

**BC Geological Survey
Assessment Report
40348**



TYPE OF REPORT [type of survey(s)]: Acquisition, processing and analyses of ground-based M: TOTAL COST: \$377,295.55

AUTHOR(S): Frederick A. Cook

SIGNATURE(S): Frederick A. Cook

Digitally signed by Frederick A. Cook
DN: cn=Frederick A. Cook, o=ou,
email=fcook@ucalgary.ca, c=CA
Date: 2022.07.15 15:26:47 -07'00'

NOTICE OF WORK PERMIT NUMBER(S)/DATE(S): _____

YEAR OF WORK: 2021-2

STATEMENT OF WORK - CASH PAYMENTS EVENT NUMBER(S)/DATE(S): Events 5934086, 5934648, 5934830

PROPERTY NAME: Moyie Anticline

CLAIM NAME(S) (on which the work was done): 604912 882449 985682 1020126 1062583 1066470 1068408 1068412 1068414

1068419 1068422 1068445 1068561 1075033 1075034 1075035 1075036 1075037 1075038 1075039 1075040 1075041

1075042 1075043 1075044 1075045 1075046 1075048 1075049 1075050 1075051 1080129 1093822 1093827 1094073 10950

COMMODITIES SOUGHT: Au, Ag, Pb, Cu, Zn

MINERAL INVENTORY MINFILE NUMBER(S), IF KNOWN: _____

MINING DIVISION: Fort Steele

NTS/BCGS: 093

LATITUDE: 53 ° 50 ' 49 " LONGITUDE: 124 ° 24 ' 01 " (at centre of work)

OWNER(S):

1) D. E. LaVoie, C. Kennedy, S. Kennedy

2) _____

MAILING ADDRESS:

2290 DeWolfe Ave.

Kimberley, BC V1A1P5

OPERATOR(S) [who paid for the work]:

1) Kootenay Resources, Inc.

2) _____

MAILING ADDRESS:

Suite 1125 - 595 Howe Street

Vancouver, British Columbia V6C 2T5

PROPERTY GEOLOGY KEYWORDS (lithology, age, stratigraphy, structure, alteration, mineralization, size and attitude):

Metasedimentary rock; massive sulphides, SedEx, Purcell anticlinorium

REFERENCES TO PREVIOUS ASSESSMENT WORK AND ASSESSMENT REPORT NUMBERS: 21786, 37386, 37418, 0001, 39050

TYPE OF WORK IN THIS REPORT	EXTENT OF WORK (IN METRIC UNITS)	ON WHICH CLAIMS	PROJECT COSTS APPORTIONED (incl. support)
GEOLOGICAL (scale, area)			
Ground, mapping	_____	_____	_____
Photo interpretation	_____	_____	_____
GEOPHYSICAL (line-kilometres)			
Ground			
Magnetic	_____	_____	_____
Electromagnetic	86 new MT stations	many - see attached list	\$325,083.09
Induced Polarization	_____	_____	_____
Radiometric	_____	_____	_____
Seismic	_____	_____	_____
Other	_____	_____	_____
Airborne		_____	_____
GEOCHEMICAL (number of samples analysed for...)			
Soil	_____	_____	_____
Silt	_____	_____	_____
Rock	_____	_____	_____
Other	_____	_____	_____
DRILLING (total metres; number of holes, size)			
Core	_____	_____	_____
Non-core	_____	_____	_____
RELATED TECHNICAL			
Sampling/assaying	_____	_____	_____
Petrographic	_____	_____	_____
Mineralographic	_____	_____	_____
Metallurgic	_____	_____	_____
PROSPECTING (scale, area)			
_____		_____	_____
PREPARATORY / PHYSICAL			
Line/grid (kilometres)	_____	_____	_____
Topographic/Photogrammetric (scale, area)	_____	_____	_____
Legal surveys (scale, area)	_____	_____	_____
Road, local access (kilometres)/trail	_____	_____	_____
Trench (metres)	_____	_____	_____
Underground dev. (metres)	_____	_____	_____
Other	Report/Admin		\$52,212.46
		TOTAL COST:	\$377,295.55



Print and Close

Cancel

Mineral Titles Online

Mineral Claim Exploration and Development Work/Expiry Date Change

Confirmation

Recorder: LAVOIE, DARLENE
ELIZABETH (132094)

Submitter: LAVOIE, DARLENE
ELIZABETH (132094)

Recorded: 2022/APR/21

Effective: 2022/APR/21

D/E Date: 2022/APR/21

Confirmation

If you have not yet submitted your report for this work program, your technical work report is due in 90 days. The Exploration and Development Work/Expiry Date Change event number is required with your report submission. **Please attach a copy of this confirmation page to your report.** Contact Mineral Titles Branch for more information.

Event Number: 5934086

Work Type: Technical Work

Technical Items: Geophysical, PAC Withdrawal (up to 30% of technical work required)

Work Start Date: 2021/NOV/01

Work Stop Date: 2021/NOV/26

Total Value of Work: \$ 30028.38

Mine Permit No: N/A

Summary of the work value:

Title Number	Claim Name	Issue Date	Good To Date	New Good To Date	# of Days Forward	Area in Ha	Applied Work Value	Sub- mission Fee
515408		2005/JUN/27	2021/DEC/18	2022/Apr/25	128	126.54	\$ 887.48	\$ 0.00
519022	KRL	2005/AUG/13	2021/DEC/18	2022/Apr/25	128	527.41	\$ 3699.07	\$ 0.00
519048	KRL 2	2005/AUG/14	2021/DEC/18	2022/Apr/25	128	400.80	\$ 2811.10	\$ 0.00
1030689	KRL 03-05-14	2014/SEP/04	2020/SEP/14	2020/SEP/14	0	189.95	\$ 0.00	\$ 0.00
1030687	KRL 04-10-14	2014/SEP/04	2020/SEP/14	2020/SEP/14	0	527.57	\$ 0.00	\$ 0.00
1030691	KRL 04-10-14	2014/SEP/04	2020/SEP/14	2020/SEP/14	0	379.94	\$ 0.00	\$ 0.00
1030770	KRL 06-10-14	2014/SEP/06	2020/SEP/14	2020/SEP/14	0	527.93	\$ 0.00	\$ 0.00
1030771	KRL 07-10-14	2014/SEP/06	2020/SEP/14	2020/SEP/14	0	528.15	\$ 0.00	\$ 0.00
1030772	KRL 08-10-14	2014/SEP/06	2021/DEC/18	2021/DEC/18	0	528.32	\$ 0.00	\$ 0.00
835425	KRL 09-10	2010/OCT/08	2021/DEC/18	2022/Apr/25	128	528.44	\$ 3706.31	\$ 0.00
835426	KRL 10-10	2010/OCT/08	2021/DEC/18	2022/Apr/25	128	528.47	\$ 3706.55	\$ 0.00
835948	KRL 12-10	2010/OCT/14	2020/SEP/14	2020/SEP/14	0	527.32	\$ 0.00	\$ 0.00
1030773	KRL 13-10-14	2014/SEP/06	2020/SEP/14	2020/SEP/14	0	506.46	\$ 0.00	\$ 0.00
1030765	KRL 14-10-14	2014/SEP/06	2020/SEP/14	2020/SEP/14	0	527.85	\$ 0.00	\$ 0.00
1030769	KRL 15-10-14	2014/SEP/06	2020/SEP/14	2020/SEP/14	0	507.01	\$ 0.00	\$ 0.00
835953	KRL 16-10	2010/OCT/14	2020/SEP/14	2020/SEP/14	0	527.19	\$ 0.00	\$ 0.00
1030775	KRL 17-10-14	2014/SEP/06	2021/DEC/18	2021/DEC/18	0	189.76	\$ 0.00	\$ 0.00
835955	KRL 18-10	2010/OCT/14	2021/DEC/18	2022/Apr/25	128	524.56	\$ 3679.08	\$ 0.00
1030774	KRL 21-10-14	2014/SEP/06	2020/SEP/14	2020/SEP/14	0	484.95	\$ 0.00	\$ 0.00
1030808	KRL 22-10-14	2014/SEP/07	2021/DEC/18	2021/DEC/18	0	526.98	\$ 0.00	\$ 0.00
836269	KRL 26-10	2010/OCT/19	2021/DEC/18	2022/Apr/25	128	528.79	\$ 3708.77	\$ 0.00
836270	KRL 27-10	2010/OCT/19	2021/DEC/18	2022/Apr/25	128	483.44	\$ 3390.71	\$ 0.00
836272	KRL 28-10	2010/OCT/19	2021/DEC/18	2022/Apr/25	128	507.56	\$ 3559.90	\$ 0.00
1030810	KRL 29-10-14	2014/SEP/07	2021/DEC/18	2021/DEC/18	0	528.96	\$ 0.00	\$ 0.00
1030811	KRL 111-11-14	2014/SEP/07	2020/SEP/14	2020/SEP/14	0	527.38	\$ 0.00	\$ 0.00
1030834	KRL 113-11-14	2014/SEP/08	2021/DEC/18	2021/DEC/18	0	253.80	\$ 0.00	\$ 0.00

986834	KRL 114-12	2012/MAY/16	2021/DEC/18	2022/Apr/25	128	337.42	\$ 2366.55	\$ 0.00
986838	KRL 115-12	2012/MAY/16	2021/DEC/18	2022/Apr/25	128	506.00	\$ 3548.92	\$ 0.00
999062	KRL 116-12	2012/JUN/19	2021/DEC/18	2022/Apr/25	128	400.36	\$ 2808.01	\$ 0.00
1019533	KRL 117-13	2013/MAY/16	2021/DEC/18	2022/Apr/25	128	252.97	\$ 1774.28	\$ 0.00
1019579	KRL 118-13	2013/MAY/17	2021/DEC/18	2022/Apr/25	128	294.98	\$ 2068.92	\$ 0.00
1019682	KRL 119-13	2013/MAY/21	2021/DEC/18	2021/DEC/18	0	21.07	\$ 0.00	\$ 0.00
1031154	KRL 120-13-14	2014/SEP/25	2021/DEC/18	2022/Apr/25	128	168.53	\$ 1182.03	\$ 0.00
1020525	KRL 121-13	2013/JUN/26	2021/DEC/18	2021/DEC/18	0	147.48	\$ 0.00	\$ 0.00
1022509	KRL 122-13	2013/SEP/22	2021/DEC/18	2021/DEC/18	0	484.79	\$ 0.00	\$ 0.00
1037431	KRL 30-15	2015/JUL/20	2021/DEC/18	2021/DEC/18	0	529.07	\$ 0.00	\$ 0.00
1037432	KRL 31-15	2015/JUL/20	2020/SEP/15	2020/SEP/15	0	841.85	\$ 0.00	\$ 0.00
1037433	KRL 32-15	2015/JUL/20	2020/SEP/15	2020/SEP/15	0	804.68	\$ 0.00	\$ 0.00
1037434	KRL 33-15	2015/JUL/20	2020/SEP/15	2020/SEP/15	0	762.69	\$ 0.00	\$ 0.00
1045018	KRL 40-16	2016/JUN/29	2020/SEP/15	2020/SEP/15	0	422.20	\$ 0.00	\$ 0.00
1045019	KRL 40-16	2016/JUN/29	2020/SEP/15	2020/SEP/15	0	547.63	\$ 0.00	\$ 0.00
1049636	KRL 42-17	2017/JAN/30	2020/SEP/15	2020/SEP/15	0	738.70	\$ 0.00	\$ 0.00
1049637	KRL 43-17	2017/JAN/30	2020/SEP/15	2020/SEP/15	0	1034.75	\$ 0.00	\$ 0.00
1049638	KRL 44-17	2017/JAN/30	2020/SEP/15	2020/SEP/15	0	1077.41	\$ 0.00	\$ 0.00

Financial Summary:

Total applied work value: \$ 42897.68

PAC name: Kootenay Gold Corp.
Debited PAC amount: \$ 12869.3
Credited PAC amount: \$ 0

Total Submission Fees: \$ 0.0

Total Paid: **\$ 0.0**

Please print this page for your records.

The event was successfully saved.

Click [here](#) to return to the Main Menu.



Print and Close

Cancel

Mineral Titles Online

Mineral Claim Exploration and Development Work/Expiry Date Change

Confirmation

Recorder: LAVOIE, DARLENE
ELIZABETH (132094)

Submitter: LAVOIE, DARLENE
ELIZABETH (132094)

Recorded: 2022/APR/24

Effective: 2022/APR/24

D/E Date: 2022/APR/24

Confirmation

If you have not yet submitted your report for this work program, your technical work report is due in 90 days. The Exploration and Development Work/Expiry Date Change event number is required with your report submission. **Please attach a copy of this confirmation page to your report.** Contact Mineral Titles Branch for more information.

Event Number: 5934648

Work Type: Technical Work

Technical Items: Geophysical, PAC Withdrawal (up to 30% of technical work required)

Work Start Date: 2021/NOV/01

Work Stop Date: 2021/NOV/26

Total Value of Work: \$ 198472.50

Mine Permit No: N/A

Summary of the work value:

Title Number	Claim Name	Issue Date	Good To Date	New Good To Date	# of Days Forward	Area in Ha	Applied Work Value	Sub- mission Fee
515408		2005/JUN/27	2022/APR/25	2022/Aug/27	124	126.54	\$ 859.74	\$ 0.00
1095262	KRL 01-22 B	2005/AUG/13	2022/APR/25	2022/APR/25	0	801.66	\$ 0.00	\$ 0.00
1095263	KRL 01-22	2005/AUG/13	2022/APR/25	2022/Aug/27	124	358.63	\$ 2436.73	\$ 0.00
1095264	KRL 2-22 B	2005/AUG/14	2022/APR/25	2022/APR/25	0	864.89	\$ 0.00	\$ 0.00
1095265	KRL 2-22	2005/AUG/14	2022/APR/25	2022/Aug/27	124	253.12	\$ 1719.82	\$ 0.00
1030689	KRL 03-05-14	2014/SEP/04	2020/SEP/14	2020/SEP/14	0	189.95	\$ 0.00	\$ 0.00
1030687	KRL 04-10-14	2014/SEP/04	2020/SEP/14	2020/SEP/14	0	527.57	\$ 0.00	\$ 0.00
1030691	KRL 04-10-14	2014/SEP/04	2020/SEP/14	2020/SEP/14	0	379.94	\$ 0.00	\$ 0.00
1030770	KRL 06-10-14	2014/SEP/06	2020/SEP/14	2020/SEP/14	0	527.93	\$ 0.00	\$ 0.00
1030771	KRL 07-10-14	2014/SEP/06	2020/SEP/14	2020/SEP/14	0	528.15	\$ 0.00	\$ 0.00
1030772	KRL 08-10-14	2014/SEP/06	2021/DEC/18	2021/DEC/18	0	528.32	\$ 0.00	\$ 0.00
1095282	KRL 09-10-22 B	2010/OCT/08	2022/APR/25	2022/APR/25	0	756.94	\$ 0.00	\$ 0.00
1095283	KRL 09-10-22	2010/OCT/08	2022/APR/25	2022/Aug/27	124	401.65	\$ 2729.00	\$ 0.00
1095284	KRL 10-10-22 B	2010/OCT/08	2022/APR/25	2022/APR/25	0	930.08	\$ 0.00	\$ 0.00
1095285	KRL 10-10-22	2010/OCT/08	2022/APR/25	2022/Aug/27	124	232.53	\$ 1579.93	\$ 0.00
835948	KRL 12-10	2010/OCT/14	2020/SEP/14	2020/SEP/14	0	527.32	\$ 0.00	\$ 0.00
1030773	KRL 13-10-14	2014/SEP/06	2020/SEP/14	2020/SEP/14	0	506.46	\$ 0.00	\$ 0.00
1030765	KRL 14-10-14	2014/SEP/06	2020/SEP/14	2020/SEP/14	0	527.85	\$ 0.00	\$ 0.00
1030769	KRL 15-10-14	2014/SEP/06	2020/SEP/14	2020/SEP/14	0	507.01	\$ 0.00	\$ 0.00
835953	KRL 16-10	2010/OCT/14	2020/SEP/14	2020/SEP/14	0	527.19	\$ 0.00	\$ 0.00
1030775	KRL 17-10-14	2014/SEP/06	2021/DEC/18	2021/DEC/18	0	189.76	\$ 0.00	\$ 0.00
835955	KRL 18-10	2010/OCT/14	2022/APR/25	2022/Aug/27	124	524.56	\$ 3564.11	\$ 0.00
1030774	KRL 21-10-14	2014/SEP/06	2020/SEP/14	2020/SEP/14	0	484.95	\$ 0.00	\$ 0.00
1030808	KRL 22-10-14	2014/SEP/07	2021/DEC/18	2021/DEC/18	0	526.98	\$ 0.00	\$ 0.00
1095288	KRL 26-10-22 B	2010/OCT/19	2022/APR/25	2022/APR/25	0	761.46	\$ 0.00	\$ 0.00
1095289	KRL 26-10-22	2010/OCT/19	2022/APR/25	2022/Aug/27	124	359.56	\$ 2443.02	\$ 0.00

1095290	KRL 27-10-22 B	2010/OCT/19	2022/APR/25	2022/APR/25	0	758.65	\$ 0.00	\$ 0.00
1095291	KRL 27-10-22	2010/OCT/19	2022/APR/25	2022/AUG/27	124	359.25	\$ 2440.95	\$ 0.00
1095292	KRL 28-10-22 B	2010/OCT/19	2022/APR/25	2022/APR/25	0	676.72	\$ 0.00	\$ 0.00
1095293	KRL 28-10-22	2010/OCT/19	2022/APR/25	2022/AUG/27	124	338.40	\$ 2299.29	\$ 0.00
1030810	KRL 29-10-14	2014/SEP/07	2021/DEC/18	2021/DEC/18	0	528.96	\$ 0.00	\$ 0.00
1030811	KRL 111-11-14	2014/SEP/07	2020/SEP/14	2020/SEP/14	0	527.38	\$ 0.00	\$ 0.00
1030834	KRL 113-11-14	2014/SEP/08	2021/DEC/18	2021/DEC/18	0	253.80	\$ 0.00	\$ 0.00
1095295	KRL 114-12-22 B	2012/MAY/16	2022/APR/25	2022/APR/25	0	738.09	\$ 0.00	\$ 0.00
1095296	KRL 114-12-22	2012/MAY/16	2022/APR/25	2022/AUG/27	124	105.45	\$ 716.45	\$ 0.00
1095297	KRL 15-12-22 B	2012/MAY/16	2022/APR/25	2022/APR/25	0	885.52	\$ 0.00	\$ 0.00
1095298	KRL 15-12-22	2012/MAY/16	2022/APR/25	2022/AUG/27	124	252.96	\$ 1718.73	\$ 0.00
1095299	KRL 116-12-22 B	2012/JUN/19	2022/APR/25	2022/APR/25	0	674.28	\$ 0.00	\$ 0.00
1095300	KRL 116-12-22	2012/JUN/19	2022/APR/25	2022/AUG/27	124	189.66	\$ 1288.62	\$ 0.00
1019533	KRL 117-13	2013/MAY/16	2022/APR/25	2022/AUG/27	124	252.97	\$ 1718.83	\$ 0.00
1095301	KRL 118-13-22 B	2013/MAY/17	2022/APR/25	2022/APR/25	0	505.69	\$ 0.00	\$ 0.00
1095302	KRL 118-13-22	2013/MAY/17	2022/APR/25	2022/AUG/27	124	252.84	\$ 1717.96	\$ 0.00
1019682	KRL 119-13	2013/MAY/21	2021/DEC/18	2021/DEC/18	0	21.07	\$ 0.00	\$ 0.00
1095303	KRL 120-13-14-22 B	2014/SEP/25	2022/APR/25	2022/APR/25	0	526.66	\$ 0.00	\$ 0.00
1095304	KRL 120-13-14-22	2014/SEP/25	2022/APR/25	2022/AUG/27	124	105.33	\$ 715.66	\$ 0.00
1020525	KRL 121-13	2013/JUN/26	2021/DEC/18	2021/DEC/18	0	147.48	\$ 0.00	\$ 0.00
1022509	KRL 122-13	2013/SEP/22	2021/DEC/18	2021/DEC/18	0	484.79	\$ 0.00	\$ 0.00
1037431	KRL 30-15	2015/JUL/20	2021/DEC/18	2021/DEC/18	0	529.07	\$ 0.00	\$ 0.00
1037432	KRL 31-15	2015/JUL/20	2020/SEP/15	2020/SEP/15	0	841.85	\$ 0.00	\$ 0.00
1037433	KRL 32-15	2015/JUL/20	2020/SEP/15	2020/SEP/15	0	804.68	\$ 0.00	\$ 0.00
1037434	KRL 33-15	2015/JUL/20	2020/SEP/15	2020/SEP/15	0	762.69	\$ 0.00	\$ 0.00
1045018	KRL 40-16	2016/JUN/29	2020/SEP/15	2020/SEP/15	0	422.20	\$ 0.00	\$ 0.00
1045019	KRL 40-16	2016/JUN/29	2020/SEP/15	2020/SEP/15	0	547.63	\$ 0.00	\$ 0.00
1049636	KRL 42-17	2017/JAN/30	2020/SEP/15	2020/SEP/15	0	738.70	\$ 0.00	\$ 0.00
1049637	KRL 43-17	2017/JAN/30	2020/SEP/15	2020/SEP/15	0	1034.75	\$ 0.00	\$ 0.00
1049638	KRL 44-17	2017/JAN/30	2020/SEP/15	2020/SEP/15	0	1077.41	\$ 0.00	\$ 0.00
984342	SPIKE'S BIG ADVENTURE	2012/MAY/07	2021/JUN/05	2022/JUL/05	395	211.02	\$ 4567.25	\$ 0.00
985682	SPIKE'S BA-02-12	2012/MAY/10	2021/JUN/05	2022/JUL/05	395	443.22	\$ 9592.99	\$ 0.00
985683	SPIKE'S BA-03-12	2012/MAY/10	2021/JUN/05	2022/JUL/05	395	337.67	\$ 7308.52	\$ 0.00
1020126	SPIKE'S BA-04-13	2013/JUN/07	2021/JUN/05	2022/JUL/05	395	253.36	\$ 5483.57	\$ 0.00
1062764	SBA 2018	2018/SEP/03	2021/JUN/05	2022/JUL/05	395	527.33	\$ 5056.61	\$ 0.00
1066457	SPIKE'S BA 06-19	2019/FEB/12	2021/JUN/05	2022/JUL/05	395	632.90	\$ 4664.37	\$ 0.00
1066458	SPIKE'S BA 07-19	2019/FEB/12	2021/JUN/05	2022/JUL/05	395	569.84	\$ 4199.66	\$ 0.00
1068199	SPIKE'S BA 06-19	2019/APR/28	2021/JUN/05	2022/JUL/05	395	358.46	\$ 2273.55	\$ 0.00
1068200	SPIKE'S BA 07-19	2019/APR/28	2021/JUN/05	2022/JUL/05	395	105.46	\$ 668.87	\$ 0.00
1068408	SPIKE'S BA 10-19	2019/MAY/08	2021/JUN/05	2022/JUL/05	395	1245.33	\$ 7727.84	\$ 0.00
1068412	SPIKE'S BA 11-19	2019/MAY/08	2021/JUN/05	2022/JUL/05	395	1901.47	\$ 11799.51	\$ 0.00
1068414	SPIKE'S BA 12-19	2019/MAY/08	2021/JUN/05	2022/JUL/05	395	865.77	\$ 5372.51	\$ 0.00
1068419	SPIKE'S BA 13-19	2019/MAY/08	2021/JUN/05	2022/JUL/05	395	1034.29	\$ 6418.29	\$ 0.00
1068422	SPIKE'S BA 14-19	2019/MAY/08	2021/JUN/05	2022/JUL/05	395	549.07	\$ 3407.24	\$ 0.00
1068560	SPIKE'S BA 15-19	2019/MAY/15	2021/JUN/05	2022/JUL/05	395	84.49	\$ 516.21	\$ 0.00
1068669	SPIKE'S BA 16-19	2019/MAY/23	2021/JUN/05	2022/JUL/05	395	506.95	\$ 3041.69	\$ 0.00
1075033	MOYIE ANTICLINE 01-20	2020/MAR/05	2021/JUN/05	2022/JUL/05	395	1923.55	\$ 10408.23	\$ 0.00
1075034	MA 02-20	2020/MAR/05	2021/JUN/05	2022/JUL/05	395	1795.55	\$ 9715.63	\$ 0.00
1075035	MA 03-20	2020/MAR/05	2021/JUN/05	2022/JUL/05	395	1648.43	\$ 8919.58	\$ 0.00

1075036	MA 04-20	2020/MAR/05	2021/JUN/05	2022/JUL/05	395	2029.86	\$ 10983.48	\$ 0.00
1075037	MA 05-20	2020/MAR/05	2021/JUN/05	2022/JUL/05	395	1523.23	\$ 8242.11	\$ 0.00
1075038	MA 06-20	2020/MAR/05	2021/JUN/05	2022/JUL/05	395	1800.07	\$ 9740.11	\$ 0.00
1075039	MA 07-20	2020/MAR/05	2021/JUN/05	2022/JUL/05	395	1524.26	\$ 8247.72	\$ 0.00
1075040	MA 08-20	2020/MAR/05	2021/JUN/05	2022/JUL/05	395	1143.19	\$ 6185.77	\$ 0.00
1075041	MA 09-20	2020/MAR/05	2021/JUN/05	2022/JUL/05	395	2073.07	\$ 11217.30	\$ 0.00
1075042	MA 10-20	2020/MAR/05	2021/JUN/05	2022/JUL/05	395	1376.74	\$ 7449.49	\$ 0.00
1075043	MA 11-20	2020/MAR/05	2021/JUN/05	2022/JUL/05	395	1080.04	\$ 5844.03	\$ 0.00
1075044	MA 12-20	2020/MAR/05	2021/JUN/05	2022/JUL/05	395	2117.45	\$ 11457.45	\$ 0.00
1075045	MA 13-20	2020/MAR/05	2021/JUN/05	2022/JUL/05	395	1353.49	\$ 7323.66	\$ 0.00
1075046	MA 14-20	2020/MAR/05	2021/JUN/05	2022/JUL/05	395	1693.96	\$ 9165.95	\$ 0.00
1075048	MA 15-20	2020/MAR/05	2021/JUN/05	2022/JUL/05	395	1947.45	\$ 10537.55	\$ 0.00
1075049	MA 16-20	2020/MAR/05	2021/JUN/05	2022/JUL/05	395	1355.84	\$ 7336.40	\$ 0.00
1075050	MA 17-20	2020/MAR/05	2021/JUN/05	2022/JUL/05	395	1395.86	\$ 7552.92	\$ 0.00
1075051	MA 18-20	2020/MAR/05	2021/JUN/05	2022/JUL/05	395	317.08	\$ 1715.68	\$ 0.00
1080129	MA 19-20	2020/DEC/19	2021/DEC/19	2022/JUL/05	198	402.32	\$ 1091.23	\$ 0.00
604912	SWEET SPOT	2009/MAY/24	2030/OCT/17	2030/OCT/17	0	423.76	\$ 0.00	\$ 0.00
882449	SWEET SPOT 04-11	2011/AUG/05	2030/OCT/17	2030/OCT/17	0	444.91	\$ 0.00	\$ 0.00
882469	SWEET SPOT 05-11	2011/AUG/05	2030/OCT/17	2030/OCT/17	0	296.67	\$ 0.00	\$ 0.00
1037318	LADY SLIPPER 01-15	2015/JUL/14	2021/JUN/05	2022/JUL/05	395	84.44	\$ 1370.75	\$ 0.00
1066459	LADY SLIPPER 02-19	2019/FEB/12	2021/JUN/05	2022/JUL/05	395	886.66	\$ 6534.57	\$ 0.00
1062583	KENCO 1-18	2018/AUG/24	2024/OCT/26	2024/OCT/26	0	169.13	\$ 0.00	\$ 0.00
1066463	KENCO 02-19	2019/FEB/12	2024/OCT/26	2024/OCT/26	0	253.67	\$ 0.00	\$ 0.00
1066460	DOWN DIP 01-19	2019/FEB/12	2021/JUN/05	2022/JUL/05	395	507.76	\$ 3742.13	\$ 0.00
1068446	DOWN DIP 02-19	2019/MAY/09	2021/JUN/05	2022/JUL/05	395	1078.94	\$ 6680.54	\$ 0.00
1066470	LEAKY PIPE 01-19	2019/FEB/12	2022/MAY/18	2022/JUL/05	48	190.21	\$ 250.14	\$ 0.00
1068445	LP 02-19	2019/MAY/09	2022/MAY/18	2022/JUL/05	48	718.56	\$ 944.96	\$ 0.00
1068561	HAZEL'S YAHK 01-19	2019/MAY/15	2022/JUN/07	2022/JUL/05	28	1078.36	\$ 827.24	\$ 0.00

Financial Summary:

Total applied work value: \$ 283532.14

PAC name: Kootenay Gold Corp.
Debited PAC amount: \$ 85059.64
Credited PAC amount: \$ 0

Total Submission Fees: \$ 0.0

Total Paid: **\$ 0.0**

Related Summary:

Existing work program 5934086
Event numbers:

Please print this page for your records.

The event was successfully saved.

Click [here](#) to return to the Main Menu.



Print and Close

Cancel

Mineral Titles Online

Mineral Claim Exploration and Development Work/Expiry Date Change

Confirmation

Recorder: LAVOIE, DARLENE
ELIZABETH (132094)

Submitter: LAVOIE, DARLENE
ELIZABETH (132094)

Recorded: 2022/APR/26

Effective: 2022/APR/26

D/E Date: 2022/APR/26

Confirmation

If you have not yet submitted your report for this work program, your technical work report is due in 90 days. The Exploration and Development Work/Expiry Date Change event number is required with your report submission. **Please attach a copy of this confirmation page to your report.** Contact Mineral Titles Branch for more information.

Event Number: 5934830

Work Type: Technical Work

Technical Items: Geophysical, PAC Withdrawal (up to 30% of technical work required)

Work Start Date: 2021/NOV/01

Work Stop Date: 2021/NOV/26

Total Value of Work: \$ 148794.67

Mine Permit No: N/A

Summary of the work value:

Title Number	Claim Name	Issue Date	Good To Date	New Good To Date	# of Days Forward	Area in Ha	Applied Work Value	Sub- mission Fee
515408		2005/JUN/27	2022/AUG/27	2022/AUG/27	0	126.54	\$ 0.00	\$ 0.00
1095263	KRL 01-22	2005/AUG/13	2022/AUG/27	2022/AUG/27	0	358.63	\$ 0.00	\$ 0.00
1095265	KRL 2-22	2005/AUG/14	2022/AUG/27	2022/AUG/27	0	253.12	\$ 0.00	\$ 0.00
1030689	KRL 03-05-14	2014/SEP/04	2020/SEP/14	2020/SEP/14	0	189.95	\$ 0.00	\$ 0.00
1030687	KRL 04-10-14	2014/SEP/04	2020/SEP/14	2020/SEP/14	0	527.57	\$ 0.00	\$ 0.00
1030691	KRL 04-10-14	2014/SEP/04	2020/SEP/14	2020/SEP/14	0	379.94	\$ 0.00	\$ 0.00
1030770	KRL 06-10-14	2014/SEP/06	2020/SEP/14	2020/SEP/14	0	527.93	\$ 0.00	\$ 0.00
1030771	KRL 07-10-14	2014/SEP/06	2020/SEP/14	2020/SEP/14	0	528.15	\$ 0.00	\$ 0.00
1030772	KRL 08-10-14	2014/SEP/06	2021/DEC/18	2021/DEC/18	0	528.32	\$ 0.00	\$ 0.00
1095283	KRL 09-10-22	2010/OCT/08	2022/AUG/27	2022/AUG/27	0	401.65	\$ 0.00	\$ 0.00
1095285	KRL 10-10-22	2010/OCT/08	2022/AUG/27	2022/AUG/27	0	232.53	\$ 0.00	\$ 0.00
835948	KRL 12-10	2010/OCT/14	2020/SEP/14	2020/SEP/14	0	527.32	\$ 0.00	\$ 0.00
1030773	KRL 13-10-14	2014/SEP/06	2020/SEP/14	2020/SEP/14	0	506.46	\$ 0.00	\$ 0.00
1030765	KRL 14-10-14	2014/SEP/06	2020/SEP/14	2020/SEP/14	0	527.85	\$ 0.00	\$ 0.00
1030769	KRL 15-10-14	2014/SEP/06	2020/SEP/14	2020/SEP/14	0	507.01	\$ 0.00	\$ 0.00
835953	KRL 16-10	2010/OCT/14	2020/SEP/14	2020/SEP/14	0	527.19	\$ 0.00	\$ 0.00
1030775	KRL 17-10-14	2014/SEP/06	2021/DEC/18	2021/DEC/18	0	189.76	\$ 0.00	\$ 0.00
835955	KRL 18-10	2010/OCT/14	2022/AUG/27	2022/AUG/27	0	524.56	\$ 0.00	\$ 0.00
1030774	KRL 21-10-14	2014/SEP/06	2020/SEP/14	2020/SEP/14	0	484.95	\$ 0.00	\$ 0.00
1030808	KRL 22-10-14	2014/SEP/07	2021/DEC/18	2021/DEC/18	0	526.98	\$ 0.00	\$ 0.00
1095289	KRL 26-10-22	2010/OCT/19	2022/AUG/27	2022/AUG/27	0	359.56	\$ 0.00	\$ 0.00
1095291	KRL 27-10-22	2010/OCT/19	2022/AUG/27	2022/AUG/27	0	359.25	\$ 0.00	\$ 0.00
1095293	KRL 28-10-22	2010/OCT/19	2022/AUG/27	2022/AUG/27	0	338.40	\$ 0.00	\$ 0.00
1030810	KRL 29-10-14	2014/SEP/07	2021/DEC/18	2021/DEC/18	0	528.96	\$ 0.00	\$ 0.00
1030811	KRL 111-11-14	2014/SEP/07	2020/SEP/14	2020/SEP/14	0	527.38	\$ 0.00	\$ 0.00
1030834	KRL 113-11-14	2014/SEP/08	2021/DEC/18	2021/DEC/18	0	253.80	\$ 0.00	\$ 0.00

1095296	KRL 114-12-22	2012/MAY/16	2022/AUG/27	2022/AUG/27	0	105.45	\$ 0.00	\$ 0.00
1095298	KRL 15-12-22	2012/MAY/16	2022/AUG/27	2022/AUG/27	0	252.96	\$ 0.00	\$ 0.00
1095300	KRL 116-12-22	2012/JUN/19	2022/AUG/27	2022/AUG/27	0	189.66	\$ 0.00	\$ 0.00
1019533	KRL 117-13	2013/MAY/16	2022/AUG/27	2022/AUG/27	0	252.97	\$ 0.00	\$ 0.00
1095302	KRL 118-13-22	2013/MAY/17	2022/AUG/27	2022/AUG/27	0	252.84	\$ 0.00	\$ 0.00
1019682	KRL 119-13	2013/MAY/21	2021/DEC/18	2021/DEC/18	0	21.07	\$ 0.00	\$ 0.00
1095304	KRL 120-13-14-22	2014/SEP/25	2022/AUG/27	2022/AUG/27	0	105.33	\$ 0.00	\$ 0.00
1020525	KRL 121-13	2013/JUN/26	2021/DEC/18	2021/DEC/18	0	147.48	\$ 0.00	\$ 0.00
1022509	KRL 122-13	2013/SEP/22	2021/DEC/18	2021/DEC/18	0	484.79	\$ 0.00	\$ 0.00
1037431	KRL 30-15	2015/JUL/20	2021/DEC/18	2021/DEC/18	0	529.07	\$ 0.00	\$ 0.00
1037432	KRL 31-15	2015/JUL/20	2020/SEP/15	2020/SEP/15	0	841.85	\$ 0.00	\$ 0.00
1037433	KRL 32-15	2015/JUL/20	2020/SEP/15	2020/SEP/15	0	804.68	\$ 0.00	\$ 0.00
1037434	KRL 33-15	2015/JUL/20	2020/SEP/15	2020/SEP/15	0	762.69	\$ 0.00	\$ 0.00
1045018	KRL 40-16	2016/JUN/29	2020/SEP/15	2020/SEP/15	0	422.20	\$ 0.00	\$ 0.00
1045019	KRL 40-16	2016/JUN/29	2020/SEP/15	2020/SEP/15	0	547.63	\$ 0.00	\$ 0.00
1049636	KRL 42-17	2017/JAN/30	2020/SEP/15	2020/SEP/15	0	738.70	\$ 0.00	\$ 0.00
1049637	KRL 43-17	2017/JAN/30	2020/SEP/15	2020/SEP/15	0	1034.75	\$ 0.00	\$ 0.00
1049638	KRL 44-17	2017/JAN/30	2020/SEP/15	2020/SEP/15	0	1077.41	\$ 0.00	\$ 0.00
984342	SPIKE'S BIG ADVENTURE	2012/MAY/07	2022/JUL/05	2023/Apr/30	299	211.02	\$ 3457.23	\$ 0.00
985682	SPIKE'S BA-02-12	2012/MAY/10	2022/JUL/05	2023/Apr/30	299	443.22	\$ 7261.53	\$ 0.00
985683	SPIKE'S BA-03-12	2012/MAY/10	2022/JUL/05	2023/Apr/30	299	337.67	\$ 5532.27	\$ 0.00
1020126	SPIKE'S BA-04-13	2013/JUN/07	2022/JUL/05	2023/Apr/30	299	253.36	\$ 4150.86	\$ 0.00
1062764	SBA 2018	2018/SEP/03	2022/JUL/05	2023/Apr/30	299	527.33	\$ 4319.79	\$ 0.00
1066457	SPIKE'S BA 06-19	2019/FEB/12	2022/JUL/05	2023/Apr/29	298	632.90	\$ 5167.22	\$ 0.00
1066458	SPIKE'S BA 07-19	2019/FEB/12	2022/JUL/05	2023/Apr/29	298	569.84	\$ 4652.41	\$ 0.00
1068199	SPIKE'S BA 06-19	2019/APR/28	2022/JUL/05	2023/Apr/29	298	358.46	\$ 2926.62	\$ 0.00
1068200	SPIKE'S BA 07-19	2019/APR/28	2022/JUL/05	2023/Apr/29	298	105.46	\$ 860.99	\$ 0.00
1068408	SPIKE'S BA 10-19	2019/MAY/08	2022/JUL/05	2023/Apr/29	298	1245.33	\$ 10167.31	\$ 0.00
1068412	SPIKE'S BA 11-19	2019/MAY/08	2022/JUL/05	2023/Apr/29	298	1901.47	\$ 15524.31	\$ 0.00
1068414	SPIKE'S BA 12-19	2019/MAY/08	2022/JUL/05	2023/Apr/29	298	865.77	\$ 7068.47	\$ 0.00
1068419	SPIKE'S BA 13-19	2019/MAY/08	2022/JUL/05	2023/Apr/29	298	1034.29	\$ 8444.37	\$ 0.00
1068422	SPIKE'S BA 14-19	2019/MAY/08	2022/JUL/05	2023/Apr/29	298	549.07	\$ 4482.82	\$ 0.00
1068560	SPIKE'S BA 15-19	2019/MAY/15	2022/JUL/05	2023/Apr/29	298	84.49	\$ 689.82	\$ 0.00
1068669	SPIKE'S BA 16-19	2019/MAY/23	2022/JUL/05	2023/Apr/29	298	506.95	\$ 4138.92	\$ 0.00
1075033	MOYIE ANTICLINE 01-20	2020/MAR/05	2022/JUL/05	2023/Apr/29	298	1923.55	\$ 9293.61	\$ 0.00
1075034	MA 02-20	2020/MAR/05	2022/JUL/05	2023/Apr/29	298	1795.55	\$ 8675.18	\$ 0.00
1075035	MA 03-20	2020/MAR/05	2022/JUL/05	2023/Apr/29	298	1648.43	\$ 7964.38	\$ 0.00
1075036	MA 04-20	2020/MAR/05	2022/JUL/05	2023/Apr/29	298	2029.86	\$ 9807.26	\$ 0.00
1075037	MA 05-20	2020/MAR/05	2022/JUL/05	2023/Apr/29	298	1523.23	\$ 7359.47	\$ 0.00
1075038	MA 06-20	2020/MAR/05	2022/JUL/05	2023/Apr/29	298	1800.07	\$ 8697.04	\$ 0.00
1075039	MA 07-20	2020/MAR/05	2022/JUL/05	2023/Apr/29	298	1524.26	\$ 7364.47	\$ 0.00
1075040	MA 08-20	2020/MAR/05	2022/JUL/05	2023/Apr/29	298	1143.19	\$ 5523.34	\$ 0.00
1075041	MA 09-20	2020/MAR/05	2022/JUL/05	2023/Apr/29	298	2073.07	\$ 10016.04	\$ 0.00
1075042	MA 10-20	2020/MAR/05	2022/JUL/05	2022/JUL/05	0	1376.74	\$ 0.00	\$ 0.00
1075043	MA 11-20	2020/MAR/05	2022/JUL/05	2023/Apr/29	298	1080.04	\$ 5218.20	\$ 0.00
1075044	MA 12-20	2020/MAR/05	2022/JUL/05	2022/JUL/05	0	2117.45	\$ 0.00	\$ 0.00
1075045	MA 13-20	2020/MAR/05	2022/JUL/05	2023/Apr/29	298	1353.49	\$ 6539.37	\$ 0.00
1075046	MA 14-20	2020/MAR/05	2022/JUL/05	2022/JUL/05	0	1693.96	\$ 0.00	\$ 0.00
1075048	MA 15-20	2020/MAR/05	2022/JUL/05	2022/JUL/05	0	1947.45	\$ 0.00	\$ 0.00

1075049	MA 16-20	2020/MAR/05	2022/JUL/05	2022/JUL/05	0	1355.84	\$ 0.00	\$ 0.00
1075050	MA 17-20	2020/MAR/05	2022/JUL/05	2023/Apr/29	298	1395.86	\$ 6744.07	\$ 0.00
1075051	MA 18-20	2020/MAR/05	2022/JUL/05	2023/Apr/29	298	317.08	\$ 1531.95	\$ 0.00
1080129	MA 19-20	2020/DEC/19	2022/JUL/05	2022/JUL/05	0	402.32	\$ 0.00	\$ 0.00
604912	SWEET SPOT	2009/MAY/24	2030/OCT/17	2030/OCT/17	0	423.76	\$ 0.00	\$ 0.00
882449	SWEET SPOT 04-11	2011/AUG/05	2030/OCT/17	2030/OCT/17	0	444.91	\$ 0.00	\$ 0.00
882469	SWEET SPOT 05-11	2011/AUG/05	2030/OCT/17	2030/OCT/17	0	296.67	\$ 0.00	\$ 0.00
1037318	LADY SLIPPER 01-15	2015/JUL/14	2022/JUL/05	2023/Apr/29	298	84.44	\$ 1368.44	\$ 0.00
1066459	LADY SLIPPER 02-19	2019/FEB/12	2022/JUL/05	2023/Apr/29	298	886.66	\$ 7239.04	\$ 0.00
1062583	KENCO 1-18	2018/AUG/24	2024/OCT/26	2024/OCT/26	0	169.13	\$ 0.00	\$ 0.00
1066463	KENCO 02-19	2019/FEB/12	2024/OCT/26	2024/OCT/26	0	253.67	\$ 0.00	\$ 0.00
1066460	DOWN DIP 01-19	2019/FEB/12	2022/JUL/05	2023/Apr/29	298	507.76	\$ 4145.56	\$ 0.00
1068446	DOWN DIP 02-19	2019/MAY/09	2022/JUL/05	2023/Apr/29	298	1078.94	\$ 8808.86	\$ 0.00
1066470	LEAKY PIPE 01-19	2019/FEB/12	2022/JUL/05	2023/Apr/29	298	190.21	\$ 1552.98	\$ 0.00
1068445	LP 02-19	2019/MAY/09	2022/JUL/05	2023/Apr/29	298	718.56	\$ 5866.60	\$ 0.00
1068561	HAZEL'S YAHK 01-19	2019/MAY/15	2022/JUL/05	2022/JUL/05	0	1078.36	\$ 0.00	\$ 0.00

Financial Summary:

Total applied work value: \$ 212560.80

PAC name: Kootenay Gold Corp.
Debited PAC amount: \$ 63766.13
Credited PAC amount: \$ 0

Total Submission Fees: \$ 0.0

Total Paid: **\$ 0.0**

Related Summary:

Existing work program 5934086, 5934648
Event numbers:

Please print this page for your records.

The event was successfully saved.

Click [here](#) to return to the Main Menu.

Assessment Report:

**Acquisition, Processing and Analyses of Ground-Based
Magnetotelluric Data on the Moyie Anticline Property,
Southeastern British Columbia**

MTO 5934086, 5934648, 5934830

North 49° 09' 07"; West 115° 50' 03.6"

UTM Zone 11N, 585000E, 5445000N

NTS map sheet 082 F, G, J, K

Fort Steele Mining Division

by

**F. A. Cook, Ph.D., P.Geo.
Salt Spring Imaging, Ltd.
128 Trincomali Heights
Salt Spring Island, B.C.**

for

***Property Operator:* Kootenay Resources, Inc.
Suite 1125-595 Howe St.
Vancouver, B.C. V6C 2T5**

***Property Owners:* D. E. Lavoie, C. Kennedy, S. Kennedy
2290 DeWolfe Ave.
Kimberley, B.C. V1A1P5**

July, 2022

Table of Contents

1.0	Summary.....	3
2.0	Introduction and Terms of Reference.....	3
	2.1 Introduction and Objectives.....	4
	2.2 Terms of Reference.....	4
3.0	Mineral Tenure Description and Location.....	5
4.0	Accessibility and Physiography.....	7
5.0	Exploration History.....	7
6.0	Geological Setting.....	7
7.0	Work Accomplished in 2021.....	10
8.0	Observations/Results.....	13
	8.1 Sweet Spot (Line SS)	13
	8.2 Line MM0.....	14
	8.3 Line MM1.....	16
	8.4 Line MM2	19
	8.5 Lines SP... ..	20
	8.6 Lines MO	23
	8.7 Conduits.....	25
9.0	Summary and Conclusions	27
10.0	References.....	28
11.0	Statement of Costs	29
12.0	Statement of Qualifications	30

Table 1

Table 1.	Tenures in the Moyie Anticline property.....	5
----------	--	---

Figures

Figure 1	Topographic image, Moyie anticline area	4
Figure 2	Map of the Moyie claims	8
Figure 3	Regional cross section.....	9
Figure 4	Map of Geology with the MT station locations	11
Figure 5	Map of geology with stations and line locations.....	12
Figure 6	2D inversions of Line SS	13
Figure 7	2D inversions of Line MM0.....	15
Figure 8	2D Inversions of Line MM1	17
Figure 9	Seismic section with Line MM1 superimposed.....	18
Figure 10	2D Inversions of Line MM2	19
Figure 11	2D Inversions of Lines SPew	21
Figure 12	2D Inversions of Lines SPns.....	22
Figure 13	2D Inversions of Line MO	24
Figure 14	Comparisons with MT data in Australia - Conduits	26

Appendices

Appendix 1	Acquisition Report - CMTS
Appendix 2	Inversion Report – CMTS
Appendix 3	Analysis Report – CMTS
Appendix 4	Recorded MT data

1.0 Summary

The purpose of this report is to describe the acquisition, processing and interpretation of a group of 86 broad-band magnetotelluric stations on the Moyie anticline in southeastern British Columbia. The data were acquired as part of a large-scale program to address the potential of the anticline where numerous showings and anomalous chemical signatures indicate that the area has significant potential, but little success, other than the St. Eugene vein system.

2.0 Introduction and Terms of Reference

2.1 Introduction and Objectives

Kootenay Resources Inc. retained Salt Spring Imaging, Ltd. to process and to design and oversee the acquisition and analyses of magnetotelluric data in southeastern British Columbia (Figure 1). The objective of the work is to evaluate the information in conjunction with the observed geological and geochemical variations of the surface rocks and soils in order to target areas for additional, more detailed geophysical and geological data. This report provides a brief description of the geological setting, of the field procedures, and of data processing and interpretation.

The author is familiar with the geology and geophysics of the region, having been responsible for acquiring geophysical data in British Columbia since 1983 and as the transect leader for the Lithoprobe Southern Canadian Cordillera Transect from 1985-1995 and Transect co-leader for the Lithoprobe Slave-Northern Cordillera Transect from 1995-2005.

This report is a description of geological and geophysical analyses undertaken in 2021. The coordinate system in use on the Property and on all maps is UTM zone 11N (NAD83). Metric units are used throughout the report.

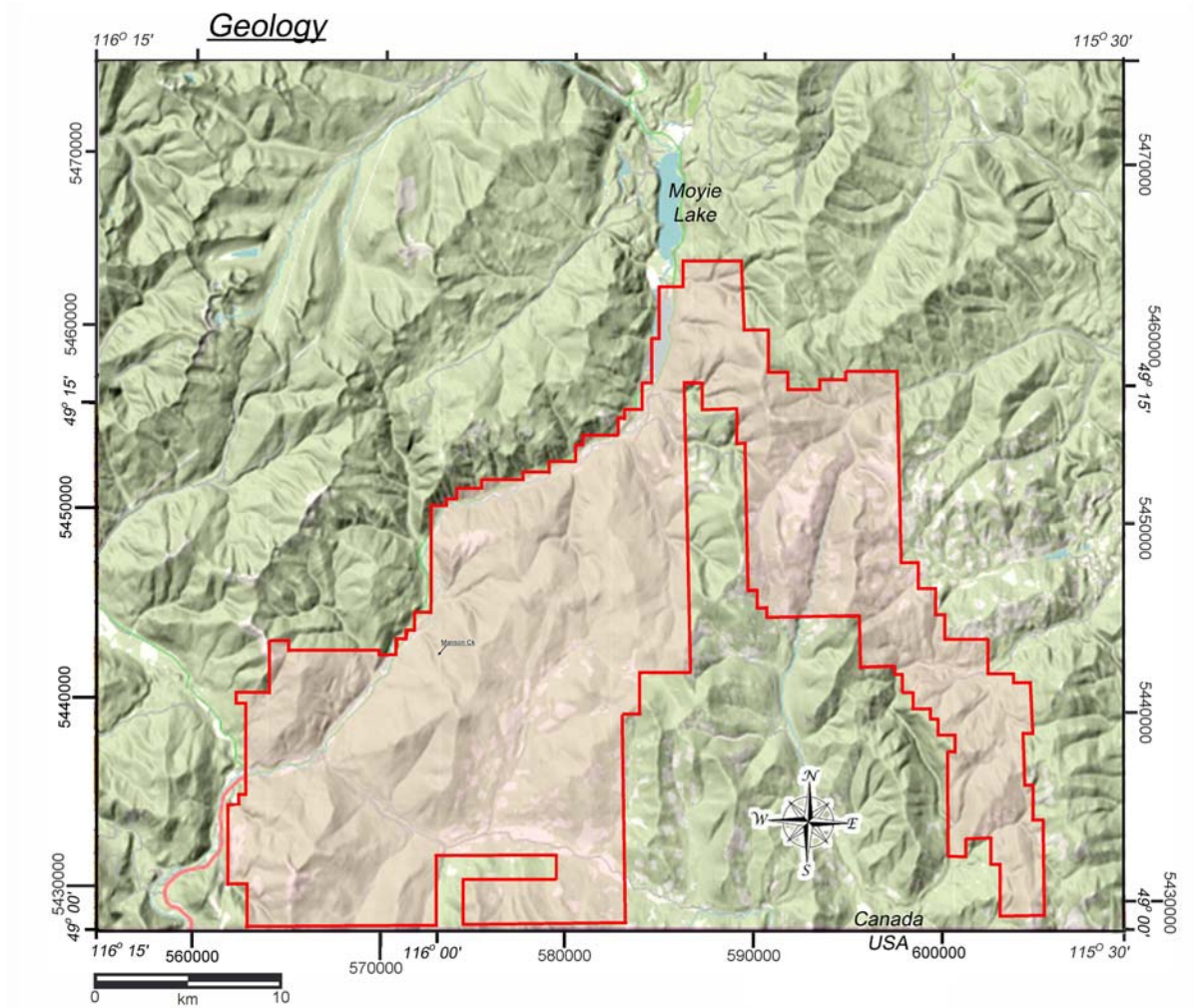


Figure 1. Image of the topography in southeastern BC with the area of the Moyie project indicated by the red shading.

2.2 Terms of Reference

Included in this report are a description of the general geological setting of the Property, a description and analysis of geophysical data and results, an interpretation and reinterpretation of geological and geophysical relationships, and an evaluation of the merits of the relevant parts of the property. Reports and publications reviewed by the author are listed in the reference section at the end of this report.

3.0 Mineral Tenure Description and Location

The Moyie property tenures total approximately 65,579 hectares (Table 1). The mineral cell titles were acquired online and as such there are no posts or lines marking the location of the property on the ground. The claims are owned by D. Lavoie, C. Kennedy and S. Kennedy of Kimberley, BC.

	Tenure Number	Claim Name	Map Number	Orig. Stake Date	Good To Date	Area
1.	515408	SP	082G.022	Jun-27-2005	Apr-30-2022	126.5350
2.	519022	KRL	082G.022	Aug-13-2005	Apr-30-2022	527.4060
3.	519048	KRL 2	082G.022	Aug-14-2005	Apr-30-2022	400.8020
4.	1030689	KRL 03-05-14	082G.022	Sep-04-2014	Apr-30-2022	189.9456
5.	1030687	KRL 04-10-14	082G.022	Sep-04-2014	Apr-30-2022	527.5704
6.	1030691	KRL 04-10-14 S/B 05-10-14	082G.012/022	Sep-04-2014	Apr-30-2022	379.9387
7.	1030770	KRL 06-10-14	082G.012	Sep-06-2014	Apr-30-2022	527.935
8.	1030771	KRL 07-10-14	082G.012	Sep-06-2014	Apr-30-2022	528.1525
9.	1030772	KRL 08-10-14	082G.012	Sep-06-2014	Apr-30-2022	528.3202
10.	835425	KRL 09-10	082G.012	Oct-08-2010	Apr-30-2022	528.4385
11.	835426	KRL 10-10	082G.012/013	Oct-08-2010	Apr-30-2022	528.4733
12.	835948	KRL 12-10	082G.022	Oct-14-2010	Apr-30-2022	527.3183
13.	1030773	KRL 13-10-14	082G.022	Sep-06-2014	Apr-30-2022	506.4601
14.	1030765	KRL 14-10-14	082G.012	Sep-06-2014	Apr-30-2022	527.8481
15.	1030769	KRL 15-10-14	082G.012	Sep-06-2014	Apr-30-2022	507.0073
16.	835953	KRL 16-10	082G.022	Oct-14-2010	Apr-30-2022	527.1879
17.	1030775	KRL 17-10-14	082G.022	Sep-06-2014	Apr-30-2022	189.7623
18.	835955	KRL 18-10	082G.012	Oct-14-2010	Apr-30-2022	524.5569
19.	1030774	KRL 21-10-14	082G.022	Sep-06-2014	Apr-30-2022	484.9516
20.	1030808	KRL 22-10-14	082G.022	Sep-07-2014	Apr-30-2022	526.9818
21.	836269	KRL 26-10	082G.002/012	Oct-19-2010	Apr-30-2022	528.7888
22.	836270	KRL 27-10	082G.002/012	Oct-19-2010	Apr-30-2022	483.4412
23.	836272	KRL 28-10	082G.003/013	Oct-19-2010	Apr-30-2022	507.5639
24.	1030810	KRL 29-10-14	082G.002/003	Sep-07-2014	Apr-30-2022	528.9604
25.	1030811	KRL 111-11-14	082G.022	Sep-07-2014	Apr-30-2022	527.3772
26.	1030834	KRL 113-11-14	082G.003/013	Sep-08-2014	Apr-30-2022	253.8027
27.	986834	KRL 114-12	082G.022	May-16-2012	Apr-30-2022	337.4181
28.	986838	KRL 115-12	082G.022	May-16-2012	Apr-30-2022	505.999
29.	999062	KRL 116-12	082G.022	Jun-19-2012	Apr-30-2022	400.3609
30.	1019533	KRL 117-13	082G.021/022	May-16-2013	Apr-30-2022	252.9734
31.	1019579	KRL 118-13	082G.021	May-17-2013	Apr-30-2022	294.9824
32.	1019682	KRL 119-13	082G.021	May-21-2013	Apr-30-2022	21.0726
33.	1031154	KRL 120-13-14	082G.022/031/C	Sep-25-2014	Apr-30-2022	168.5311
34.	1020525	KRL 121-13	082G.021/031	Jun-26-2013	Apr-30-2022	147.4793
35.	1022509	KRL 122-13	082G.021	Sep-22-2013	Apr-30-2022	484.7929
36.	1037431	KRL 30-15	082G.002/003	Jul-20-2015	Apr-30-2022	529.073
37.	1037432	KRL 31-15	082G.002/003	Jul-20-2015	Apr-30-2022	841.8493
38.	1037433	KRL 32-15	082G.002/003	Jul-20-2015	Apr-30-2022	804.6822
39.	1037434	KRL 33-15	082G.002/003	Jul-20-2015	Apr-30-2022	762.6852
40.	1045018	KRL 40-16	082G.012	Jun-29-2016	Apr-30-2022	422.1983
41.	1045019	KRL 40-16 S/B KRL 41-16	082G.031/032	Jun-29-2016	Apr-30-2022	547.6297
42.	1049636	KRL 42-17	082G.012/022	Jan-30-2017	Apr-30-2022	738.6997
43.	1049637	KRL 43-17	082G.012	Jan-30-2017	Apr-30-2022	1034.7539
44.	1049638	KRL 44-17	082G.012	Jan-30-2017	Apr-30-2022	1077.413
45.	984342	SPIKE'S BIG ADVENTURE	082G.021	May-07-2012	Apr-30-2022	211.0183
46.	985682	SPIKE'S BA-02-12	082G.011/021	May-10-2012	Apr-30-2022	443.2206

Table 1: Tenures in the Moyie Anticline property for Events 5934086, 5934648, 5934830

	Tenure Number	Claim Name	Map Number	Orig. Stake Date	Good To Date	Area
47.	985683	SPIKE'S BA-03-12	082G.011/021	May-10-2012	Apr-30-2022	337.6723
48.	1020126	SPIKE'S BA-04-13	082G.011	Jun-07-2013	Apr-30-2022	253.355
49.	1062764	SPIKE'S BA-05-18	082G.021	Sep-03-2018	Apr-30-2022	527.3321
50.	1066457	SPIKE'S BA 06-19	082G	Feb-12-2019	Apr-30-2022	632.8979
51.	1066458	SPIKE'S BA 07-19	082G.011/021	Feb-12-2019	Apr-30-2022	569.8422
52.	1068199	SPIKE'S BA 08-19	082G	Apr-28-2019	Apr-30-2022	358.4649
53.	1068200	SPIKE'S BA 09-19	082G.021	Apr-28-2019	Apr-30-2022	105.4582
54.	1068408	SPIKE'S BA 10-19	082G.011/021	May-08-2019	Apr-30-2022	1245.3251
55.	1068412	SPIKE'S BA 11-19	082G.011	May-08-2019	Apr-30-2022	1901.4669
56.	1068414	SPIKE'S BA 12-19	082G.011	May-08-2019	Apr-30-2022	865.7686
57.	1068419	SPIKE'S BA 13-19	082G.011/021	May-08-2019	Apr-30-2022	1034.2941
58.	1068422	SPIKE'S BA 14-19	082G.011	May-08-2019	Apr-30-2022	549.0701
59.	1068560	SPIKE'S BA 15-19	082G.011	May-15-2019	Apr-30-2022	84.4913
60.	1068669	SPIKE'S BA 16-19	082G.011	May-23-2019	Apr-30-2022	506.9488
61.	1075033	MOYIE ANTICLINE 01-20	082G	Mar-05-2020	Apr-30-2022	1923.5462
62.	1075034	MA 02-20	082G	Mar-05-2020	Apr-30-2022	1795.5462
63.	1075035	MA 03-20	082G	Mar-05-2020	Apr-30-2022	1648.4287
64.	1075036	MA 04-20	082G	Mar-05-2020	Apr-30-2022	2029.8579
65.	1075037	MA 05-20	082G	Mar-05-2020	Apr-30-2022	1523.226
66.	1075038	MA 06-20	082G	Mar-05-2020	Apr-30-2022	1800.0711
67.	1075039	MA 07-20	082G	Mar-05-2020	Apr-30-2022	1524.2624
68.	1075040	MA 08-20	082G	Mar-05-2020	Apr-30-2022	1143.1928
69.	1075041	MA 09-20	082F	Mar-05-2020	Apr-30-2022	2073.0702
70.	1075042	MA 10-20	082F	Mar-05-2020	Apr-30-2022	1376.7417
71.	1075043	MA 11-20	082G	Mar-05-2020	Apr-30-2022	1080.0364
72.	1075044	MA 12-20	082F	Mar-05-2020	Apr-30-2022	2117.4524
73.	1075045	MA 13-20	082F	Mar-05-2020	Apr-30-2022	1353.4861
74.	1075046	MA 14-20	082F	Mar-05-2020	Apr-30-2022	1693.9612
75.	1075048	MA 15-20	082F	Mar-05-2020	Apr-30-2022	1947.4455
76.	1075049	MA 16-20	082F	Mar-05-2020	Apr-30-2022	1355.8405
77.	1075050	MA 17-20	082F	Mar-05-2020	Apr-30-2022	1395.8553
78.	1075051	MA 18-20	082F	Mar-05-2020	Apr-30-2022	317.0756
79.	1080129	MA 19-20	082F	Dec-19-2020	Apr-30-2022	402.324
80.	604912	SWEET SPOT	082G.001	May-24-2009	Oct-17-2030	423.7554
81.	882449	SWEET SPOT 04-11	082G.001	Aug-05-2011	Oct-17-2030	444.908
82.	882469	SWEET SPOT 05-11	082G.001	Aug-05-2011	Oct-17-2030	296.6665
83.	1037318	LADY SLIPPER 01-15	082G.011	Jul-14-2015	Apr-30-2022	84.4428
84.	1066459	LADY SLIPPER 02-19	082G.011	Feb-12-2019	Apr-30-2022	886.6607
85.	1062583	KENCO 1-18	082F	Aug-24-2018	Oct-26-2024	169.1282
86.	1066463	KENCO 02-19	082F	Feb-12-2019	Oct-26-2024	253.6748
87.	1066460	DOWN DIP 01-19	082G	Feb-12-2019	Apr-30-2022	507.7618
88.	1068446	DOWN DIP 02-19	082G	May-09-2019	Apr-30-2022	1078.9372
89.	1066470	LEAKY PIPE 01-19	082F	Feb-12-2019	May-18-2022	190.214
90.	1068445	LP 02-19	082F	May-09-2019	May-18-2022	718.5603
91.	1068561	HAZEL'S YAHK 01-19	082F.010/020	May-15-2019	Jun-07-2022	1078.3606
					Total HA	65579.237

Table 1: Tenures in the Moyie Anticline property (continued).

4.0 Accessibility and Physiography

The Moyie Anticline property stretches from Moyie Lake (at about 49° 20' N. Latitude) in the north to the U. S. border (49° 00' N. Latitude) in the south (Figure 1). Access is via the major Cranbrook – Creston highway, and then by a series of logging roads into different regions of the property. The physiography in the vicinity of the property consists of rolling hills punctuated by linear lakes and valleys. Logging has been a mainstay of economic activity in the area. Geological exposure is fair to good throughout much of the area.

5.0 Exploration History

The region in the vicinity of the property has been prospected heavily ever since the Sullivan deposit was found near Kimberley in 1892. However, the only significant developed deposit in the Moyie anticline area is the St. Eugene polymetallic vein system that was found in 1893. Indeed, the St. Eugene deposit was the subject of the first BC Mines Assessment Report (Smith, 1948). Numerous showings have been described in assessment reports, but no deposits of sufficient size for development have been found.

6.0 Geological Setting

The Moyie anticline property is situated in the southeastern corner of British Columbia and includes part of the Purcell anticlinorium, a group of stacked, crustal-scale anticlinorial structures that formed as the result of orogenic episodes between about 1.5 Ga and 0.6 Ga. The deepest of the anticlinorial structures is the subject of this project: the Moyie anticline (Figure 2).

The Moyie anticline formed as a thick basin of Mesoproterozoic strata (primarily the Aldridge Formation) were detached and thrust eastward above the westward thinning underlying North American (Laurentian) craton. The exact thicknesses of the strata beneath the Moyie anticline are unknown because the base of the strata in the anticline has not been observed. Nevertheless, the large volume of strata approaching the craton responded by forming the large, north-striking Moyie anticline. In other words, the Moyie anticline is an example of an inverted basin.

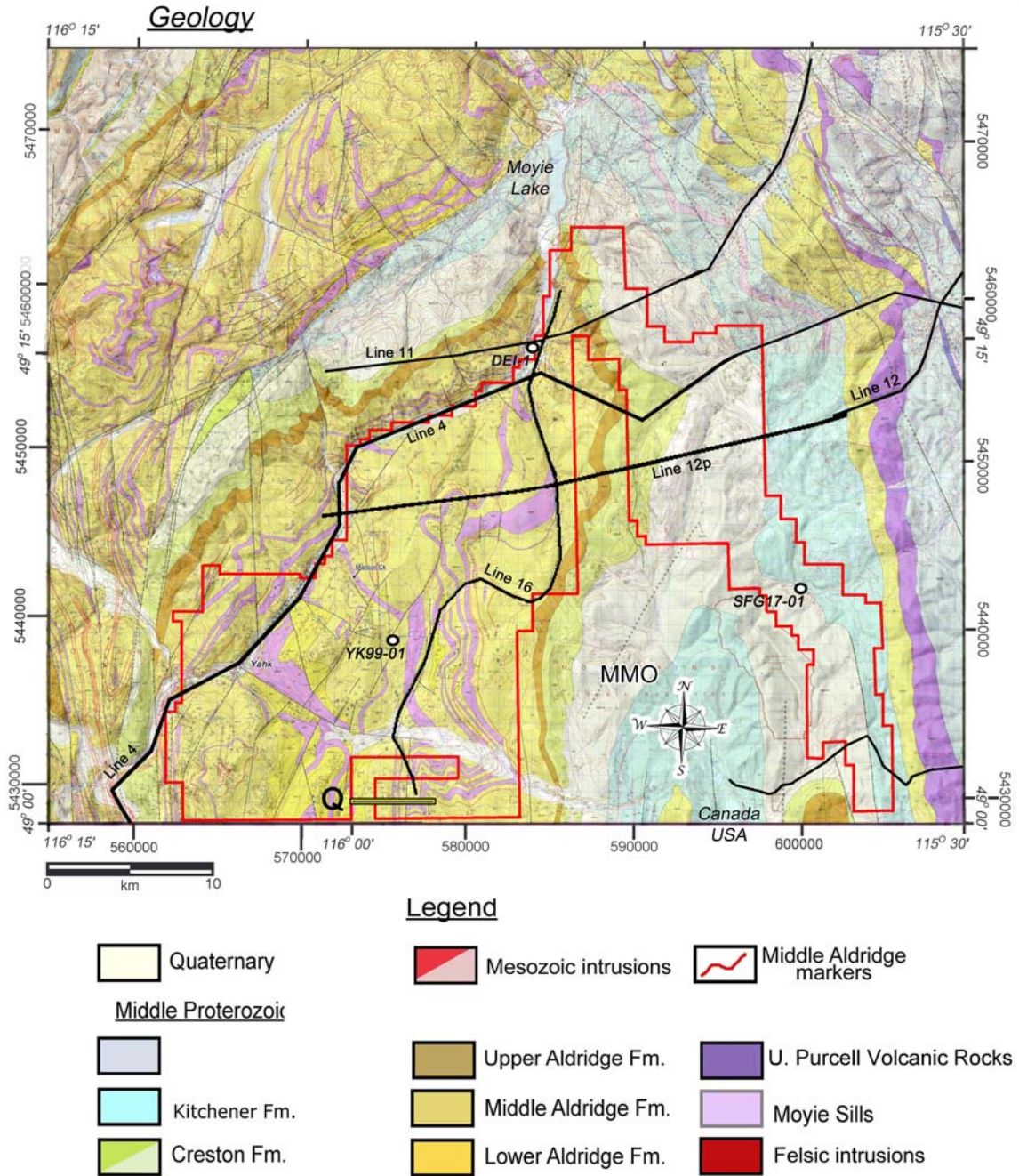


Figure 2. Moyie anticline claim group in southeastern BC (red outline) superimposed on the geological map of the area. Geological map compiled from Glombick et al. 2010, Brown and Macleod, 2011 and Brown et al., 2011.

Figure 3 is a regional seismic reflection cross section of the area to illustrate some of the key stratigraphic and structural relationships. The section extends from east of the Rocky Mountain Trench to west of the Moyie anticline. The Duncan drill hole (DEI Moyie #1) drilled through the Sundown sill (Middle Aldridge) into a prominent reflections from the Lower Aldridge sills.

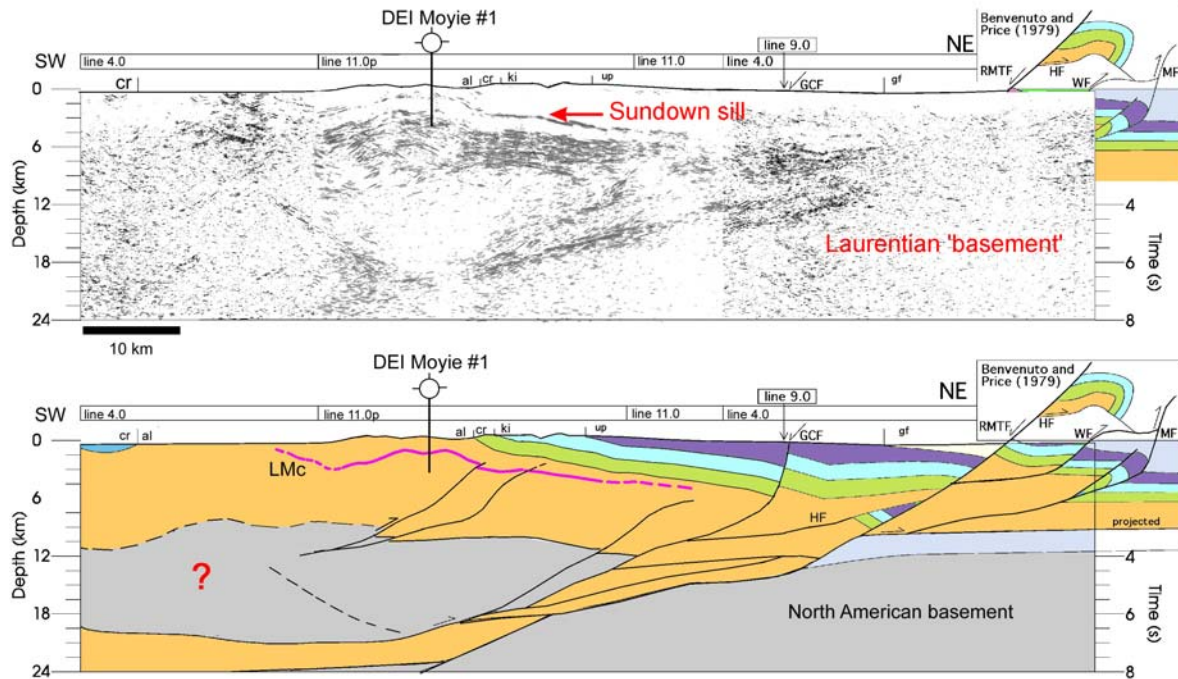


Figure 3. Regional east-west cross section constructed from several segments of seismic data combined into a continuous cross section. The section shows the position of the Duncan Energy drill hole (DEI Moyie #1) near the axis of the Moyie anticline, seismic lines 4 and 11, and the Southern Rocky Mountain Trench fault (RMTF). Note that beneath the DEI drill hole, the autochthonous ‘basement’ (Laurentian craton) is observed near 24 km depth with a slice of basement shown between ~7 and ~20 km. It is also possible that the interpreted basement ‘slice’ is Aldridge Formation strata.

7.0 Work Accomplished in 2021

Kootenay Resources, Inc contracted Complete MagnetoTelluric Solutions (CMTS) to record and analyse the magnetotelluric data. Data were recorded at 86 points scattered throughout the anticline during October-November, 2021 (Figure 4). Details of the acquisition are described in Appendix 1. Key points are: 1) some of the original station locations had to be moved due to road closures, and, 2) The weather was generally good for most of the survey.

Once acquisition was complete, data analysis was undertaken by CMTS in communication with Kootenay Resources, Inc. Of particular note is that initial analyses of the data focused on determining the optimal way to analyse and present the data and results. Because there is not enough detail for a full 3D analysis, it was decided that a series of 2D lines would be the most useful presentation. Accordingly, Figure 5 shows eight lines:

Line SS (east-west) – green line near the international border

Line MM0 (east-west) – light blue line ~10-15km north of the border;

Line MM1 – Long line (~70-80 km east-west) that includes 12 stations recorded for Duncan Energy in the mid-1980s.

Line MM2 – Short line (east-west) about 2-3 km north of Line MM1;

Lines SP(east-west and north-south) – Pink lines, including four stations from Duncan Energy;

Lines MO – Dark blue lines at the northern end of the property.

The contractor analysed the data quality and consistency and provided analyses of geoelectric strike (Appendices 2 and 3) in order to optimize the projections for the cross sections. During the analyses for geoelectric strike, it was observed that the strike sometimes varies as a function of frequency/depth. For example, near the US-Canada border (Sweet Spot area) the geoelectric strike for high frequencies (shallow depth) is about N12E, whereas for the low frequencies (deep) the calculated geoelectric strike is about N55W. When this was found (different strikes for different depths), two inversions are calculated: one for the shallow section and one for the deep.

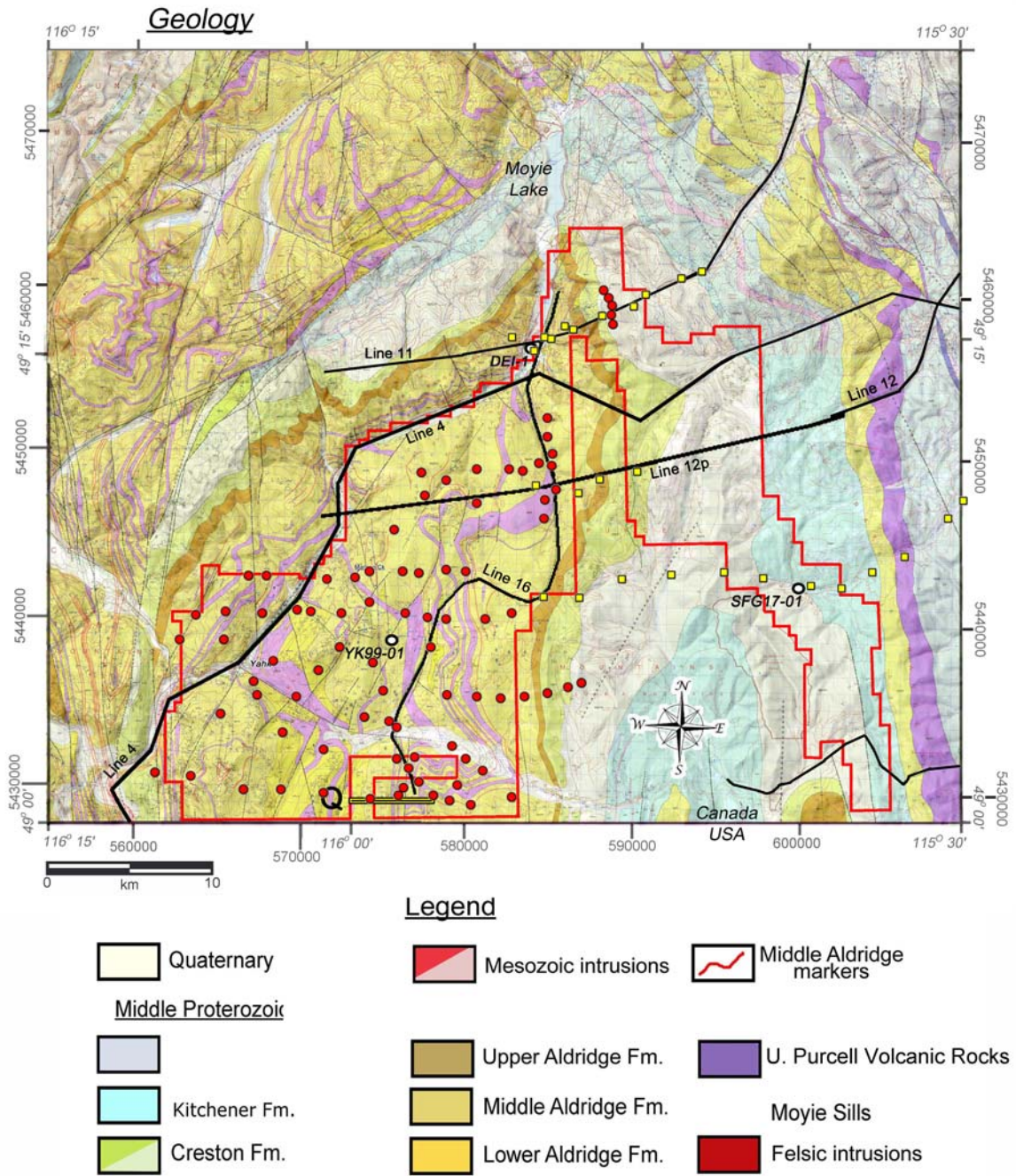


Figure 4. Map of the Moyie anticline property with the recorded data shown by the colored lines. Black lines = seismic profiles; red dots: 2021 stations; yellow dots = Duncan Energy 1985 stations. 'Q' is a short, high-resolution MT line recorded by Quantec for Teck in 2017.

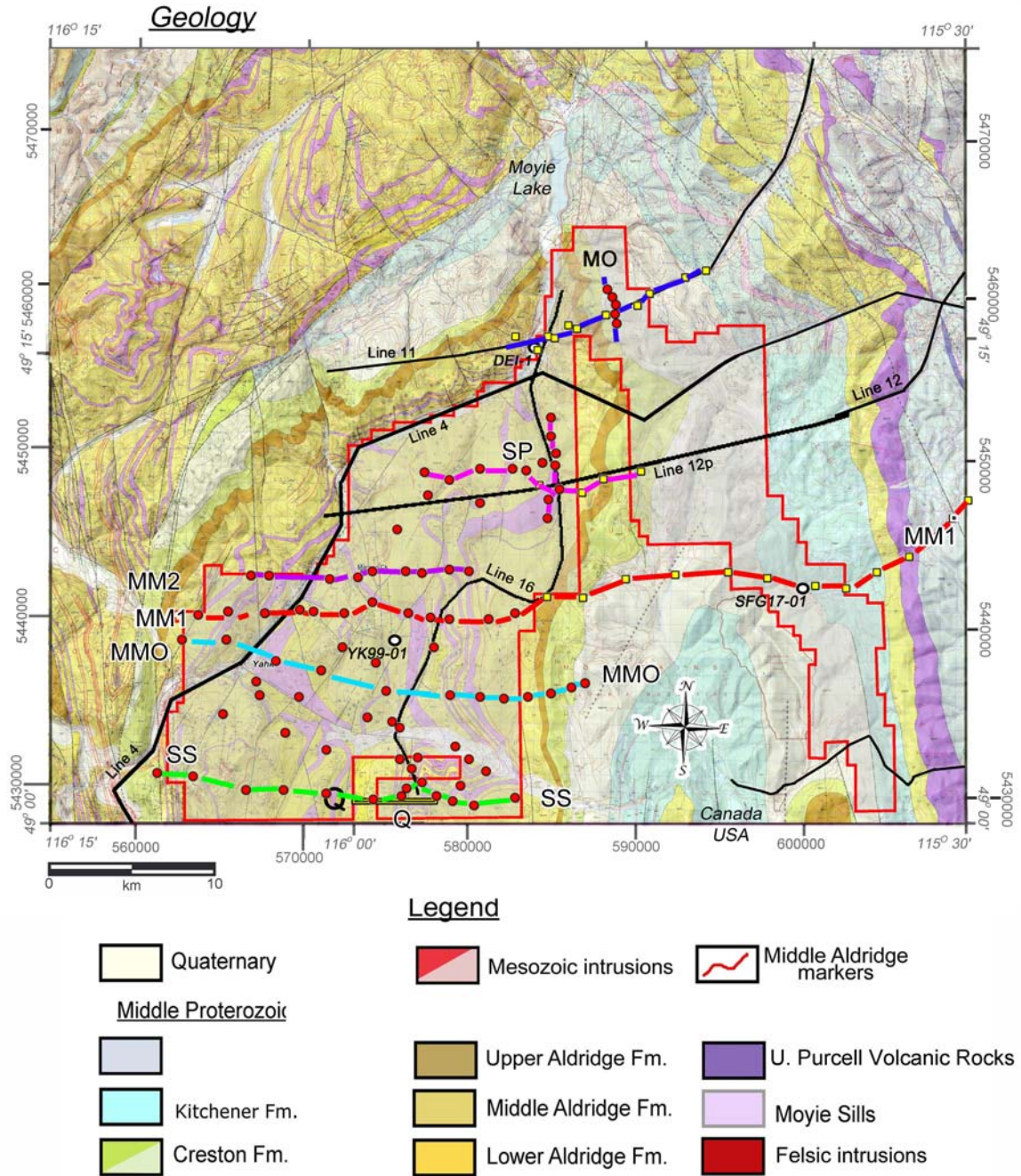


Figure 5. Same map as in Figure 4 with the proposed east-west 2D line; green line = Sweet Spot (SS) line of section; blue line = Line MM0; red line = Line MM1. Note Line MM1 includes 12 stations on the east (yellow dots) recorded for Duncan Energy in the 1980's; purple line = Line MM2; pink line = Spike's Big Adventure (N-S and E-W); dark blue lines = Line MO near Moyie.

8.0 Observations/Results

8.1 Sweet Spot (Line SS)

The Sweet Spot line (SS) extends from near highway 3 on the west end for about 22 km to the east. On its eastern end the line intersect the Sweet Spot property (originally known as the Can-Am property) that has strong showings in soil geochemistry as well as several rounds of drilling. The most recent drilling was completed by Teck Resources in 2019 (Boucher and Thomson, 2019). During the work preceding the drilling, Teck recorded a single east-west MT line (labeled 'Q' near the international border at approximately $115^{\circ} 55'$ W. longitude on Figure 5).

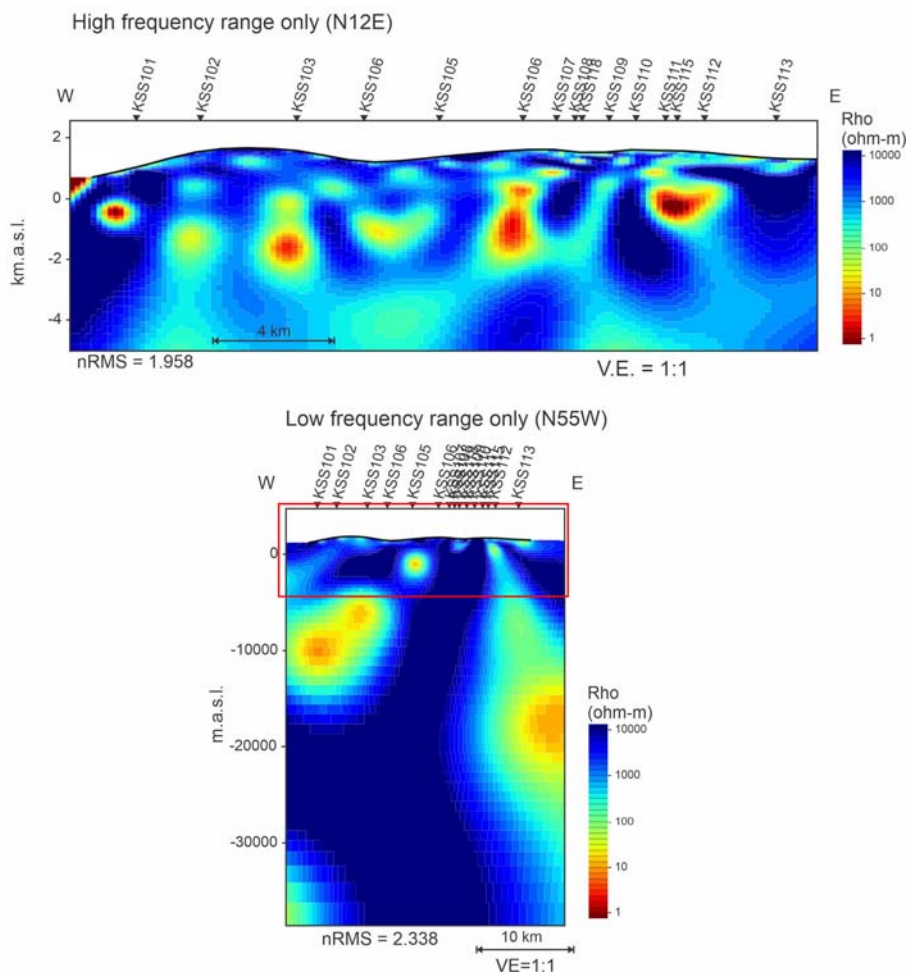


Figure 6 (upper image). 2D Inversion of Line SS for the shallow section (< 5km below sea level) with geoelectric strike = N12E; (lower image) 2D Inversion of Line SS for the deep (> 5km below sea level) with geoelectric strike = N55W. The red rectangle at the top of the lower section is the area enhanced in the shallow section above.

8.2 Line MM0

Line MM0 is constructed from stations located approximately 10 km north of Line SS (Figure 5). As in the case of Line SS, the geoelectric strike was found to be N12E for the shallow section and N55W for the deep (low frequency) section. The inversion results indicate the presence of a very large (~4-5 km east-west, and 1-2 km vertical thickness; Figure 7). The eastern limit of the anomaly is not well constrained due to the end of the line. The line was extended beyond the eastern edge of the claim block because anomaly definition requires three or more stations; once the anomaly was observed, additional tenures were added to the claim block to include the anomaly. The northern and southern limits of the anomaly are not constrained by the existing control as the line is oriented east-west. Future work may include additional stations to define the MM0 anomaly.

Based on the surface geology and estimated stratigraphic thicknesses, the MM0 anomaly occurs between the Sundown sill above and the lower Aldridge sills (~Bootleg sill) below. The centre of the MM0 anomaly is located about 2 km below the surface, although the depth may be different to the north or to the south of the line. This is a target for future work.

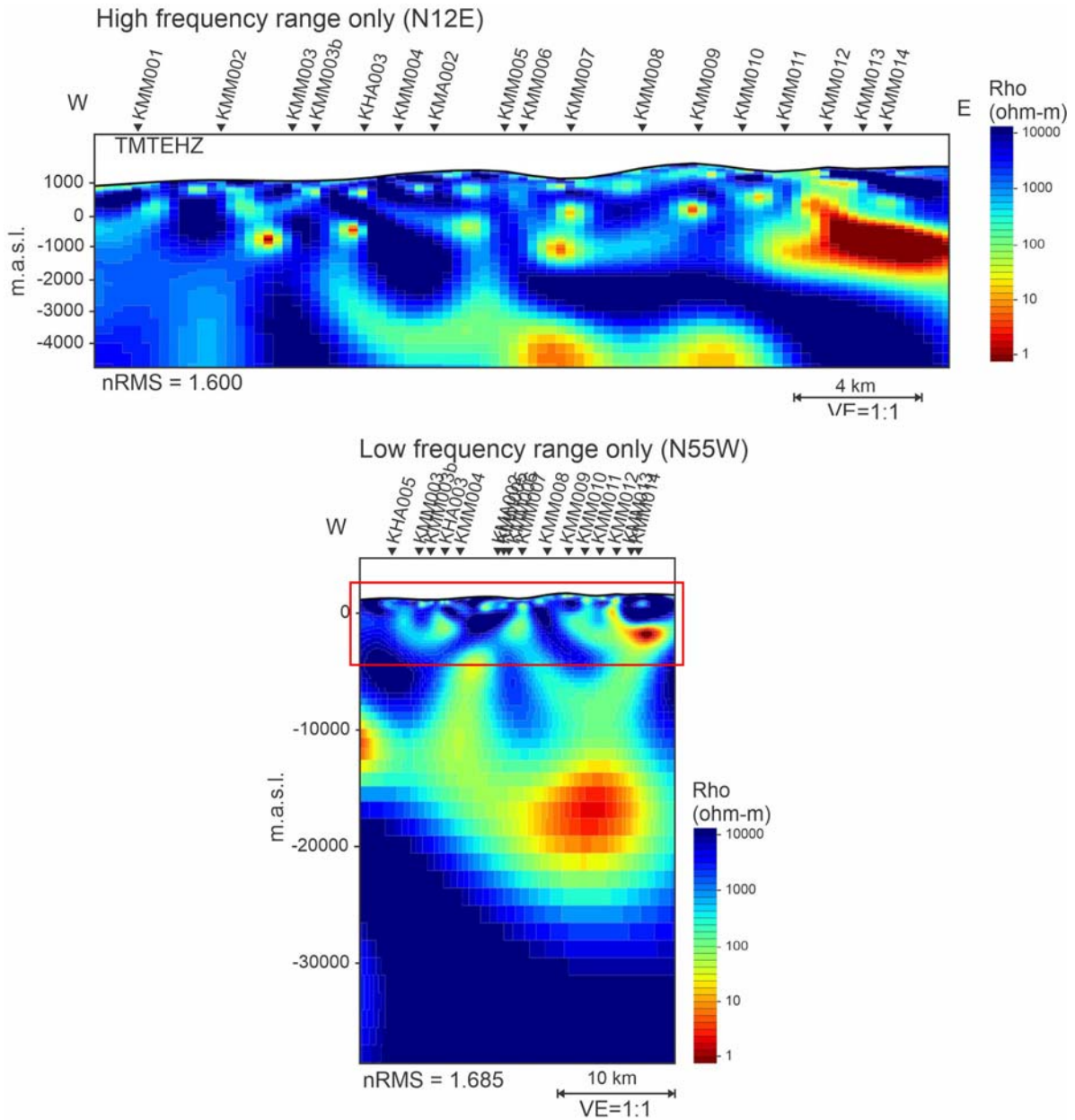


Figure 7 (upper image): 2D Inversion of Line MMO for the shallow (< 5km below sea level) with geoelectric strike = N12E; (lower image) 2D Inversion of Line MM0 for the deep (> 5km below sea level) with geoelectric strike = N55W. The red rectangle in the lower (deep) section is the area of the shallow section above.

8.3 Line MM1

Line MM1 is oriented ~east-west and is located approximately 6-10 km north of Line MM0 (Figure 5). The positions of the new stations along this line were located in order to allow data recorded for Duncan Energy (yellow dots on Figures 4 and 5) to be included into a long regional line across the Moyie anticline. The 2D inversion results are shown in Figure 8. For these inversions, the geoelectric strikes used were N55W for the deep section and N10E for the shallow section (Appendix 2).

Inclusion of the Duncan Energy stations on the east with the new stations on the west produces a cross section that is ~50km long (Figure 8). However, during the analysis and inversion, J. Spratt recognized that the Duncan Energy data for the deep section are not as high quality as the rest of the data and should be used with caution.

The inversion results are illustrated in Figures 8 and 9. The shallow section (<5 km below sea level) displays four prominent conductors that dip eastward. The SFG17-01 drill hole is located very near MT station DUN115 and may have intersected the upper part of the conductivity anomaly below DUN115 (Figure 9). The hole was drilled to 588m below surface and intersected a broad zone of hematite mineralization, some of which was replaced by chalcocite and bornite (S. Kennedy, 2019). The drill hole did not penetrate into the main part of the conductivity anomaly (Figure 9), as the main part of the conductor beneath the drill hole is at about 1 km below sea level (Figure 8). Two additional anomalies (Figure 9), one beneath station DUN 503, and a second, shallower anomaly, beneath stations DUN303 and DUN403 have not been tested by drilling. All of the anomalies appear to be in the Upper Aldridge or lower Creston strata.

The inversion for the deep section (>5 km depth) in Figure 8 (lower) appears to illustrate a large, near-vertical anomaly between about 8 km and 20 km depth. As noted previously, however, the deep data for the Duncan stations are generally not high quality and should therefore be interpreted with caution.

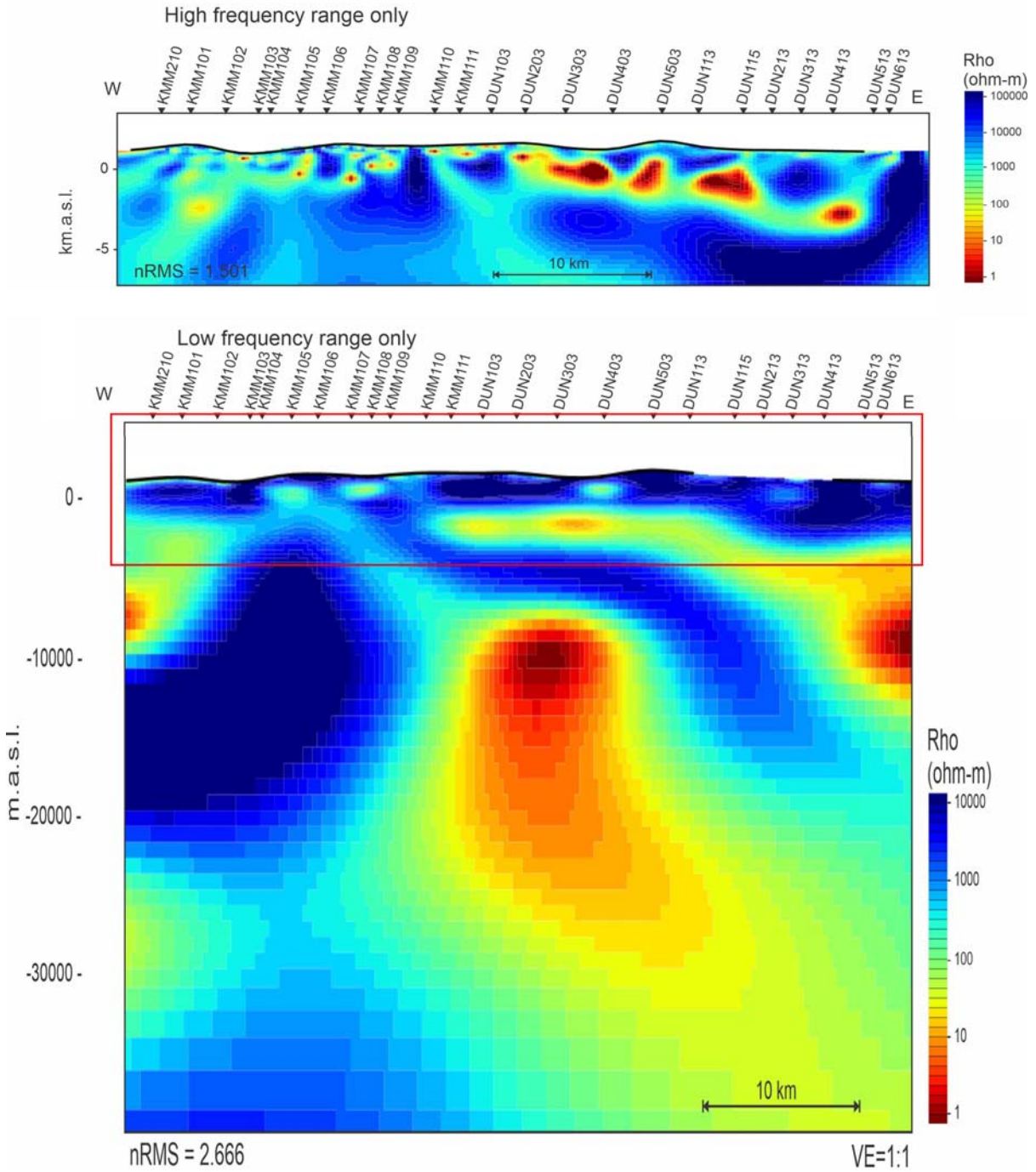
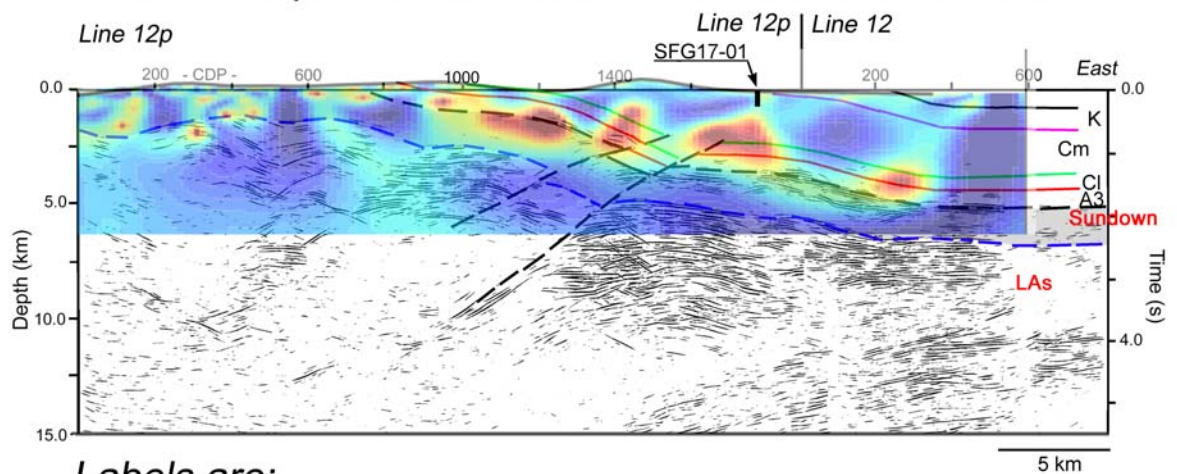


Figure 8 (upper image). 2D Inversion of Line MM1 for the shallow (< 5 km below sea level) with Geoelectric strike = N10E; (lower image) 2D Inversion of Line MM1 for the deep (> 5km below sea level) with geoelectric strike = N55W.

Seismic profile 12 with MM1 MT inversion overlainLabels are:

A3 = Upper Aldridge; Cl = Lower Creston;

Cm = Middle Creston; K = Kitchener;

LAs = Lower Aldridge sills; Sundown = Sundown sill/marker

SFG17-01

- drilled to 588m; intersected copper minerals
in lower part of hole; casing still down hole.

Note:

- MT anomalies appear to cluster between
Middle Aldridge (Sundown) and Middle Creston

Figure 9. Seismic section 12 (lines 12p and 12) with the approximate stratigraphic boundaries (coloured lines) and the conductivity anomalies along profile MM1 superimposed. Note that the two central anomalies appear to be spatially associated with the two interpreted faults.

8.4 Line MM2

Line MM2 is located approximately 4-5 km north of line MM1 (Figure 5). The inversions are shown in Figure 10. Although the shallow (high frequency) section displays a number of apparent conductors, they appear to be quite small. However, because the line is 2D, it is possible that one or more of the conductors is larger to the north or to the south of the line. There are indications on the surface that the area has significant potential (e.g., Cook, 2019).

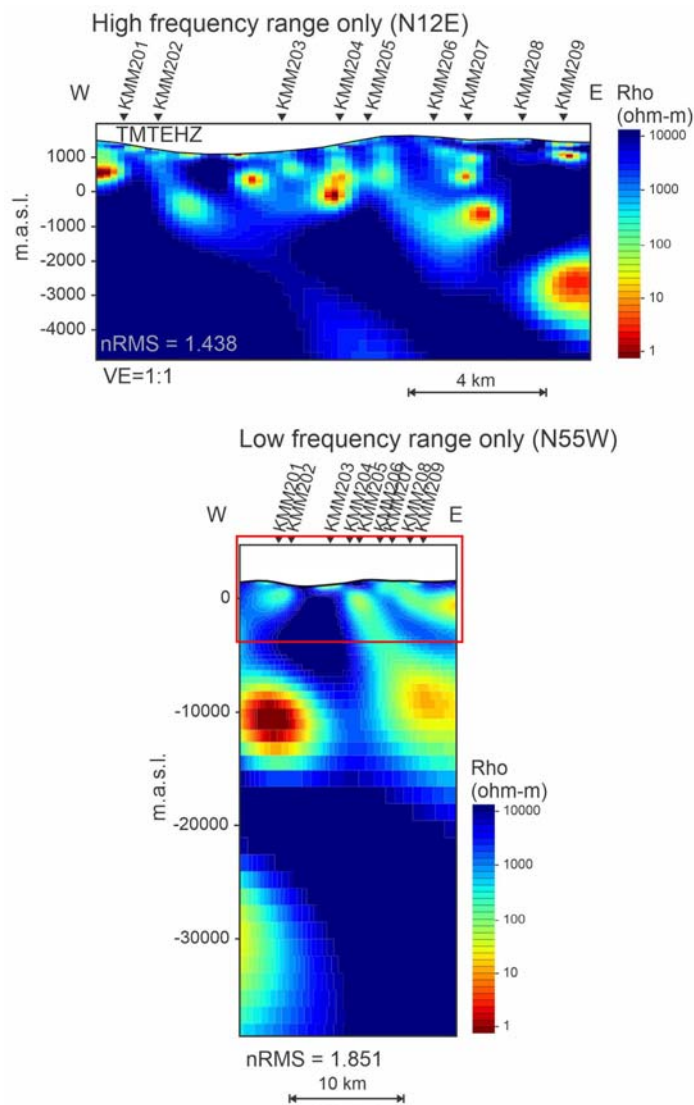


Figure 10. (upper image) 2D Inversion of Line MM2 for the shallow (< 5km below sea level) with Geoelectric strike = N45W; (lower image) Inversion of Line MM2 for the deep (> 5km below sea level) with geoelectric strike = N55W.

8.5 Lines SP

The data near the Spike's Big Adventure property (abbreviated SP) were projected into both an east-west line and a north-south line; they are labeled here SPew and SPns. In addition, there were five Duncan Energy stations (labeled with 'X...') that were used on the east-west line.

Although the area is relatively small (compared to the long lines farther south), there are a number of features that are visible on the inversions. First, there do not appear to be any very large conductors, either in terms of the magnitude of conductivity or the size of the anomalous conductivity. However, on SPew (Figure 11), there is a conductor beneath station X86d006 at about 3 km below sea level and a similar conductor appears at about 2 km depth beneath station KSP106 on line SPns. It is possible that these may be the same conductor and thus that it may be quite large. Although these are too deep to be within drilling depth, they may coalesce into a single large conductive zone.

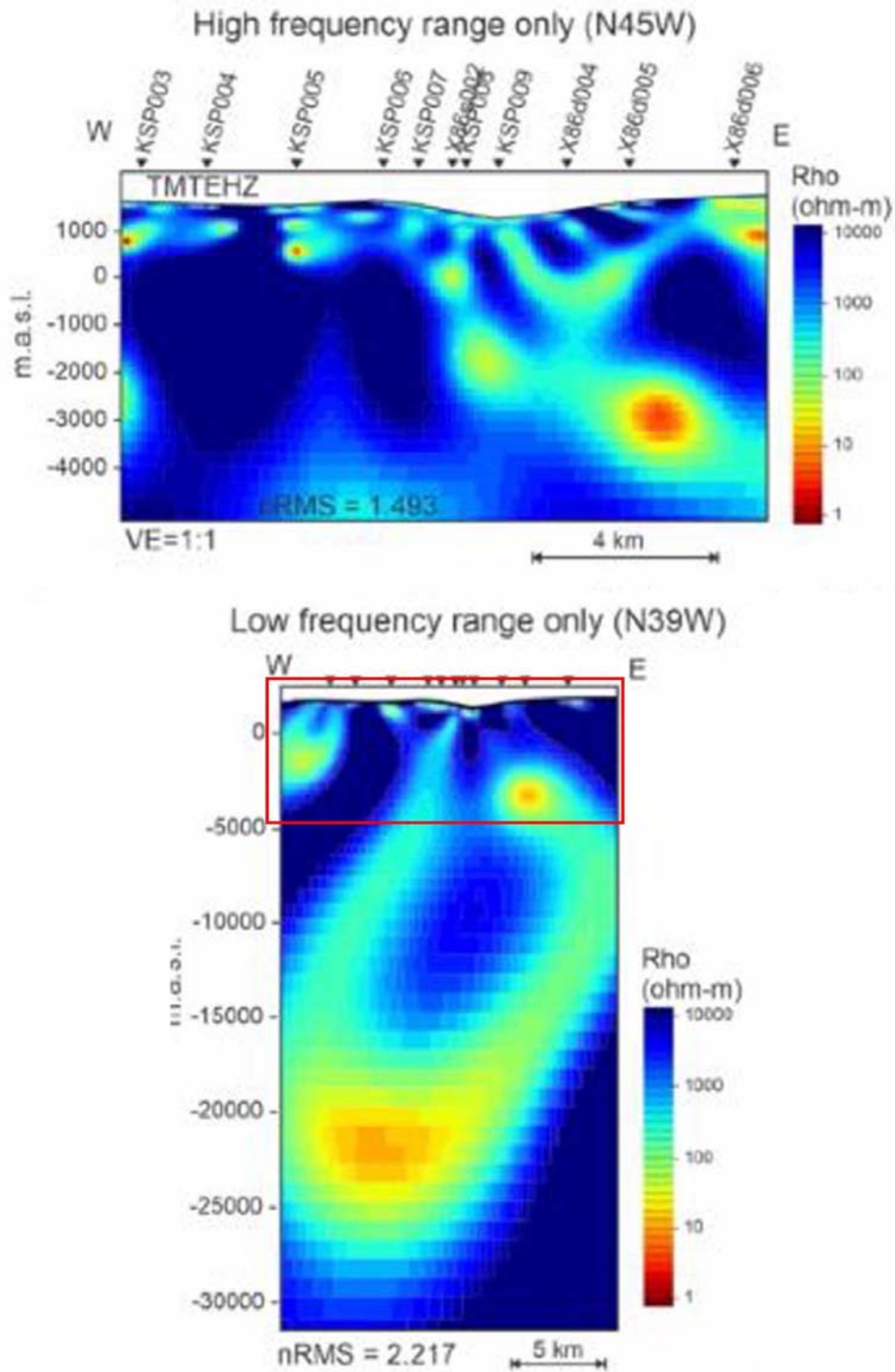


Figure 11 (upper image): 2D Inversion of Line SPew for the shallow (< 5km below sea level) with geoelectric strike = N45W; (bottom) 2D Inversion of Line MM2 for the deep (> 5km below sea level) with geoelectric strike = N39W.

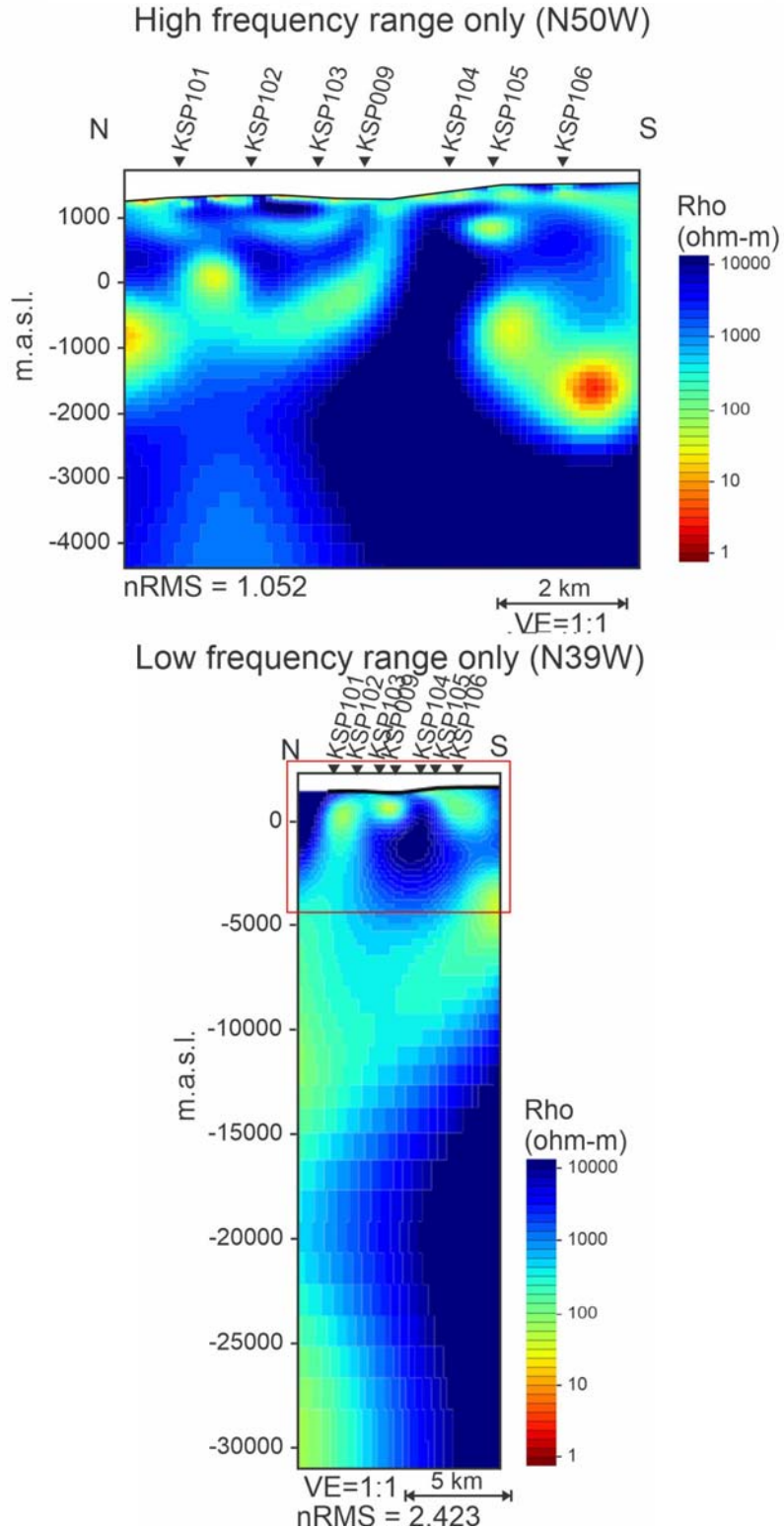


Figure 12 (top). 2D Inversion of Line SPns for the shallow section (< 5km below sea level) with geoelectric strike = N50W; (bottom) 2D Inversion of Line SPns for the deep section (> 5km below sea level) with geoelectric strike = N39W.

8.6 Lines MO

Two short lines were recorded near the St. Eugene and Society Girl deposits near the northern end of the property (Figure 4). The longest is about 10 km, is oriented east-west and utilizes nine (9) stations recorded for Duncan Energy in the mid-1980s (Figure 13). Significantly, this area is the only region with the same geoelectric strike (N39W) for the shallow as well as the deep sections; thus it is not necessary to display separate inversions for the high frequency (shallow) and the low frequencies (deep). Both the east west (MOew) and north-south (MOns) are shown in Figure 13.

The east-west line includes nine (9) stations from the Duncan Energy data (labeled 'DUN...', 'KB...', and '11-...'). The north-south line is short (only 5 stations). As previously, the inversions do not include low frequency (deep) data due to serious questions concerning the data quality. Thus, the east-west line is calculated only for the shallow data (to about 5 km below sea level). The north south line is constructed only from five (5) stations recorded in 2021 (Figure 13).

Six or more shallow (<2 km) conductors were detected along the MOew (Figure 13). Similar shallow conductors are visible along MOns, but it is not yet clear how they relate to the anomalies along MOew. Similarly, line MOns appears to have an image of a deeply penetrating narrow zone that is similar to interpreted 'conduits' (see next section).

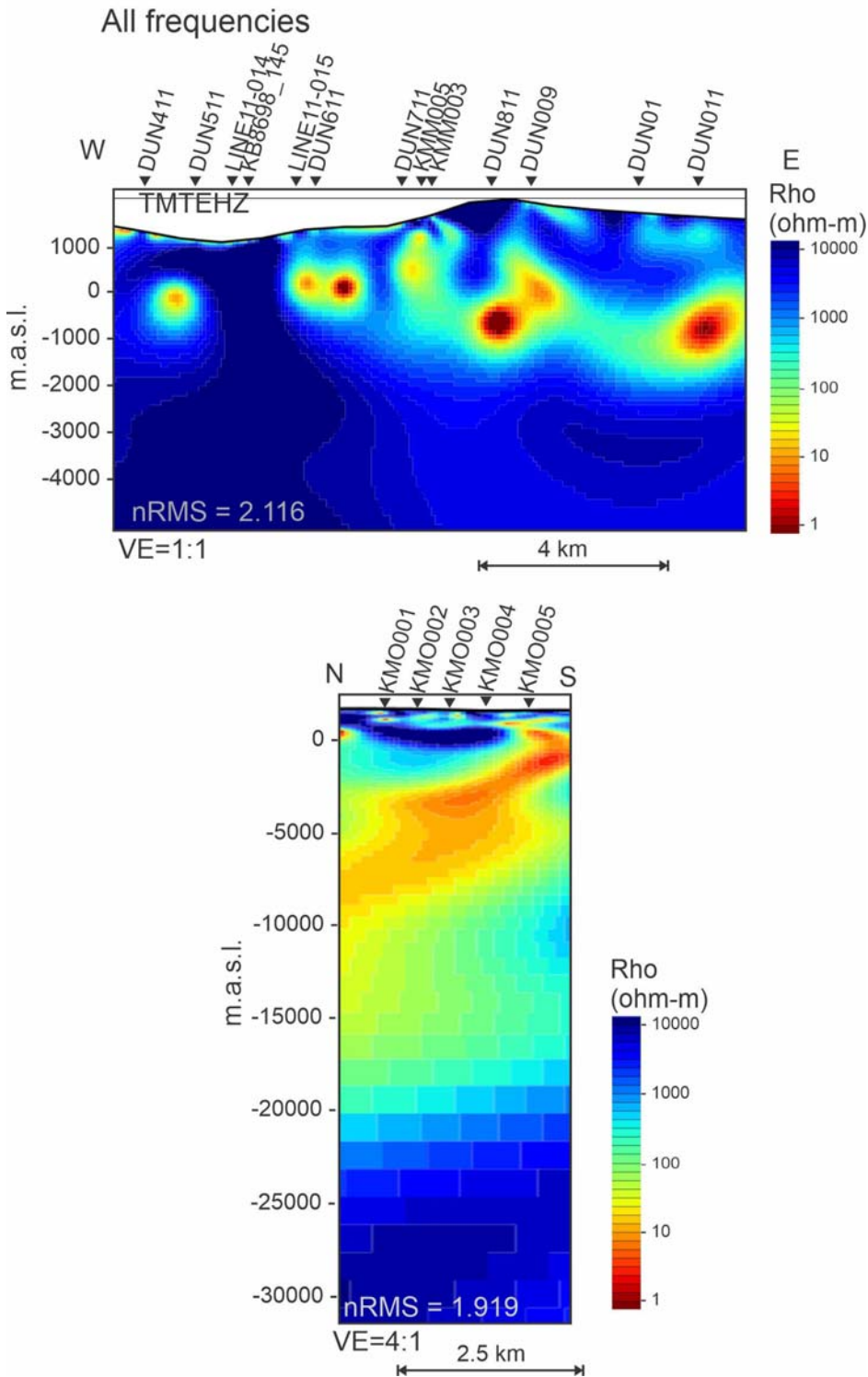


Figure 13 (top). 2D Inversion of Lines MOew for the shallow (< 5km below sea level) with geoelectric strike = N39W; (bottom) 2D Inversion of Line MOs for the deep (> 5km below sea level) with geoelectric strike = N39W. Note that the geoelectric strike is the same for both the shallow and the deep sections.

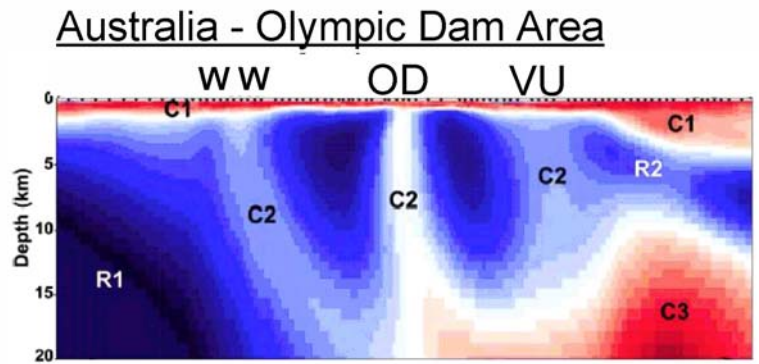
8.7 Conduits

Regional magnetotelluric data from southern British Columbia and southern Australia appear to have images of vertical to near-vertical features that are often interpreted as fluid conduits that have slightly higher conductivity values than the surrounding rocks. Although the first mention of MT images of conduits that I can find is in Gupta and Jones (1995), these features are relatively shallow (upper few kilometers); it is not clear how deeply they penetrate into the crust.

Large-scale (hundreds of km) cross sections that include both magnetotelluric data and seismic reflection data have been interpreted to have images of vertical zones of elevated conductivity. Most importantly, in productive mining areas (e.g., Ernest Henry, Olympic Dam deposits) vertical 'conduits' appear to spatially correlate with deposits discovered on the surface. As shown in Figure 14, three major vertical conductivity zones point to and correlate with three important mineral deposits; Wirrda Well (WW), Vulcan (VU) and Olympic Dam (OD). Each of these is located at the surface where a deeply penetrating vertical conductor reaches the surface. The spatial relationships of these features has led many authors to suggest that there is a genetic relationship between the vertical conductors and the deposits (e.g., Heinson et al. 2018).

The cause(s) of the vertical conductivity are not known at this time. Indeed they may even vary from one area to another. Nevertheless, these observations lead to the suggestion that such vertical conduits are common, if not necessary features to delineate the locations, geometry and potential for areas under exploration.

In the Moyie anticline, a number of conduit-like structures are observed on the data. Two of the most prominent are associated with the Sweet Spot property and the large anomaly on line MM0 (Figure 14). Then Sweet Spot conduit anomaly appears to project to the surface where a large, untested anomaly is visible on the east end of the 2017 MT line (Boucher and Thomson, 2019). Similarly, the MM0 conduit appears to project to the surface at the location of anomaly MM0.



Comparison of MT results across the Olympic Dam deposit (upper image) with the low-frequency inversions of Line MM0 and Line SS below

Southeast BC - Moyie Anticline

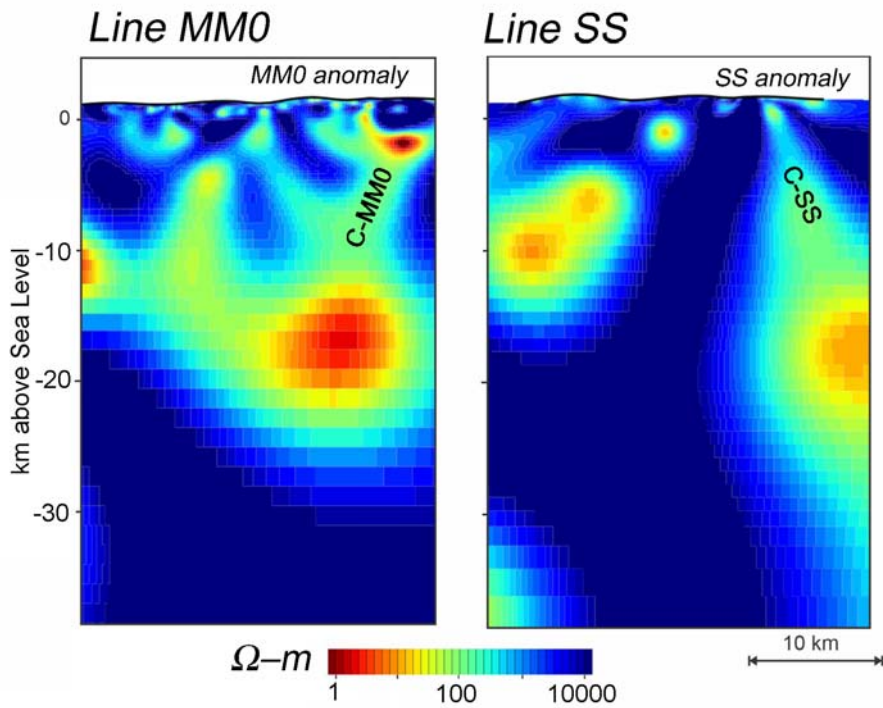


Figure 14. (upper) Regional cross section through the Olympic dam (OD), Wirrda Well (WW) and Vulcan (VU) deposits in southern Australia. Conductors are labeled with 'C' and resistive areas are marked with 'R'. Note that each of the deposits is associated (spatially) with a vertical conductor.

9.0 Summary and Conclusions

Application of the magnetotelluric technique in the Moyie anticline of southeastern BC has resulted in detection of several conductivity anomalies that, when coupled with the geology and geochemistry of surface rocks and in drill holes, lead to the identification of areas for enhanced exploration and, eventually, drilling.

Some of the anomalous areas observed so far include the following:

1. Sweet Spot anomaly – Originally known as the CanAm property (Anderson, 1991) – has a significant anomaly, first identified on 2017 MT data (Boucher and Thomson, 2019) - that correlates spatially with the deep ‘conduit’.
2. MM0 anomaly – a new discovery – has unknown size due to its location at the east end of line MM0. Along – strike projections indicate that the anomaly is located between the Sundown sill (Middle Aldridge) and the Lower Aldridge sills, the top of which is equivalent (stratigraphically) to the Bootleg sill at the Sullivan mine.
3. MM1 anomalies – are a series of four (40 conductors that dip eastward). They are shallow (3 km or less) and they are untested by drilling. As is visible in Figure 9, these conductors are located above, or at, the Sundown sill (Middle Aldridge) and at least two of the conductors appear to be spatially associated with faults (i.e., shallow conduits).
4. Line MM2 has a number of small apparent conductors and a possible conduit on the east.
5. Lines SPes and SPns display a moderately strong conductor at 2-3 km below sea level as well as numerous apparent shallow conduits.

Taken together, these results have allowed the identification and enhancement of a number of anomalous areas in the Moyie anticline even though the area has been actively explored for more than 100 years.

10.0 References

- Anderson, D. 1991. Diamond drilling report: CANAM property, British Columbia Ministry of Energy and Mines, Assessment Report 21786, 23 pp.
- Boucher and Thomson, 2019. Assessment report on Magnetotelluric (MT) geophysics at the Sweet Spot mineral tenure, British Columbia Ministry of Energy and Mines, Assessment Report 37386, 170pp.
- Brown, D. and Macleod, R. F. 2011. Geology, Yahk River, British Columbia, Geological Survey of Canada, Open File 6304, scale 1:50,000.
- Brown, D. A., Macleod, R. F., Wagner, C. L., and Chow, W. 2011, Geology, Moyie Lake, British Columbia, Geological Survey of Canada, Open File 6303, scale 1:50,000.
- Cook, F. 2019. Analyses of Digitized Airborne Magnetic Data and VLF-EM Data on the Leaky Pipe Property, Southeastern British Columbia, British Columbia Ministry of Energy and Mines, Assessment Report, 31pp.
- Cook, F. and Van der Velden, A. 1995. Three dimensional crustal structure of the Purcell Anticlinorium of Southwestern Canada, Geological Society of America Bulletin, v. 107, p. 642-664.
- Glombick, P., Brown, D. A., and Macleod, R. F., 2010. Geology, Yahk, British Columbia, Geological Survey of Canada, Open File 6153, scale 1:50,000.
- Gupta, J. and A. Jones, 1995. Electrical conductivity structure of the Purcell Anticlinorium in southeast British Columbia and northwest Montana, Canadian Journal of Earth Sciences, v. 23, p. 1564-1583.
- Heinson, G., Didana, Y., Soeffky, P., Thiel, S., and Wise, T. 2018. The crustal geophysical signature of a world-class magmatic mineral system. Scientific Reports, v. 8, 10608 (2018). <https://doi.org/10.1038/s41598-018-29016-2>
- Kennedy, S. 2018. Assessment report for diamond drilling: Silver Fox Property, British Columbia Ministry of Energy and Mines, Assessment Report 37418, 177pp.
- Smith, A. 1948. Report and geological maps submitted for assessment work on the Moyie groups 1-6 and the ML #55 M. C., British Columbia Ministry of Energy and Mines, Assessment Report 0001.

11.0 Statement of Costs

Moyie Anticline Geophysics 2021 - 2022		Days			Totals
Personnel (Name)* / Position	Field Days (list actual days)	Days	Rate	Subtotal*	
Fred Cook/Geoscientist	Oct 29, 30, 31,	3	\$840.00	\$2,520.00	
				\$2,520.00	\$2,520.00
Office Studies	List Personnel (note - Office only, do not include field days)				
Program Preparation	Fred Cook Sep 2, 4,	2.0	\$840.00	\$1,680.00	
Report preparation	Fred Cook	1.0	\$3,150.00	\$3,150.00	
Data Management/Analyses	Fred Cook Feb 10 - April 22	9.0	\$840.00	\$7,560.00	
				\$12,390.00	\$12,390.00
Ground geophysics	Line Kilometres / Enter total amount invoiced list personn		\$0.00	\$0.00	
MT Survey	Complete MT Solutions - All in Costs	1.0	\$275,310.00	\$275,310.00	
2D Inversion MT Data	Complete MT Solutions	1.0	\$18,375.00	\$18,375.00	
Analyses of Feild Data	Complete MT Solutions	1.0	\$14,175.00	\$14,175.00	
				\$307,860.00	\$307,860.00
Accommodation & Food	Rates per day				
Travel & L/O	Fred Cook Oct 28, Nov 7, Apr 19, 23	4.0	\$840.00	\$3,360.00	
	Flights/Accommodations/Meals	1.0	\$1,953.09	\$1,953.09	
				\$5,313.09	\$5,313.09
<i>Subtotal</i>					\$328,083.09
15% Administration Fee on Subtotal				\$49,212.46	\$49,212.46
TOTAL Expenditures					\$377,295.55

12.0 Statement of Qualifications

I, **Frederick A. Cook** do hereby certify that:

I attained the degree of Doctor of Philosophy (Ph.D.) in geophysics from Cornell University in Ithaca, New York in 1981.

I have a B.Sc. in geology (1973) and an MSc. in Geophysics (1975) from the University of Wyoming in Laramie, Wyoming.

I am a registered member of the Association of Professional Engineers and Geoscientists of British Columbia (P. Geo. 2009). Previously, from 1984-2009, I was registered with the Association of Professional Engineers, Geologists and Geophysicists of Alberta as both a P. Geol. and a P. Goph.

I am a member of the American Geophysical Union and the Geological Society of America.

In 2011 I was awarded the J. Tuzo Wilson medal from the Canadian Geophysical Union.

I have worked as a geophysicist/geologist for a total of 45 years since my graduation from university.

I have worked for the Continental Oil Company (1975-1977) and the University of Calgary (1982-2010).

I was the Director of the Lithoprobe Seismic Processing Facility at the University of Calgary from 1987-2003.

In 2011 I was appointed an International Consultant for the Chinese SinoProbe project.

I have a thorough knowledge of the geology and geophysics of southern British Columbia based on extensive geological and geophysical fieldwork.

I have authored more than 125 scholarly publications in peer-reviewed journals and books.

I am the author of this report.

I am not aware of any material fact or material change with respect to the subject matter of this report, which is not reflected in this report.

“signed and sealed” at Salt Spring Island, B.C.

Frederick A. Cook, P. Geo.

Salt Spring Imaging, Ltd

128 Trincomali Heights

Salt Spring Island, B.C. V8K1M8

Dated at Salt Spring Island, B.C. this 10th day of July, 2022

Registration License No. 34585

Association of Professional Engineers and Geoscientists of British Columbia

Appendix 1: Acquisition Report - CMTS



**COMPLETE MT
SOLUTIONS**

CMTS Contract CMTS-2021-KootenayResources

Report CMTS-2021- KootenayResources-R1

Logistics Report: Acquisition of magnetotelluric
data in SW BC

for

Kootenay Resources Inc.

Ms. Jessica Spratt, M.Sc.

Dr. Alan G. Jones, P.Geo.

6th December, 2021

TABLE OF CONTENTS

EXECUTIVE SUMMARY2

1. INTRODUCTION.....3

2. SURVEY LOGISTICS4

2.1. SURVEY PRODUCTION SUMMARY4

2.2. MOOMBARRIGA PERSONNEL.....4

2.3. HEALTH AND SAFETY PROTOCOLS5

2.3.1. RISK ASSESSMENT AND CONTROL5

3. SURVEY DETAILS6

3.1. EQUIPMENT AND INSTRUMENTATION6

3.2. SITE LAYOUT7

3.3. INSTALLATION MEASUREMENTS AND NOTES7

3.4. PROCESSING PARAMETERS.....7

3.4.1. CALIBRATION FILES7

3.4.2. K- INDEX8

3.4.3. REMOTE REFERENCING.....8

3.5. COMMENTS ON MT DATA RESPONSES9

4. DECLARATIONS AND SIGNATURE10

REFERENCES11

Executive Summary

On a sub-contract from Complete MT Solutions Inc. (“CMTS”), Moombarriga Canada Inc., the Canadian arm of Moombarriga Geoscience, “MGS”), undertook acquisition of very broadband magnetotelluric (MT) data at a total of 84 locations in the southern Kootenays, British Columbia.

The general data quality is excellent, and there were no serious impediments to operations.

1. Introduction

Moombarriga Canada Inc (the Canadian arm of Moombarriga Geoscience, “MGS”) was sub-contracted by Complete MT Solutions Inc (“CMTS”) to undertake the acquisition of audio (AMT) and broadband (MT) magnetotelluric data in the southern Kootenays of British Columbia for Kootenay Resources Inc.

This report presents the logistical operations of the Kootenay MT survey completed for Kootenay Resources Inc from October 29th to November 26th throughout the southern Kootenay region.

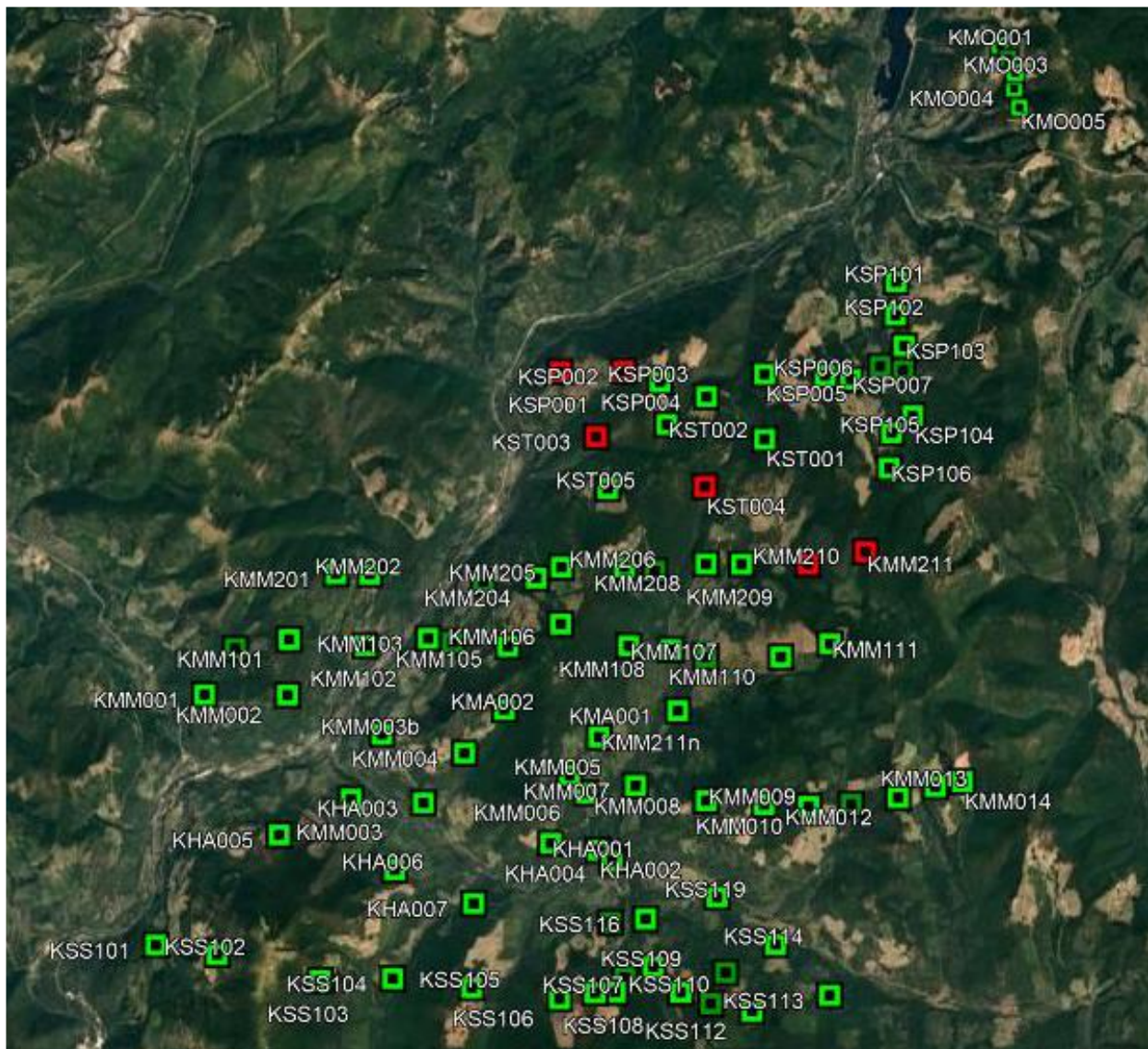


Figure 1: MT sites locations in the southern Kootenay region. Red sites are those that were planned but which could not be accessed.

Magnetotelluric data were acquired at the sites shown in Figure 1. The red sites on the figure denote those that were planned but which could not be accessed.

2. Survey Logistics

Survey base of operations was in Cranbrook, B.C. Access to survey locations was primarily by with minimal installation by foot. Survey site locations were provided by client prior to survey execution in both UTM as well as latitude and longitude coordinates. Sites were acquired in geomagnetic coordinates and processed to geographic coordinates, the survey area declination is 13.8 degrees.

2.1. Survey Production Summary

Details of the survey production are shown in Appendix A. Duration of the survey was from October 29th to November 30th for a total of 32 survey days. These included 4 scheduled days off, 0 weather days, and all equipment testing, preparation and arranging shipping.

A total of 86 sites were acquired. Five (5) of the initial site locations were deemed inaccessible due to road conditions and were all relocated at the client's request.

2.2. Moombarriga Personnel

Project Manager:	Jessica Spratt
Field/Operations Manager:	Jessica Spratt
	Thomas Pegg
Data Processor (s):	Jessica Spratt
MT Operators (s):	Thomas Pegg
	Toby Richards
	Erhan Erdogan
	Caroline Finateau
Field Technicians (s):	Jason Leus
	Rosanna Wijenberg
	Grace Stewart
	Onur Uyar

2.3. Health and Safety Protocols

MGS is committed to achieving the highest standards in occupational health and safety (OHS) with the aim of sustaining a safe and health working environment.

In achieving this, MGS will continue to:

- incorporate the OHS Management System as the foundation for the management of occupational health and safety across the organisational operational activities;
- consult with employees in the development and improvement of OHS policies, procedures and work instructions, wherever practicable;
- provide employees with the necessary information, instruction, training and supervision to enable them to work in a safe and healthy manner;
- enable team leaders and employees to undertake their work safely and hold them accountable for their area of responsibility;
- ensure hazards are identified, risk assessed and controlled in a timely and effective manner;
- comply with all applicable OHS and injury management legislation, standards and guidance in codes of practice as applies to our operational activities;
- expect that all persons at the workplace, including contractors and visitors, abide by our policies and procedures that have been created in the interest of occupational health and safety;
- communicate openly with employees and others about OHS.

Upon arrival in the field survey area, one person was designated as health and safety representative. Jason Leus, Rosanna Wijenberg, and Grace Stewart are all local residents and volunteer firefighters with experience in remote safety procedures particular to the BC forest and mountain terranes.

2.3.1. *Risk Assessment and Control*

Prior to mobilization, MGS compiled a risk assessment for the proposed survey and all tasks involved in conducting the work. Job Safety Analyses (JSA) were generated and discussed defining safe work procedures based on the risk assessment.

2.3.1.1. *In field procedures*

All personnel were equipped with any personal protective equipment (PPE) required for the work.

Daily “toolbox” morning safety meetings of all in field MGS personnel were conducted prior to commencement of work to review safe work procedures and discuss any prior incidents, daily plans and potential hazards.

All vehicles were equipped with first aid kits, fire extinguishers, radios, navigational aids, and satellite phones.

Vehicle and trailer circle checks were completed by drivers prior to departure.

3. Survey Details

3.1. Equipment and Instrumentation

The data were acquiring using Phoenix built MTU-5C recording instruments (see http://umt.phoenix-geophysics.com/pdf/MTU-5C_brochure.pdf for product details).

The horizontal magnetic field components were measured using Phoenix MTC-150 coils and the vertical field was measured using Phoenix MTC-180 coils (see <http://mtc-100-series.phoenix-geophysics.com/> for product specifications).

Newly constructed electrodes (either made by Moombarriga Geosciences or provided by Phoenix Geophysics) were used to acquire the electric field components.

Table 1 lists the serial numbers for each sensor and recording unit.

Type	Owner	Serial #	Cals
MTC-150	Phoenix	57240	Yes
MTC-150	Phoenix	57241	Yes
MTC-150	Phoenix	57243	Yes
MTC-150	Phoenix	57254	Yes
MTC-150	Moombarriga	57199	Yes
MTC-150	Moombarriga	57209	Yes
MTC-150	Moombarriga	57218	Yes
MTC-150	Moombarriga	57226	Yes
MTC-150	Moombarriga	57236	Yes
MTC-150	Moombarriga	57246	Yes
MTC-180	Phoenix	53318	Yes
MTC-180	Phoenix	53334	Yes
MTC-180	Moombarriga	53313	Yes
MTC-180	Moombarriga	53314	Yes
MTC-180	Moombarriga	53317	Yes
MTU-5C	Phoenix	10124	Yes
MTU-5C	Phoenix	10467	Yes
MTU-5C	Moombarriga	10127	Yes
MTU-5C	Moombarriga	15019	Yes

MTU-5C	Moombarriga	15025	Yes
--------	-------------	-------	-----

Table 1: List of equipment used on survey.

3.2. Site Layout

Three orthogonal components of the magnetic field (H_x , H_y , H_z) and two horizontal components of the electric field (E_x , E_y) comprise the principle measurements of each site and will be laid out as shown in the schematic of Figure 2.

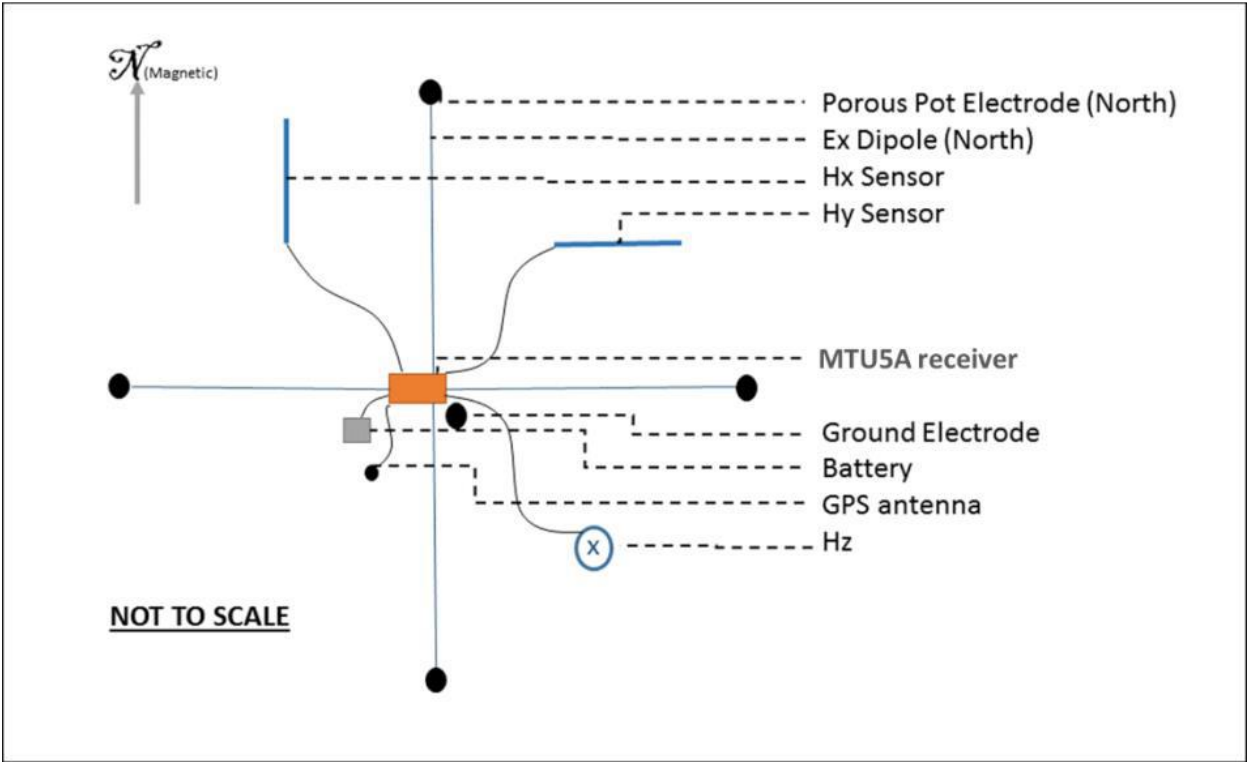


Figure 2: MT site layout.

3.3. Installation Measurements and Notes

Sites were installed as close to the requested site locations as possible. Where possible e-line dipole lengths of 100m were used; however steep terrane, road access and thick forest limited the maximum e-line lengths. The data recorded for 2 seconds at 24000 samples/s every 30 seconds and recorded continuously at 150 samples/s. The sites were installed for at least 1 night of recording at each location. Appendix B gives the measured and recorded layout details for each site acquired.

3.4. Processing Parameters

3.4.1. Calibration files

Each of the MTU-5C recording units and magnetic field sensors were calibrated in the field prior to recording data. The coil calibrations were performed at the site location for KSP101, latitude

49.21504 N and longitude 115.83914 W. The calibration curves for each type are shown in Appendix C. The field derived calibration files were used for processing all sites in the survey.

3.4.2. *K-Index*

The K-index is a measure of average low frequency (<8 Hz) geomagnetic activity. Figure 3 shows the K-index for each day of acquisition during the Southern Kootenay MT survey.

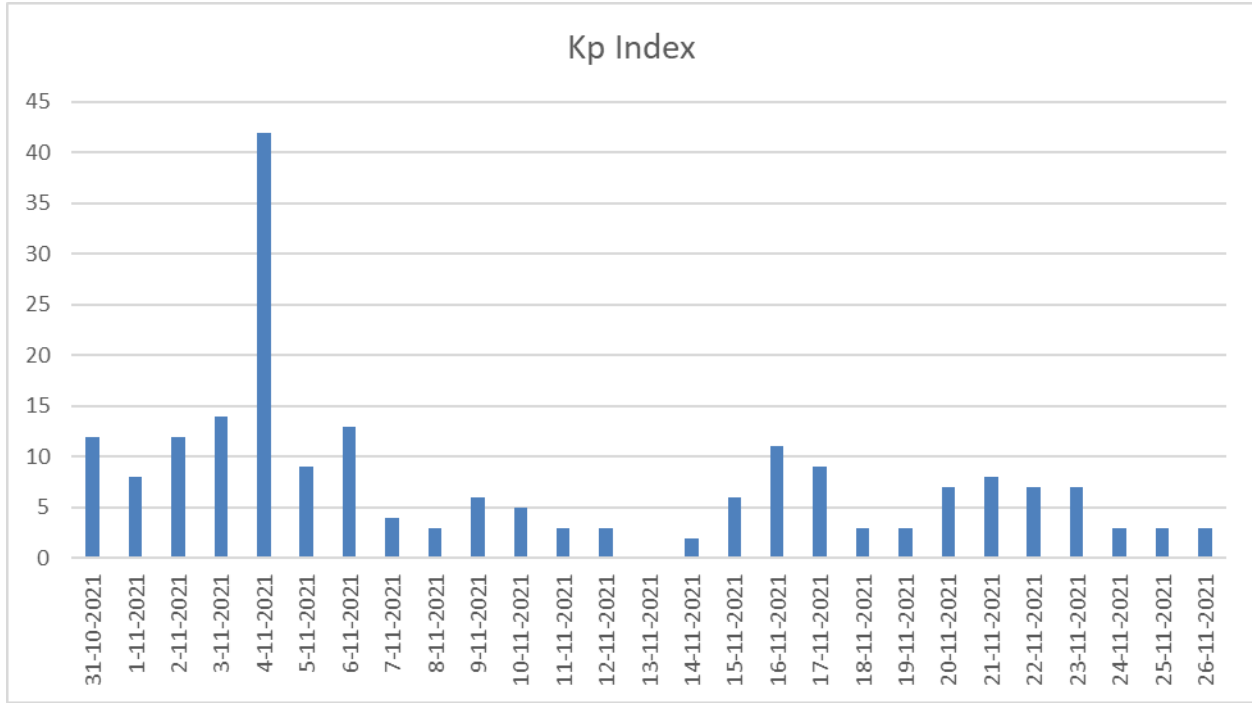


Figure 3: K-index during acquisition of MT data.

3.4.3. *Remote referencing*

Due to the relatively large survey area for AMT acquisition (~ 25 x 25 km) and the overall quiet locations for the sites, in discussion with the client, we opted to have a moving remote reference site rather than a permanent location. Table 2 shows the remote reference site used in the data processing.

Kootenay Silver (Southern BC-2021) MT Data Processing Table

Site ID	Date		EDI	Site ID	Date		EDI
	Acquired	Processed	Remote site		Acquired	Processed	Remote site
KHA004	02-Nov-21	06-Nov-21	KSP103H	KMM006	15-Nov-21	17-Nov-21	KSS109H
KMM012	03-Nov-21	04-Nov-21	KMM014	KMM007	15-Nov-21	17-Nov-21	KSS109H
KMM013	03-Nov-21	04-Nov-21	KSP101BH	KHA003	16-Nov-21	18-Nov-21	KHA003H
KMM014	03-Nov-21	05-Nov-21	KSP101BH	KSS116	16-Nov-21	18-Nov-21	KHA003H
KMM104	08-Nov-21	10-Nov-21	KST001RH	KHA001	16-Nov-21	18-Nov-21	KSS116E

KMM203	09-Nov-21	09-Nov-21	KST001RH	KSS119	16-Nov-21	18-Nov-21	KHA003H
KMM204	09-Nov-21	09-Nov-21	KST001RH	KMM107	17-Nov-21	18-Nov-21	KMM009E
KMM205	08-Nov-21	08-Nov-21	KSP004H	KMM009	17-Nov-21	18-Nov-21	KMM206H
KSP003	07-Nov-21	08-Nov-21	KSS115H	KMM008	17-Nov-21	18-Nov-21	KMM206E
KSP004	08-Nov-21	08-Nov-21	KMM205H	KMM206	17-Nov-21	18-Nov-21	KMM009E
KSP005	05-Nov-21	06-Nov-21	KSP006H	KMM207	18-Nov-21	19-Nov-21	KMM011H
KSP006	05-Nov-21	06-Nov-21	KSS112H	KMM010	18-Nov-21	19-Nov-21	KMM207H
KSP007	09-Nov-21	10-Nov-21	KMM204H	KMM005	18-Nov-21	19-Nov-21	KMM011J
KSP009	04-Nov-21	05-Nov-21	KSS114H	KMM011	18-Nov-21	21-Nov-21	KMM005H
KSP101	02-Nov-21	05-Nov-21	KHA004H	KMM211B	20-Nov-21	21-Nov-21	KMO002H
KSP102	04-Nov-21	05-Nov-21	KSS114H	MTO002	20-Nov-21	23-Nov-21	KMM211BH
KSP103	02-Nov-21	21-Nov-05	KHA004H	MTO004	20-Nov-21	22-Nov-21	KMM211BH
KSS110	07-Nov-21	08-Nov-21	KST002H	MTO005	20-Nov-21	22-Nov-21	KMM211BH
KSS111	06-Nov-21	08-Nov-21	KST002H	MTO001	22-Nov-21	23-Nov-21	KSS103H
KSS112	05-Nov-21	06-Nov-21	KSP006H	MTO003	21-Nov-21	22-Nov-21	KSS117E
KSS113	05-Nov-21	06-Nov-21	KSP006H	KHA002	21-Nov-21	22-Nov-21	KSS117H
KSS114	04-Nov-21	05-Nov-21	KSP009H	KMM001	21-Nov-21	22-Nov-21	KHA002H
KSS115	07-Nov-21	08-Nov-21	KST002H	KSS117	21-Nov-21	22-Nov-21	KHA002E
KST001R	09-Nov-21	10-Nov-21	KMM204H	KSS103	22-Nov-21	23-Nov-21	KMO001RH
KST002	07-Nov-21	07-Nov-21	KSP003H	KMM101	22-Nov-21	23-Nov-21	KSS013H
KST005	08-Nov-21	08-Nov-21	KSP004H	KMO001	22-Nov-21	23-Nov-21	KSS103H
KSP105	10-Nov-21	11-Nov-21	KMM106E	KSS102	23-Nov-21	24-Nov-21	KMM202H
KSP106	10-Nov-21	11-Nov-21	KMM105H	KMM201	23-Nov-21	24-Nov-21	KSS102H
KMM106	10-Nov-21	11-Nov-21	KSP106H	KMM002	24-Nov-21	25-Nov-21	KMM004H
KMM105	10-Nov-21	11-Nov-21	KSP105H	KMM004	24-Nov-21	25-Nov-21	KMM002H
KMM003b	10-Nov-21	11-Nov-21	KSP106H	KMM202	23-Nov-21	24-Nov-21	KSS102H
KMM110	11-Nov-21	12-Nov-21	KSP008H	KSS104	24-Nov-21	25-Nov-21	KMM202H
KMM111	11-Nov-21	12-Nov-21	KSP008H	KMM102	24-Nov-21	25-Nov-21	KMM004E
KSP008	11-Nov-21	12-Nov-21	KMM111H	KHA005	25-Nov-21	26-Nov-21	KHA007H
KSP104	11-Nov-21	12-Nov-21	KMM111H	KMA002	25-Nov-21	27-Nov-21	KSS101H
KMM209	13-Nov-21	15-Nov-21	KSS107H	KSS101	25-Nov-21	27-Nov-21	KMA002H
KMM108	14-Nov-21	15-Nov-21	KSS118H	KHA007	25-Nov-21	27-Nov-21	KMM210H
KSS106	13-Nov-21	15-Nov-21	KMM109H	KMM210	25-Nov-21	27-Nov-21	KMA002H
KSS107	13-Nov-21	15-Nov-21	KMM109H	KMM103	26-Nov-21	29-Nov-21	KSS105H
KSS108	14-Nov-21	15-Nov-21	KMA001H	KHA006	26-Nov-21	29-Nov-21	KSS105H
KSS118	14-Nov-21	15-Nov-21	KMM208H	KMM003	26-Nov-21	29-Nov-21	KSS105H
KMM208	14-Nov-21	15-Nov-21	KSS108H	KSS105	26-Nov-21	29-Nov-21	KMM103H
KMA001	14-Nov-21	15-Nov-21	KSS118H	KMO003	21-Nov-21	22-Nov-21	KSS117E
KMM109	13-Nov-21	15-Nov-21	KSS107H				

Table 2: Remote reference site used for data processing.

4. Declarations and Signature

I, Jessica Spratt, do hereby certify that:

- I am a Senior Geophysicist with residence in Wakefield, Quebec and I am presently working in this capacity as Director of Moombarriga Canada Inc. of Ottawa Ontario; responsible for data acquisition.
- I obtained a B.Sc. (Hons, Geology, Carleton University, Ottawa Canada) in 1998, an M.Sc. (Applied Geophysics, Syracuse University, New York) in 2004
- I have derived the results presented in this report without consultation with any other person or persons, except for Alan Jones of CMTS and Shane Evans of Moombarriga Geosciences.
- I have no interest, nor do I expect to receive any interest in the properties or securities of Kootenay Resources Inc., its subsidiaries, or its joint-venture partners.

Signed:

A handwritten signature in black ink, appearing to read 'J. Spratt', written in a cursive style.


Jessica Spratt
Complete MT Solutions Inc.

I, Alan G. Jones, do hereby certify that:

- I am a Senior Geophysicist with residence in Ottawa, Ontario and I am presently working in this capacity as President and Managing Director of Complete MT Solutions Ltd. of Ottawa, Ontario and President and Managing Director of ManoTick GeoSolutions Ltd. of Ottawa, Ontario and Vice-President of Moombarriga Canada Ltd. of Ottawa, Ontario;
- I obtained a B.Sc. in Hons. Physics at the Univ. Nottingham, England in 1972, an M.Sc. in Applied Geophysics at the Univ. Birmingham, England in 1973, and a Ph.D. in Geophysics at the Univ. Edinburgh, Scotland in 1977;
- I undertook PostDoctoral Fellowships in Germany at the Univ. Munster from 1977 to mid-1981, in Sweden at the Swedish Geological Survey in 1981, and in Canada at the Univ. Toronto in 1982-1983;

- I subsequently joined the Geological Survey of Canada (Ottawa) in 1984 to 2003, rising from Research Scientist RES-2 level to Senior Research Scientist RES-5 level (the top level in the Canadian Government).
- I then became the Senior Professor and Head of Geophysics at the Dublin Institute for Advanced Sciences from 2004 to January, 2015.
- I am a registered geophysicist and a member in good standing with a license to practice in the Province of Ontario (PGO member #2790);
- I have been awarded academic distinction in Canada (J. Tuzo Wilson medal, Canadian Geophysical Union, 2006), in the USA (Fellow, American Geophysical Union, 2019), in Ireland (Member, Royal Irish Academy, 2010), in Europe (Member, Academia Europaea, 2010), in China (International Member, Geo-Electromagnetism Committee, Chinese Geophysical Society, 2009), and in South Africa (Life Affiliate member, Geological Society of South Africa, 2016).
- I am also a member of the Society of Exploration Geophysicists (SEG) and the Canadian Exploration Geophysical Society (KEGS);
- I have reviewed and approve the results presented in this report, and have done so without consultation with any other person or persons, except for Jessica Spratt;
- I have no interest, nor do I expect to receive any interest in the properties or securities of Kootenay Resources Inc., its subsidiaries, or its joint-venture partners.

Signed:



Alan G. Jones, Ph.D., P.Geo. (PGO #2790)
President, Complete MT Solutions Inc.

Appendix 2: Inversion Report - CMTS



**COMPLETE MT
SOLUTIONS**

CMTS Contract CMTS-2021-Kootenay
Resources
Report CMTS-2021-KootenayResources-R3
2D modelling of MT data in the Southern
Kootenays
for
Kootenay Resources Inc.

Ms. Jessica Spratt, M.Sc.

Dr. Alan G. Jones, P.Geo.

23rd March 2022

FINAL

Table of Contents

EXECUTIVE SUMMARY	5
1. INTRODUCTION	5
1.1. PRIMARY AND SECONDARY TARGET DEPTHS	6
1.2. EXISTING DATA	6
1.3. COMPARISONS OF NEW AND OLD DATA	7
1.3.1. KSP104 AND 86D003	7
1.3.2. KSP105 AND 86D003	11
1.3.3. KMO004 AND DUN711	13
1.3.4. KSS106 AND SS_14	16
1.3.5. KSS108 AND SS_32	18
1.4. PROFILES	20
1.5. EXISTING MODELS	22
2. NEW ACQUISITION	23
2.1. CONTACT RESISTANCES	23
2.2. DC VALUES	27
2.3. AC VALUES	28
3. MT QUALITY FACTORS	28
3.1. QF PLOTS	29
3.1.1. CHANGE OF QF WITH SURVEY TIME	38
3.2. EXAMPLE SITES	40
3.2.1. EXAMPLE OF EXCELLENT QUALITY SITES, QF = 1.00 – 1.25	40
3.2.2. EXAMPLE OF VERY HIGH-QUALITY SITES, QF = 1.25 – 1.50	41
3.2.3. EXAMPLE OF HIGH QUALITY SITES, QF = 1.5 – 2.0	41
3.2.4. EXAMPLE OF GOOD TO MEDIUM QUALITY SITES, QF = 2.0 – 3.0	42
3.2.5. EXAMPLE OF MEDIOCRE QUALITY SITES, QF = 3.0 – 4.25	43
3.3. QF CF. ELECTRODE ARRAY PARAMETERS	45
3.4. QF CONCLUSIONS	47
4. TIPPER QUALITY FACTORS	48
5. AVERAGE RHOA/PHA CURVES	50

6.	QUALITATIVE IMAGES	53
6.1.	FREQUENCIES FOR PRIMARY DEPTHS OF INVESTIGATION	53
6.2.	DEPTHS OF PENETRATION FOR VARIOUS FREQUENCIES	55
6.3.	APPROXIMATE RESISTIVITY IMAGES FOR VARIOUS DEPTHS	57
6.4.	QUALITATIVE DIMENSIONALITY PLOTS	61
7.	GEOELECTRICAL STRIKE – PHASE TENSORS	63
7.1.	PHASE TENSOR DIMENSIONALITY	64
7.2.	PHASE TENSOR DIRECTIONALITY	65
8.	VERTICAL FIELD TRANSFER FUNCTIONS	66
8.1.	INDUCTION VECTORS	66
8.2.	TIPPER MAGNITUDE	67
8.3.	INDUCTION VECTOR AND TIPPER PLOTS	67
9.	STRIKE DECOMPOSITION	71
9.1.	SINGLE SITE ANALYSES	73
9.1.1.	SINGLE-SITE, DECADE-WIDE BANDS	73
9.1.2.	SINGLE-SITE, SINGLE FREQUENCY BANDS	76
9.1.2.1.	10 kHz – 3 Hz	77
9.1.2.2.	800 Hz – 8 Hz	79
9.1.3.	SINGLE-SITE: MISFIT SENSITIVITY WITH STRIKE DIRECTION	80
9.1.4.	SINGLE-SITE: CONCLUSIONS	83
9.2.	MULTI-SITE BY PROFILE	83
9.2.1.	PROFILE MM1	83
9.2.1.1.	Whole profile analysis	84
9.2.1.2.	Lateral variation along profile	85
9.2.1.3.	Imposed strike directions – N10E and N35W	86
9.2.1.4.	Conclusions	87
9.2.2.	PROFILE MO	88
9.2.3.	PROFILE SS	92
9.2.4.	PROFILE MM0	93
9.2.5.	PROFILE MM2	94
9.2.6.	PROFILE SP-EW	95
9.2.7.	PROFILE SP-NS	97
9.2.8.	AREA SP: PROFILES SP-NS & SP-EW TAKEN TOGETHER	97
9.2.8.1.	High frequencies: 10 kHz – 3 Hz	98

9.2.8.2.	Low frequencies: 3 Hz – 0.01 Hz	98
9.2.8.3.	All frequencies: 10 kHz – 0.01 Hz	98
9.2.9.	AREA SOUTH	99
9.2.9.1.	High frequency robust fitting	102
9.2.9.2.	Low frequency robust fitting	102
9.2.10.	PROFILE AND AREA STRIKE DIRECTIONS: CONCLUSIONS	103
9.3.	STRIKE: CONCLUSIONS	104
9.4.	CORRECTION FOR LOCAL SITE ANISOTROPY	104
10.	<u>RHO⁺ CONSISTENCY CHECK</u>	105
11.	<u>CONCLUSIONS</u>	107
12.	<u>RECOMMENDATIONS</u>	108
13.	<u>DELIVERABLES</u>	108
14.	<u>DECLARATION AND SIGNATURE</u>	108
15.	<u>REFERENCES</u>	110
16.	<u>APPENDIX A: MT ACQUISITION EQUIPMENT</u>	113
16.1.	RECORDERS	113
16.2.	MAGNETIC SENSORS	113
16.3.	ELECTRODES	114
16.3.1.	GENERAL	114
16.3.2.	ELECTRODES AND ELECTRODE ARRAY	115
16.3.3.	ELECTRIC ARRAY MEASUREMENTS	115
17.	<u>APPENDIX B: AMT DEADBAND</u>	117
18.	<u>APPENDIX C: QUALITY FACTORS DETERMINATION</u>	118
18.1.	MT QUALITY FACTORS	118
18.2.	TIPPER QUALITY FACTORS	120

Executive Summary

Newly-acquired data in the Kootenays were analysed together with older (1980s vintage) existing data from Duncan Oil. Quantec data along the southernmost profile give responses that are not consistent with the newly-acquired ones, especially for the diagonal terms (XX and YY), so are not used.

Generally the response estimates of the newly-acquired are of high quality, except for estimates in the AMT deadband (4 kHz – 900 Hz) and the MT deadband (10 Hz – 0.1 Hz) during times of low signal. Appropriate error floors are 3.5% in RhoA and 1° in Pha.

Consideration of depth penetration shows that the estimates from 10 kHz – 3 Hz optimally sense the depths of primary interest (to 4 km), and lower frequencies (3 Hz – 0.001 Hz) sense down to the base of the crust.

Some areas of interest are inferred from the qualitative maps of phases, resistivities and induction vectors.

The data can be inverted in 2-D but with varying strike direction for the high and low frequencies, and with larger error floors.

3-D inversion is recommended for the southern sites.

1. Introduction

Complete MT Solutions Inc. (“CMTS”) was contracted by Kootenay Resources Inc. (“Kootenay” or “client”) to acquire and process new data, and to analyse and model the new data together with existing data at locations shown in Figure 1.

The new data were acquired for the client under sub-contract by Moombarriga Canada Ltd. of Ottawa, a subsidiary of Moombarriga Geoscience Pty. Ltd. of Perth, Australia. Data were acquired at eighty-six (86) locations, (red circles in Figure 1). as described in report CMTS-2021-KootenayResources-R1. Direction during fieldwork was through daily contact with the client’s representative, Professor Fred Cook (“Cook” or “client’s representative”).

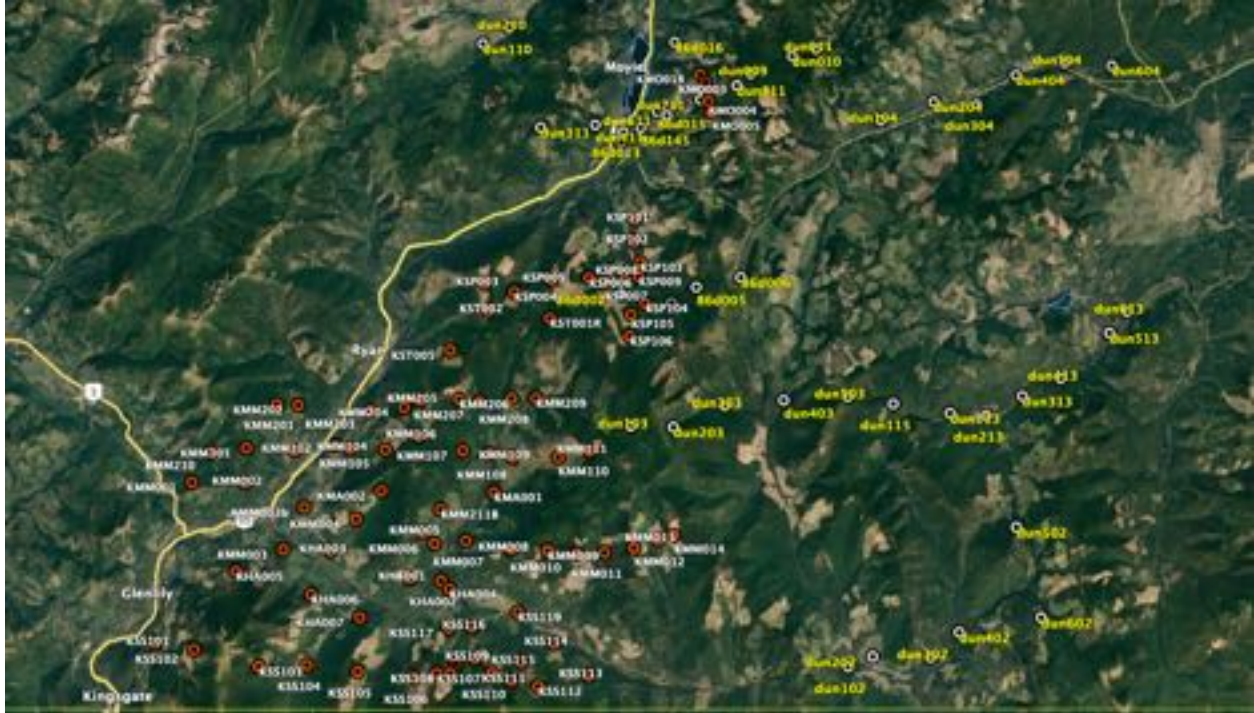


Figure 1: New MT data acquired for the client (red circles, white names). Also shown are the locations of existing data (white circles, yellow names).

1.1. Primary and Secondary target depths

As per the email from Fred Cook on 7th Nov, 2021:

“The primary target depth has to be the upper 2-4 km as that represents drilling depths.

We are also trying to image conduits in order to link them to conductors/showings near the surface. So, deeper information (middle to lower crust) will also be valuable.”

1.2. Existing data

In addition, existing data were included for consideration. These comprised two separate sets of data.

First, high-quality MT data in southeastern British Columbia were collected in 1985 (sites named “dunxxx”) and 1986 (sites named “86dxxx”) by Phoenix Geophysics Ltd. for Duncan Exploration Co. (Denver, Colo.). The locations are denoted by white circles in Figure 1. These data were donated to the Lithoprobe project by Duncan Exploration, and are now in the public domain. These data, and data over the Purcell Anticlinorium in the adjacent U.S.A., were analysed and modelled previously by Gupta and Jones (1995).

Second, a 5 km dense, high-resolution profile of 46 stations was acquired by Quantec Geoscience Ltd. (“Quantec”) for Teck Resources just north of the Canada/US border. These are named “SS_xx”, and were made available to Kootenay Resources.



1.3. Comparisons of new and old data

1.3.1. *KSP104 and 86d003*

The centres of new site KSP104 and Duncan site 86d003 are 240 m apart (Figure 2). Side-by-side comparisons of the two are shown in the upper row of Figure 3, and an overlap of them on top of each other in the lower row of Figure 3, with “1” being KSP104 and “2” being 86d003.

Both sets of estimates were derived using Phoenix equipment and Phoenix processing, but the equipment used in 2021 was very different from the MT-16 system used in 1986. Also, the new hybrid coils were used in 2021 whereas the older broadband MTC50 coils were used in 1986. The processing was essentially the same though. Note that site 86d003 only has estimates to 384 Hz as Phoenix did not have AMT acquisition until the very late-1980s.

There is visually significant differences between the two sets of estimates. But clearly there are significant galvanic distortions on both sets of data. The KSP104 PhaYX goes out of quadrant at frequencies <1 Hz.

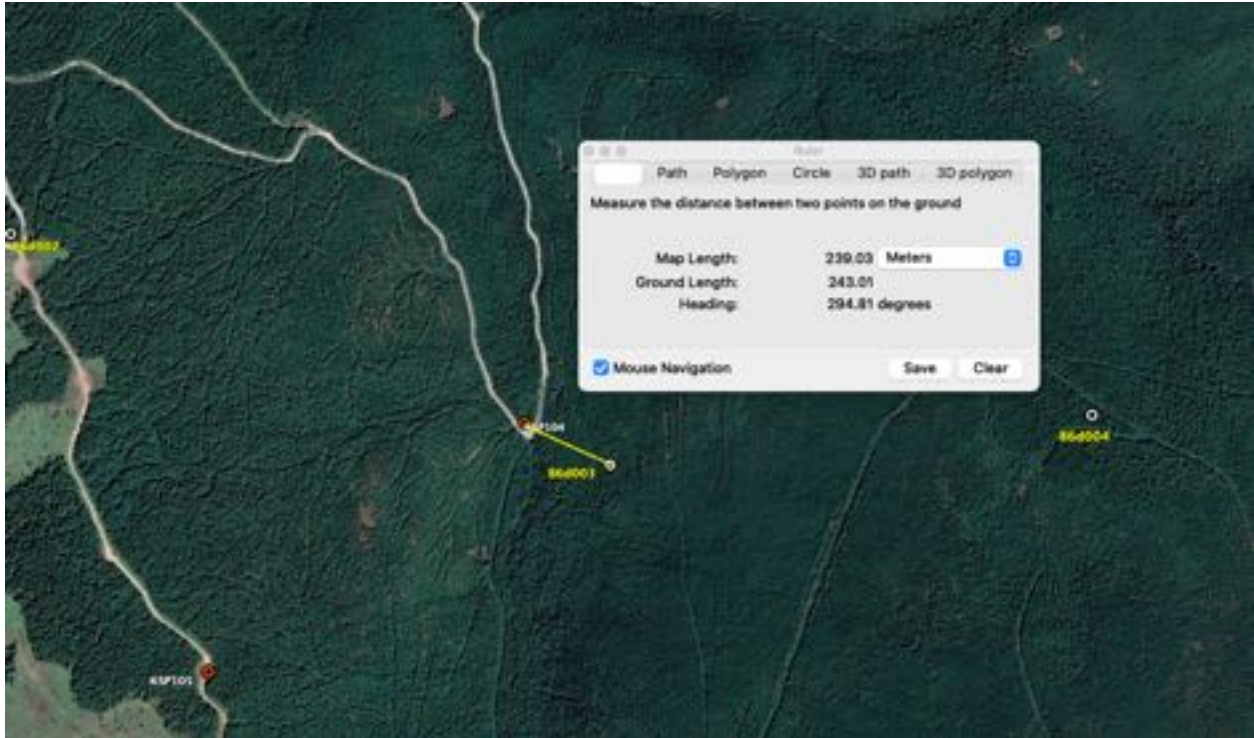
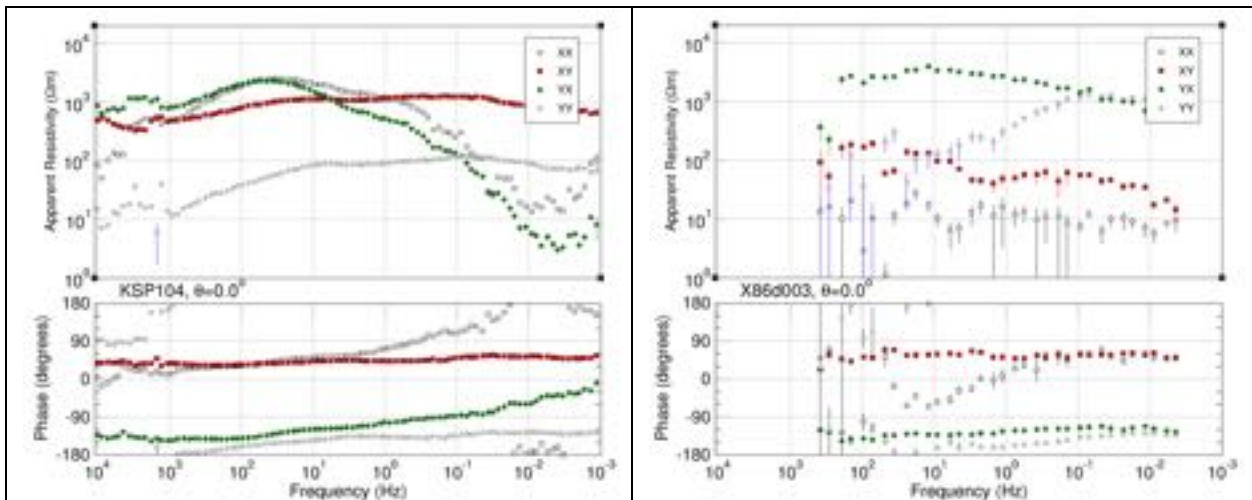


Figure 2: Locations of new site KSP104 and existing Duncan site 86d003.



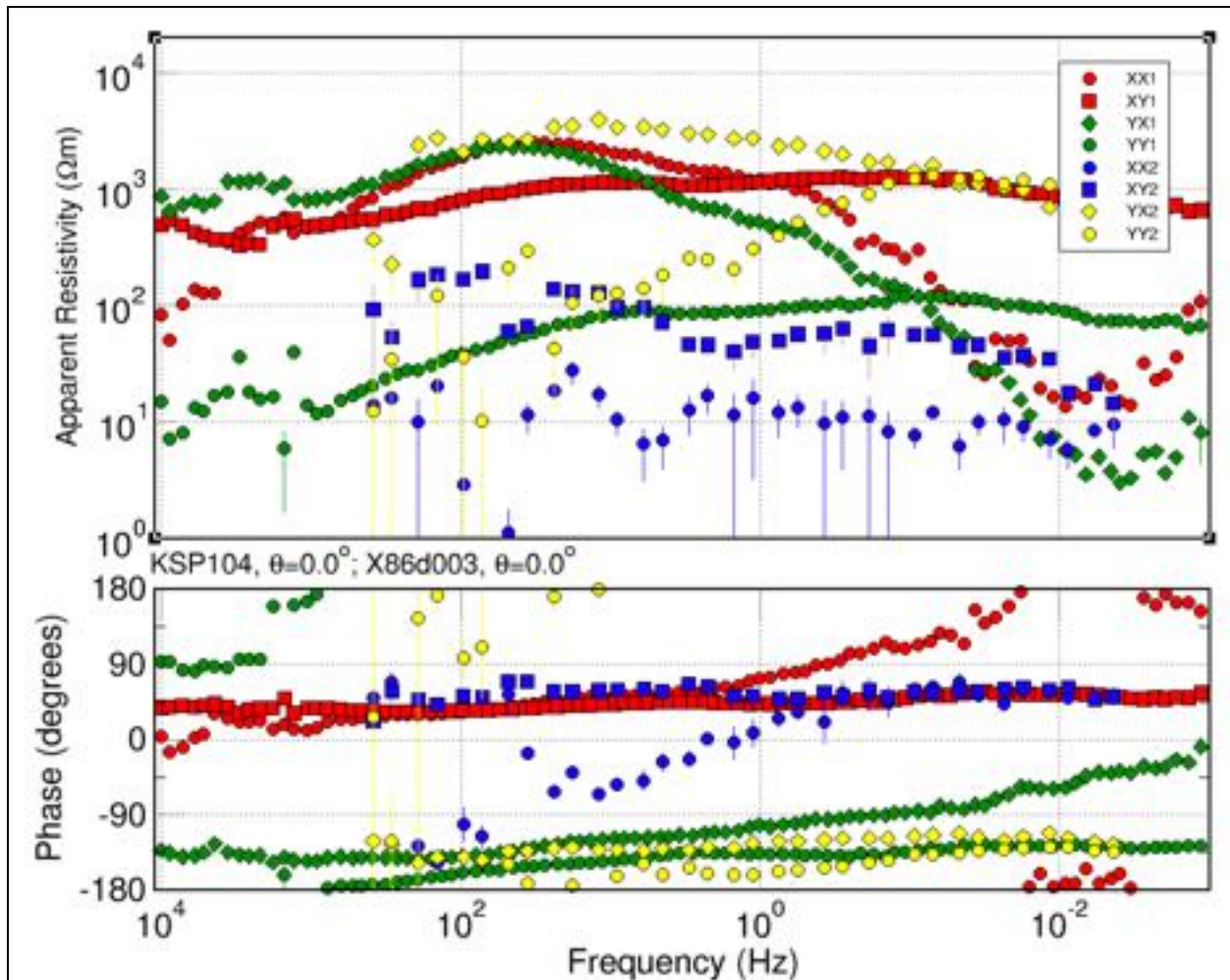


Figure 3: Comparison of new site KSP104 with Duncan site 86d003. Top row: Plots of separate sites. Bottom row: Overlay of the two sets of data - "1" is KSP104 and "2" is 86d003.

We can see if galvanic distortion decomposition removal will bring these two into better agreement – see description of the McNeice and Jones (2001) approach in the section below on *Strike decomposition*.

Performing single-site, multi-frequency decompositions for the frequency band 400 – 1 Hz yields the 2-D regional responses in Figure 4. There is some scatter in the Duncan data, but the phases are now in substantial agreement, and the RhoA curves have the same shapes but are displaced by residual static shift effects.

The only problem is that the geoelectricstrike direction determined from the new data, KSP104, is N24W, whereas the strike direction from the older data, 86d003, is N29E!

This may infer that one or both of the phases of the diagonal terms, XX and YY, in the original data are in opposite quadrants from each other. A comparison of the two (Figure 5) shows that indeed the PhaXX data (black and blue squares) are 90° apart.

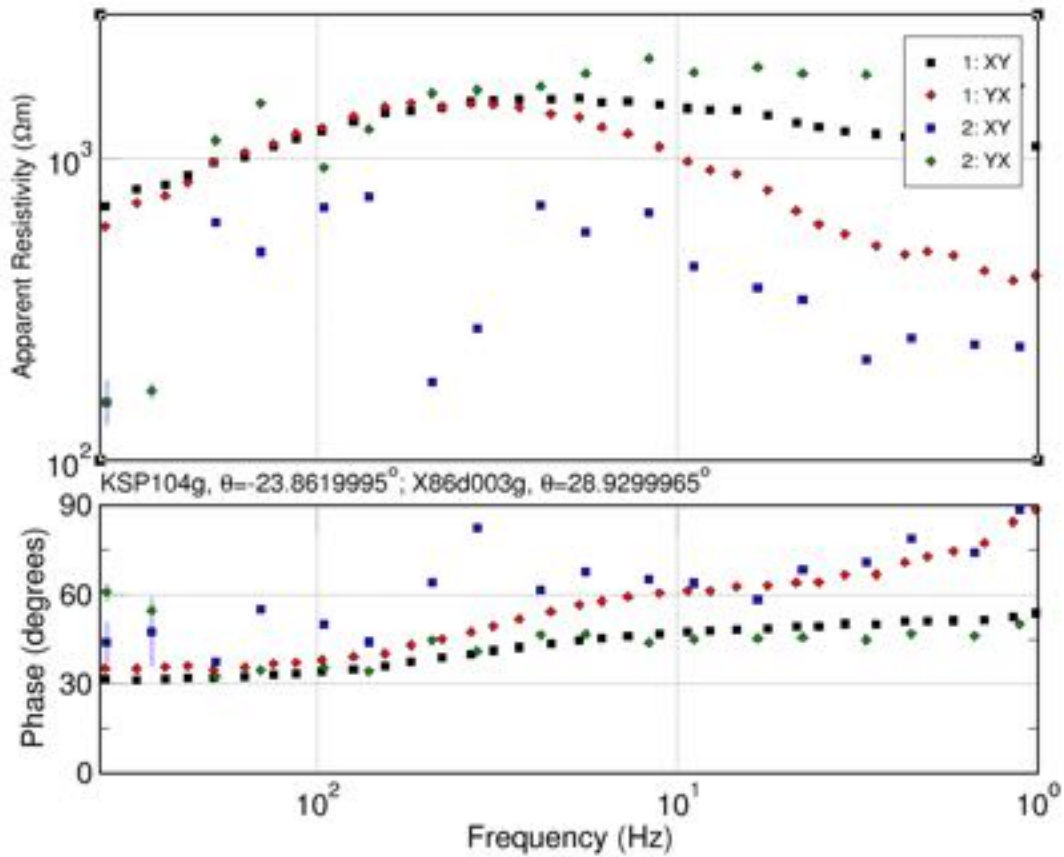


Figure 4: Comparison of KSP104 ("1") and 86d003 ("2") after distortion decomposition.

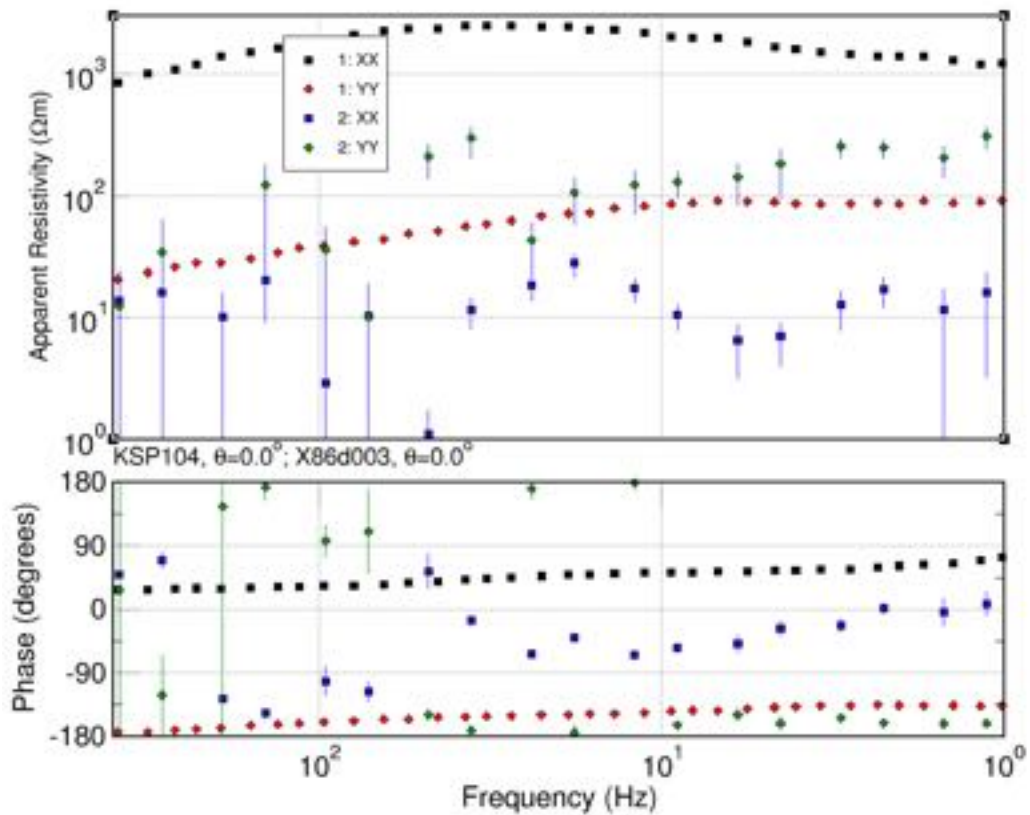


Figure 5: Comparison of the XX and YY estimates for new site KSP104 and Duncan site 86d003.

1.3.2. *KSP105 and 86d003*

The centres of new site KSP105 and Duncan site 86d002 are just over 1 km apart (Figure 6), so their high-frequency estimates may differ to about 100 Hz, but their lower frequency responses should be comparable.

Side-by-side comparisons of the two are shown in the upper row of Figure 7, and an overlap of them on top of each other in the lower row of Figure 7, with “1” being KSP105 and “2” being 86d002.

Again, both sets of estimates were derived using Phoenix equipment and Phoenix processing, site 86d003 used older BBMT coils (MTC-50s) and receiver (MT-16), whereas KSP105 used very modern coils (MTC-150s) and receiver (MTU-5C v2)

There is very good agreement of the off-diagonal (XY and YX, squares and diamonds) estimates – the phases overlap and the RhoA curves have the same shape but are slightly shifted from each other. The diagonal estimates are though not in agreement.

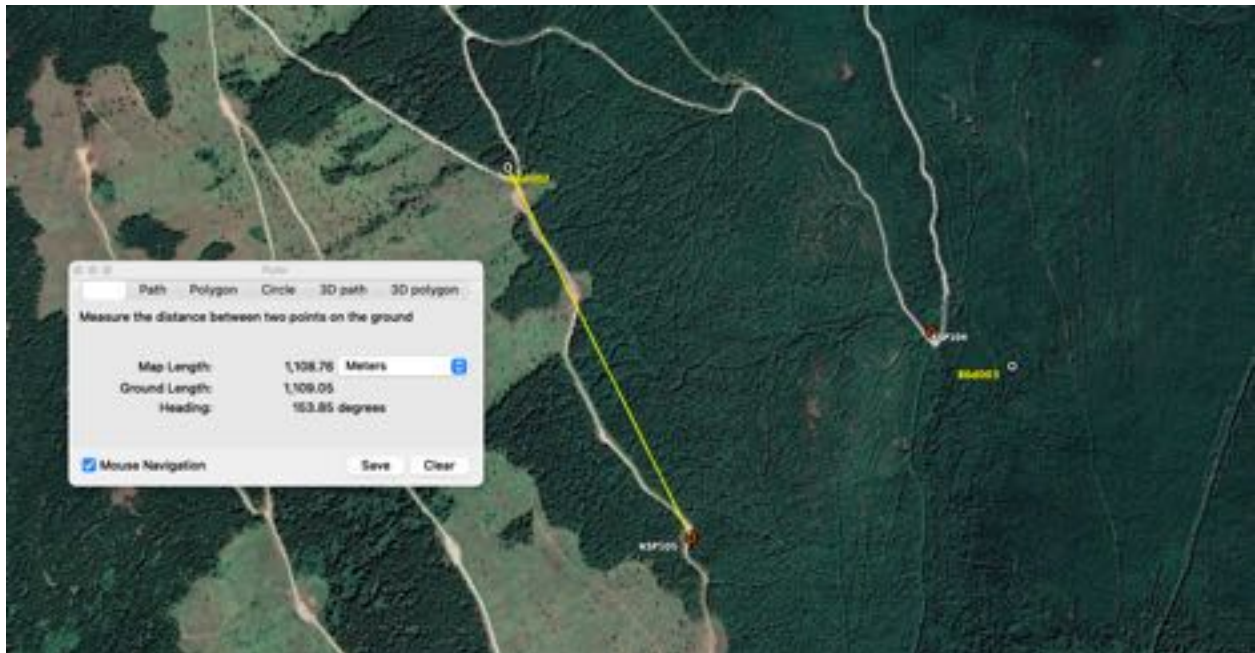


Figure 6: Locations of new site KSP105 and existing Duncan site 86d002.

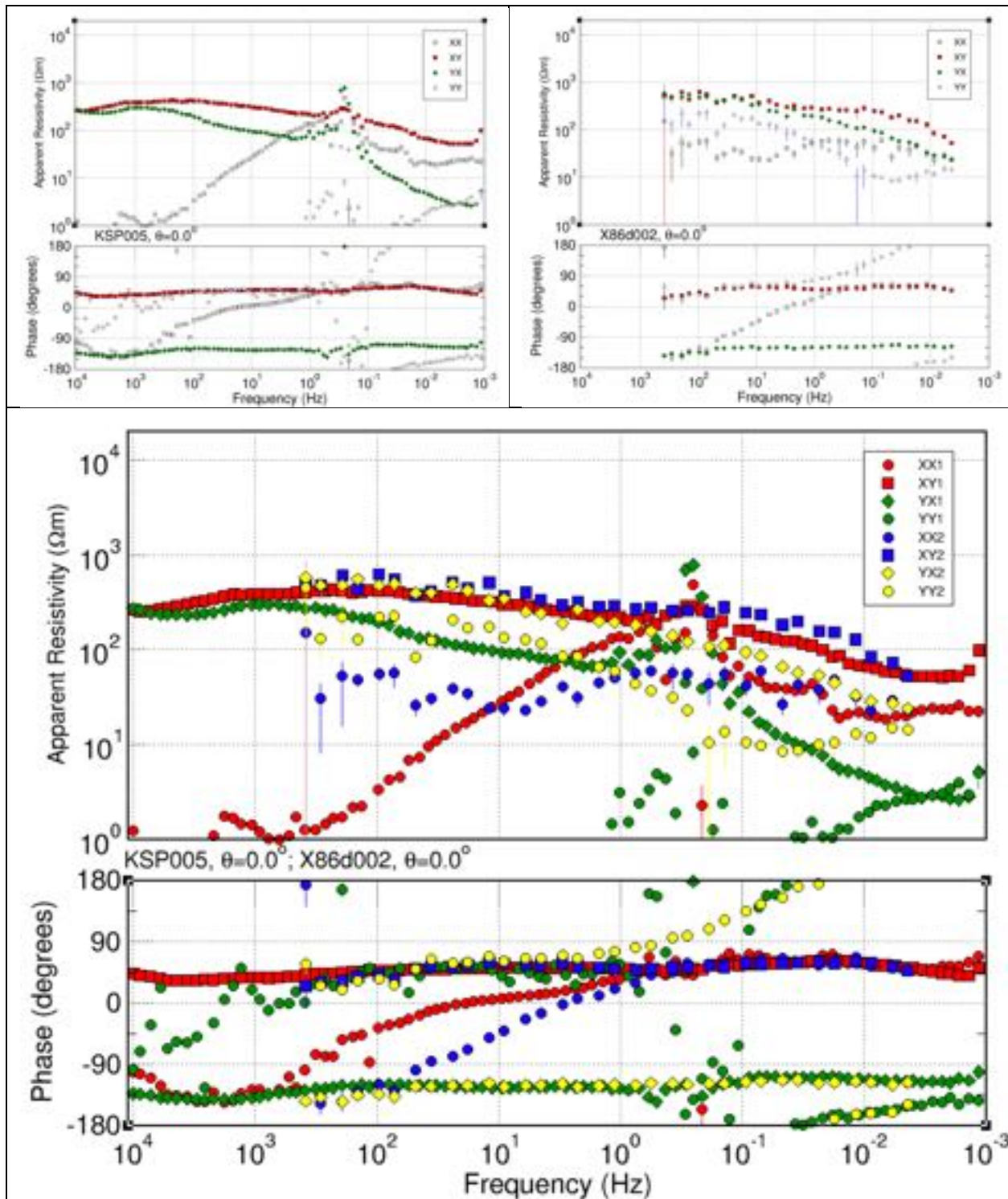


Figure 7: Comparison of new site KSP105 with Duncan site 86d002. Top row: Plots of separate sites. Bottom row: Overlay of the two sets of data - "1" is KSP105 and "2" is 86d002.

Again, we can see if galvanic distortion decomposition removal will bring these two into better agreement. Undertaking independent model fits we find geoelectric strikes of N43W and N45W (or N47E and N45E) for KSP005 and 86d002 respectively in the frequency band of 400 – 0.05 Hz.

A multi-station, multi-site decomposition of the two simultaneously yields a geoelectrical strike of N44E (or N46W), and the data are in excellent agreement (Figure 8). The phases are the same to 1 Hz, and the RhoA curves have the same shape but are displaced from each other by static shift effects.

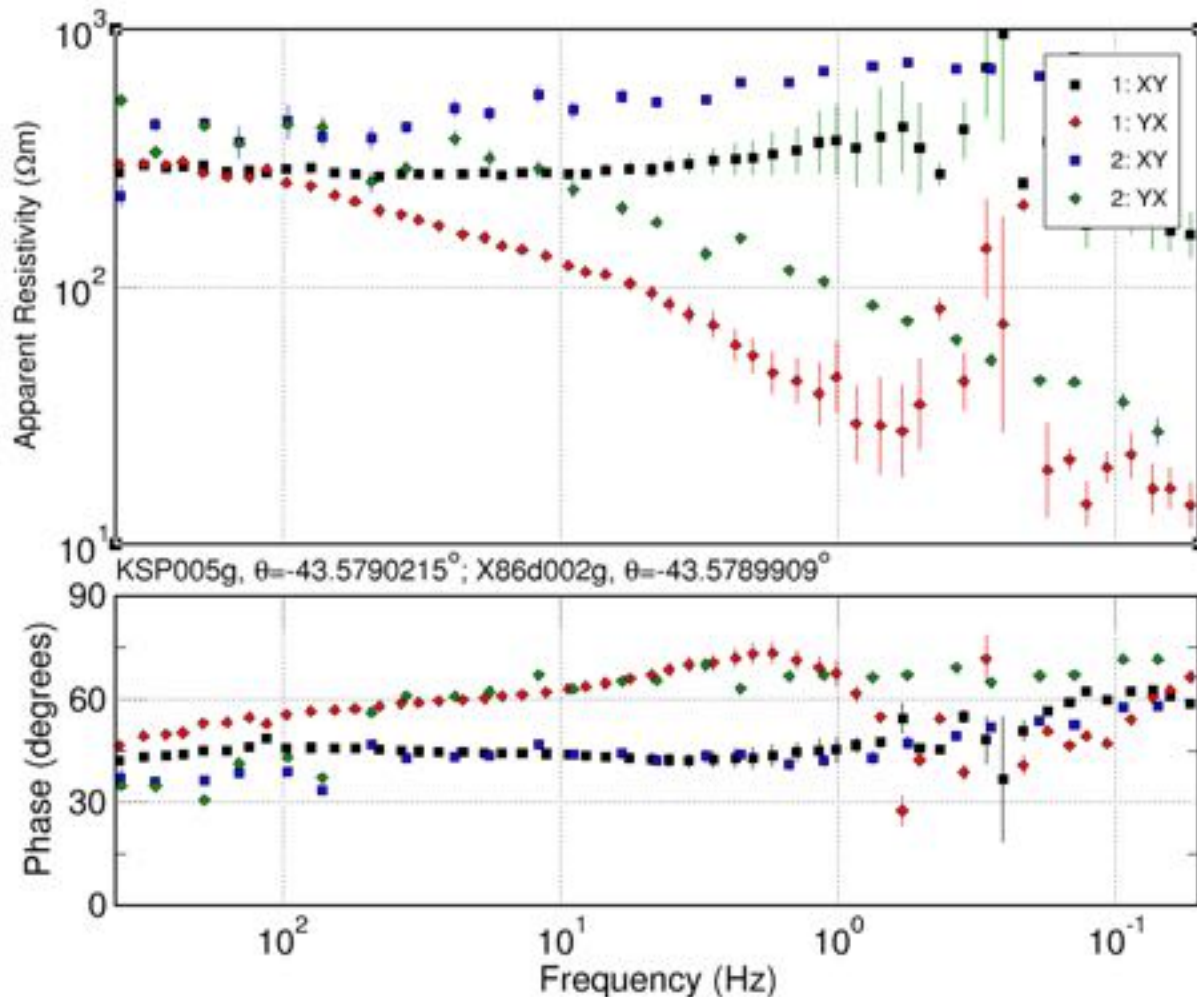


Figure 8: Comparison of KSP105 ("1") and 86d002 ("2") after distortion decomposition.

1.3.3. KMO004 and dun711

The centres of sites KMO004 and dun711 are 430 m from each other (Figure 9). Unfortunately, the dun711 data are very poor and are only over a very restricted frequency range of 384 – 1 Hz.

Nevertheless, the overlap comparison plot (Figure 10, bottom row) shows excellent agreement in the off-diagonals, XY (red and blue squares) and YX (green and tallow diamonds), even the RhoA levels are the same. There is though no agreement in the diagonal estimates, XX (red and blue circles) and YY (blue and yellow circles).

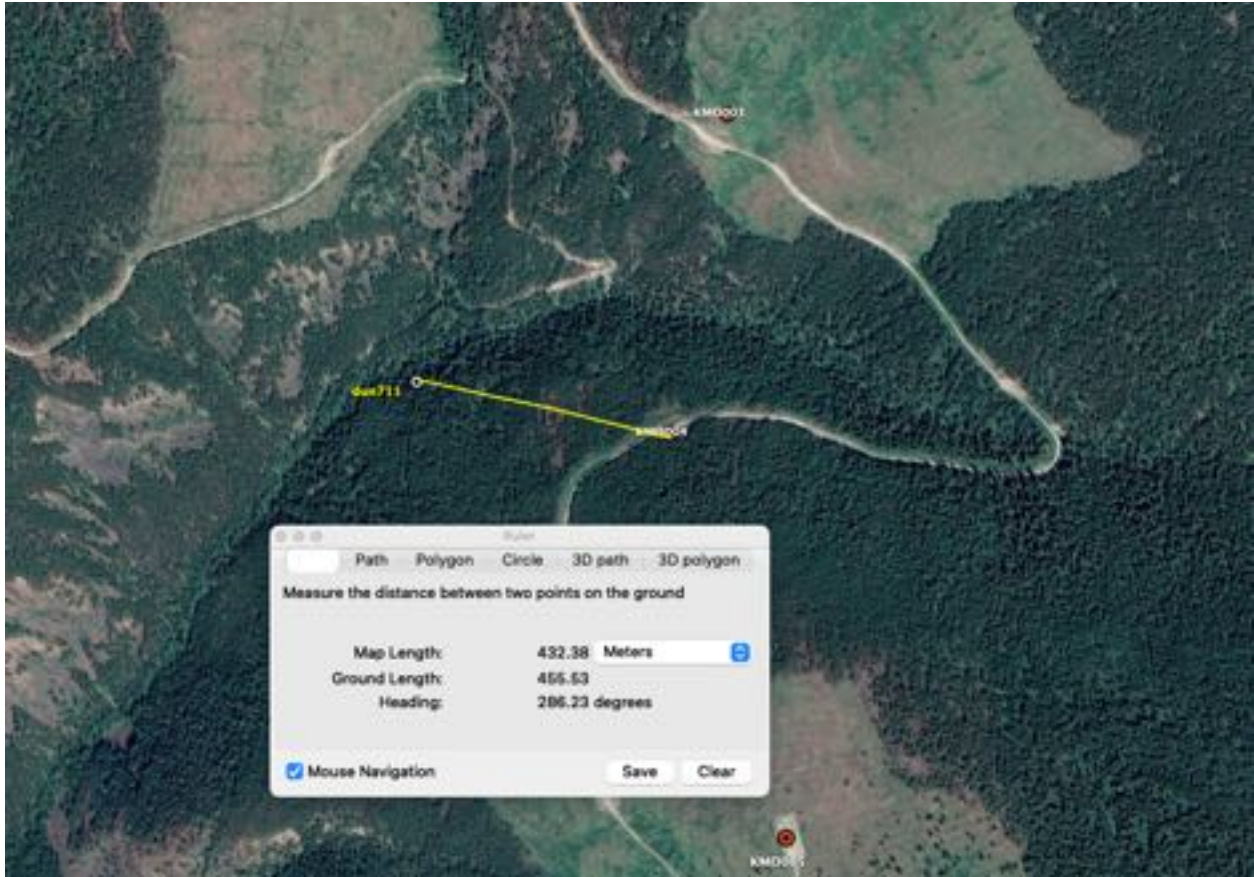
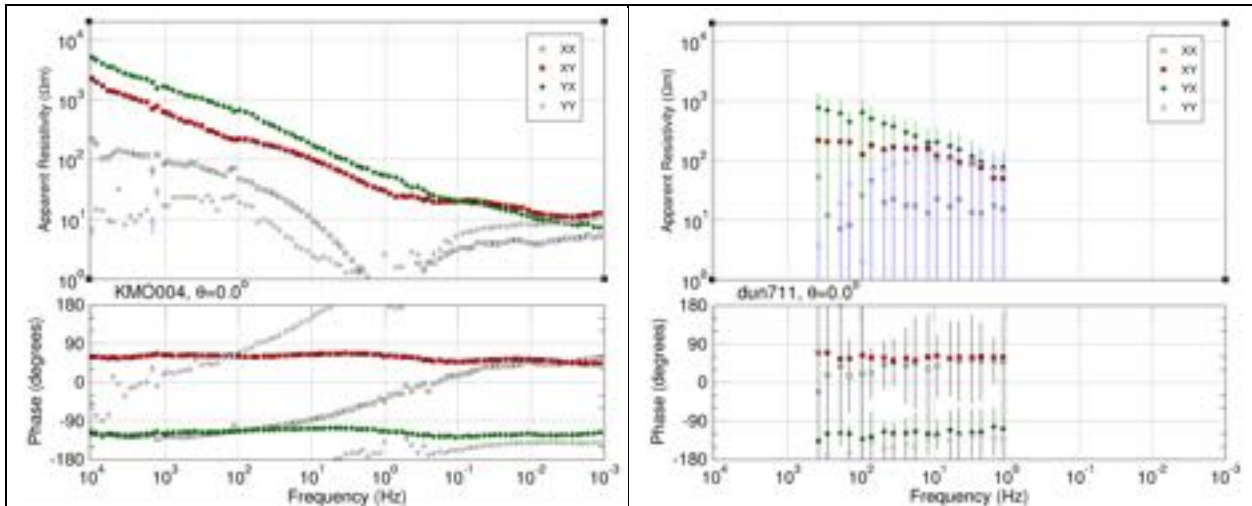


Figure 9: Locations of new site KMO004 and existing Duncan site dun711.



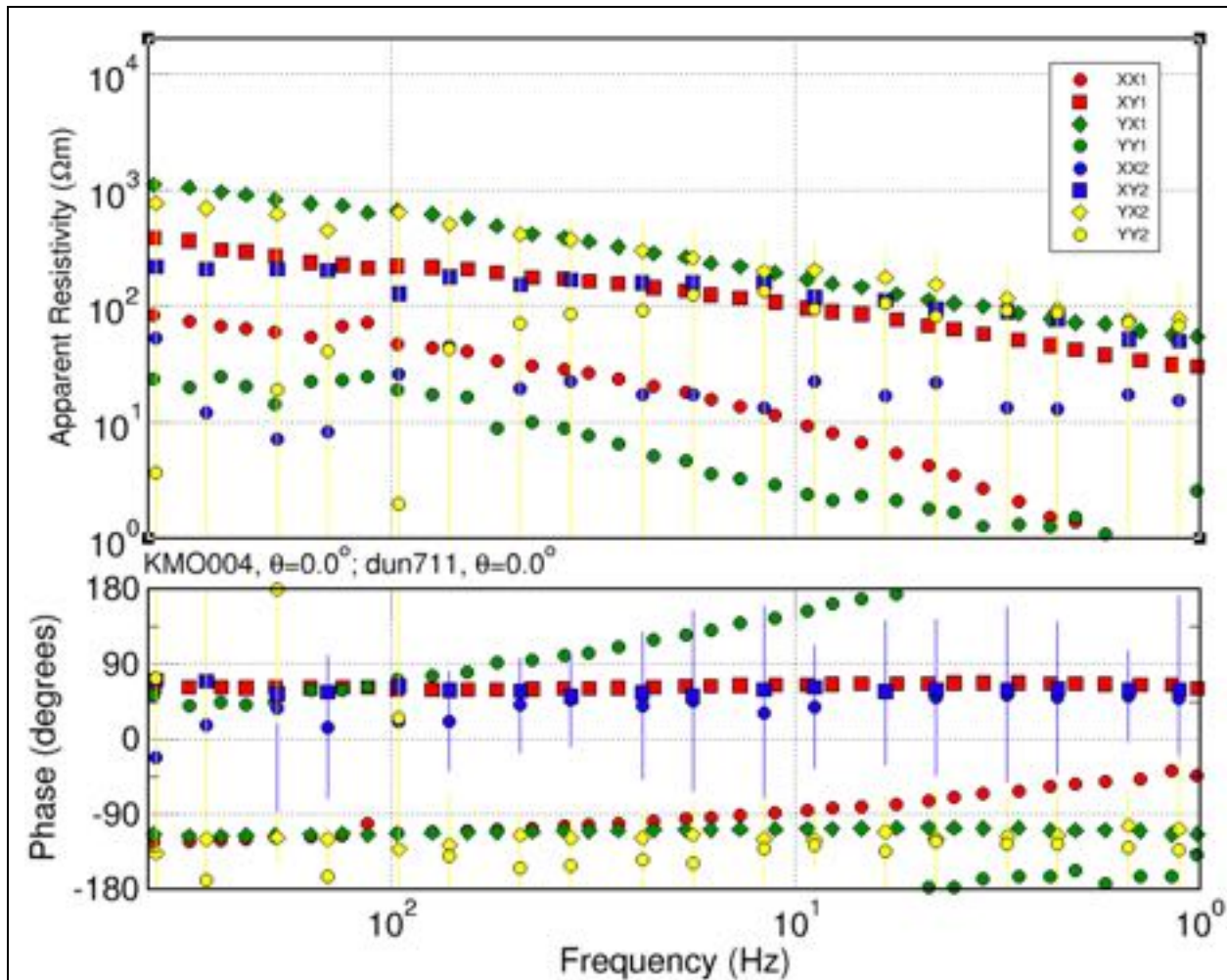


Figure 10: Comparison of new site KMO004 with Duncan site dun711. Top row: Plots of separate sites. Bottom row: Overlay of the two sets of data - "1" is KMO004 and "2" is dun711.

In contrast though to the first pair of sites, KSP104 and 86d003, separate distortion decompositions yield approximately the same strike directions, N29W for KMO004 and N33W for 86d003. Fitting the two together simultaneously in multi-site, multi-frequency mode yields 2-D response estimates with a common geoelectrical strike of N29W shown in Figure 11, and given the 35 years between the two, there is very good agreement (the shifts in the ρ_a curves are static shifts that are easily corrected for).

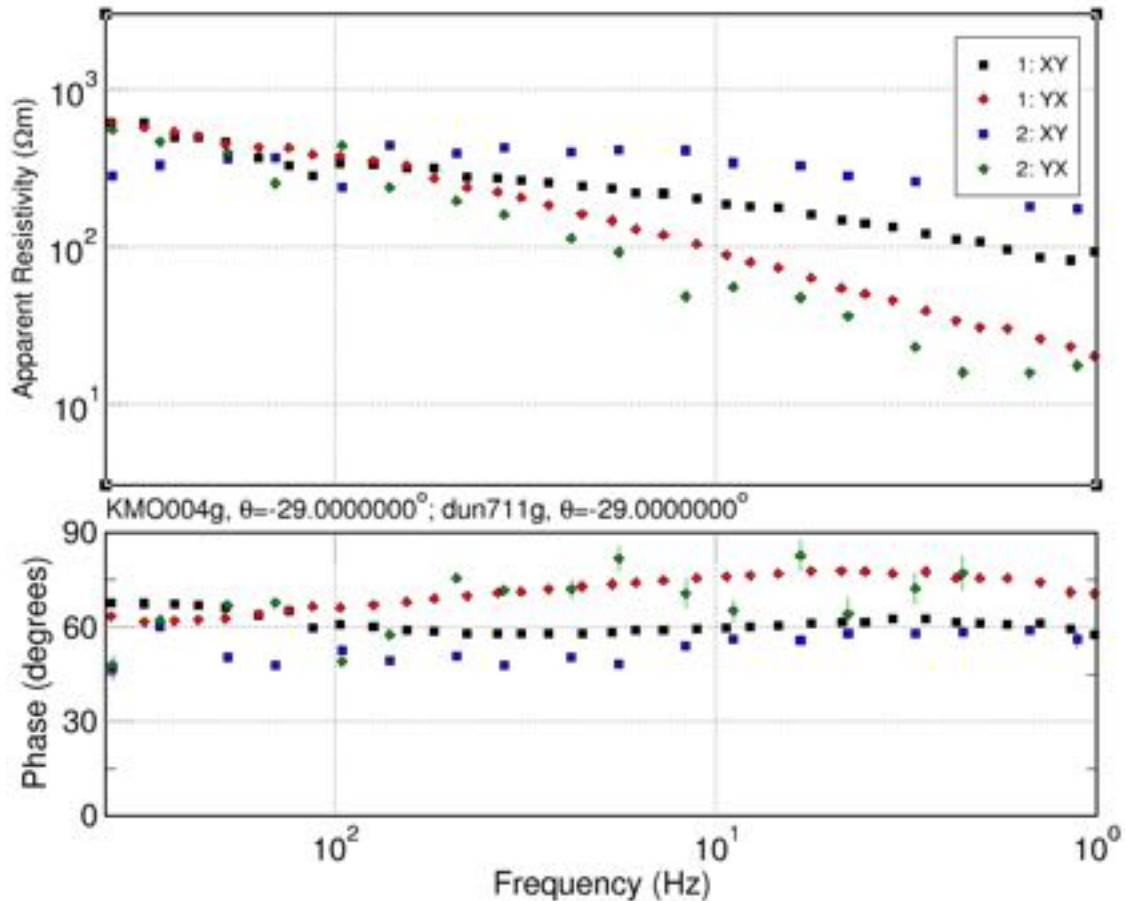


Figure 11: Comparison of distortion decomposed new site KMO004 and Duncan site dun711.

➔ We can conclude that the Duncan data is usable at most sites.

1.3.4. KSS106 and SS_14

New site KSS106 lies 400 m directly north of Quantec station SS_14 (Figure 12).

A comparison of the two sets of data is shown in Figure 13. The upper row plots the two sites separately, and the lower row overlays the two – “1” is KSS106 and “2” is SS_14.

Note that there is reasonable agreement between the off-diagonal estimates, XY and YX. There is some static shift effects evident in the Quantec data, but the ρ_{XY} and ρ_{YX} curves have mostly the same shape at frequencies >0.1 Hz. Below 0.1 Hz the Quantec Pha_{XY} estimates are very different from the new ones, with Quantec Pha_{XY} estimates leaving the 1st quadrant.

Of serious concern is the differences observable in the diagonal estimates, XX and YY. There is clearly a “tear” in the Quantec ρ_{YY} estimates at 10 Hz – such problems have been observed before in Quantec data provided by other clients and it appears to be at the overlap between the high frequency (HF) coil and the low frequency (LF) coil.

→ If the data are truly 2-D with a strike of N-S, then the diagonal terms are not used and this issue is unimportant. However, if the subsurface is 3-D, OR the strike is not exactly N-S, then all four elements of the impedance tensor are needed, and problems with the diagonal terms will influence the model of the subsurface.

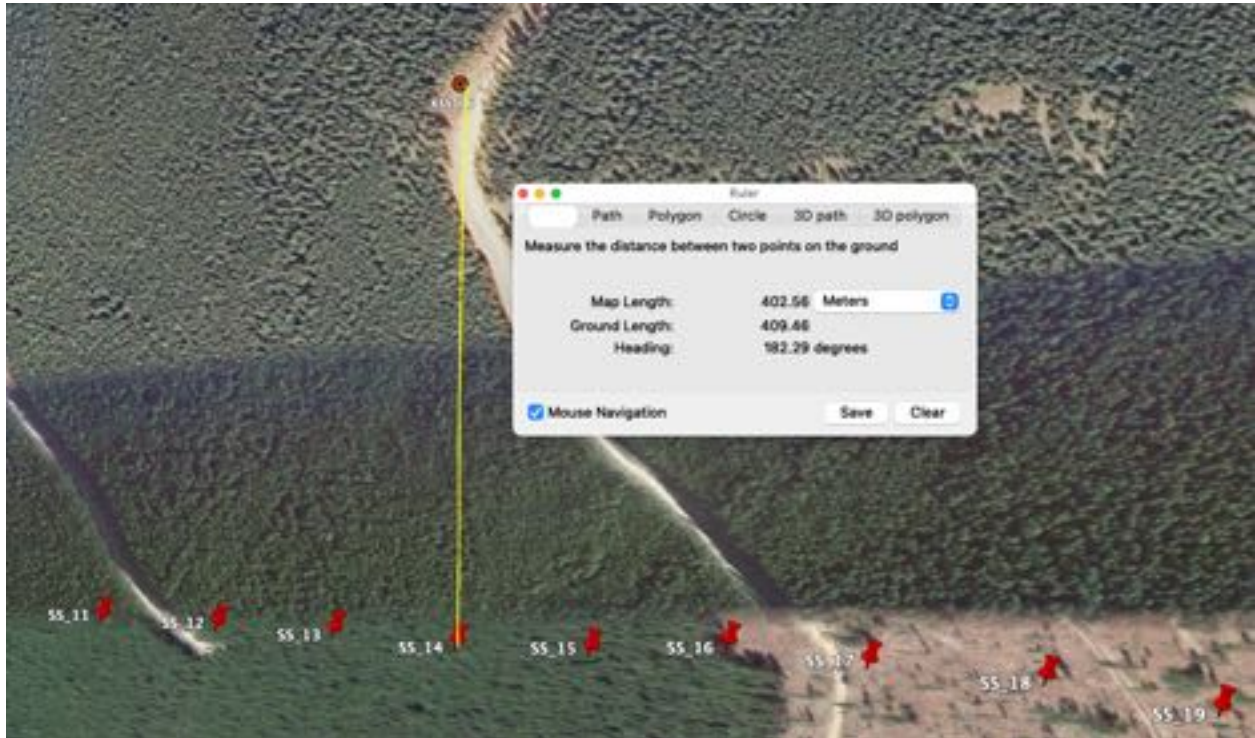
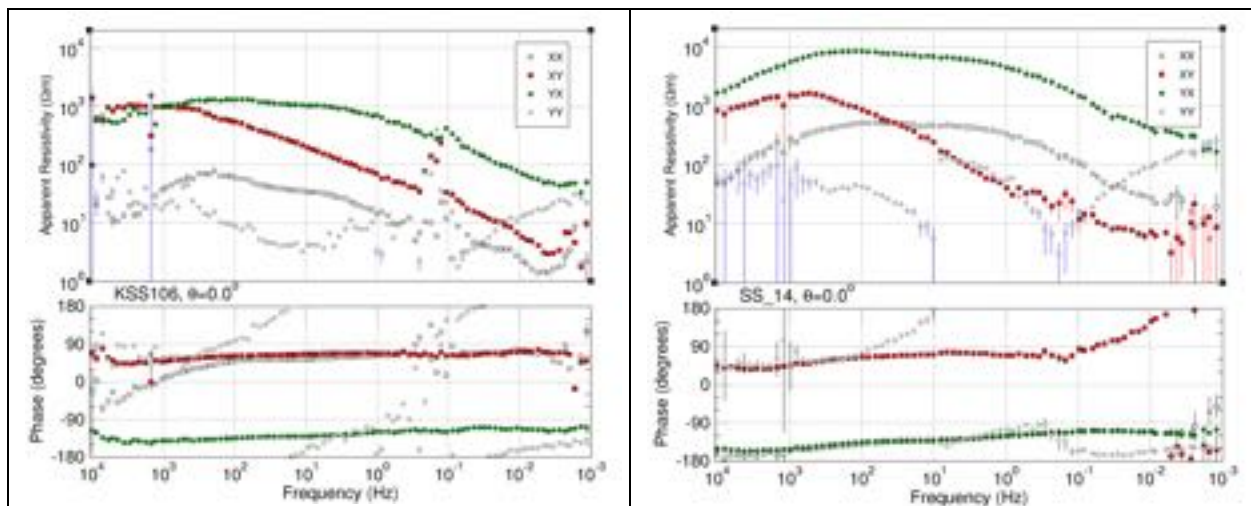


Figure 12: Locations of new site KSS106 and existing Quantec site SS_14.



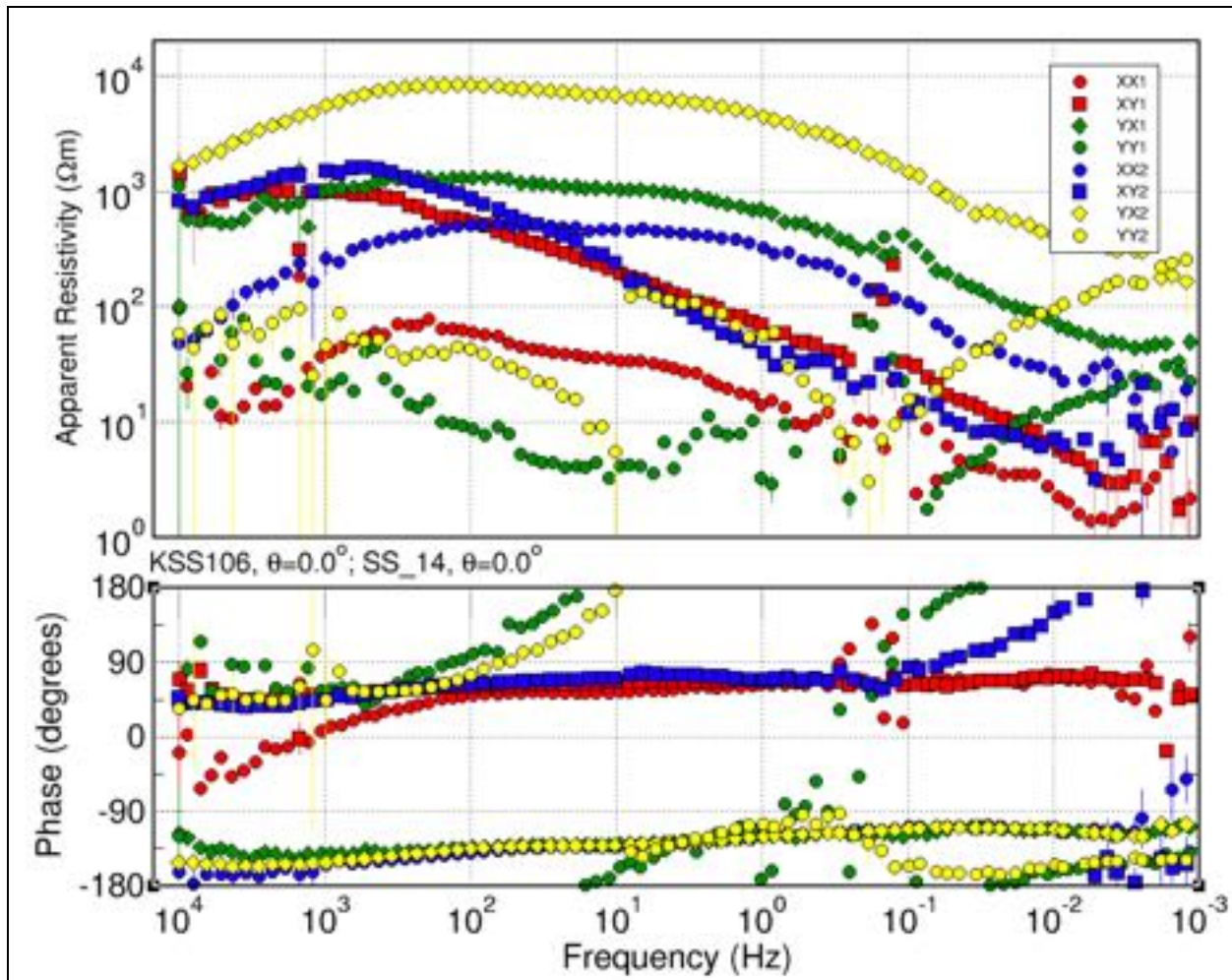


Figure 13: Comparison of new site KSS106 with Quantec site SS_14. Top row: Plots of separate sites. Bottom row: Overlay of the two sets of data - "1" is KSS106 and "2" is SS_14.

1.3.5. KSS108 and SS_32

Sites KSS108 and Quantec site SS_32 are 640 m from each other (Figure 14). Their comparison (Figure 15) is again somewhat reasonable for the off-diagonal components, XY and YX, but the diagonal terms are in very poor agreement.

In particular the PhaYY estimates (green and yellow circles) are 180° different from each other at high frequencies, but come into agreement at very low frequencies (<0.001 Hz). This problem has also been observed on data from other clients.

➔ **The Quantec diagonal elements are not in good agreement with the new Phoenix estimates, and should be used with caution.**

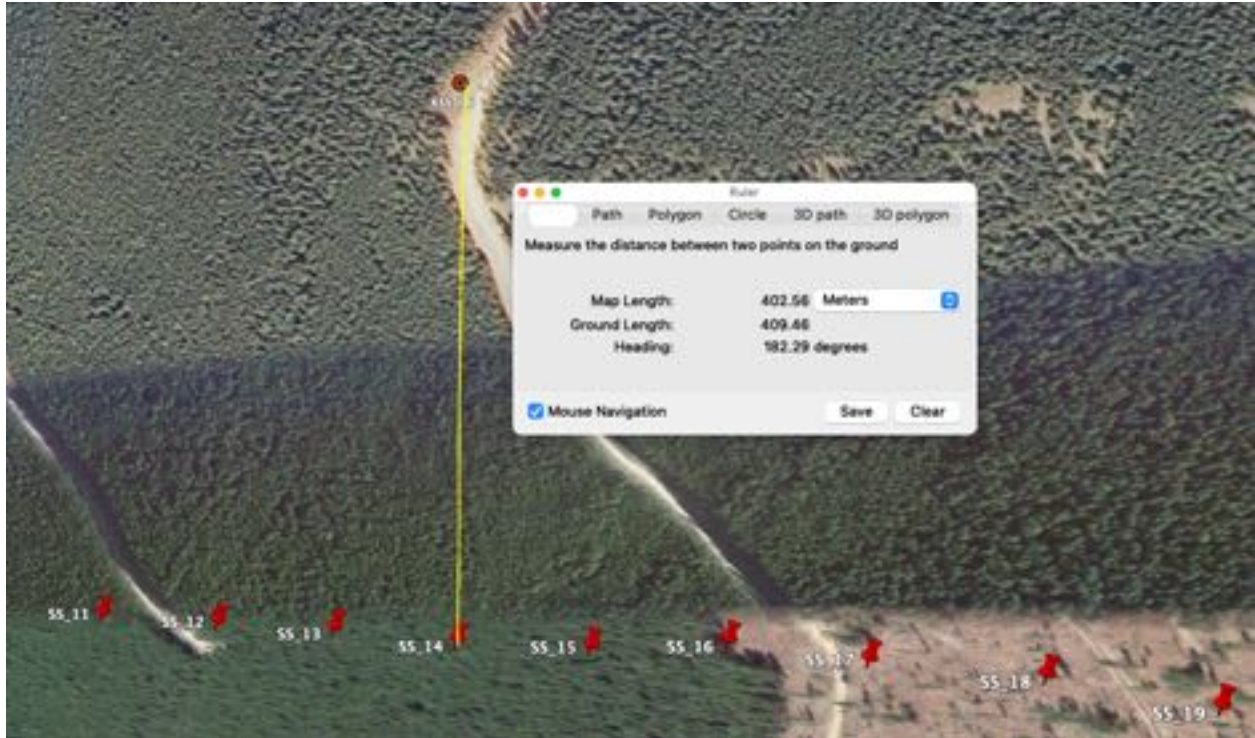
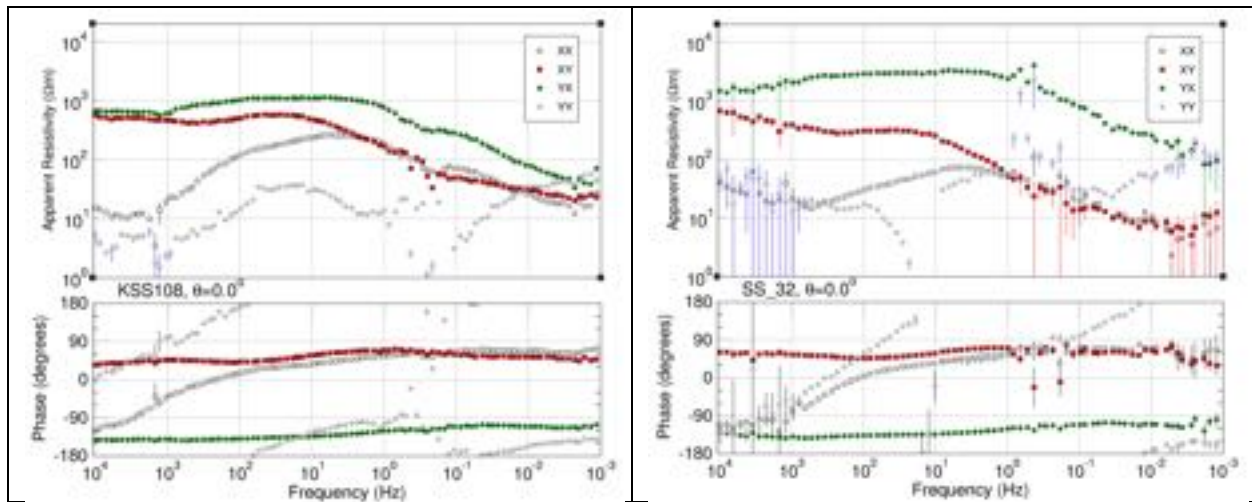


Figure 14: Locations of new site KSS108 and existing Quantec site SS_32.



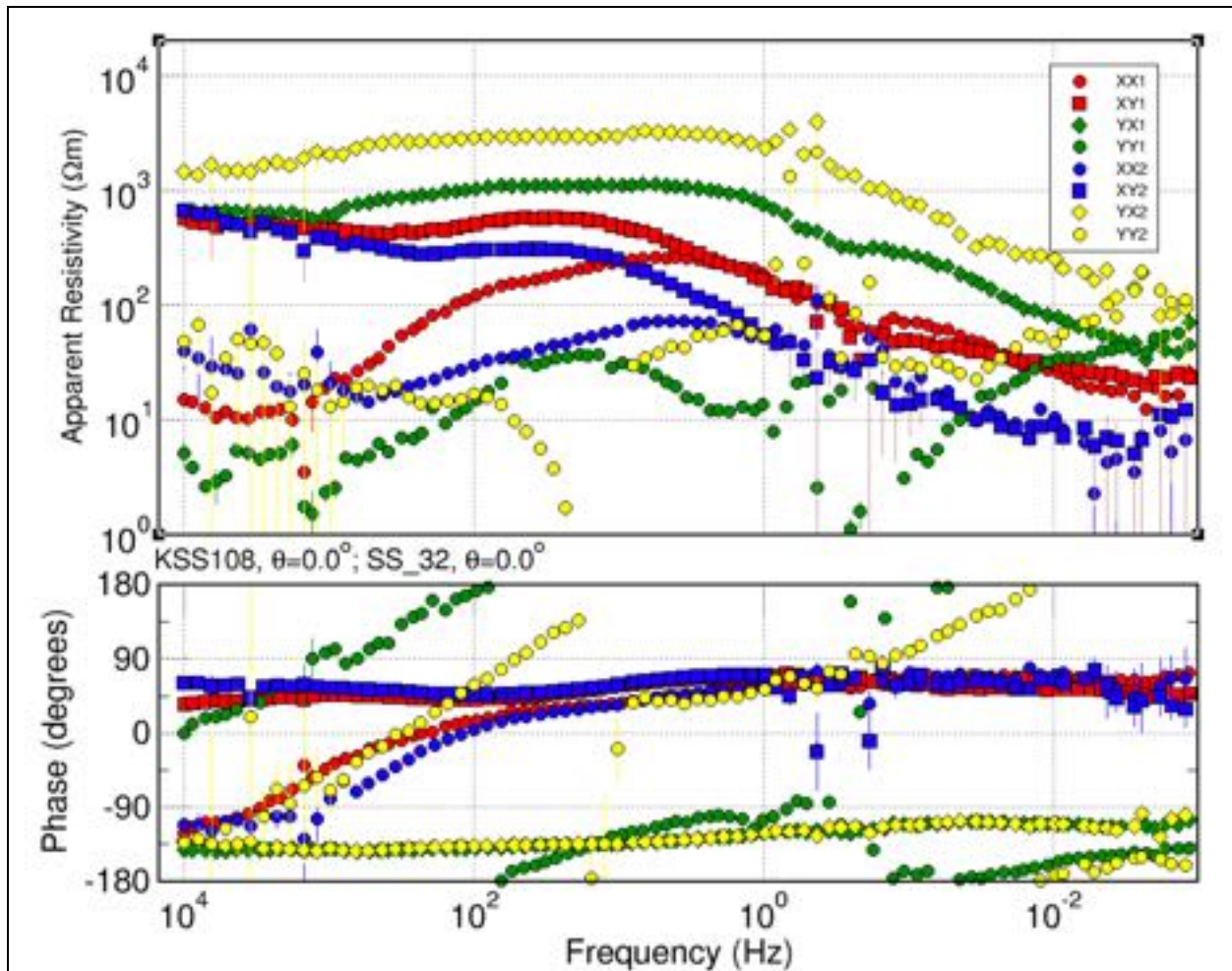


Figure 15: Comparison of new site KSS108 with Quantec site SS_32. Top row: Plots of separate sites. Bottom row: Overlay of the two sets of data - "1" is KSS108 and "2" is SS_32.

1.4. Profiles

The client's representative, Fred Cook, defined seven profiles of interest (Figure 16), with the cross-lines SP defined as two profiles, SP-EW and SP-NS. Profile MM1 uses both new data and Duncan data, and profile MO is only Duncan data for which a model already exists (see below).

Sites were assigned to the profiles as follows, from west to east.

Table 1: Site assignment to profiles.

Profile	Nsites	Sites
SS	15	KSS101, KSS102, KSS103, KSS104, KSS105, KSS106, KSS107, KSS108, KSS118, KSS109, KSS110, KSS111, KSS115, KSS112, KSS113
MM0	17	KMM001, KMM002, KMM003, KMM003b, KMM004, KMA002, KMM005, KMM006, KMM007, KMA001, KMM008, KMM009, KMM010, KMM011, KMM012, KMM013, KMM014
MM1	24	KMM210, KMM101, KMM102, KMM103, KMM104, KMM105, KMM106, KMM107, KMM108, KMM109, KMM110, KMM111, dun103, dun203,

		dun303, dun403, dun503, dun115, dun113, dun213, dun313, dun413, dun513, dun613
MM2	9	KMM201, KMM202, KMM203, KMM204, KMM205, KMM206, KMM207, KMM208, KMM209
SP-EW	12	KSP003, KSP004, KSP005, KSP006, KSP007, 86d002, KSP008, KSP009, KSP104, 86d004, 86d005, 86d006
SP-NS	9	KSP106, KSP105, KSP104, 86d002, KSP009, KSP008, KSP103, KSP102, KSP101
MO	14	dun311, dun411, dun511, 86d014, 86d145, 86d015, dun611, dun711, KMO004, KMO003, dun811, dun009, dun010, dun011

Note that the Quantec data are not assigned to profile SS.

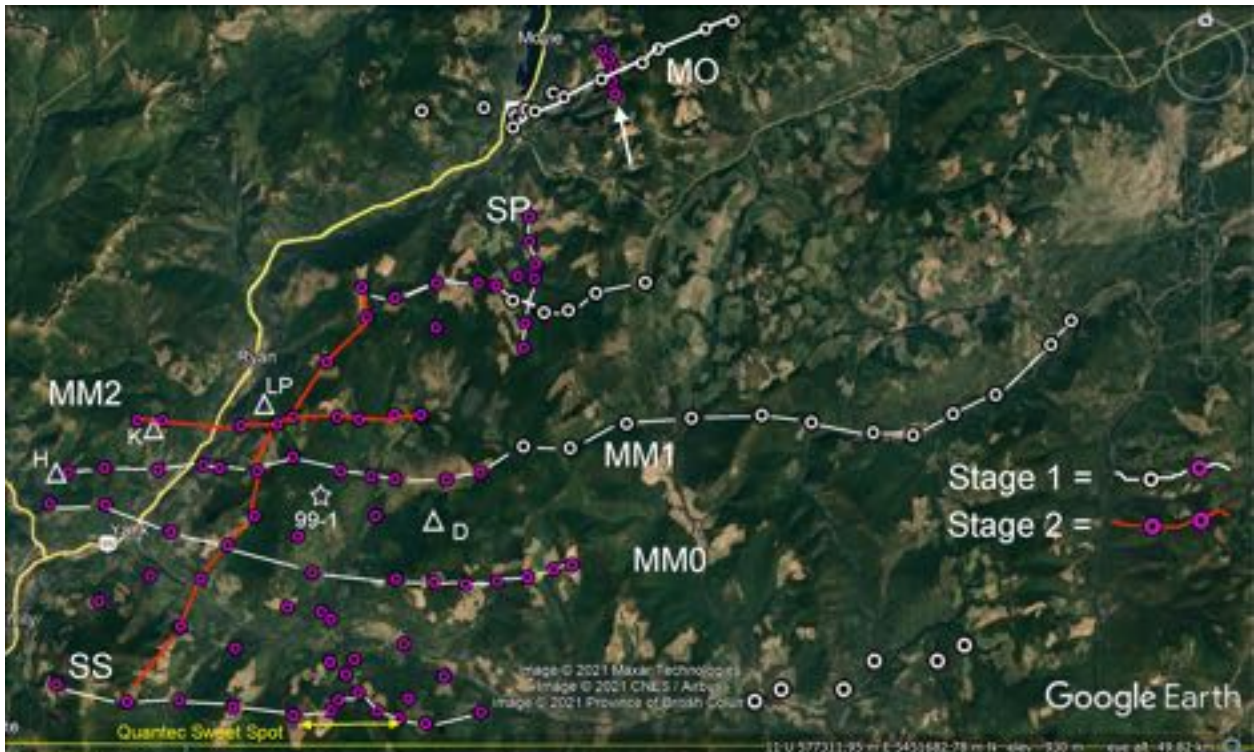


Figure 16: 2-D profiles defined by the client's representative. Purple sites are new sites and white ones are existing Duncan data.

Some of these existing data, namely stations along Duncan profile 3 (dunxx3) are used to extend profile "MM1", others to extend profile SP-EW to the east (86d0xx), and others are used to define profile MO along Duncan profile 11.

Note that these existing data are broadband MT (BBMT) only, and the highest frequency of them is 384 Hz. Also note that they are on a different frequency set than the new data, so interpolation has to occur to get all 190 sites on the same set for inversion.

1.5. Existing models

Also note that profile MO, for Moyie, was modelled by Gupta and Jones (1995) where it is named the “Longfarrell” profile, as it combines sites along Farrell Creek and those along Teepee Creek. It is labelled profile B in Gupta and Jones (1995). These data were also modelled by Cook and Jones (1995).

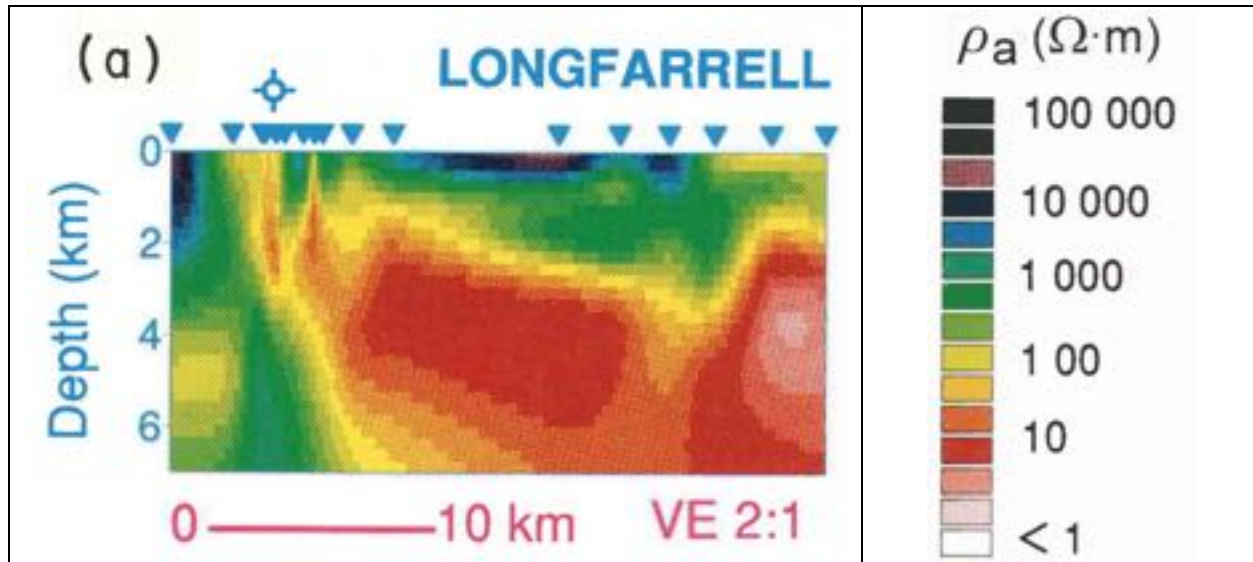


Figure 17: 2-D model derived by Gupta and Jones (1995) for the MO (Longfarrell) profile data.

The 2-D model derived for those data by Gupta and Jones (1995) is shown in Figure 17. This model was derived using the Rapid Relaxation Inversion (RRI) 2-D code that was current for the day, but modern codes are far superior. It will be interesting to see the model that we derive from these data.

Cook and Jones (1995) focus on only those sites in the close proximity to the drillhole at Moyie, and their model is shown in Figure 18.

Note that these two models had different adopted geoelectrical strike directions. The more regional Gupta and Jones (1995) model assumed a strike of N30W, whereas the more focussed Cook and Jones (1995) model had a strike of N50W.

The adopted strike angle is absolutely critical for correct modelling of the subsurface. If the wrong strike direction is chosen, then there is “mode switching”, i.e., the TE-mode data are modelled as TM-mode data, and vice-versa.

As we will discuss below, it is possible that both Gupta and Jones (1995) and Cook and Jones (1995) made errors in their assumed strike directions, and the correct strike directions were orthogonal to those assumed, i.e., N60E and N40E.

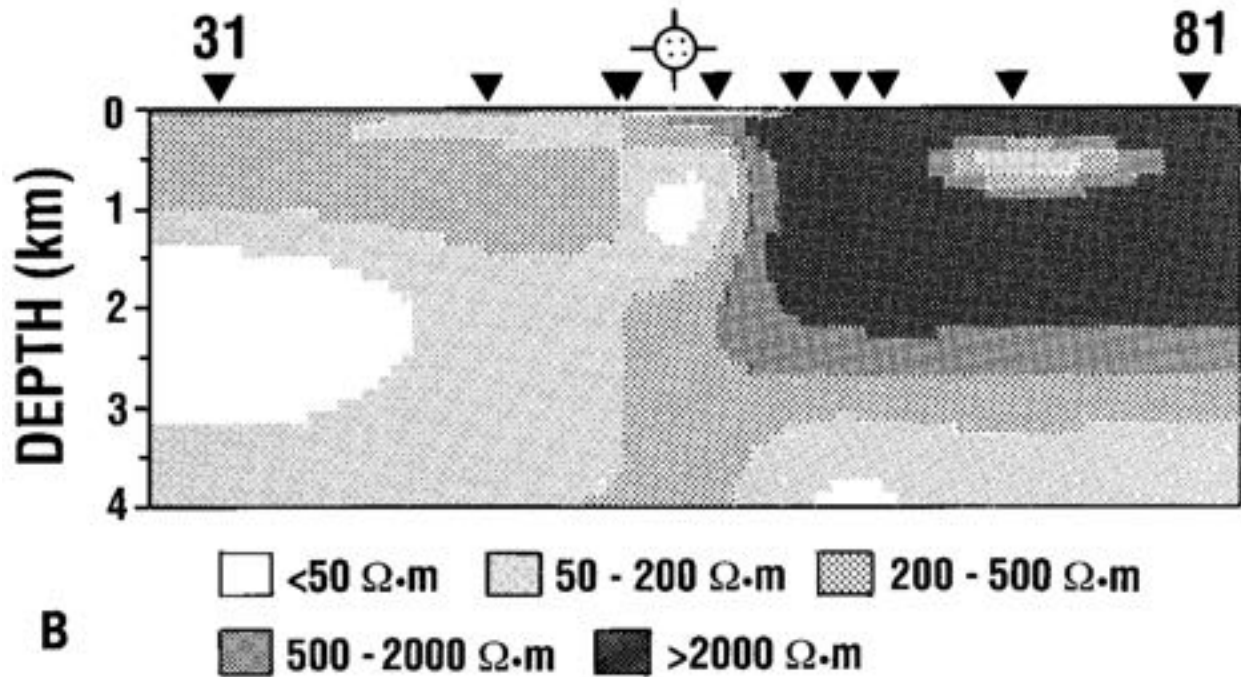


Figure 18: 2-D model derived by Cook and Jones (1995) for the sites around the Moyie drillhole.

2. New Acquisition

As described in the Logistics report, CMTS-2021-KootenayResources-R1, data were acquired at the 86 sites, and prior to each run measurements were made of the electric field parameters; contact resistances, AC and DC levels. For a discussion of these, see Appendix A.

The electrode array parameters measured at the commencement of acquisition are plotted in Figure 24.

2.1. Contact resistances

The contact resistances are, for the most part, reasonably low. The median values for E_x and E_y are $3.4 \Omega\mu$ and $3.6 \Omega m$, with the third quartiles of $5.9 \Omega m$ and $6.5 \Omega m$. The five sites in the NE corner, sites KMOxxx, all have high contact resistances, likely due to the surface conditions.

Ex Contact Resistance	Ey Contact Resistance
-----------------------	-----------------------

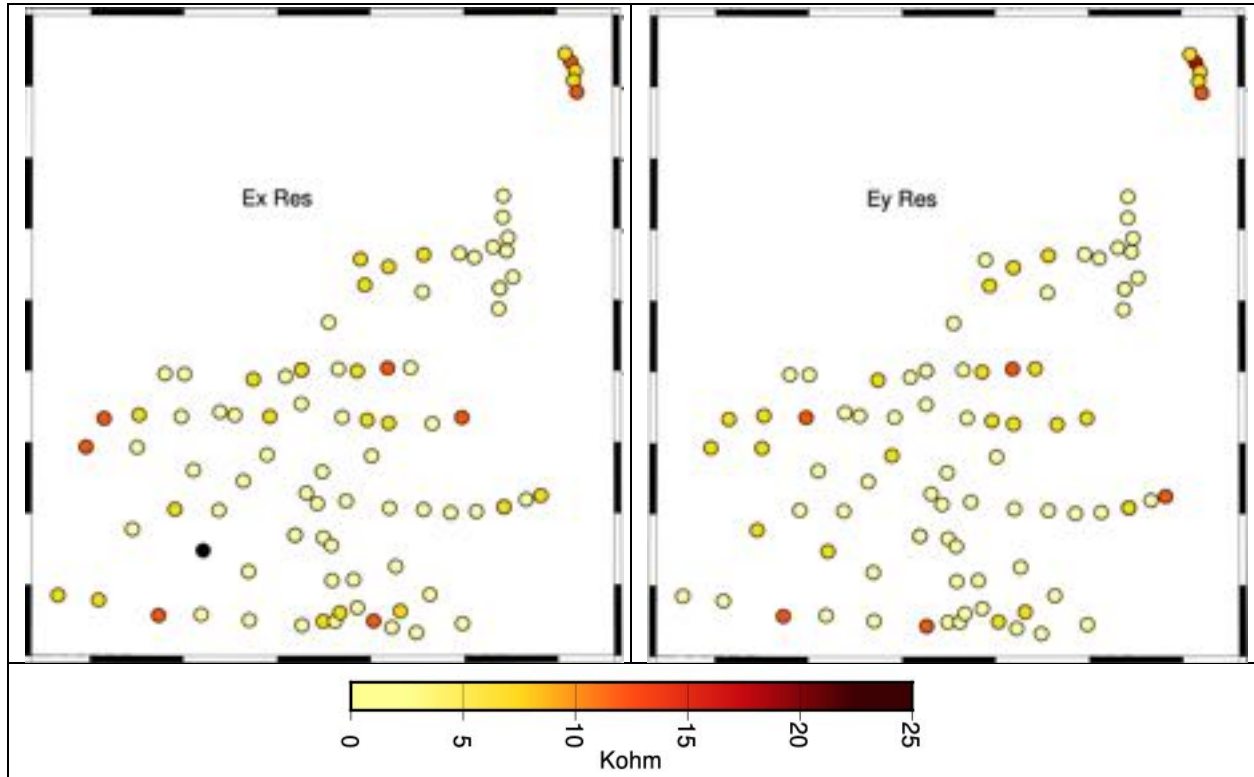


Figure 19: Electrode contact resistance measurements.

The most extreme value of 29.1 Ωm was recorded for the Ex line at site KHA006. The corresponding Ey line recorded a far lower value of 8.4 Ωm . The MT off-diagonal (XY & YX) estimates for this site exhibit high-frequency “pull-ups” in RhoXY and PhaXY (black squares, Figure 20) which may be a consequence of the high Ex contact resistance.

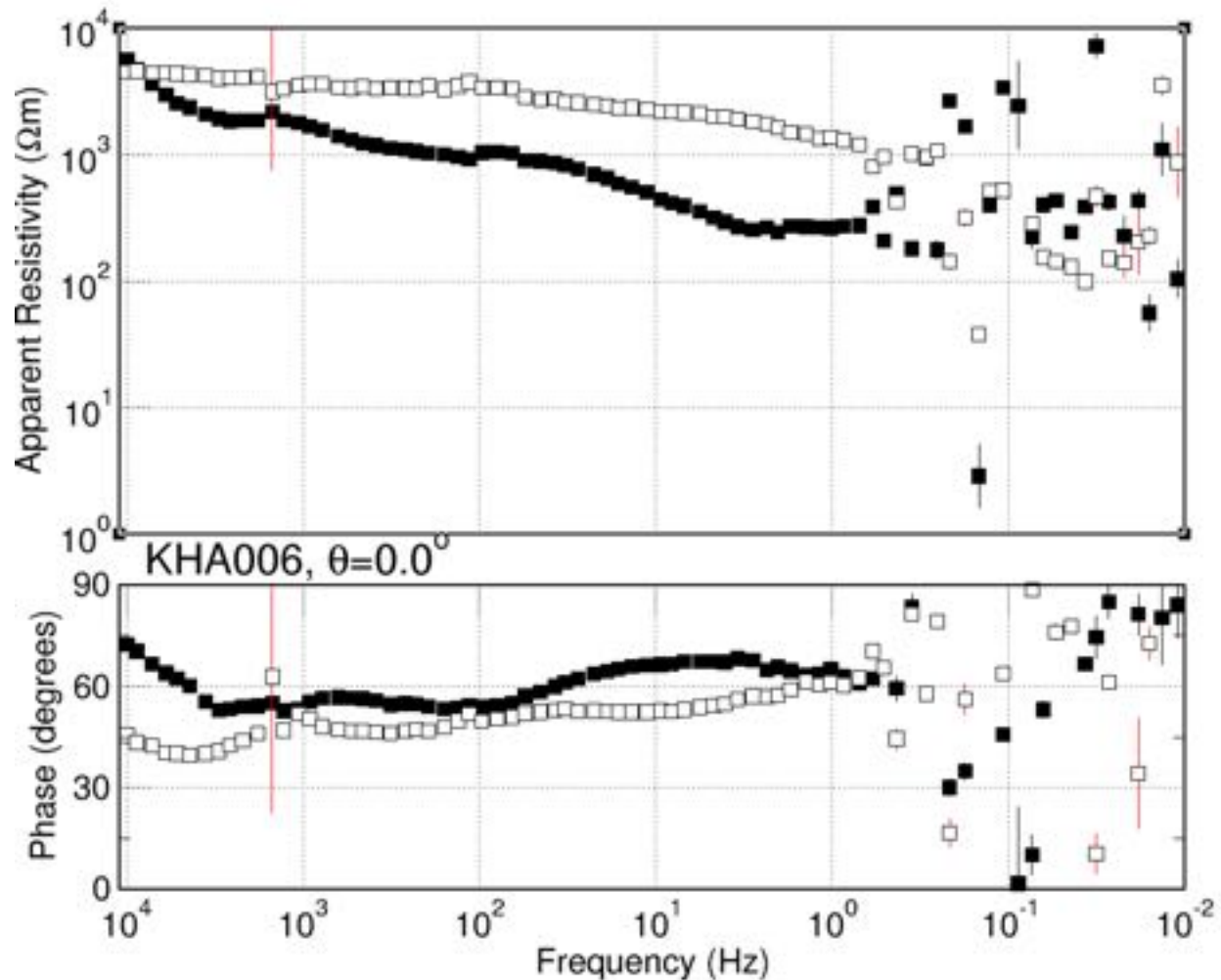


Figure 20: MT off-diagonal estimates for site KHA006.

We can check this by plotting the E_x contact resistance against the high frequency Pha_{XY} , and E_y against Pha_{YX} , for all sites. The cross-plot (Figure 21) shows that apart from this one outlier, there is the statistically weak suggestion of an increasing high frequency phase with increasing contact resistance. The best-fit linear regression through the data, excluding the anomalous KHA006 Pha_{XY} value, is

$$\text{Pha} = 31.1 (33.8 - 40.5) + 1.25 (0.67 - 1.84) R$$

(red line, Figure 21) where R = contact resistance and the ranges are the 95% confidence intervals of the intercept and the gradient. However, the R-squared goodness-of-fit statistic is only 0.097, which indicates very low confidence in the relationship.

Taking the logarithm of the contact resistances, the R-squared goodness-of-fit statistic is even lower at 0.081 with the linear regression model

$$\text{Pha} = 35.1 (30.5 - 39.6) + 13.60 (6.61 - 20.60) \log_{10}(R)$$

(blue line, Figure 21).

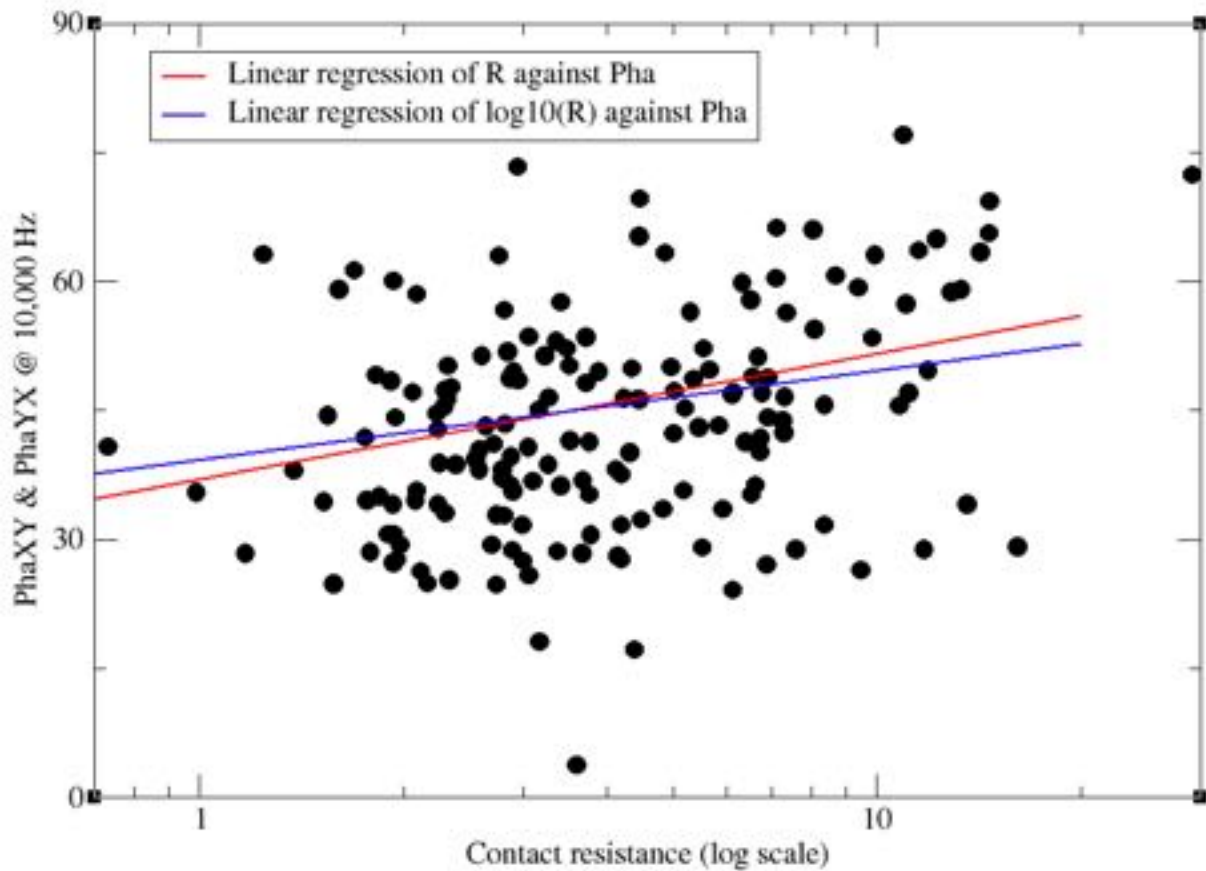


Figure 21: High frequency (10 kHz) PhaXY and PhaYX phase compared to contact resistance measured. Linear regression lines of R against Pha and $\log_{10}(R)$ against Pha shown.

One could conclude that there is a weak correlation of contract resistance with high frequency phase, but one must beware that correlation does not mean causation.

Plotted in Figure 22 are maps of the high frequency phases, plus smoothed median versions. The sites exhibiting anomalous phases compared to their neighbours can be compared with the sites showing high contact resistances in Figure 19.

There are some correlations, but others not.

→ Care should be taken when modelling sites with high contact resistances as the very high frequency phases may have been affects.

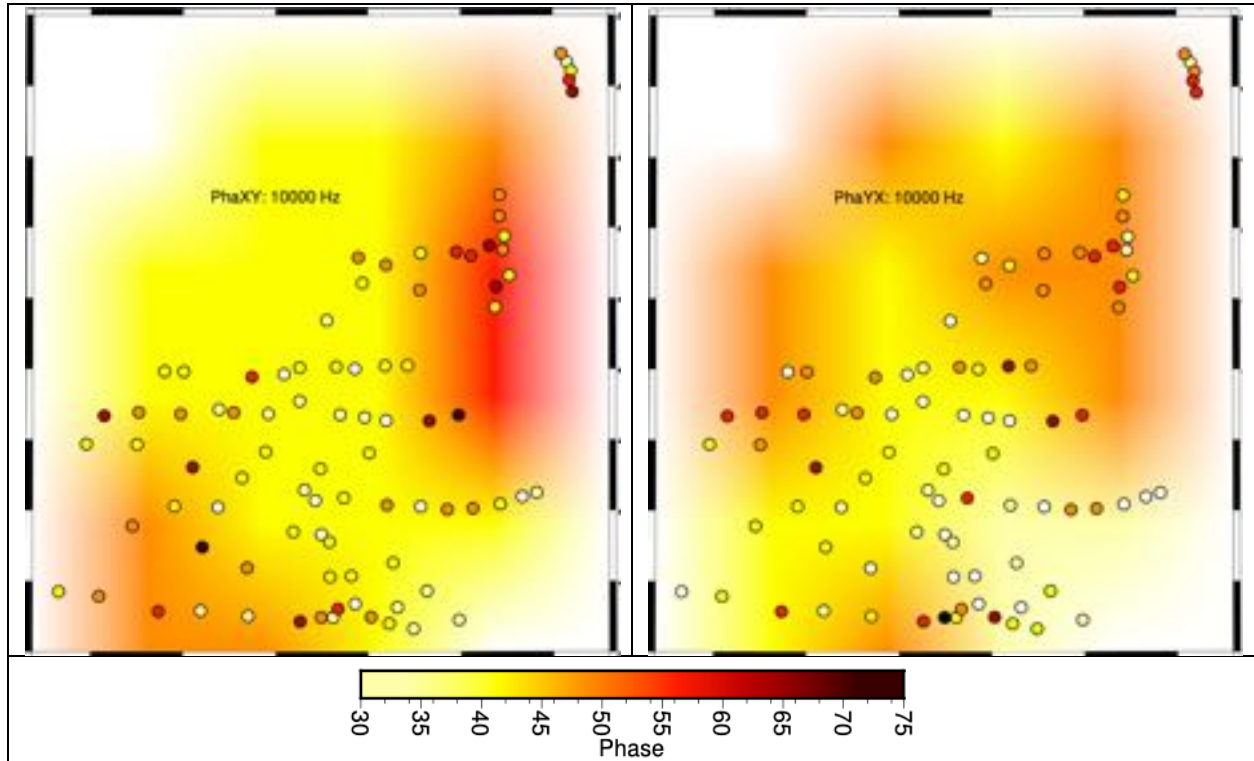
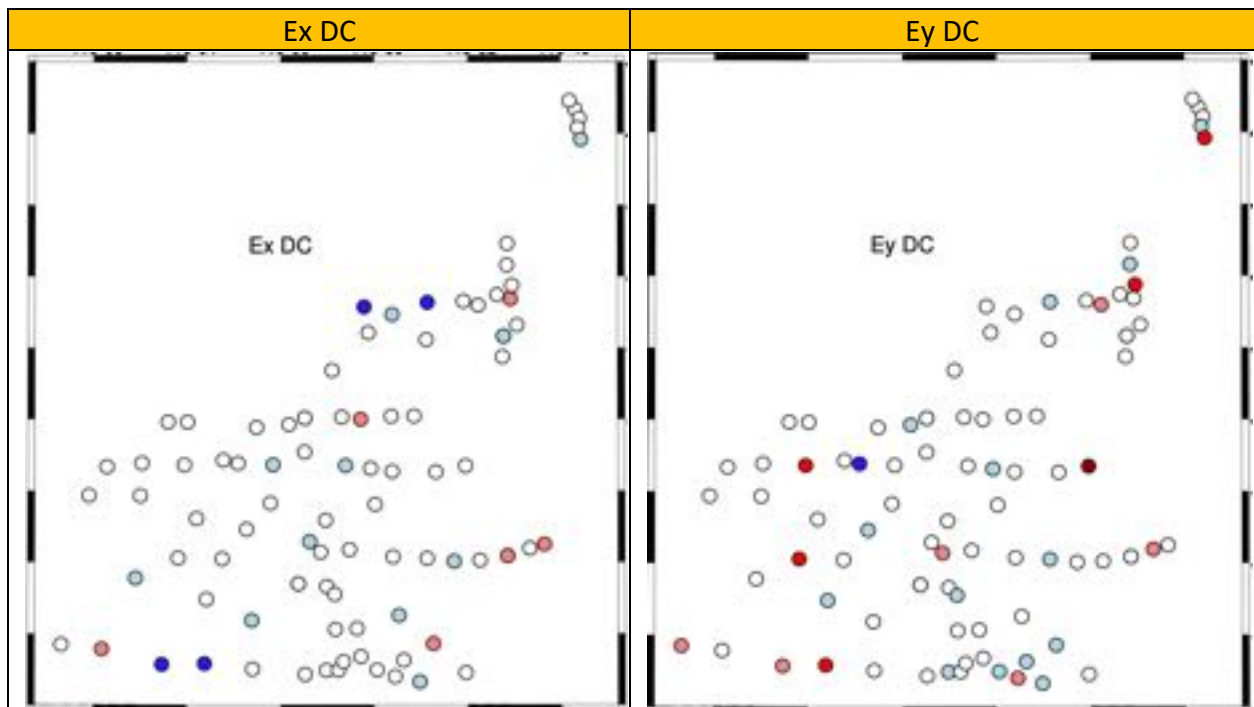


Figure 22: 10 kHz PhaXY (left) and PhaYX (right). Values at each site are shown by the coloured circles, and the contours are smoothed median maps of the values..

2.2. DC values

The DC values show that the electrodes were in good to very good condition



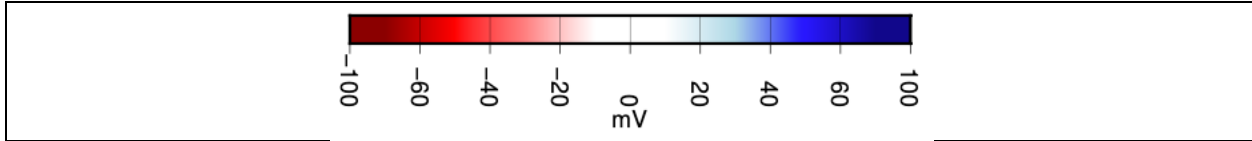


Figure 23: Electrode DC measurements.

2.3. AC values

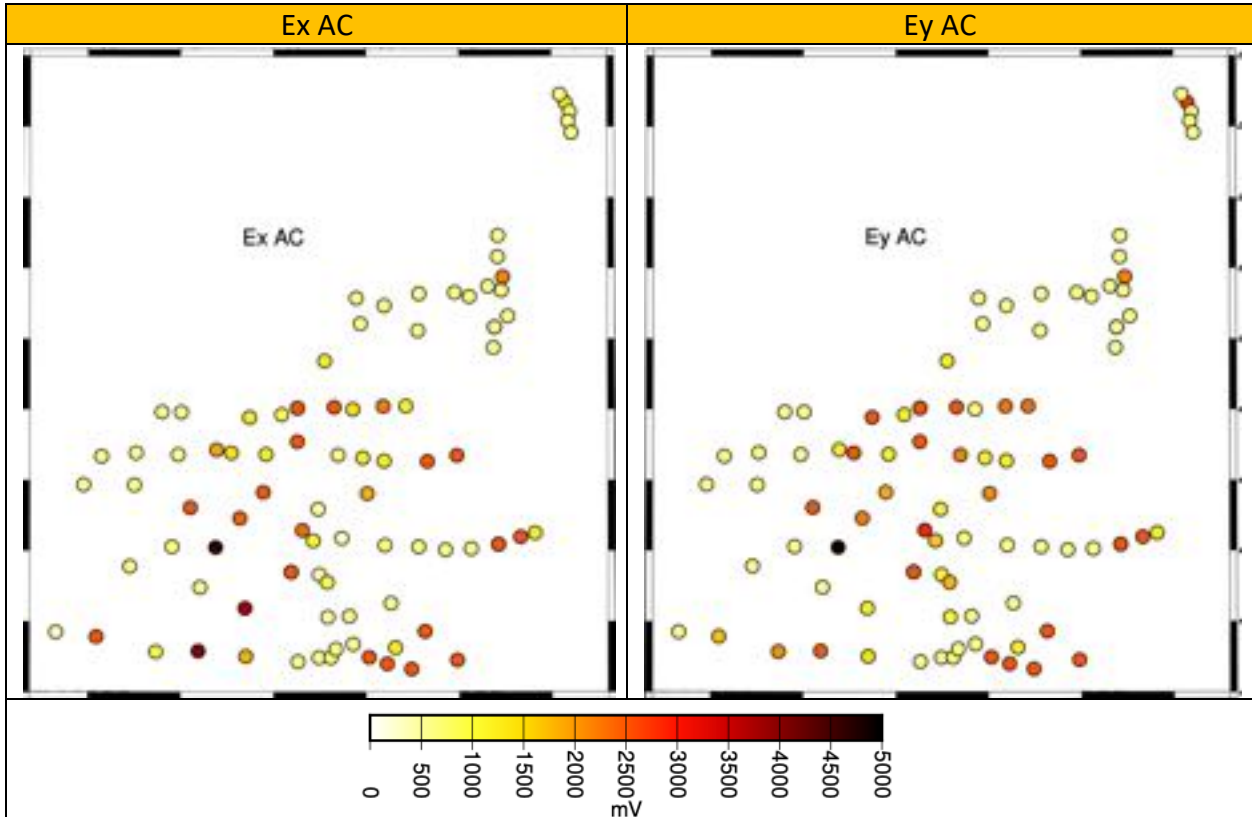


Figure 24: Electrode AC measurements.

3. MT Quality Factors

The derivation of the Smoothness Factor (SF), Error Factor (EF) and Quality Factor (QF) is described in Appendix C.

3.1. QF Plots

I plot sets of SF, EF and QF maps for each of five frequency/period bands for the MT data (Figure 25), assuming an error floor of 1° in phase/3.5% in apparent resistivity (which are levels for high quality data in the MT community).

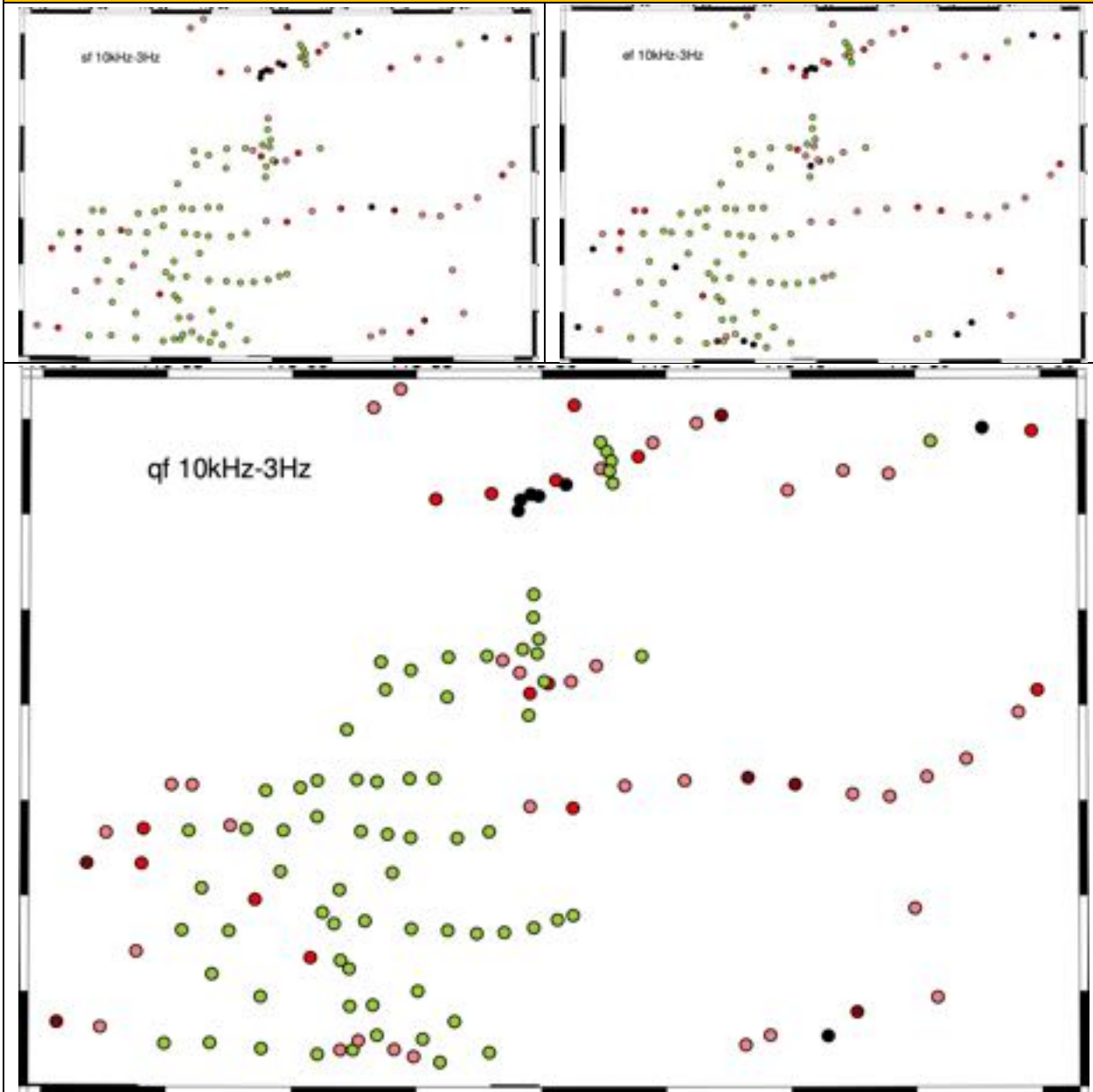
The frequency/period bands are:

- 1) 10 kHz – 3 Hz: These three-and-a-half decades cover all of the data that may be of interest, penetrating down to on average 4-5 km at the lowest frequency.
- 2) 3 Hz – 0.001 Hz: These three-and-a-half decades cover all of the data that may be of interest for crustal imaging, penetrating down to below the Moho at the lowest frequency.
- 3) 4 kHz – 800 Hz: This half decade covers the AMT dead-band, and has a depth penetration on average of 150 – 400 m.
- 4) 8 Hz – 0.1 Hz: This decade-and-a-half covers the MT deadband.
- 5) 800 Hz – 8 Hz: These two decades are where the best signals are that are sensing from 400 m to 3-4 km.
- 6) 0.1 Hz – 0.002 Hz (10 s – 500 s): This decade-and-a-half are where the best signals are sensing from 8 km to 25 km.

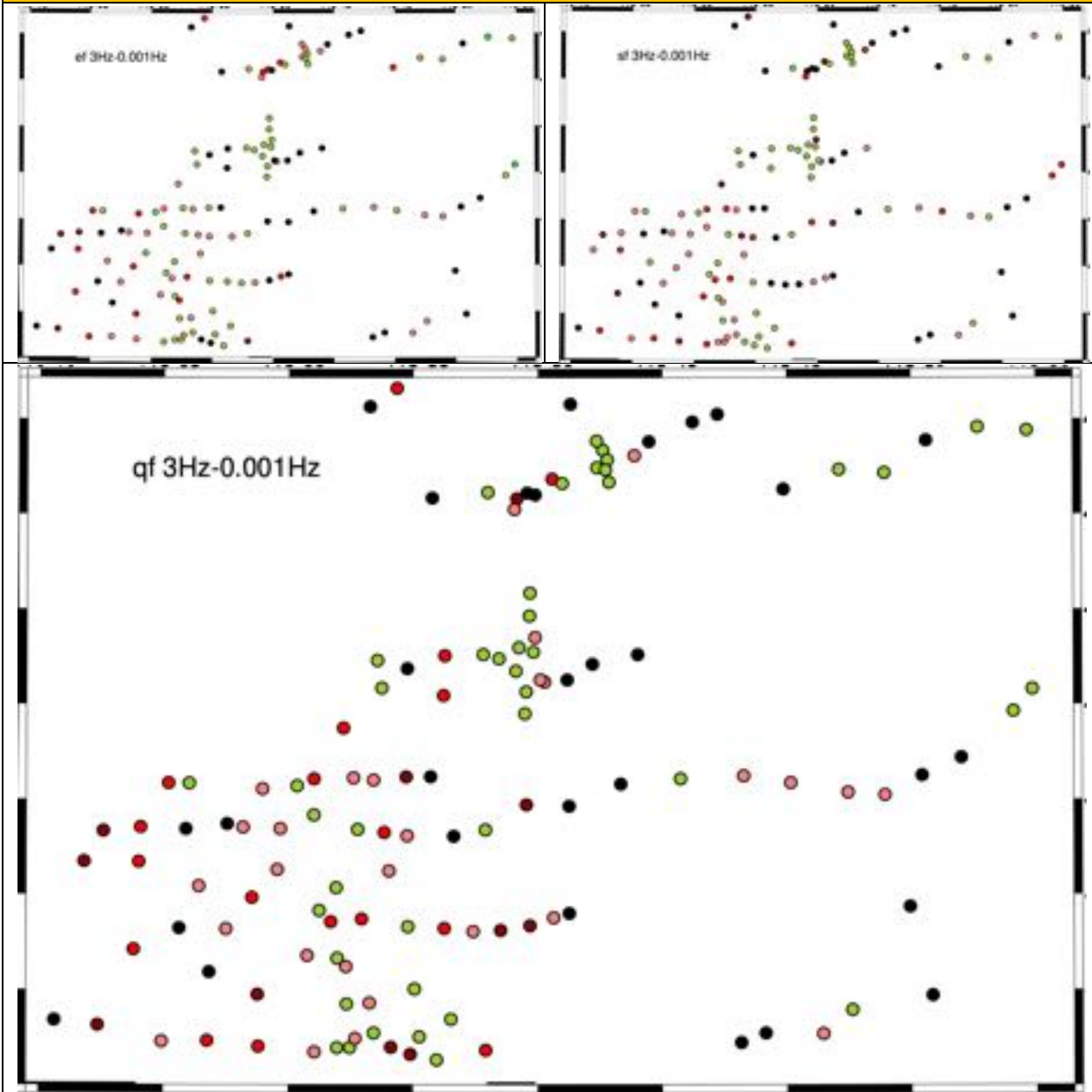
The median PHA errors for the frequency band 800 Hz – 8 Hz (avoiding the scatter in the AMT deadband) are $\text{PhaXY} = 0.025^\circ$ and $\text{PhaYX} = 0.0046^\circ$, which are ridiculously low. Even the diagonal phases are very low, $\text{PhaXX} = 0.17^\circ$ and $\text{PhaYX} = 0.11^\circ$. There is no way that errors can be that low. The problem is the Stodt parametric error estimator used by Phoenix to calculate the errors.

A brute force way of dealing with them is to assume an error floor, i.e., error estimates LESS than the floor are raised to the floor, and estimates greater than the floor are unchanged. An error floor of 1° in phase/3.5% in apparent resistivity was assumed – such an error floor is appropriate for high quality MT response estimates. Viewing the plots this is appropriate at some sites for some frequencies, but certainly not appropriate at all sites for all frequencies.

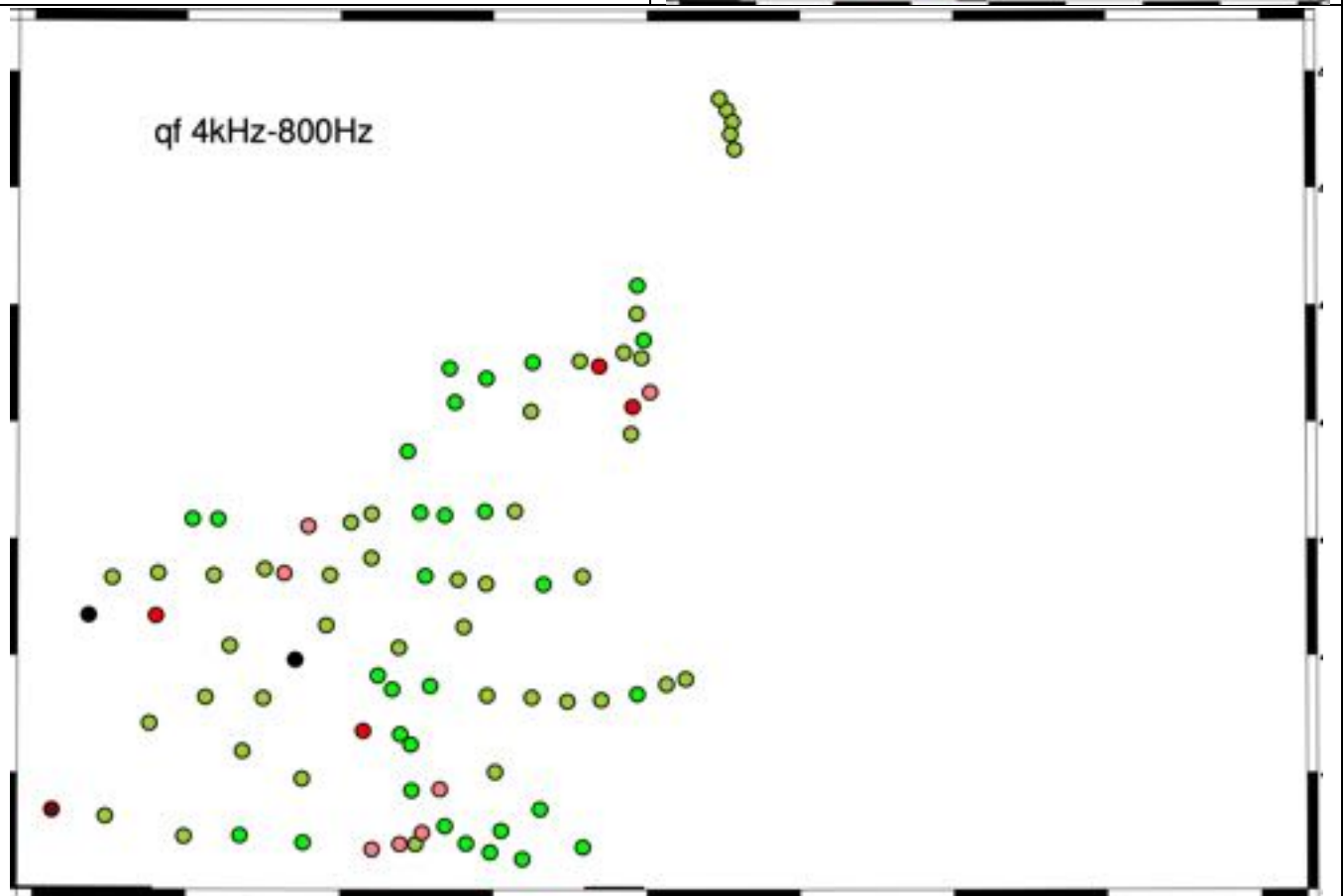
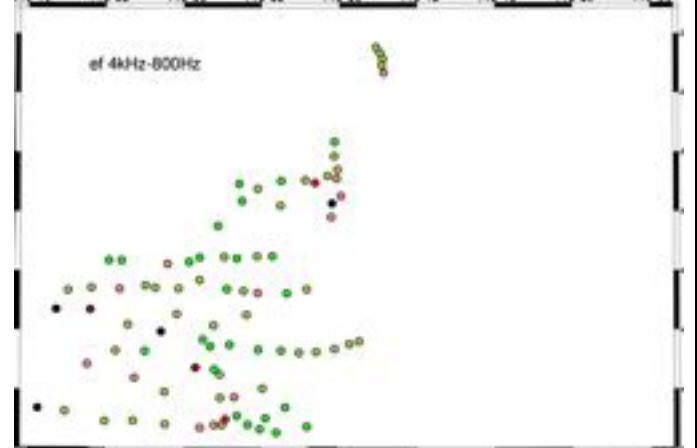
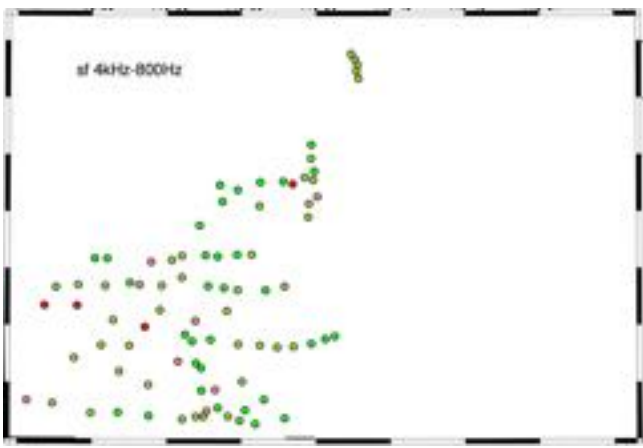
10 kHz – 3 Hz: Surface to 4-5 km



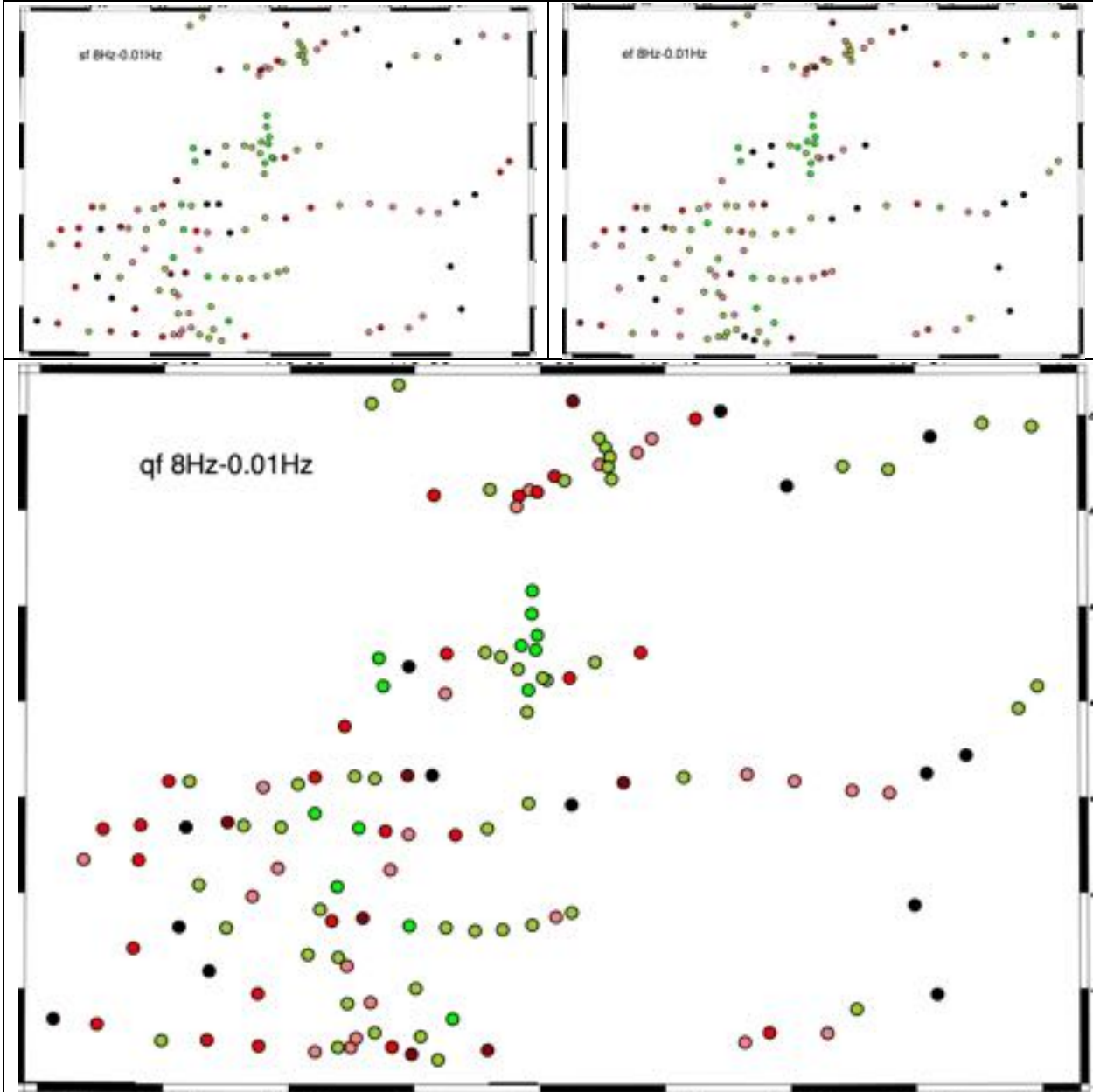
3 Hz – 0.001 Hz: 4-5 km to Moho



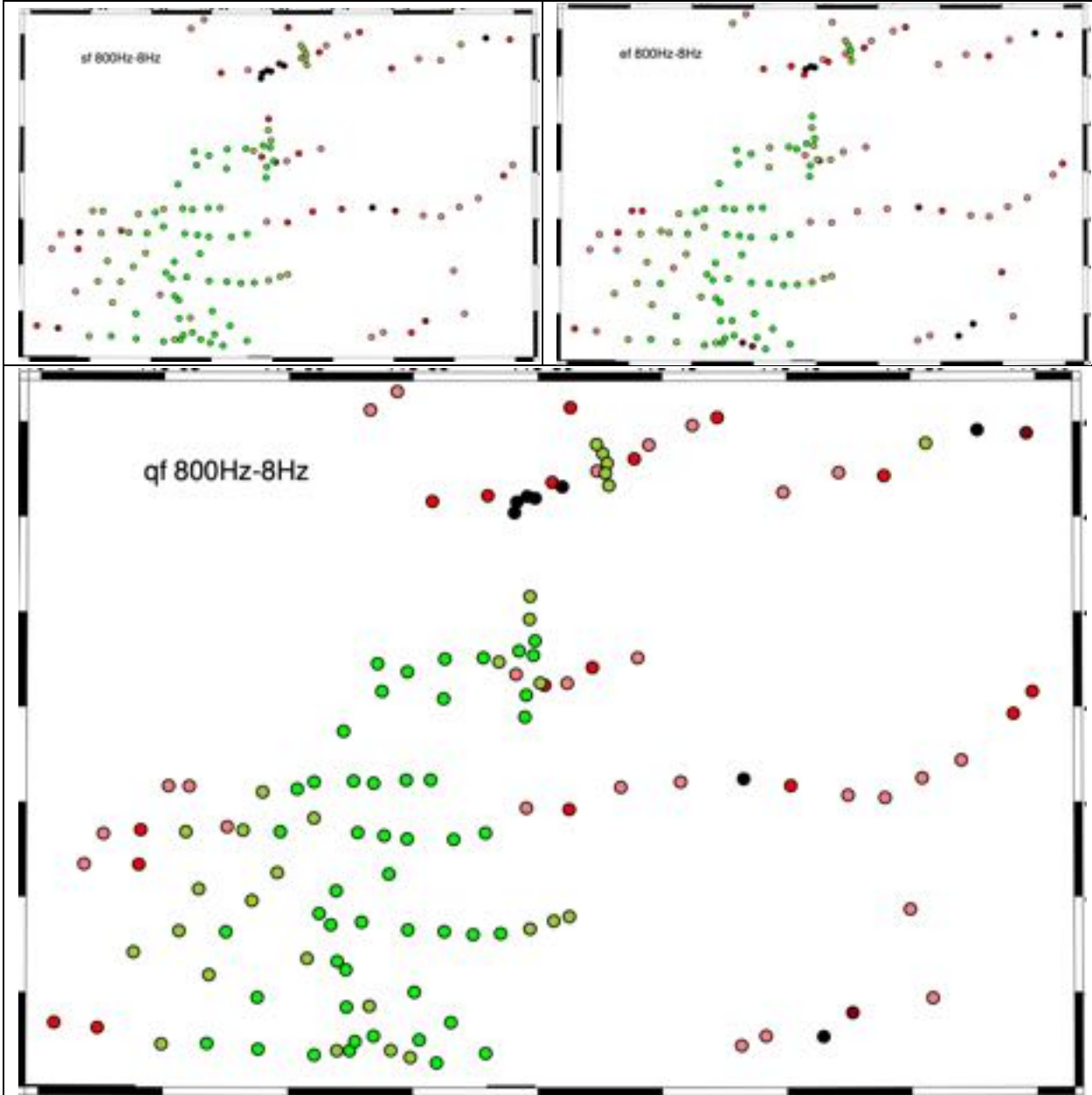
4 kHz – 800 Hz: AMT deadband



8 Hz – 0.1 Hz: MT deadband



800 Hz – 8 Hz: Optimum frequency band for shallow imaging



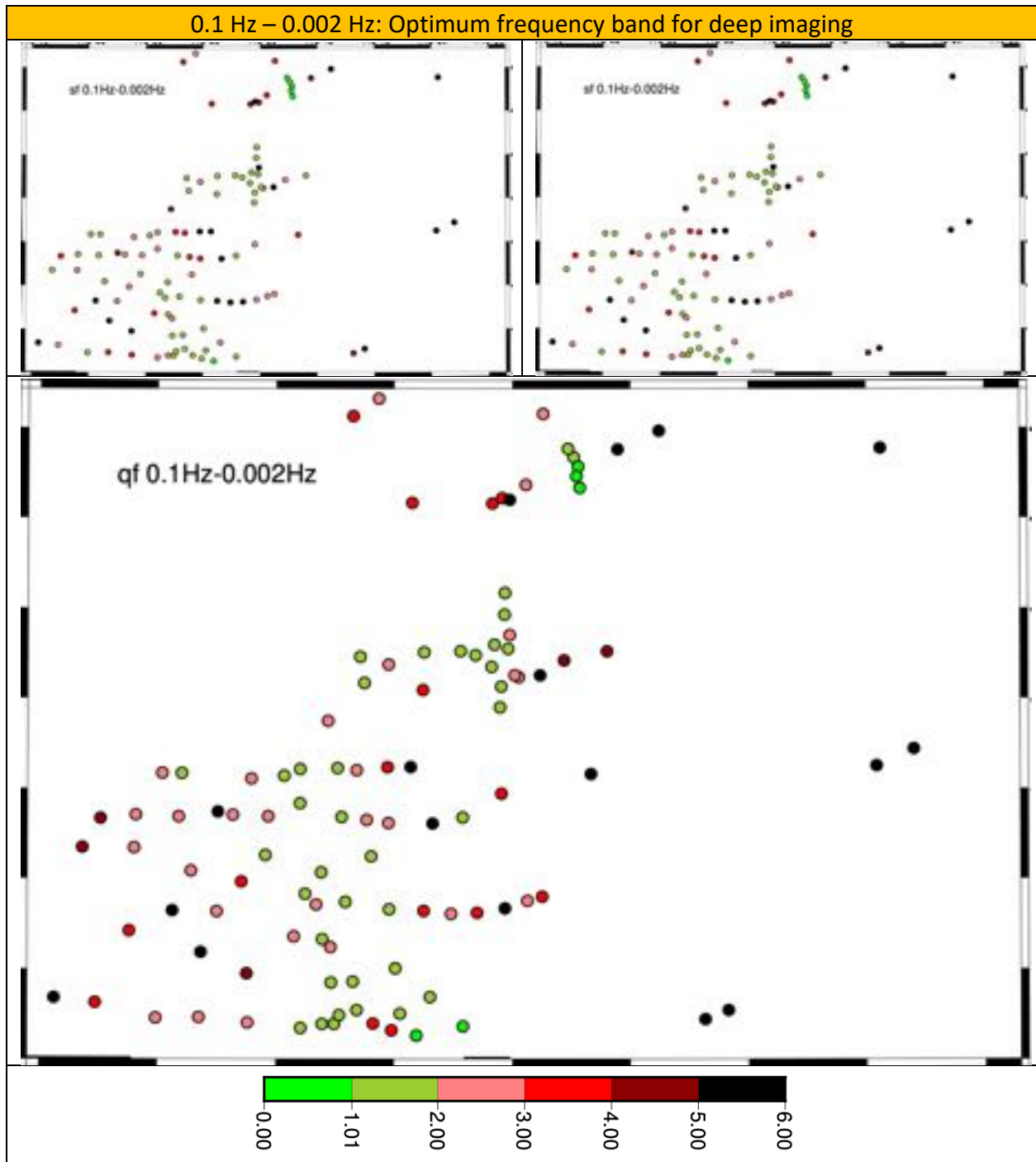
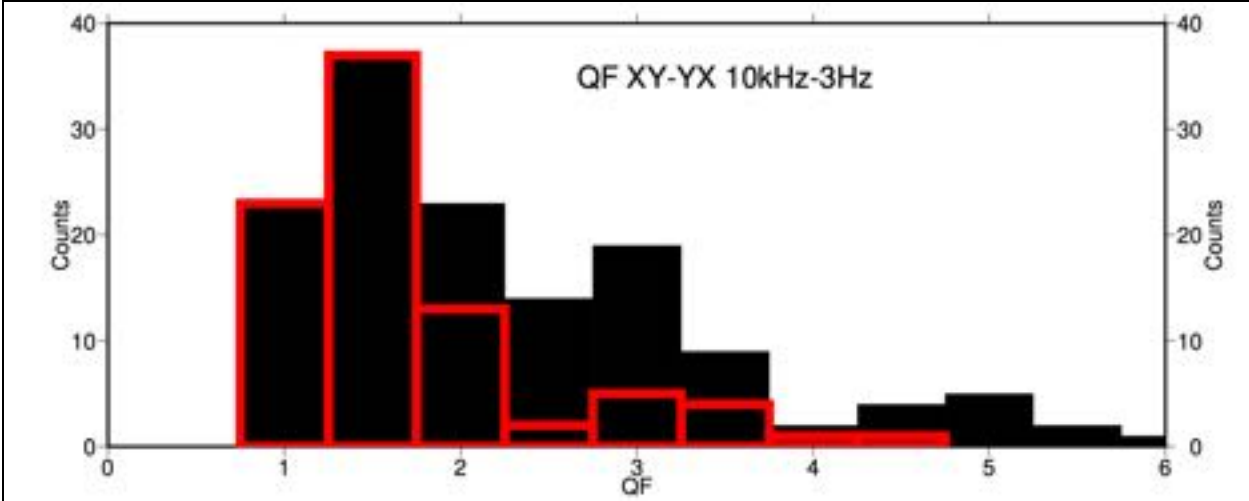


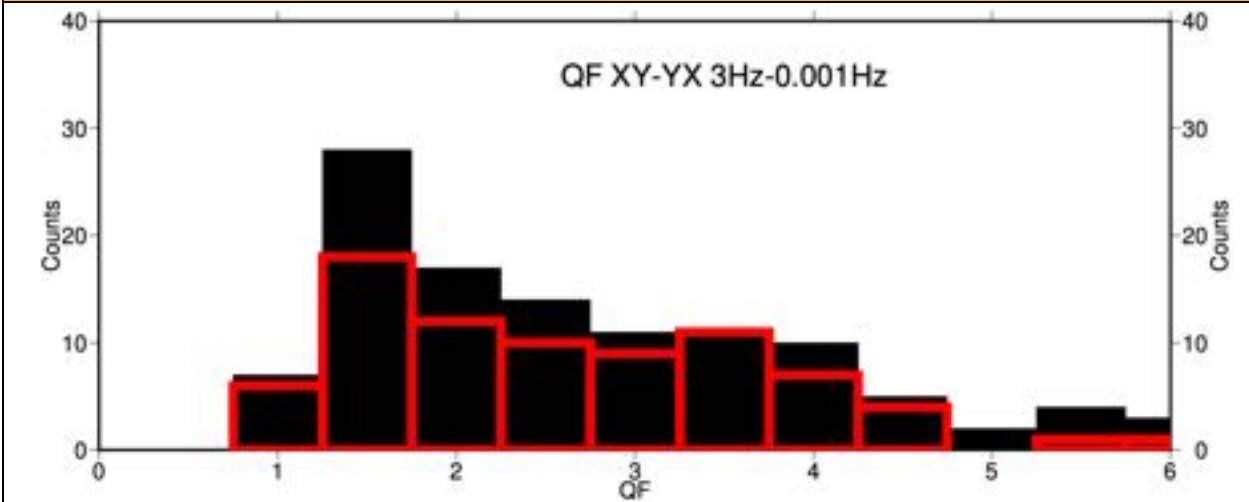
Figure 25: Maps of the Smoothness Factor (SF, left column), Error Factor (EF, right column) and Quality Factor (QF, bottom row), for an adopted error floor of 1° in Pha and 3.5% in RhoA..

The histograms of the QFs are shown in Figure 26. Histograms for all data are plotted in black, and those for the new Kootenay data only are with thick red lines.

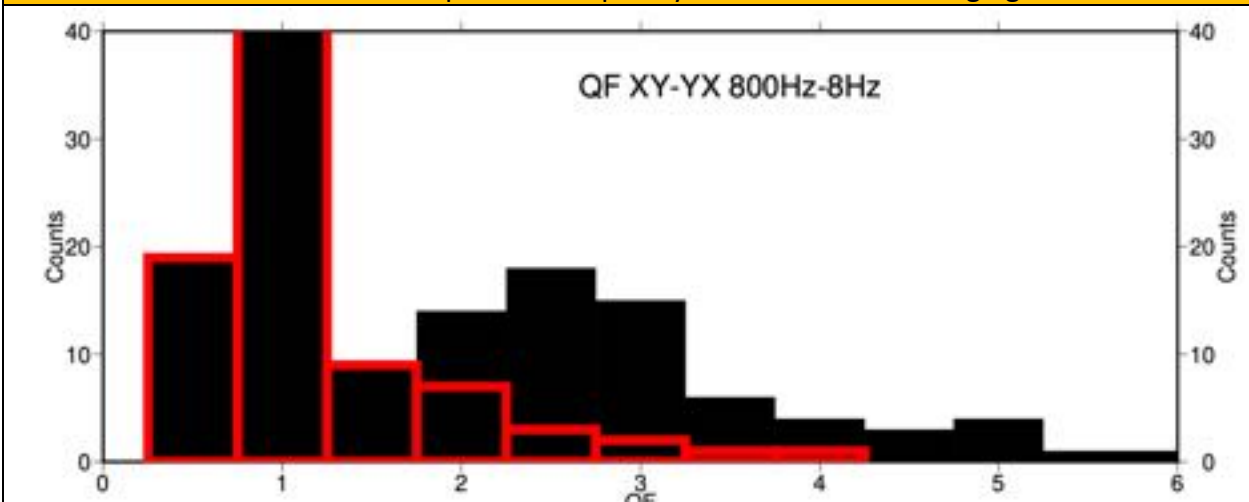
10 kHz – 3 Hz: Surface to 4-5 km



3 Hz – 0.001 Hz: 4-5 km to Moho



800 Hz – 8 Hz: Optimum frequency band for shallow imaging



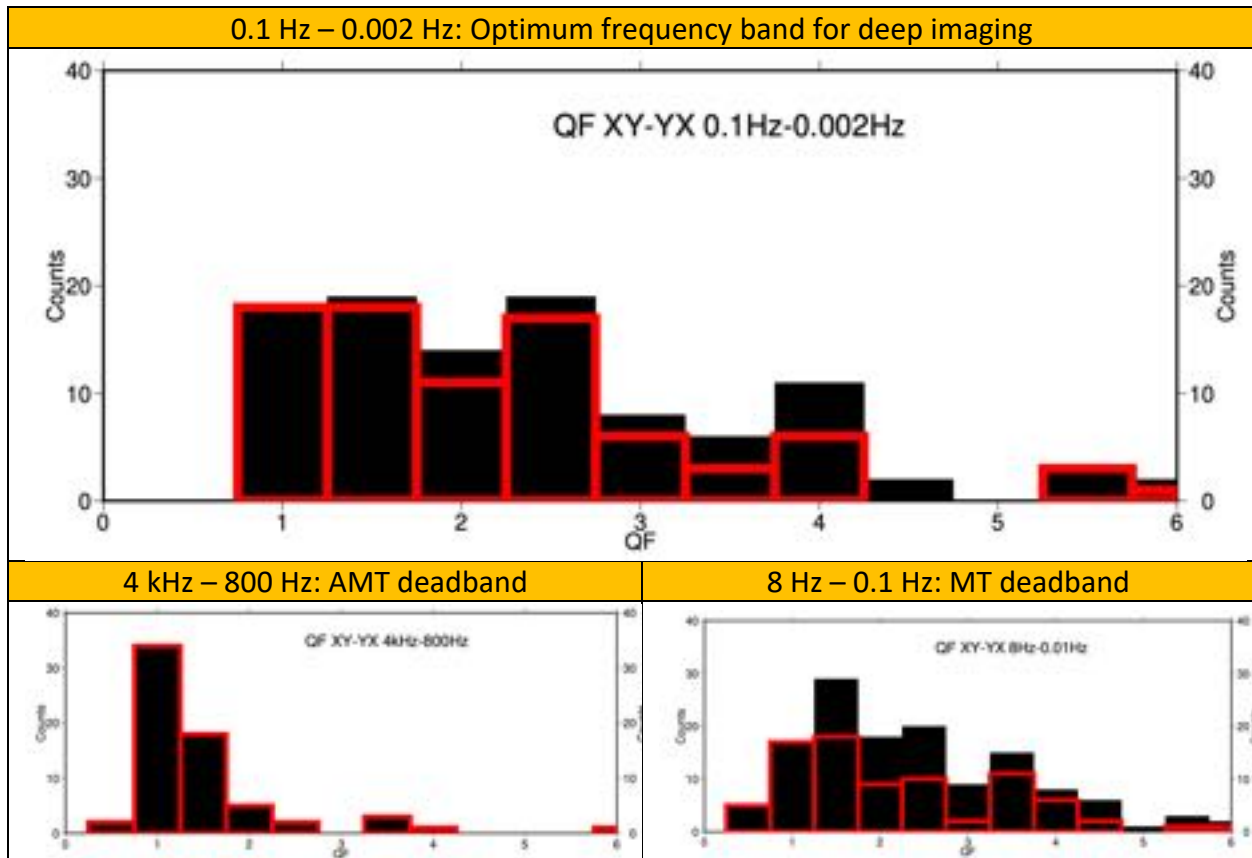


Figure 26: Histograms of the Quality Factors for various frequency bands for an adopted error floor of 1° in Pha and 3.5% in RhoA. Note: Only QFs to 6 are plotted, larger values are omitted from these plots. The black histograms are for all data, and the red lines indicate the new Kootenay data only

Overall, in the 10 kHz – 3 Hz band the QFs are well peaked at QF=1.25-1.75, with the Kootenay data having far lower QFs (= better quality) than the older Duncan data. The overall mean and median are 2.49 and 2.09, with first and third quartiles of 1.34 and 2.89. For the Kootenay data only, the mean and median are 1.71 and 1.44, with first and third quartiles of 1.23 and 1.82, statistical testament to the far higher quality of the new Kootenay data compared to the older Duncan data in this frequency band. Recall also that the older data only goes to a maximum frequency of 384 Hz.

At the lower frequency band however of 3 Hz – 0.001 Hz, the QF histogram is flatter, but nevertheless exhibits a peak at 1.25-1.75, albeit not as strong a peak. Also the distribution is very long tailed, with almost 25% of the QFs being >6 so not plotted. The overall mean and median are 4.32 and 2.89, with first and third quartiles of 1.75 and 5.73. For the Kootenay data only, the mean and median are 2.69 and 2.44, with first and third quartiles of 1.62 and 3.41, meaning there are fewer sites with very high QF so generally the Kootenay data are superior.

In the optimum frequency band of 800 Hz – 8 Hz, the Kootenay data are clearly far superior to the older data. The overall mean and median are 2.23 and 1.58, with first and third quartiles of 0.89 and 2.92. For the Kootenay data only, the mean and median are 1.18 and 0.94, with first

and third quartiles of 0.76 and 1.27. For the Duncan data, these values are 3.80, 3.04, 3.42 and 3.86. This again provides statistical evidence of the far higher quality of the new Kootenay data compared to the older Duncan data at frequencies probing down to 4-5 km.

→ We can conclude that the appropriate error floors for the new Kootenay data is 3.56%/1° for RhoA and Pha respectively for frequencies probing down to 4-5 km, whereas for the Duncan data higher error floors of 10.86%/3° are appropriate.

→ At the deeper-probing frequencies down to the Moho, then overall error floors of 9.61%/2.7° are appropriate for the Kootenay data

3.1.1. Change of QF with survey time

The QFs over the length of the survey for the new Kootenay data are shown in Figure 27 for the shallow-probing (red) and deep-probing (black) frequency bands.

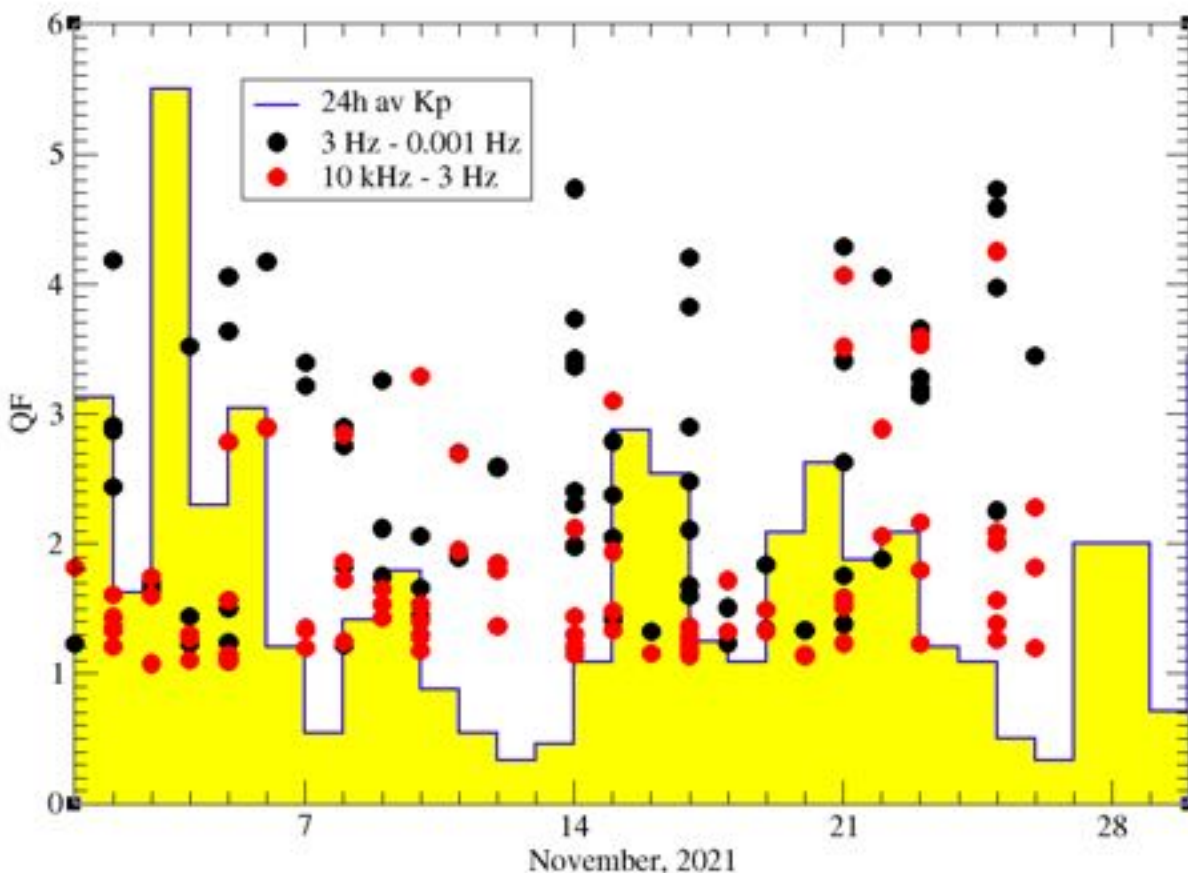


Figure 27: QFs in the frequency ranges 10 kHz - 3 Hz (black) and 10 kHz - 3Hz (red), with acquisition start day since 1st November, 2021. The yellow histogram gives the daily averaged Kp values.

There is clearly variation with time of the quality of the data in both bands. These are both signal related. The 3 hour Kp indices ⁽¹⁾ for November have been averaged from midday to midday on the day. There was significant low frequency (<8 Hz) magnetic activity at the beginning of November, and again from 15th onwards, but there was a deep lull in magnetic activity from 7th to 14th.

A plot of the Kp indices against derived QFs for the impedance estimates in the 3 Hz – 0.001 Hz band (Figure 28) shows a strong visual relationship; high Kp correlates with low QF (= high quality data), and vice-versa. Omitting the three anomalous points with very high Kp of 5.5, the others are fit to a linear regression (red line) with a correlation coefficient of -0.42.

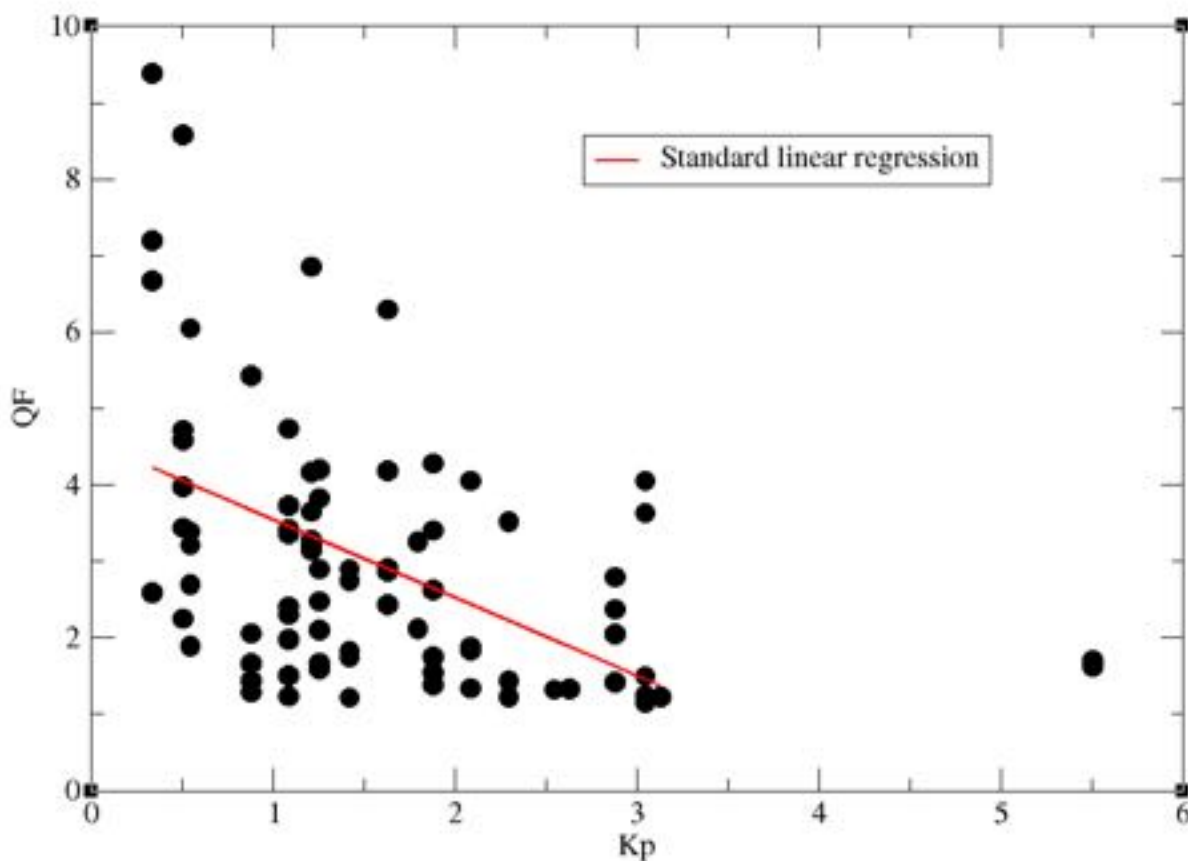


Figure 28: Kp indices against QFs for 3 Hz - 0.001 Hz band

¹ The Kp-index is the global geomagnetic activity index that is based on 3-hour measurements from ground-based magnetometers around the world. The Kp-index is a three hour long quasi-logarithmic index of the geomagnetic activity. The Kp-index ranges from 0 to 9 where a value of 0 means that there is very little geomagnetic activity and a value of 9 means extreme geomagnetic storming.

→ The quality of the low frequency responses (<8 Hz) is directly correlated with signal activity.

3.2. Example sites

Below I show examples of data for varying quality sites for the band 10 kHz to 3 Hz, which is the band of primary interest to the client.

3.2.1. Example of excellent quality sites, $QF = 1.00 - 1.25$

Of the 86 sites, over one quarter (23) have a $QF < 1.25$. The lowest of all is site KSS114 with a QF of 1.077 (Figure 29). These are really beautiful data – both the main off-diagonals (XY & YX) are smooth, and the diagonal elements (XX & YY) are well-determined.

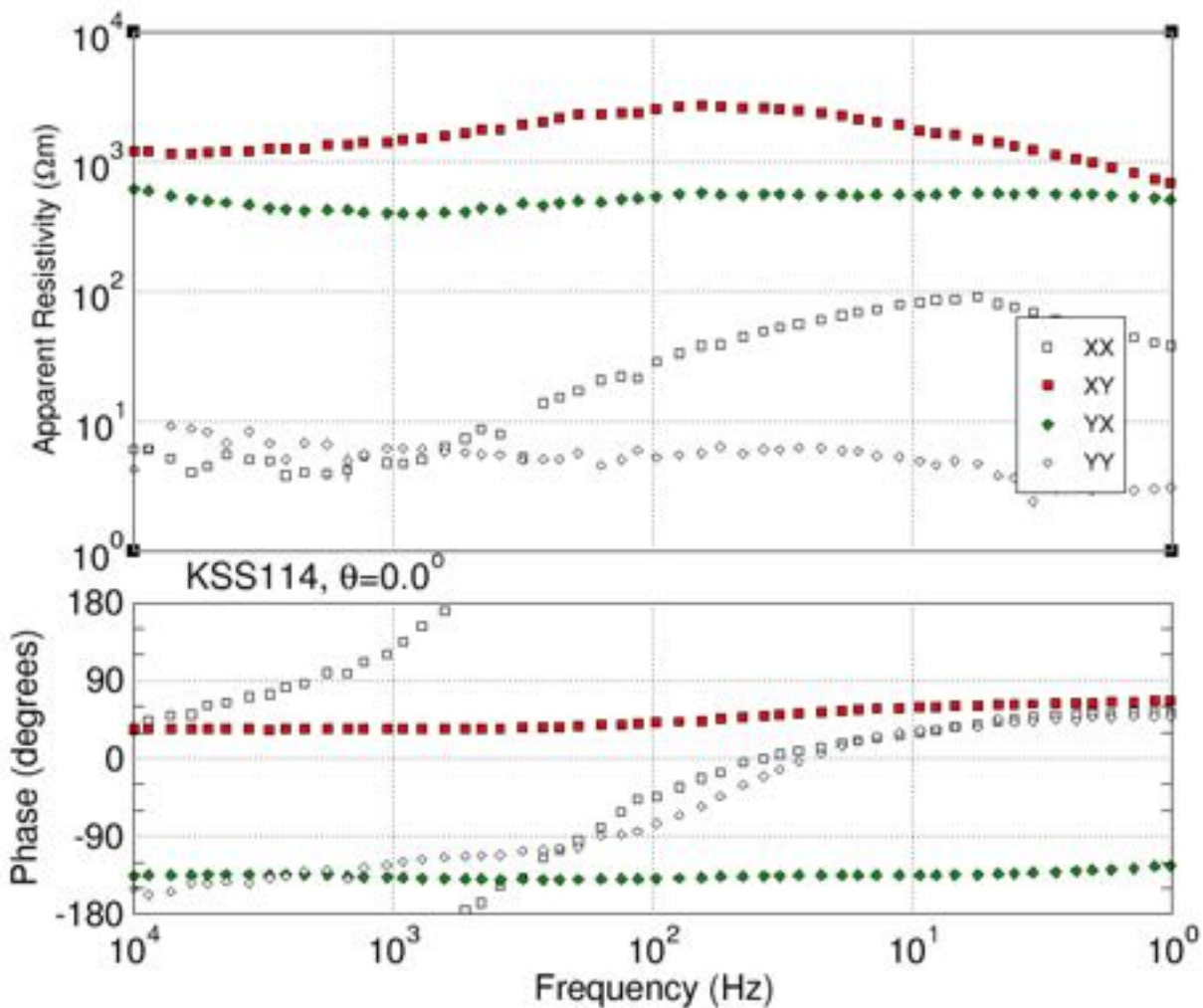


Figure 29: Example of excellent quality sites with lowest QF in the range 1.00 – 1.25.

One point to note is that at frequencies <300 Hz the Pha_{XX} and Pha_{YY} curves are on top of each other. This is a sign that the data can be validly fit with an anisotropic 1-D model.

3.2.2. Example of very high-quality sites, $QF = 1.25 - 1.50$

The next one quarter (23 sites) have a QF in the range 1.25 – 1.50. The example chosen is in the middle of this range, and is site KMM209 with $QF = 1.367$

There is now some visible scatter, particularly at a couple of frequencies in the AMT deadband and into the MT deadband, which is why the QFs are not 1. Note also the more poorly determined diagonal elements at low frequency, particularly XX.

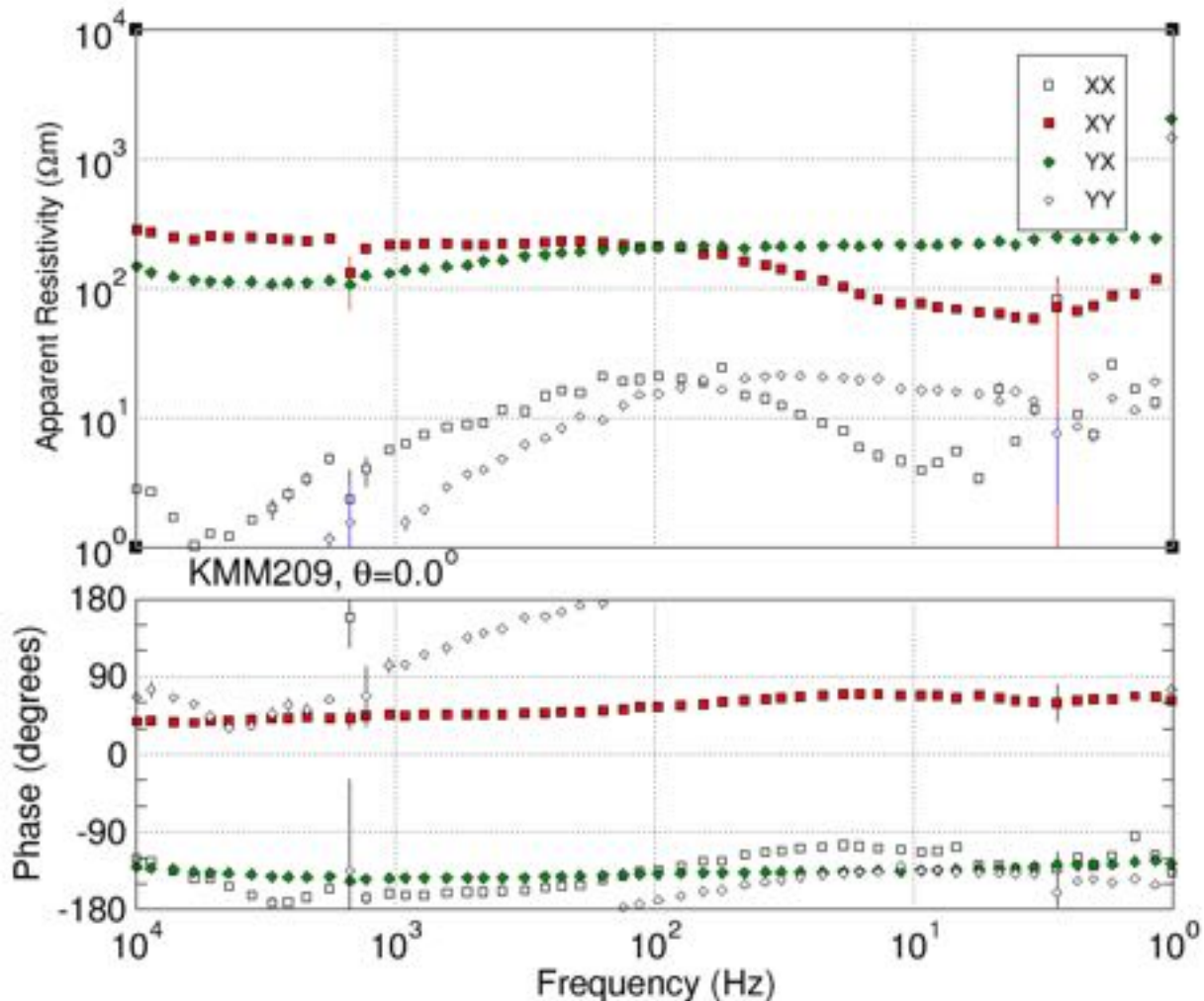


Figure 30: Example of very high quality site with QF in the range 1.25 – 1.50

3.2.3. Example of high quality sites, $QF = 1.5 - 2.0$

The next quarter (22) of sites have QF in the range 1.5 – 2.0. The site with the QF closest to the middle of this range is KSP009 with a $QF = 1.743$ (Figure 31).

Most of the XY and YX estimates are visibly very good, but with a small amount of scatter visible at the AMT deadband frequencies and up to 10 kHz, especially in YX (green diamonds). The diagonal elements XX and YY are more scattered above 1 kHz, especially YY (open diamonds).

These two shared the same electric field, E_y , so the high frequency noise was predominantly on that channel.

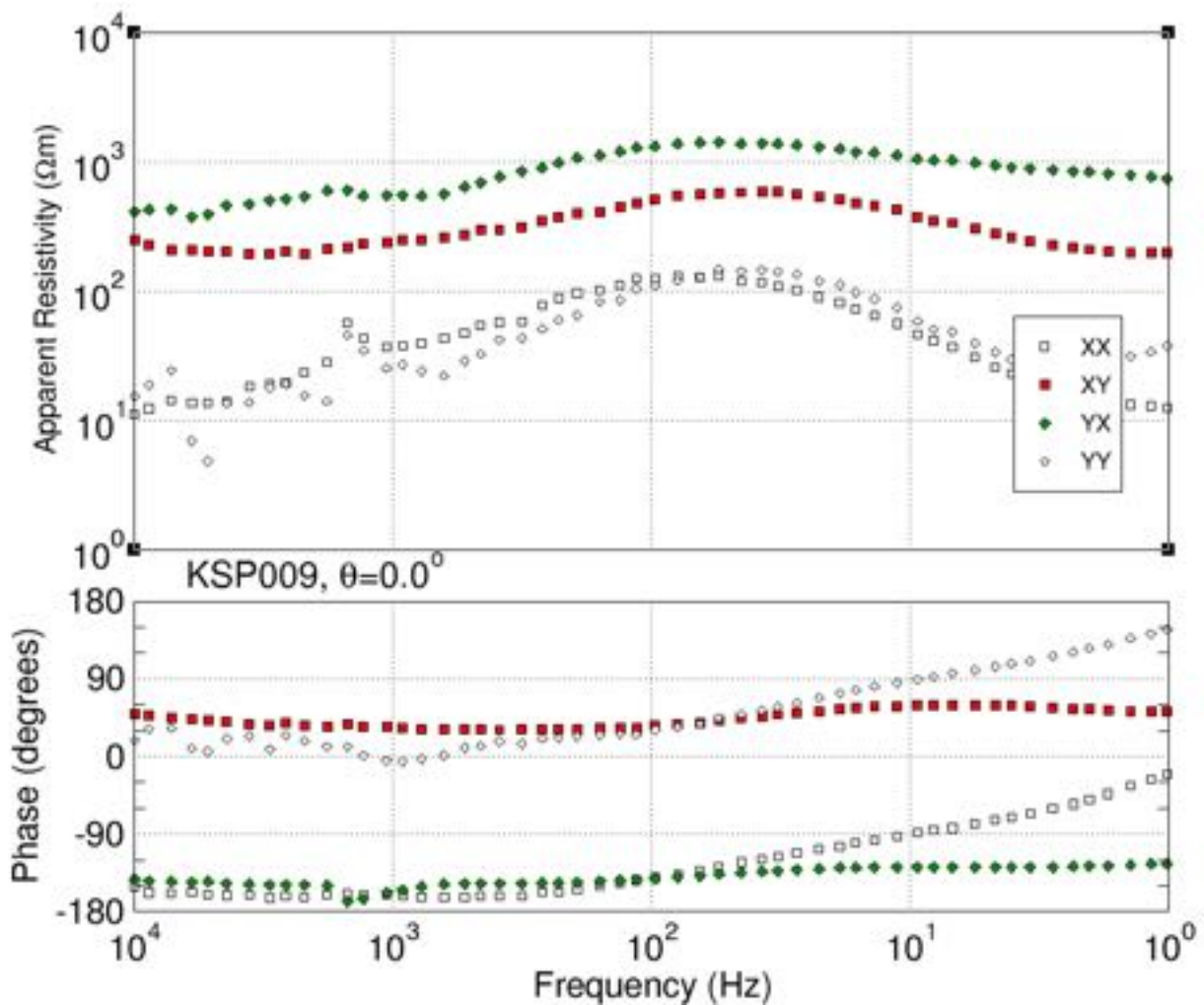


Figure 31: Example of high quality site with the QF in the range 1.5 – 2.0

3.2.4. Example of good to medium quality sites, QF = 2.0 – 3.0

There are eleven (11) sites with QF between 2.0 to 3.0. (Figure 32). The example is site KSS107 with QF = 2.688.

There is now far more visible scatter at high frequencies above 900 Hz, but the lower frequencies are still beautiful.

The diagonal elements, especially YY, are poorly estimated with a lot of scatter at high frequencies, and also below 10 Hz.

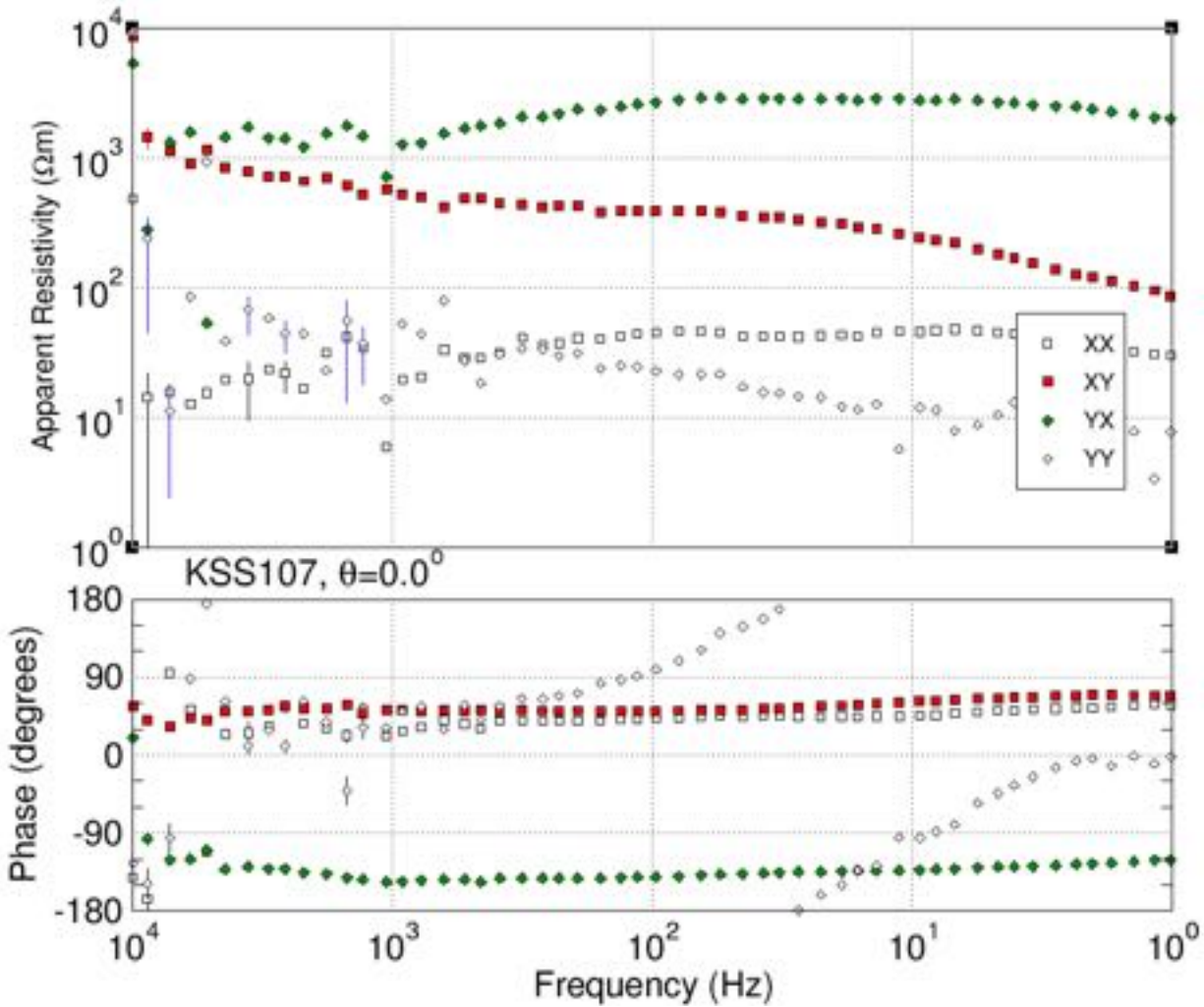


Figure 32: Example of good quality site with QF in the range 2.0 - 3.0.

3.2.5. Example of mediocre quality sites, QF = 3.0 – 4.25

Finally, there are eight (8) sites with QF in the range 3.0 – 4.25. The worst quality is KSS101 with QF = 4.251 (Figure 33).

For this site the scatter is primarily between 300 – 100 Hz, not in the AMT or MT deadbands.

Site KSS101 was located up the Emer Creek Forest Service Road some 1 km off Highway 95, and is some 3 km from the border areas of Kingsgate (CA) and Eastport (USA), with significant industrial structures and railways. I suspect that the scatter is caused by electrical interference from harmonics of 60 Hz (120 Hz, 180 Hz, 240 Hz, 300 Hz) that is not being adequately rejected by the processing software.

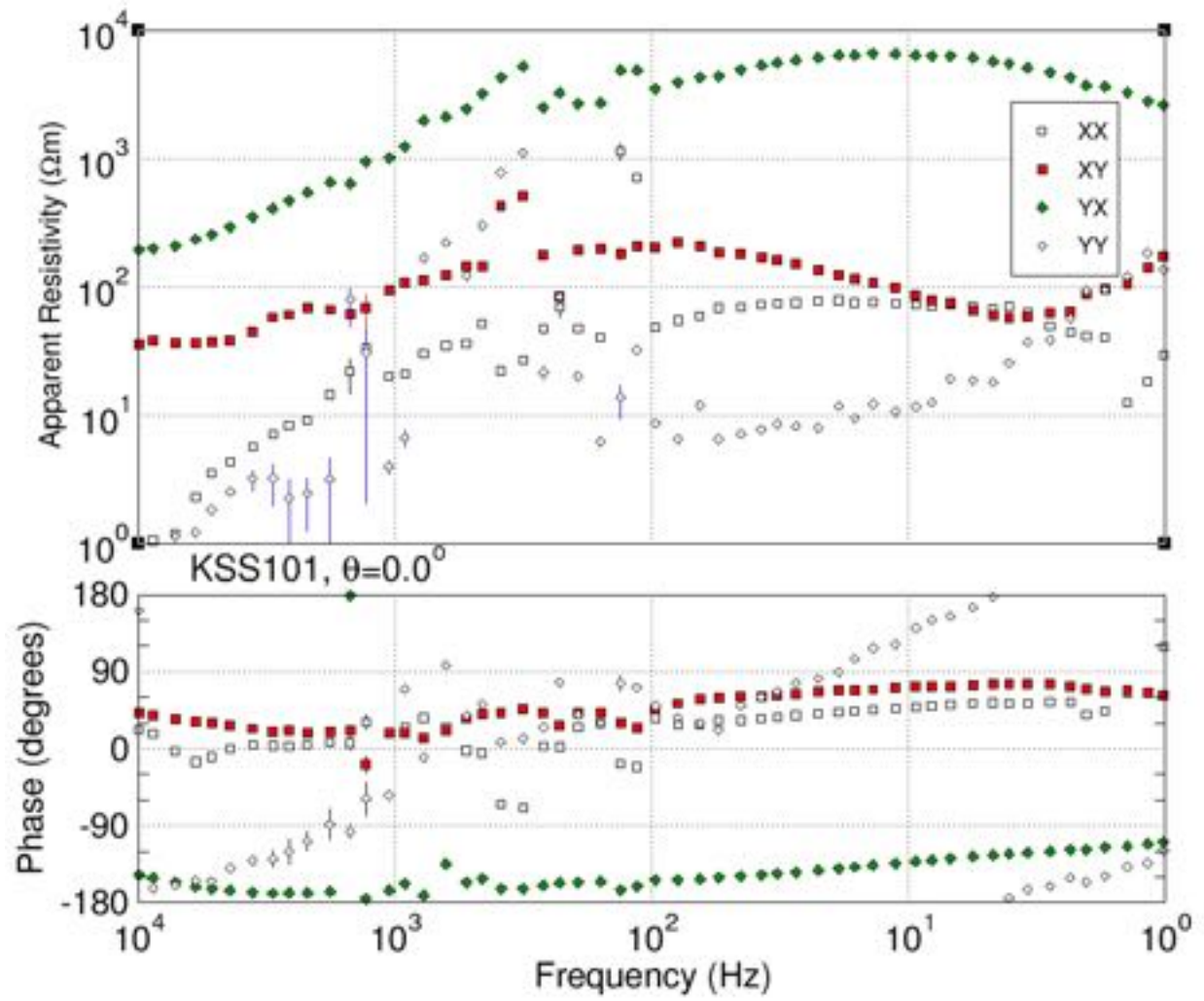


Figure 33: Example of mediocre quality sites with QF in the range 3.0 – 4.25.

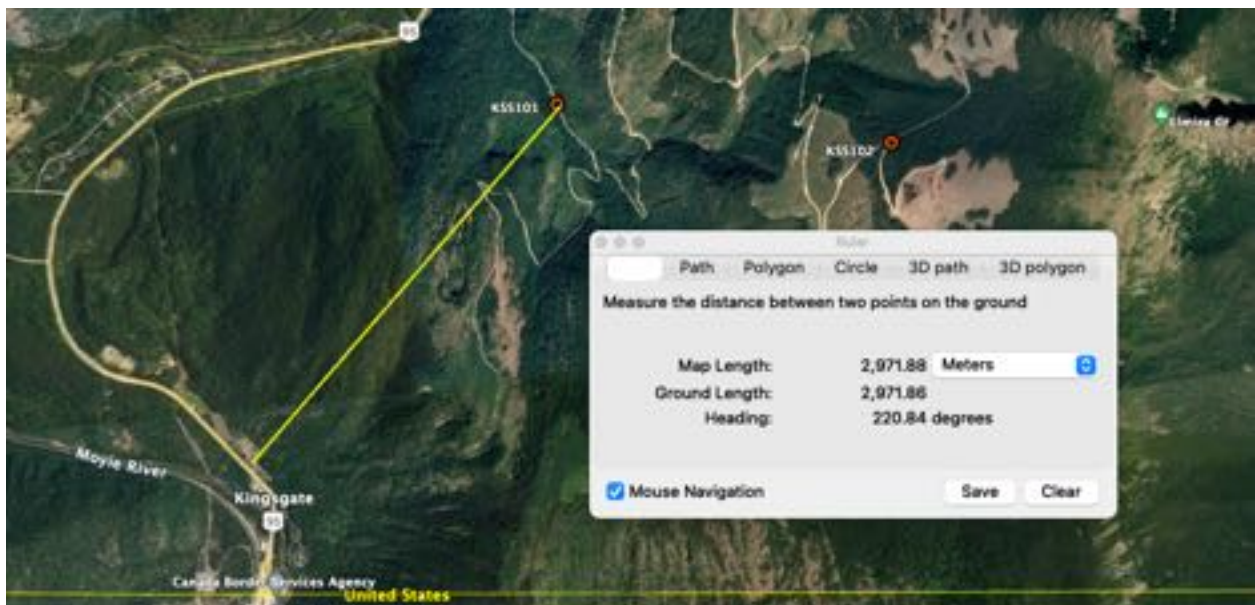


Figure 34: Location of site KSS101.

3.3. QF cf. electrode array parameters

Finally, we cross-plot the QF values derived in the frequency band 10 kHz – 3 Hz against the electrode array parameters, contact resistance, AC and DC values, to see if electrode array installation affected the quality of the data.

The plot of QFs against contact resistances (Figure 35) do not show any correlation between contact resistance and the QF values.

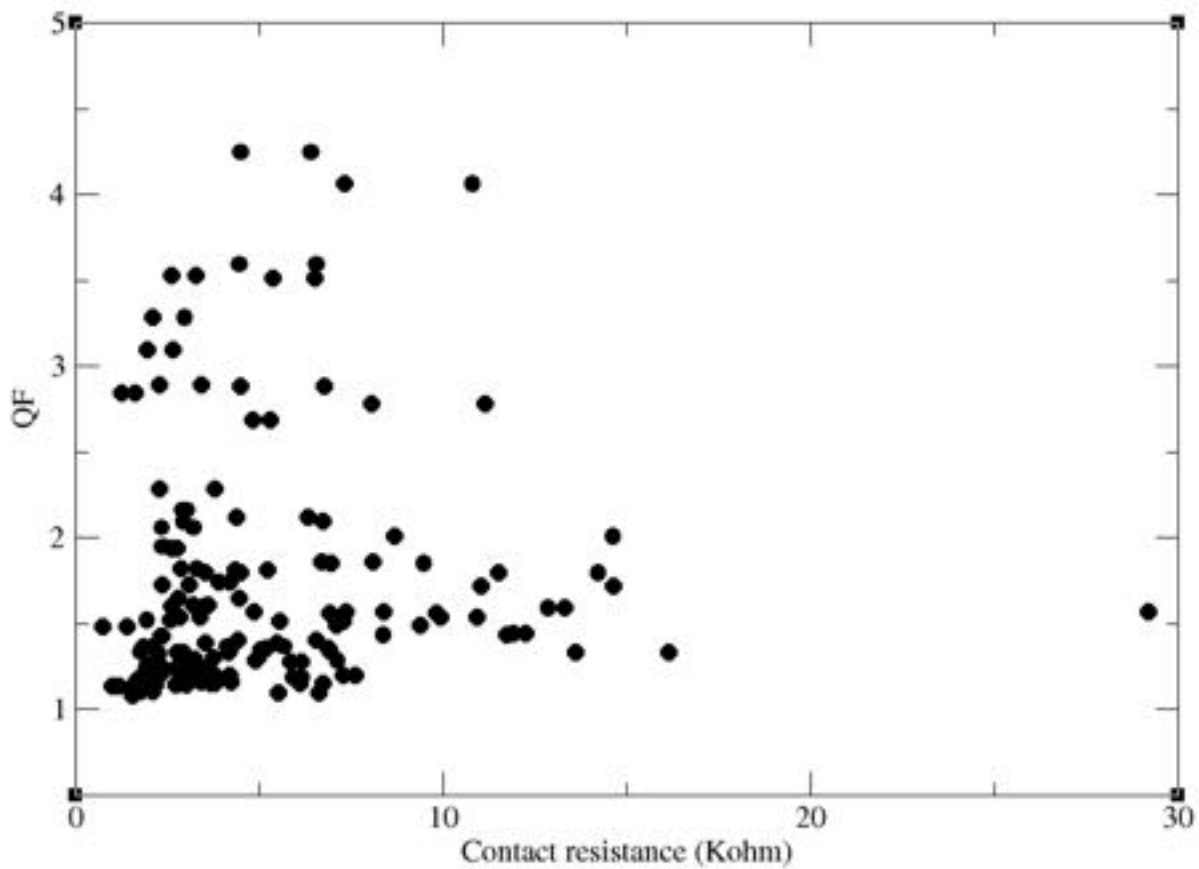


Figure 35: Cross-plot of QFs against contact resistances.

The cross-plot of measured AC against QFs is plotted in Figure 36. Again, no visible correlation of the two is evident.

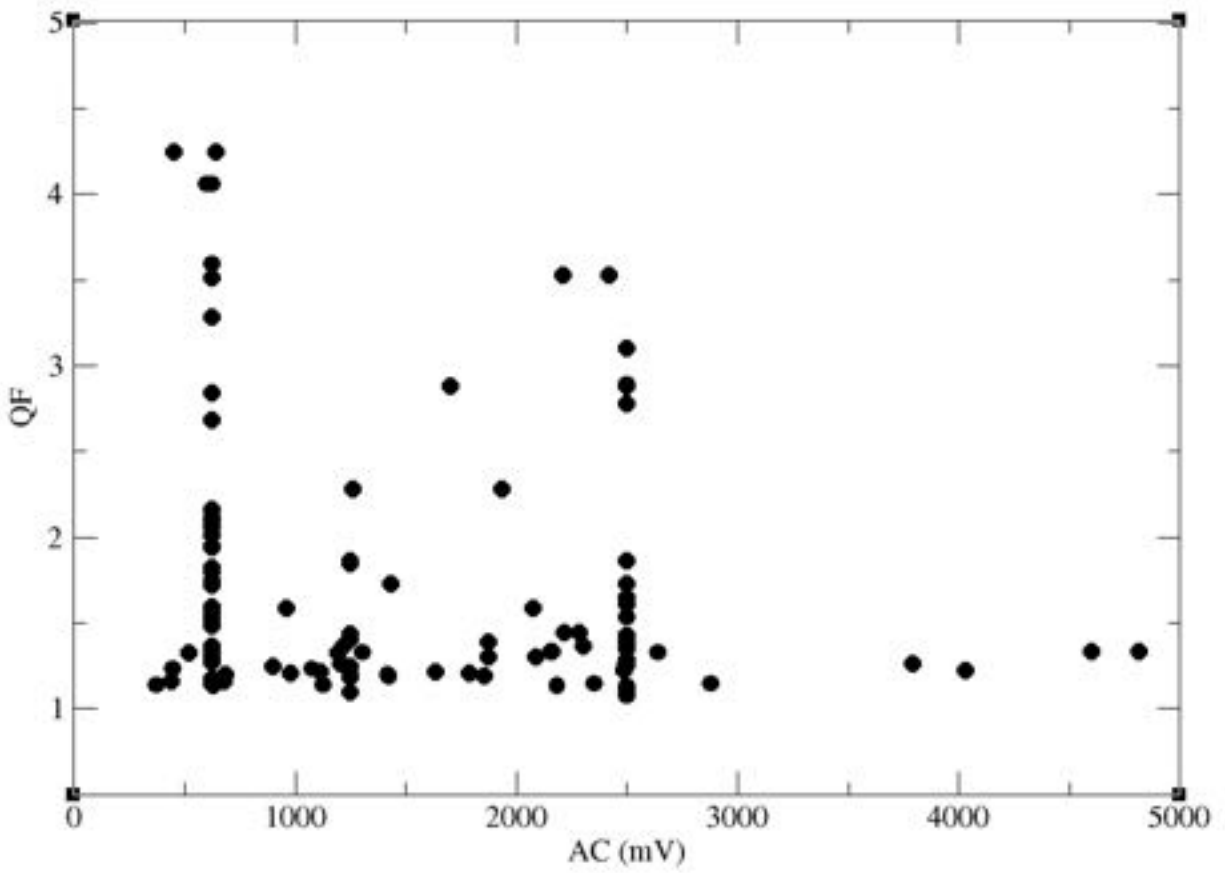


Figure 36: Cross-plot of AC against QFs

The cross-plot of the absolute values of the measured DC against QFs is plotted in Figure 37. Again, no discernible correlation is evident.

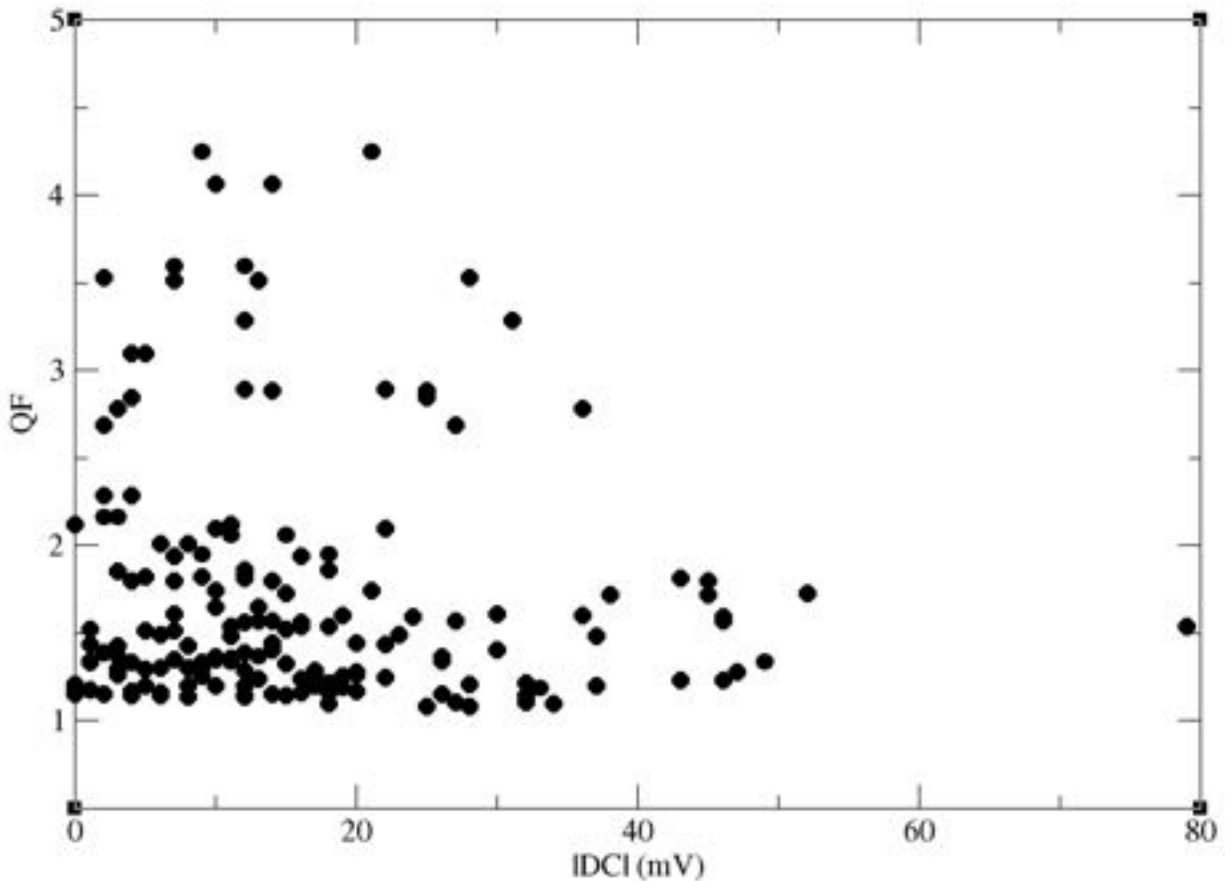


Figure 37: Cross-plot of DC against QFs

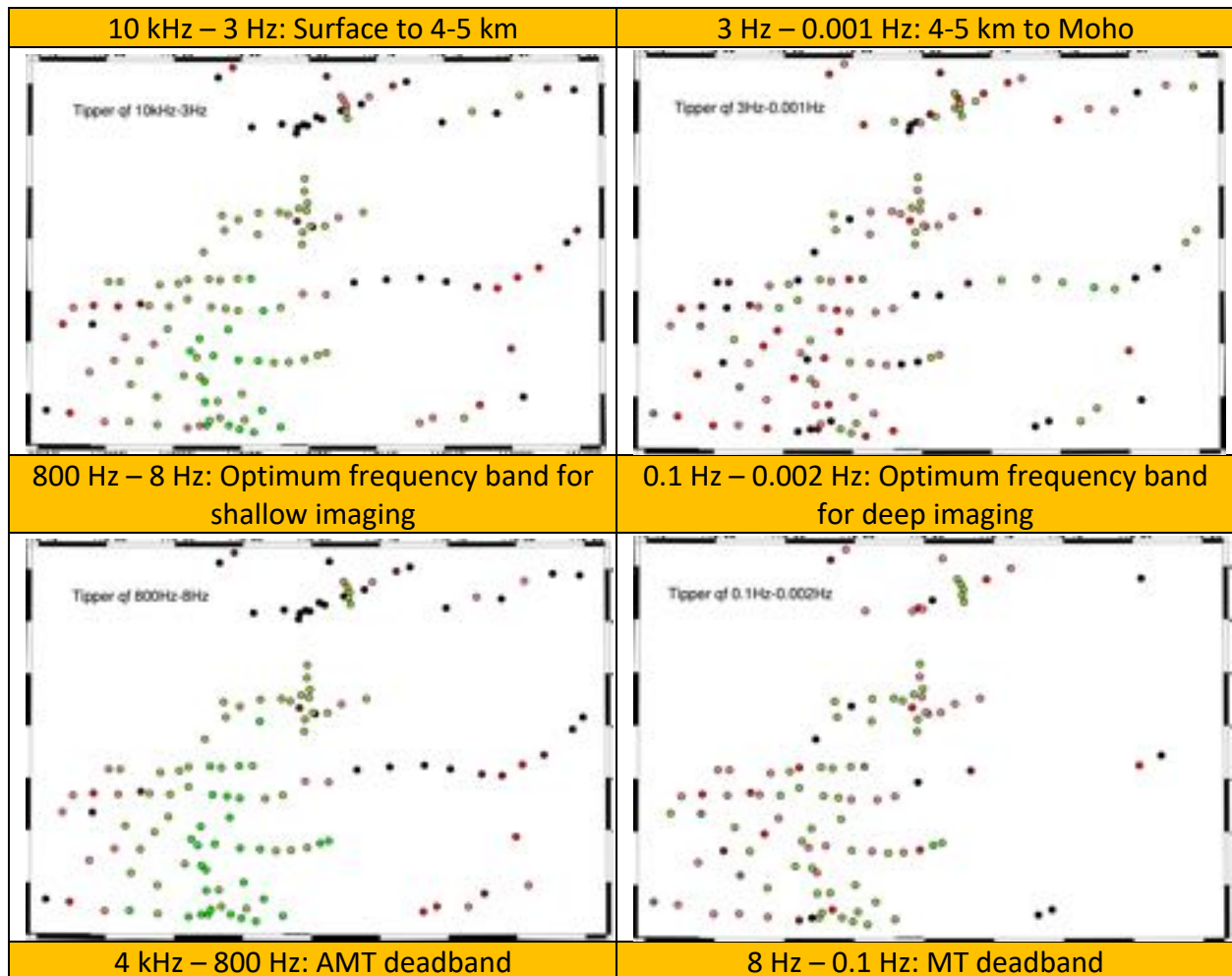
3.4. QF Conclusions

1. At the high frequencies probing down to 4-5 km, Quality Factor analyses of the data have shown that for most sites the newly-acquired data are very good to excellent, especially in the frequency range of most importance from 800 Hz – 8 Hz. For those with somewhat higher QFs, most of the noisy data are in the AMT or MT deadbands. The appropriate error floors to use are 3.56% in RhoA and 1.0° in Pha for all newly-acquired data. The existing Duncan data are poorer in quality, and the appropriate error floors to use are of order three times higher, i.e., 10.68% in RhoA and 3.0° in Pha.
2. At the lower frequencies, both the newly-acquired data and the Duncan data have appropriate error floors of order 8.90% in RhoA and 2.5° in Pha.
3. There is a strong correlation of data quality (measured by QF) with signal strength (measured by Kp). When Kp was high, QF was low.
4. There are no discernible correlations of QFs with any of the electrode array parameters.

4. Tipper Quality Factors

The vertical magnetic fields (Hz) were acquired for the newly-acquired data, so we can perform a Quality Factor analysis of the Tipper estimates, as described in Appendix C. I adopt an error floor of 0.02 for these data, which is the error level one would expect for high quality data.

The QF maps for the same frequency bands as the MT data are shown in Figure 38. Clearly the newly-acquired data are superior than the existing Duncan data.



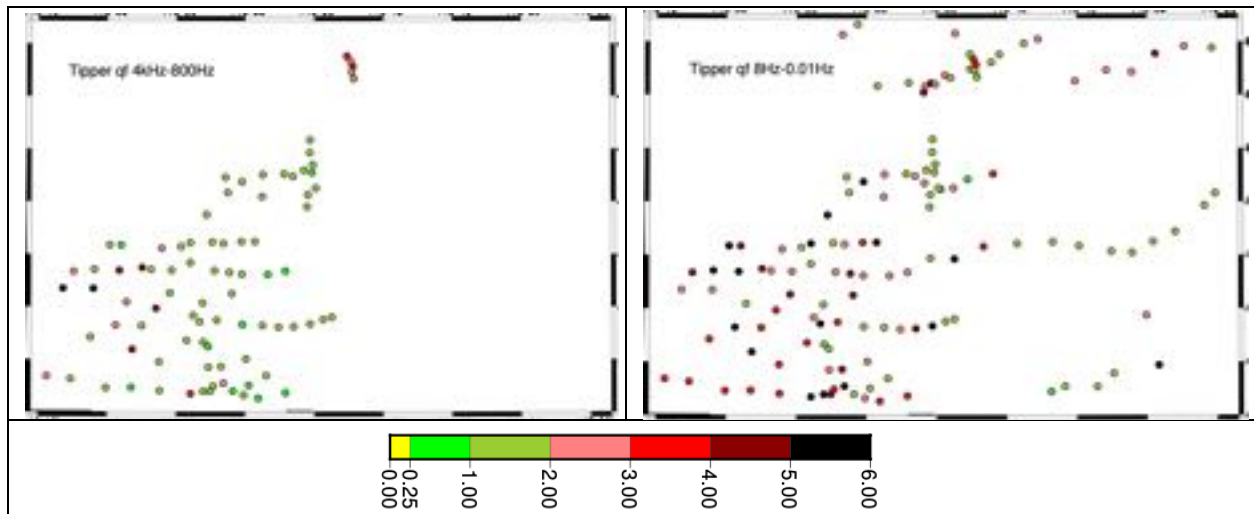


Figure 38: Tipper QFs in various frequency bands.

Histograms of the Tipper QFs are shown in Figure 39, and the 1st, median and 3rd quartiles of them are listed in Table 2. The superior quality of the newly-acquired data is proven statistically.

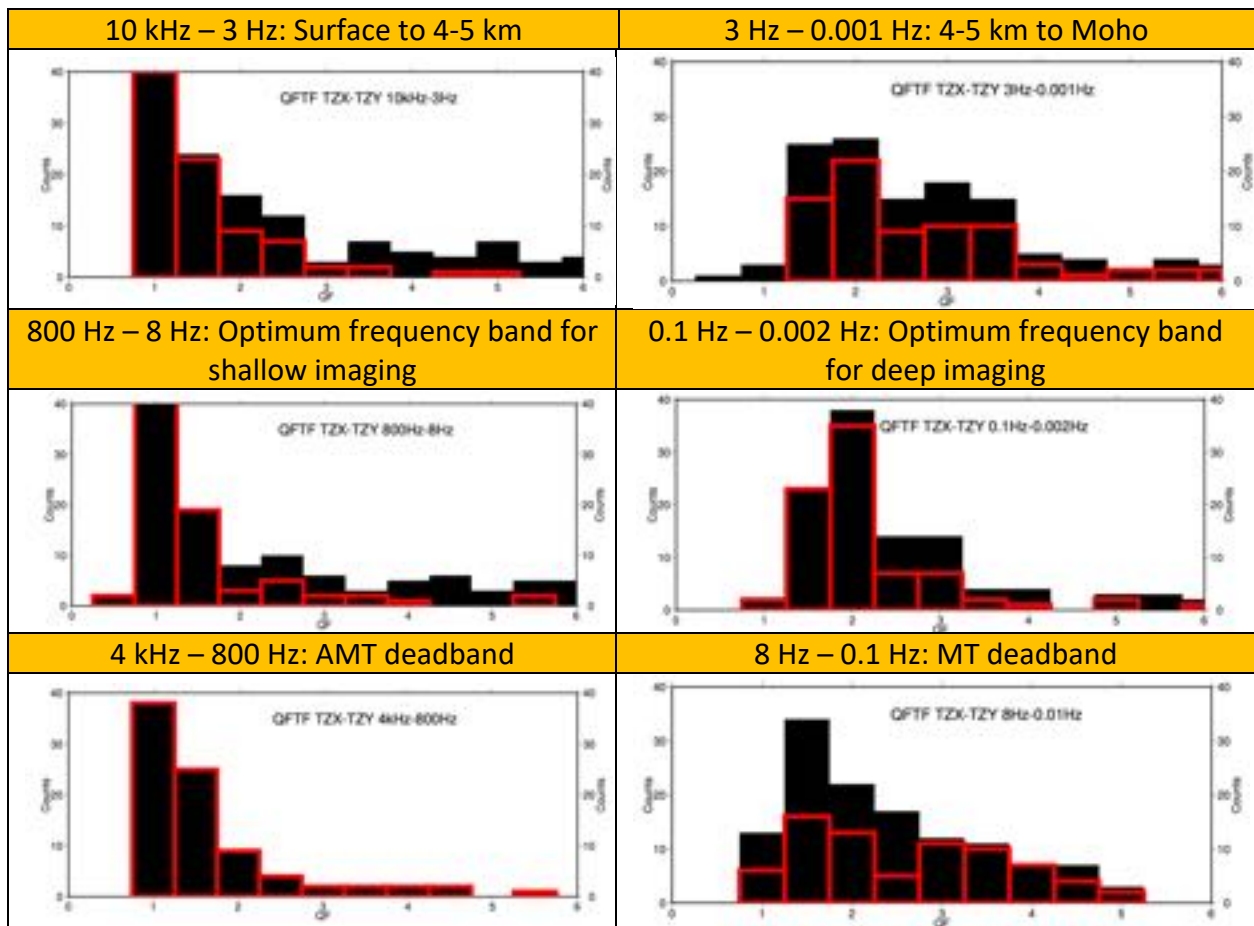


Figure 39: Histograms of Tipper QFs in various frequency bands.

Table 2: First quartile, median, and third quartile for all data and for the new Kootenay data only in the frequency bands indicated.

Frequency band	All data			New data			Duncan data		
	Q1	Median	Q3	Q1	Median	Q3	Q1	Median	Q3
10 kHz – 3 Hz	1.22	1.93	4.22	1.04	1.28	1.80	3.04	4.92	6.60
3 Hz – 0.001 Hz	1.90	2.76	3.86	1.90	2.63	3.58	1.72	3.03	5.31
800 Hz – 8 Hz	1.06	1.78	4.53	0.92	1.11	1.39	3.07	5.36	7.82
0.1 Hz – 0.002	1.77	2.12	2.96	1.69	1.91	2.26	1.28	3.09	5.07
4 kHz – 800 Hz*	1.10	1.28	1.76	1.10	1.28	1.76	-	-	-
8 Hz – 0.1 Hz	1.51	2.30	3.61	1.72	2.83	4.02	1.34	1.90	2.60

*: No Duncan data above 384 Hz

- ➔ At high frequencies, 10 kHz – 3 Hz, the error floor of 0.025 is appropriate for the newly-acquired Kootenay data, but for the existing Duncan data the appropriate error floor is higher at 0.1, which is 5 times the assumed floor of 0.02.
- ➔ At low frequencies, 3 Hz – 0.001 Hz, both the newly-acquired data and the existing Duncan data can take as their error floor a value of 0.05.

5. Average RhoA/Pha curves

To get a sense of the average resistivity structure, I average the RhoA and Pha curves from all of the sites to give the averaged XY and YX curves. This is done in a logarithmic manner for the RhoA curves and in an arithmetic manner for the Pha curves.

These averaged curves are plotted in Figure 40, where XY data are plotted as full squares, and YX data as open squares. Both curves start at some 800-1,000 Ωm . The RhoYX curve stays at 1,000 Ωm to 3 Hz, then starts to descend. The RhoXY curve starts to descend already from 30 Hz, and always lies below the RhoYX curve, indicating less penetration at the same frequency.

The Niblett-Bostick penetration depth for 1,000 Ωm at 10 kHz is 100 m. At the low frequency of 0.001 Hz (1,000 s period) the RhoA values are 10 Ωm and 30 Ωm for RhoXY and RhoYX respectively. These imply penetration to 36 km and 60 km respectively.

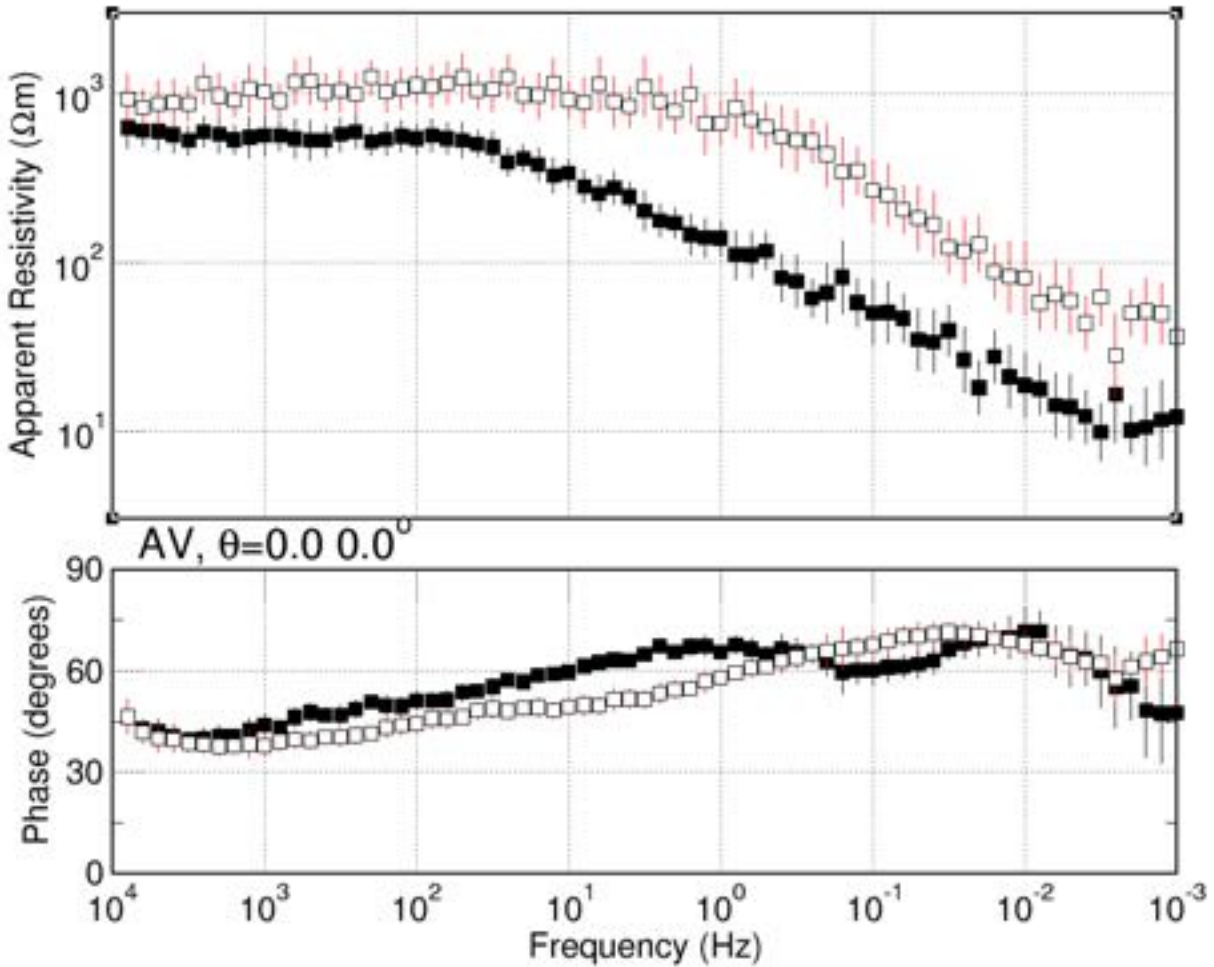


Figure 40: Averaged curves for all sites.

These estimates are transformed from period into the approx. depth, using the Niblett-Bostick transformation (Jones, 1983), in Figure 41 (top: depths to 3,000 m; bottom: depths to 30 km). The data are colour coded in with:

black: 10 kHz – 1 kHz red: 1 kHz – 100 Hz blue: 100 Hz – 10 Hz
 green: 10 Hz – 1 Hz orange: 1 Hz – 0.1 Hz magenta: 0.1 Hz – 0.01 Hz
 violet: 0.01 Hz – 0.001 Hz

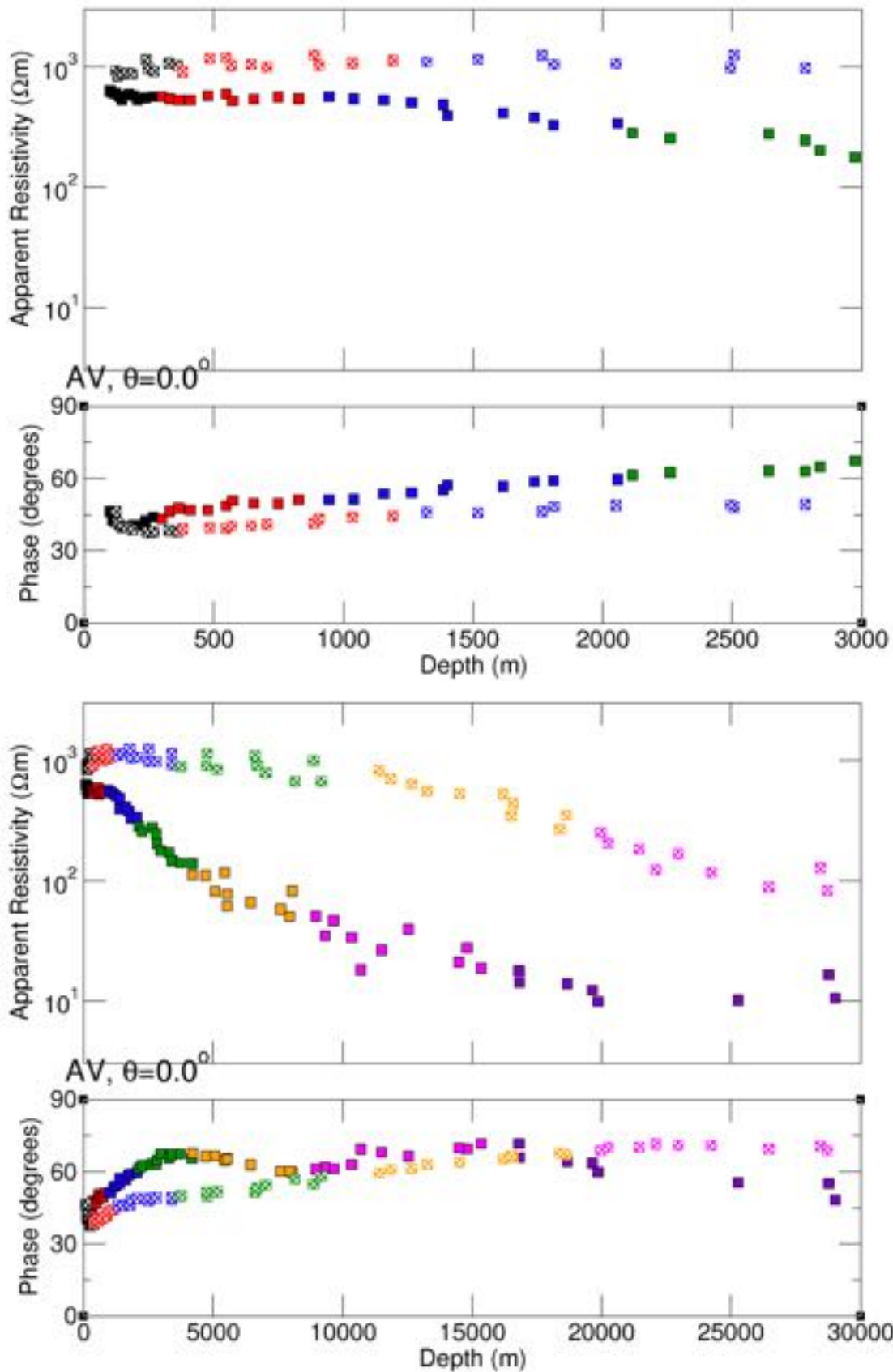


Figure 41: Averaged estimates plotted against approximate depth. Top: to 3000 m. Bottom: to 30 km

The Niblett-Bostick approximate average depths for the frequency/period bands are listed in Table 3. Taking data at frequencies much lower than 30 Hz serves no purpose for detecting the presence and imaging the top of structures at depths to 2,500 m. However, for delineation and full resolution, given the strong attenuation within any conductor present, data to 30 Hz are required.

Table 3: Niblett-Bostick penetration depths (below surface) for the XY and YX data averages.

Frequency band	XY (m)	YX (m)
10 kHz – 1 kHz	100 – 250	120 – 350
1 kHz – 100 Hz	250 – 825	350 – 1,200
100 Hz – 10 Hz	825 – 2,000	1,200 – 3,500
10 Hz – 1 Hz	2,000 – 4,000	3,500 – 9,000
1 Hz – 0.1 Hz	4,000 – 8,000	9,000 – 18,000
0.1 Hz – 0.01 Hz	8,000 – 15,000	18,000 – 32,000
0.01 Hz – 0.001 Hz	15,000 – 40,000	32,000 – 68,000

→ This defines for us the data of primary interest for imaging depths of 2-4 km, which lies in the four decades 10 kHz – 1 Hz.

→ The secondary depth of interest to the base of the crust comes from data down to 0.001 Hz.

6. Qualitative images

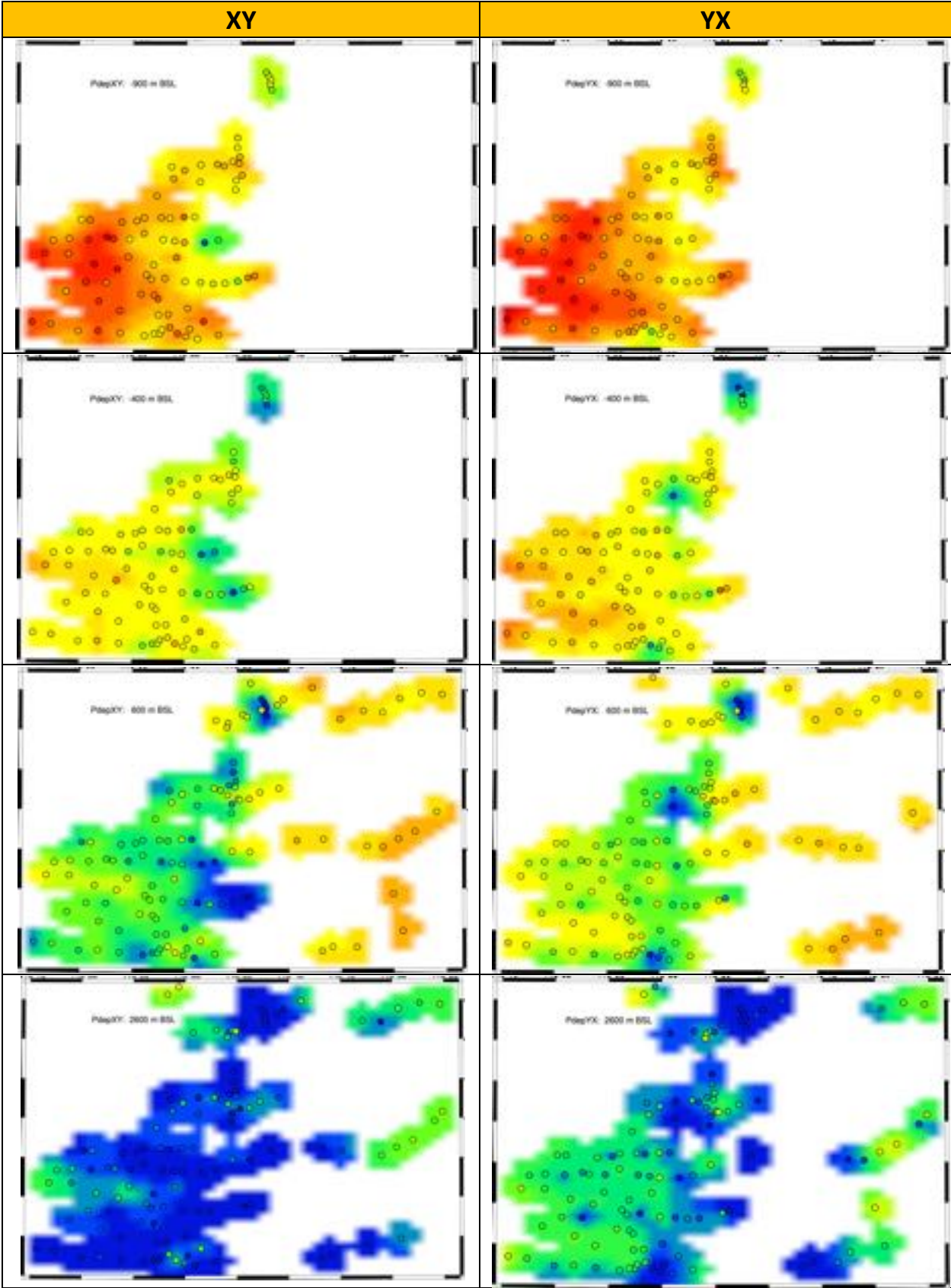
I obtain qualitative information from these data to guide analyses and subsequent inversions.

6.1. Frequencies for primary Depths of Investigation

The frequency at each site for a given Depth of Investigation is useful for identifying those frequencies most sensitive to the target depths. Below are plotted the frequencies sensing depths, defined as the Niblett-Bostick depths (Jones, 1983) rather than skin depths, for approximate depths of 500 m, 1000 m, 2000 m, and 4000 m bs (below surface) (Figure 42) for the XY and YX data at each site. The actual depths are -900 m, -400 m, 600 m and 1600 m below sea level at each site, and the approximate depths below surface are derived using the average elevation of 1400 m.

Both the XY and YX plots are visually very similar, attesting to rotational invariance at the large scale.

Note that the penetration depth of the highest frequency of the Duncan data is greater than 1000 m, hence those data do not plot on the first two rows.



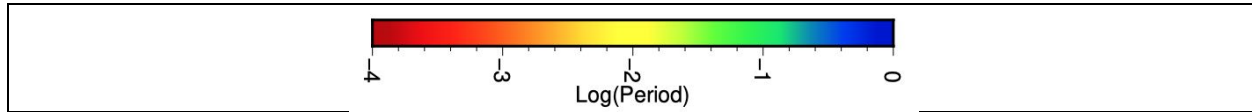


Figure 42: Frequency for Niblett-Bostick penetration to approximate depths of 500 m (top row, -900 m below sea level), 1000 m (2nd row, -400 m bsl), 2000 m (3rd row, 600 m bsl), and 4000 m (bottom row, 2600 m bsl). Left: XY; Right: YX.

From the data plotted in Figure 42 we can derive the frequencies most sensitive to the four depths are given by Table 4, which lists the median frequency plus the first and third quartiles to penetrate to each depth. Thus, the frequency range of 5 kHz to 100 Hz will cover depths of 500 m to 2,500 m on average. Where there are conductors present however, then we will need to use data to lower frequency. This is true of some parts of the grid, where frequencies down to 10 Hz appear to be needed to penetrate to 2,500 m at some sites.

Table 4: Median and 1st and 3rd quartiles for frequency to penetrate to the given depths.

Depth	XY			YX		
	Q1 (Hz)	Median (Hz)	Q3 (Hz)	Q1 (Hz)	Median (Hz)	Q3 (Hz)
500 m	800	400	160	920	460	260
1000 m	160	80	30	260	120	65
2000 m	100	25	7	145	45	25
4000 m	6	2	0.8	15	7	2

Note that this is an important point – there is no point modelling/inverting data at frequencies that penetrate too deeply to be of interest. The fit to those inconsequential data contaminates the overall fit and biases the search for the minimum to the inversion objective function. The problems associated with overfitting data of little consequence are discussed and demonstrated in Jones (1993).

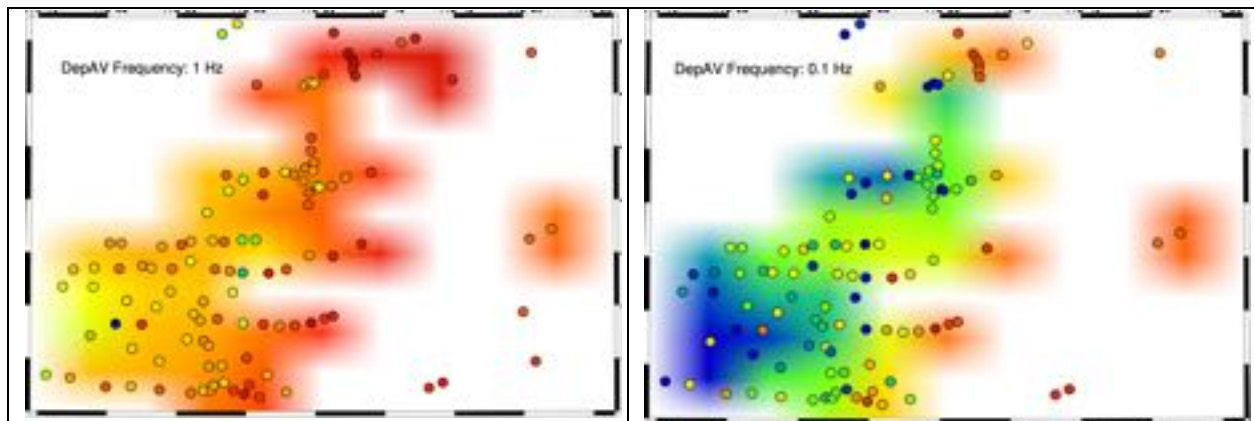
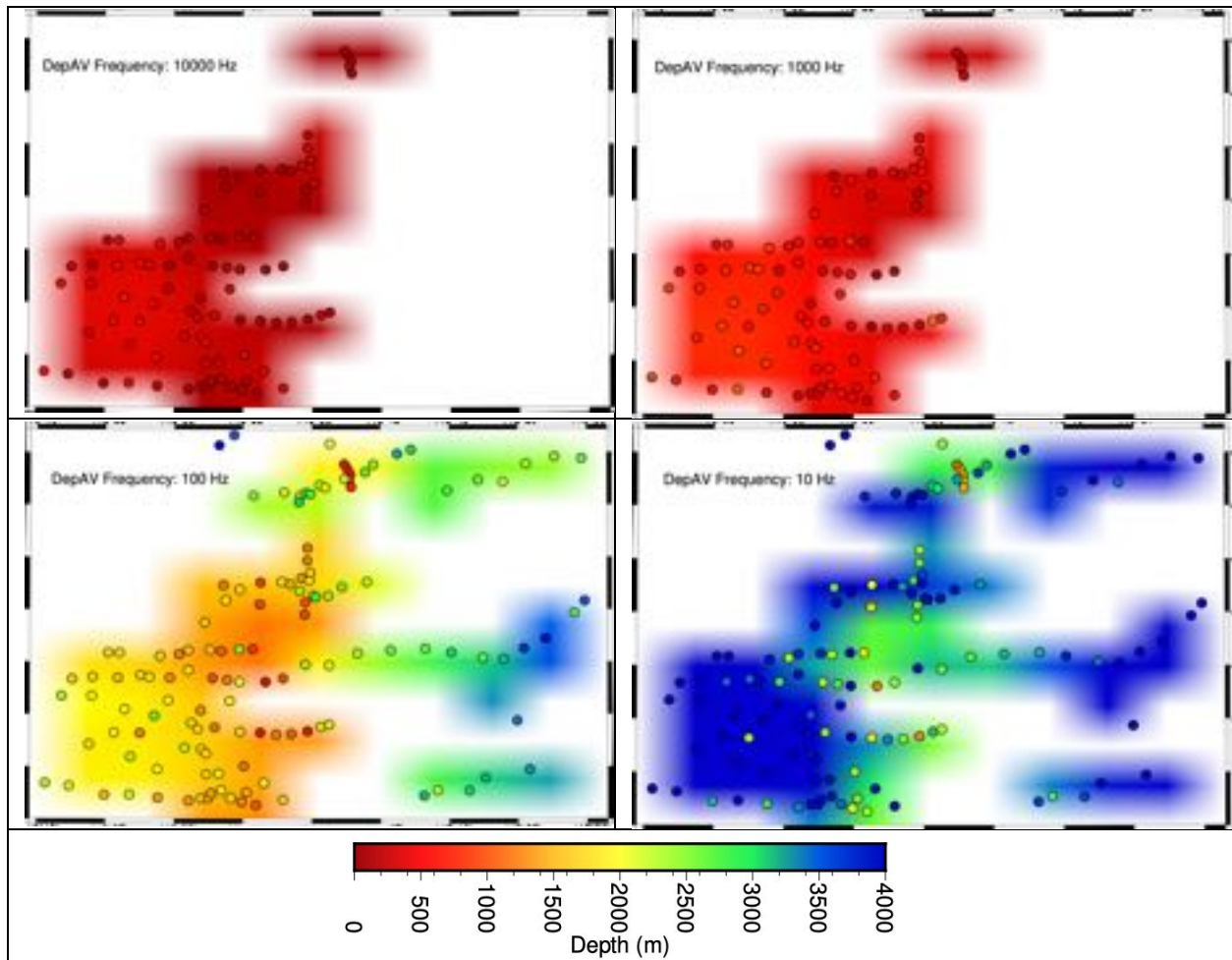
Of course, the frequencies required for optimum resolution of the subsurface are not generally known beforehand, as the conductivity structure is unknown – which is the whole point of the survey – so it always makes sense to analyse data half a decade on either side of those inferred from penetration depth arguments.

➔ **Modelling of the data needs to use frequencies from 10.5 kHz to 3 Hz for the primary target depths**

6.2. Depths of penetration for various frequencies

Another way to view the penetration information is to consider the depths for given frequencies. Below in Figure 43 are the plots of the Niblett-Bostick penetration depths (below surface) for frequencies of 10 kHz (top left row), 1 kHz (top right), 100 Hz (2nd row left), 10 Hz (2nd row right), 1 Hz (3rd row left), 0.1 Hz (3rd row right), 0.01 Hz (bottom left), and 0.001 Hz (bottom right), for the averaged impedances. Depths here are depths below surface, for an assumed average elevation of 1,400 m.

Note that the maps for frequencies above 1 Hz are on a different depth scale from those 1 Hz and below.



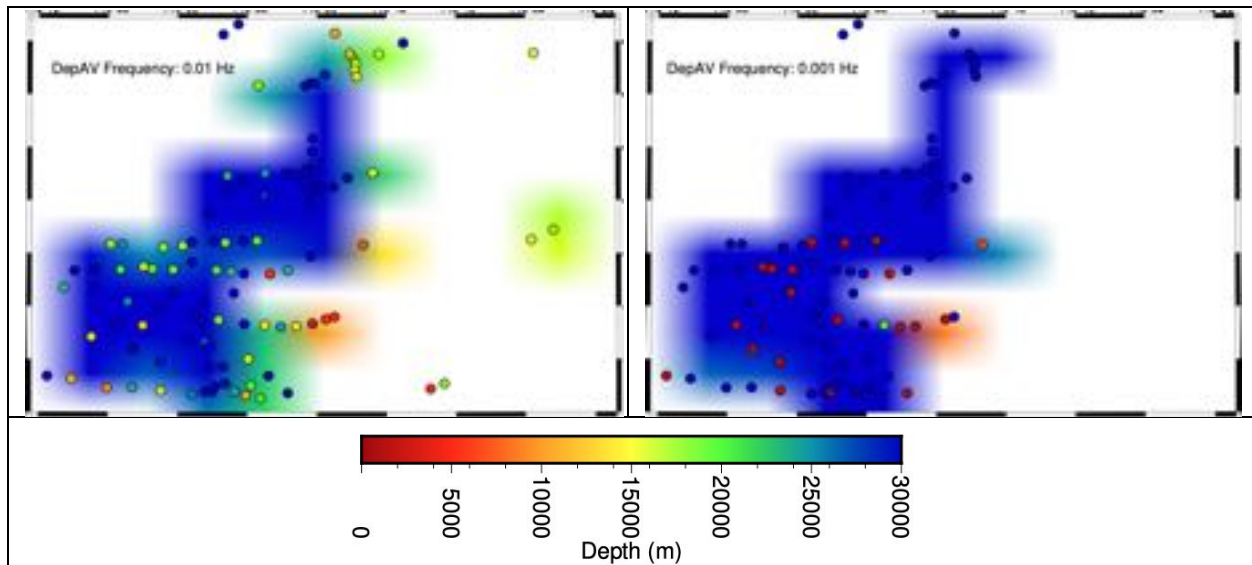


Figure 43: Depth of penetration (based on Niblett-Bostick) below surface for averaged impedances at frequencies of 10 kHz (top left), 1 kHz (top right), 100 Hz (2nd row left), 10 Hz (2nd row right), 1 Hz (3rd row left), 0.1 Hz (3rd row right), 0.01 Hz (bottom left) and 0.001 Hz (bottom right). Note the change of colour scale for frequencies above and below 1 Hz.

The statistics of the penetration depths are given in Table 5.

Table 5: Median and 1st and 3rd quartiles for depth of penetration at each frequency.

Frequency	Q1 (m)	Median (m)	Q3 (m)
10,000 Hz	8	120	260
1,000 Hz	260	440	590
100 Hz	1,225	1,800	2,500
10 Hz	2,800	3,900	4,800
1 Hz	5,650	8,675	11,700
0.1 Hz	10,700	17,700	24,150
0.01 Hz	17,750	28,600	38,700
0.001 Hz	36,500	63,500	92,500

This confirms that the frequencies of primary interest for imaging the top 4 km are from 10 kHz to around 3 Hz, and that the lower frequencies down to 0.001 Hz are essential to reach the base of the crust.

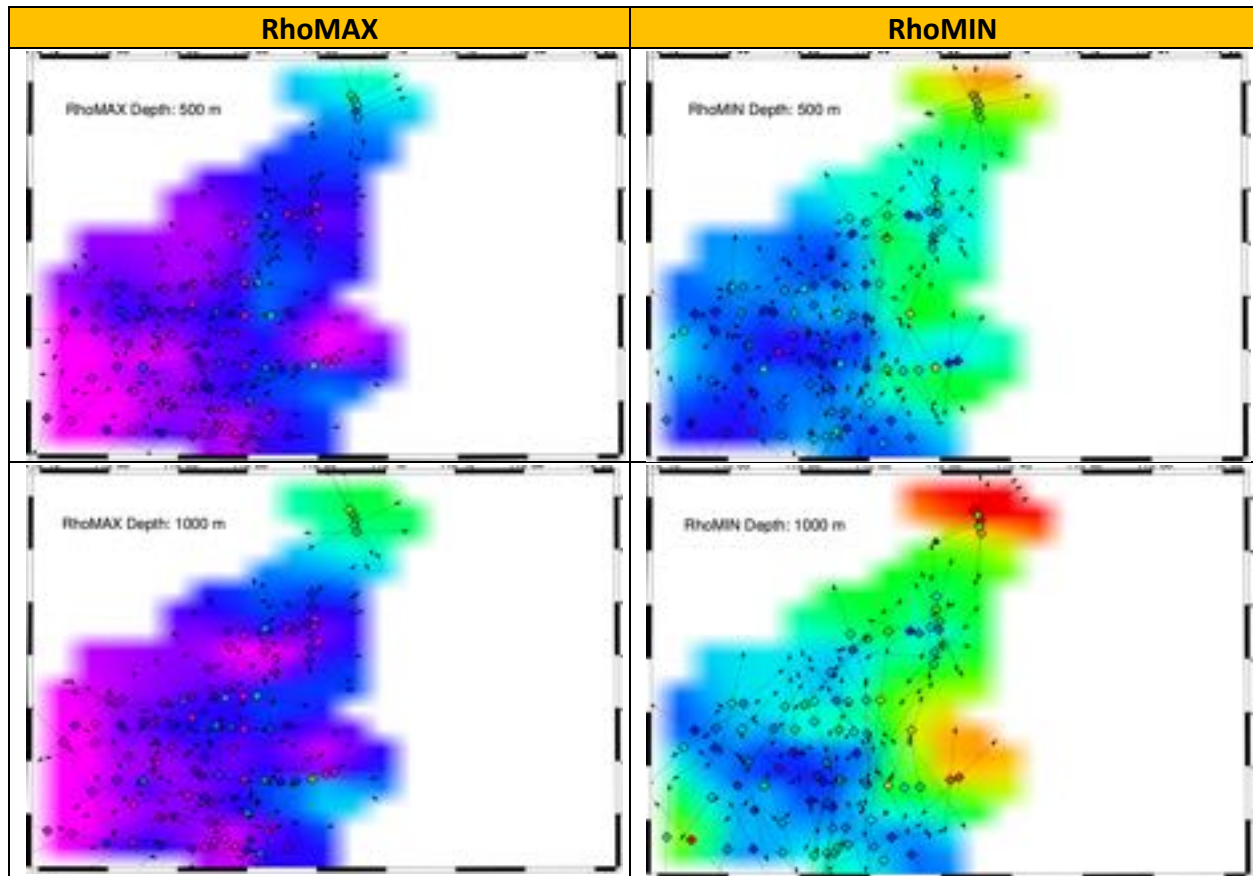
6.3. Approximate resistivity images for various depths

A quickview way of imaging the data is to obtain an approximate resistivity at a given depth using the Niblett-Bostick transform (Jones, 1983). This is done for depths of -900 m, -400 m, 600

m and 1600 m below sea level at each site for RhoMAX and RhoMIN ⁽²⁾. These depths are approx. 500 m, 1000 m, 2000 m and 4000 m below surface given the average elevation of 1400 m.

The maps for RhoMAX (left) and RhoMIN (right) are shown in Figure 44. Sites are plotted only when both orthogonal directions (XY and YX) reach to the desired depth.

The arrows indicate the direction of RhoMAX for the RhoMAX maps, and RhoMIN for the RhoMIN plots.



² RhoMAX is the maximum resistivity at that depth, and RhoMIN is the minimum resistivity. These RhoMAX and RhoMIN values are determined by rotating the data through 90° at each frequency for each site and recording the maximum and minimum resistivities and their directions. Note that these two directions are not necessarily at right angles to one another.

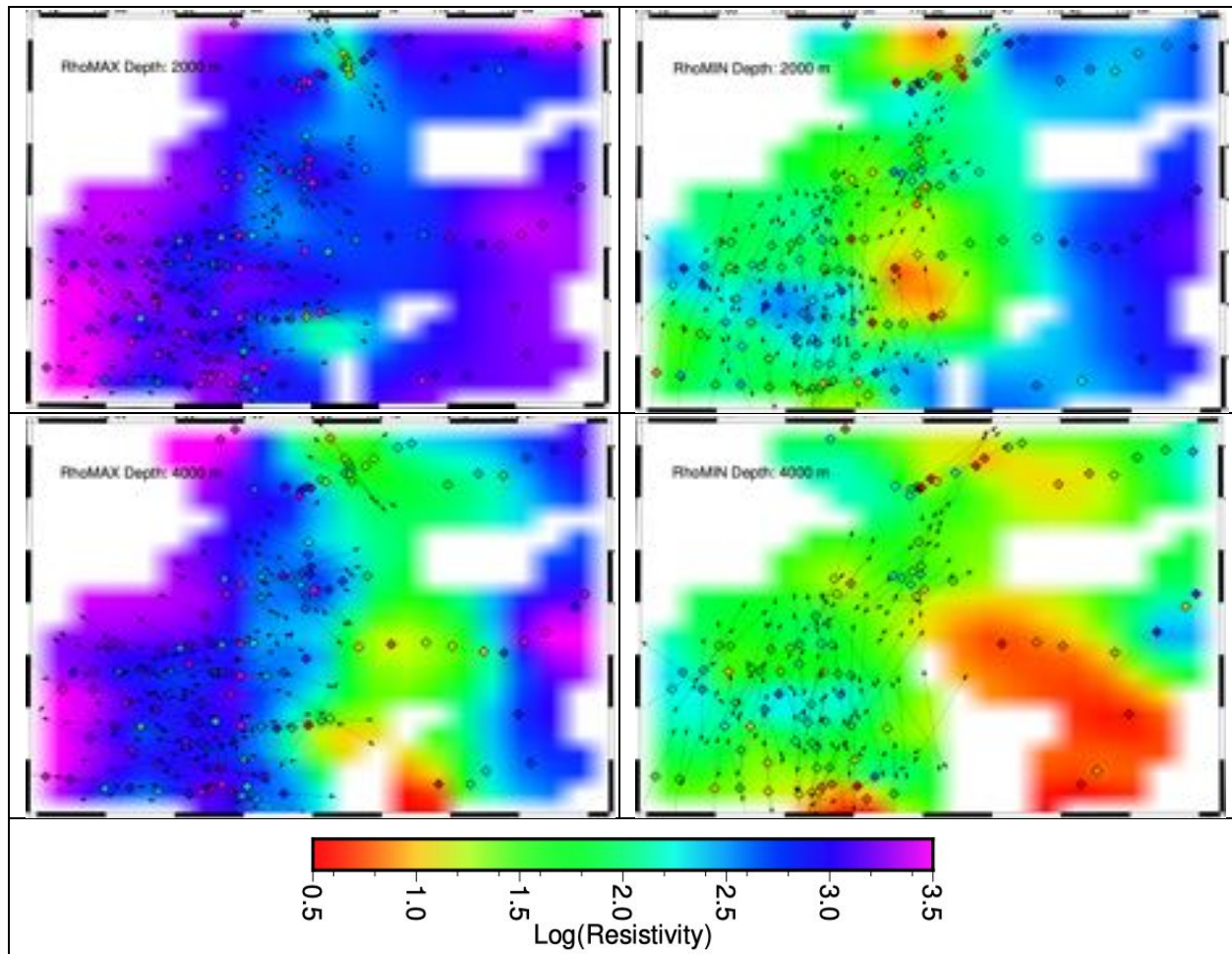


Figure 44: RhoMAX (left) and RhoMIN (right) approx. resistivity maps at depths (below sea level) of -900 m (top row, 500 m below surface), -400 m (2nd row, 1000 m bs), 600 m (3rd row, 2000 m bs), and 2600 m (4th row, 4000 m bs). Note: sites are plotted only when both orthogonal directions (XY and YX) reach to the desired depth.

There are some regions of interest in these maps. Three prominent ones are indicated in the RhoMIN plot at 4 km Figure 45, and are:

Anomaly A: A low conductivity anomaly associated with the eastern sites along the southern profile KSS.

Anomaly B: A low conductivity anomaly associated with the Purcell sulphides and mapped by Gupta and Jones (1995).

Anomaly C: A low conductivity anomaly also associated with the Purcell sulphides and mapped and modelled by Gupta and Jones (1995) – see Figure 17 above.

➔ **There are a number of regions of interest identified in the RhoMIN plots. The main new one, labelled Anomaly A, is in the eastern part of line KSS (see RhoMIN @ 4000 m depth).**

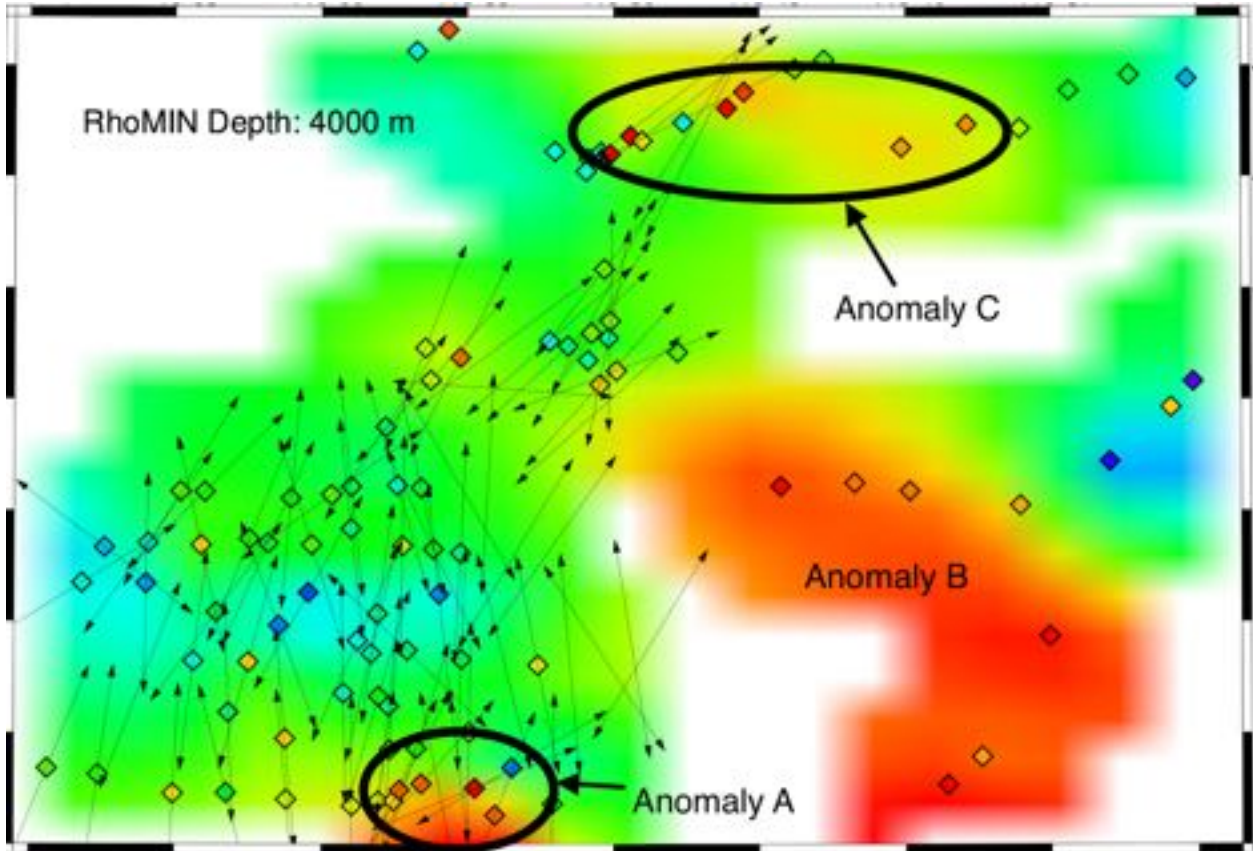


Figure 45: RhoMIN plot at approximate depth of 4 km.

The directions of the arrows are plotted as histograms on Figure 46.

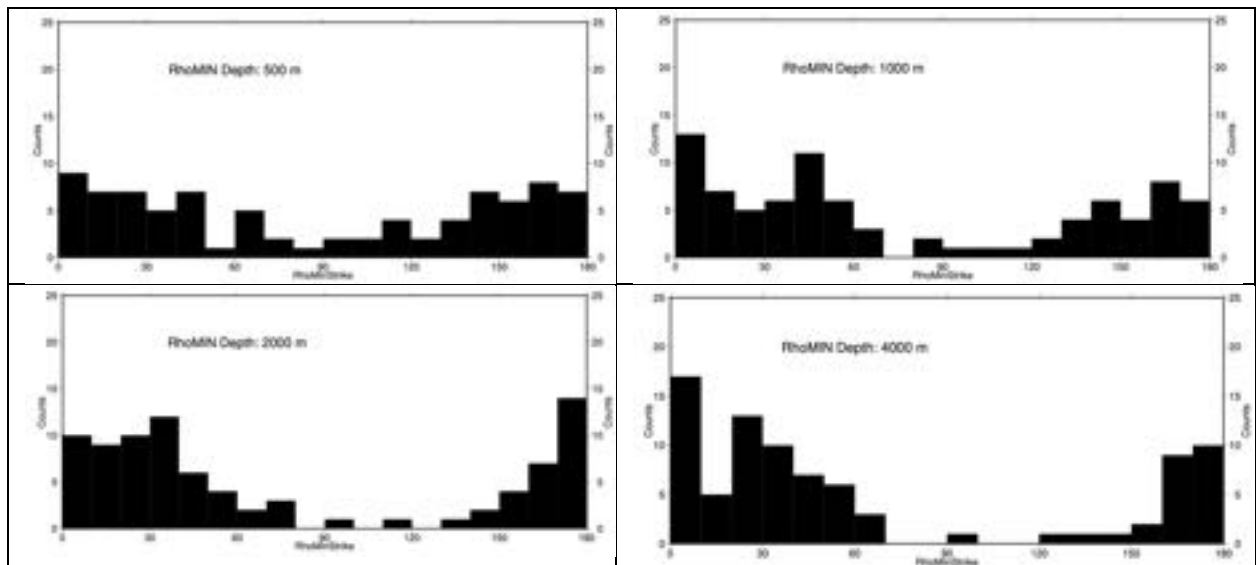


Figure 46: Histograms of RhoMIN strike directions for depths (below sea level) of -900 m (top left, 500 m below surface), -400 m (top right, 1000 m bs), 600 m (bottom left, 2000 m bs), and 2600 m (bottom right, 4000 m bs).

Using circular statistics with a pi repetition (Mardia, 1972), the means of these histograms are N11E, N14E, N15E and N2E for depths of 500 m, 1000 m, 2000 m and 4000 m respectively.

There is though clearly S-N variation, with the southern sites striking more N-S and the northernmost sites striking NNE-SSW.

6.4. Qualitative Dimensionality plots

Given the observed differences in the RhoXY and RhoYX plots at different depths shown in Figure 44, we can obtain qualitative information about the strength of dimensionality by considering the maximum differences in phase in orthogonal directions when the data are rotated through 360°.

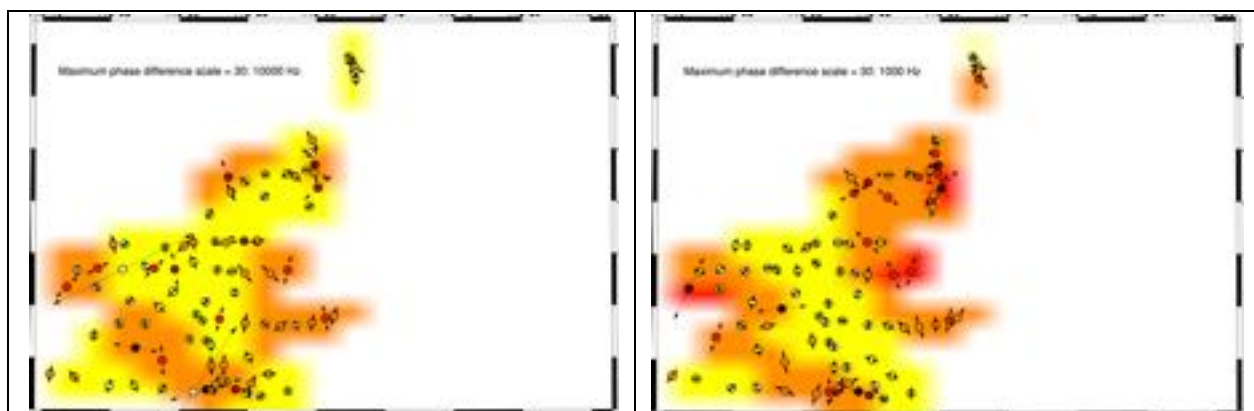
For a 1-D Earth, the phase is the same regardless of strike direction, so the phase difference is zero.

For a 2-D Earth phase difference maximises when the data are in the strike and orthogonal-to-strike directions, so the direction of maximum phase difference is indicative of geoelectrical strike.

For a 3-D Earth the extent of “3-Dness” affects whether the phase maximises at the quasi-2-D direction or not.

Below are plotted the phase difference maps at four frequencies, 10 kHz, 1 kHz, 100 Hz and 10 Hz (Figure 47), which are approximately penetrating to maximum depths of 120 m, 440 m, 1,800 m and 4,000 m respectively (Table 5).

Yellow means very little phase difference with rotation (<10 degrees), which means 1-D or subtle 2-D/3-D. Red and dark red indicate areas with strong sensitivity of phase to strike direction, so are areas that are 2-D or 3-D.



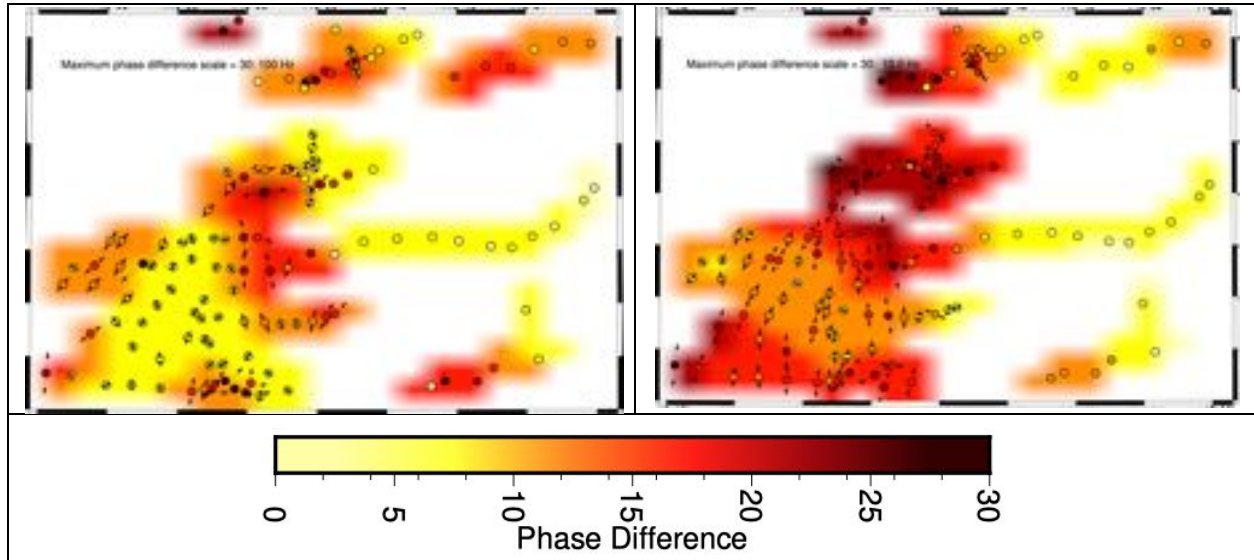


Figure 47: Phase differences at 10 kHz (top left), 1 kHz (top right), 100 Hz (bottom left) and 10 Hz (bottom right).

For much of the grid there are no strong phase differences in orthogonal directions at high frequencies. Strong phase sensitivity comes in below 100 Hz, i.e., below 2 km depth.

The directions of maximum phase difference are plotted as histograms in Figure 48. Note that these are the directions of the higher phase, and the strike direction changes by 90 degrees on either side of a boundary in conductivity (see the footnote about Phase Tensor direction – the same applies to anisotropy direction).

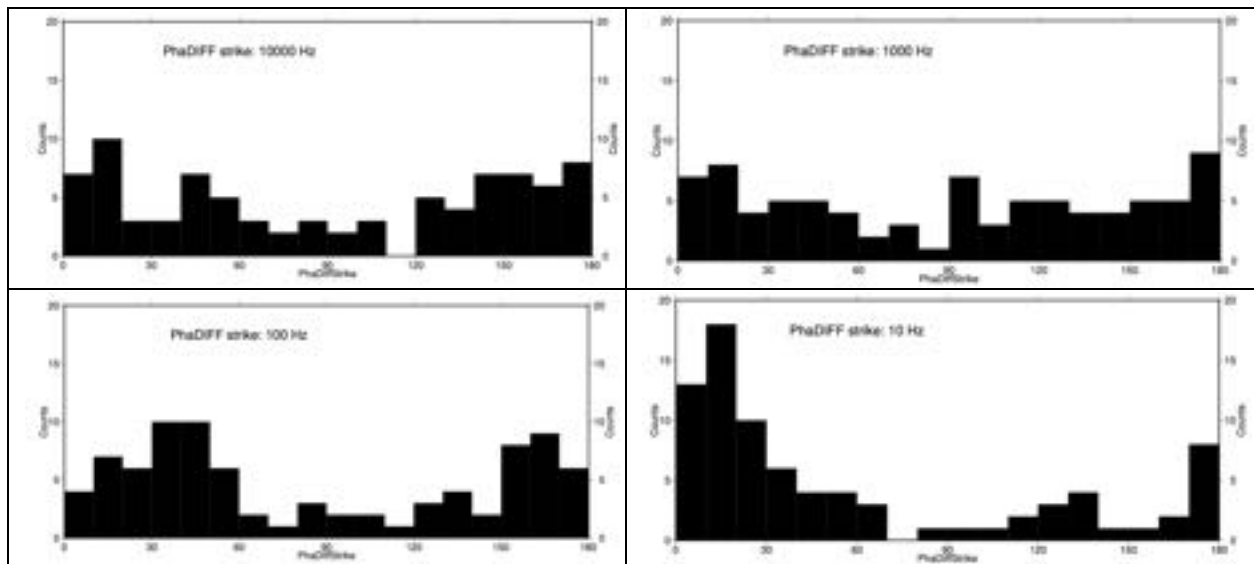


Figure 48: Histograms of maximum phase differences at frequencies of 10 kHz (top left), 1 kHz (top right), 100 Hz (bottom left) and 10 Hz (bottom right).

At high frequencies the strike is poorly defined, as we would expect from a quasi-1-D-subsurface down to 500 m. A predominant strike direction is formed by 100 Hz, with a peak at NE-SW and another at the almost conjugate direction. By 10 Hz there is one single dominant

peak at N15E. Circular statistical analyses of these histograms, assuming a repetition of π , yields means of N10E, N11E, N12E and N14E for 10 kHz, 1 kHz, 100 Hz and 10 Hz respectively, with the standard deviation reducing with decreasing frequency.

7. Geoelectrical strike – Phase Tensors

For two-dimensional (2-D) structures, in conventional MT the along-strike e-field (E_x , where “x” is defined as being along strike) divided by the across-strike h-field (H_y , “y” is across strike) is defined as the transverse-electric (TE) mode⁽³⁾ of induction in MT. In contrast, the across-strike e-field (E_y) divided by the along strike h-field (H_x) is defined as the transverse magnetic (TM) mode.

It is vitally important that the correct geoelectrical strike be defined for 2-D data – an incorrect strike direction will lead to erroneous models, and thereby erroneous interpretations and conclusions.

A rapid visual way for assessing dimensionality and directionality is to plot the MT Phase Tensors (Caldwell et al., 2004). The great attraction of Phase Tensors (PT) is that local galvanic distortion caused by near-surface inhomogeneities of no interest is removed, and only directionality and dimensionality of the Earth structure are indicated in the PT parameters. However, as discussed by Jones (2012), Phase Tensors should only be used in a qualitative manner as their determination is unstable in the presence of high noise and/or high distortion. For quantitative assessment then more sophisticated approaches must be adopted.

The Phase Tensors at frequencies of 3 kHz, 300 Hz, 30 Hz, 3 Hz, 0.3 Hz and 0.03 Hz, which are on average approximately penetrating to maximum depths of approx. 200 m, 650 m, 2,000 m, 6,500 m, 15 km, 22 km and 50 km respectively (Table 5), are plotted in Figure 49.

Note that there are no PTs at 3,000 Hz for the existing data as the highest frequency for those data is 384 Hz.

³ In 2-D, Maxwell’s Equations separate into two independent sets. One set describes electric currents travelling along the structures, and is called the TE mode. The other set describes electric currents travelling perpendicular to structures, and is called the TM mode. Essentially, the TE mode is responsive to current flow, whereas the TM mode is responsive to charge distribution. Hence, the two sense the subsurface resistivity distribution differently, and a joint inversion of both TE and TM mode data together is a true Joint Inversion in an inversion manner as the two trade-off against each other.

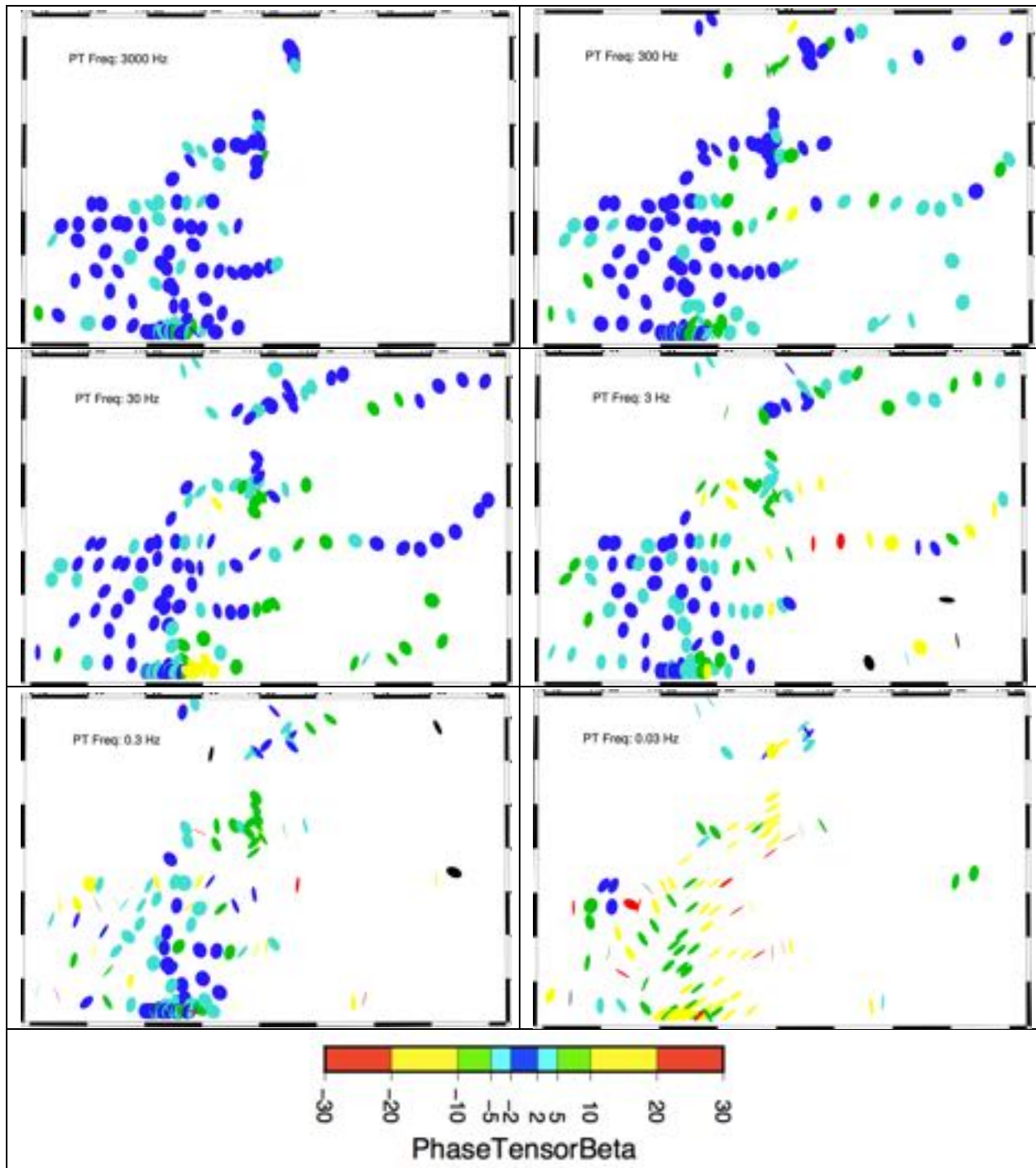


Figure 49 : Phase Tensors at frequencies of 3 kHz (top left), 300 Hz (top right), 30 Hz (middle left), 3 Hz (middle right), 0.3 Hz (bottom left), and 0.03 Hz (bottom right). The colours of the ellipses are the phase tensor beta values.

7.1. Phase Tensor Dimensionality

The colours of the ellipses indicate the PT absolute beta angle ($|\beta|$) values, which is a measure of 3-dimensionality, and the axes indicate the geoelectric co-ordinate system at that depth for that site. Low beta values (dark or light blue, $<5^\circ$) means that the data conform to either a 1-D

or 2-D representation of the structure below. High beta values (yellows and reds) indicate that the data are either representative of 3-D structures, OR that the data are scattered and noisy. (Note that the estimation of PT values is from algebraic manipulation of the MT impedance tensors, and so is totally non-robust.)

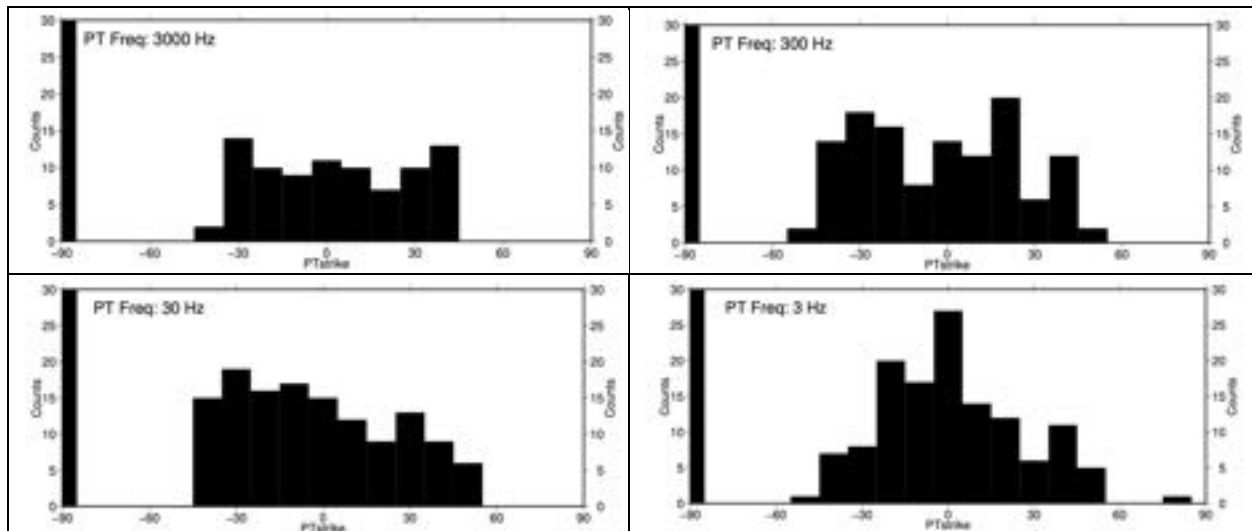
Disregarding a few obviously noisy sites (very high betas and/or very strongly distorted ellipses), at the high frequencies >3 Hz of primary interest to the client, most of the ellipses are dark to light blue, which indicates very low to low PT absolute skew ($|\beta|$) below 5° . For those sites an assumption of 1-D or 2-D interpretation is valid. Some of the dark blue ellipses are almost circular, which is evidence of a 1-D subsurface, and 1-D tools can be used for the data from those sites for imaging the top 4-5 km.

As frequency decreases below 0.3 Hz, then the data become more 3-D, and/or become very noisy.

7.2. Phase Tensor Directionality

The shape of the ellipses indicates whether the data are 1-D, which is true if the ellipse is near circular, or 2-D for low beta. If 2-D then the geoelectric strike direction is represented by the major or minor axis, depending on whether the site is on or off a conductor.

Histograms of the PT strike directions for the six frequencies are shown in Figure 50. PT-defined strike directions are scattered at high frequencies, indicative of no strong strike direction across the area, but show peaks at lower frequencies of 3 Hz and below, with directions consistent with prior observations.



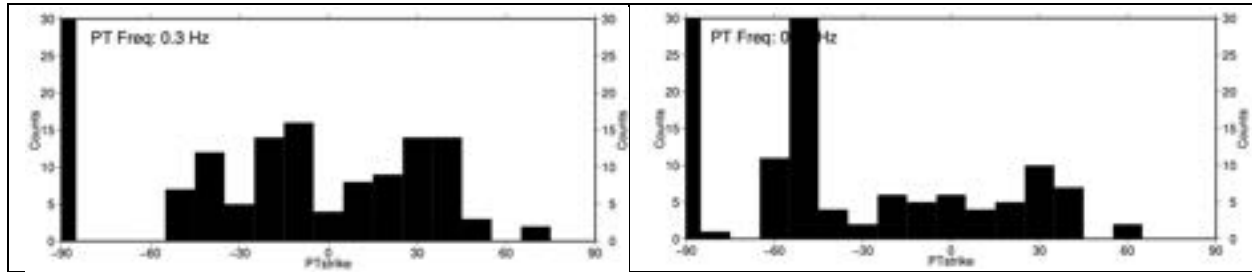


Figure 50: Histograms of the Phase Tensor strike direction for frequencies of 3 kHz (top left), 300 Hz (top right), 30 Hz (middle left), 3 Hz (middle right), 0.3 Hz (bottom left), and 0.03 Hz (bottom right).

There is in MT a 90° ambiguity in the determination of geoelectrical strike from MT data alone – there is no intrinsic way to know which is the TE mode and which is the TM mode; mode assignment must be done through considering other factors, such as the tipper induction arrow vectors (but these were not acquired), or local geology.

8. Vertical field transfer functions

There is a linear transfer functions between the observed vertical magnetic field and the two components of the horizontal magnetic field, viz.

$$H_z = T_{zx} H_x + T_{zy} H_y$$

(dependence on frequency assumed). The two transfer functions T_{zx} and T_{zy} are commonly referred to as “tippers”, taken from AFMAG, and are a measure of how much horizontal field is “tipped” into the vertical field. For a uniform source field there are no tippers over an isotropic 1-D Earth, so the presence of tippers is indicative of either a non-uniform source field (Jones & Spratt, 2002) or of non-isotropic 1-D subsurface, i.e. anisotropic 1-D, or isotropic or anisotropic 2-D or 3-D.

Tippers have not been much used in the mineral exploration industry, as often the vertical magnetic field, H_z , is not recorded in an attempt to reduce costs. This is a mistake in my view, as the tippers contain complementary information to the MT responses.

8.1. Induction vectors

The two transfer functions T_{zx} and T_{zy} are usually represented graphically as real and imaginary “induction vectors”, where the real induction vector is given by the amplitude and direction of the real parts of T_{zx} and T_{zy} , and the imaginary induction vector given by the same for the imaginary parts of T_{zx} and T_{zy} . The real part is usually reversed in the so-called Parkinson convention to point towards current concentration in conductors (Parkinson, 1959, 1962), except at high frequencies above the skin depth to the conductor (Jones, 1986). When not reversed the real vector is in the so-called Wiese convention, and the arrows point away from

structures of interest. The visually-confusing Wiese convention is generally used by central Europeans, and the far more sensible Parkinson convention by everyone else. The imaginary arrow is not reversed, as it undergoes a direction change at the frequency where the real arrow maximises – this is because the two induction arrows form a Hilbert transform pair.

Besides being used as part of inversion for structure, one common use of induction vectors is to define strike direction for 2-D modelling, given by the direction perpendicular to the real vector.

8.2. Tipper magnitude

Another informative plot is that of the tipper magnitude, given by

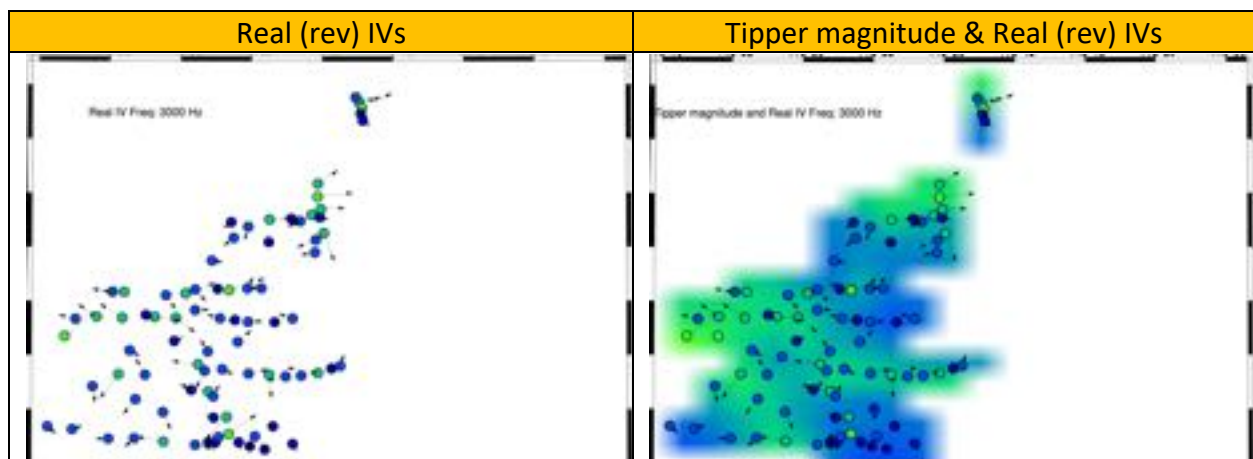
$$T = \text{SQRT} (T_{zx}^2 + T_{zy}^2).$$

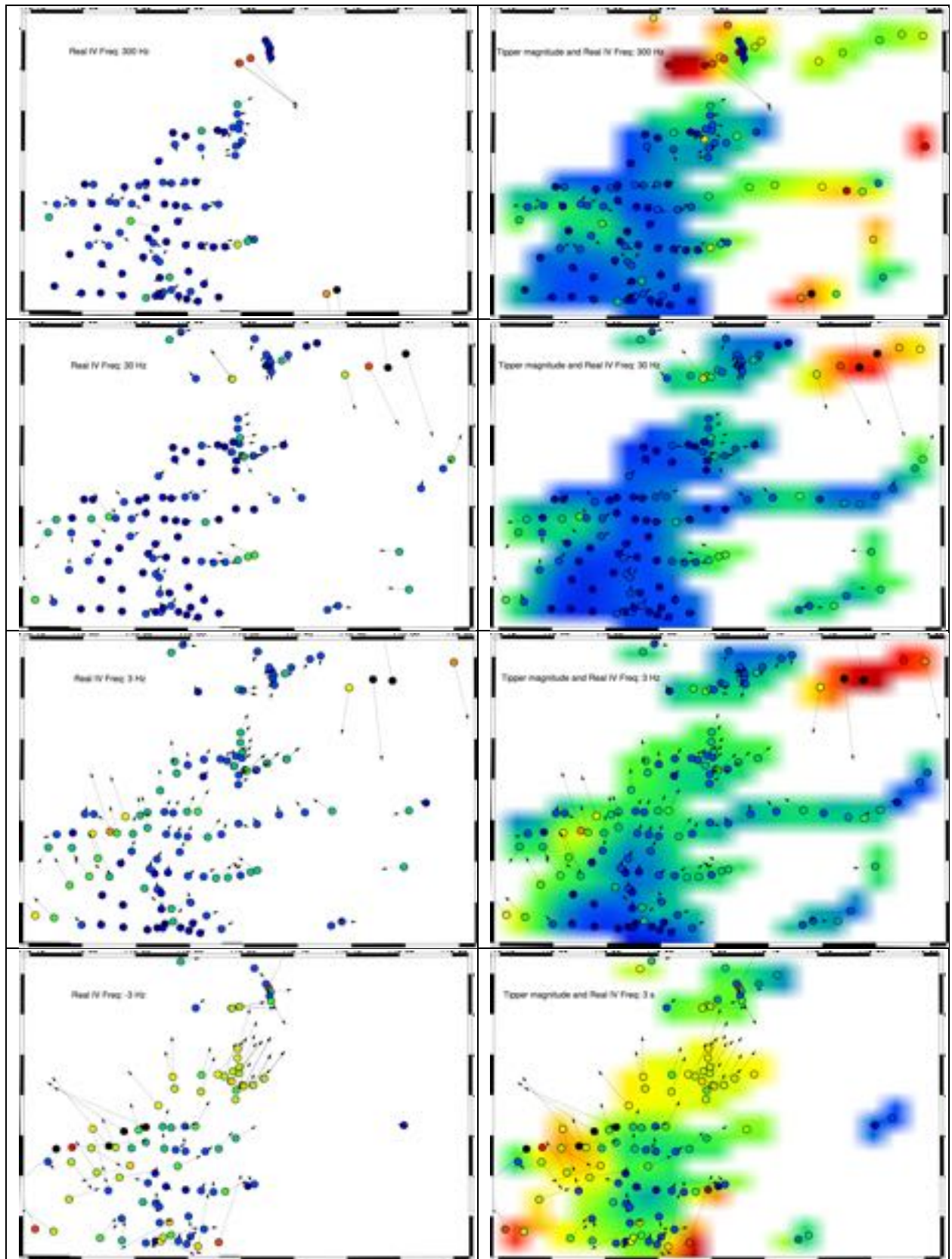
A recent paper discussing the advantages of considering Tipper Magnitude is that of Shalivahan et al. (2017)

8.3. Induction Vector and Tipper plots

Below are plots of the real (reversed) induction arrows at frequencies of 3 kHz, 300 Hz, 30 Hz, 3 Hz, 0.3 Hz and 0.03 Hz. For comparison to approximate depth, refer to Table 3, but recall that vertical magnetic field (Hz) penetration is less than electric field penetration (E_x or E_y), so tipper penetration (which is the ratio $\text{Hz}/(H_x, H_y)$) is less than MT penetration (which is the ratio $(E_x, E_y)/(H_x, H_y)$).

Real (reversed) induction vectors point towards current concentration, and in a 2-D case this means they are orthogonal to the strike of the 2-D anomaly. Note that on either side of a 2-D conductor, the vectors will have opposite directions, i.e., for a N-S striking 2-D conductor, on the east side the vectors will point west, and on the west side the vectors will point east. Thus there will be two peaks in a histogram plot of directions.





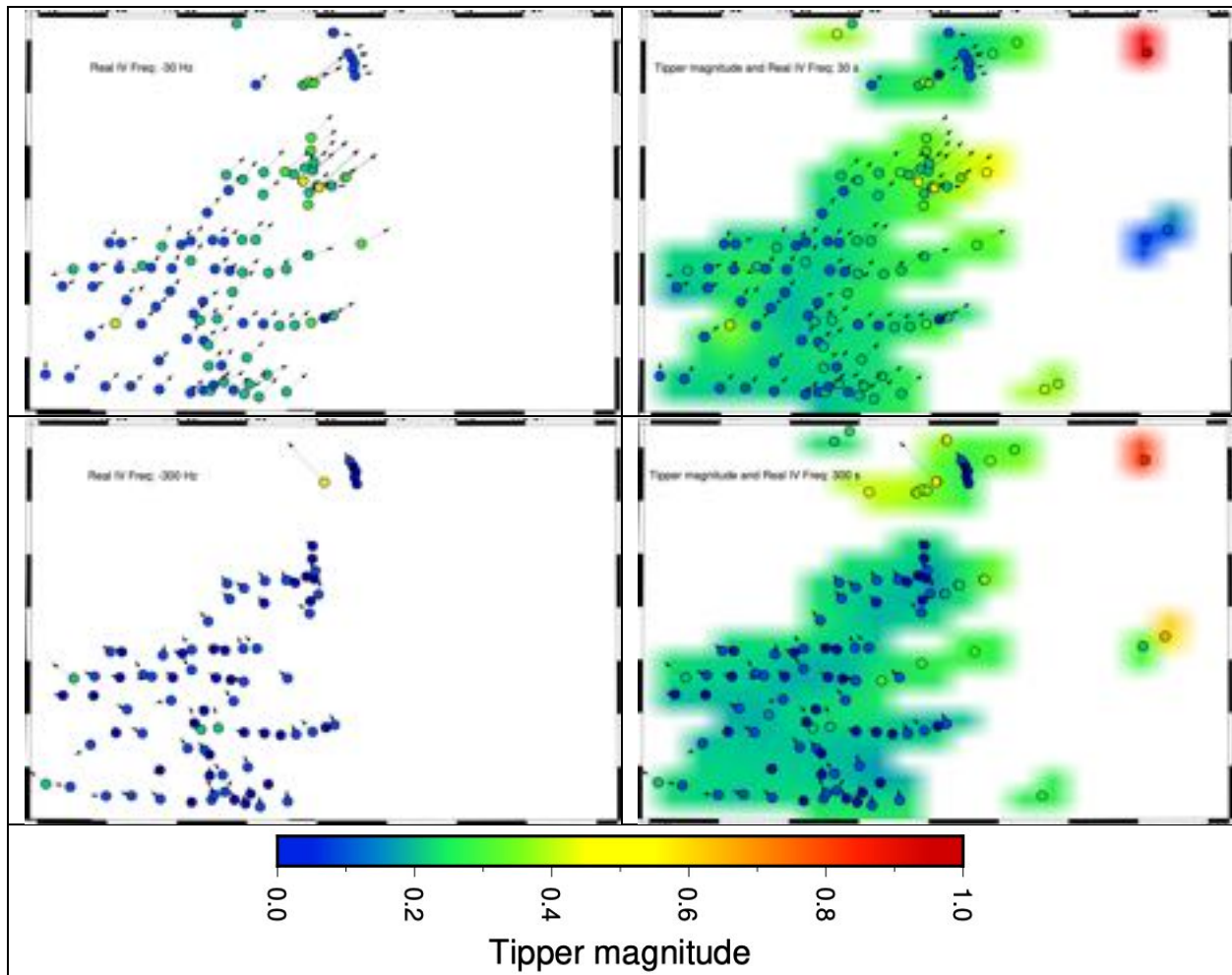


Figure 51: Plots of the real (reversed) induction arrows (left) and of the arrows and tipper magnitude (right) at frequencies of 3000 Hz (top row), 300 Hz (2nd row), 30 Hz (3rd row), 3 Hz (4th row), 0.3 Hz (3 s, 5th row), 0.03 Hz (30 s, 6th row), and 0.003 Hz (300 s, bottom row). The colour of the symbol is the magnitude of the real arrow, and the colour contour is that of the smoothed tipper magnitude.

Histograms of the induction arrow directions at the frequencies above plus the intermediate frequencies are shown in Figure 52.

The Duncan data are clearly noisy, with induction arrows that are far too large in places. There are no high frequency (>384 Hz) estimates at any Duncan sites, and also no low frequency estimates at most Duncan sites (acquisition time too short for determining estimates at low frequencies).

At high frequencies >100 Hz, generally, the tipper is relatively small, below 0.4, and is scattered without any strong dominant direction. This is indicative of small scale structures without a dominant trend.

The only immediately strongly anomalous region is in the NE at 3 Hz, but those sites are from Duncan data, and are not reliable – especially when two stations right next to each other point in opposite directions (could imply that one of the mag coils was laid in the wrong way).

At 0.3 Hz (3 s), there is some lateral variation, indicative of lateral variation in electrical conductivity. There is a strong peak at N30E – N60E that is maintained down to 0.01 Hz (100 s).

It is interesting to note the arrows and Tipper Magnitude in the location identified as Anomaly A at the eastern end of profile KSS.

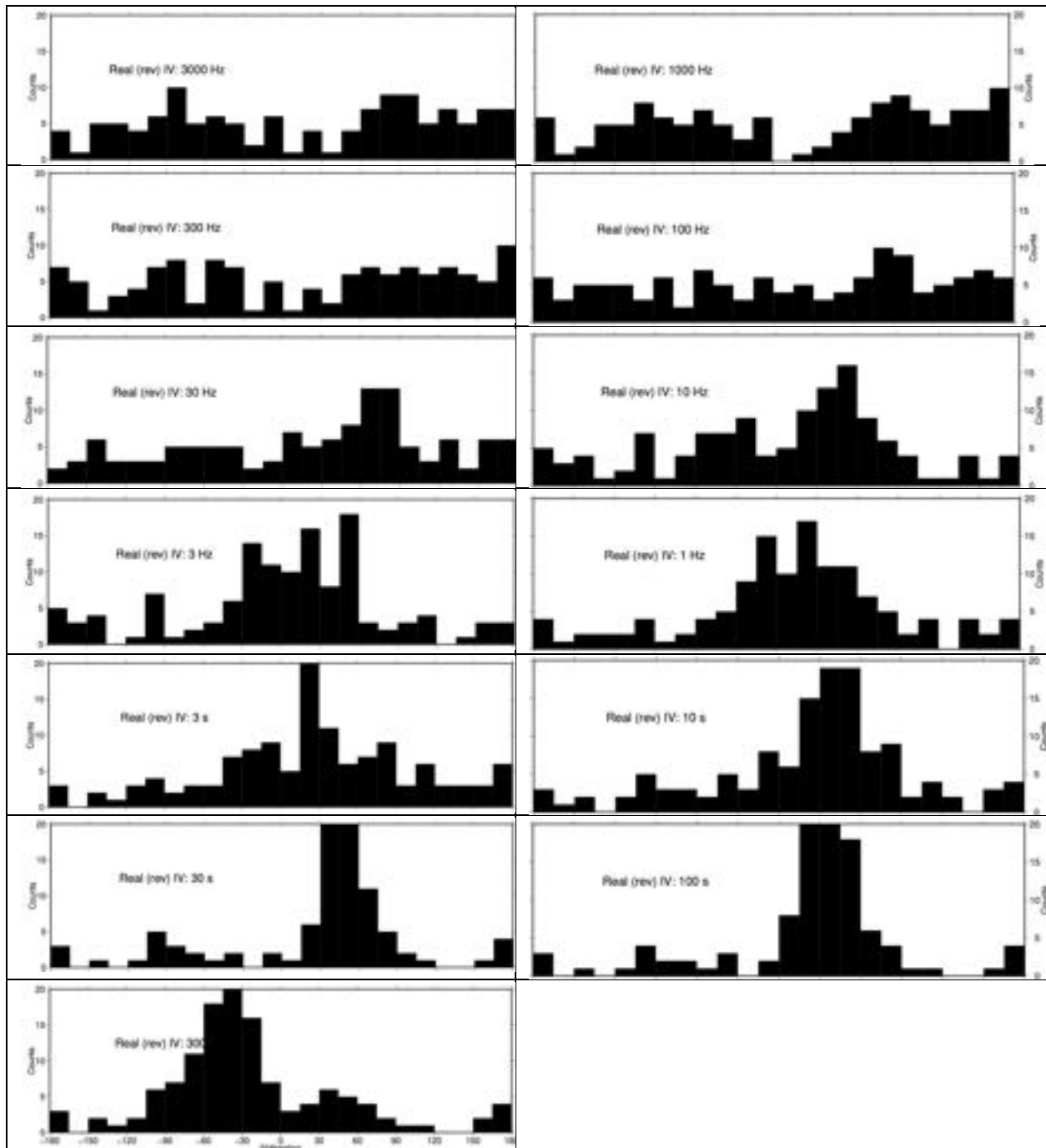


Figure 52: Histograms of Real (rev) IVs at various frequencies/periods.

- At high frequencies >100 Hz, there is no dominant strike direction apparent for the whole region.
- The induction arrows below 100 Hz are predominantly pointing NE – this means that the dominant geoelectric strike of the major structures is NW.

This justifies the choices made by Gupta and Jones (1995) and Cook and Jones (1995) of N50W and N30W respectively, rather than the orthogonal direction of N20E for the regional strike chosen by Marquis et al. (1995).

9. Strike decomposition

The purpose of geoelectrical strike determination is two-fold; first it is to ascertain **IF** a 2-D model of the data is valid, and second, if a 2-D model is valid then to derive the best strike angle to adopt for 2-D inversion and to derive the regional responses in that strike angle ⁽⁴⁾. This has to be performed in a statistical manner to derive the angle that fits the data at most sites and most frequencies.

The most-consistent geoelectrical strike over a series of sites and frequencies is best determined using the multi-site, multi-frequency distortion decomposition code of McNeice and Jones (2001), based on the approach of *Groom and Bailey* (1989, 1991). The primary objective when using any strike approach is to determine the most consistent strike direction acceptable to the majority of sites for the majority of frequencies. The optimum manner to determine that direction is in a stepwise mode, going from single-station to multi-station and from a few frequencies to broad frequency bands, to locate significant departures from uniformity, rather than utilizing all data immediately.

Strike decompositions were previously performed for this region by Gupta and Jones (1995) over decade-wide frequency bandwidths (Figure 53).

- One important point is that Gupta and Jones (1995) assumed that strike was dominantly WEST of North.

From MT data alone, there is a 90° ambiguity in the direction of strike.

⁴ Note: The data are NOT rotated into the strike direction, but a distortion model fit with that direction and estimates made of the regional responses. Jones and Groom (1993) and McNeice and Jones (2001) show the superiority of distortion model fitting over rotation.

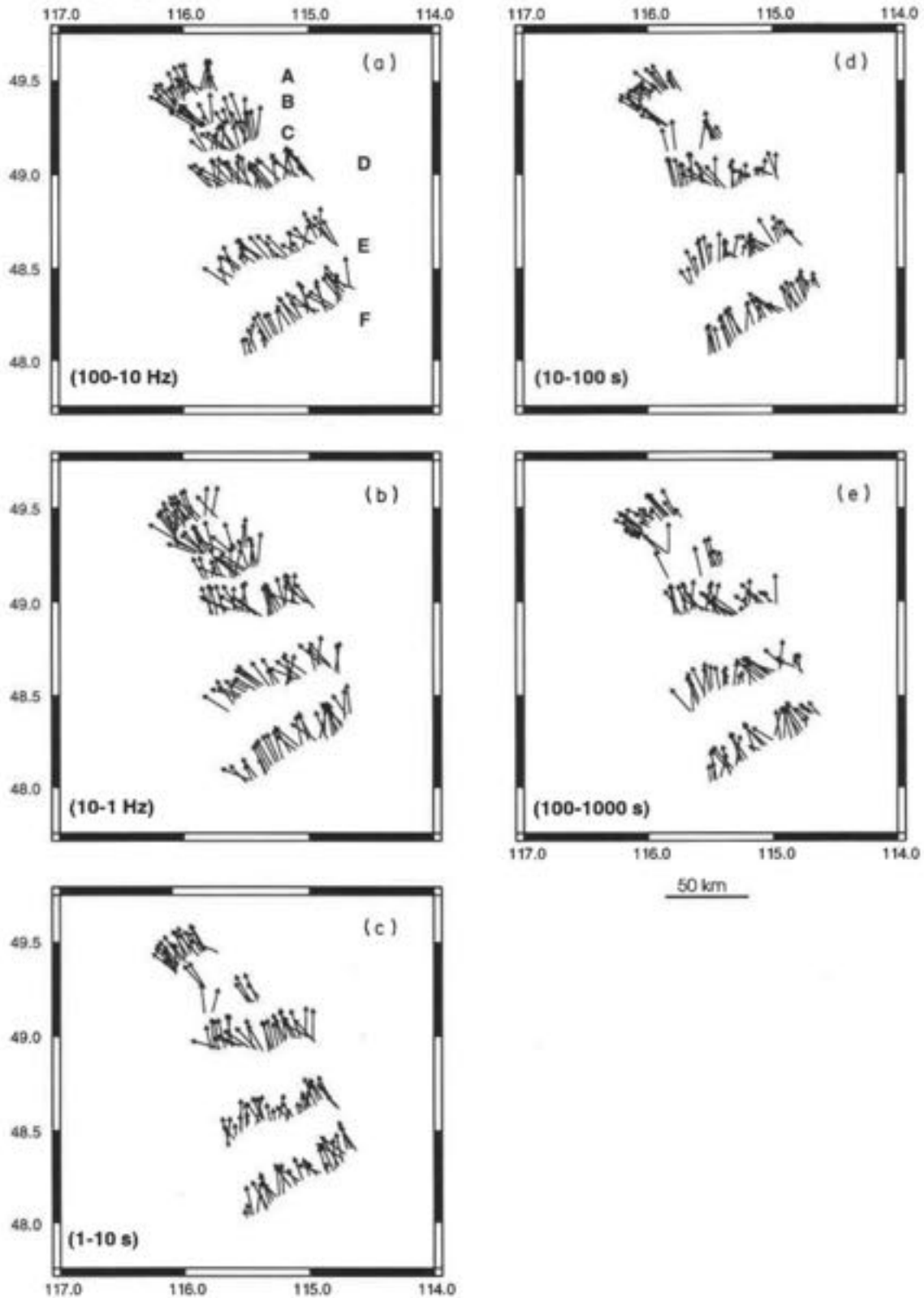


Figure 53: Strike directions calculated for five period bands: (a) 100-10 Hz; (b) 10-1 Hz; (c) 1-10 s; (d) 10-100 s; and (e) 100- 1000 s. The length of an arrow is a measure of the fit of the data to a Groom-Bailey distortion model calculated for the ID or 2D Earth under the influence of a 3D body that distorts the electric field only: long arrows indicate a good fit between the data and the model and the short arrows imply a poor fit between the two. Copied from Figure 4 in Gupta and Jones (1995).

9.1. Single site analyses

First, we run the code in single-site, multi-frequency mode, averaging data in various frequency or depth bands. We assume an error floor ⁽⁵⁾ of 1.75% in impedance throughout; this is equivalent to 3.56% in apparent resistivity and 1° in phase.

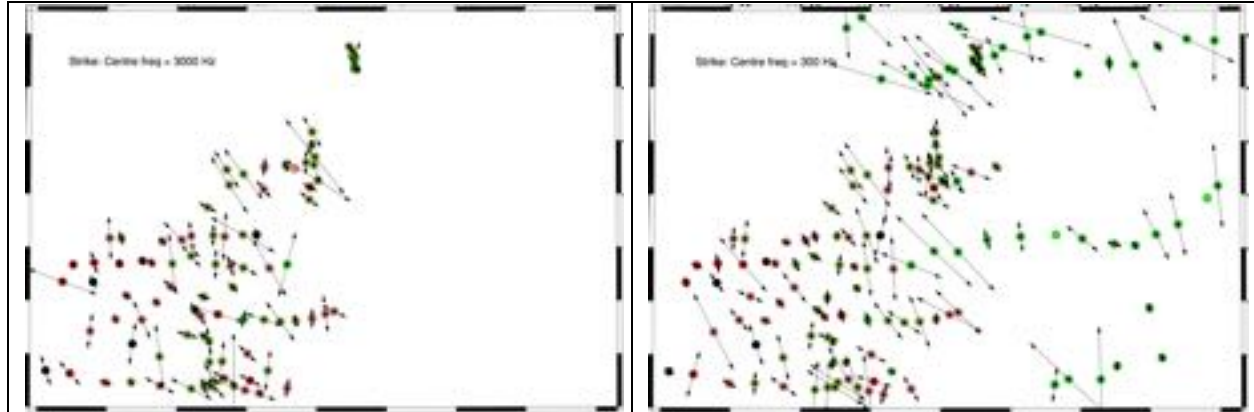
9.1.1. *Single-site, decade-wide bands*

We start by analysing data in seven decade-wide bands, from 10 kHz to 0.001 Hz.

The geoelectric strike directions for the seven are shown in Figure 54.

The lengths of the arrows indicate the phase difference between modes at the middle of each range, i.e., the phase in the strike direction minus the phase in the perpendicular-to-strike direction, which is a measure of the strength of the dimensionality. This phase difference is zero for 1-D structures, and is large for strong 2-D or 3-D structures.

The colours at each site indicate how well the model of distortion fits the data. Light green (RMS<1) and dark green (1<RMS<2) are both acceptable, pink (2<RMS<3) is moderately acceptable, and >4 (red, brown black) is not acceptable and is indicative of either 3-D structures or errors that are too low. Single site outliers are expressions of noisy scattered data.



⁵ An error floor is the minimum value of the error. Errors that are less than the error floor are increased to the error floor value, whereas errors that are greater than the error floor are unchanged. We routinely adopt an error floor when undertaking data fitting as most error estimates are derived from parametric error estimators, and are known to be far too small (see, e.g. (Chave & Jones, 1997)).

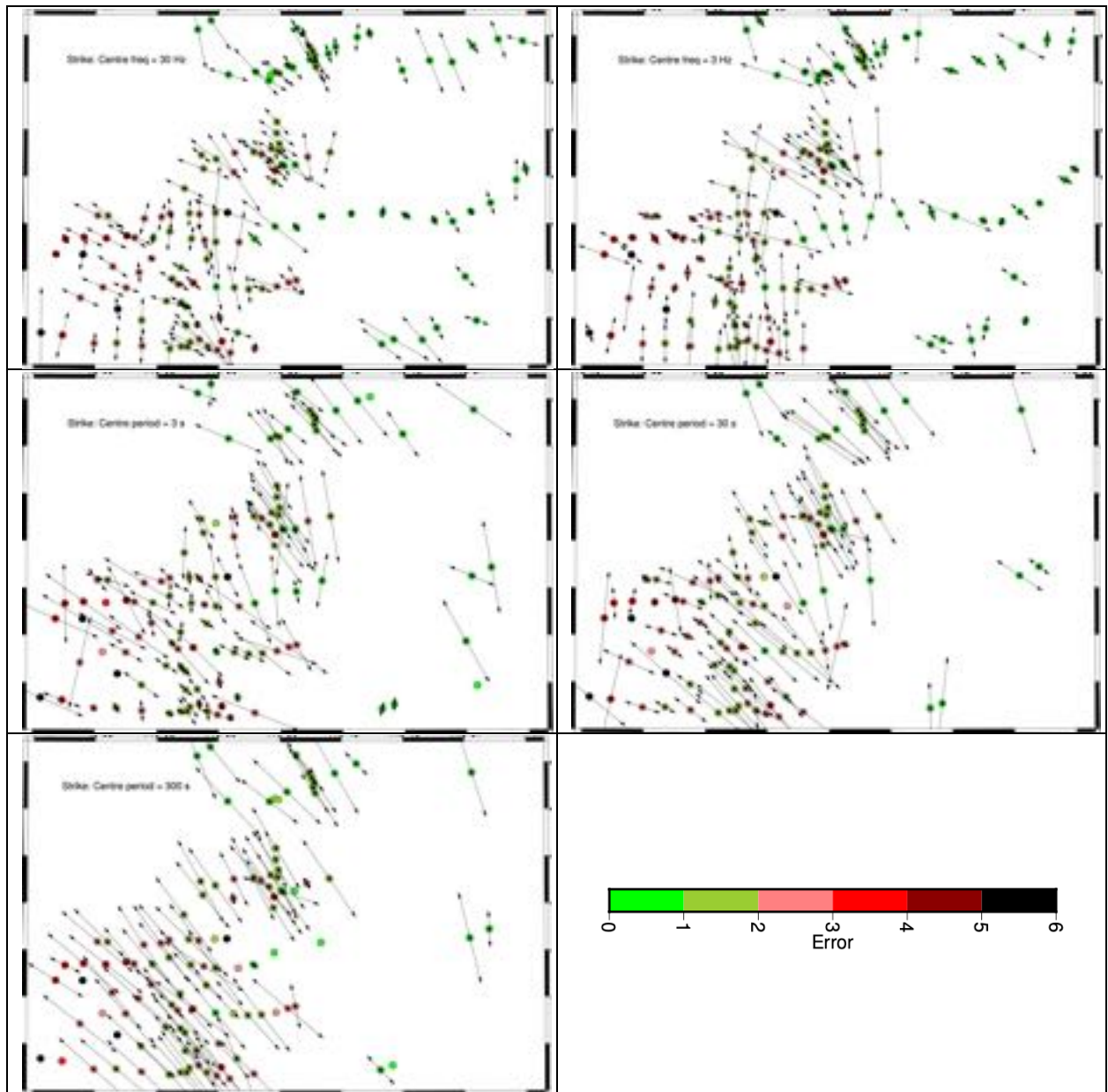
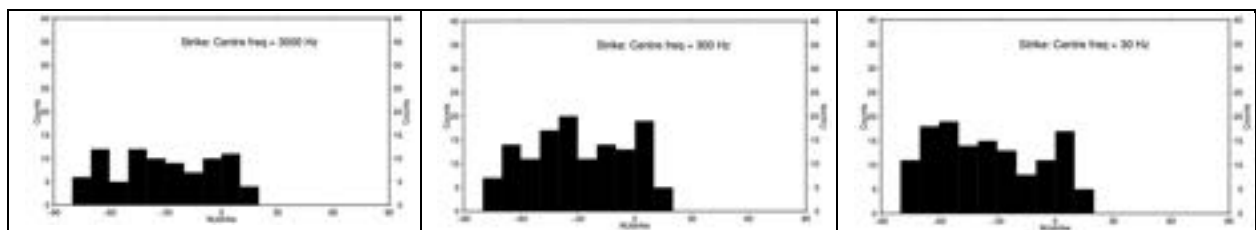


Figure 54: Single-site, multi-frequency strike directions for decade-wide bands from 10 kHz to 0.001 Hz. The length of the arrows indicates the phase difference, which is a measure of the strength of dimensionality, and the colour indicates the nRMS, with green inferring an acceptable fit and red and black unacceptable.



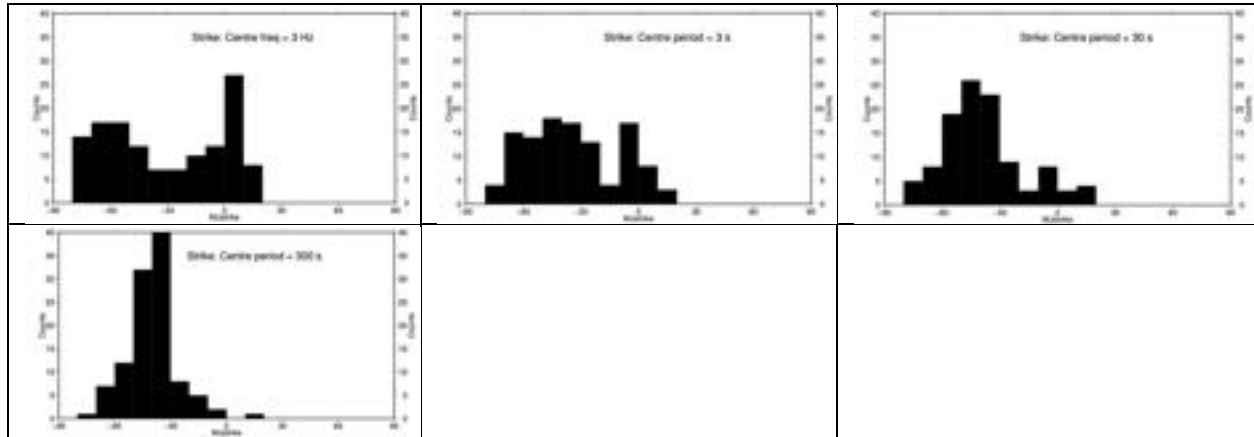


Figure 55: Histograms of the strike directions in decade-wide frequency bands from 10 kHz – 0.001 Hz.

Both visibly in the strike maps (Figure 54) and in the histograms (Figure 55) there is certainly an increasing concentration on a strike direction of initially N-S then NW-SE with decreasing frequency then finally rotating around to N30W at almost all sites at the lowest frequencies.

This rotation with decreasing frequency (=increasing period) is consistent with the directions observed by Marquis et al. (1995) to the west at the Intermontane/Omineca boundary (Figure 55).

→ However, Marquis et al. (1995) decided that the low frequencies were directed N30E, whereas here we prefer N60W, consistent with the strike directions of Gupta and Jones (1995).

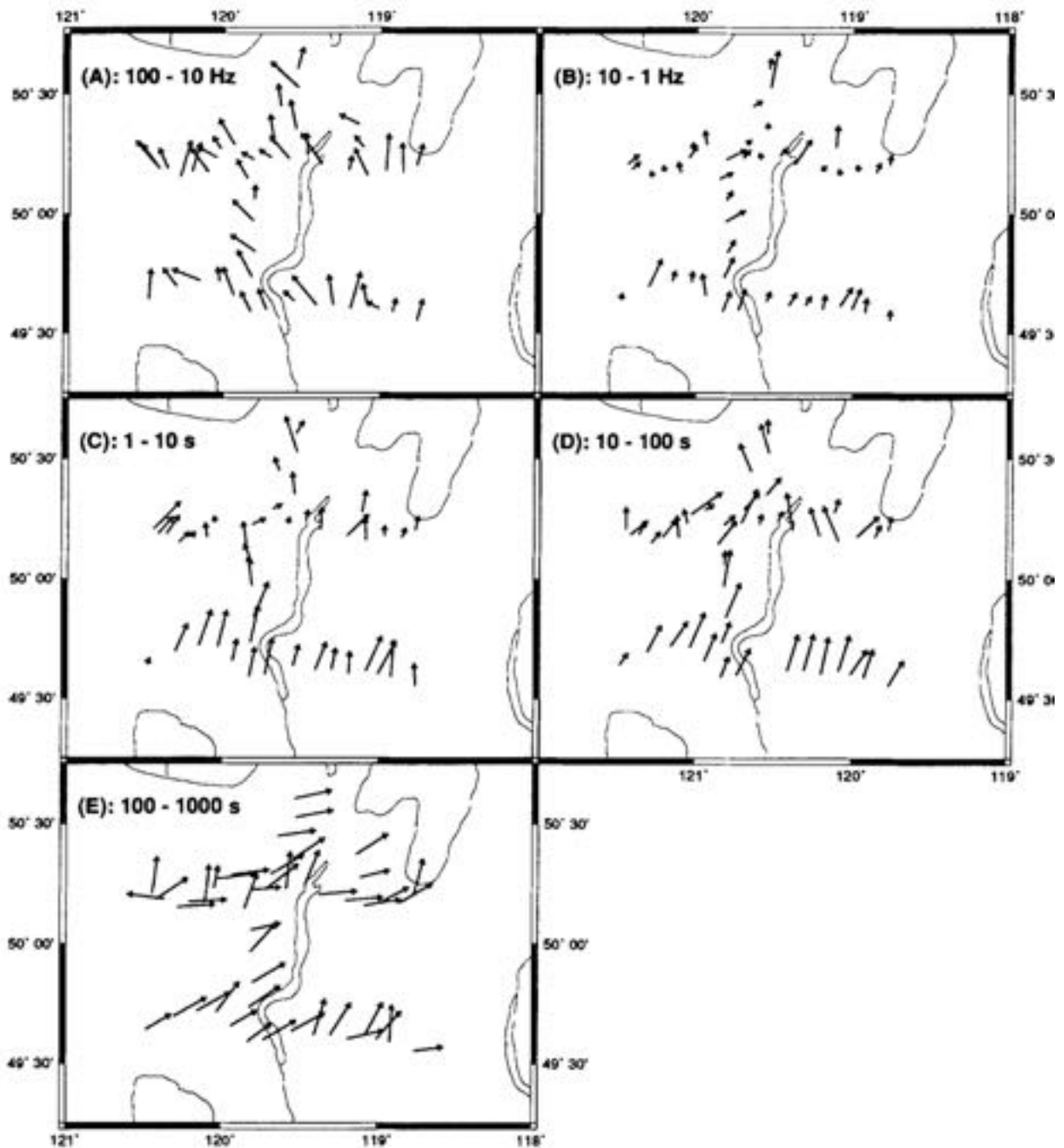


Figure 56: Strike directions for sites at the boundary of the Omineca and Intermontane Belts. Taken from Marquis et al. (1995).

9.1.2. Single-site, single frequency bands

Next we examine the strike directions determined when we seek the strike that is acceptable at each site for all frequencies in single bands.

9.1.2.1. 10 kHz – 3 Hz

The first set is the almost four-decade band of 10 kHz – 3 Hz, which is sampling from 100 m down to 4-5 km. The strike directions and error of distortion model fits at each site are shown in Figure 57, a histogram of the errors in Figure 58, and a histogram of the strike directions in Figure 59.

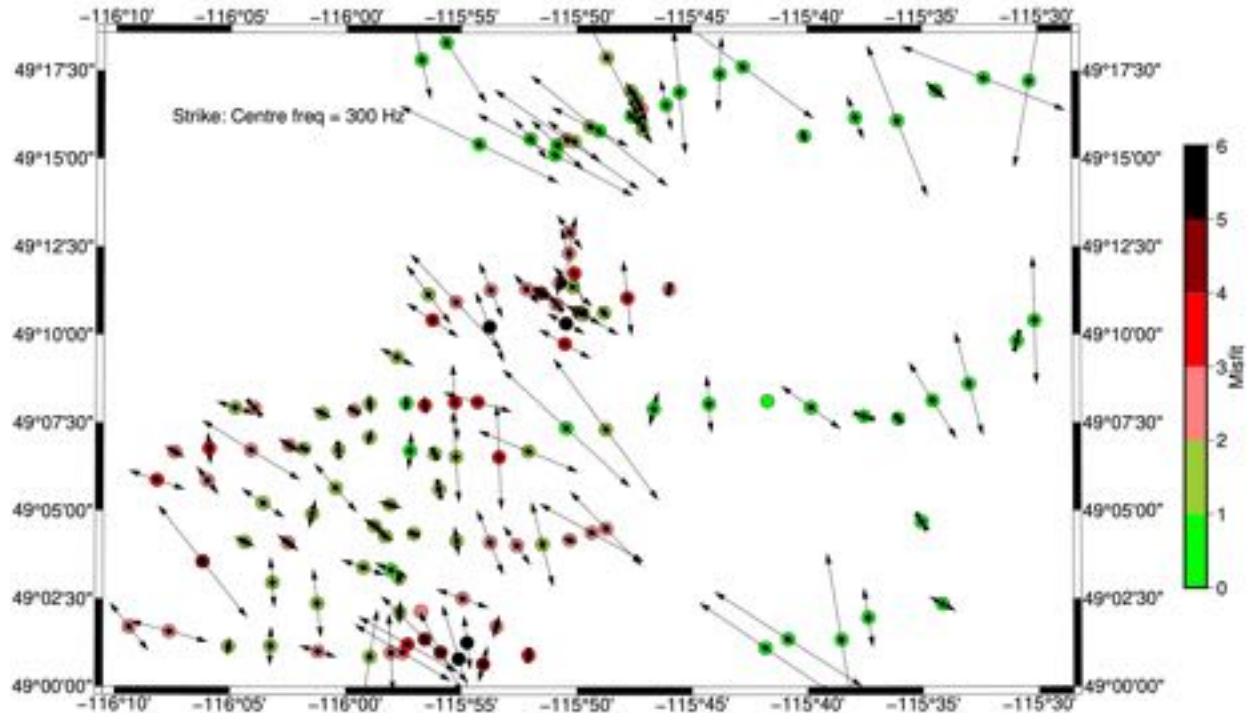


Figure 57: Strike direction for each site in the frequency band 10 kHz – 3 Hz. The scale is the average error of misfit of the distortion model to the data. Green = acceptable; Red = unacceptable.

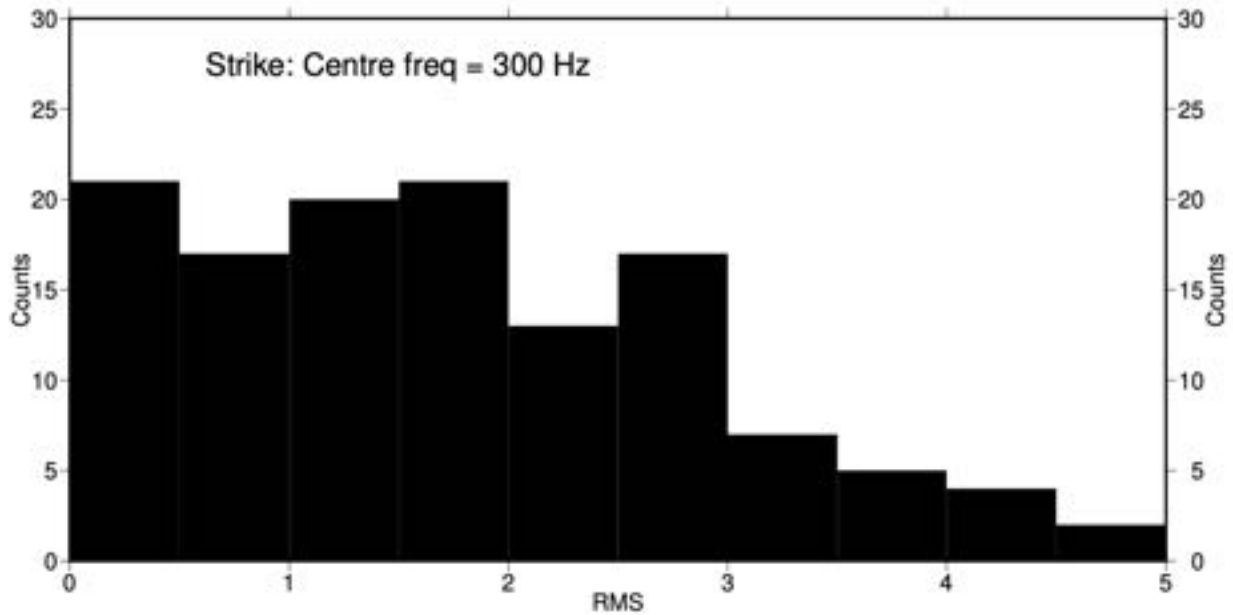


Figure 58: Histogram of nRMS misfits to the distortion model at each site as shown in Figure 57.

Of the 112 sites analysed, over half of them (759, have an nRMS < 2, so the 2-D distortion model with a single strike direction over the whole band of 10 kHz – 3 Hz is acceptable to them. A further 30 are marginally acceptable (2 < nRMS < 3), which means if the error floor is increased x1.5 from 3.75%/1° for RhoA/Pha to 5.625%/1.5°, those 30 would be acceptable also.

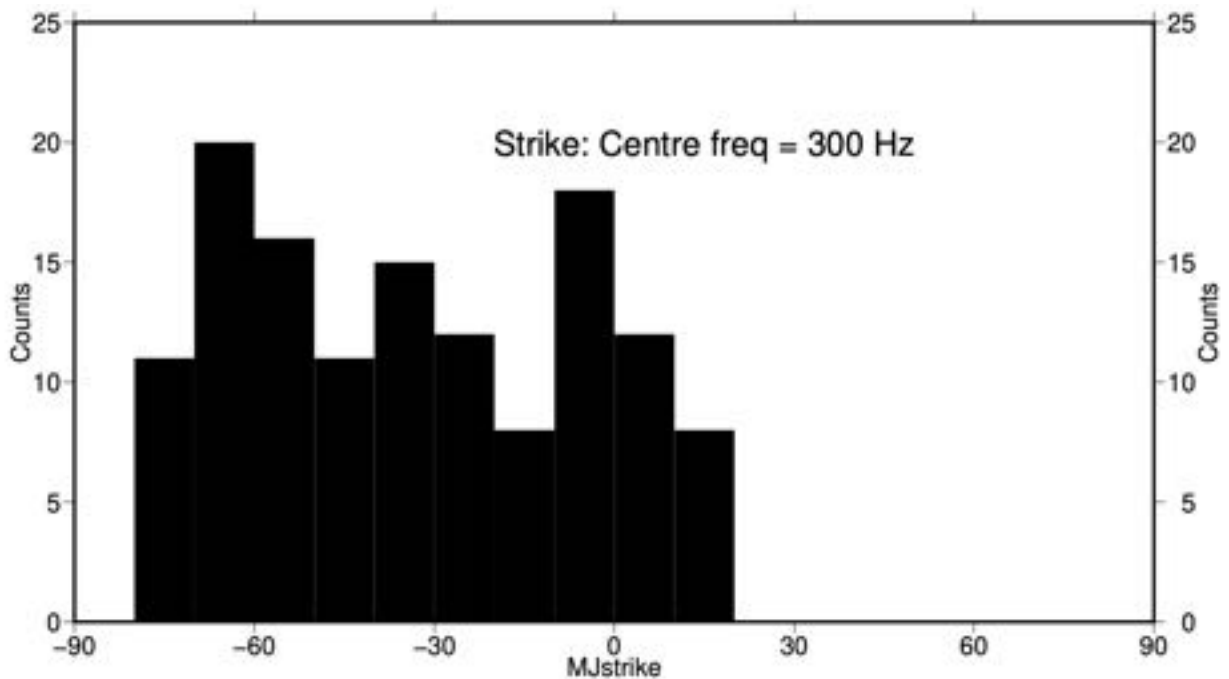


Figure 59: Histogram of strike directions in the three-decade band 10 kHz - 3 Hz.

The histogram of the strike directions is shown in Figure 59, and there are three visible peaks, at -70° - -60°, at -40° - -30° and at -10°- 0° (or their orthogonal directions).

9.1.2.2. 800 Hz – 8 Hz

The next band to analyse is the two decades of highest quality data from 800 Hz – 8 Hz. This band is primarily sensing depths from 500 m to 3-4 km. Here we see decent fits to most of the sites, with nRMS < 2.00 for about 2/3 of them.

Strike directions show the same three peaks as for the broader frequency range (Figure 61) at -70°- -60°, at -30° - -20° and at -10° - 00°, but with the peak at -70°- -60° far more pronounced.

The distortion models fits the sites excellently well (Figure 62), with over one third half (51 of 144) having an nRMS misfit <1, and two-thirds (92 of 144) having a misfit <2. There are 27 marginally-fit sites with misfit between 2 – 3, so those would be acceptable with a 50% increase in the adopted error floor. Only four sites poorly fit the distortion model with misfit >3.

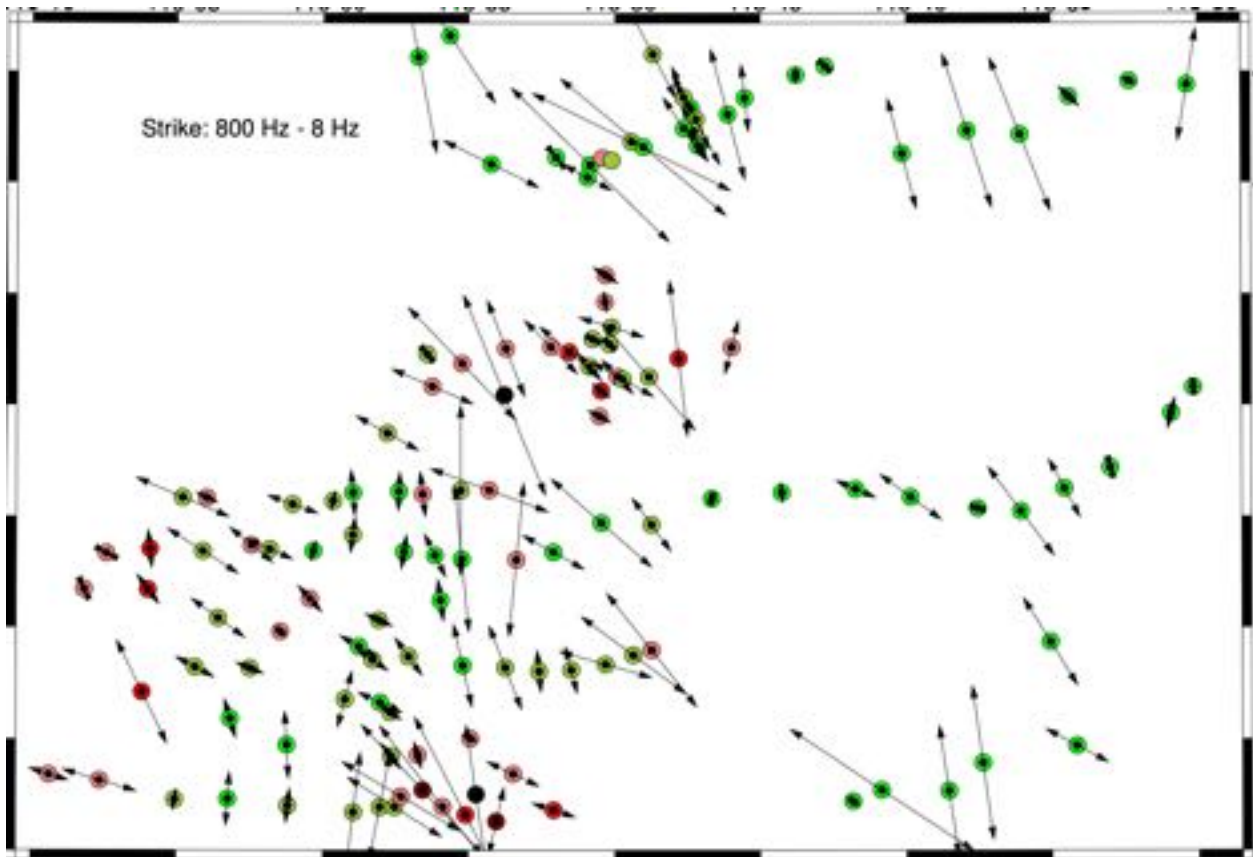


Figure 60: Strike direction for each site in the frequency band 800 Hz – 8 Hz. The scale is the average error of misfit of the distortion model to the data. Green = acceptable; Red = unacceptable.

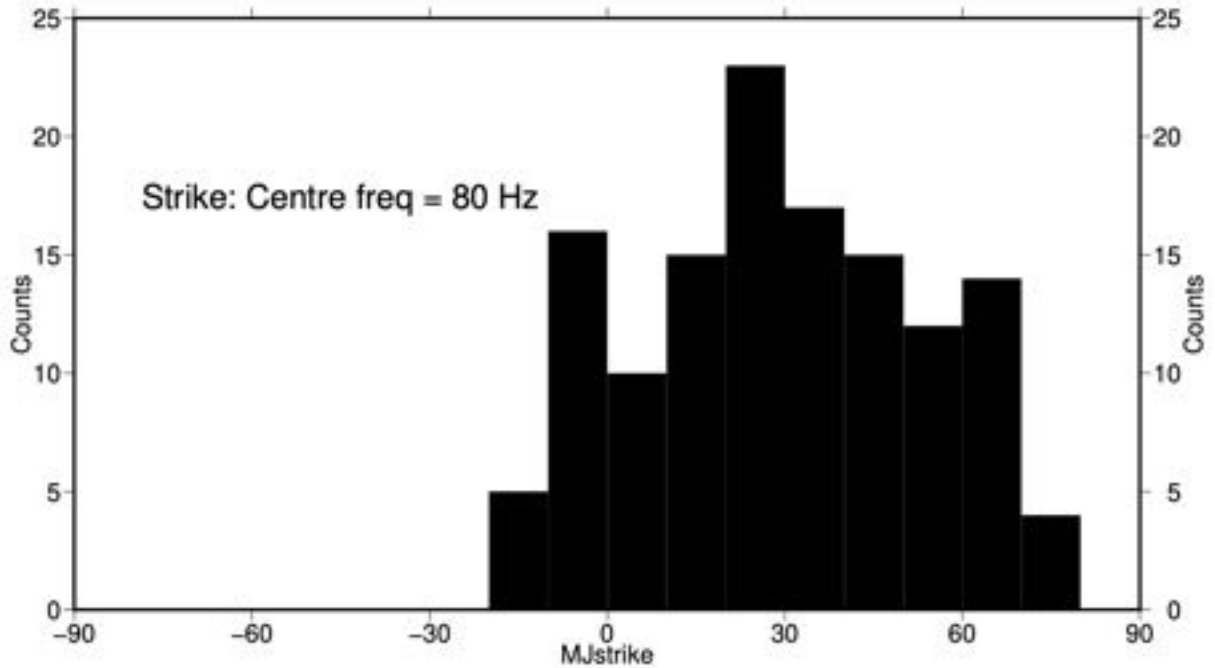


Figure 61: Histogram of strike directions in the two decade band 800 Hz - 8 Hz.

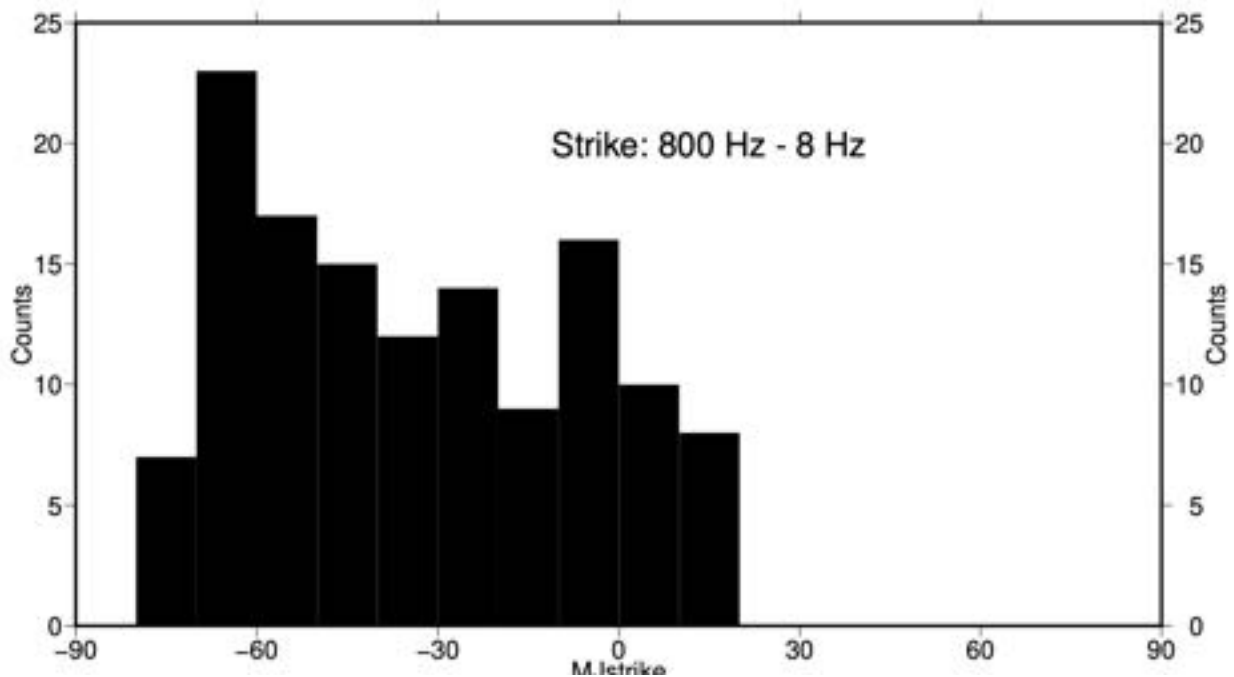


Figure 62: Histogram of strike directions in the two-decade band 800 Hz - 8 Hz.

9.1.3. Single-site: Misfit sensitivity with strike direction

One way of determining sensitivity to strike direction, i.e., intrinsic dimensionality, is to rotate the data at each site through 90° by 1° increments, and determine the minimum and maximum misfits found, then derive the ratio of the maximum RMS/minimum RMS. This ratio is plotted in

Figure 63 for the whole band 10 kHz – 3 Hz, and the sites with greatest sensitivity to strike are shown in dark red and black squares.

The histogram of the ratios (Figure 64).

The sites with little sensitivity to strike can be modelled in 1-D or anisotropic 1-D, and that is over one third (56 of 144) of them (ratio <1.5, white circles). The next 51 sites are mildly dimensional, with a ratio in the range 1.5 – 2.0 (yellow circles). Only 16 sites exhibit sensitivity to strike direction, with a ratio >2.5. These are mostly rather scattered, and most likely the sensitivity is more a function of the noise in the data than the dimensionality of the subsurface.

There is though a cluster of sites in the middle of the long central E-W profile, labelled MM1 by the client’s representative. These sites do show sensitivity to strike direction.

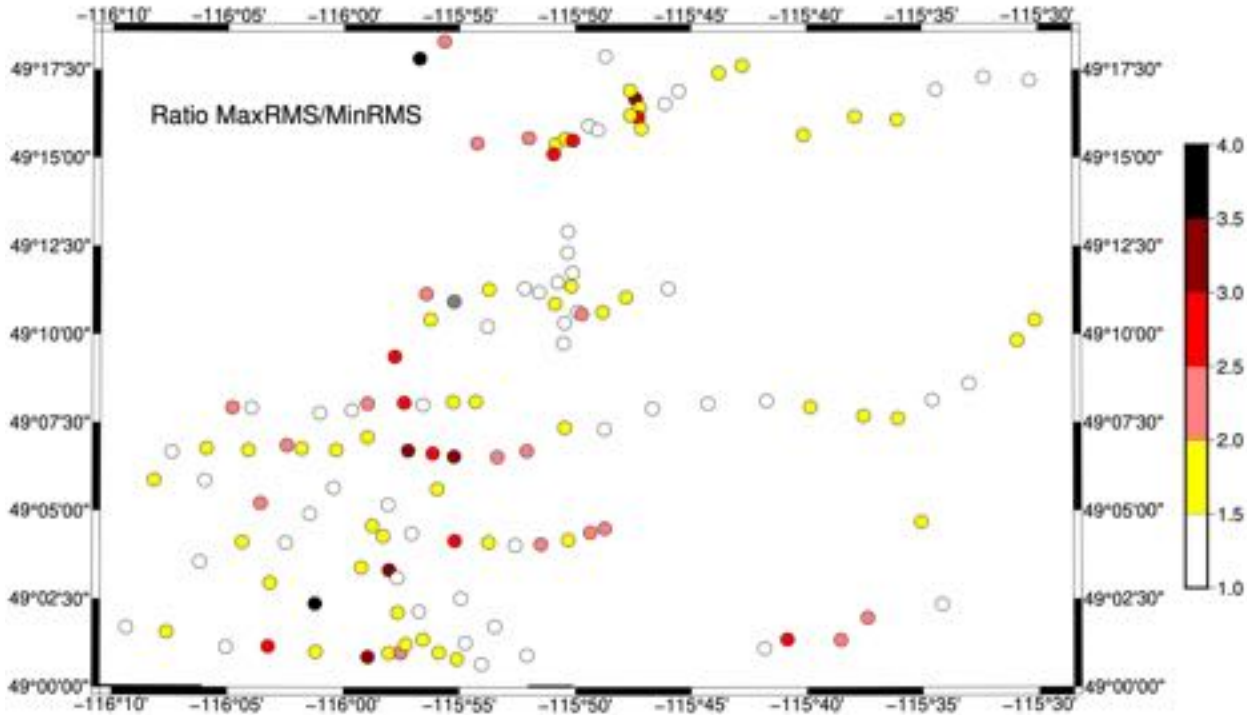


Figure 63: Ratio of the maximum RMS/minimum RMS for each site for the frequency band 10 kHz – 3 Hz.

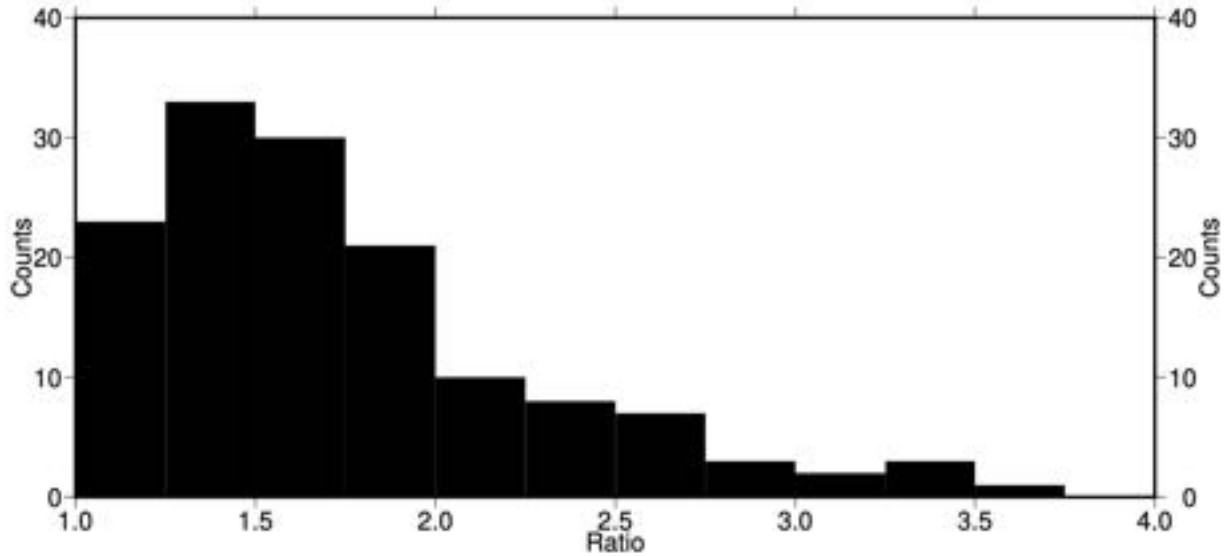


Figure 64: Histogram of the ratios of MaxRMS/MinRMS for single-site strike directions in the frequency band 10 kHz – 3 Hz.

The same plots but for the two decades 800 Hz – 8 Hz are shown in Figure 65 and Figure 66, and essentially the same information is portrayed. 51 sites have a ratio <1.5, and a total of 89 have a ratio <2.0. Only 25 sites have a ratio > 2.5.

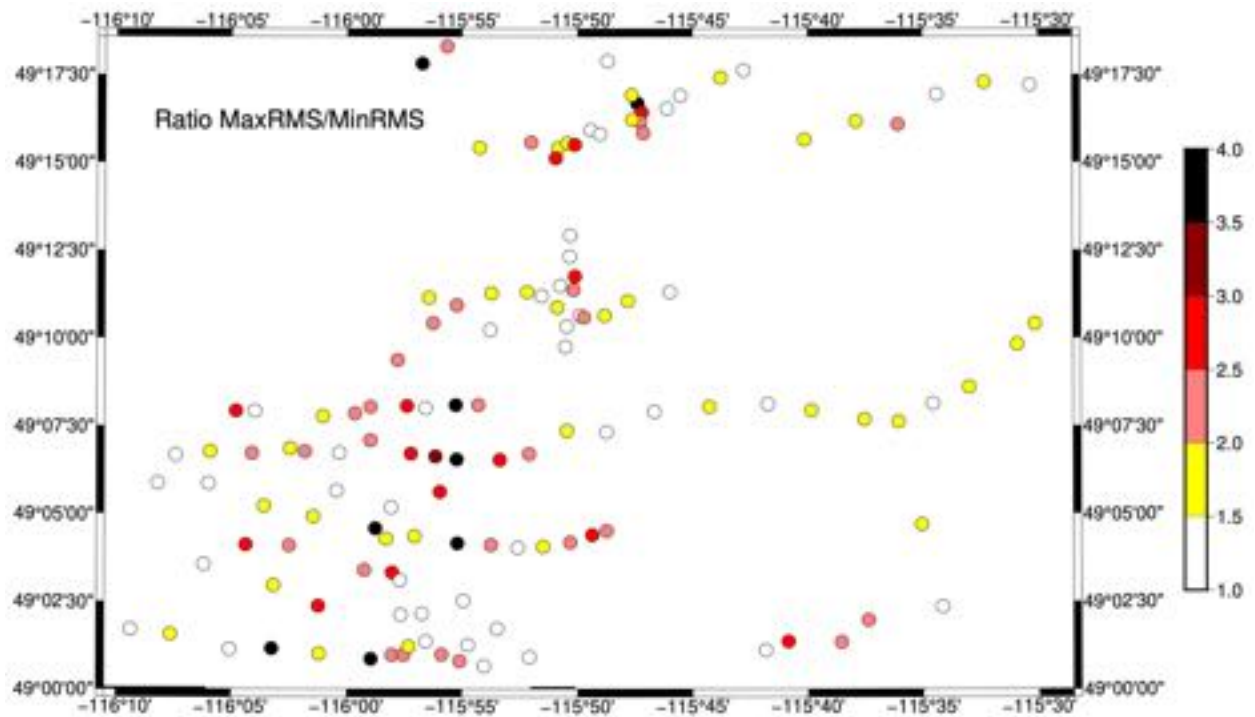


Figure 65: Ratio of the maximum RMS/minimum RMS for each site for the frequency band 800 Hz – 8 Hz.

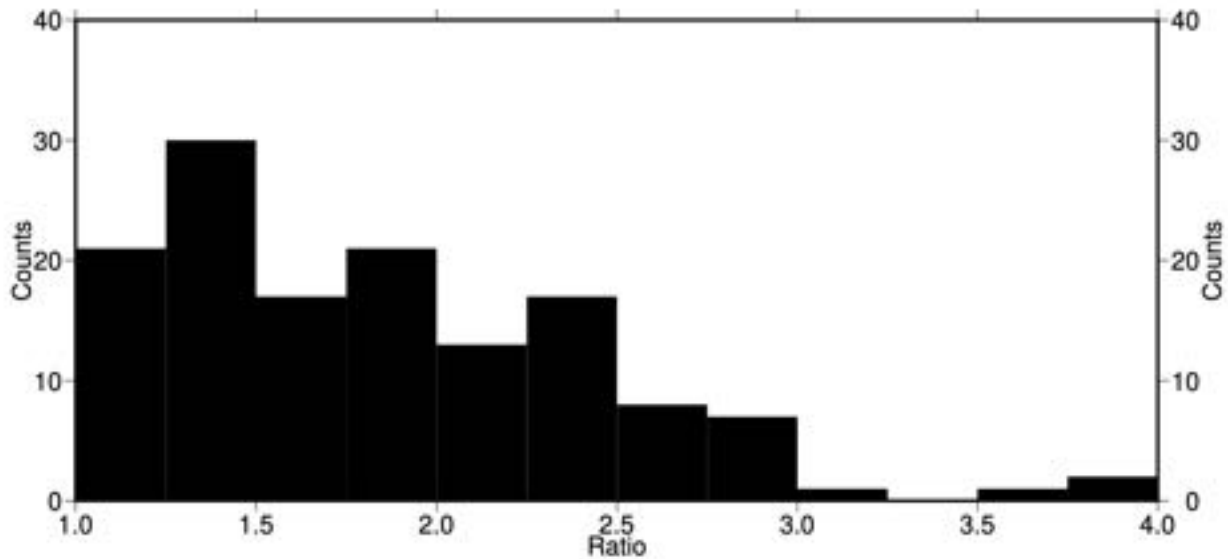


Figure 66: Histogram of the ratios of MaxRMS/MinRMS for single-site strike directions in the frequency band 800 Hz – 8 Hz.

9.1.4. *Single-site: Conclusions*

Single site analysis shows that the area is varying somewhat laterally and but very strongly vertically in the direction of strike of electrical conductivity. Some sites may be amenable to anisotropic 1-D inversion, and some small groups of sites to 2-D inversion.

Generally, the high frequencies strike N-S, the mid-frequencies NW-SE, and the lowest frequencies N60W. Hence the three peaks observed in the strike direction histograms.

9.2. Multi-site by profile

Multi-site, multi-frequency analyses were performed along each profile. The stations on each profile are listed in Table 1. Given the priority of analyses to provide Spratt with regional responses for 2-D parameter testing, the profiles were analysed starting with MM1 and MO.

Extra effort was expended on profile MM1 given its length and its importance for defining the parameters for 2-D inversion.

9.2.1. *Profile MM1*

Profile MM1 comprises 24 sites, 12 newly-acquired sites and 12 from the 1985 Duncan survey line 3 (Figure 67). The Duncan sites only have data up to 384 Hz, and are of poorer quality.

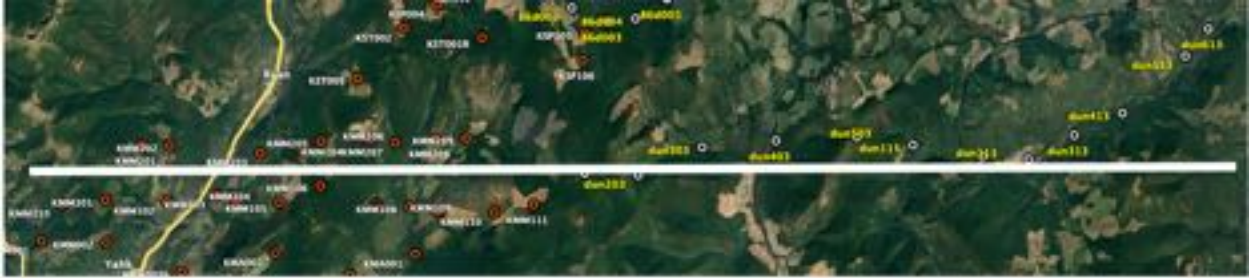


Figure 67: Profile MM1

9.2.1.1. Whole profile analysis

Performing single frequency, multi-site analyses of all the sites simultaneously along the profile (black points in Figure 68), there is significant scatter, but nonetheless a transition is visible from around N-S at the highest frequencies rotating clockwise to N45E at the lowest frequencies. This is consistent with what is being observed regionally.

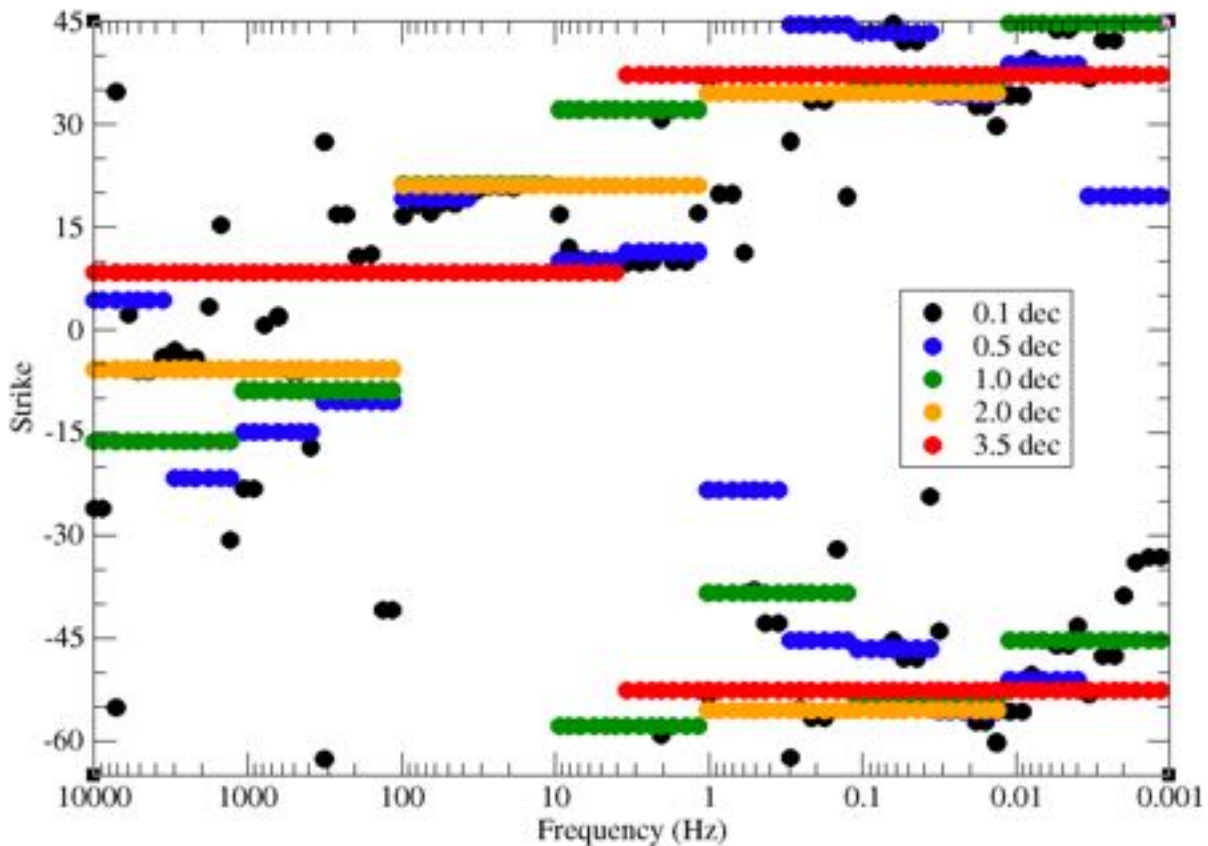


Figure 68: Strike directions for multi-site analyses with different bandwidths for sites on profile MM1.

Multi-site, multi-frequency analysis, with increasing widths of the frequency band from 0.5 decades to 3.5 decades, confirms this trend.

The 3.5 decade directions, from 10 kHz – 3 Hz and from 3 Hz – 0.001 Hz (red points) are essentially a N08E geoelectric strike direction to around 4 km and a N55W or (N35E) strike direction for the rest of the crust.

Such a layered situation was observed by Marquis et al. (1995) for sites at the boundary of the Omineca and Intermontane Belts (Figure 56). Marquis et al. (1995) found that the strike directions above 10 Hz were on average N25W, which is very different from those below 10 Hz, N20E, and at the lowest frequency of N60E.

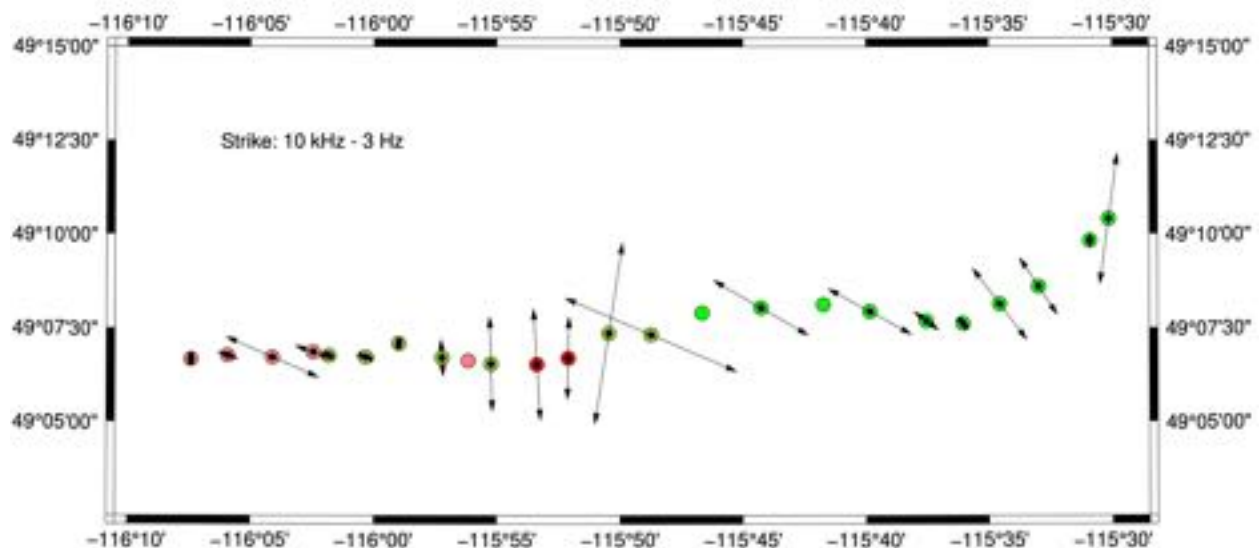
The interpretation of Marquis et al. (1995) was that the high frequency strike represents the geoelectrical strike of the allochthonous terranes, whereas the lower frequency strike is the strike of autochthonous basement. And the lowest frequency strike is that of the lowermost crust/upper mantle.

However, based on the Induction Vector directions, we assume that crustal strike is WEST of north.

9.2.1.2. *Lateral variation along profile*

To test variation of preferred strike direction along the profile, groups of sites were taken. Each group was of 5 sites, the centre one and its two neighbours on either side. The end sites were modified to include only one or two neighbours.

The analyses were performed for the two frequency bands of interest, namely 10 kHz – 3 Hz for the upper 4-5 km or so, and 3 Hz – 0.001 Hz for the middle and lower crust to the Moho. Analysis was also performed of the two-decade band from 800 Hz – 8 Hz, as these represent the best quality data. (Remember though that the Duncan data only goes to 384 Hz.)



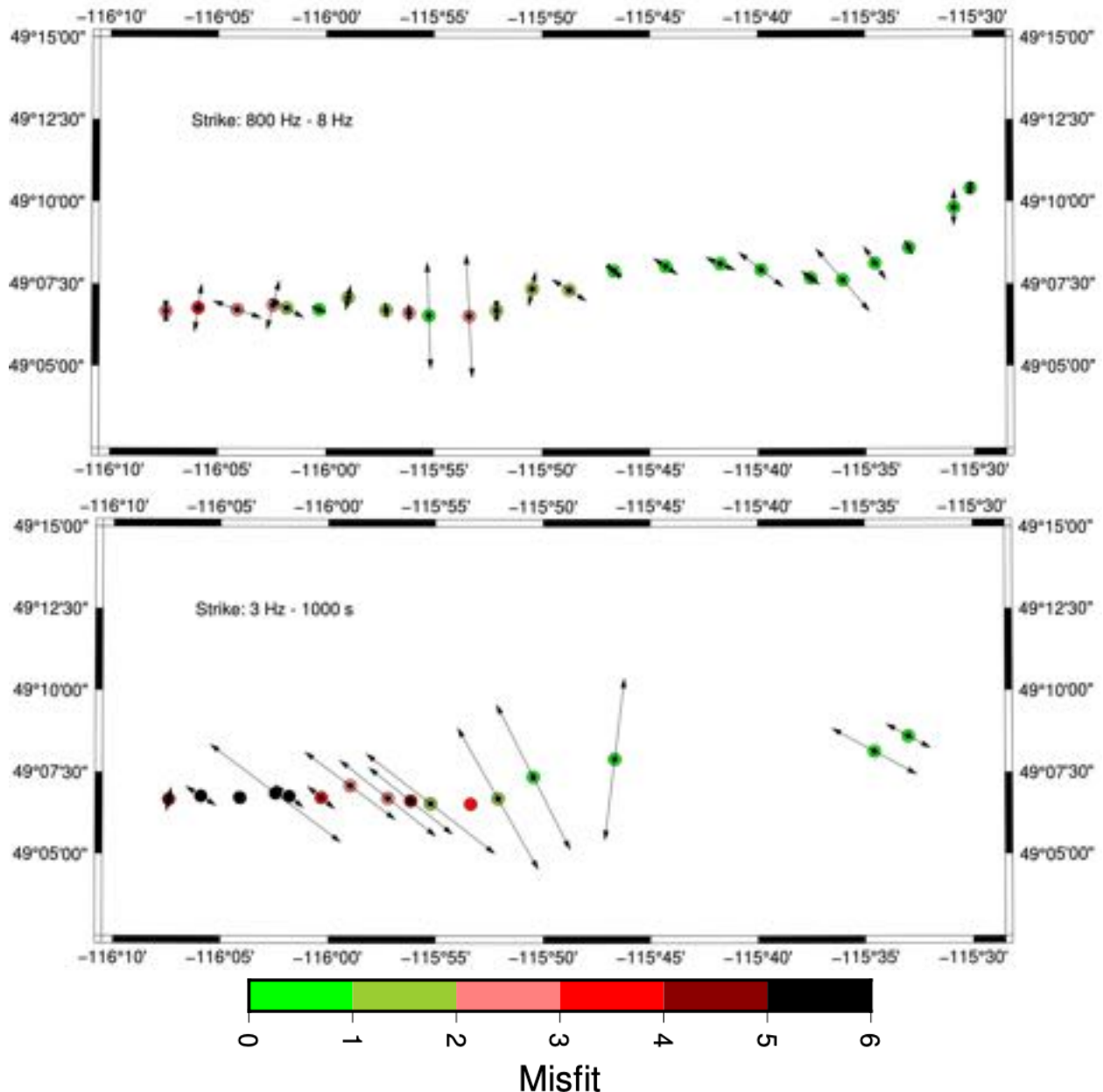


Figure 69: Strike directions for groups of five sites in the three frequency bands.

We still see a strong preference for approx. N-S at high frequencies and approx. NW-SE at the low frequencies.

9.2.1.3. Imposed strike directions – N10E and N35W

Finally, we can impose a single strike direction on all of the data, and see how well the distortion model fits.

We impose two directions, the uppermost crust direction of N10E (Figure 70, top) and the rest-of-the-crust direction of N35W (Figure 70, bottom) for all frequencies from 10 kHz – 0.001 Hz.

What we find is that the Duncan sites to the east are really not that sensitive to strike direction, and accept both directions over all frequencies. However the newly-acquired sites to the west are far more sensitive, and they poorly accept one direction over all frequencies.

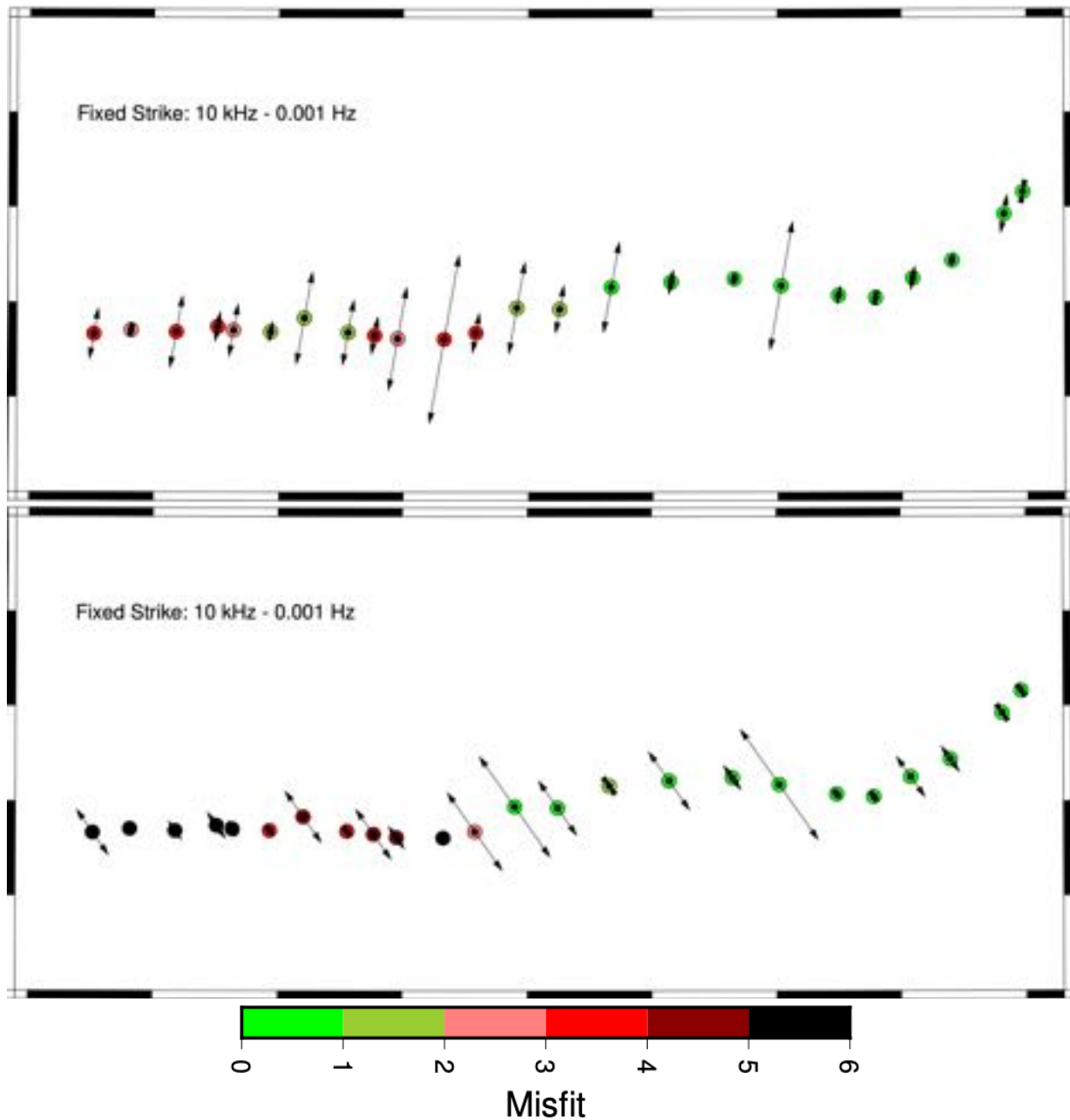


Figure 70: Imposed strike directions of N10E (top) and N35W (bottom) for all sites and all frequencies from 10 kHz – 0.001 Hz.

9.2.1.4. Conclusions

1. Profile MM1 exhibits both lateral and vertical variation in geoelectrical strike direction.
2. Sites to the east – the existing Duncan data – allow a broad range of strike directions, whereas those to the west – the newly-acquired Kootenay data – are more selective.

3. Generally, the data require a direction on N10E for frequencies sampling the top 4-5 km and N35W for the rest of the crust.
4. For optimal imaging, two models need to be generated, one for the upper 4 km with an assumed strike of N10E and using frequencies from 10 kHz – 3 Hz, and the other for the whole of the crust with an assumed strike of N35E and using frequencies from say 30 Hz – 0.001 Hz.
5. A single crustal model with a strike of N10E would be reasonable for the upper crust, but would not optimally image structures in the middle and lower crust.
6. Similarly, a single crustal model with a strike of N34E would be reasonable for the middle and lower crust, but would not optimally image structures in the upper crust.

→ **Two sets of final estimates were prepared, one set at N10E and the other set at N35E.**

9.2.2. Profile MO

Profile MO (Moyie) is the most northern sites and is an ENE-SWS one comprising primarily existing Duncan data (Figure 71). In addition, a short N-S profile of five sites labelled KMOxxx was newly-acquired, and all of those data are included in the analysis to define the appropriate strike direction(s).



Figure 71: Profile MMO. Existing Duncan data shown in yellow, and newly-acquired KMOxxx sites in white. The location of the Moyie drillhole is indicated by the blue triangle.

Thus, the 17 sites assigned to this profile are:

dun311, dun411, dun511, 86d014, 86d145, 86d015, dun611, dun711, KMO01R, KMO002, KMO003, KMO004, KMO005, dun811, dun009, dun010, dun011.

The Duncan data were previously modelled by Gupta and Jones (1995), with an assumed strike of N50W, and their model is shown in Figure 17. A subset of the data around the Moyie drillhole was previously modelled by Cook and Jones (1995), with an assumed strike of N30W, and their model is shown in Figure 18.

The multi-site analyses for different frequency bandwidths is shown in Figure 72, and there is certainly stability with frequencies lower than 10 Hz.

Note that the high frequency strike of N32W and a lower frequency strike of N43W is fully consistent with the prior analyses of Cook and Jones (1995), for the high frequency data, and Gupta and Jones (1995) for the regional scale data.

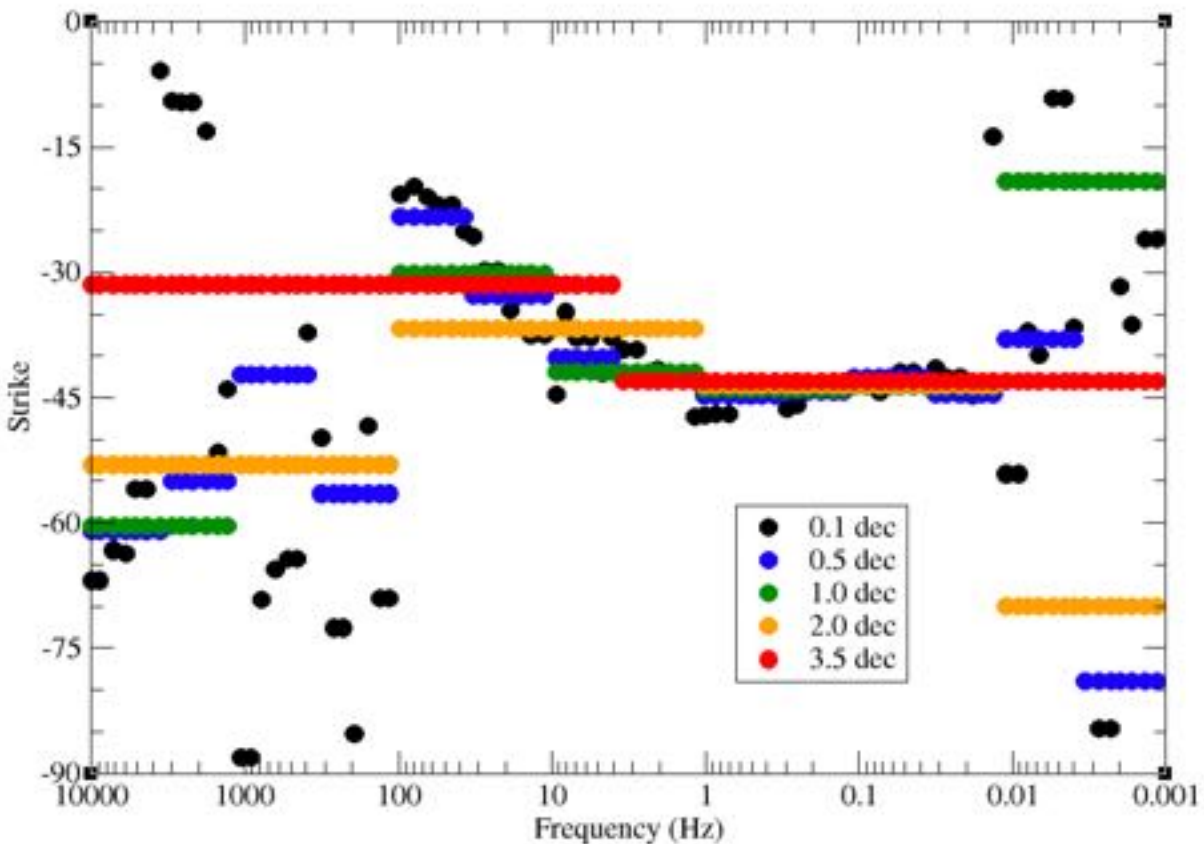


Figure 72: Strike directions for multi-site analyses with different bandwidths for sites on profile MO

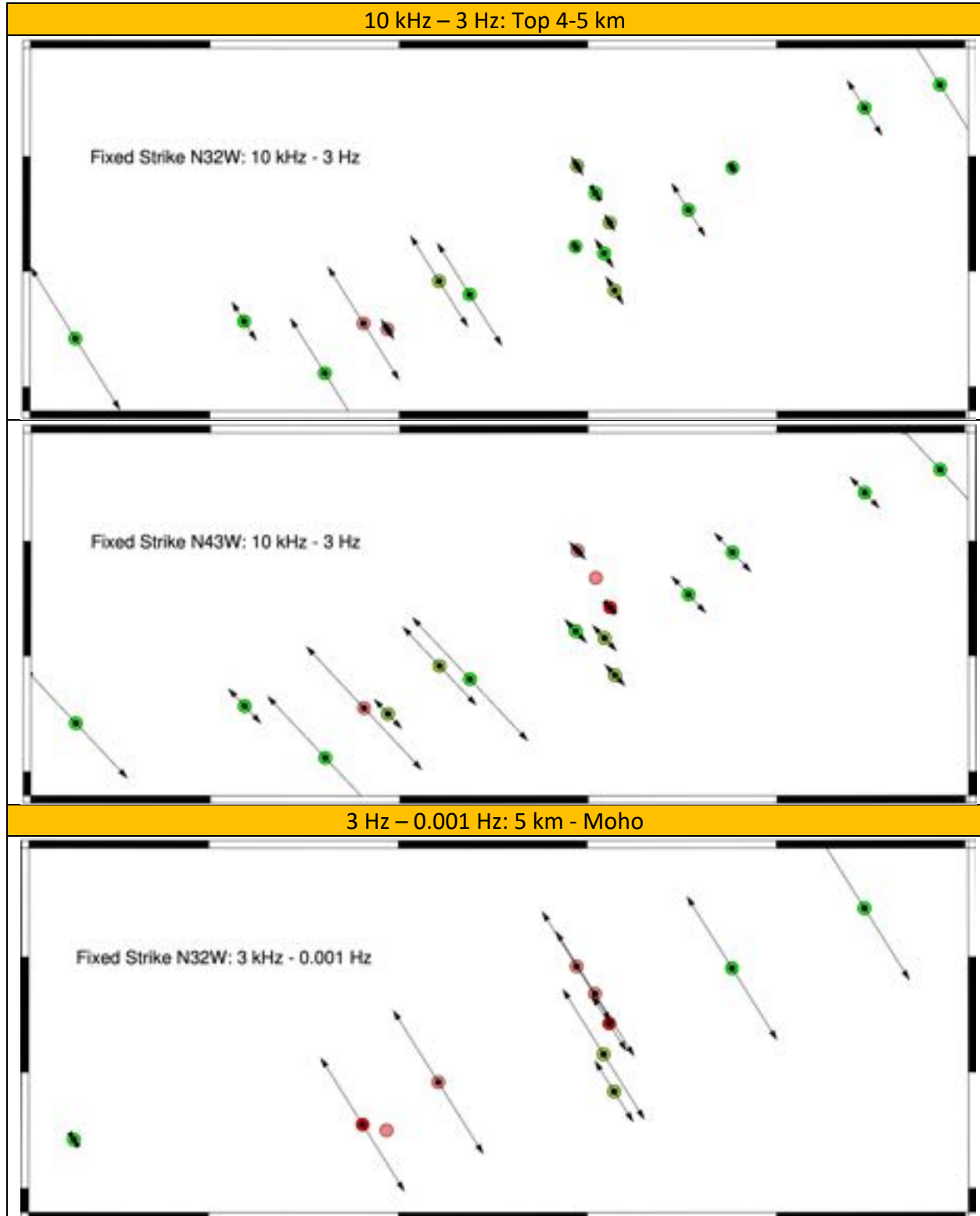
Taking all six decades from 10 kHz to 0.01 Hz together, the most consistent strike direction found is N39W, and the misfit is acceptable for most sites with an average RMS = 1.06 and first and third quartiles of 0.30 and 1.60, which is acceptable.

Fixing the strike to either N32W or N43W for the frequency band 10 kHz – 3 Hz (appropriate for N32W), 3 Hz to 0.001 Hz (appropriate for N43W), and for the whole bandwidth of 10 kHz – 0.001 Hz, we can judge how well a single strike direction fits the data.

As we can see in the error plots (Figure 73) that one strike direction is poorly appropriate for the whole frequency band of 10 kHz – 0.001 Hz (depths from the surface to the Moho). The top 4-5 km require a strike of N32W, especially the newly-acquired data. The 5 km to Moho best accepts a direction of N43W.

→ Optimally, the data from this profile should also be modelled in two bands with two different strikes, for the upper 5 km and for 5 km to the Moho.

→ However, a good first-order model for the whole crust can be obtained at N39W.



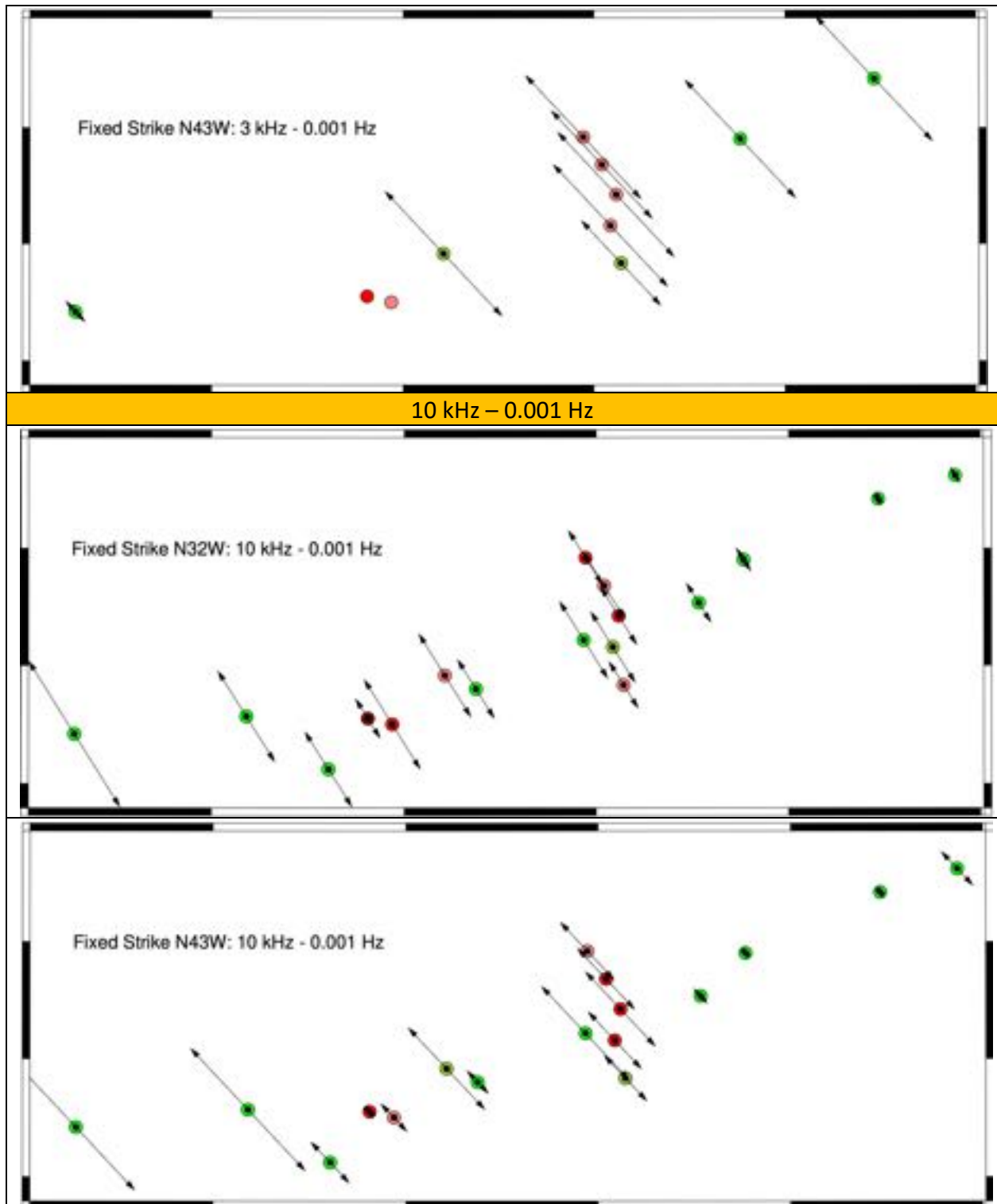


Figure 73: Errors for fixed strike directions. Top panels: Upper 5 km strike of N32W (top is correct, bottom is incorrect). Middle panels: 5 km to Moho strike of N43W (top is incorrect, bottom is correct). Bottom panels: Fixed strikes over the whole frequency band.

9.2.3. Profile SS

Profile SS comprises 14 sites KSSxxx:

KSS101, KSS102, KSS103, KSS104, KSS105, KSS106, KSS107, KSS108, KSS118, KSS109, KSS110, KSS111, KSS115, KSS112, KSS113

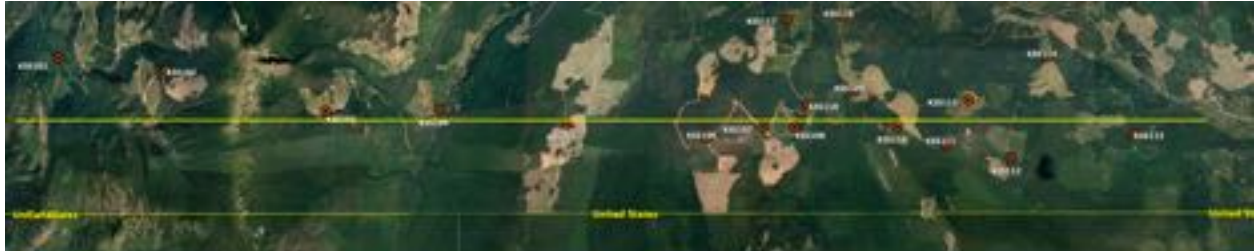


Figure 74: Sites along profile SS.

Four other KSS sites, namely KSS114, KSS116, KSS117, and KSS119, were deemed to be too far off the profile.

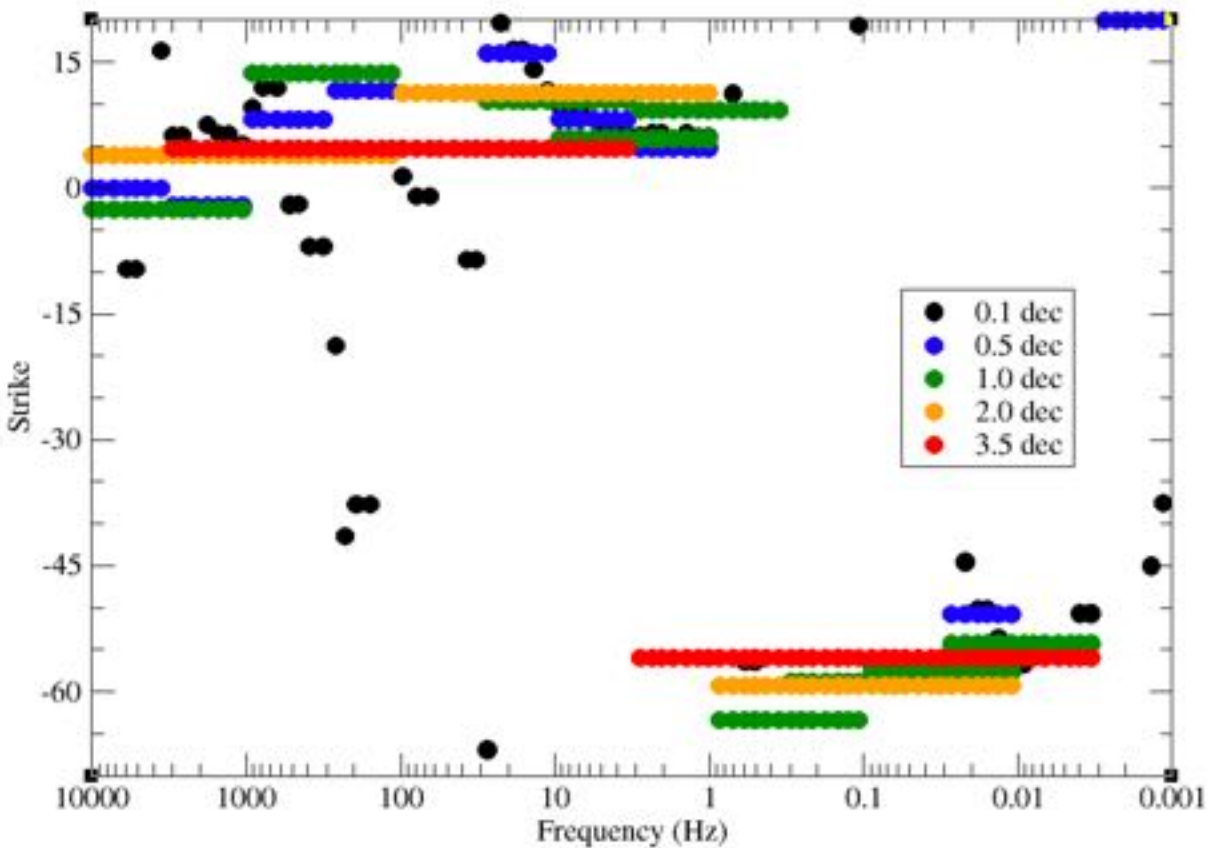


Figure 75: Strike directions for multi-site analyses with different bandwidths for sites on profile SS.

Multi-site, multi-frequency analyses with different frequency bandwidths are shown in Figure 75. As with the prior profiles, we see a systematic change in strike direction from approx. N-S (N05E) at high frequencies to N55W at low frequencies, with a cross-over at around 3 Hz.

9.2.4. Profile MM0

Profile MM0 comprises 17 sites, 15 KMM0xx and 2 KMA00x (Figure 76).

KMM001, KMM002, KMM003, KMM003b, KMM004, KMA002, KMM005, KMM006, KMM007, KMA001, KMM008, KMM009, KMM010, KMM011, KMM012, KMM013, KMM014



Figure 76: Sites along profile MM0.

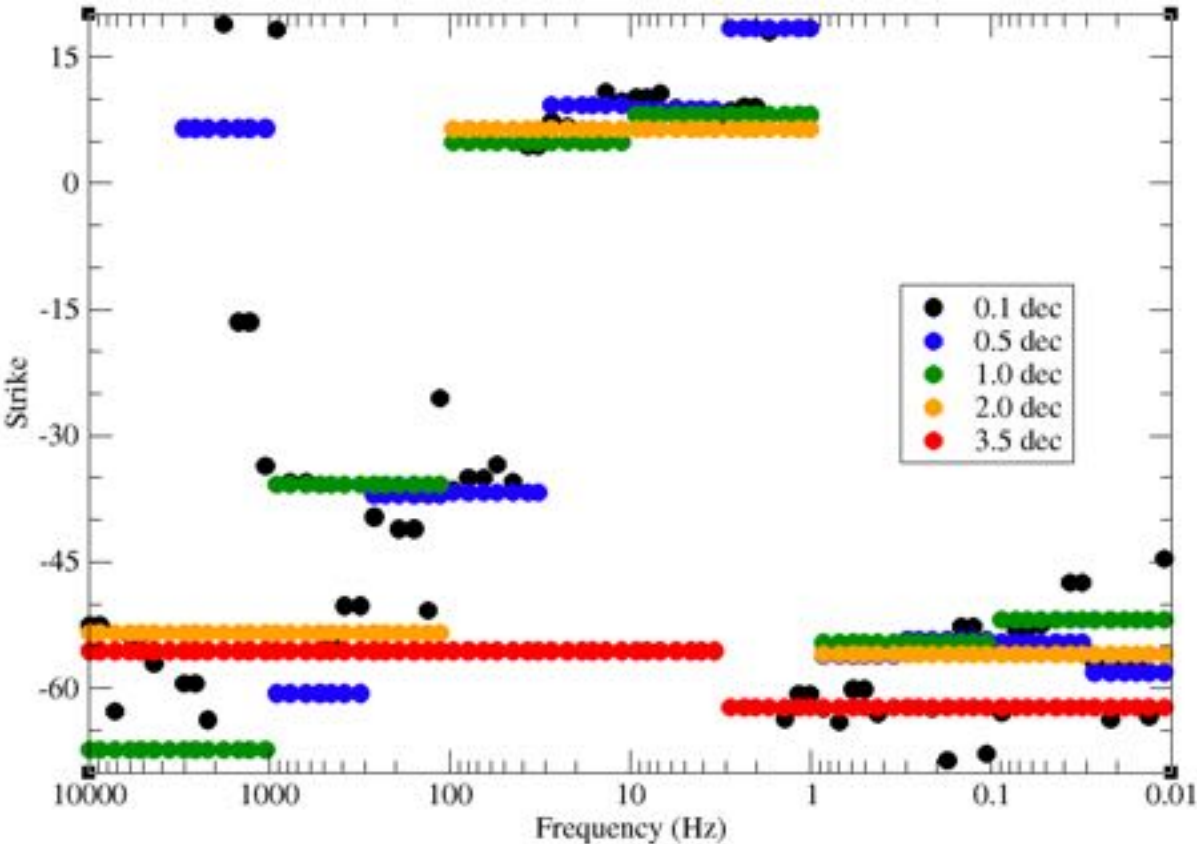


Figure 77: Strike directions for multi-site analyses with different bandwidths for sites on profile MM0.

Multi-site, multi-frequency analyses with different frequency bandwidths are shown in Figure 77. We see now a difference compared to the profile to the South (profile SS), in that the top layer to around 200 Hz has a strike direction of N55W, whereas the layer from 200 Hz to around 30 Hz has a strike of N35W, and from 30 Hz to 0.1 Hz a strike of N05E, as we saw for profile SS. Beneath that is a layer with a strike of N60W, again as we saw for profile SS.

At 200 Hz the maximum depth of penetration is of order 800 m. So we have a 4-layered strike, with N55E from the surface to 800 m (200 Hz), N35E from 800 m to 2,000 m, N05E from 2,000 m to 10,000 m, and N60W below that for the rest of the crust.

The best-fit average strike from 10 kHz – 3 Hz is N56W, and from 3 Hz – 0.01 Hz is N62W, and for the whole 6-decade frequency band of 10 kHz – 0.01 Hz is N66W.

9.2.5. Profile MM2

Profile MM2 comprises 9 sites KMM20x (Figure 78):

KMM201, KMM202, KMM203, KMM204, KMM205, KMM206, KMM207, KMM208, KMM209



Figure 78: Sites along profile MM2.

Multi-site, multi-frequency analyses with different frequency bandwidths are shown in Figure 79. The highest frequencies >1 kHz, i.e. to a depth of order 300 m, show significant change, but from 1 kHz down to 3 Hz there is strike stability in the direction N10E. As with the other profiles, at low frequencies <3 Hz the strike rotates around clockwise to N65W.

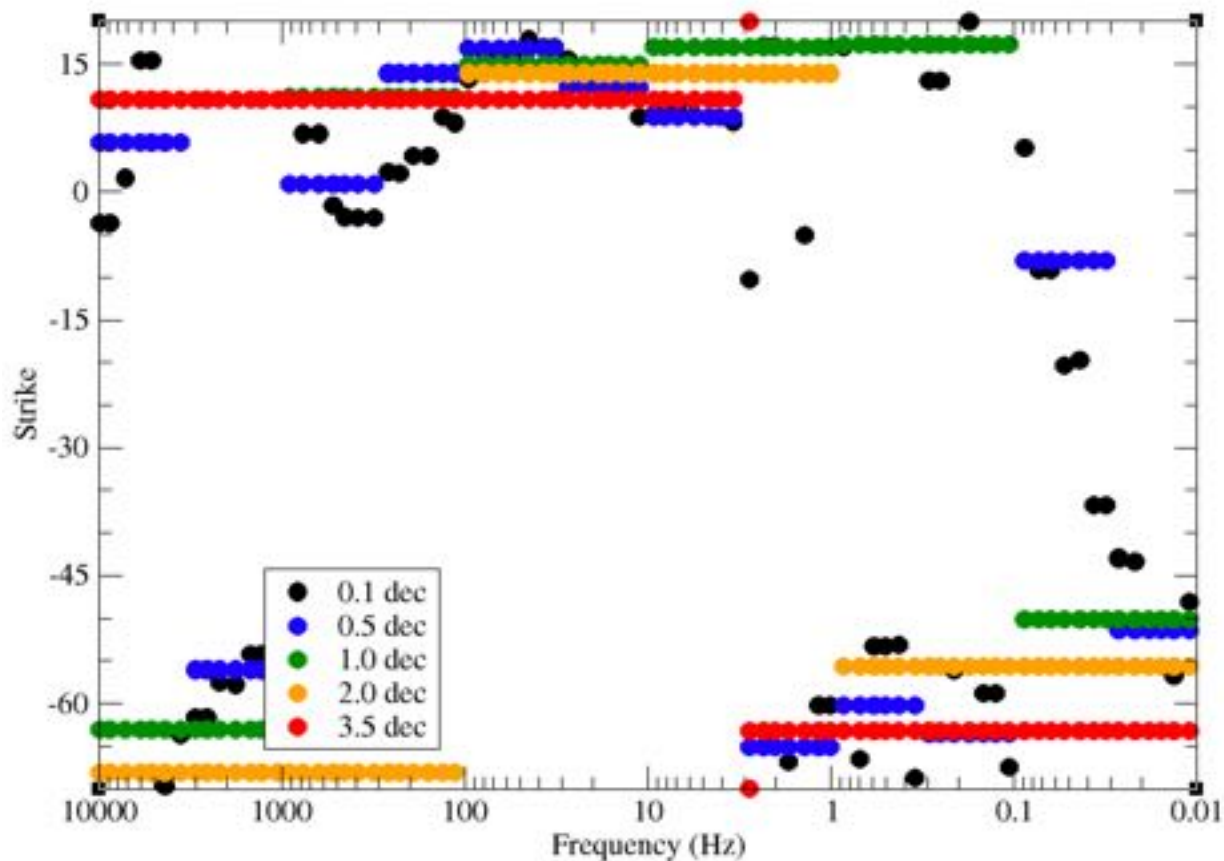


Figure 79: Strike directions for multi-site analyses with different bandwidths for sites on profile MM2.

9.2.6. Profile SP-EW

Profile SP-EW comprises 12 sites, 8 newly-acquired ones (KSPxxx) and 4 Duncan ones (86d00x) (Figure 80):

KSP003, KSP004, KSP005, KSP006, KSP007, 86d002, KSP008, KSP009, KSP104, 86d004, 86d005, 86d006

Recall that the Duncan sites only go to 384 Hz as their highest frequency.

Multi-site, multi-frequency analyses with different frequency bandwidths are shown in Figure 81. There is clearly for this profile greater agreement in strike direction between the uppermost parts of the crust and the bulk of the crust, with a direction of N45W for the upper 4 km and N35W for the rest of the crust.

Analysing all 6 decades of frequency from 10 kHz to 0.01 Hz together, the common strike direction is N44W (NW-SE).



Figure 80: Sites along profiles SP-EW (red) and SP-NS (blue).

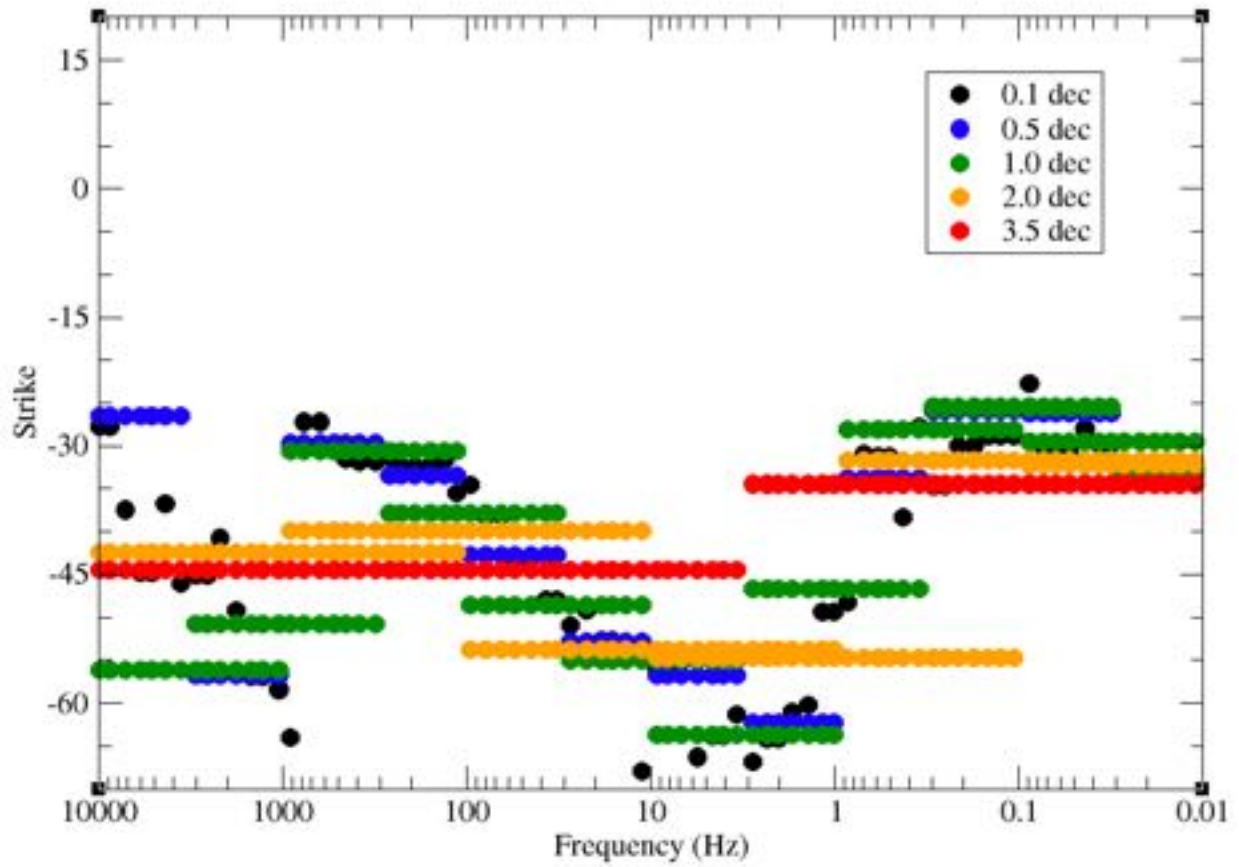


Figure 81: Strike directions for multi-site analyses with different bandwidths for sites on profile SP-EW.

9.2.7. Profile SP-NS

Profile SP-NS comprises 9 sites, 8 newly-acquired ones (KSPxxx), and one Duncan one (Figure 80):

KSP106, KSP105, KSP104, 86d002, KSP009, KSP008, KSP103, KSP102, KSP101

Multi-site, multi-frequency analyses with different frequency bandwidths are shown in Figure 82. High frequencies show a strike around N62W, whereas low frequencies show a strike of N36W.

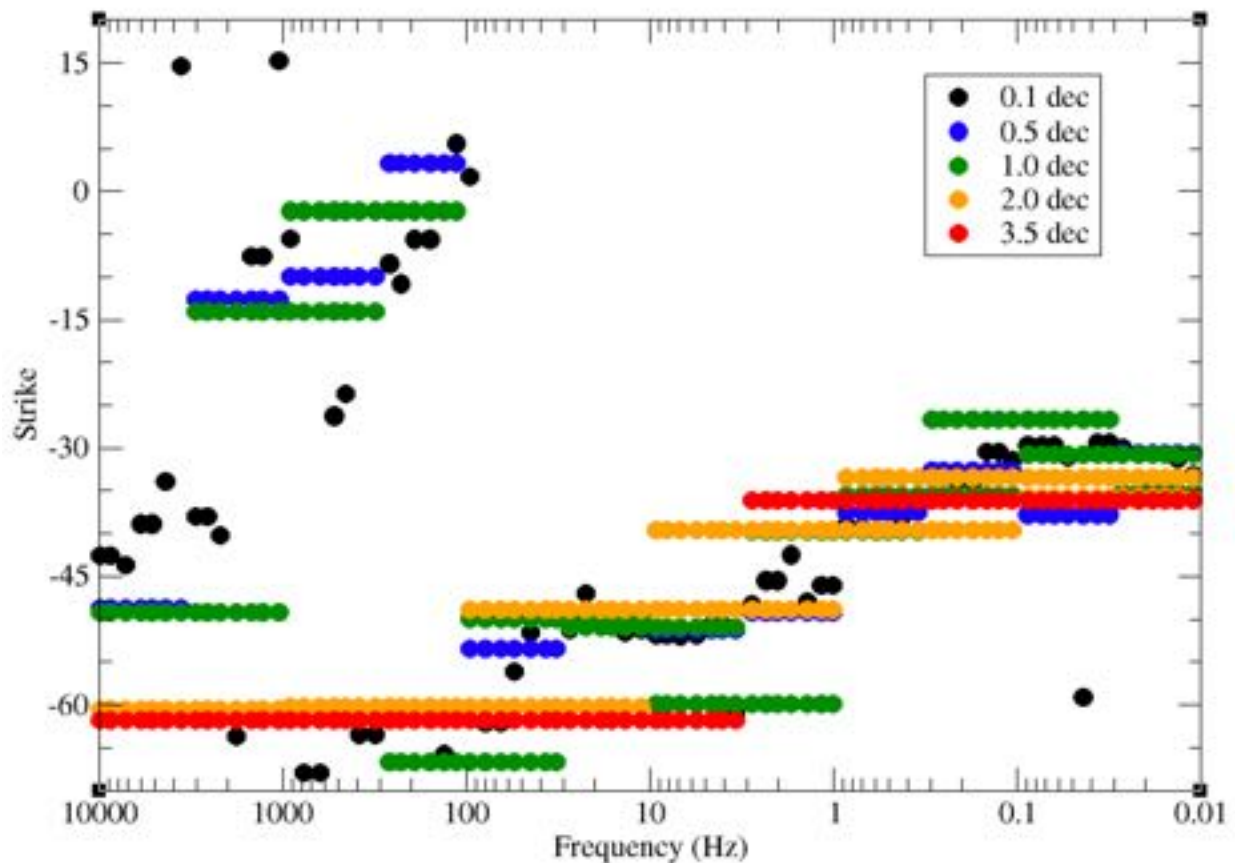


Figure 82: Strike directions for multi-site analyses with different bandwidths for sites on profile SP-NS.

9.2.8. Area SP: Profiles SP-NS & SP-EW taken together

Given that the two profiles SP-NW and SP-NS give very close strike directions at angles to them both, we can analyse all 17 sites simultaneously.

Multi-site, multi-frequency analyses with different frequency bandwidths are shown in Figure 83. High frequencies show a strike around N50W, whereas low frequencies show a strike of N39W.

9.2.8.1. *High frequencies: 10 kHz – 3 Hz*

The average misfit at high frequencies (10 kHz – 3 Hz) for a strike of N50W is 3.02, with first and third quartiles of 2.31 and 3.36. This means that the 2-D model of the subsurface is not statistically acceptable to most sites when error floors are set to 3.5% in RhoA and 1° in Pha. Again, to be statistically acceptable, 95% of the sites have to have an RMS < 2.00 (95% confidence limit). We can achieve this by doubling the error floor to 7% in RhoA and 2° in Pha.

9.2.8.2. *Low frequencies: 3 Hz – 0.01 Hz*

The average misfit at low frequencies (3 Hz – 0.01 Hz) for a strike of N39W is 1.62, with first and third quartiles of 2.44 and 3.83. This means that the 2-D model of the subsurface is not statistically acceptable to most sites when error floors are set to 3.5% in RhoA and 1° in Pha. To be statistically acceptable, 95% of the sites have to have an RMS < 2.00 (95% confidence limit). We can achieve this by doubling the error floor to 7% in RhoA and 2° in Pha

9.2.8.3. *All frequencies: 10 kHz – 0.01 Hz*

Taking all 6 decades of frequency from 10 kHz to 0.01 Hz, the best-fitting strike direction is N44E for all sites simultaneously. But this strike has a high average RMS misfit = 4.5, with three four sites disagreeing vehemently with RMS >7.0 (86d006 RMS = 8.13; 86d005 = 7.96, KSP104 = 8.30). Those three sites could potentially distort the strike direction acceptable to the rest of the sites because of their “leverage” effect on the least-squares model fitting.

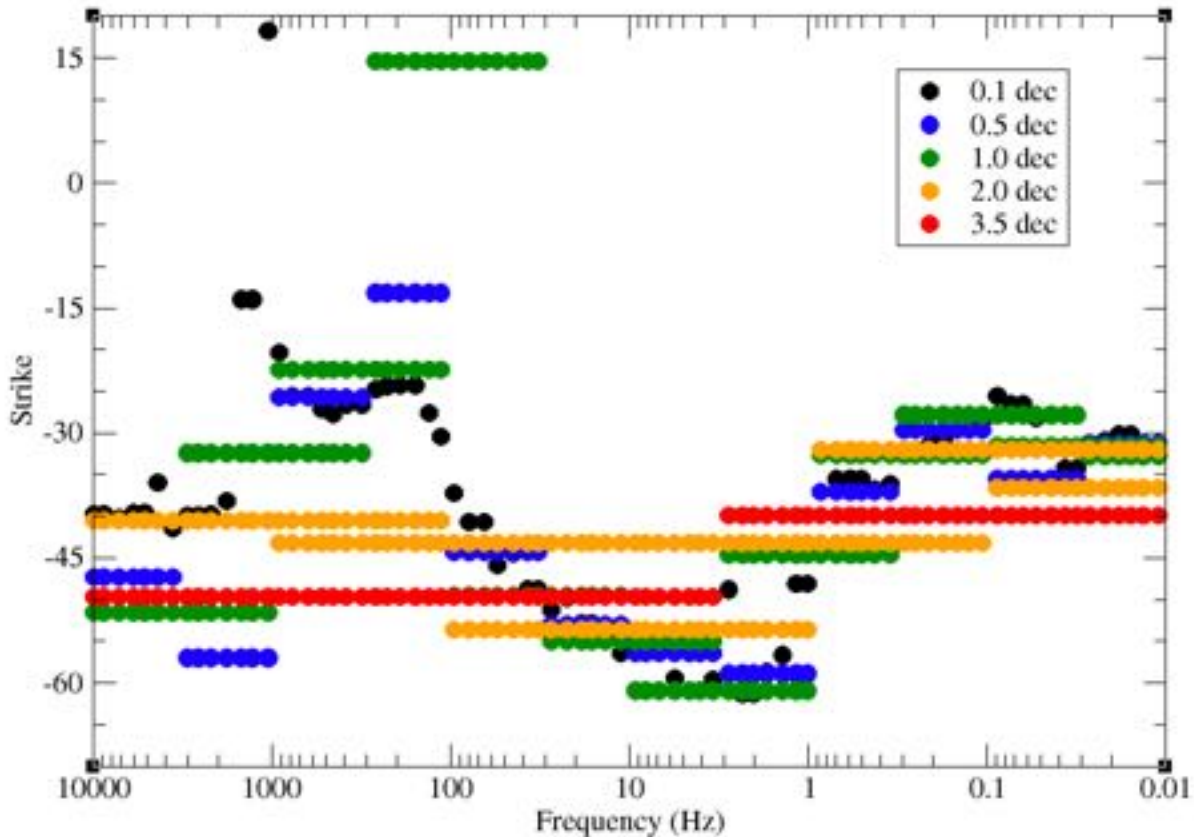


Figure 83: Strike directions for multi-site analyses with different bandwidths for sites in area SP.

Taking the reduced set of 14 sites, the best-fitting strikes is N45E with average RMS misfit = 3.73 with first and third quartiles of 2.50 and 4.31.

To make these data acceptable for 2-D inversion, 95% of them (12) should have an RMS <2.00 (95% confidence interval). If we increase the error floor from 3.5% in RhoA and 1° in Pha to 4x those values, i.e., 14% in RhoA and 4° in Pha, then the strike is N44W and the average misfit is RMS = 1.00, which is too good a fit as all sites have an RMS <1.5. Reducing the error floor to 3x original values, i.e., 10.5% in RhoA and 3° in Pha, results in a strike of N45W and an average RMS = 1.32, which is acceptable.

9.2.9. Area South

In a similar manner, we can take all 65 sites in the south, KSSxxx, KHAxxx and KMMxxx, and analyse them together for unified strike directions. (Given the high number of sites, it is not possible to conduct multi-frequency analysis with more than 28 frequencies (due to memory limitations), so the 3.5 decade wide bands are not computed.)

Multi-site, multi-frequency analyses with different frequency bandwidths are shown in Figure 85. High frequencies show a strike around N10E, whereas low frequencies show a strike of N54W, with the change in strike occurring at around 1 Hz (approx. 5 km).



Figure 84: Locations of sites in area "South".

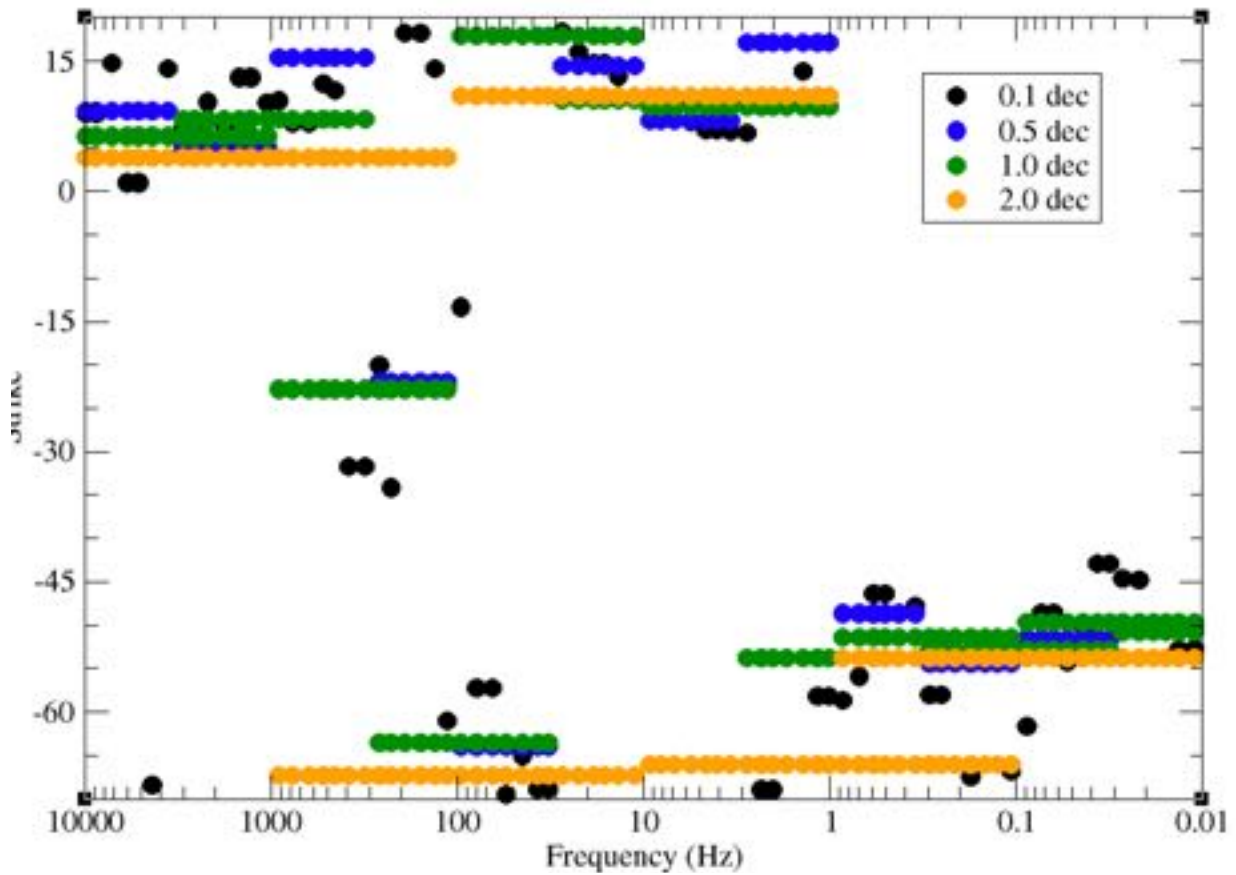


Figure 85: Strike directions for multi-site analyses with different bandwidths for sites in area "South".

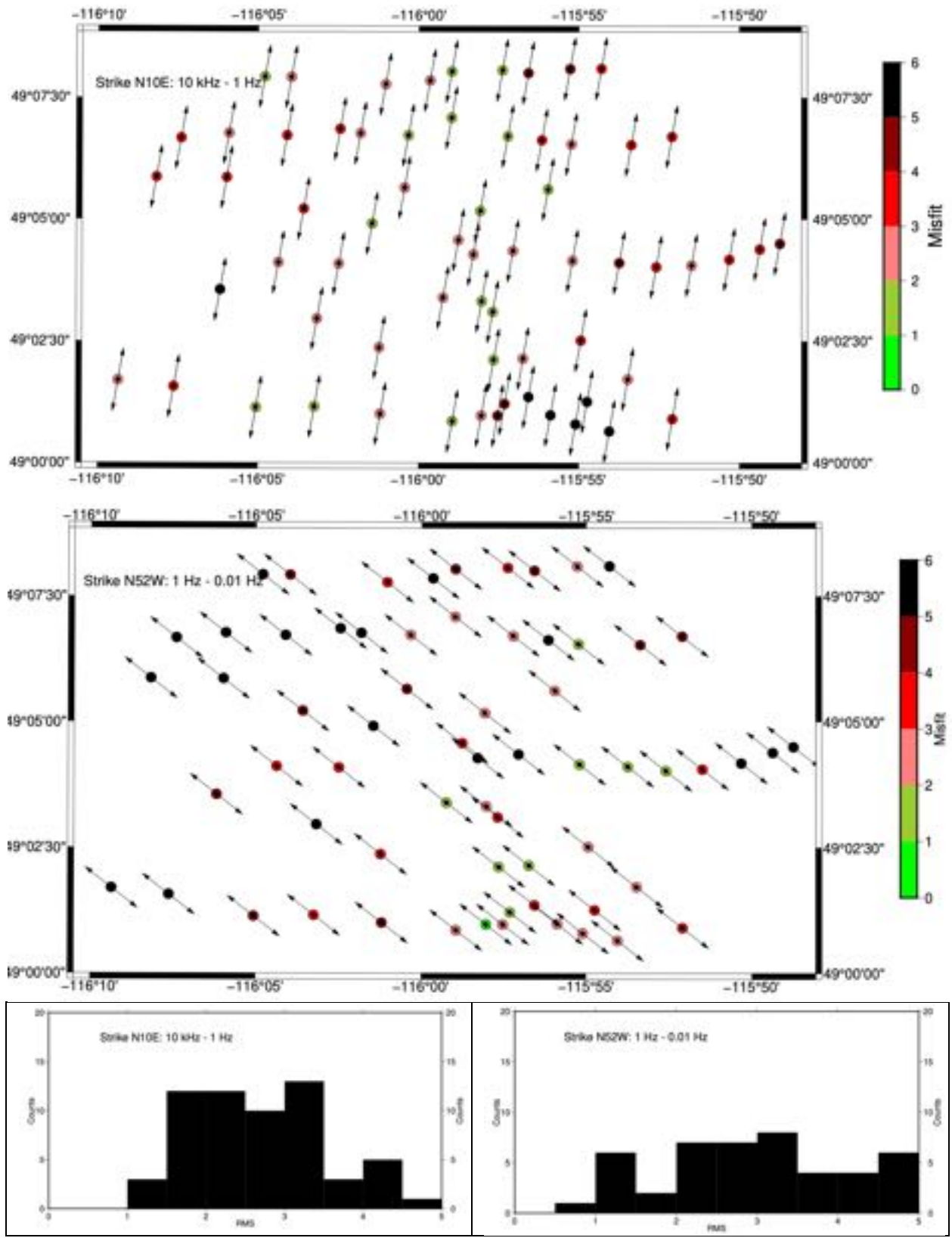


Figure 86: Fixed strike direction of N10E at high frequencies (top row) and N52W at low frequencies (middle row), and the misfit histograms (bottom row).

Note that the RMS misfits (Figure 86) show that most sites are >2.0 , which means that the distortion model does not fit the data within the errors of the data – an error floor of 1.75% in $|Z|$ was assumed, which is 3.5% in RhoA and 1° in Pha . These were judged to be the error floors for the newly-acquired data in the Quality Factor analysis. Below we adjust those floors to accommodate the data.

9.2.9.1. High frequency robust fitting

The misfits of the distortion model to the high frequency data (10 kHz – 1 Hz, Figure 86, bottom left) have a median of 2.6 with first and third quartiles of 2.03 and 3.37. The “problem” with high misfits is that with a least-squares approach those with high misfits are outliers than can distort the model, the so-called “leverage effect”.

To address this and to fit the data robustly, if we increase the error floor to 1.5 times the prior values, then approx. 3/4 of the misfits will be acceptable (<2.0) and the effect of high misfits will be less severe. Also, to guard against outlier leverage effects, we remove the four sites that fit most poorly (RMS >6.0), namely KSS115 (RMS=11.19), KSS111 (9.83), KSS109 (7.08) and KSS110 (6.01).

When we do this, we find a consistent angle for high frequencies >1 Hz of N12E (Figure 87). The RMS errors are now statistically acceptable, with 58 (=93%) falling within the 95% confidence limit (RMS < 2.00).

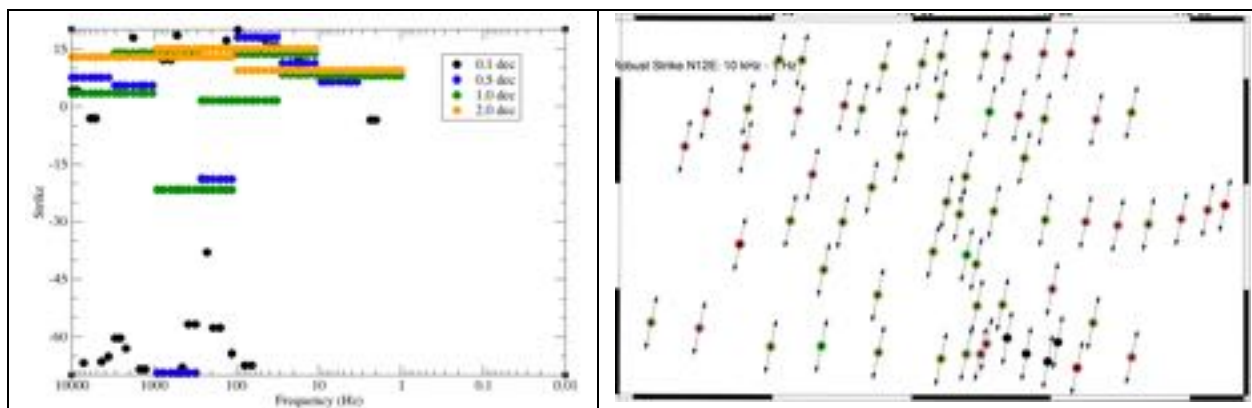


Figure 87: High frequency strike directions for multi-site analyses with different bandwidths for the reduced set of sites in area “South” with error floors set to 5.25% for RhoA and 1.5° for Pha .

9.2.9.2. Low frequency robust fitting

At low frequencies (1 Hz – 0.01 Hz, Figure 86, bottom right), misfits are higher, with a mode of 3.76 and first and third quartiles of 2.45 and 5.32. We need to increase the error floor by 2.5x to get most sites fitting acceptably, and to guard against outlier leverage, we remove seven sites with high misfit above 7.0, namely KMM102 (RMS=9.42), KHA006 (8.59), KMM103 (8.19), KSS101 (7.46), KSS102 (7.34), KMM007 (7.28), and KMM002 (7.03).

When we do this, we find a consistent angle for low frequencies <1 Hz of N55W (Figure 88). The RMS errors are now statistically acceptable, with 45 (=89%) falling within the 95% confidence limit (RMS < 2.00).

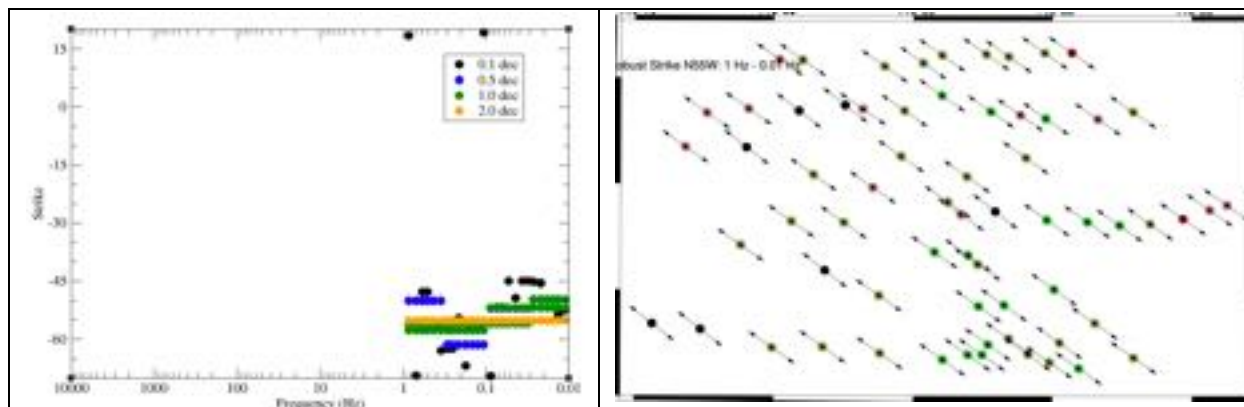


Figure 88: Low frequency strike directions for multi-site analyses with different bandwidths for the reduced set of sites in area “South” with error floors set to 8.75 % for RhoA and 2.5° for Pha.

9.2.10. Profile and Area Strike directions: Conclusions

A summary of the strike directions found for each profile and for the two areas is given in Table 6.

Table 6: Summary of strike directions along profiles and for areas.

Profile	High frequency 10 kHz – 3 Hz	Low frequency 3 Hz – 0.01 Hz	Comments
SS	N05E	N55W	
MM0	N56W	N62W	High frequency strike not consistent with neighbouring profiles SS, MM1 and MM2 nor with Area “South”.
MM1	N10E	N35W	Low frequency strike not consistent with neighbouring profiles SS, MM0 and MM2, nor with Area “South”.
MM2	N10E	N65W	
Area South	N12E	N55W	Combines all 65 newly-acquired sites KSSxxx, KHAXxx and KMMxxx. Cross-over at 1 Hz. Strikes are from reduced sets with larger error floors. Error floors for the newly-acquired data should be set to 5.25% for RhoA and 1.5° for Pha for the high frequency data (10 kHz – 3 Hz), and to 8.75 % for RhoA and 2.5° for Pha for the low frequency data (3 Hz – 0.001 Hz) for 2-D inversion
SP-EW	N45W	N35W	
SP-NS	N62W	N36W	
Area SP	N50W	N39W	Combines sites on SP-EW and SP-NS. Error floors of 7% in RhoA and 2° in Pha required at both HF and LF.
	N45E		Can use N45E for all freqs. Need to set error floors to 10.5% in RhoA and 3° in Pha.

MO	N32W	N43W	Can use N39W for all freqs. Error floors set to 3.5% in RhoA and 1° in Pha.
	N39W		

9.3. Strike: Conclusions

1. Southern profiles – SS, MM0, MM1 & MM2:

- 1.1. The southern profiles are all consistent with a two-layered crust, with a top layer striking N12E down to of order 5 km, and the rest of the crust striking N55W.
- 1.2. Error floors for the newly-acquired data should be set to 5.25% for RhoA and 1.5° for Pha for the high frequency data (10 kHz – 3 Hz), and to 8.75 % for RhoA and 2.5° for Pha for the low frequency data (3 Hz – 0.001 Hz) for 2-D inversion.

2. Central profiles – SP-EW & SP-NS:

- 2.1. For the central SP cross, the strike is consistent for both SP-EW and SP-NS, with again a two-layer crust with the uppermost crust striking N50W and the rest of the crust striking N39W. Error floors need to be set to 7% in RhoA and 2° in Pha
- 2.2. A single strike of N45E is acceptable when the error floors are increased to 10.5% in RhoA and 3° in Pha.

3. Northern profile – MO:

- 3.1. Again a two-layered Earth is found in strike, but with directions very close to each other, N32W for the upper 4 km and N43W for the rest of the crust.
- 3.2. A single strike direction of N39W is acceptable for all data, with error floors set to 3.5% in RhoA and 1° in Pha.

9.4. Correction for local site anisotropy

The final distortion correction that can be applied is for local site anisotropy, “*a*” in Groom-Bailey parlance, whereby the high frequency asymptotes of the two apparent resistivity curves are moved to their geometric mean values at each site. This is performed on the “*dcmp*” files output by the proprietary *strike* code using another proprietary code *dcmp2j*.

An example is for a site named P3-24 from another client’s survey. The original data (left, Figure 89) show RhoXY and RhoYX curves that are parallel but separated at high frequencies. Application of the site anisotropy correction brings them together (right, Figure 89).

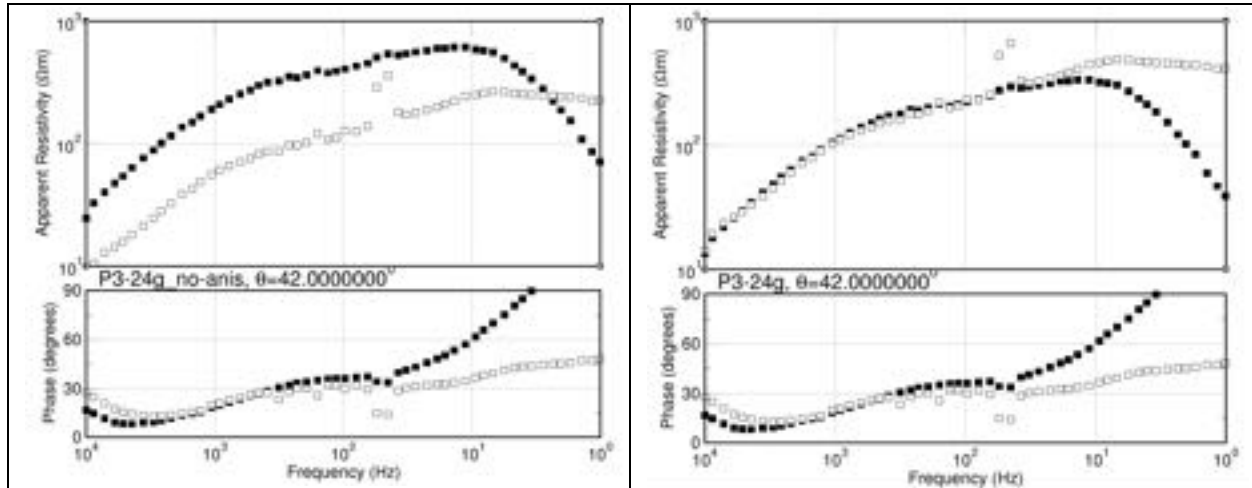


Figure 89: Example of application of anisotropy correction for site P3-24. The decomposed data (left) show Rho_{XY} and Rho_{YX} curves that are parallel but separated at high frequencies. Application of the site anisotropy correction brings them together (right).

10. Rho^+ consistency check

Formally in 1-D (Weidelt, 1972) and for the TM mode in 2-D (Weidelt & Kaikkonen, 1994) the MT responses at a site must be internally consistent such that the apparent resistivity Rho_A curve and the phase Pha curve are the Hilbert Transform of each other. There are also a number of other constraints on the nature of the impedances when expressed as impulse response functions in the time domain, but these are rarely exploited (Jones, 1980).

For extreme numerical models this is not upheld in the TE mode in 2D (Parker, 2010), but experience shows that there are few 2-D TE data for which this Hilbert Transformation relationship is not valid. It also has some merit in 3-D for testing internal compatibility the off-diagonal terms (Z_{xy} and Z_{yx}), but the diagonal terms (Z_{xx} and Z_{yy}) cannot be tested in the same manner as they are routinely “out-of-quadrant”.

Parker and Booker (1996) present an algorithm, called Rho^+ , which tests this compatibility between the Rho_A and Pha curves. This is an extension of a previous algorithm, called D^+ , of Parker (1980) that yields the best-fitting model possible to a 1-D MT response but operated on the real and imaginary parts of the impedances ⁽⁶⁾.

⁶ Note: All physically realizable systems do not respond before input is received. This means that the impulse response function describing the system must be zero for lags less than zero. This leads to a Hilbert Transformation relationship between the real and imaginary parts of the frequency domain response function. This was used by Jones [1980]. For some special systems, called “minimum phase” systems, then the amplitude and phase also form a Hilbert Transform pair.

I have adapted the Rho^+ algorithm and made it robust to outliers, that would otherwise perturb the results, using a Least Trimmed Squares approach (Rousseeuw & Leroy, 1987). This iterative procedure identifies those points that are inconsistent, to within statistical error, of the Hilbert Transform relationship between the RhoA and Pha curves. The outliers are replaced by their predictions, and errors are assigned to signify the magnitude of the shift involved.

For the example of site P3-24, the data after distortion decomposition and anisotropy correction are shown in Figure 90 (left plot), and clearly even after distortion decomposition there are problems with scatter in the especially the YX component. The Robust Rho^+ algorithm smoothed through the obvious scatter in the data, as shown in the right plot.

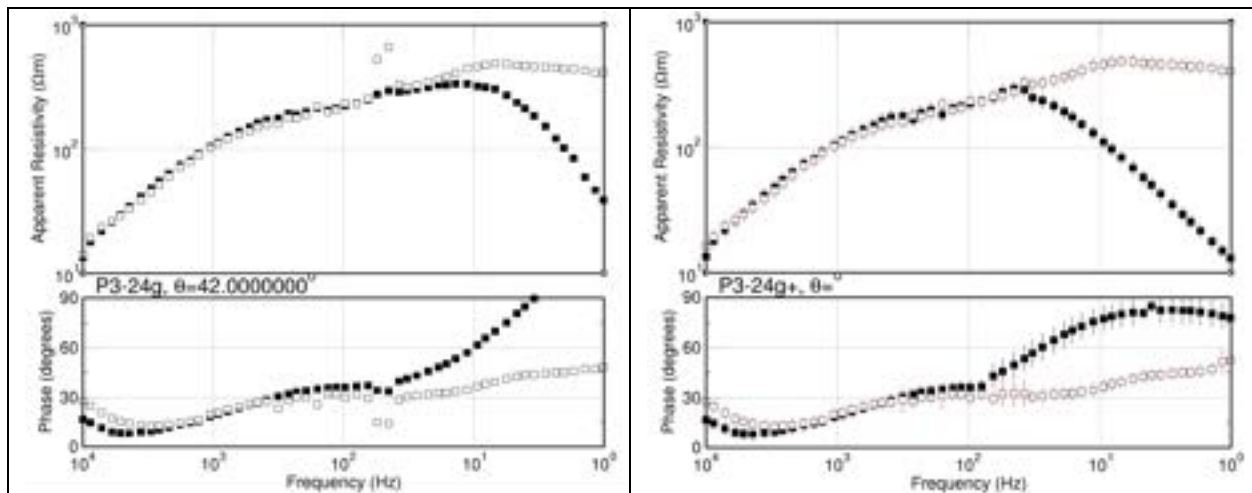


Figure 90: Site P3-24: Left plot is the distortion decomposed and anisotropy-corrected data. Right plot: Robust Rho^+ corrected data. Filled circles are XY (=TE) data, open circles are YX (=TM) data.

Some of the sites in this survey exhibit the same behaviour of Phase Roll Out of Quadrant (PROQ).

This is an important pre-processing step prior to inversion, as otherwise all least-squares based inversion codes will try to reduce the misfit to the largest outliers, if they are not culled before initiation of inversion. It is important to ensure that RhoA and Pha are consistent, and that outliers are dealt with prior to inversion, or a lot of human and computer time will be wasted.

Note: It should be noted that no-one else, neither in academia nor industry, offers such a robust Rho^+ algorithm to apply to the data. In Geotools there is the standard Rho^+ algorithm, but I have developed this robust variant that is proprietary to ManoTick GeoSolutions (MTGS).

Decomposition and Rho^+ does not necessarily result in 2-D responses that should be inverted for structure. In some cases, one of the phases rolls out-of-quadrant (PROQ – phase roll out of quadrant) and the apparent resistivity curves rise or drop at >45 degrees. Such behaviour is impossible in the TM mode in 2-D, and is only seen in the TE mode for extremely paranoid and

sharp structures, such as the corner of an ocean basin (Ichihara & Mogi, 2009), and even then the departure from the correct phase quadrant for the TE phase is less than 10 degrees.

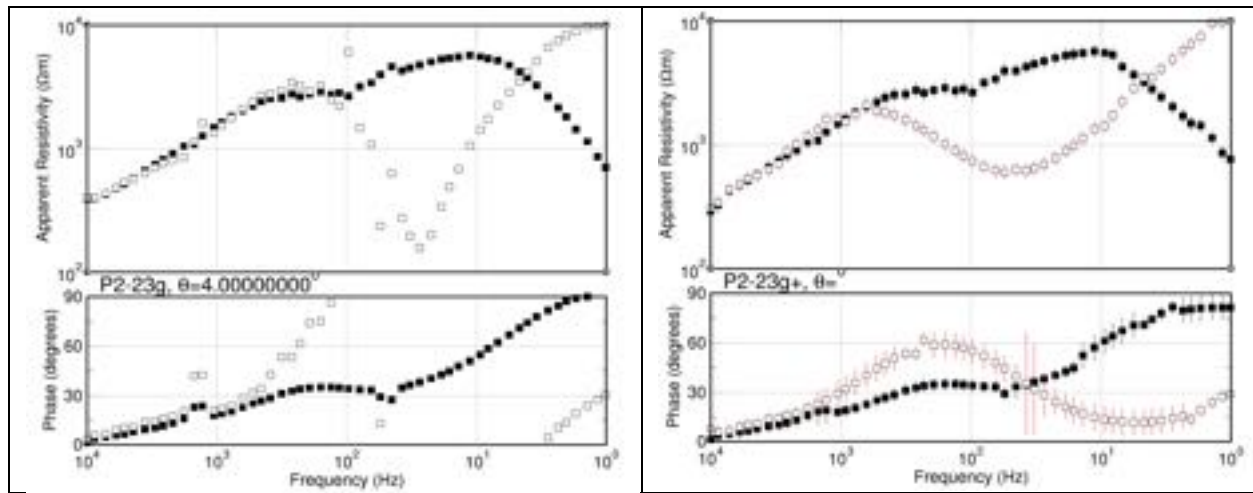


Figure 91: Site P2-23: Left plot is the distortion decomposed and anisotropy-corrected data. Right plot: Robust Rho+ corrected data. Filled circles are XY (=TE) data, open circles are YX (=TM) data.

An example is shown for site P2-23 of another client, where the original data and the decomposed data both exhibit phases rolling out-of-quadrant at frequencies <100 Hz (Figure 91, left). Applying robust Rho⁺ forces the PhaXY to stay within quadrant (Figure 91, right), but one cannot have any confidence in the XY responses below 300 Hz as the shapes of the curves have been dramatically modified. In this case the suspect data are culled prior to inversion.

To guard against this issue, visual inspection of the comparisons of before-and-after application of robust Rho⁺ must be performed for all sites prior to inversion, and suspect/inconsistent data must be culled.

11. Conclusions

Deep analyses of the data show that they are of generally high quality, except for some bands (especially the AMT and MT deadbands) due to low signal during those times of acquisition.

Quantec data along the southernmost profile give responses that are not consistent with the newly-acquired ones, especially for the diagonal terms (XX and YY), so are not used.

For the depths of interest to the client, the high frequencies from 10 kHz – 3 Hz probe down to 4 km. For crustal probing, frequencies from 3 Hz down to 0.01 Hz or even 0.001 Hz need to be taken.

Qualitative mapping of the responses does show some areas of potential interest.

Careful and exhaustive geoelectrical strike analyses shows that the southern area sites are all consistent expressing a two-layer situation, with a top layer striking approx. N-S, and the lower

layer striking approx. NW-SE. This lower strike is consistent with prior work (Gupta & Jones, 1995).

Strikes directions and appropriate error floors to use for 2-D inversion are summarized in Table 6.

Subsequently, the 2-D regional response estimates were checked for internal consistency.

12. Recommendations

- 1) Perform 2-D inversions along the profiles using the distortion-corrected data.
- 2) Perform 3-D inversion of the southern sites.

13. Deliverables

The deliverables for this part of the contract comprise:

1. Deliverables/Report: This report.
2. Deliverables/*profile*/Appendix A: Plots of all four MT components and both Tipper components for all sites.
3. Deliverables/*profile*/Appendices B: Plots of all distortion decomposed and Rho+ distortion decomposed MT components and for all sites along each of the profiles
4. Deliverables/*profile*/Appendices C: Plots of all Rho+ distortion decomposed MT components compared with the original data and for all sites along each of the profiles
5. Deliverables/*profile*/Appendices D: Plots of all Rho+ distortion decomposed MT components compared with the distortion decomposed data and for all sites along each of the profiles
6. Deliverables/*profile*/Appendices E: Plots of all distortion decomposed MT components compared with the original data and for all sites along each of the profiles
7. Deliverables/*profile*/Appendices F: Distortion-corrected (“g.edi”) and Rho+ distortion-corrected (“g+.edi”) estimates in EDI format.


14. Declaration and Signature

I, Alan G. Jones, do hereby certify that:

- I am a Senior Geophysicist with residence in Ottawa, Ontario and I am presently working in this capacity as President and Managing Director of Compete MT Solutions Ltd. of Ottawa (Ontario), President and Managing Director of ManoTick GeoSolutions Ltd. of Ottawa (Ontario), and Vice-President of Moombarriga Canada Ltd. of Ottawa (Ontario);

- I obtained a B.Sc. in Hons. Physics at the Univ. Nottingham (England) in 1972, an M.Sc. in Applied Geophysics at the Univ. Birmingham (England) in 1973, and a Ph.D. in Geophysics at the Univ. Edinburgh (Scotland) in 1977;
- I undertook PostDoctoral Fellowships in Germany at the Univ. Munster from 1977 to mid-1981, in Sweden at the Swedish Geological Survey in 1981, and in Canada at the Univ. Toronto in 1982-1983;
- I subsequently joined the Geological Survey of Canada (Ottawa) in 1984 to 2003, rising from Research Scientist RES-2 level to Senior Research Scientist RES-5 level (the top scientist level in the Canadian Government).
- I then became the Senior Professor and Head of Geophysics at the Dublin Institute for Advanced Sciences (Ireland) from 2004 to January, 2015.
- I am a registered geophysicist and a member in good standing with a license to practice in the Province of Ontario (PGO member #2790);
- I have been awarded academic distinction in Canada (J. Tuzo Wilson medal, Canadian Geophysical Union, 2006), in the USA (Fellow, American Geophysical Union, 2019), in Ireland (Member, Royal Irish Academy, 2010), in Europe (Member, Academia Europaea, 2010), in China (International Member, Geo-Electromagnetism Committee, Chinese Geophysical Society, 2009), and in South Africa (Life Affiliate member, Geological Society of South Africa, 2016).
- I am also a member of the Society of Exploration Geophysicists (SEG), the Canadian Exploration Geophysical Society (KEGS), and the South African Geophysical Association (SAGA);
- I have derived the results presented in this report without consultation with any other person or persons;
- I have no interest, nor do I expect to receive any interest in the properties or securities of Kootenay Resources Inc., any of its subsidiaries or controlling interests, or any of its joint-venture partners.

Signed:



Alan G. Jones, Ph.D., P.Geo.
President, Complete MT Solutions Inc.

15. References

- Caldwell, T. G., Bibby, H. M., & Brown, C. (2004). The magnetotelluric phase tensor. *Geophysical Journal International*, 158(2), 457-469. Article.
- Chave, A. D., & Jones, A. G. (1997). Electric and magnetic field galvanic distortion decomposition of BC87 data. *Journal of Geomagnetism and Geoelectricity*, 49(6), 767-789.
- Chave, A. D., & Jones, A. G. (Eds.). (2012). *The Magnetotelluric Method - Theory and Practice*: Cambridge University Press.
- Cook, F. A., & Jones, A. G. (1995). Seismic reflections and electrical conductivity: A case of Holmes' curious dog? *Geology*, 23(2), 141-144. Article.
<http://homepages.dias.ie/~ajones/papers/58.pdf>
- Evans, S., Jones, A. G., Spratt, J., & Katsube, J. (2005). Central Baffin electromagnetic experiment (CBEX): Mapping the North American Central Plains (NACP) conductivity anomaly in the Canadian arctic. *Physics of the Earth and Planetary Interiors*, 150(1-3), 107-122.
- Ferguson, I. J. (2012). Instrumentation and field procedures. In A. D. Chave & A. G. Jones (Eds.), *The Magnetotelluric Method: Theory and Practice* (pp. 421-479). Cambridge, UK: Cambridge University Press.
- Garcia, X., & Jones, A. G. (2002). Atmospheric sources for audio-magnetotelluric (AMT) sounding. *Geophysics*, 67(2), 448-458.
- Groom, R. W., & Bailey, R. C. (1989). Decomposition of magnetotelluric impedance tensors in the presence of local three dimensional galvanic distortion. *Journal of Geophysical Research*, 94, 1913-1925.
- Groom, R. W., & Bailey, R. C. (1991). Analytical investigations of the effects of near surface three dimensional galvanic scatterers on MT tensor decomposition. *Geophysics*, 56(4), 496-518. Article.
- Gupta, J. C., & Jones, A. G. (1995). Electrical conductivity structure of the Purcell Anticlinorium in southeast British Columbia and northwest Montana. *Canadian Journal of Earth Sciences*, 32, 1564-1583.
- Haines, G. V., & Jones, A. G. (1988). Logarithmic Fourier Transformation. *Geophysical Journal*, 92, 171-178. <http://homepages.dias.ie/~ajones/papers/28.pdf>
- Hutton, V. R. S., & Jones, A. G. (1980). Magnetovariational and magnetotelluric investigations in S. Scotland. In U. Schmucker (Ed.), *Electromagnetic Induction in the Earth and Moon* (pp. 141-150): Centr. Acad. Publ. Japan, Tokio and D. Reidel Publ. Co., Dordrecht.
- Ichihara, H., & Mogi, T. (2009). A realistic 3-D resistivity model explaining anomalous large magnetotelluric phases: the L-shaped conductor model. *Geophysical Journal International*, 179(1), 14-17.
- Jones, A. G. (1980). Geomagnetic induction studies in Scandinavia - I. Determination of the inductive response function from the magnetometer data. *Journal of Geophysics (Zeitschrift fuer Geophysik)*, 48, 181-194.
- Jones, A. G. (1983). On the equivalence of the Niblett and Bostick transformations in the magnetotelluric method. *Journal of Geophysics-Zeitschrift Fur Geophysik*, 53(1), 72-73. Letter.

- Jones, A. G. (1986). Parkinson's pointers' potential perfidy! *Geophysical Journal of the Royal Astronomical Society*, 87, 1215-1224. <http://homepages.dias.ie/~ajones/papers/25.pdf>
- Jones, A. G. (1993). The COPROD2 dataset - tectonic setting, recorded MT data, and comparison of models. *Journal of Geomagnetism and Geoelectricity*, 45(9), 933-955.
- Jones, A. G. (2012). Distortion of magnetotelluric data: its identification and removal. In A. D. Chave & A. G. Jones (Eds.), *The Magnetotelluric Method: Theory and Practice*. Cambridge (UK): Cambridge University Press.
- Jones, A. G., & Groom, R. W. (1993). Strike angle determination from the magnetotelluric impedance tensor in the presence of noise and local distortion - rotate at your peril. *Geophysical Journal International*, 113(2), 524-534. Note.
- Jones, A. G., & Spratt, J. (2002). A simple method for deriving the uniform field MT responses in auroral zones. *Earth Planets and Space*, 54(5), 443-450.
- Mardia, K. V. (1972). *Statistics of Directional Data*: Academic Press, New York.
- Marquis, G., Jones, A. G., & Hyndman, R. D. (1995). Coincident conductive and reflective middle and lower crust in Southern British Columbia. *Geophysical Journal International*, 120(1), 111-131. Article.
- McNeice, G. W., & Jones, A. G. (2001). Multisite, multifrequency tensor decomposition of magnetotelluric data. *Geophysics*, 66(1), 158-173.
- Parker, R. L. (1980). The inverse problem of electromagnetic induction: Existence and construction of solutions based on incomplete data. *Journal of Geophysics*, 85(B8), 4421-4428.
- Parker, R. L. (2010). Can a 2-D MT frequency response always be interpreted as a 1-D response? *Geophysical Journal International*, 181(1), 269-274. <Go to ISI>://WOS:000275884300015
- Parker, R. L., & Booker, J. R. (1996). Optimal one-dimensional inversion and bounding of magnetotelluric apparent resistivity and phase measurements. *Physics of the Earth and Planetary Interiors*, 98(3-4), 269-282. <Go to ISI>://WOS:A1996WB25300010
- Parkinson, W. D. (1959). Directions of rapid geomagnetic fluctuations. *Geophysical Journal of the Royal Astronomical Society*, 2(1), 1-14. <Go to ISI>://WOS:A1959WW35400001
- Parkinson, W. D. (1962). The influence of continents and oceans on geomagnetic variations. *Geophysical Journal of the Royal Astronomical Society*, 6(4), 441-449. <Go to ISI>://WOS:A1962WU73100003
- Petiau, G., & Dupis, A. (1980). Noise, temperature-coefficient, and long-time stability of electrodes for telluric observations. *Geophysical Prospecting*, 28(5), 792-804. <Go to ISI>://WOS:A1980KM25200009
- Rousseeuw, P. J., & Leroy, A. M. (1987). *Robust Regression and Outlier Detection*: Wiley.
- Shalivahan, Maurya, V. P., Bhattacharya, B. B., & Singh, R. K. (2017). Tipper Magnitude Revisited. In *15th International Congress of the Brazilian Geophysical Society & EXPOGEEF, Rio de Janeiro, Brazil, 31 July-3 August 2017* (pp. 189-193).
- Weidelt, P. (1972). The inverse problem of geomagnetic induction. *Geophysical Journal of the Royal Astronomical Society*, 35(1-3), 379-379. Abstract of Published Item.
- Weidelt, P., & Kaikkonen, P. (1994). Local 1-D interpretation of magnetotelluric B-polarization impedances. *Geophysical Journal International*, 117(3), 733-748. Article.

16. Appendix A: MT acquisition equipment

16.1. Recorders

MT recorders are often specially designed for MT, such as those used by Phoenix, Metronix, and Lviv. Some contractors use generic recorders, such as RefTeks (Quantec) or gDAS (Southernrock Geophysics).

What is important in a recorder is a high dynamic range, true 24-bit A/D at a minimum, and a high input impedance.

16.2. Magnetic sensors

In induction coil design there is a trade-off to be made between having greater sensitivity, which comes from having more windings around the core (i.e., a longer, heavier sensor) and minimising eddy current noise, which comes from having fewer windings and a smaller core. Induction coil design is discussed in detail in Ferguson's Chapter 9 (Ferguson, 2012) in Chave and Jones (2012).

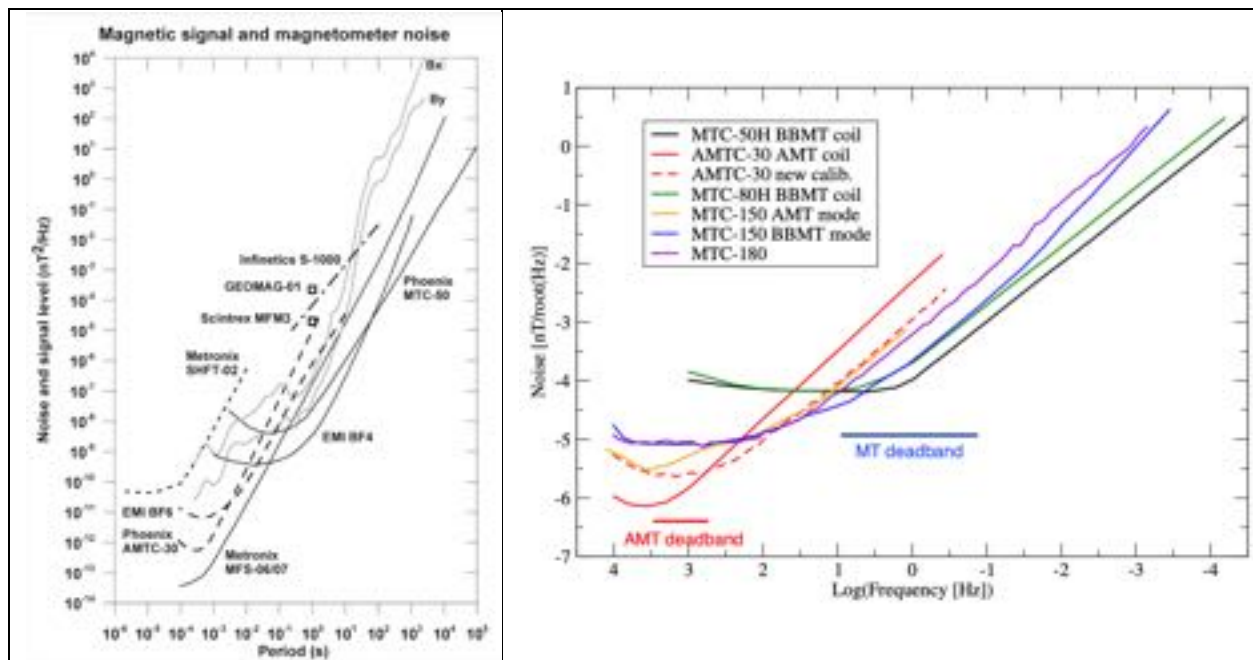


Figure 92: Left: Noise levels of common MT coils, from Ferguson (2012). Right: Noise levels of Phoenix's family of coils.

A comparison of common MT coils is shown in Figure 92. Left shows a number of manufacturers and was compiled by Ferguson (2012), and right compares the Phoenix family of coils and was compiled by me.

16.3. Electrodes

16.3.1. General

Electric field sensors, called “electrodes”, in the early days of MT were initially solid metal, such as steel, Pb or Cu in rods, tubes or plates. However, it was realized in the late-1970s that polarization charges on metal surfaces caused significant noise on the electric fields, particularly in the MT deadband of 8 Hz to 0.1 Hz where signal is very low and noise is high (due primarily to microseismic activity caused by e.g. wind coupling to the ground through tree roots). Hence non-polarizing electrodes came into common use for MT from the late-1970s onwards.

Non-polarizing electrodes comprise a metal and its salt, and for land acquisition are usually Pb-PbCl₂ or Cu-CuSO₄. Pb-PbCl₂ are intrinsically lower noise, given the lower potential between Pb and its salt. For marine use, the more expensive Ag-AgCl electrodes are used as Ag-AgCl has the lowest potential between a metal and its salt of all three, so give the lowest noise specs.

Parallel comparison tests by Petiau and Dupis (1980) showed the superiority of non-polarizing electrodes, particularly at lower frequencies Figure 93.

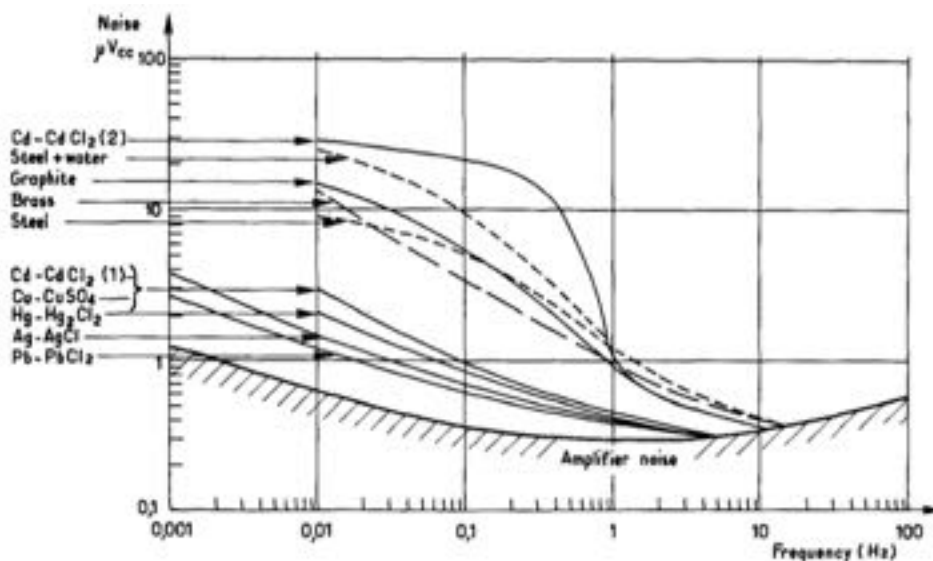


Figure 93: Noise of different electrodes 30 min – 1 hour after setting up. Taken from Petiau and Dupis (1980).

For the late-1970s recording system used by Petiau and Dupis (1980), all electrodes performed as well as each other at frequencies above 10 Hz. Modern systems are far more sensitive, so the difference between polarizing and non-polarizing electrodes persists to higher frequencies, to at least 100 Hz.

Care has to be taken of electrodes, however they are constructed. Metal ones need to be cleaned daily to ensure there are no oxidation effects on them, and non-polarizing ones have to

be checked for DC levels to ensure that there is no precipitation of the salt on the metal surface causing internal resistances. Any of these effects cause noise on the electric field.

16.3.2. *Electrodes and electrode array*

Acquisition was performed using stainless steel rods. As shown above, these are noisier than non-polarizing electrodes, by more than half an order of magnitude, even to high frequencies.

Solid metal electrodes have a high contact resistance. For a rod of length L , diameter a , in a half-space of resistivity ρ , the Faradaic contact resistance R is given by

$$R = \frac{\rho}{2\pi L} \left[\ln\left(\frac{2L}{a}\right) - 1 \right]$$

(Ferguson, 2012). Assume a 1 cm diameter rod pushed 50 cm into the ground with an intrinsic resistance of 2,000 Ωm , this yields a Faradaic resistance of 2.3 k Ω . That is assuming 100% contact along the whole surface of the rod and that there is no rusting or other effects that will cause resistance to be increased.

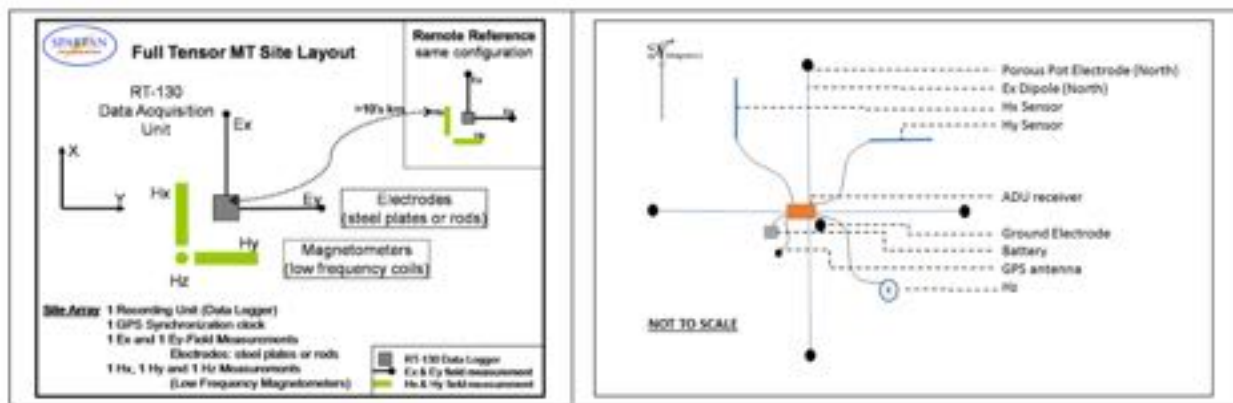


Figure 94: L-shaped (left, typically used by Quantec) and X-shaped (right, used by CMTS) electrode arrays.

Two electrode arrays are shown in Figure 94.

16.3.3. *Electric array measurements*

It is necessary when performing MT acquisition to make three measurements at the beginning and the end of acquisition of the electrode array. These are:

1) **DC voltages between various pairs of electrodes.**

- The point of measuring the DC voltages between various pairs of electrodes, N-S, N-G, S-G, etc., is to determine whether an electrode is holding charge. Charges on electrodes introduce noise into the electric channels.

- Solid metal electrodes intrinsically have this problem, as discussed above.
- Excellent, newly-made, non-polarizing electrodes should have very low DC, of order 5 mV. Over time, and especially if the electrodes are not properly cared-for, the salt paste begins to dry, and this causes precipitation of the salt onto the metal. This introduces noise in the electrode, and its effect is to make the electrode hold charge, ie it turns the electrode into a weak battery. The DC level will rise to large values above say 25 mV. Any electrode that shows high DC levels should be immediately taken out of service and reconditioned or discarded.

2) AC voltages between N-S and E-W electrodes.

The AC voltage is measured for the two pair of electric field channels in order to ensure that ambient AC noise, from nearby powerlines, will not swamp the input and cause clipping. This was more of a problem when recorders were only 16 bit in the 1980s. The 24 bit recorders used by both Quantec and Moombarriga will have had sufficient dynamic range for this not to be an issue. Also, as noted in Moobarriga's report, there is no cultural noise in the vicinity of the project area.

3) Contact resistance between N-S and E-W electrodes.

The issue with contact impedance is the circuit between the electrodes, the ground, and the receiver, such that if the contact impedance approaches the input impedance of the receiver, then there are *RL* inductive effects on the data due to attenuation (and phase advances) of the electric field amplitudes at high frequencies. The most egregious example in the literature is that from a recently-deglaciated site on Baffin Island acquired by Evans et al. (2005) with a measured contact resistance of 2 M Ω . No data at high frequencies >5 Hz (periods <0.2 s) are usable (Figure 95).

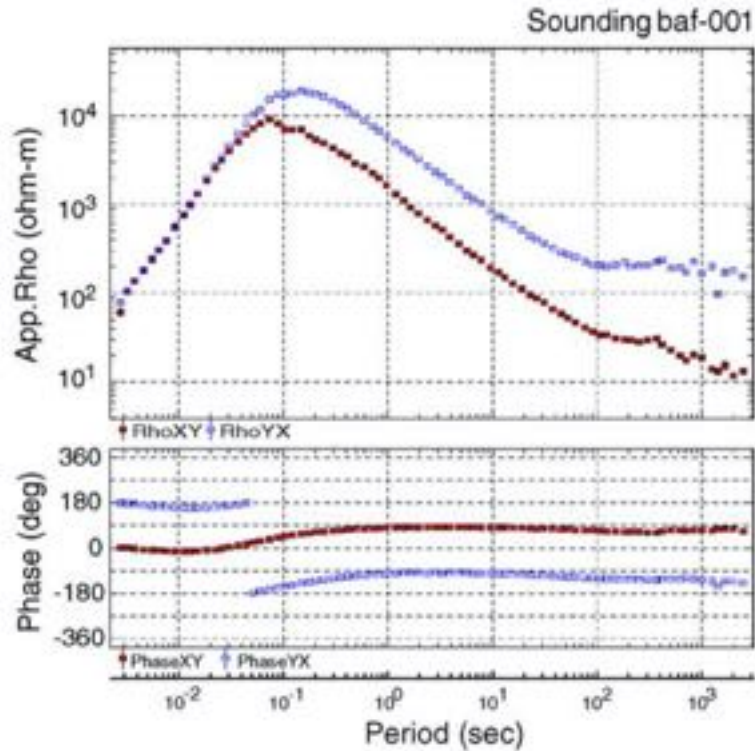


Figure 95: Site baf001 of Evans et al. (2005).

The information on these values should be read from the EDI files. Note that many contractors do not provide this information, or if they do it is not within the EDI file.

17. Appendix B: AMT deadband

The sensitivity of the available coils is important for assessing the likely quality of the time series, especially in the AMT deadband⁽⁷⁾. Tests by Garcia and Jones (2002) analysing data acquired with the Phoenix AMTC-30 sensors showed that typically signal was estimated to be one to two orders of magnitude less than sensor noise, at about 5×10^{-8} nT/sqrt(Hz) at 1 kHz (based on the electric field amplitudes), during the daytime. As soon as the Sun rises atmospheric electrical conductivity goes up by two to three orders of magnitude due to solar ionization of the atmosphere. Thus, energy from distant lightning storms travelling along sunlit paths are attenuated by 100 to 1,000 times more than nighttime paths. This phenomenon is shown in the Hx and Hy spectral amplitudes at 1 kHz over 24 hours of Figure 96. There is decent signal from sunset at 21:00 to sunrise at 06:30, but as soon as the Sun rises the signal level

⁷ The AMT deadband is the band of frequencies from around 5 kHz to around 800 Hz, and is caused by a natural low in the signal spectrum from the two different sources of lightning energy. High frequency cloud-to-ground energy is at frequencies from 5 kHz and above, and low frequency cloud-to-ionsphere energy is from around 800 Hz to the Schumann resonance (7.8 Hz).

drops instantly and decreases to below sensor noise levels, and the spectral amplitude hovers at the sensor noise level.

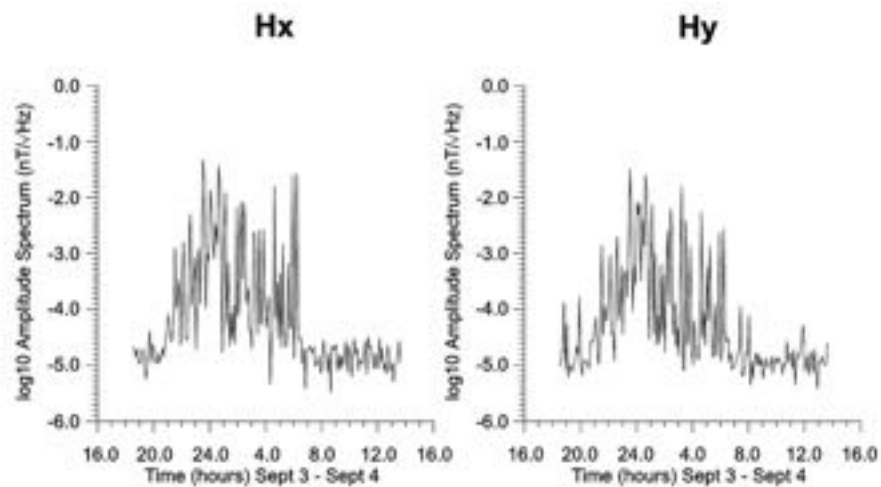


Figure 96: Power spectra amplitude calculated for a frequency of 1000 Hz for the two magnetic channels recorded between the afternoon of September 3 and the morning of September 4. (Reproduced from Fig. 6 of Garcia and Jones (2002).)

The important point here is that it is virtually impossible to obtain high quality data in the AMT deadband during sunlit acquisition with any sensors, even with the currently very best AMT coils available (Metronix MFS-06/07 coils, Figure 92), if one uses normal processing methods that derives estimates the continuum.

18. Appendix C: Quality Factors determination

18.1. MT Quality Factors

Currently, there is no accepted way in the MT community of quantitatively assessing the quality of MT response curves. Generally, curves can be rated on a 5-point qualitative scale from excellent (1) to good (2) to average (3) to poor (4) to unusable (5), based on visual inspection. However, the response estimates usually vary in their quality with period – data in the AMT deadband (5 kHz – 800 Hz) and the MT deadband (10 Hz – 0.1 Hz) are often far poorer than neighbouring data, especially if acquisition was in the daytime only. The lowest frequency/longest period data can also be poor due to insufficient recording times, non-uniform source fields, lack of source field energy (=low sunspot number), etc.

The quality of the RhoA and Pha curves is basically a function of the smoothness of the curves, i.e., point to point consistency, and the errors associated with the estimates. Smooth XX, XY, YX and YY curves that have consistent errors such that small scale scatter of the estimates lies within small errors are desirable. To undertake quantitative assessment of quality, and to

automate the process of poor data identification, I devised a “Quality Factor” of the XY and YX curves that is a combination of a measure of smoothness and a measure of error.

Smoothness Factor (SF): For this I use the Rho+ algorithm of Parker and Booker (1996). This algorithm tests the compatibility of the off-diagonal RhoA and Pha curves to each other. High quality response curves should have a chi-squared misfit of the best-fitting possible model (which is of conductance spikes) equivalent to a normalised RMS (nRMS) of one. Formally, this Rho+ test only applies for 1-D data (Weidelt, 1972) and the TM mode in 2-D data (Weidelt & Kaikkonen, 1994), and in practice to almost all TE mode data. Some extreme and pathological theoretical models in the TE-mode in 2-D fail this test as their phases go slightly outside the 0-90 degree phase bounds (Ichihara & Mogi, 2009; Parker, 2010), but only by a few degrees. In 3-D there is no general statement, but it often is applicable. There are two SFs, one for the XY component (SF_{xy}) and one for YX (SF_{yx}).

Error Factor (EF): The error factor is the average error divided by the assumed error floor. Typically, we assume a minimum error floor of order 1° in phase/3.5% in apparent resistivity for high quality data. When an error floor is set, the EF has a minimum value of 1.

Alternatively, if no error floor is set, then the EF is the average error without normalization. There are four EFs, for each off-diagonal element there is one for RhoA and one for Pha, and for each component these are arithmetically averaged, i.e., EF_{xy} = (EFRhoXY + EFPhaXY)/2, and similarly for EF_{yx}.

For each component, XY and YX, the Quality Factor is given by the geometric mean of the SF and EF, i.e., QF_{xy} = SQRT(SF_{xy} * EF_{xy}), and similarly for QF_{yx}.

The **Average Quality Factor** is given by **QF_{av} = SQRT(QF_{xy} * QF_{yx})**

Quality Factors will be of order 1 for high quality data, and QF increases with decreasing quality of data.

→ Note: The QFs are only for the XY and YX off-diagonal elements of the MT impedance tensor. I do not test the XX and YY diagonal elements, but they are just as important when one wants to undertake anything that involves the complete tensor (e.g., dimensionality analyses, anisotropic 1-D inversion, 2-D inversion with strike not perpendicular to the profile direction, 3-D inversion).

18.2. Tipper Quality Factors

Given the potential importance of tippers in MT, Quality Factor determinations for tippers would be highly useful to identify those sites with problems and those with good quality data without laboriously viewing all of the tipper plots.

As with MT responses, there is no accepted automated way of assessing the quality of the tipper responses, and so I have developed one. I have used the fact that the Real and Imaginary parts of the tipper responses, T_{zx} and T_{zy} , given by

$$H_z = T_{zx} H_x + T_{zy} H_y$$

(dependence on frequency assumed), must form a Hilbert Transform pair relationship as the tipper equation describes a realizable, linear system. By “realizable” that means that there is no output to the system before there is any input, i.e., the impulse response functions in the lag domain are zero for lags less than zero. That translates into the Hilbert Transform relationship in the frequency domain. This relationship was discovered independently in a number of fields, and is called the Kramers-Kronig relationship in atomic scattering theory, Bode’s relations in servo-mechanics, and the Kertz operator in Geomagnetic Depth Sounding studies.

This relationship is the basis of the D^+ and Rho^+ algorithms of Parker (1980) and Parker and Booker (1996), but otherwise is little exploited in MT. Jones (1980) used Hilbert Transformation to show that the real part of his Scandinavian C-response function was consistent with the imaginary part through Hilbert transformation.

The Hilbert transformation integral is

$$H_R(\omega) = \mathcal{H}\{H_I(\omega)\} = \frac{1}{\pi} P \int_{-\infty}^{\infty} \frac{H_I(w)}{\omega - w} dw$$
$$H_I(\omega) = -\mathcal{H}\{H_R(\omega)\} = -\frac{1}{\pi} P \int_{-\infty}^{\infty} \frac{H_R(w)}{\omega - w} dw$$

where $H_R(\omega)$ and $H_I(\omega)$ are the real and imaginary parts of the transfer function $H(\omega)$, and P denotes the Cauchy principal value of the integral. The integral is defined over all frequencies in a linear manner, so is difficult to implement. It is usually determined using Fourier Transformation, but as our data are in a log domain, we would have to interpolate significantly at 10 kHz sampling to cover the whole range to 1,000 s (=time series of 10^7 points). This could be performed more efficiently using the Logarithmic Fourier Transform of Haines and Jones (1988), but still the computational effort is large.

Instead, I adopted an approximate method using a 5-point numerical differentiation to determine the predicted Imaginary part from the Real part.

An example is shown for the tippers from a site named L50N_2750W. The Real parts are shown as filled circles, and the imaginary parts as unfilled circles in Figure 97. Also shown for the imaginary data are the ± 0.02 ranges (dashed lines), which represents a realistic error floor for tipper estimates. The 5-point numerical differentiation of the real part (after 5-point smoothing to reduce scatter effects) as an estimate of the predicted imaginary part is shown as the blue line (Tz-i pred).

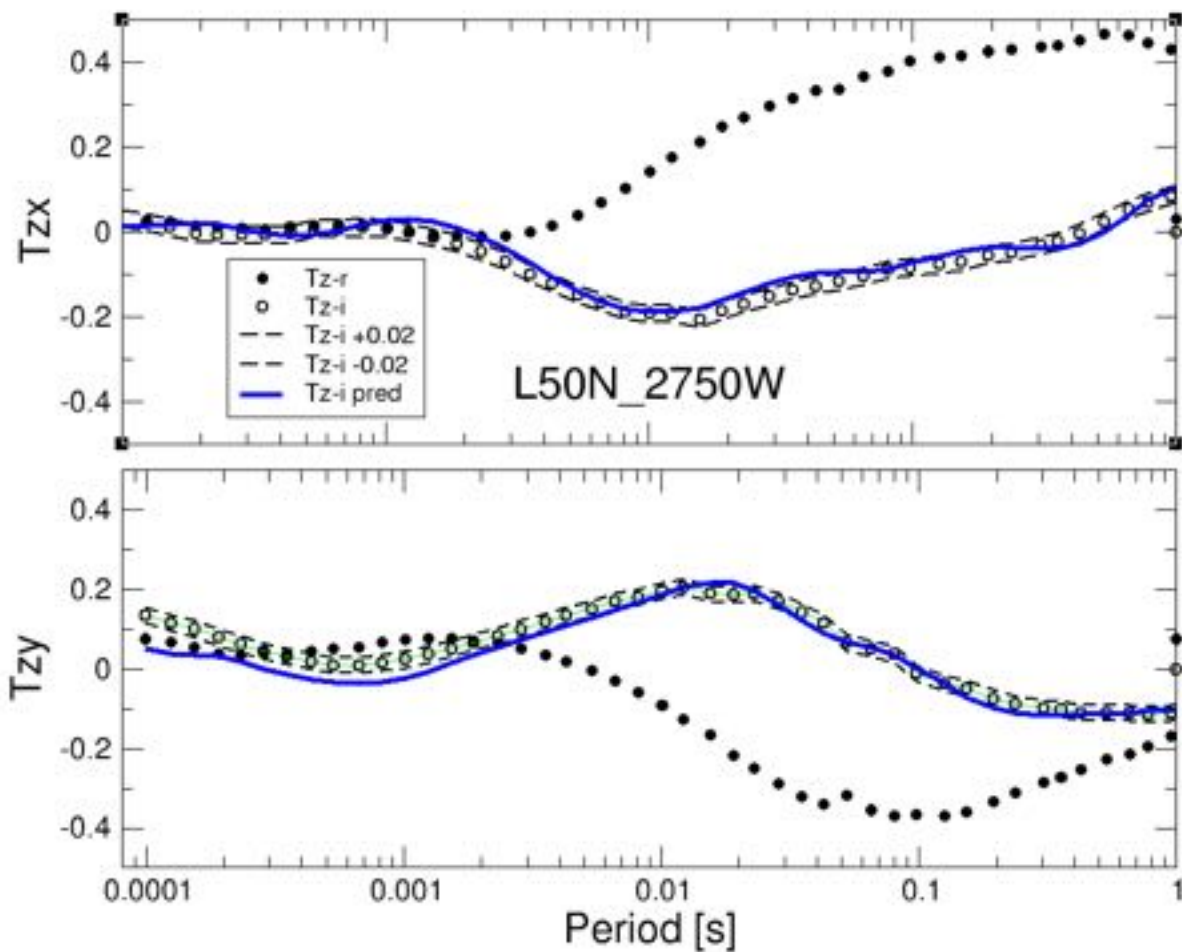


Figure 97: Tippers for site L50N_2750W shown as filled (Real, $Tz-r$) and unfilled (Imaginary, $Tz-i$) points. An error floor of 0.02 is shown as the black dashed lines on the imaginary parts. The 5-point numerical differentiation prediction of $Tz-i$ from $Tz-r$ is shown as the blue lines ($Tz-i$ pred).

The averaged absolute difference between the $\text{Im}(Tz_x)$ and $\text{Im}(Tz_y)$ and their predictions for the 46 data points between 10 kHz and 1 Hz is 0.017 and 0.026 respectively, which is consistent with an assumed error floor of 0.02. The higher Tz_y prediction difference is due to the rising $\text{Im}(Tz_y)$ at high frequencies, which may not be real. So these data would have Smoothness Factors of 0.85 and 1.30 for Tz_x and Tz_y respectively for an adopted error floor of 0.02.

This approach can be used as a tool to determine the Smoothness Factors in exactly the same way as for MT data. The Error Factors can be derived in the same manner also, as the average

error over an interval scaled by the error floor. And the Quality Factors are the average of these two.

TABLE OF CONTENTS

EXECUTIVE SUMMARY 3

1. PRIOR REPORTS 3

2. INTRODUCTION..... 4

3. DATA ASSESSMENT 5

3.1. PROFILE MM1 5

3.2. PROFILE SS 9

3.3. PROFILE SP-EW 12

3.4. PROFILE SP-NS 14

3.5. PROFILE MO 16

3.6. PROFILE MM0 19

3.7. PROFILE MM2 21

4. PARAMETER TESTING..... 23

4.1. PROFILE MM1 HIGH FREQUENCIES 23

4.1.1. SMOOTHING PARAMETERS 24

4.1.2. DATA COMPONENTS AND ERROR FLOOR 29

4.1.3. STARTING RESISTIVITY 31

4.1.4. ADDING THE VERTICAL FIELD DATA 31

4.2. PROFILE MM1 LOW FREQUENCIES..... 32

4.2.1. SMOOTHING PARAMETERS 32

4.2.2. DATA COMPONENTS AND ERROR FLOOR 37

4.2.3. STARTING RESISTIVITY 38

4.2.4. ADDING THE VERTICAL FIELD DATA 39

4.3. PROFILE SS HIGH FREQUENCIES 40

4.3.1. SMOOTHING PARAMETERS 40

4.3.2. DATA COMPONENTS AND ERROR FLOOR 45

4.3.3. STARTING RESISTIVITY 46

4.3.4. ADDING THE VERTICAL FIELD DATA 47

4.4. PROFILE SP-EW LOW FREQUENCIES 48

4.4.1. SMOOTHING PARAMETERS 48

4.4.2. DATA COMPONENTS AND ERROR FLOOR 53

4.4.3. STARTING RESISTIVITY 54

4.4.4. ADDING THE VERTICAL FIELD DATA 55

4.5. RESULTS OF PARAMETER TESTING..... 56

4.5.1. HIGH FREQUENCY RANGE	56
4.5.2. LOW FREQUENCY RANGE	56
5. PREFERRED 2D MODELS	57
5.1. PROFILE MM1	57
5.2. PROFILE SS	59
5.3. PROFILE SP-EW.....	61
5.4. PROFILE SP-NS.....	64
5.5. PROFILE MO	67
5.6. PROFILE MM0	71
5.7. PROFILE MM2	73
6. CONCLUSIONS.....	76
7. DECLARATIONS AND SIGNATURE	77
REFERENCES.....	78

Executive Summary

Two-dimensional inversions have been performed on the AMT/MT data from southern Kootenay region using both data acquired by Moombarriga Canada in 2021 and previously existing sites. Inversions were undertaken on the distortion-decomposed and Rho+ internally consistent data derived during the Analyses phase. Some data were excluded from inversion as they demonstrated contradictions or discrepancies with a 2D description of the subsurface. Prior to inversion, comprehensive tests were executed to determine the appropriate inversion parameters to adopt. The preferred models derived are from jointly inverting the TE and TM mode MT data and the vertical field tipper data simultaneously.

1. Prior reports

Prior reports related to this contract are:

CMTS-2021-KootenayResources-R1: Acquisition Report

CMTS-2021-KootenayResources-R2: Analyses of Data and Maps of Parameters of MT data

2. Introduction

Complete MT Solutions Inc. (“CMTS”) was contracted by Kootenay Resources Inc. (“Kootenay Resources” or “client”) to undertake analyses and 2-D inversions of magnetotelluric data around in the southern Kootenay region, as shown in Figure 1. The data were acquired in four main areas of interest, Mount Mahon (profiles MM*), Sweet Spot (profile SS), Spike (profiles SP), and Moyie (profile MO) and 2D models have been generated along 6 east-west profiles and 2 north-south profiles.

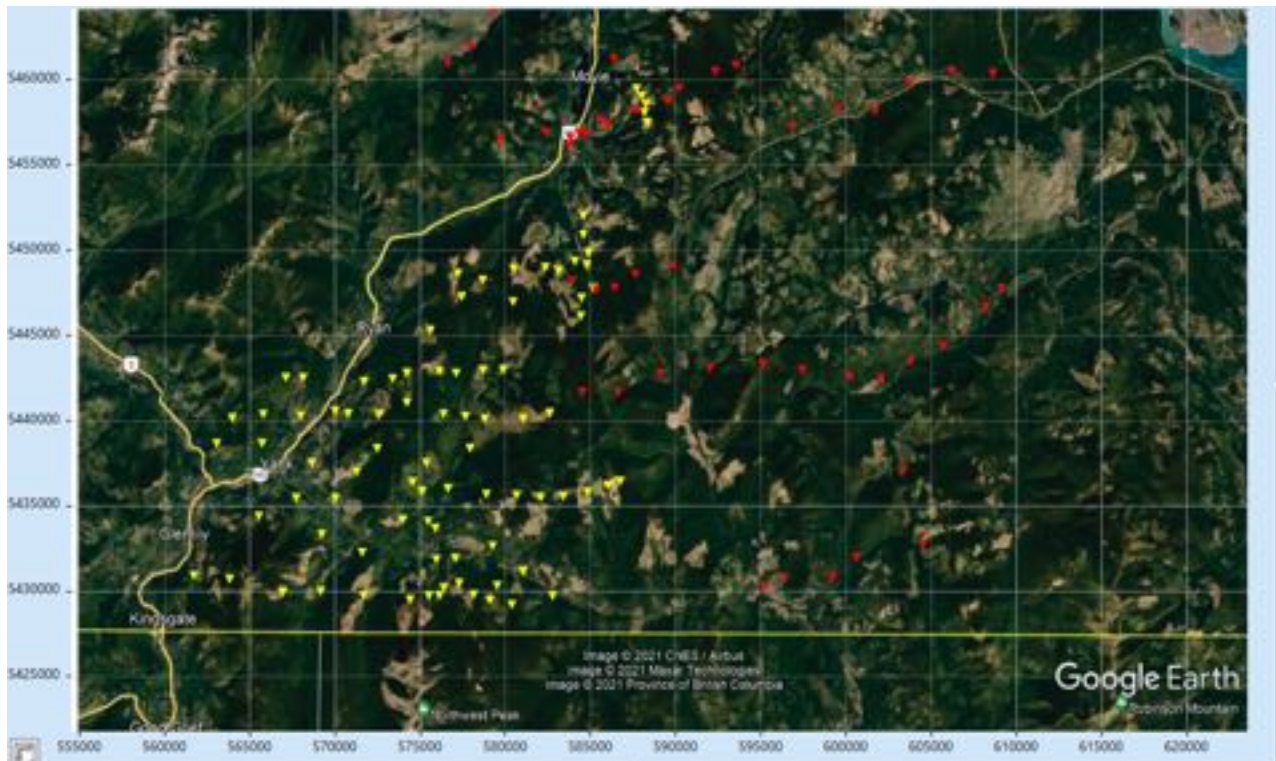


Figure 1: MT site locations. Yellow are the newly acquired data and red are the previously existing sites.

Analysis of the MT data showed that the dominant geoelectric strike angle through most of the survey area is frequency dependent (see report CMTS-2021-Kootenay Resources-R2), where the high frequencies (10k – 3 Hz) have a different preferred strike and from the lower frequencies. For the purposes of the 2D Inversions performed herein. Based on the Analysis, the high frequency range are the frequencies/periods that optimally image the depth range of interest of ~4000 mbsl as requested by the client.

3. Data assessment

3.1. Profile MM1

In order to generate models with the highest resolution and accuracy for the appropriate depths, 2D inversions have been executed along profile MM1. Analysis of the data showed that a geoelectric strike angle of N10E was appropriate for the high frequency data (10kHz – 3Hz) and N55W for the low frequency data (3 Hz – 1000s). The profile has been divided into two separate frequency ranges to independently model the shallow and deep structure at the appropriate strike angle. The high frequency data include the distortion corrected Rho^+ response curves of MT sites in the four-decade period range of 10,000 – 3 Hz at a strike angle of N10E and the low frequency data include response curves from 3 Hz – 0.001 Hz at a strike angle of N55W. These distortion-free, internally consistent regional responses were derived in the Analysis phase (report CMTS-2021-KootenayResources-R2). Where the data show a high degree of scatter with large error bars (see example for site KMM103 in Figure 2), where phases are out of quadrant (i.e., TE-mode phases outside 0° to 90° and TM-mode phases outside -90° to -180° see example at site KMM110 in Figure 2) or where the Rho^+ response varies significantly from the decomposed MT response (example is shown for site KMM101 in Figure 2) the data have been masked (=culled) prior to 2D inversion.

→ This is important, as outliers highly perturb any least-squares minimization scheme.

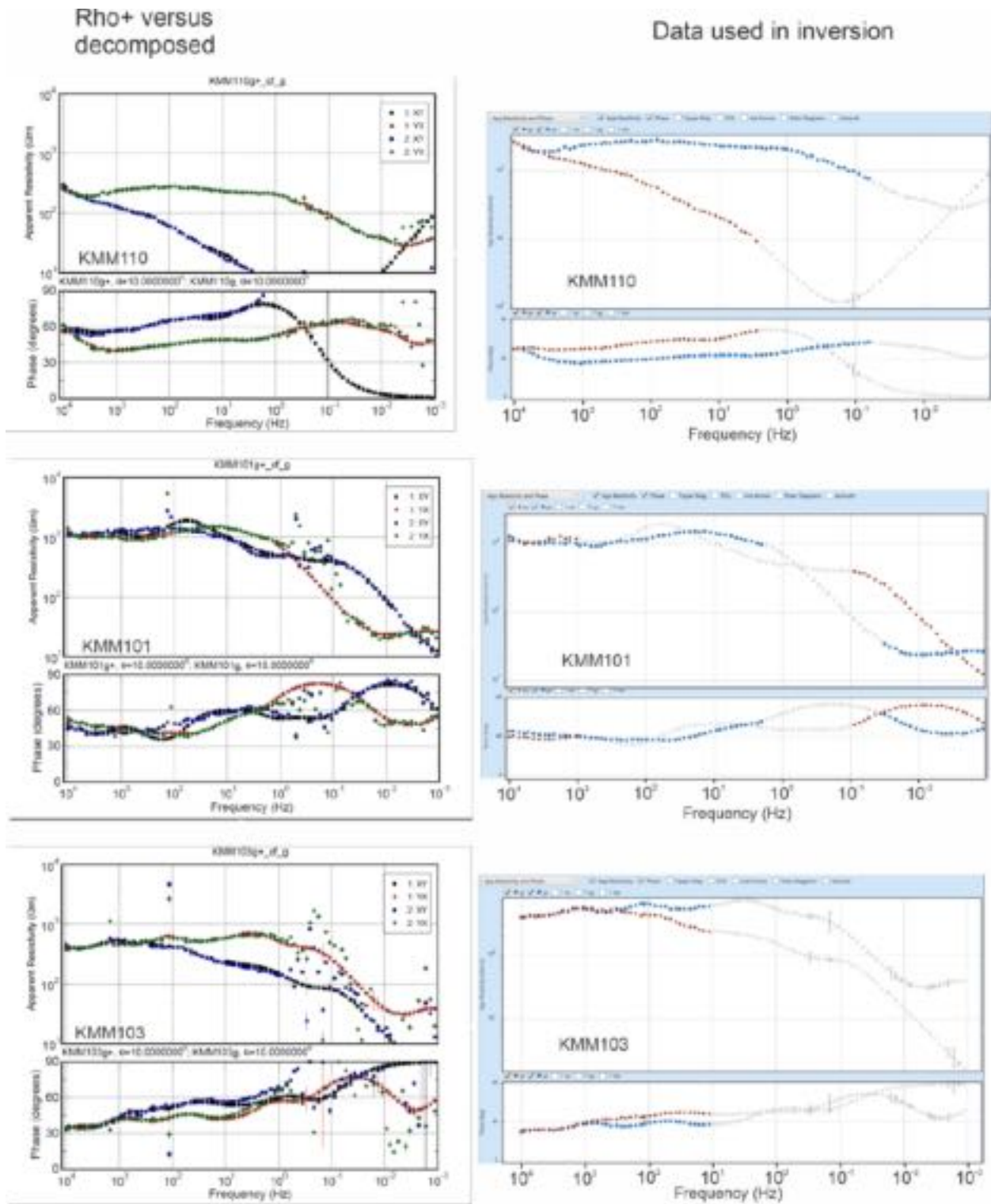


Figure 2: Examples of data masking (right) for inversion based on Rho^+ analysis (left).

Pseudosections of the high frequency range (10,000 – 3 Hz) phase and apparent resistivity response estimates for each of the sites along the profile has been generated for both the TE- and TM-modes as well as for the vertical field tipper magnitude for data points deemed

acceptable for 2D inversion (Figure 3). Pseudosections of the low frequency range (3 Hz – 0.001 Hz) are shown in Figure 4. As apparent resistivities may be affected by static shift, the phase pseudosections are typically inspected to determine areas that are relatively one-dimensional (1D). The Earth can be regarded as 1D at periods where the phases in the TE- and TM-modes are similar and the 2D models will be independent of the geo-electric strike angle.

In general, moderate vertical streaking is observed in the apparent resistivity pseudosection plots with lateral difference of at approximately 1 order of magnitude. However these correlate with changes in the phases, particularly beneath the western end of the profile in the high frequency data range. This is an indication that there is minimal residual static shift effects present in the data that need to be accounted for in the 2D inversion process, but that there are complex structural changes along the profile. The profile has been selected for high frequency range and low frequency range parameter testing.

It should be noted that for the DUN sites, much of the existing data was determined to be of poor quality and no useable for 2D inversion. The pseudosection plots show these data to be largely 1-dimensional with similar response in the TE and TM-modes.

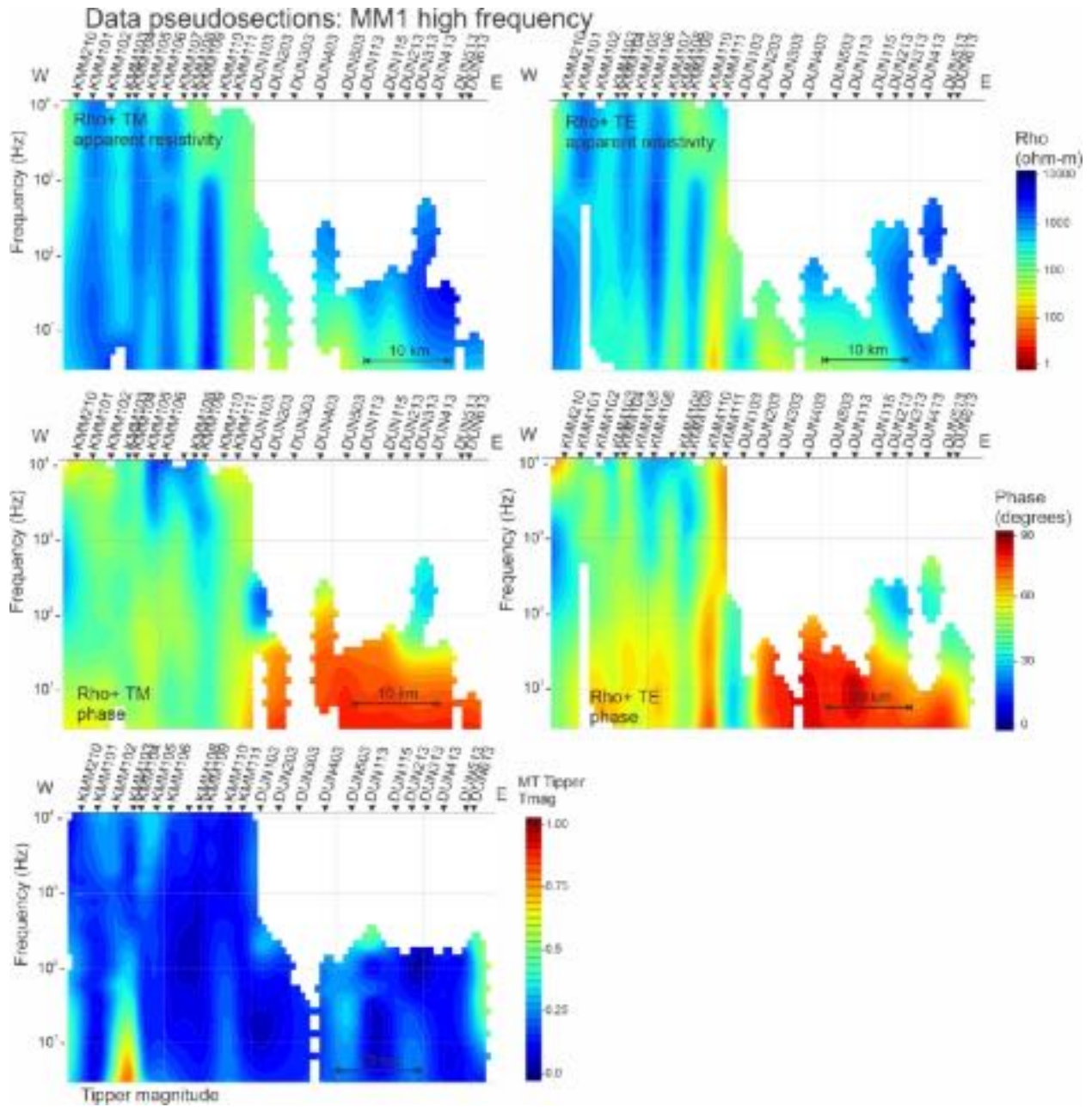


Figure 3: Pseudosections of the high frequency data used in inversions along profile MM1 for apparent resistivity and phase in the TE and TM-modes and the vertical field tipper magnitude.

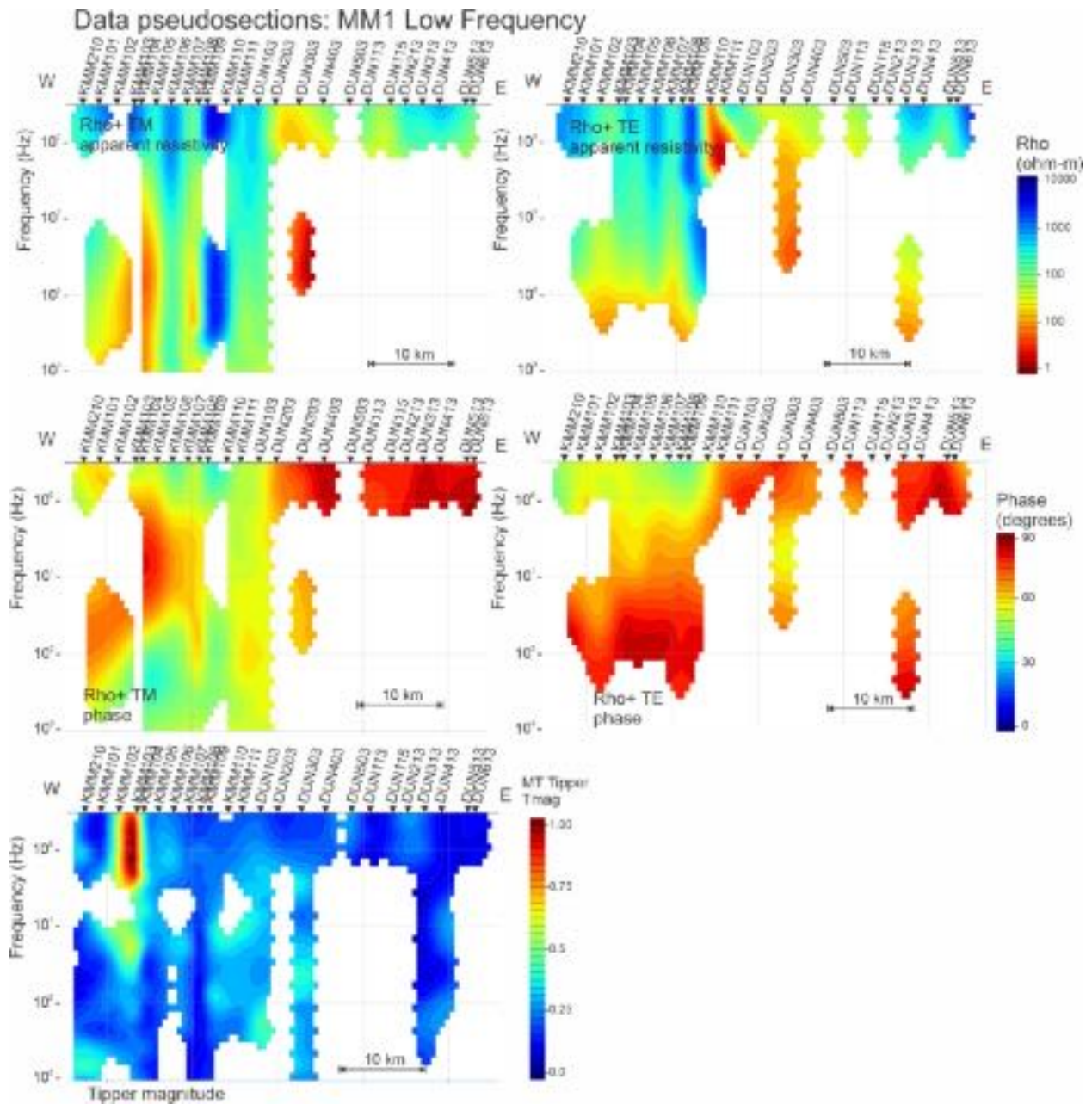


Figure 4: Pseudosections of the low frequency data used in inversions along profile MM1 for apparent resistivity and phase in the TE and TM-modes and the vertical field tipper magnitude.

3.2. Profile SS

Analysis of the data along profile SS showed that a geoelectric strike angle of N12E was appropriate for the high frequency data (10 kHz – 3 Hz) and N55W for the low frequency data (3 Hz – 0.001 Hz). The profile has been divided into two separate frequency ranges to independently model the shallow and deep structure at the appropriate strike angle. The high frequency data include the distortion corrected Rho^+ response curves of MT sites in the four-decade period range of 10,000 – 3 Hz at a strike angle of N12E and the low frequency data

include response curves from 3 Hz – 0.001 Hz at a strike angle of N55W. Where the data show a high degree of scatter with large error bars with phases that are out of quadrant or where the Rho^+ response varies significantly from the decomposed MT response, the data have been masked prior to 2D inversion. Note that for several sites, particularly at the western end of the profile where increased noise levels resulted in lower short frequency (long period) data quality, much of the data have been removed. Figure 5 shows an example where most of the TM-mode data and all of the TE-mode data has been masked for the low frequency range.

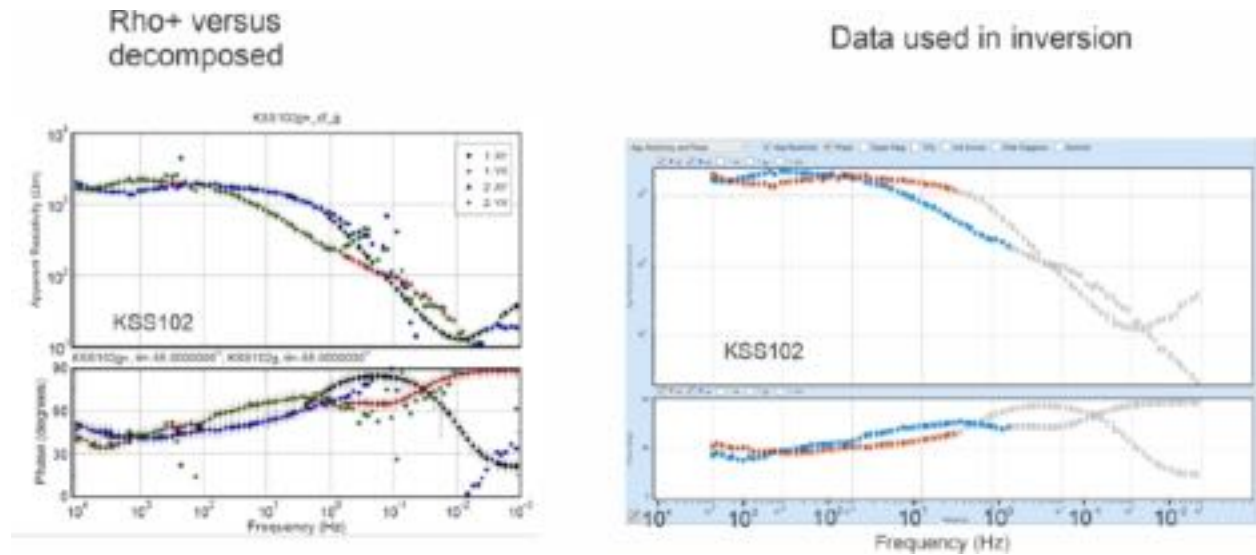


Figure 5: Examples of data masking (right) for inversion based on Rho^+ analysis (left).

Pseudosections of the high frequency range (10,000 – 3 Hz) phase and apparent resistivity response estimates for each of the sites along the profile have been generated for both the TE- and TM-modes as well as the vertical field tipper magnitude for data points deemed acceptable for 2D inversion (Figure 6). Pseudosections of the low frequency range (3 Hz – 0.001 Hz) are shown in Figure 7.

In general, moderate vertical streaking is observed in the apparent resistivity pseudosection plots with lateral difference of at approximately 1 order of magnitude, but similar to MM1 these correlate with changes in the phases. This is an indication that there are minimal residual static shift effects present in the data that need to be accounted for in the 2D inversion process, but that there are complex structural changes along the profile. This profile has been selected for high frequency range parameter testing.

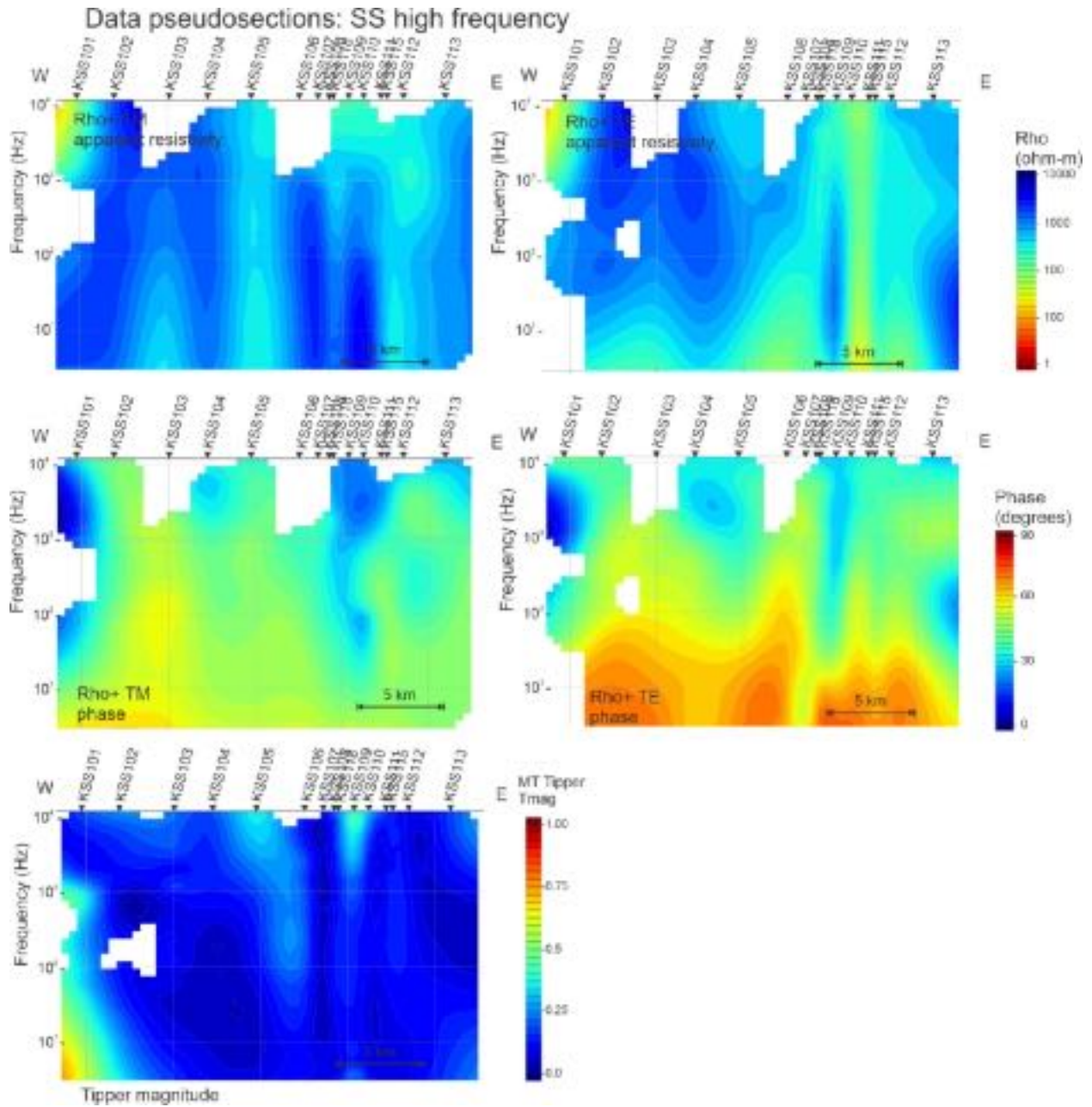


Figure 6: Pseudosections of the high frequency data used in inversions along profile SS for apparent resistivity and phase in the TE and TM-modes and the vertical field tipper magnitude.

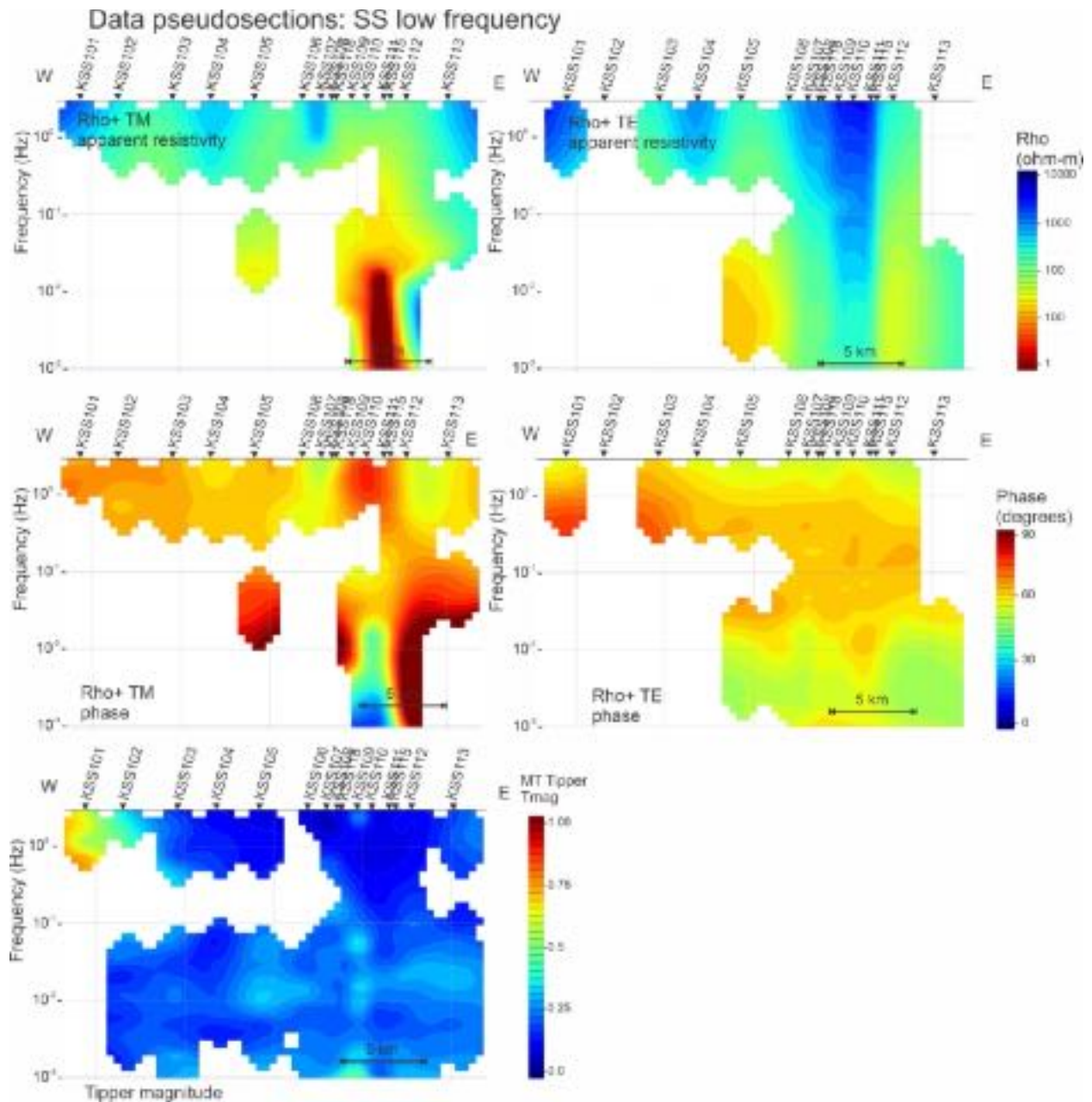


Figure 7: Pseudosections of the low frequency data used in inversions along profile SS for apparent resistivity and phase in the TE and TM-modes and the vertical field tipper magnitude.

3.3. Profile SP-EW

Analysis of the data along profile SP-EW showed that a geoelectric strike angle of N50W was appropriate for the high frequency data (10 kHz – 3 Hz) and N39W for the low frequency data (3 kHz – 0.001 Hz). Where the data show a high degree of scatter with large error bars with phases out of quadrant or where the Rho⁺ response varies significantly from the decomposed MT response, the data have been masked prior to 2D inversion.

Pseudosections of the high frequency range (10,000 – 3 Hz) phase and apparent resistivity response estimates for each of the sites along the profile has been generated for both the TE- and TM-modes as well as the vertical field tipper magnitude for data points deemed acceptable for 2D inversion (Figure 8). Pseudosections of the low frequency range (3 Hz – 0.001 Hz) are shown in Figure 9. This profile has been selected for low frequency range parameter testing.

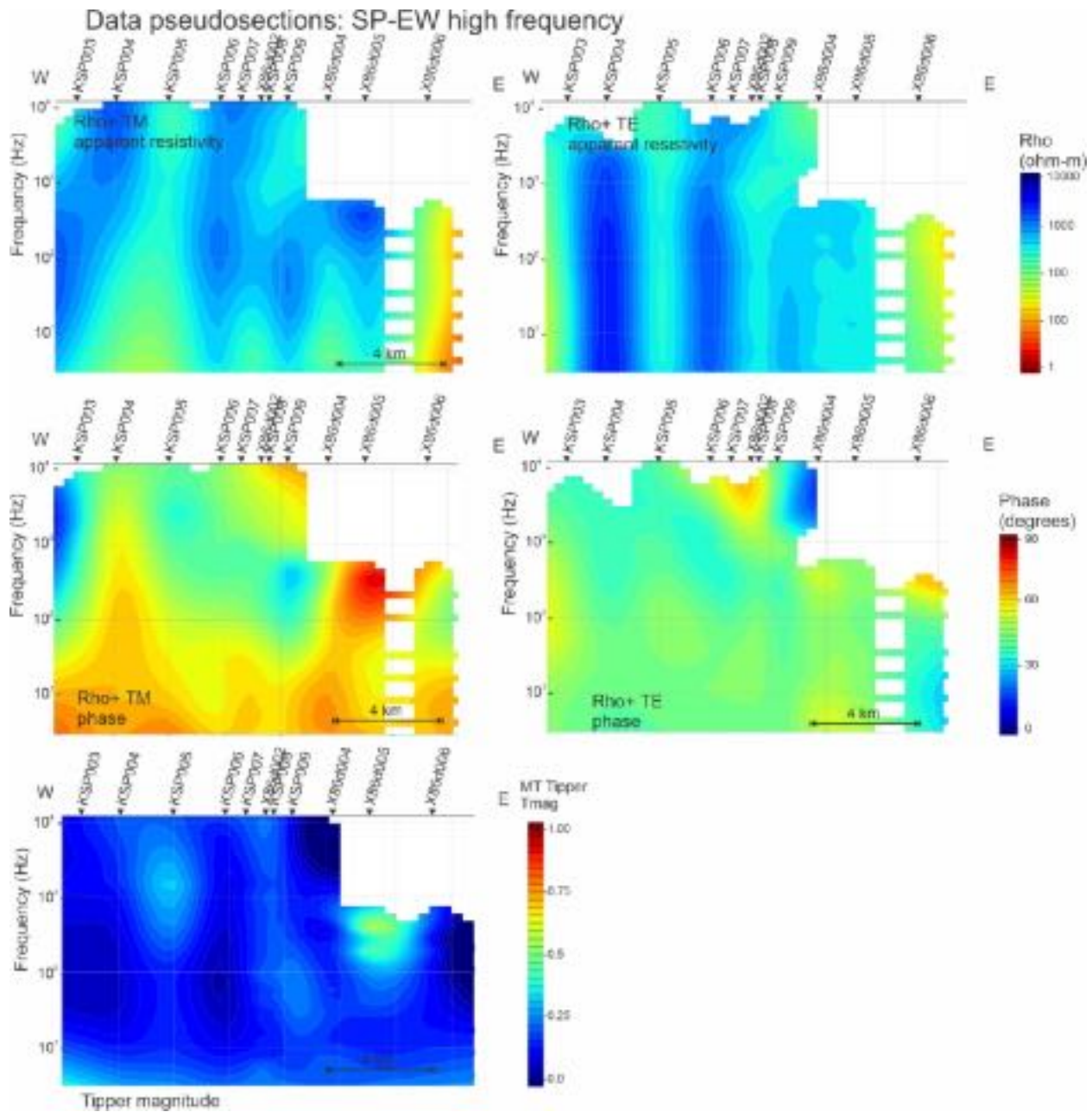


Figure 8: Pseudosections of the high frequency data used in inversions along profile SP-EW for apparent resistivity and phase in the TE and TM-modes and the vertical field tipper magnitude.

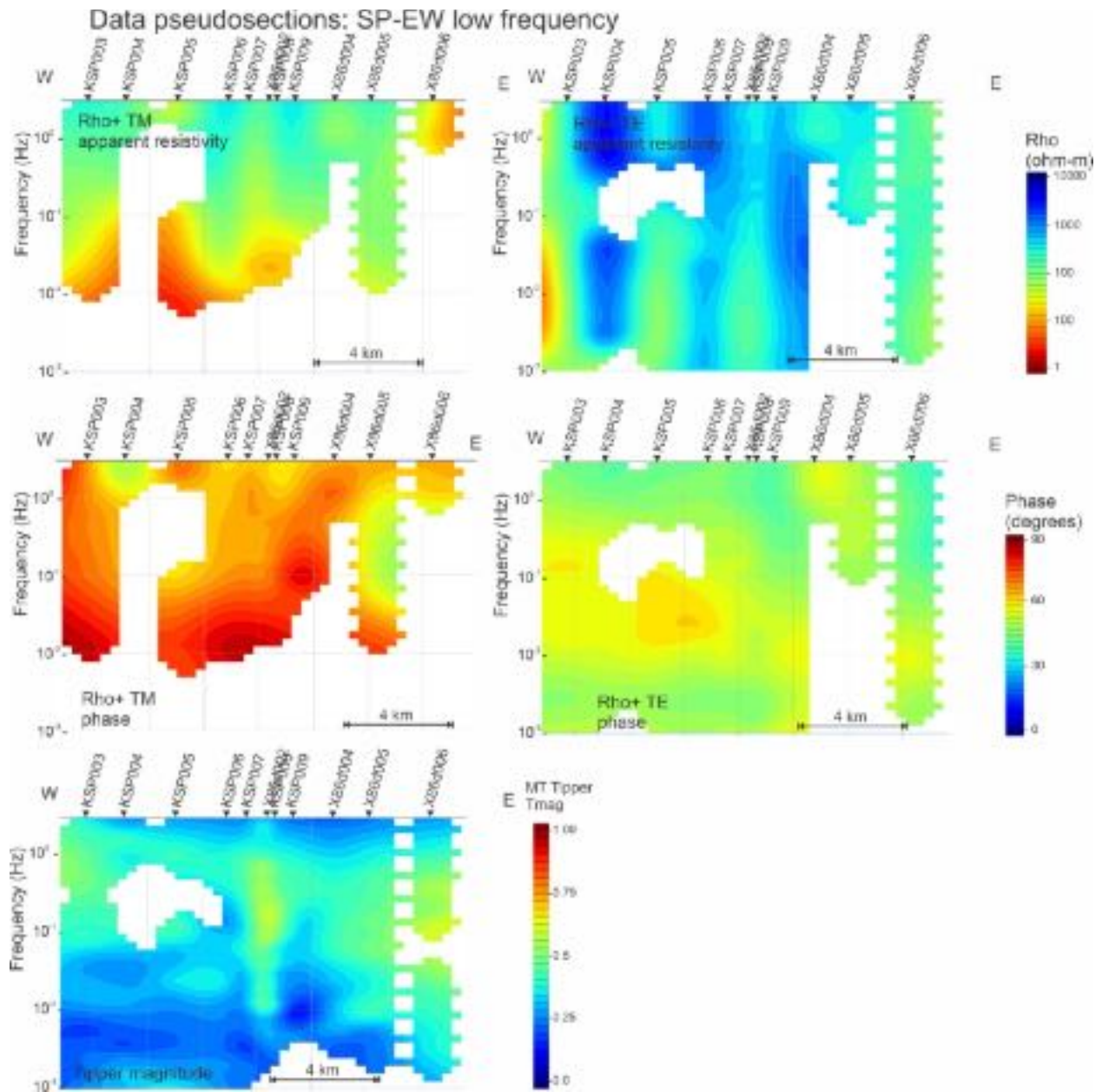


Figure 9: Pseudosections of the low frequency data used in inversions along profile SP-EW for apparent resistivity and phase in the TE and TM-modes and the vertical field tipper magnitude.

3.4. Profile SP-NS

Analysis of the data along profile SP-NS showed that a geoelectric strike angle of N50W was appropriate for the high frequency data (10 kHz – 3 Hz) and N39W for the low frequency data (3 kHz – 0.001 Hz). Where the data show a high degree of scatter with large error bars where phases are out of quadrant or where the Rho^+ response varies significantly from the decomposed MT response, the data have been masked prior to 2D inversion.

Pseudosections of the high frequency range (10,000 – 3 Hz) phase and apparent resistivity response estimates for each of the sites along the profile has been generated for both the TE- and TM-modes as well as the vertical field tipper magnitude for data points deemed acceptable for 2D inversion (Figure 10). Pseudosections of the low frequency range (3 Hz – 0.001 Hz) are shown in Figure 11.

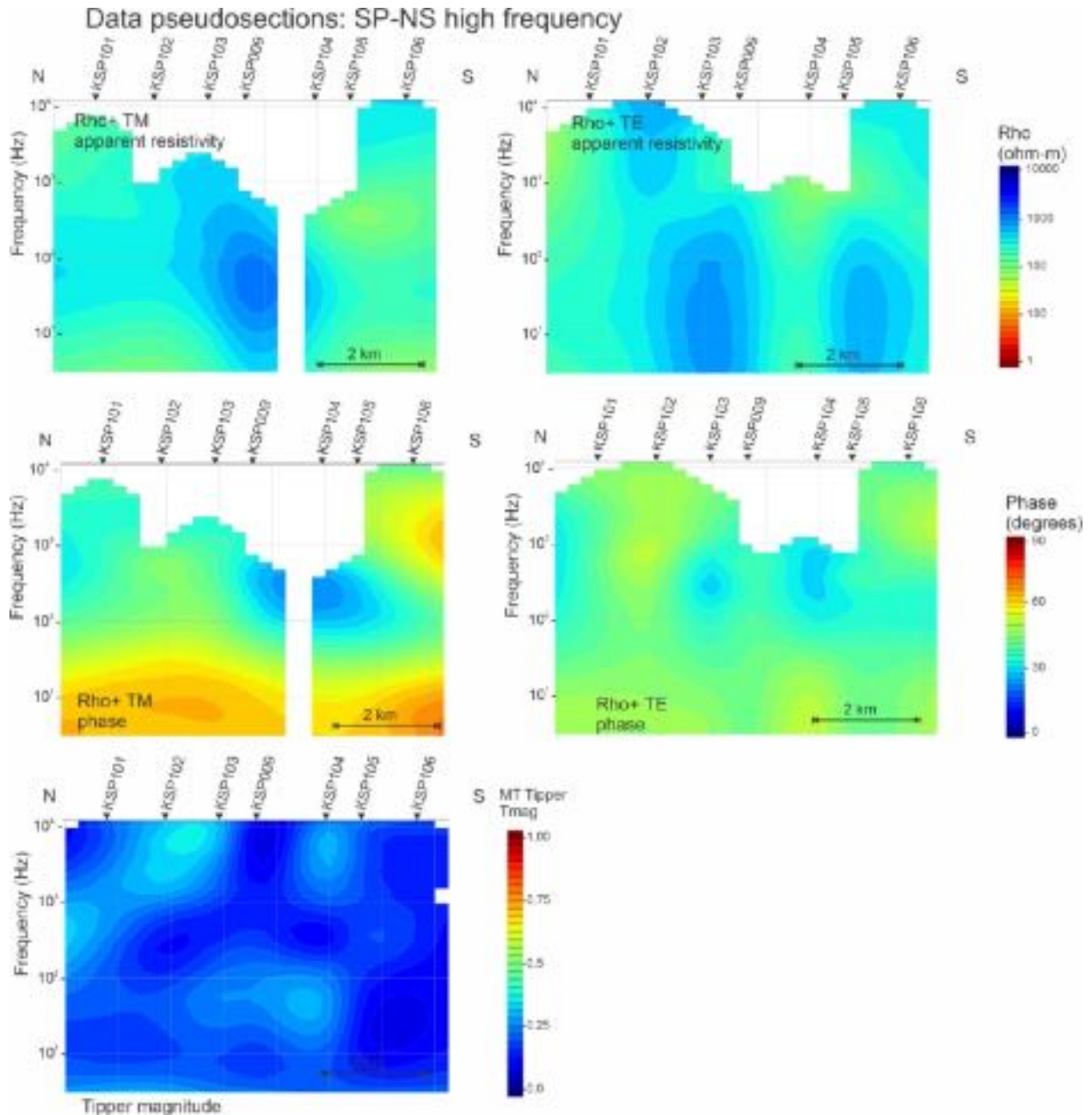


Figure 10: Pseudosections of the high frequency data used in inversions along profile SP-NS for apparent resistivity and phase in the TE and TM-modes and the vertical field tipper magnitude.

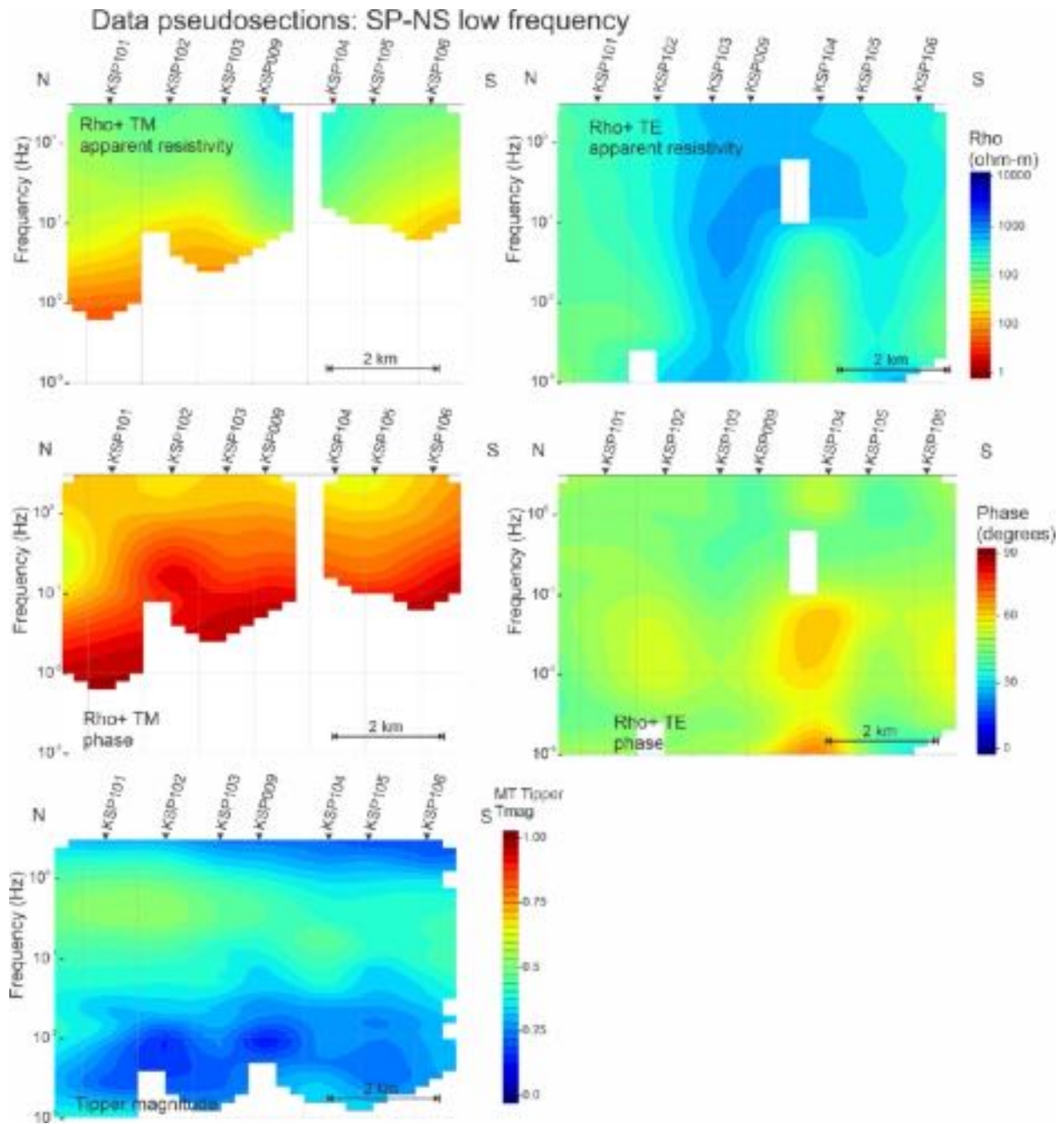


Figure 11: Pseudosections of the low frequency data used in inversions along profile SP-NS for apparent resistivity and phase in the TE and TM-modes and the vertical field tipper magnitude.

3.5. Profile MO

Analysis of the data along profile MO showed that a geoelectric strike angle of N39W was appropriate for the entire frequency data (10 kHz – 0.001 Hz). Where the data show a high degree of scatter with large error bars or where phases are out of quadrant or where the Rho+ response varies significantly from the decomposed MT response, the data have been masked prior to 2D inversion.

Pseudosections of the entire frequency range (10,000 Hz – 0.001 Hz) phase and apparent resistivity response estimates for each of the sites along the profile have been generated for both the TE- and TM-modes as well as the vertical field tipper magnitude for data points deemed acceptable for 2D inversion (Figure 12). The newly-acquired data run along a profile that is roughly parallel to the strike direction, for this reason only 2 of the new sites have been included on the regional MO profile. It should be noted that much of the DUN data have been deemed unreliable for 2D inversion, particular in the TM-mode, for frequencies below 1 Hz.

In an attempt to define the structure beneath the new data, inversions were run along a local MO profile; however, the orientation of the profile might result in unreliable models.

Pseudosections for the local MO profile are shown in Figure 13.

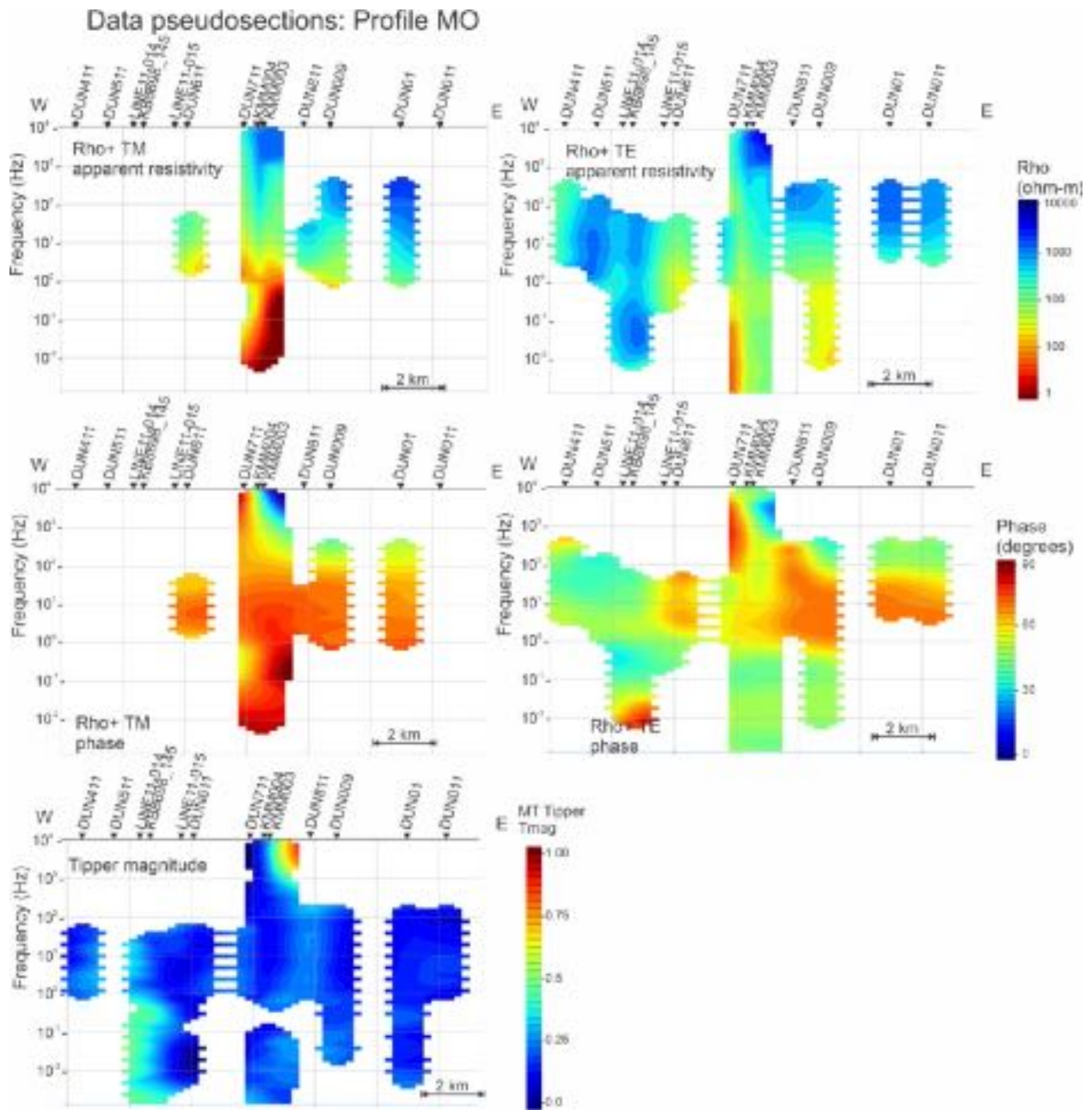


Figure 12: Pseudosections of the entire frequency data used in inversions along the regional profile MO for apparent resistivity and phase in the TE and TM-modes and the vertical field tipper magnitude.

Data pseudosections: Profile MO new data

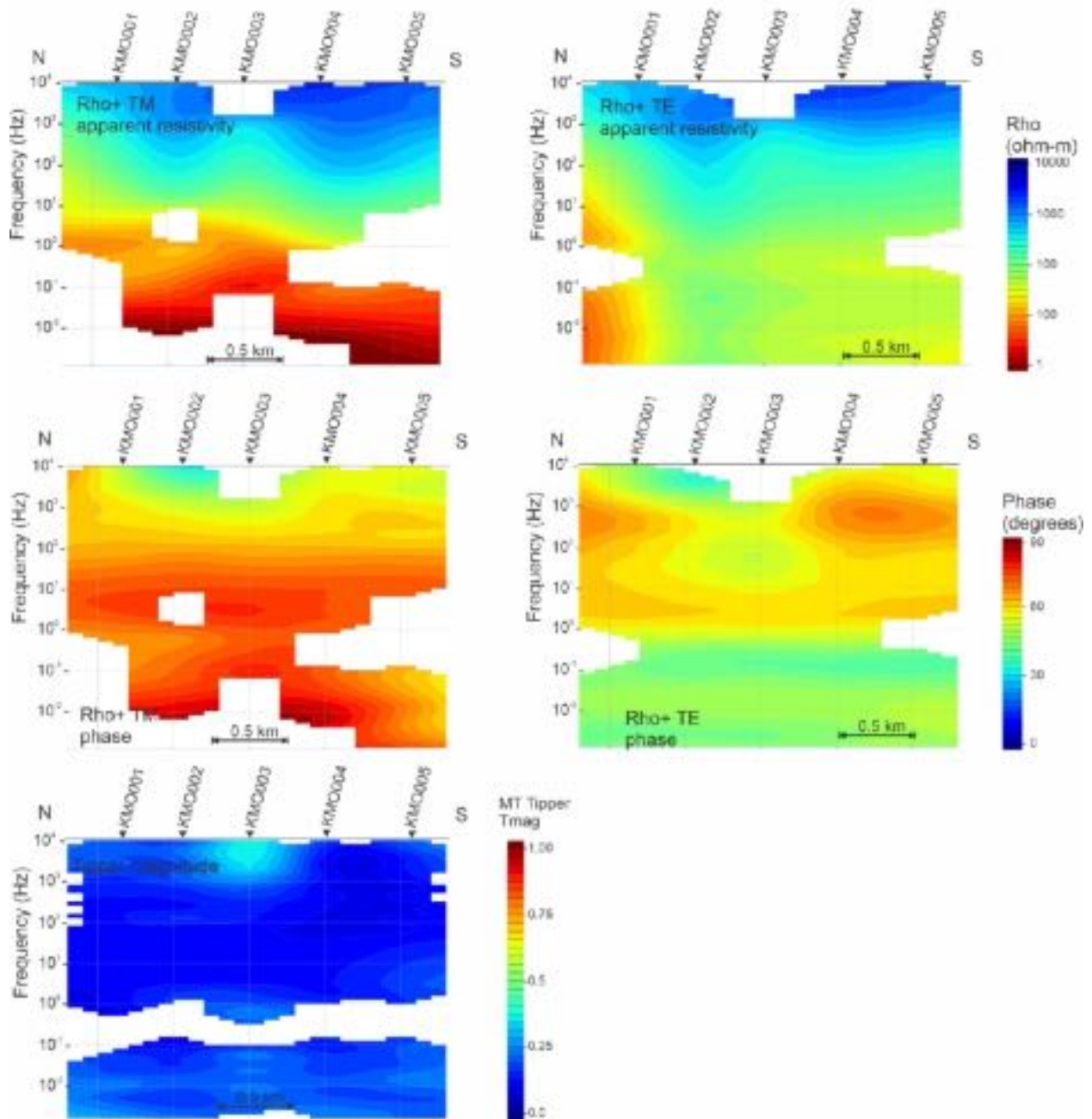


Figure 13: Pseudosections of the entire frequency data for newly recorded sites used in inversions along the local profile MO for apparent resistivity and phase in the TE and TM-modes and the vertical field tipper magnitude.

3.6. Profile MM0

Analysis of the data along profile MM0 showed that a geoelectric strike angle of N12E was appropriate for the high frequency data (10 kHz – 3 Hz) and N55W for the low frequency data (3 kHz – 0.001 Hz). Where the data show a high degree of scatter with large error bars or where

phases are out of quadrant or where the Rho^+ response varies significantly from the decomposed MT response, the data have been masked prior to 2D inversion.

Pseudosections of the high frequency range (10,000 – 3 Hz) phase and apparent resistivity response estimates for each of the sites along the profile has been generated for both the TE- and TM-modes as well as the vertical field tipper magnitude for data points deemed acceptable for 2D inversion (Figure 14). Pseudosections of the low frequency range (3 Hz – 0.001 Hz) are shown in Figure 15.

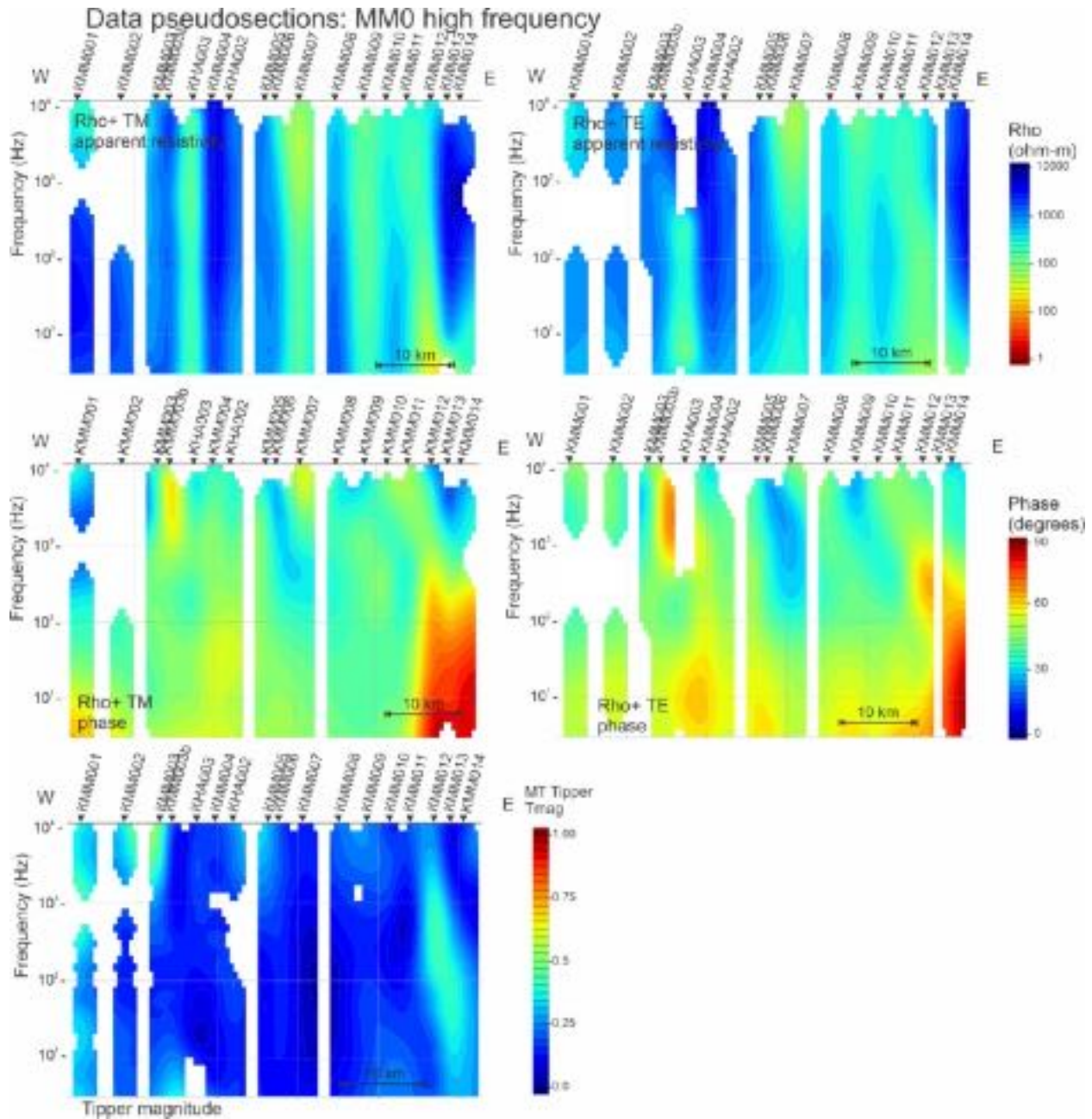


Figure 14: Pseudosections of the high frequency data used in inversions along profile MM0 for apparent resistivity and phase in the TE and TM-modes and the vertical field tipper magnitude.

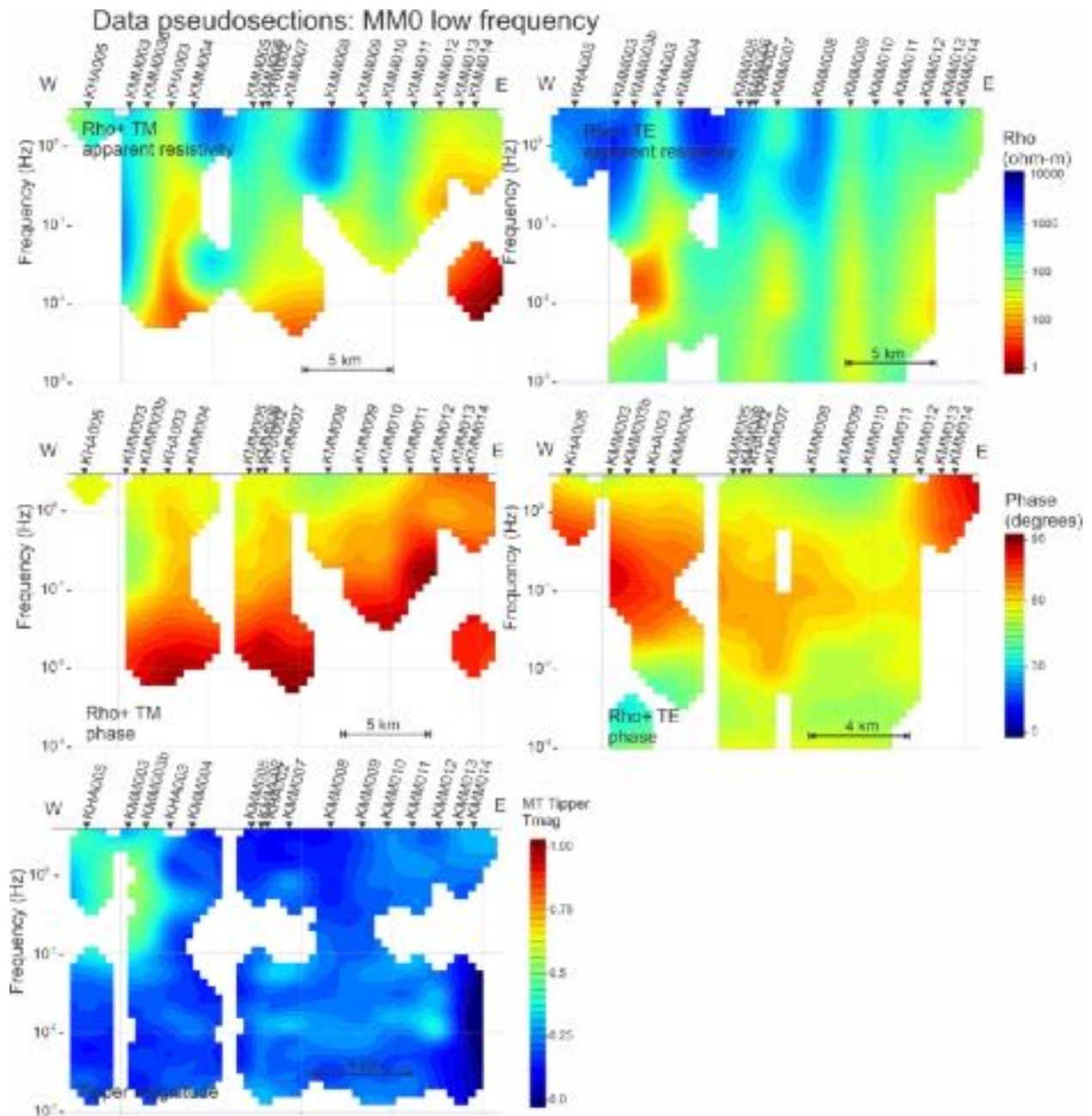


Figure 15: Pseudosections of the low frequency data used in inversions along profile MM0 for apparent resistivity and phase in the TE and TM-modes and the vertical field tipper magnitude.

3.7. Profile MM2

Analysis of the data along profile MM2 showed that a geoelectric strike angle of N12E was appropriate for the high frequency data (10 kHz – 3 Hz) and N55W for the low frequency data (3 kHz – 0.001 Hz). Where the data show a high degree of scatter with large error bars or where phases are out of quadrant or where the Rho^+ response varies significantly from the decomposed MT response, the data have been masked prior to 2D inversion.

Pseudosections of the high frequency range (10,000 – 3 Hz) phase and apparent resistivity response estimates for each of the sites along the profile has been generated for both the TE- and TM-modes as well as the vertical field tipper magnitude for data points deemed acceptable for 2D inversion (Figure 16). Pseudosections of the low frequency range (3 Hz – 0.001 Hz) are shown in Figure 17.

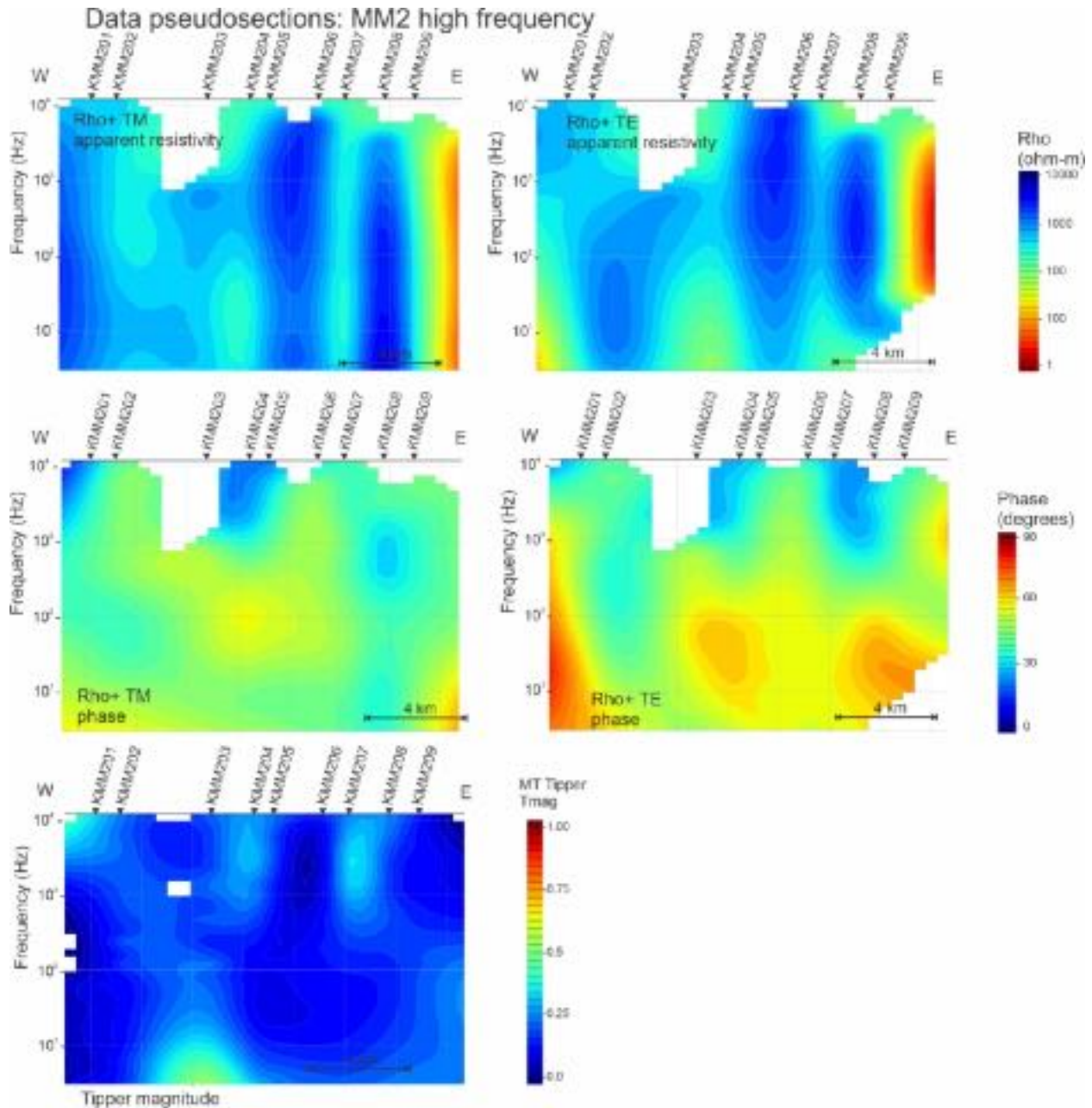


Figure 16: Pseudosections of the high frequency data used in inversions along profile MM2 for apparent resistivity and phase in the TE and TM-modes and the vertical field tipper magnitude.

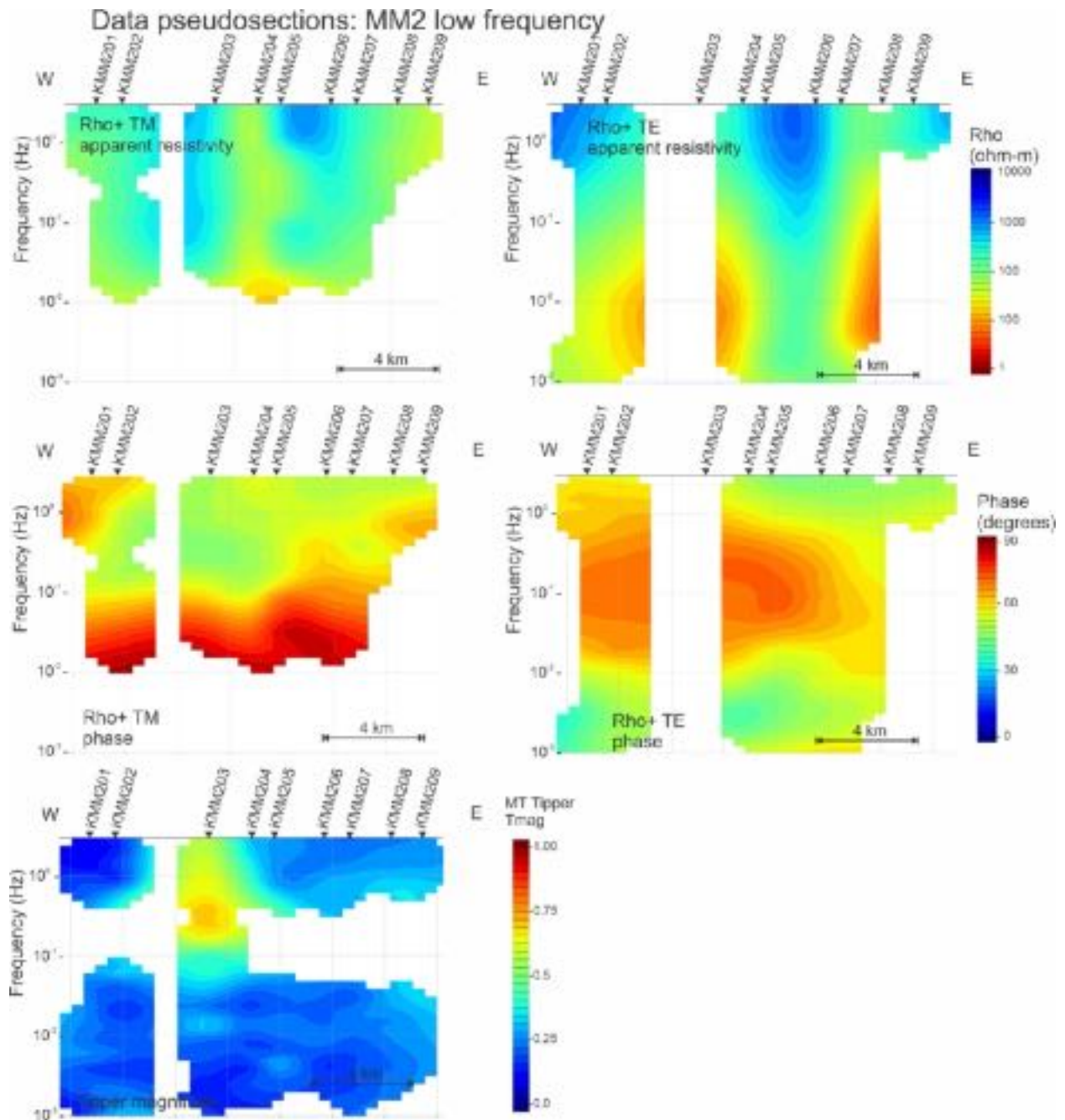


Figure 17: Pseudosections of the low frequency data used in inversions along profile MM2 for apparent resistivity and phase in the TE and TM-modes and the vertical field tipper magnitude.

4. Parameter testing

4.1. Profile MM1 High Frequencies

CGG's Geotools interpretation software package that implements the latest version of the *Rodi and Mackie* [2001] inversion algorithm was used to derive two-dimensional models along the

profiles through objective regularized inversion. The inversion program searches for the smoothest model with an acceptable fit to the data, with optionally the least deviation from the *a priori* starting model. The models derived, therefore, represent the minimum structure required to fit the data with an acceptable misfit. If performed correctly, there can be more structure in the Earth than that represented by the model, but not less. Given known sensitivity to the start model and to the selection of inversion parameters, it is necessary to perform the inversion multiple times with successive start models and inversion parameters in order to obtain the optimum model from the optimum set of inversion parameters.

A series of inversion parameters and settings were tested on the data to determine their influence on final results and to identify optimal parameters. Parameters tested include the smoothing weight (τ , this is the so-called Tikhonov trade-off parameter that balances misfit against smoothness), the horizontal and vertical smoothing values (Hsm and Vsm), the minimum resolution scale ($Z0$), and the starting resistivity half-space value ($Rho0$). The inversion models were also tested by inverting various components of the data with different assigned error floors; varying error floor for apparent resistivity is one approach for identifying and dealing with the effects of static shift on the data. The resulting optimal parameters for inversion have been applied to the remaining profiles.

4.1.1. *Smoothing Parameters*

The model results for various values of τ (Figure 18), Hsm (Figure 19), Vsm (Figure 20), and $Z0$ (Figure 21) are shown for Profile MM1 high frequencies only. Models were generated using the TE-mode and TM-mode data only, with an error floor of 10% on apparent resistivity and 5% on phase, and a starting uniform half-space of 100 ohm-m. The overall resistivity structure is similar between each of the resulting models. The τ and Hsm values appear to have a large influence on the resulting model structure whereas variations the $Z0$ value has minimal effect.

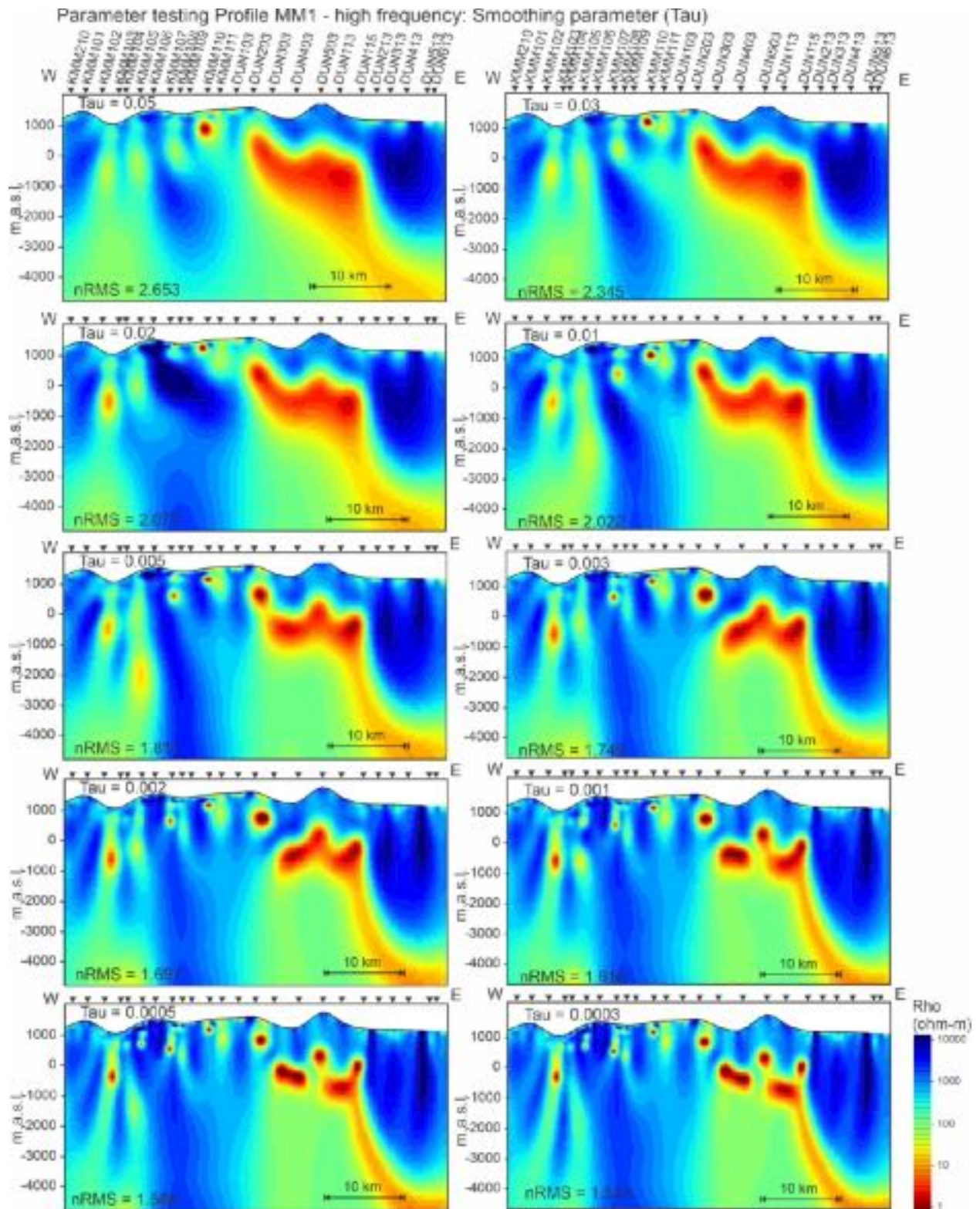


Figure 18: Results of variations of tau (smoothing parameter) on Profile MM1_HF.

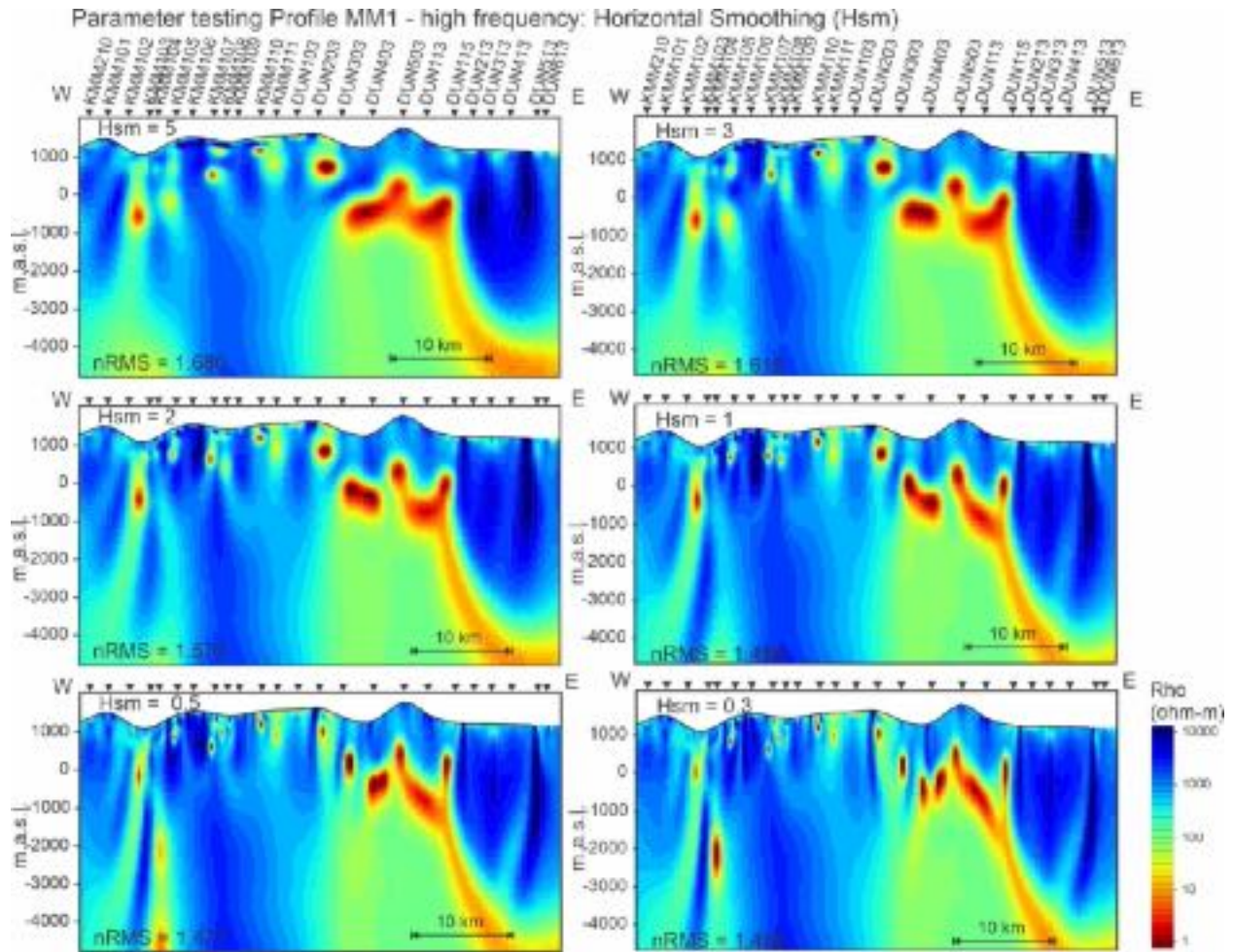


Figure 19: Results of variations of Hsm (horizontal smoothing parameter) on Profile MM1_HF.

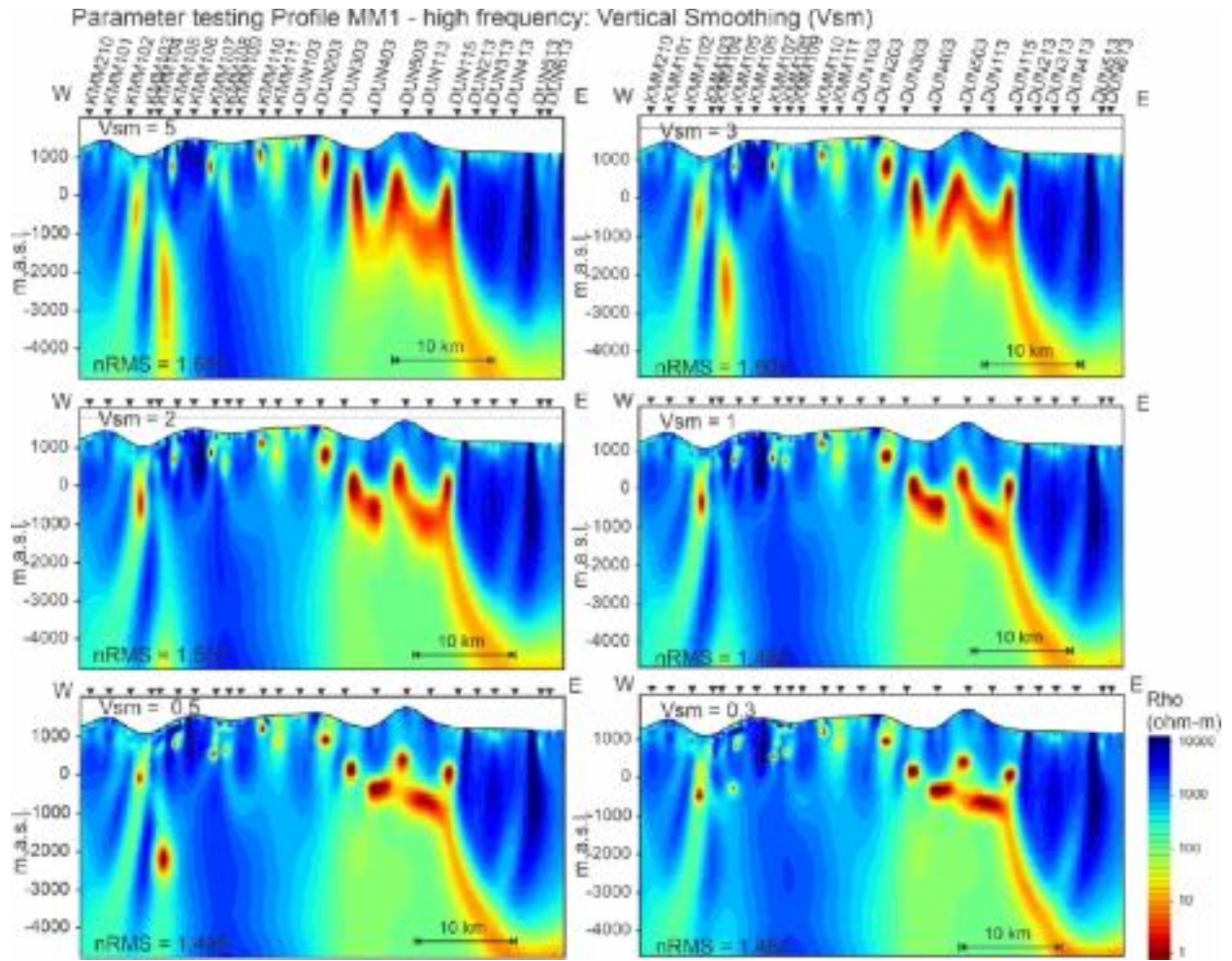


Figure 20: Results of variations of Vsm (vertical smoothing parameter) on Profile MM1_HF.

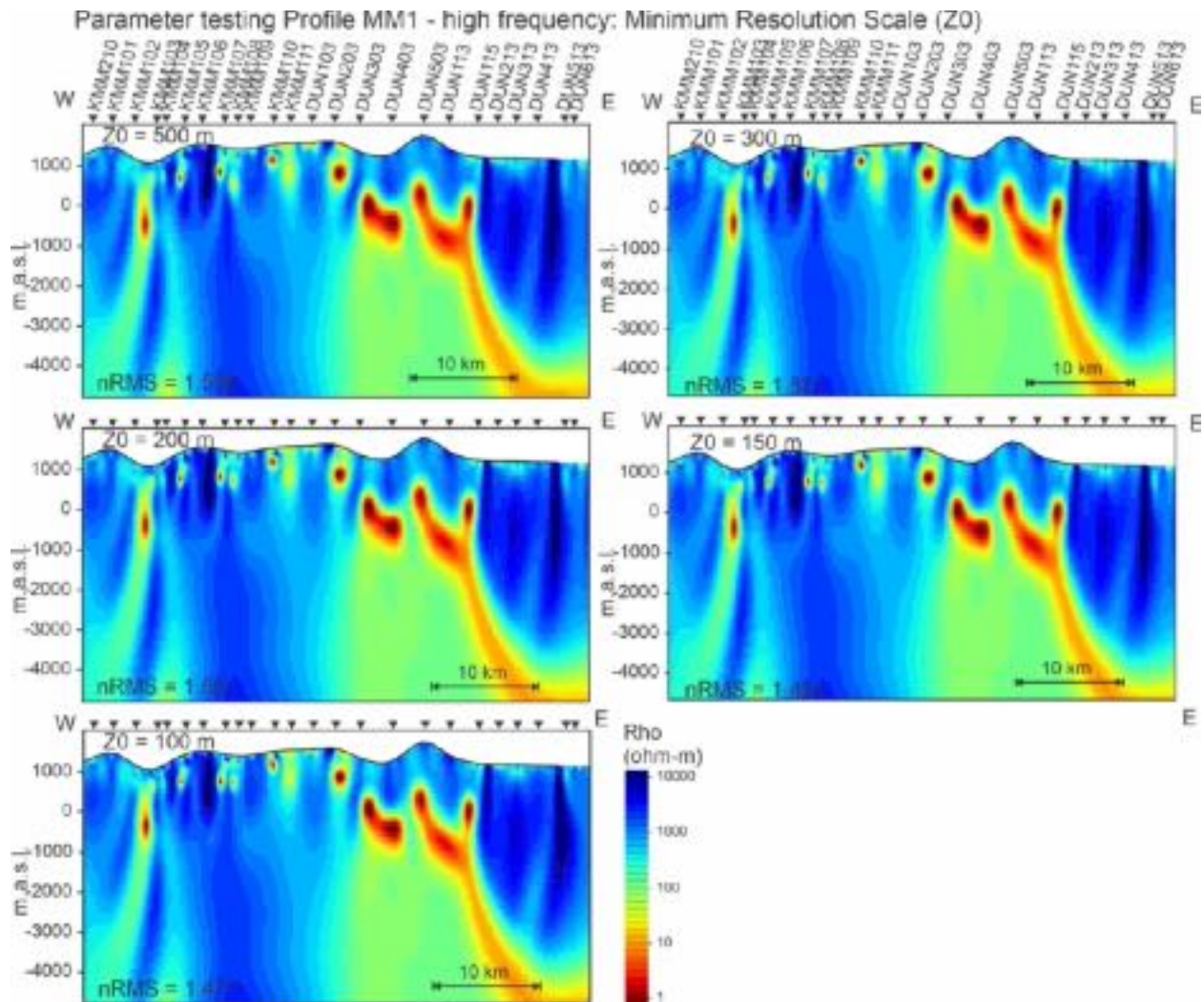


Figure 21: Results of variations of Z_0 (minimum resolution scale) on Profile MM1_HF.

Trade-off curves between the roughness of the model, defined by the various smoothing parameters, and the fit of the model to the data (the nRMS values) have been plotted for each smoothing parameter (Figure 22). Where possible, the value that yields the minimum nRMS with maximum smoothing has been selected as the optimal value in the so-called L-curve criterion [Hansen, 1992].

Figure 22 illustrates the trade-off between the roughness of the model and the fit of the model to the data for each parameter. The trade-off curve and resulting models show that the optimal values resulting in the smoothest model with the best fit to the data are: smoothing weight (τ) of 0.0005 - 0.001, horizontal smoothing (Hsm) of 1, vertical smoothing (Vsm) of 1, and minimum resolution scale (Z_0) of 200 - 300 m.

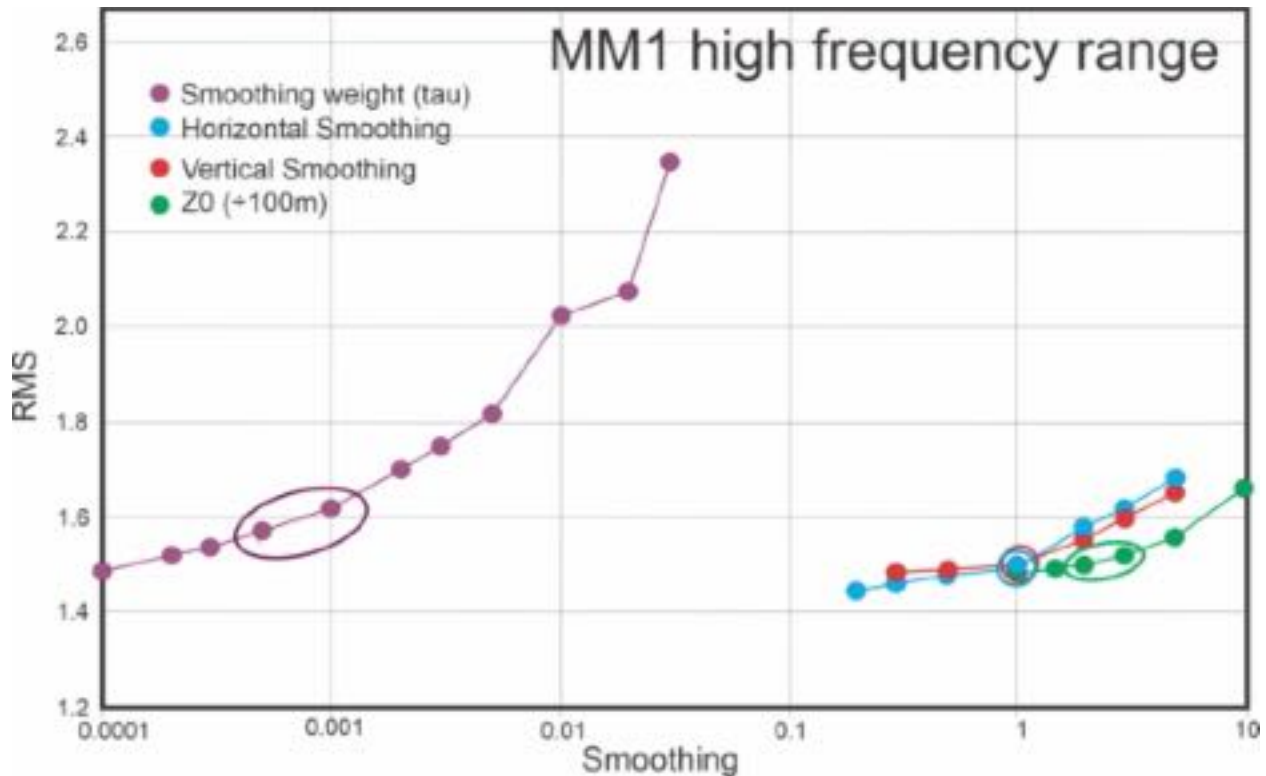


Figure 22: Plot of RMS misfit versus smoothing parameter values for Profile MM1_HF. The ovals mark the optimal value for final models.

4.1.2. Data components and error floor

Models were generated along the profile using various data components and error floors on the apparent resistivities and phases. A series of models were generated using the TM-mode only (i.e., for currents flowing *across* structures), the TE-mode only (currents flowing *along* structures) and inverting the TM and TE-modes jointly together. Apparent resistivity error floors varied from 20% to 4% and phases from 5% to 2%, and finally the data were inverted for static shift effects at each site.

The overall subsurface resistivity structure imaged when inverting the TM-mode only data is consistent with varying error floors and when inverting for static shift and the nRMS value is low for all models (left column in Figure 23). This suggests that there is minimal static shift in the TM data (or that inversions are accounting for them) and that the error floors derived in the Rho^+ data analysis are appropriate for 2D inversion. Models generated using the TE-mode only data (middle column, Figure 23) image fairly consistent structure beneath the profile for error floors down to 4% rho and 2% phase. When inverting the data for static shift effects the nRMS value is significantly reduced from 3.073 to 0.879, suggesting that some static shift effects are may be present and unaccounted for in the TE-mode. A reasonably low nRMS value of 2.486 and structure consistent with the static shift inversion is obtained with and error floor of 7% on TE apparent resistivity. When the TM and TE-mode data are inverted together (right column,

Figure 23) the results the overall structure is very similar between the different models. We conclude that a TM apparent resistivity error floor of 4%, a TE apparent resistivity error floor of 7 - 20 %, and phase error floor of 2% are most appropriate for this data. Note that upon further analysis by Alan Jones, the minimum error floors for this data set are 5.25% for apparent resistivity and 1.5 degrees for phase. These values have been used for our preferred models.

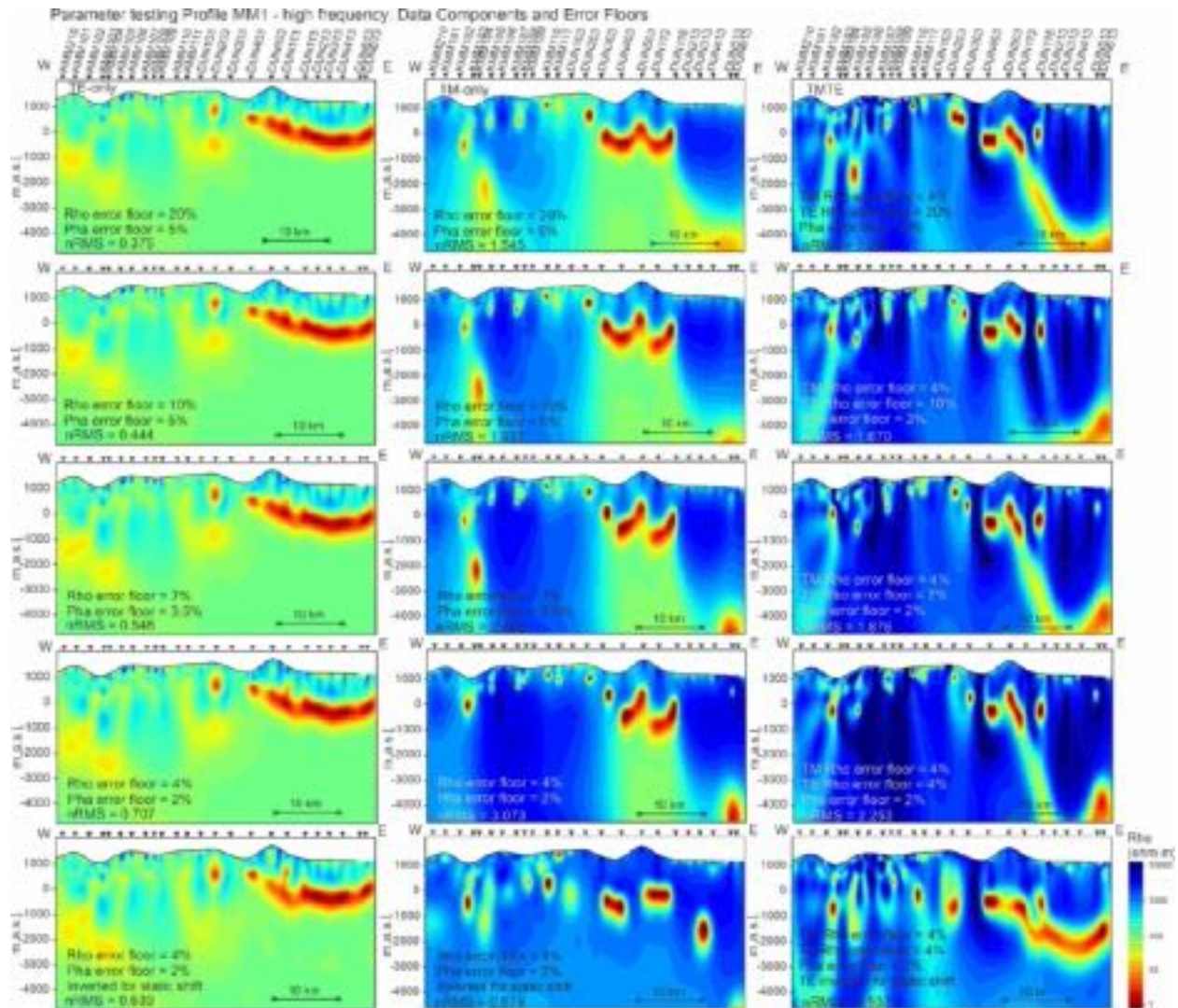


Figure 23: Results of 2D inversions using various data components and error floors for Profile MM1_HF.

Note: Keep in mind the different sensitivities of the TE and TM mode data as a consequence of their separation of Maxwell's Equations. The TE mode data essentially "sees" current flow and yields a resistivity model consistent with the geometry of that flow. The TM mode data essentially "sees" charges on lateral boundaries and yields a resistivity model consistent with the geometry of those charges. Inverting the two together is truly a Joint Inversion as the two sense the Earth differently.

4.1.3. Starting Resistivity

Inversions were initiated from various starting models and allowed to run to convergence to observe the effects on the model outputs (Figure 24). Initial models included uniform half-space resistivity values of 100 Ωm , 500 Ωm , 1000 Ωm , 5000 Ωm , and a layered structure of 1000 Ωm to 800 masl, 10 Ωm from 800 to -1000 masl underlain by 5000 Ωm . Inversions were run with the starting model as the *a priori* model. Results show strong similarities in the resistivity structure to depths of at least -2000 masl. This is an indication that for most of the profile the resulting model is independent of the starting half space. The lowest nRMS of 1.798 was obtained using a layered starting model.

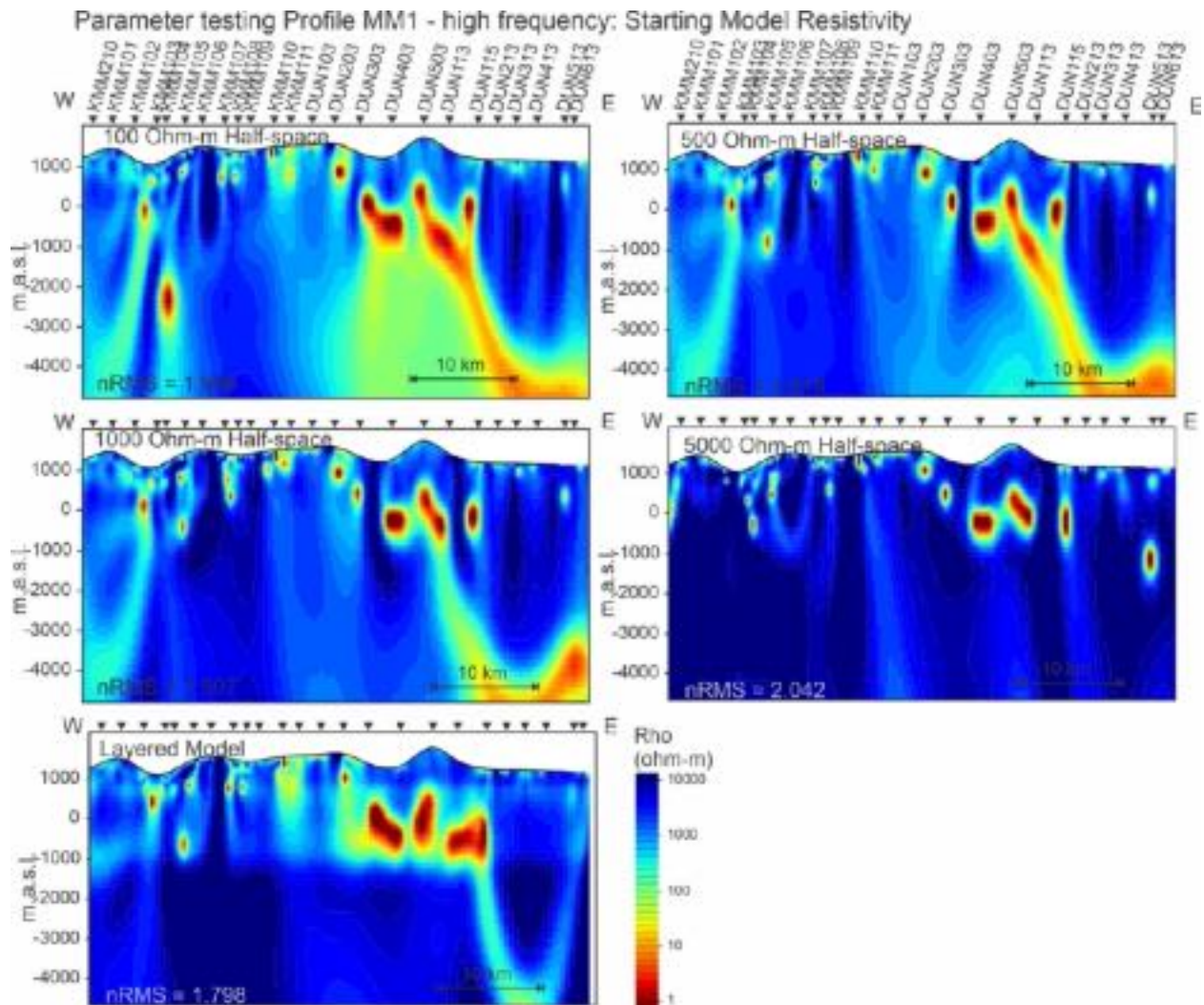


Figure 24: 2D inversion results using varying starting models for Profile MM1_HF.

4.1.4. Adding the vertical field data

Models were generated using the TMTE-only data and using the TMTE+vertical field data (HZ). Inversions were initiated from a layered starting model and the *a priori* model was set to current

model which uses the previous inversion result as the *a priori* model (Figure 25). Given the limited frequency range and data quality of the DUN sites, inversions were initiated using the KMM sites only to observed changes in the model structure. Beneath the western half of the profile (KMM sites) the structure remains fairly consistent, but extremely complex.

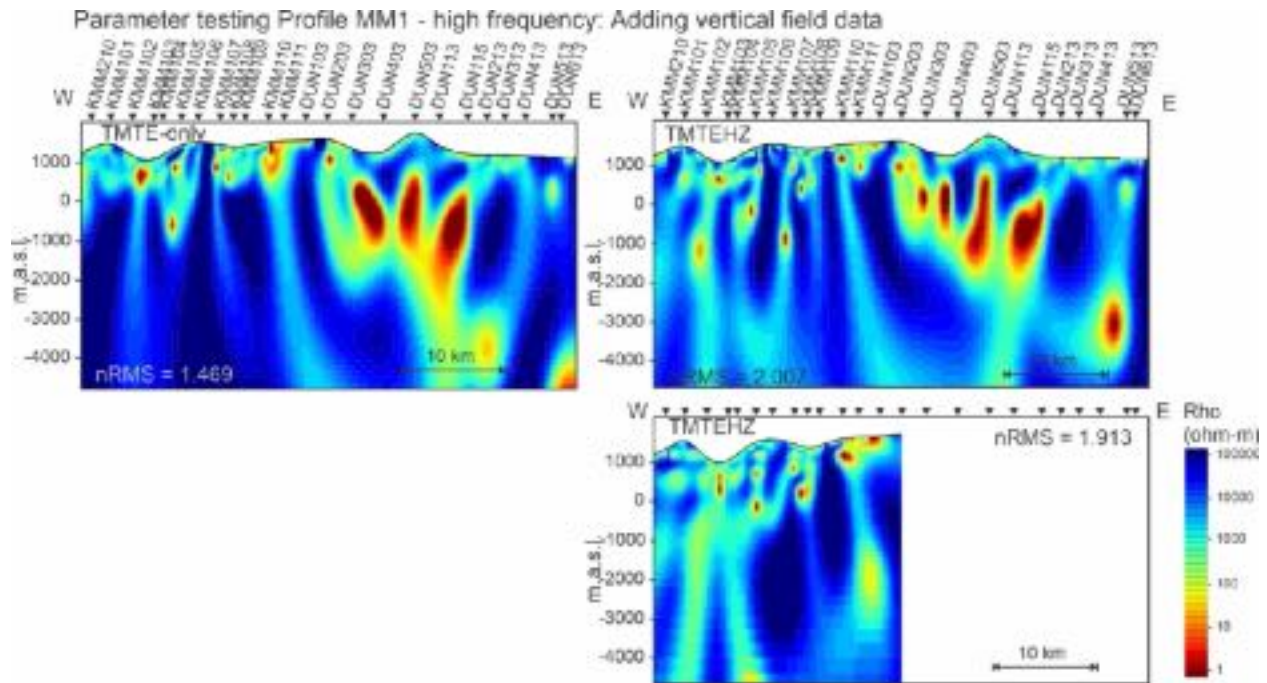


Figure 25: Results of using optimal parameters with the TMTE-only data (left) and the TMTEHZ data (right) for Profile MM1_HF.

4.2. Profile MM1 Low Frequencies

4.2.1. Smoothing Parameters

The model results for various values of τ (Figure 26), Hsm (Figure 27), Vsm (Figure 28), and $Z0$ (Figure 29) are shown for Profile MM1 low frequencies only. Models were generated using the TE-mode and TM-mode data only, with an error floor of 10% on apparent resistivity and 5% on phase, and a starting uniform half-space of 1000 ohm-m. The overall resistivity structure is similar between each of the resulting models.

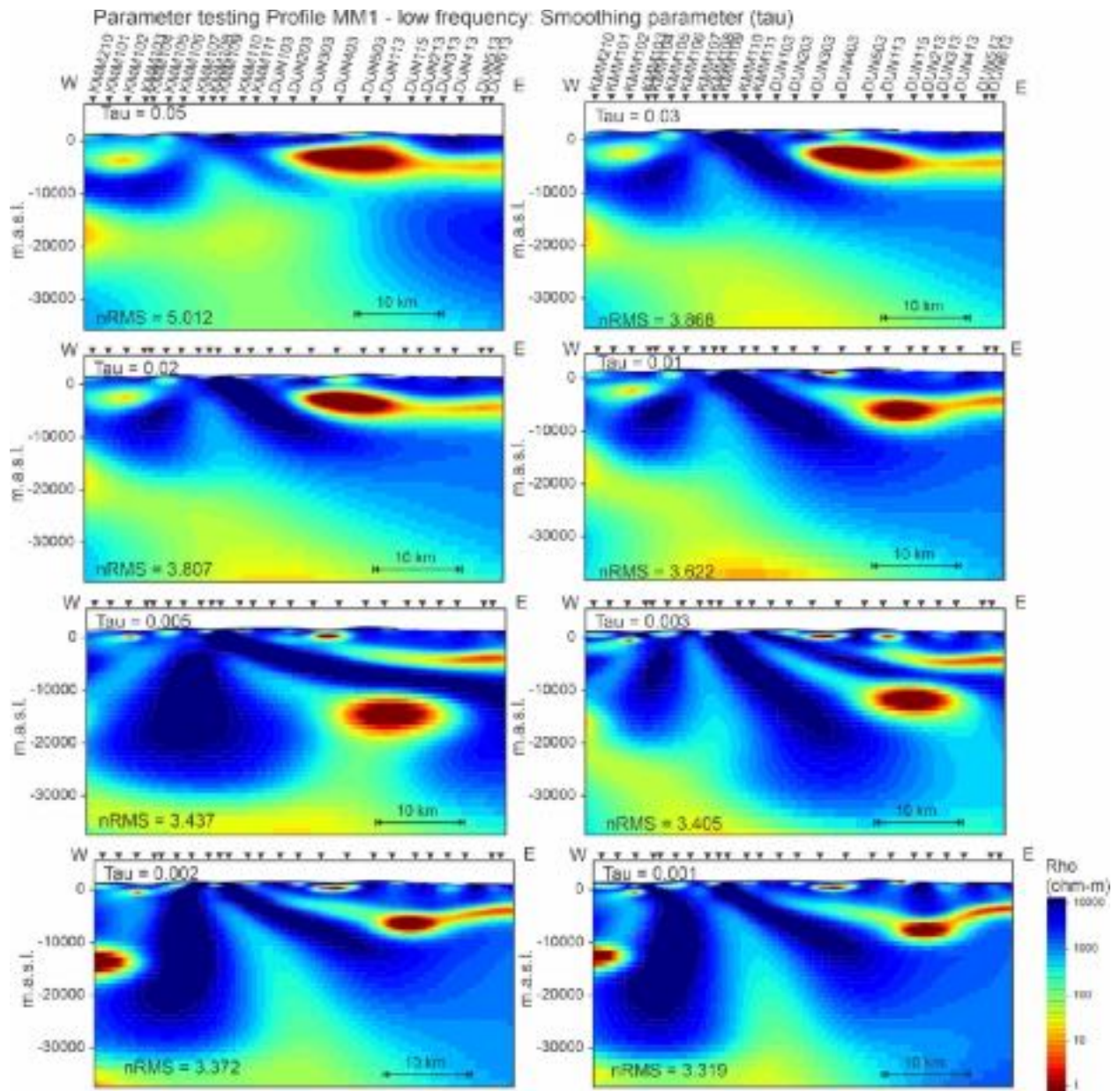


Figure 26: Results of variations of tau (smoothing parameter) on Profile MM1_LF.

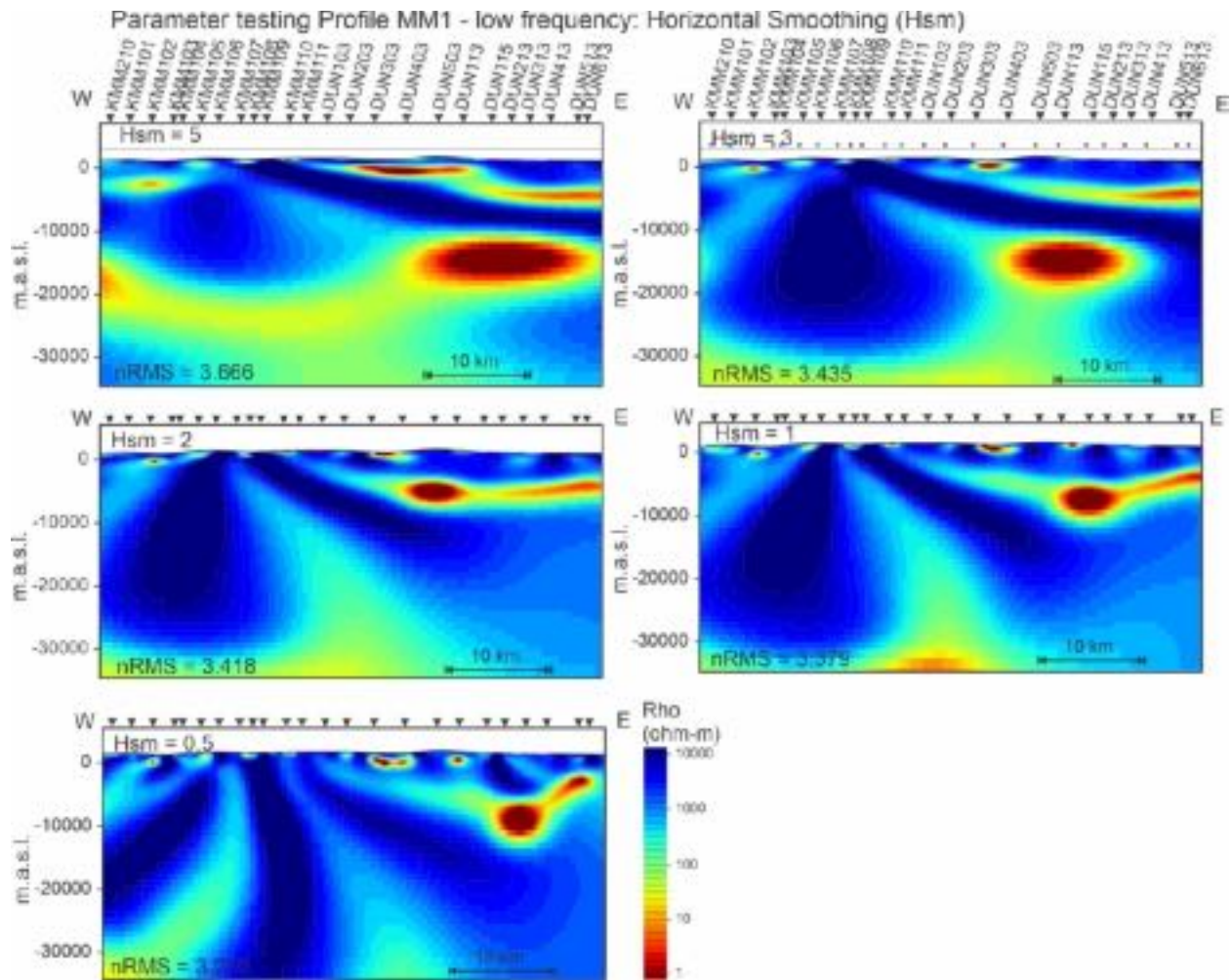


Figure 27: Results of variations of Hsm (horizontal smoothing parameter) on Profile MM1_LF.

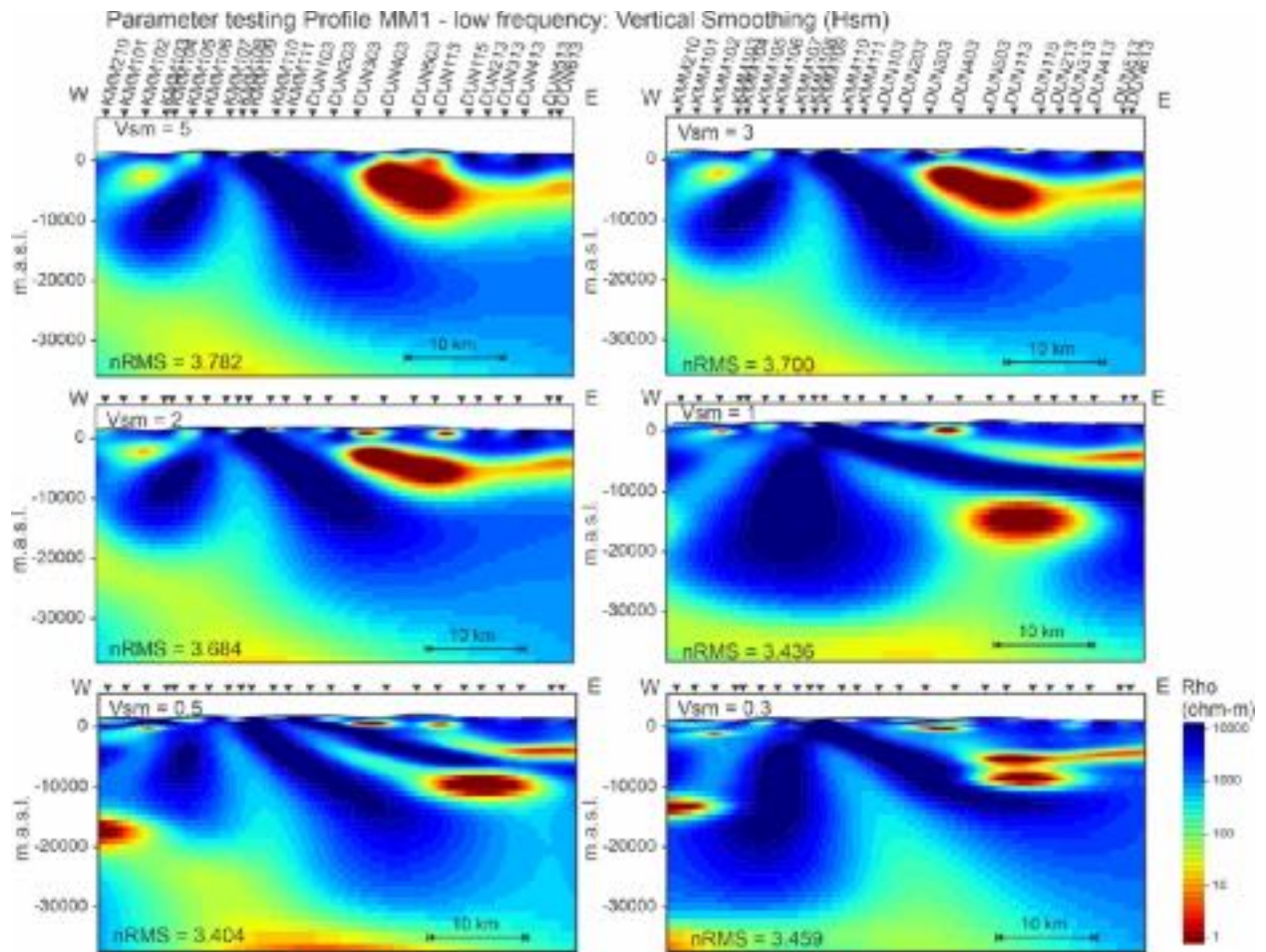


Figure 28: Results of variations of Vsm (vertical smoothing parameter) on Profile MM1_LF.

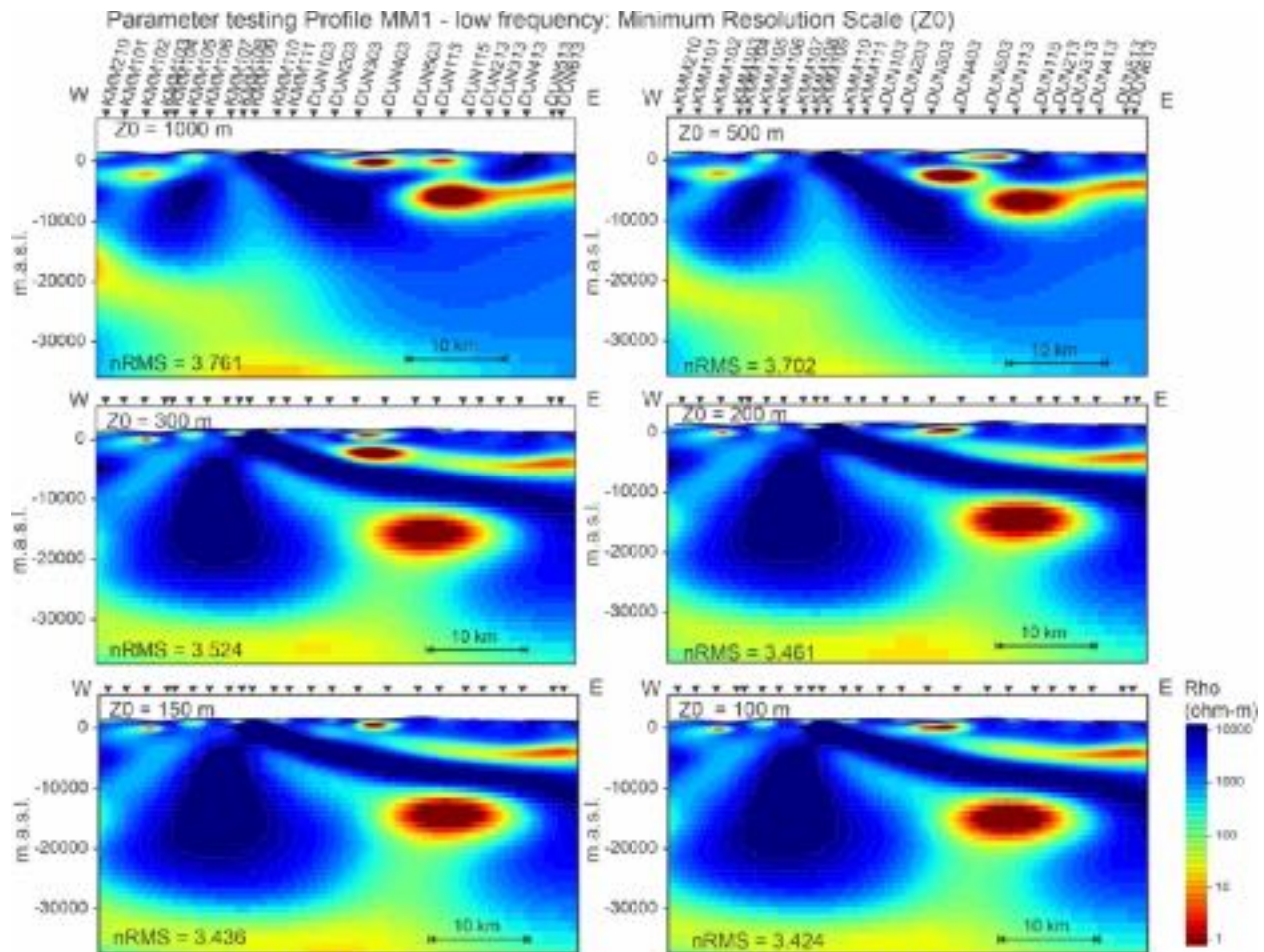


Figure 29: Results of variations of Z_0 (minimum resolution scale) on Profile MM1_LF.

Trade-off curves between the roughness of the model and the fit of the model to the data have been plotted for each smoothing parameter for profile MM1 in the low frequency data range (Figure 30: Plot of RMS misfit versus smoothing parameter values for Profile MM1_LF. The ovals mark the optimal value for final models.). The trade-off curve and resulting models show that the optimal values resulting in the smoothest model with the best fit to the data are: smoothing weight (τ) of 0.005, horizontal smoothing (Hsm) of 3, vertical smoothing (Vsm) of 1, and minimum resolution scale (Z_0) of 200 – 300 m.

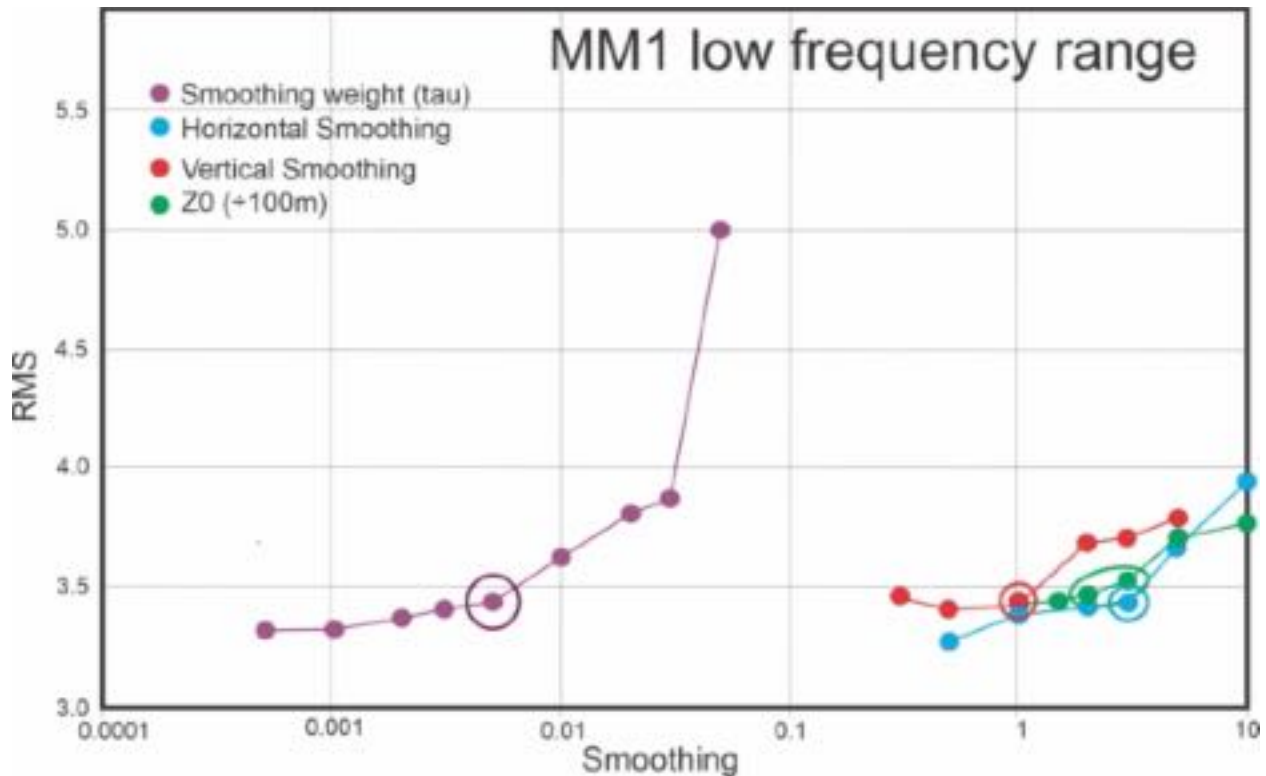


Figure 30: Plot of RMS misfit versus smoothing parameter values for Profile MM1_LF. The ovals mark the optimal value for final models.

4.2.2. Data components and error floor

Models were generated along the profile using various data components and error floors on the apparent resistivities and phases. A series of models were generated using the TM-mode only (i.e., for currents flowing *across* structures), the TE-mode only (currents flowing *along* structures) and inverting the TM and TE-modes jointly together. Apparent resistivity error floors varied from 20% to 8.75% and phases from 5% to 4.375%, and finally the data were inverted for static shift effects at each site.

The overall subsurface resistivity structure imaged when inverting the TM-mode only data is consistent with varying error floors and when inverting for static shift and the nRMS value is low for all models (left column in Figure 31). This suggests that there is minimal static shift in the TM data (or that inversions are accounting for them) and that the error floors derived in the ρ^+ data analysis are appropriate for 2D inversion. Models generated using the TE-mode only data (middle column, Figure 31) image fairly consistent structure beneath the profile for error floors down to 8.75% rho and 4.375% phase. When inverting the data for static shift effects the nRMS value is significantly reduced from 5.308 to 1.827, suggesting that static shift effects may be present and unaccounted for in the TE-mode. A reasonably low nRMS value of 3.058 and structure consistent with the static shift inversion is obtained with an error floor of 20% on TE apparent resistivity. When the TM and TE-mode data are inverted together (right column,

Figure 31) the results of varying error floors are similar to those for the TE-model only inversions. We conclude that a TM apparent resistivity error floor of 8.75% a TE apparent resistivity error floor of 20 %, and phase error floor of 4.375% are most appropriate for these data.

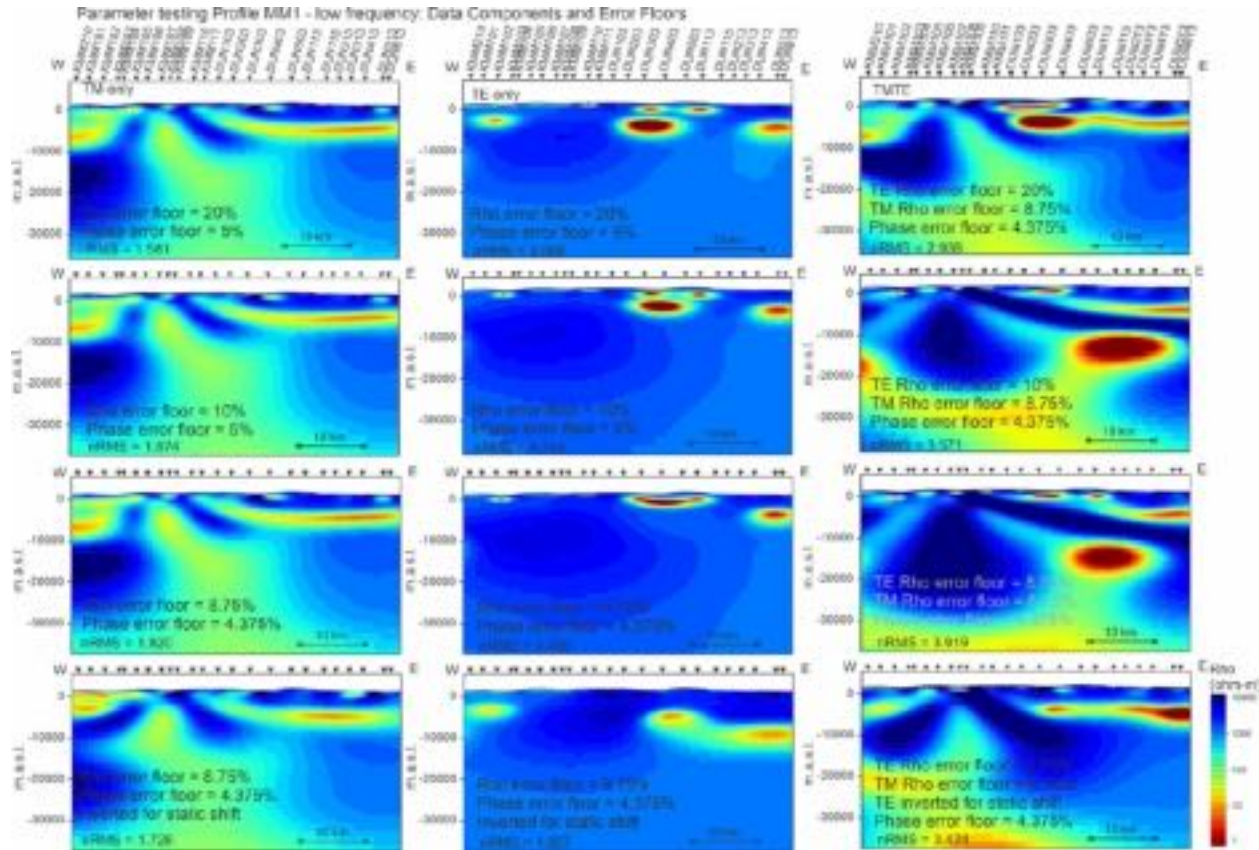


Figure 31: Results of 2D inversions using various data components and error floors for Profile MM1_LF.

4.2.3. Starting Resistivity

Inversions were initiated from various starting models and allowed to run to convergence to observe the effects on the model outputs (Figure 32). Initial models included uniform half-space resistivity values of 100 Ωm , 500 Ωm , 1000 Ωm , 5000 Ωm , and a layered structure of 4000 Ωm to -2000 masl, 10 Ωm from -2000 to -5500 masl underlain by 1000 Ωm . Inversions were run with the starting model as the *a priori* model. Results show strong similarities in the resistivity structure to depths of \sim 8000 masl; however, the deeper structure shows significant variations. This is an indication that the data may not be sensitive to the deeper structure. The lowest nRMS of 2.659 was obtained using a 500 Ωm uniform half-space as the starting model.

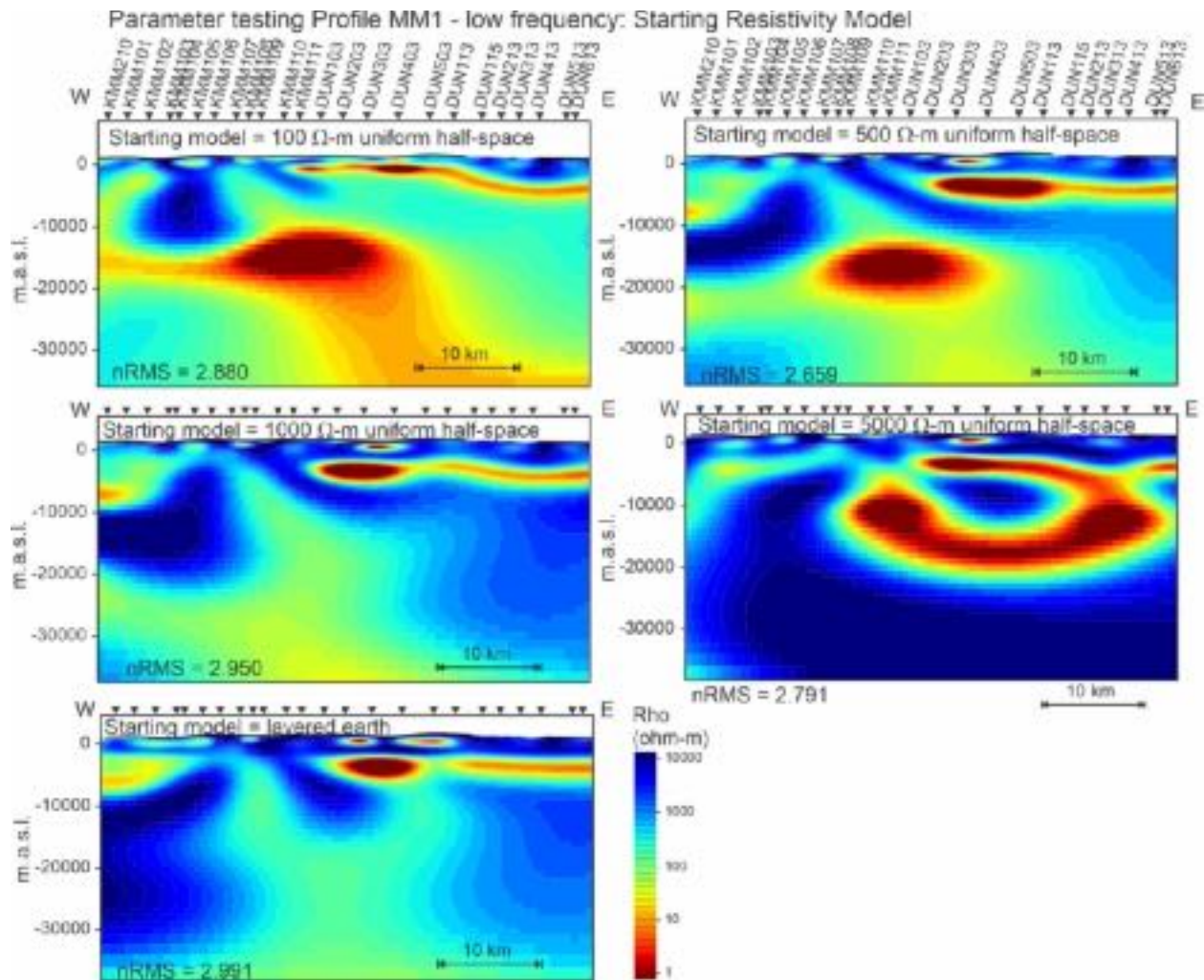


Figure 32: 2D inversion results using varying starting models for Profile MM1_LF.

4.2.4. Adding the vertical field data

Models were generated using the TMTE-only data and using the TMTE+vertical field data (HZ). Inversions were initiated from a 500 Ω m uniform starting model and the *a priori* model was set to current model which uses the previous inversion result as the *a priori* model (Figure 33). Given the limited data deemed invertible of the DUN sites, inversions were initiated using the KMM sites only to observed changes in the model structure. Beneath the western half of the profile (KMM sites) significant differences in model conductivity values are observed at depths $> \sim 15$ km and sensitivity of the data to this area of the model should be tested.

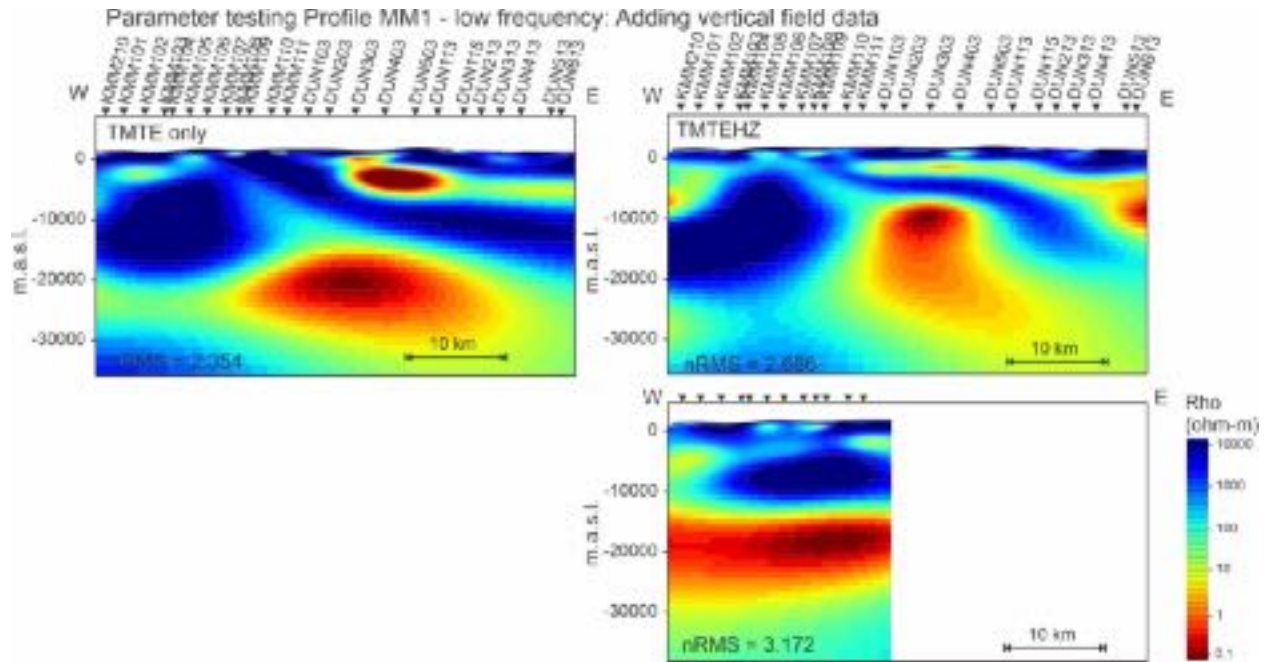


Figure 33: Results of optimal parameters using the TMTE-only data (left) and the TMTEHZ data (right) along Profile MM1_LF.

4.3. Profile SS High Frequencies

4.3.1. Smoothing Parameters

The model results for various values of τ (Figure 34), Hsm (Figure 35), Vsm (Figure 36), and $Z0$ (Figure 37) are shown for Profile SS high frequencies only. Models were generated using the TE-mode and TM-mode data only, with an error floor of 10% on apparent resistivity and 5% on phase, and a starting uniform half-space of 1000 ohm-m. The overall resistivity structure is similar between each of the resulting models.

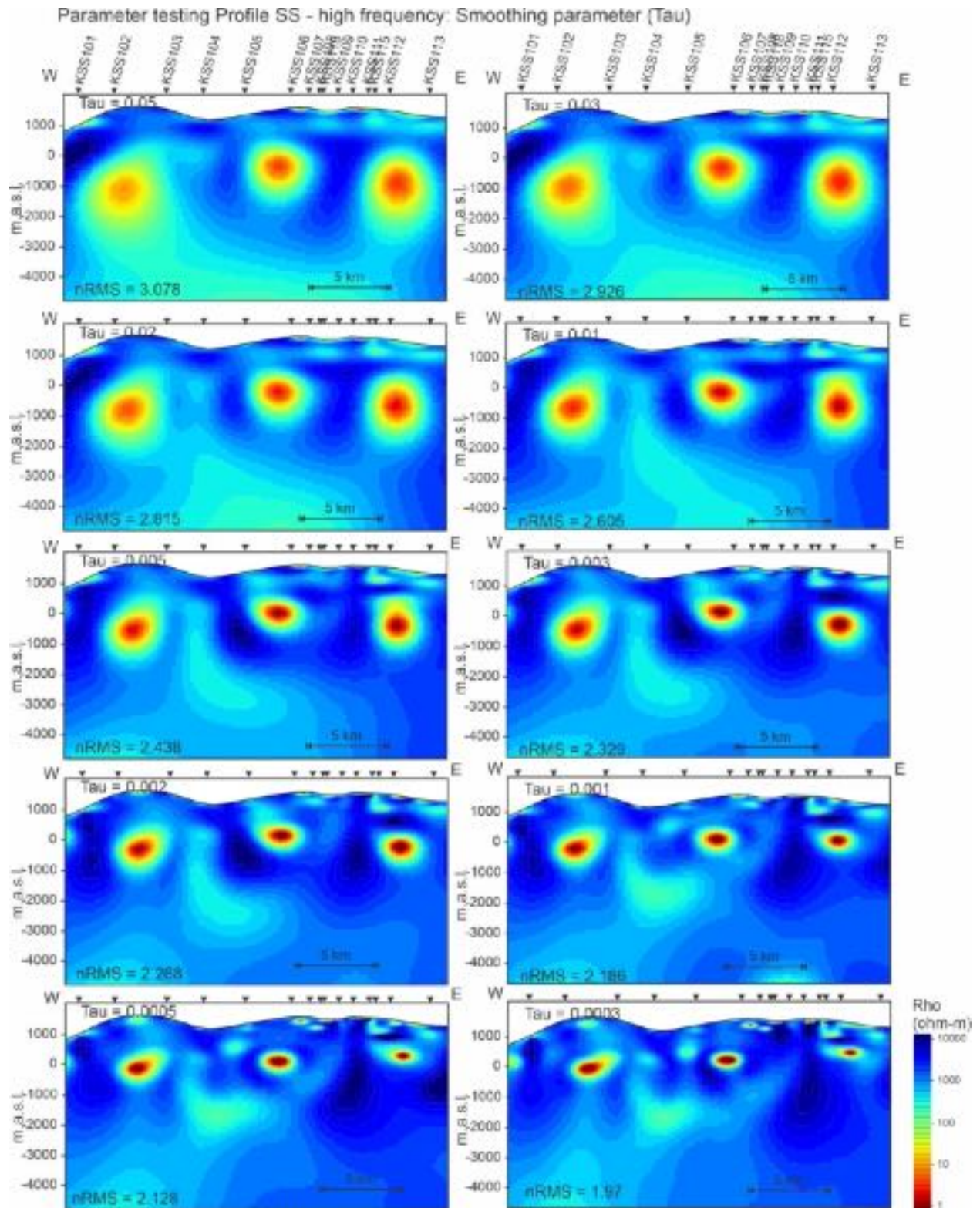


Figure 34: Results of variations of tau (smoothing parameter) on Profile SS_HF.

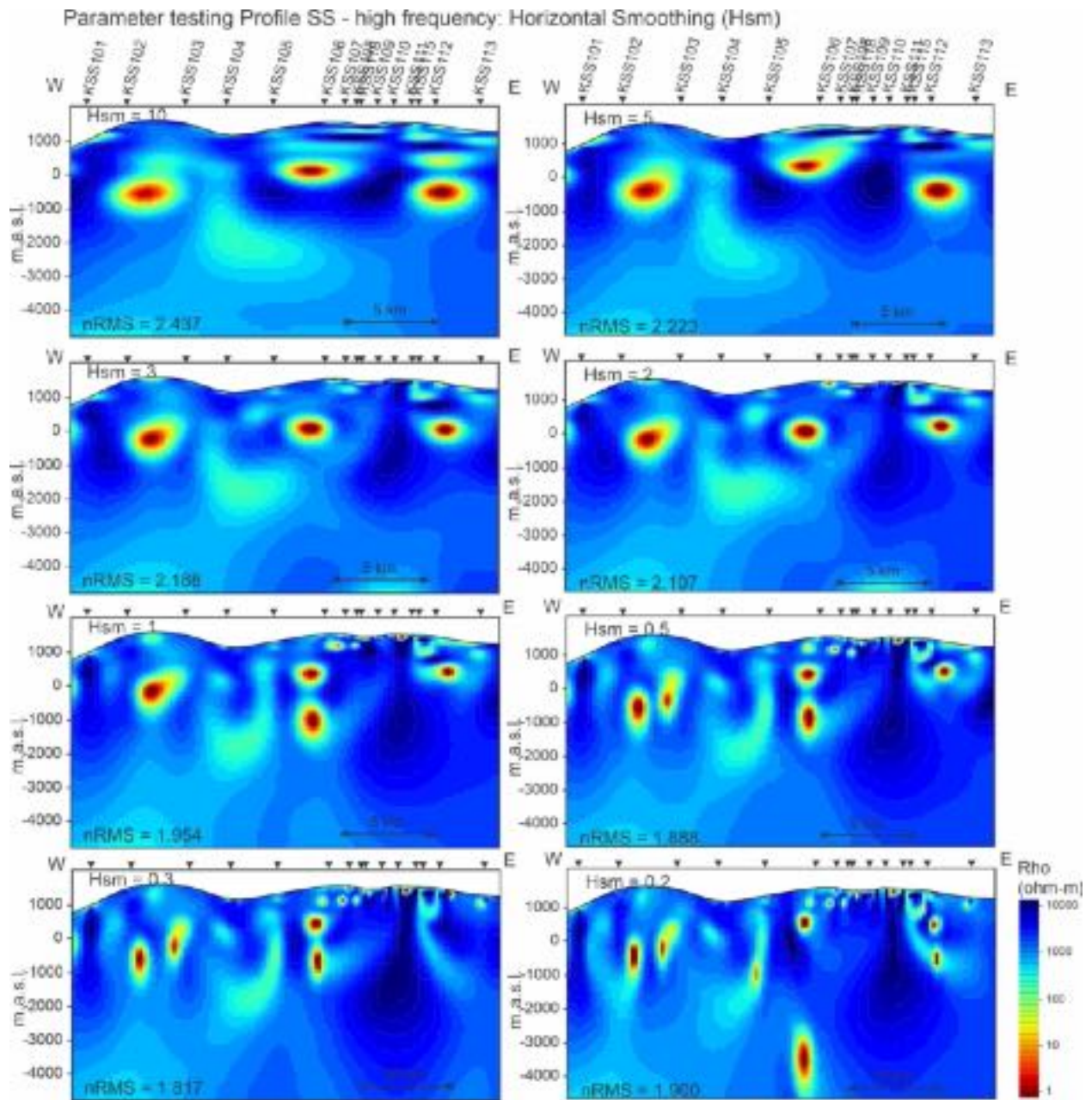


Figure 35: Results of variations of Hsm (horizontal smoothing parameter) on Profile SS_HF.

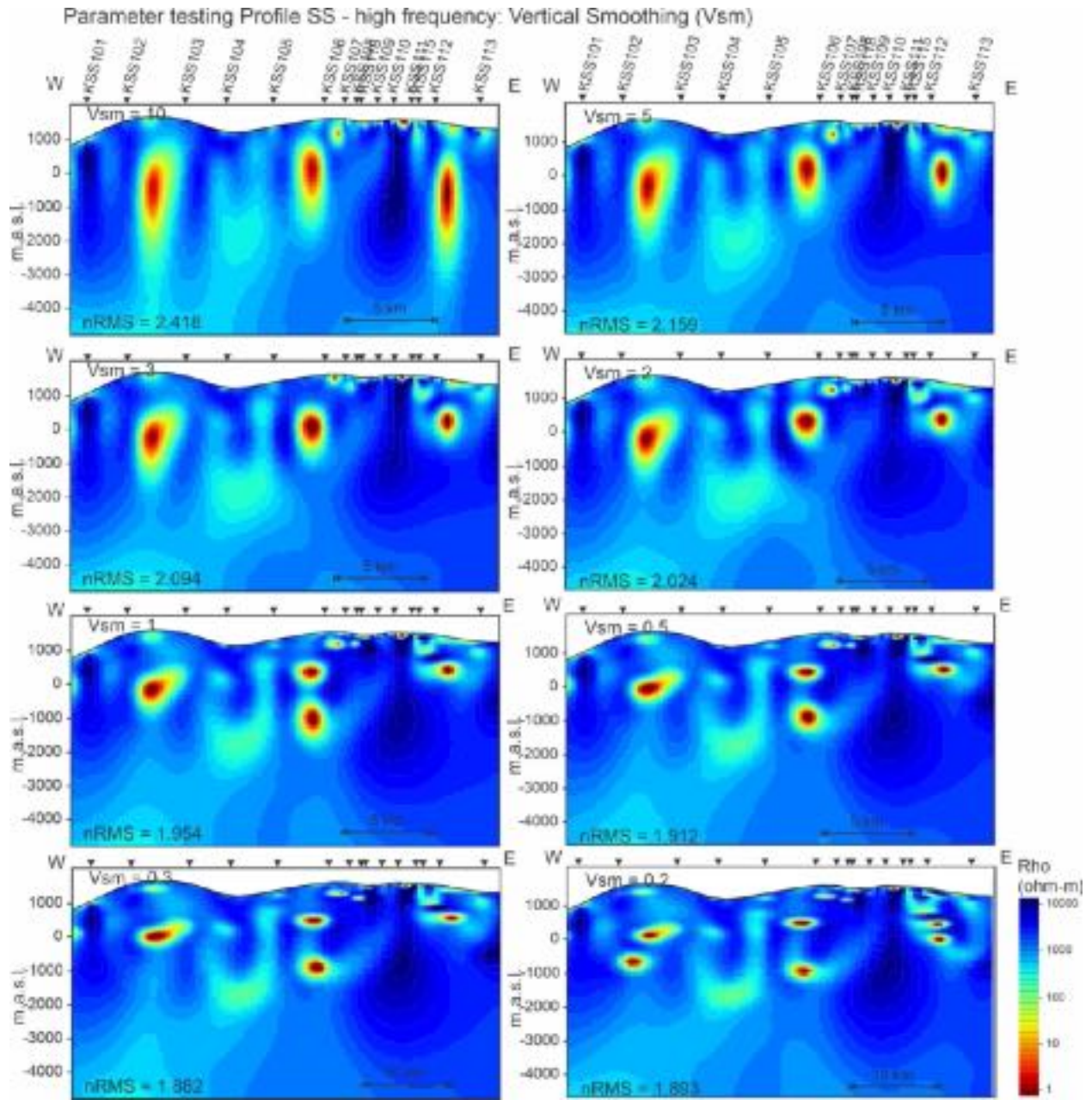


Figure 36: Results of variations of Vsm (vertical smoothing parameter) on Profile SS_HF.

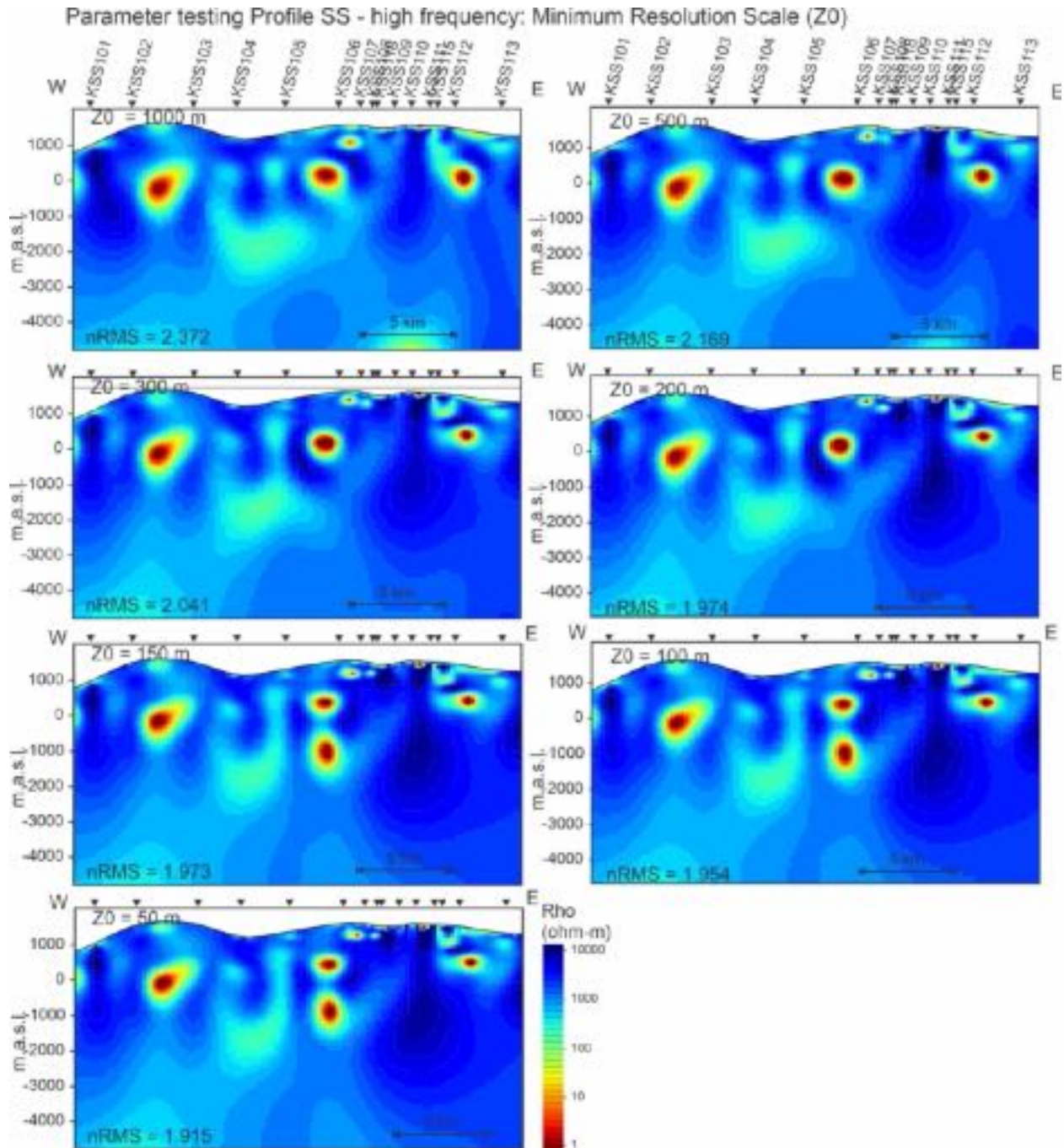


Figure 37: Results of variations of Z_0 (minimum resolution scale) on Profile SS_HF.

Trade-off curves between the roughness of the model and the fit of the model to the data have been plotted for each smoothing parameter for profile SS in the high frequency data range (Figure 38). The trade-off curve for τ shows the nRMS value to continue to drop even with unrealistically low values. Figure 35 shows that the overall structure remains very consistent for values below 0.001 and is an acceptable value. The trade-off curves and resulting models show that the optimal values resulting in the smoothest model with the best fit to the data are: smoothing weight (τ) of 0.001, horizontal smoothing (Hsm) of 1, vertical smoothing (Vsm) of

1, and minimum resolution scale (Z0) of 200 m consistent with those obtained for the high frequency data along MM1.

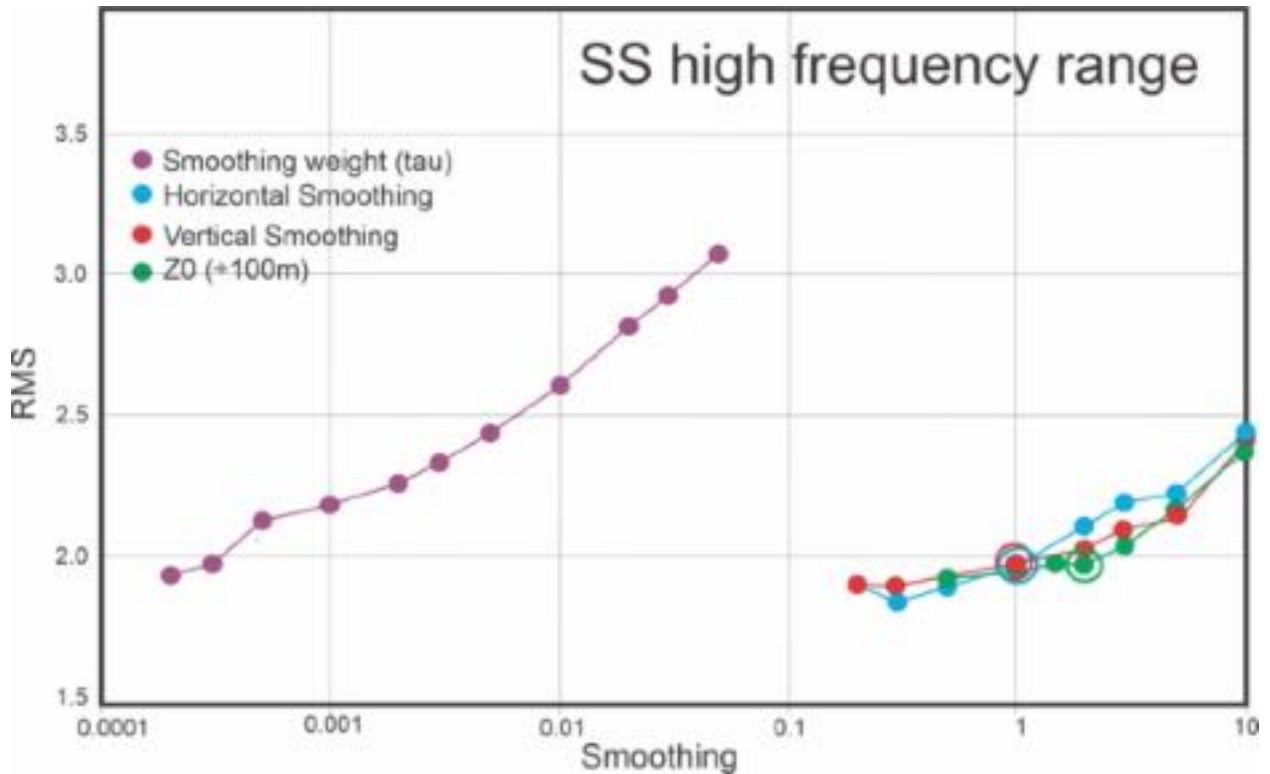


Figure 38: Plot of RMS misfit versus smoothing parameter values for Profile SS_HF. The ovals mark the optimal value for final models.

4.3.2. Data components and error floor

Models were generated along the profile using various data components and error floors on the apparent resistivities and phases. Apparent resistivity error floors varied from 20% to 5.25% and phases from 5% to 2.625%, and finally the data were inverted for static shift effects at each site.

The overall subsurface resistivity structure imaged when inverting the TM-mode only data is consistent with varying error floors and when inverting for static shift and the nRMS value is low for all models (left column in Figure 39). This suggests that there is minimal static shift in the TM data (or that inversions are accounting for them) and that the error floors derived in the ρ^+ data analysis are appropriate for 2D inversion. Models generated using the TE-mode only data (middle column, Figure 39) also image fairly consistent structure beneath the profile. When inverting the data for static shift effects the nRMS value is significantly reduced from 4.540 to 0.760, suggesting that static shift effects may be present and unaccounted for in the TE-mode. A reasonably low nRMS value of 1.899 and structure consistent with the static shift inversion is obtained with an error floor of 20% on TE apparent resistivity. When the TM and TE-mode data are inverted together (right column, Figure) the results of varying error floors are

similar to those for the TE-model only inversions. We conclude that a TM apparent resistivity error floor of 5.25%, a TE apparent resistivity error floor of 20 %, and phase error floor of 2.625% are most appropriate for this data.

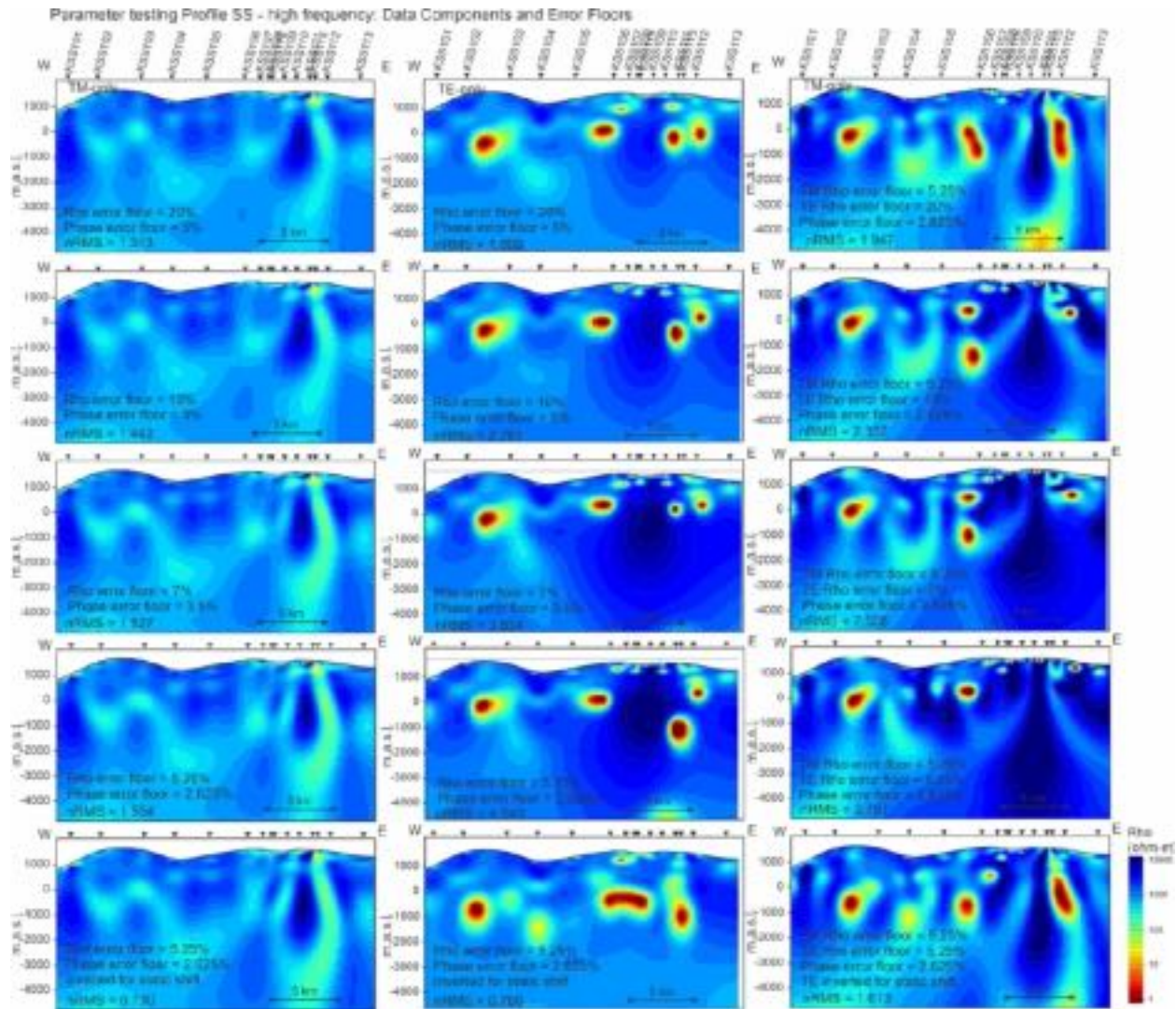


Figure 39: Results of 2D inversions using various data components and error floors for Profile SS_HF.

4.3.3. Starting Resistivity

Inversions were initiated from various starting models and allowed to run to convergence to observe the effects on the model outputs (Figure 40). Initial models included uniform half-space resistivity values of 100 Ωm , 500 Ωm , 1000 Ωm , 5000 Ωm , and a layered structure of 1000 Ωm to 400 masl, 10 Ωm from 400 to -900 masl underlain by 5000 Ωm . Inversions were run with the starting model as the *a priori* model. Results show strong similarities in the resistivity structure to depths of \sim 2000 masl. The lowest nRMS of 1.966 was obtained using a 5000 Ωm uniform half-space as the starting model.

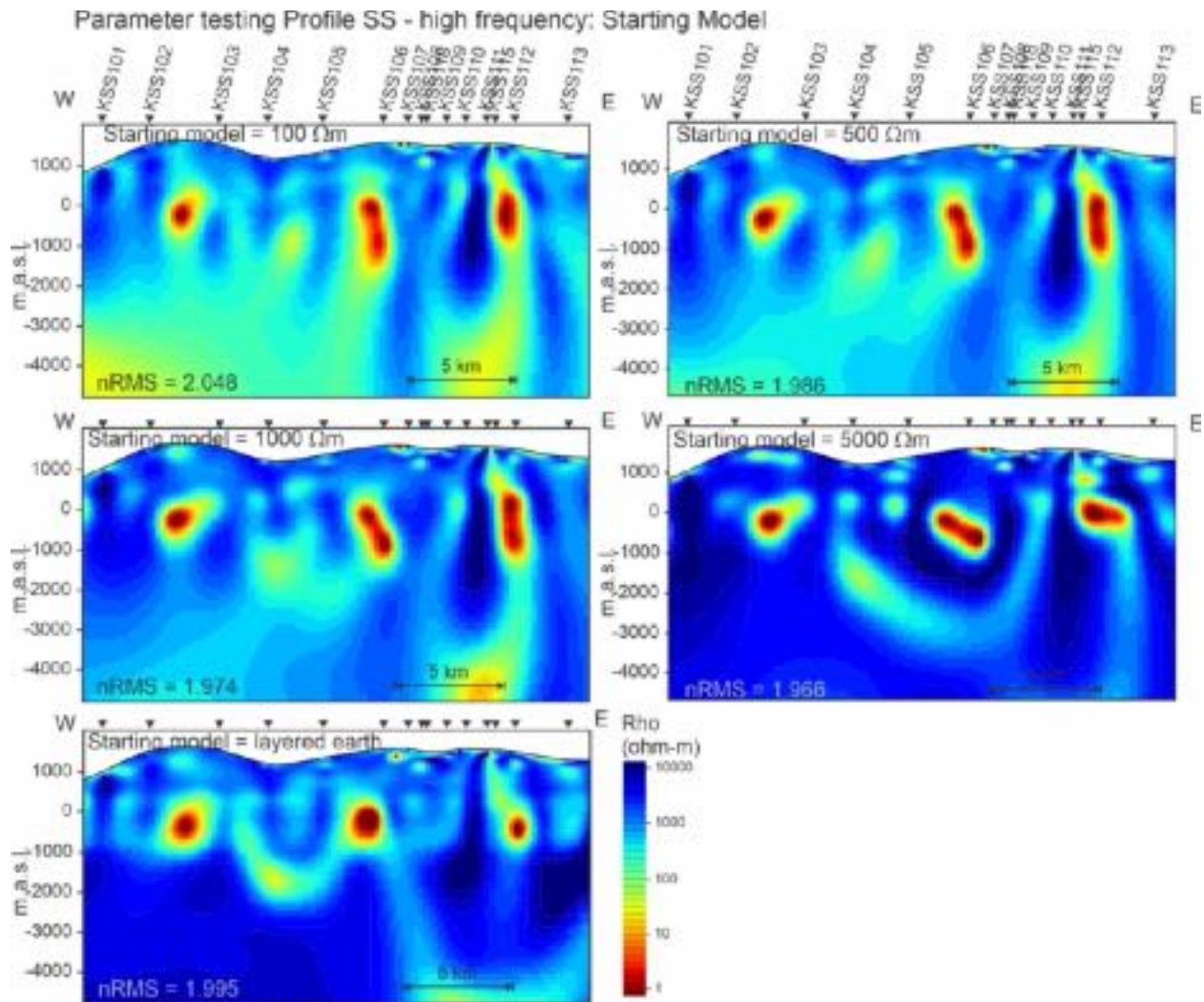


Figure 40: 2D inversion results using varying starting models for Profile SS_HF.

4.3.4. Adding the vertical field data

Models were generated using the TMTE-only data and using the TMTE+vertical field data (HZ). Inversions were initiated from a 5000 Ω m uniform starting model and the *a priori* model was set to current model which uses the previous inversion result as the *a priori* model (Figure 41). There are strong similarities between the two models with a good overall fit to the data. Results indicate complex structural features beneath the entire profile.

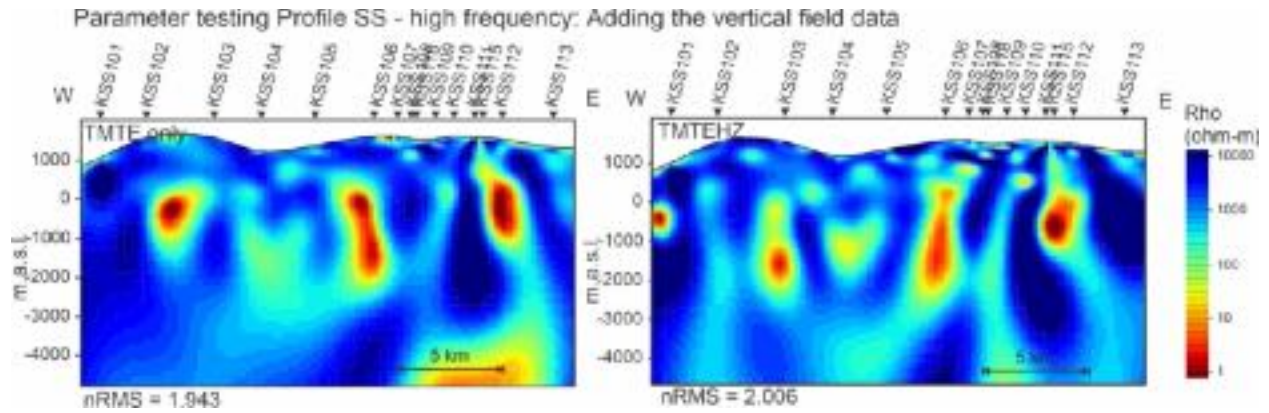


Figure 41: Results of optimal parameters using the TMTE-only data (left) and the TMTEHZ data (right) along Profile SS_HF.

4.4. Profile SP-EW Low Frequencies

4.4.1. Smoothing Parameters

The model results for various values of τ (Figure 42), Hsm (Figure 43), Vsm (Figure 44), and $Z0$ (Figure 45) are shown for Profile SP-EW for the high frequency range only. Models were generated using the TE-mode and TM-mode data only, with an error floor of 10% on apparent resistivity and 5% on phase, and a starting uniform half-space of 1000 Ωm . Several of the inversions appear to get stuck in local minima where there is a significant jump in the nRMS value, and sometimes an increase with lower smoothing value (for example the result for τ 0003 in Figure 42 and $Z0$ of 100 m in Figure 45). Where the nRMS values are reasonable, there are large similarities between the various models.

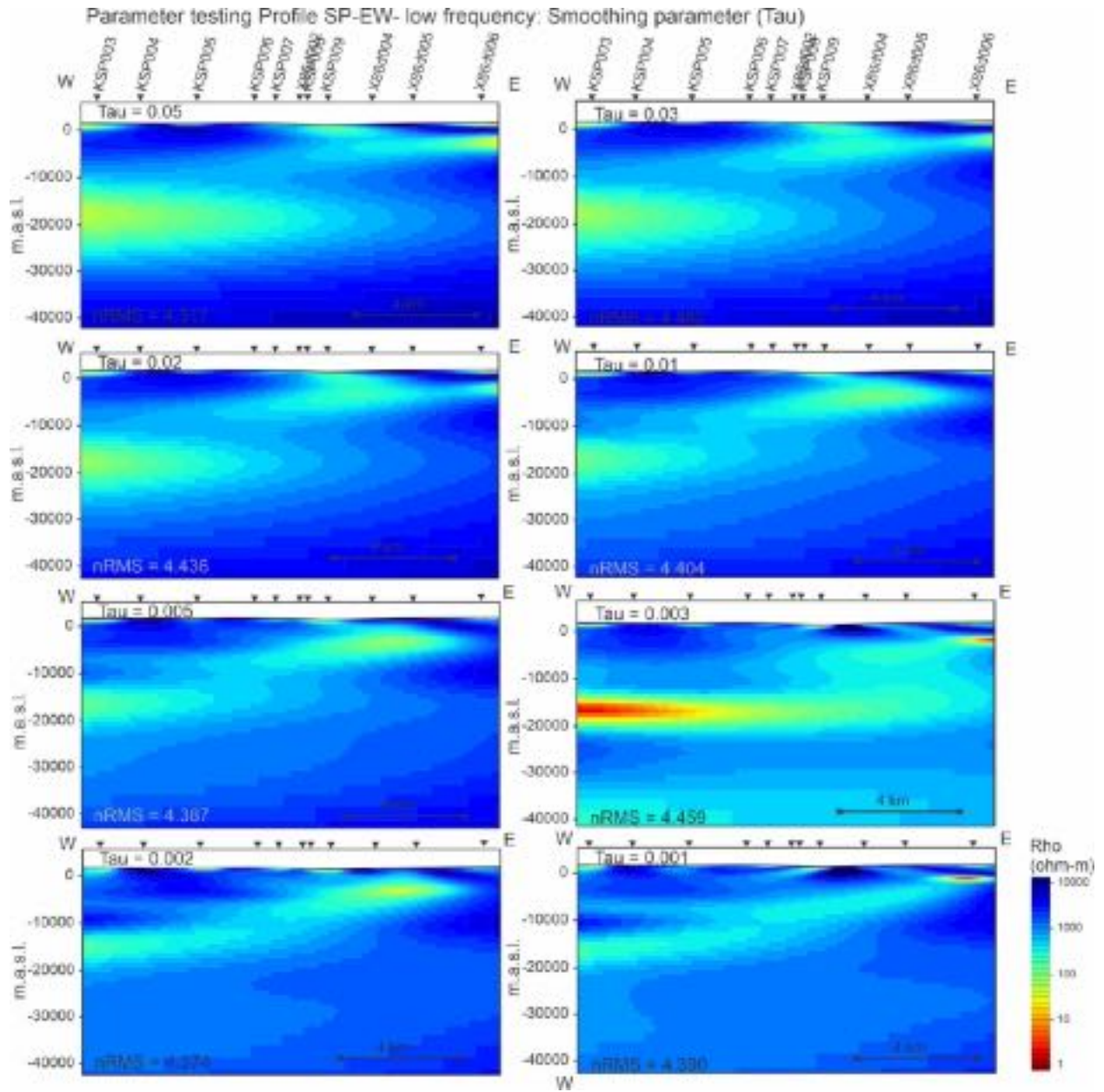


Figure 42: Results of variations of tau (smoothing parameter) on Profile SP-EW_LF.

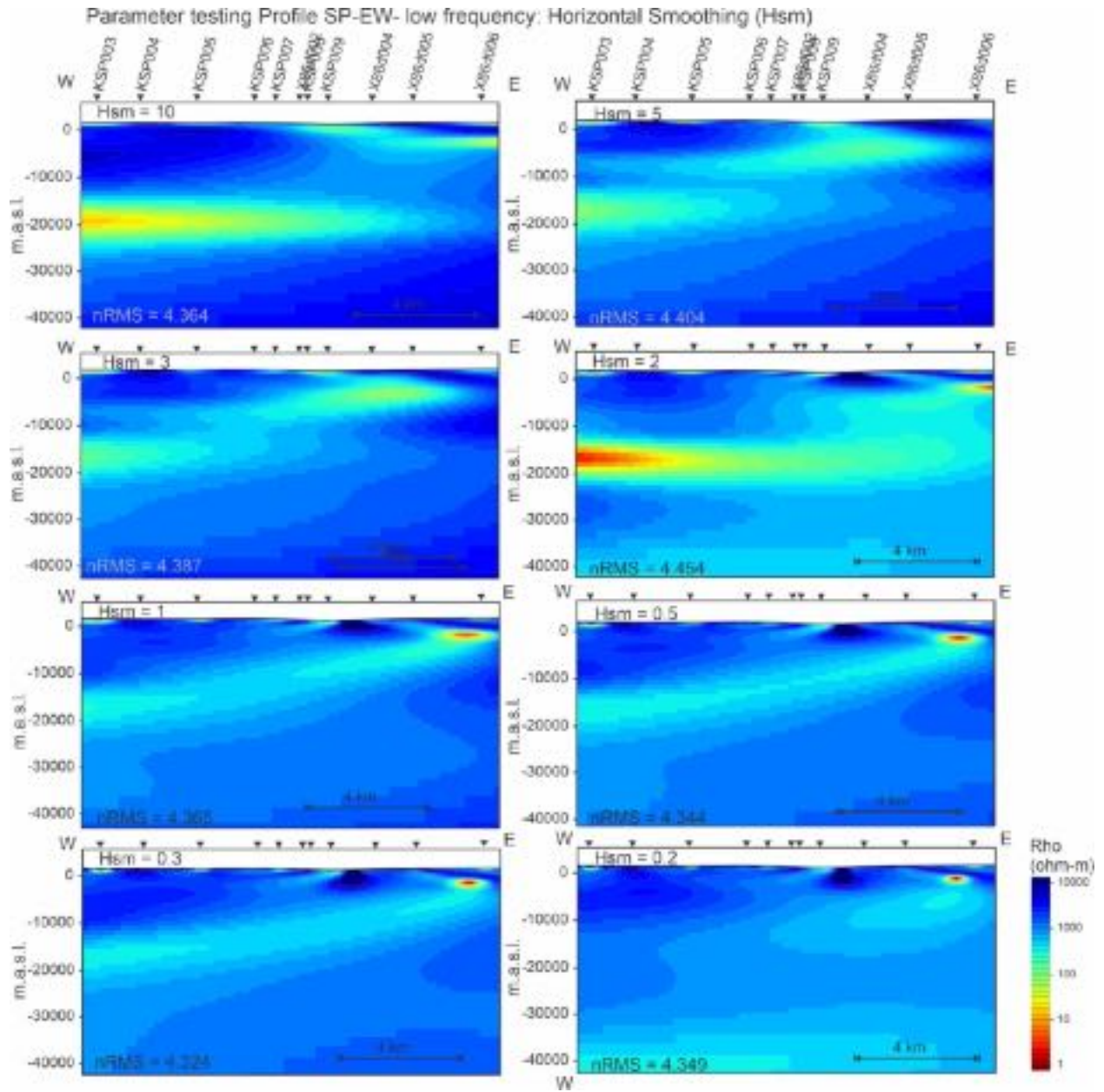


Figure 43: Results of variations of Hsm (horizontal smoothing parameter) on Profile SP-EW_LF.

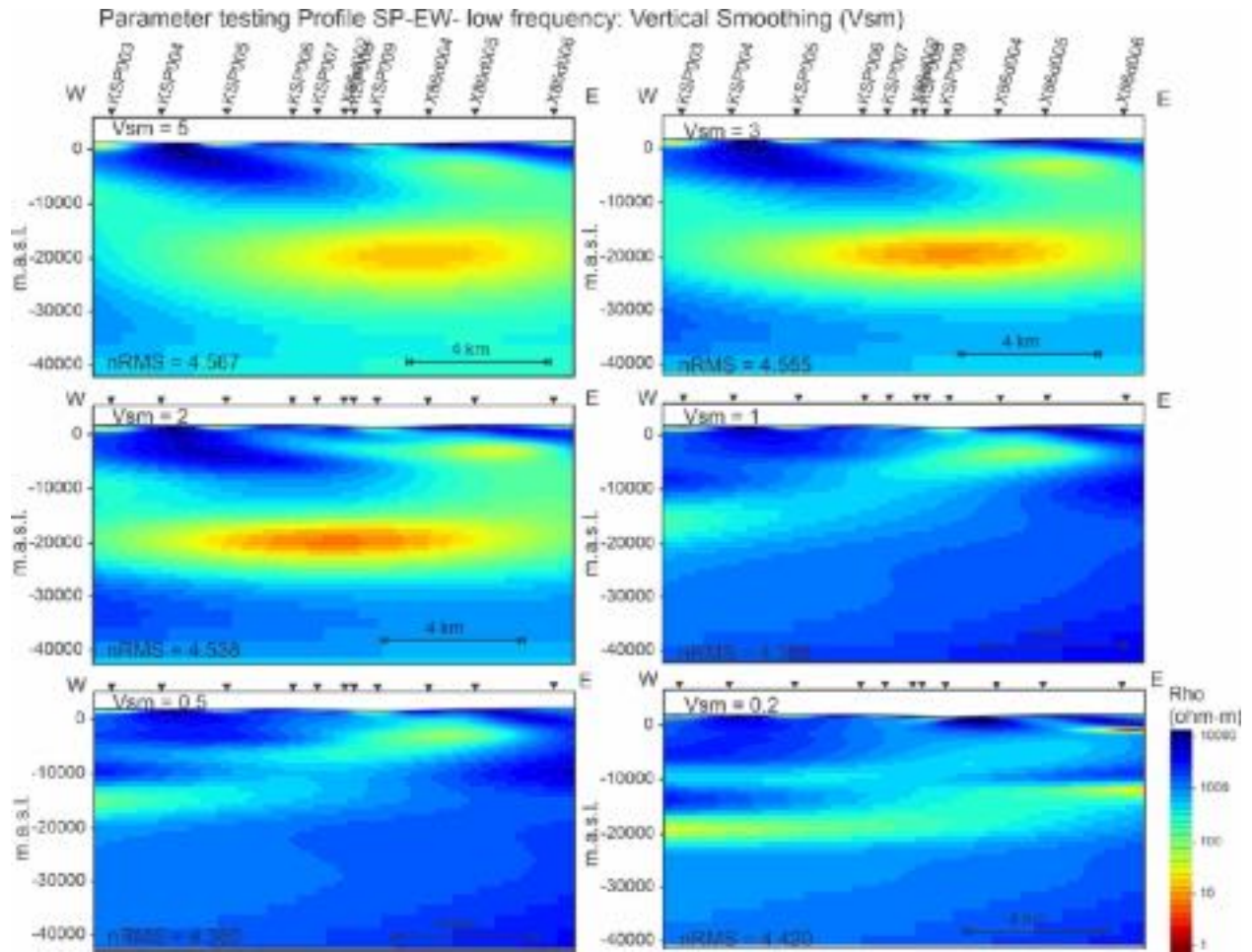


Figure 44: Results of variations of Vsm (vertical smoothing parameter) on Profile SP-EW_LF.

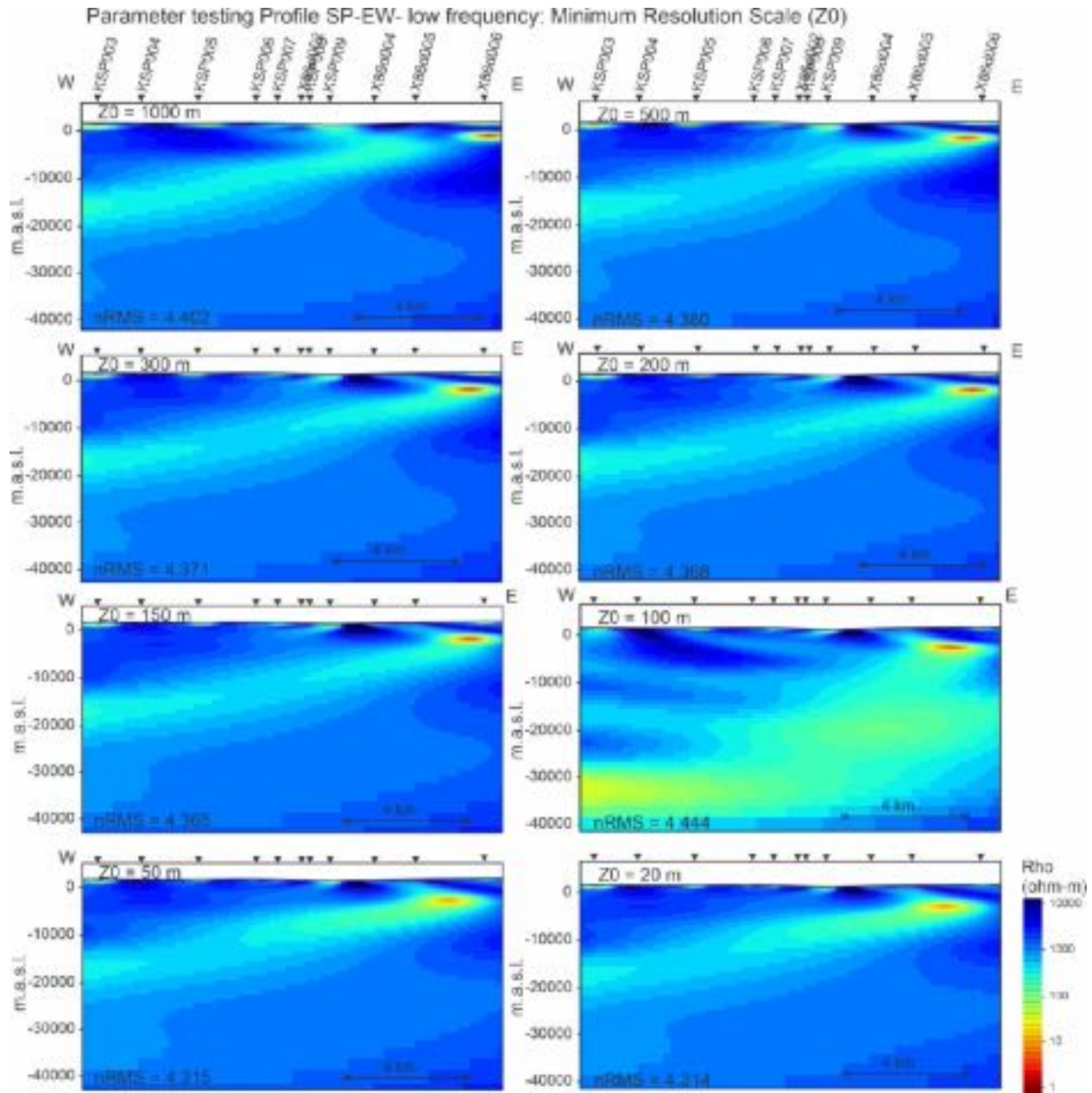


Figure 45: Results of variations of Z0 (minimum resolution scale) on Profile SP-EW_LF.

Trade-off curves between the roughness of the model and the fit of the model to the data have been plotted for each smoothing parameter for profile SP-EW in the low frequency data range (Figure 46). The trade-off curve and resulting models show that the optimal values resulting in the smoothest model with the best fit to the data are: smoothing weight (τ) of 0.002 or 0.005, horizontal smoothing (Hsm) of 0.5 - 1, and vertical smoothing (Vsm) of 1. The minimum resolution scale (Z0) shows a large jump in the nRMS value below 100 m; however, the resulting models (with the exception of the Z0=100 m model) show nearly identical structure indicating that this value has little effect on the overall result (Figure 45).

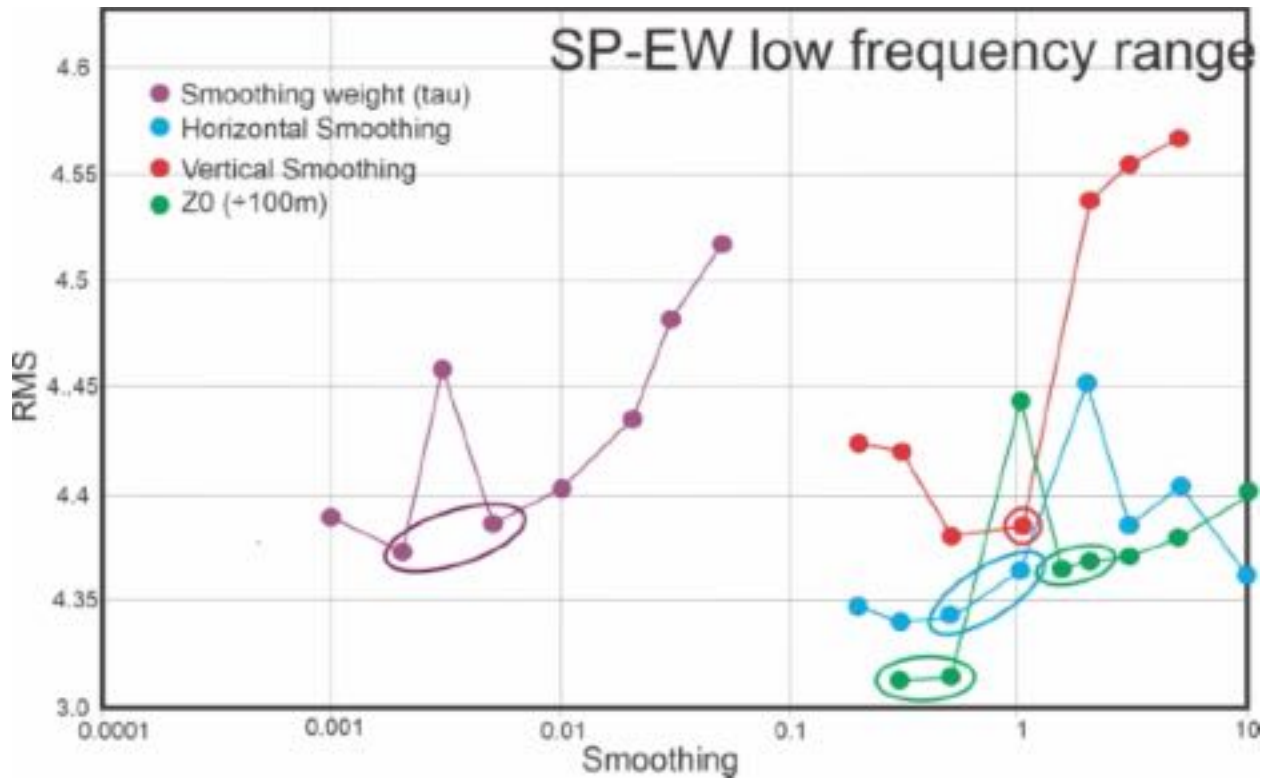


Figure 46: Plot of RMS misfit versus smoothing parameter values for Profile SP-EW. The ovals mark the optimal value for final models.

4.4.2. Data components and error floor

Models were generated along the profile using various data components and error floors on the apparent resistivities and phases. A series of models were generated using the TM-mode only (i.e., for currents flowing *across* structures), the TE-mode only (currents flowing *along* structures) and inverting the TM and TE-modes jointly together. Apparent resistivity error floors varied from 20% to 7% and phases from 5% to 3.75%, and finally the data were inverted for static shift effects at each site.

The overall subsurface resistivity structure imaged when inverting the TM-mode only data is consistent with varying error floors and when inverting for static shift and the nRMS value is low for all models (left column in Figure 47). Models generated using the TE-mode only data (middle column, Figure 47) image fairly consistent structure beneath the profile for error floors down to 7% rho and 3.75% phase; however, the nRMS value is unacceptably high at 7.474. When inverting the data for static shift effects the nRMS value is significantly reduced from 1.818, suggesting that static shift effects are present and unaccounted for in the TE-mode. Aside from one small conductor, the TE-only models are largely devoid of any structure. When the data are inverted for static shift, the conductor is imaged further to the west. When the TM and TE-mode data are inverted together (right column, Figure 47) the results of varying error floors are similar to those for the TE-model only inversions. A reasonably low nRMS value of

2.665 is obtained with and error floor of 20% on TE apparent resistivity. Note that even with 30% error floor the structure remains different from that inverted for static shift. We conclude that a TM apparent resistivity error floor of 7% a TE apparent resistivity error floor of 20%, and phase error floor of 3.75% are most appropriate for this data.

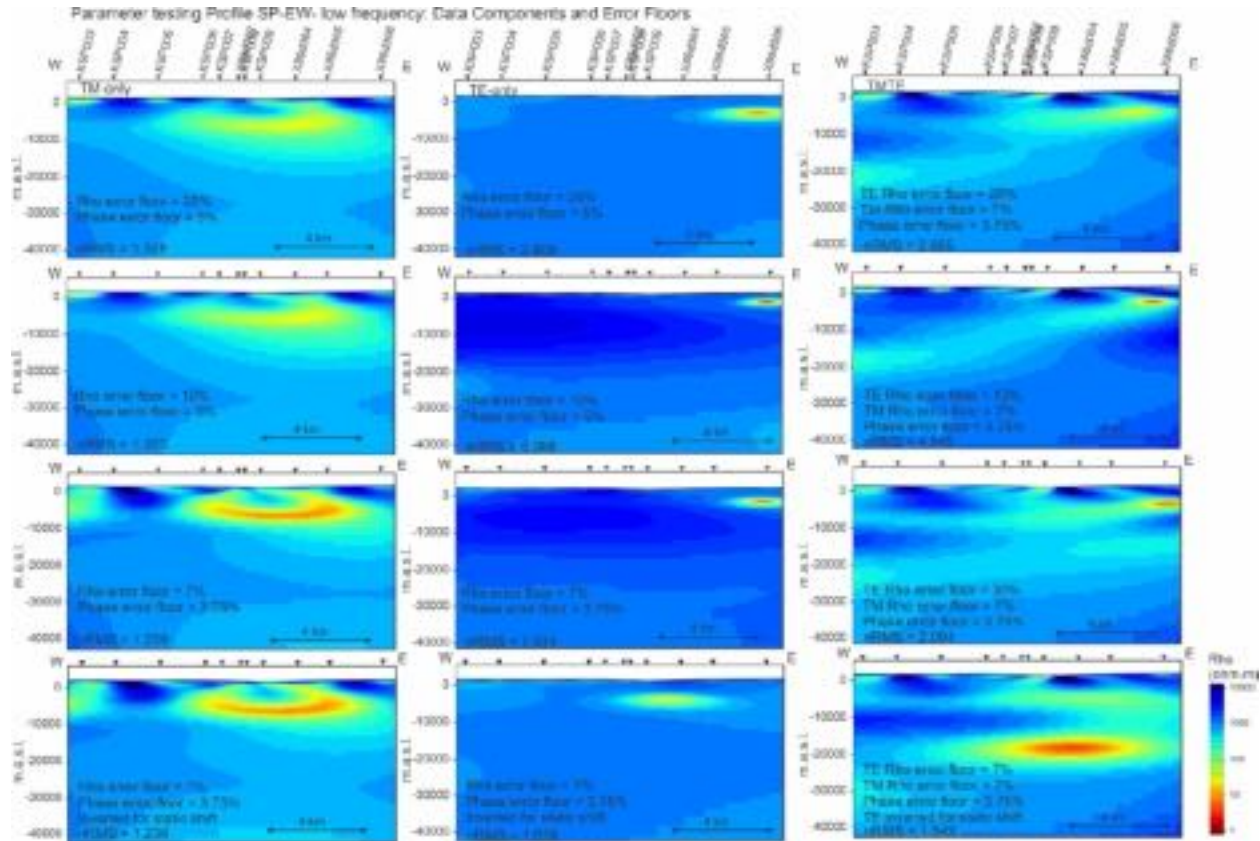


Figure 47: Results of 2D inversions using various data components and error floors for Profile SP-EW_LF.

4.4.3. Starting Resistivity

Inversions were initiated from various starting models and allowed to run to convergence to observe the effects on the model outputs (Figure 48). Initial models included uniform half-space resistivity values of 100 Ωm , 500 Ωm , 1000 Ωm , 5000 Ωm , and a layered structure of 4000 Ωm to -2000 masl, 10 Ωm from -2000 to -5500 masl underlain by 1000 Ωm . Inversions were run with the starting model as the *a priori* model. Results show strong similarities in the resistivity structure to depths of \sim 8000 masl; however, the deeper structure shows significant variations. This is an indication that the data may not be sensitive to the deeper structure. The lowest nRMS of 2.651 was obtained using a 5000 Ωm uniform half-space as the starting model.

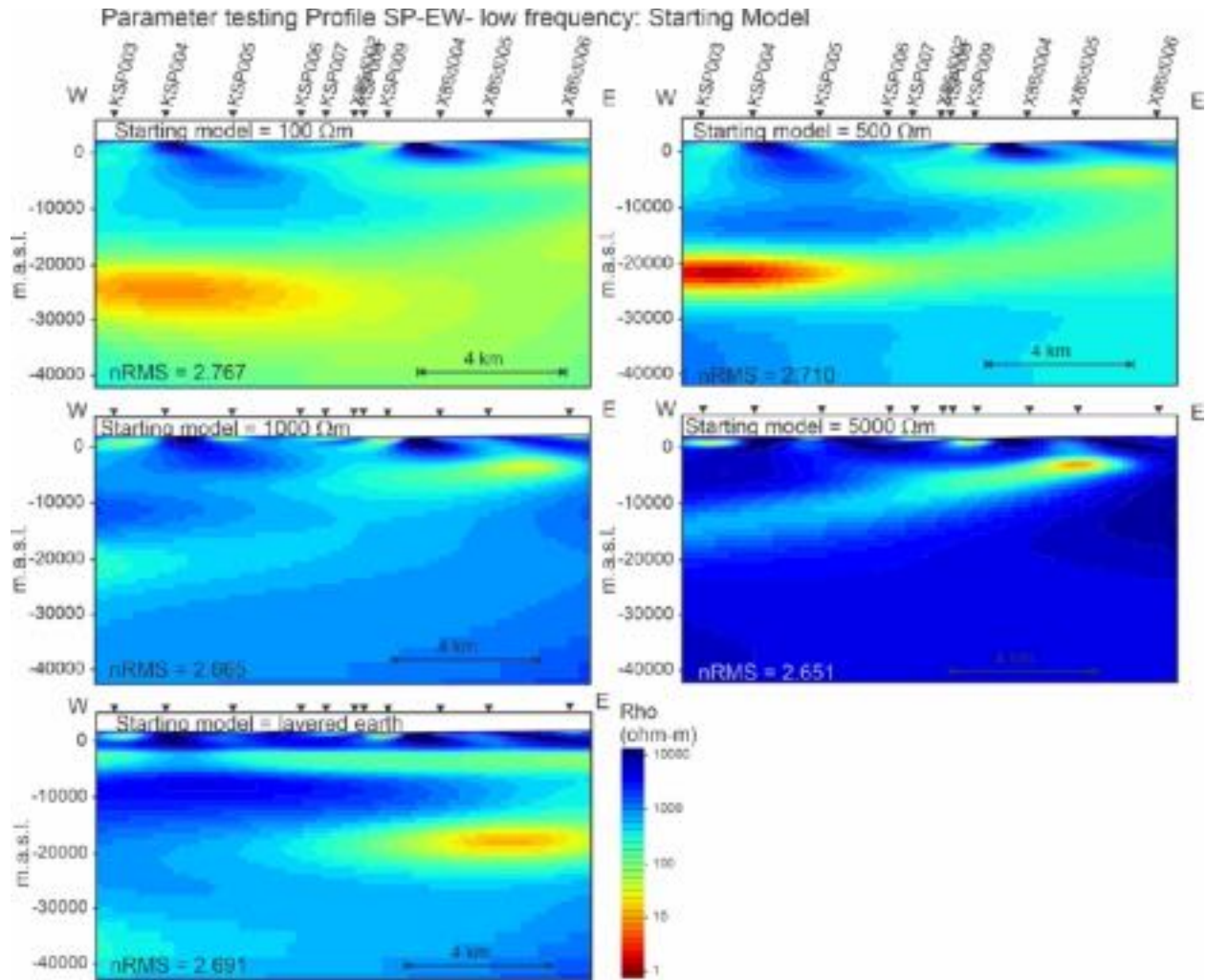


Figure 48: 2D inversion results using varying starting models for Profile SP-EW_LF.

4.4.4. Adding the vertical field data

Models were generated using the TMTE-only data and using the TMTE+vertical field data (HZ). Inversions were initiated from a 5000 Ωm uniform starting model and the *a priori* model was set to current model which uses the previous inversion result as the *a priori* model (Figure 49).

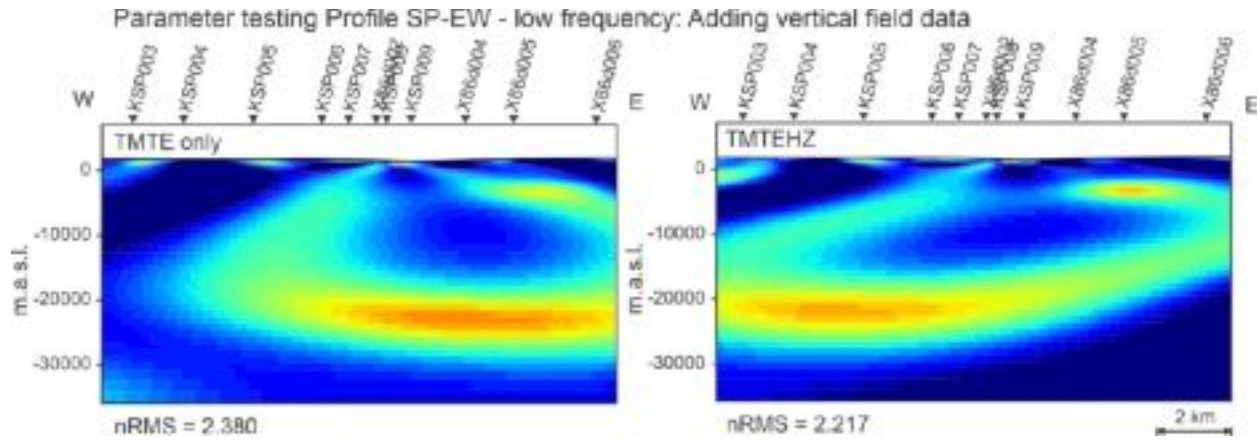


Figure 49: Results of optimal parameters using the TMTE-only data (left) and the TMTEHZ data (right) for the low frequency range along Profile SP-EW_LF.

4.5. Results of parameter testing

The above analyses the optimal parameters for model inversion.

4.5.1. High frequency range

For the high frequency ranges Smoothing values of τ of 0.001, horizontal smoothing (Hsm) of 1, vertical smoothing (Vsm) of 1, and minimum resolution scale ($Z0$) of 200 m were found to be optimal for both profiles MM1 and SS. Analysis of profile MM1 shows a preferred layered starting model whereas profile SS preferred a starting model of 5,000 Ωm ; however, the resulting model structure was very similar for all starting models.

Models have been generated using the TE-mode TM-mode with and without the vertical field data with an error floor of 5.25% on TM apparent resistivity, 20% on TE apparent resistivity, 2.625% on phase, and absolute value of 0.025 on vertical field data. Our preferred model includes the TM-mode, TE-mode, and HZ (vertical field data).

4.5.2. Low frequency range

For the low frequency ranges Smoothing values of τ of 0.005, horizontal smoothing (Hsm) of 1, vertical smoothing (Vsm) of 1, and minimum resolution scale ($Z0$) of 200 m were found to be optimal for both profiles MM1 and SS. Analysis of profile MM1 shows a preferred a starting model of 500 Ωm whereas profile SS preferred a starting model of 5,000 Ωm ; however, the next lowest nRMS value for MM1 was with a starting model of 5,000 Ωm . We have used starting model of 5,000 Ωm as the starting model for the remainder of the low frequency profiles.

Parameter testing of data components and error floors showed that the minimum error floor recommended in the analysis report can be used for the TM-mode apparent resistivities and phases, but that the TE-mode should use an error floor of 20%.

5. Preferred 2D Models

Here we show the preferred model inverted using the distortion corrected responses for the TMTE and vertical field data (HZ) for the high frequency range of 10,000 Hz – 3 Hz, the low frequency range 3 Hz – 0.001 Hz, and the entire frequency range for all profile (see profile map Figure 50). For the entire frequency range, the strike direction and optimal parameters for the high frequency range were applied as the shallow structure is of greater interest. Note that inverting the entire frequency range can help to understand the relationship between the shallow and deeper structure, the independent high and low frequency inversions are deemed more reliable and should be used for interpretation purposes. All models were inverted to use previous inversion results as the *a priori* model.

Difference pseudosections of the measured data and the responses calculation from the preferred high frequency models are shown to highlight areas of the model that do not adequately fit the data and may not be deemed reliable or need to be further tested.

Figure 50: 2D profile map.

5.1. Profile MM1

The high frequency model was generated with the data at a strike angle of N10E from a layered starting model and obtained an overall nRMS value of 1.501 (Figure 51). Error floors of 5.25% on TM-mode apparent resistivity, 20% on TE-mode apparent resistivity, 2.625% for both TM- and TE-mode phase, and an absolute value of 0.02 on the vertical field data were applied. The low frequency model was generated with the data at a strike angle of N55W from a starting model of 500 Ω m. Error floors of 8.75% TM apparent resistivity, 20% TE apparent resistivity, 4.375% phase, and an absolute value of 0.025 on the vertical field data were applied.

Difference pseudosections of the high frequency model show an excellent fit to all components of the data over the entire frequency range (Figure 52).

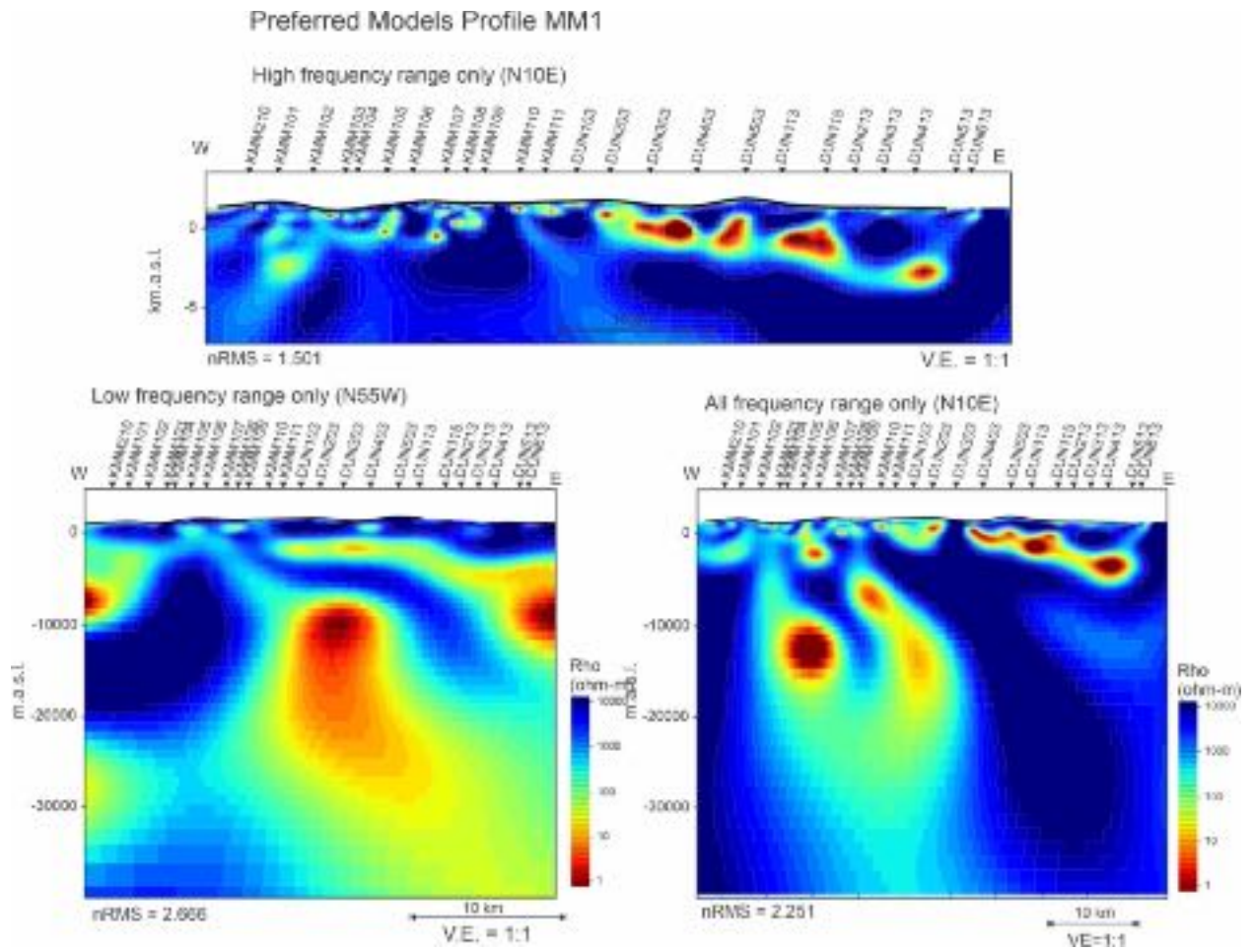


Figure 51: Preferred 2D models along Profile MM1.

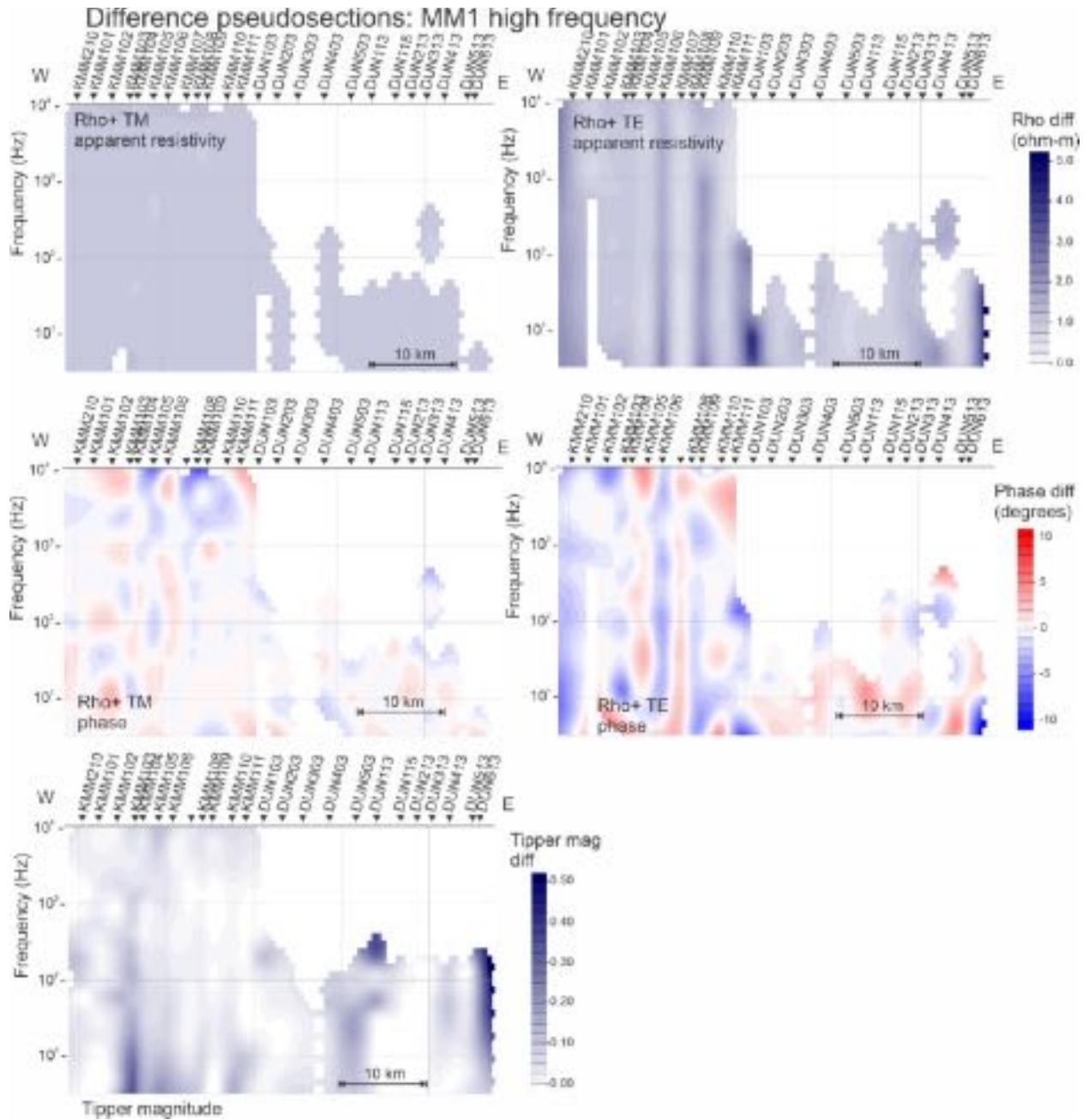


Figure 52: Difference pseudosections for the high frequency model along profile MM1.

5.2. Profile SS

The high frequency model was generated with the data at a strike angle of N12E from a starting model of 5,000 Ωm and yielded an overall nRMS value of 1.958 (Figure 53). Error floors of 5.25% on TM-mode apparent resistivity, 20% on TE-mode apparent resistivity, 2.625% for both TM- and TE-mode phase, and an absolute value of 0.025 on the vertical field data were applied. The low frequency model was generated with the data at a strike angle of N55W from a starting

model of 5000 Ωm . Error floors of 8.75% TM apparent resistivity, 20% TE apparent resistivity, 4.375 % phase, and an absolute value of 0.025 on the vertical field data were applied.

Difference pseudosections of the high frequency model show a reasonable fit to all components of the data over the entire frequency range (Figure 54).

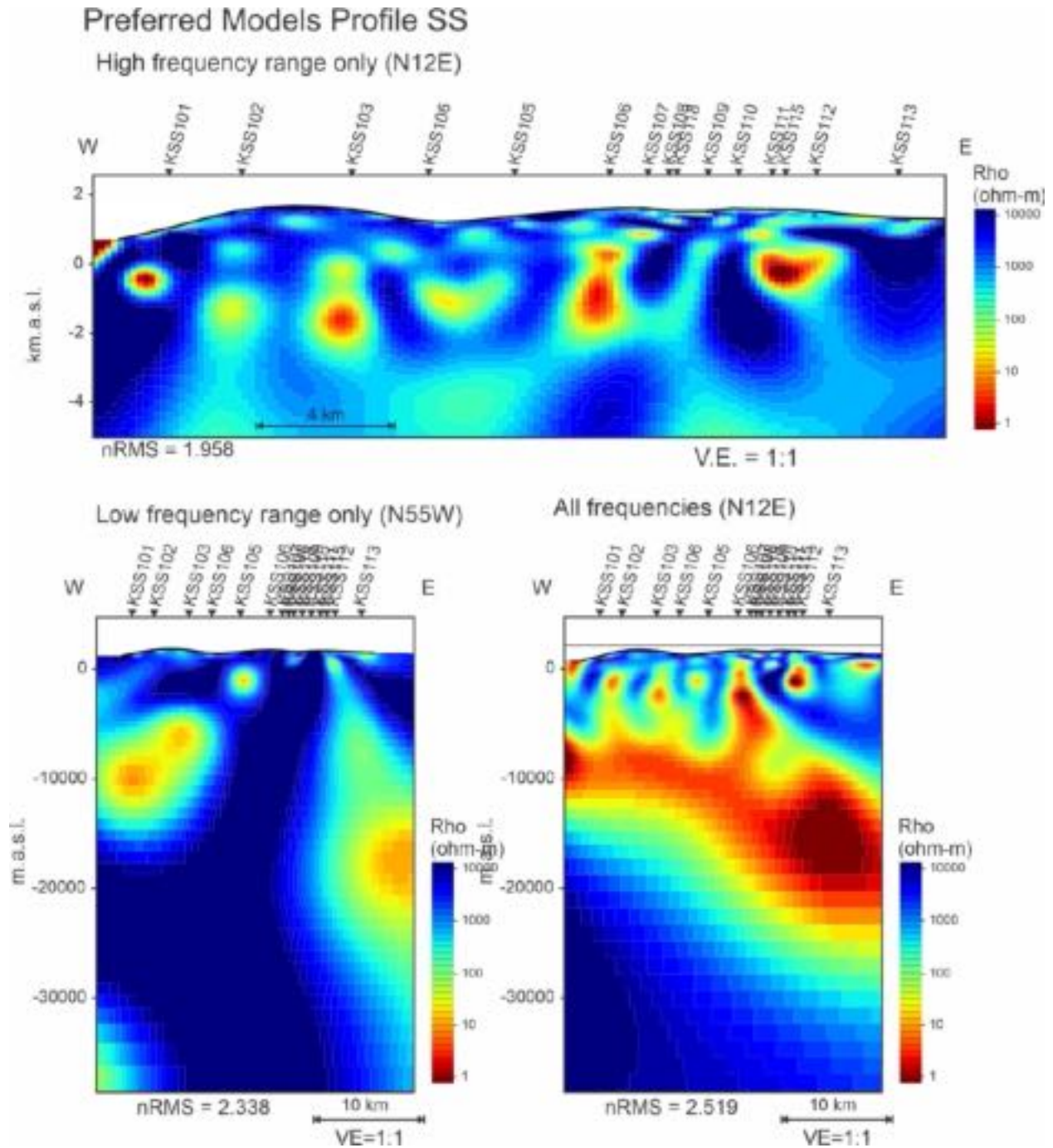


Figure 53: Preferred 2D models along Profile SS.

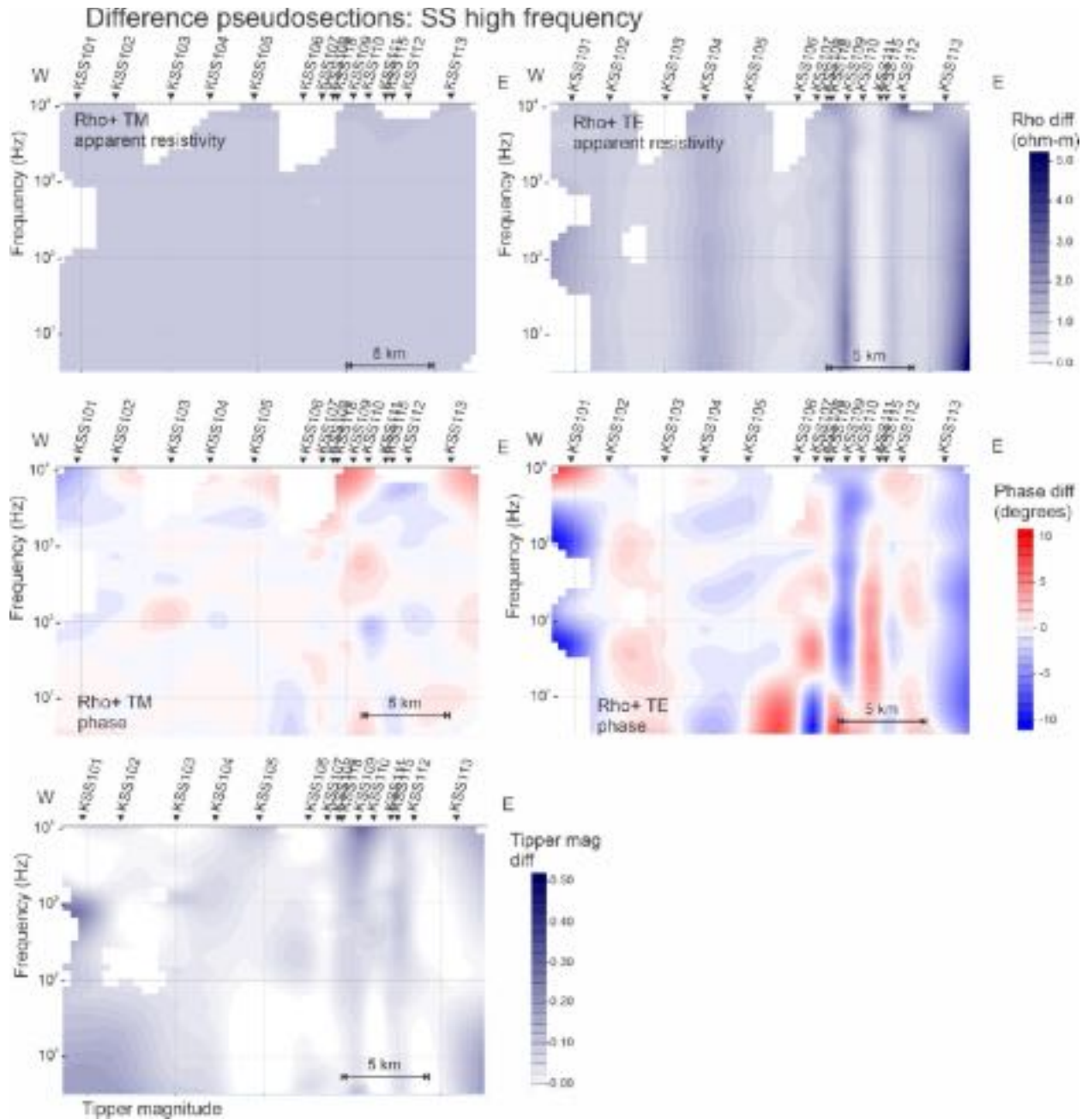


Figure 54: Difference pseudosections for the high frequency model along profile SS.

5.3. Profile SP-EW

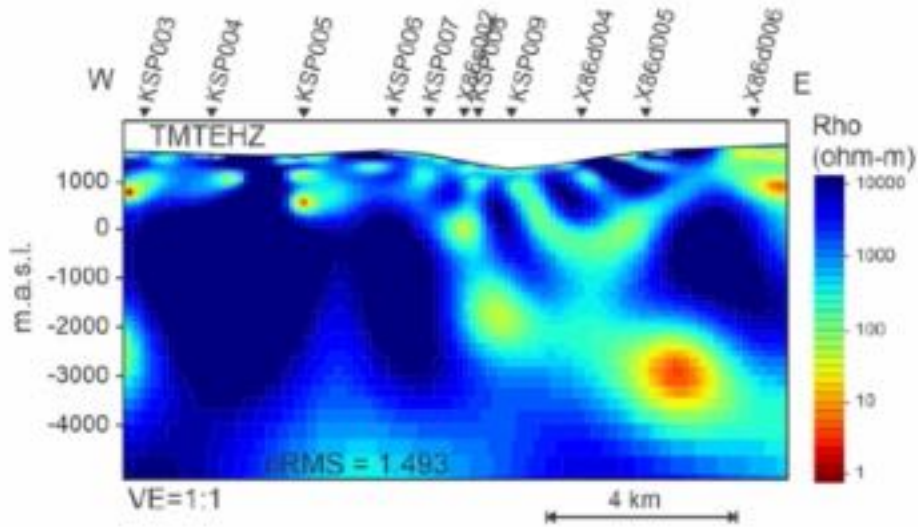
The high frequency model was generated with the data at a strike angle of N45W from a layered starting model and resulted in an overall nRMS value of 1.493 (Figure 55). Error floors of 7% on TM-mode apparent resistivity, 20% on TE-mode apparent resistivity, 3.5% for both TM- and TE-mode phase, and an absolute value of 0.025 on the vertical field data were applied. The low frequency model was generated with the data at a strike angle of N39W from a starting

model of 5000 Ωm . Error floors of 7% TM apparent resistivity, 20% TE apparent resistivity, 3.5 % phase, and an absolute value of 0.025 on the vertical field data were applied.

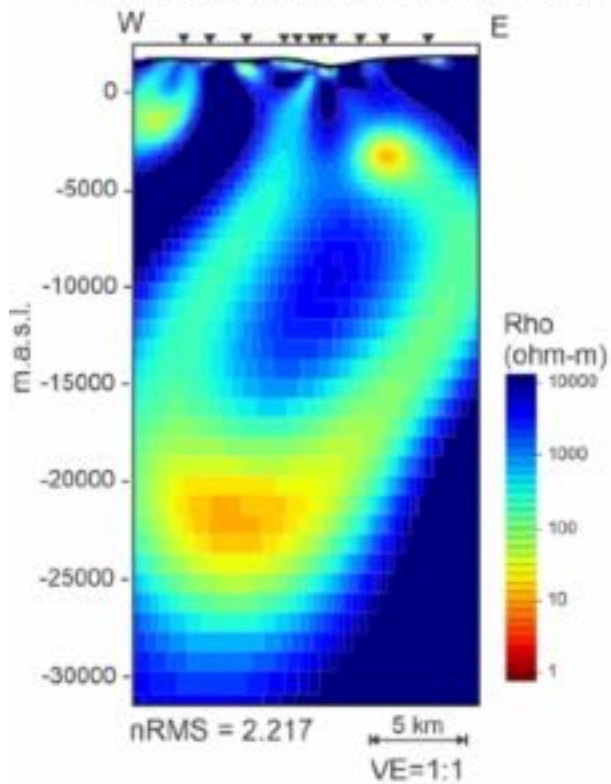
Difference pseudosections of the high frequency model show a reasonable fit to all components of the data over the entire frequency range (Figure 56). One exception is the TE-mode apparent resistivity at site KSP004. The increased difference between the model response and data is relatively uniform over the whole frequency range. This is typical of static shift effects likely present at site KSP004.

Preferred Models: Profiles SP-EW

High frequency range only (N45W)



Low frequency range only (N39W)



All frequencies (N45W)

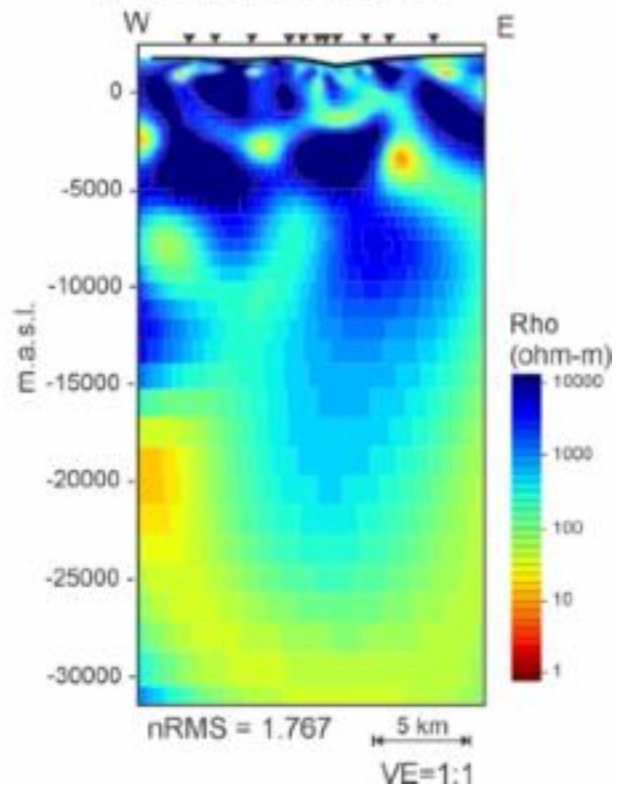


Figure 55: Preferred 2D models along Profile SP-EW.

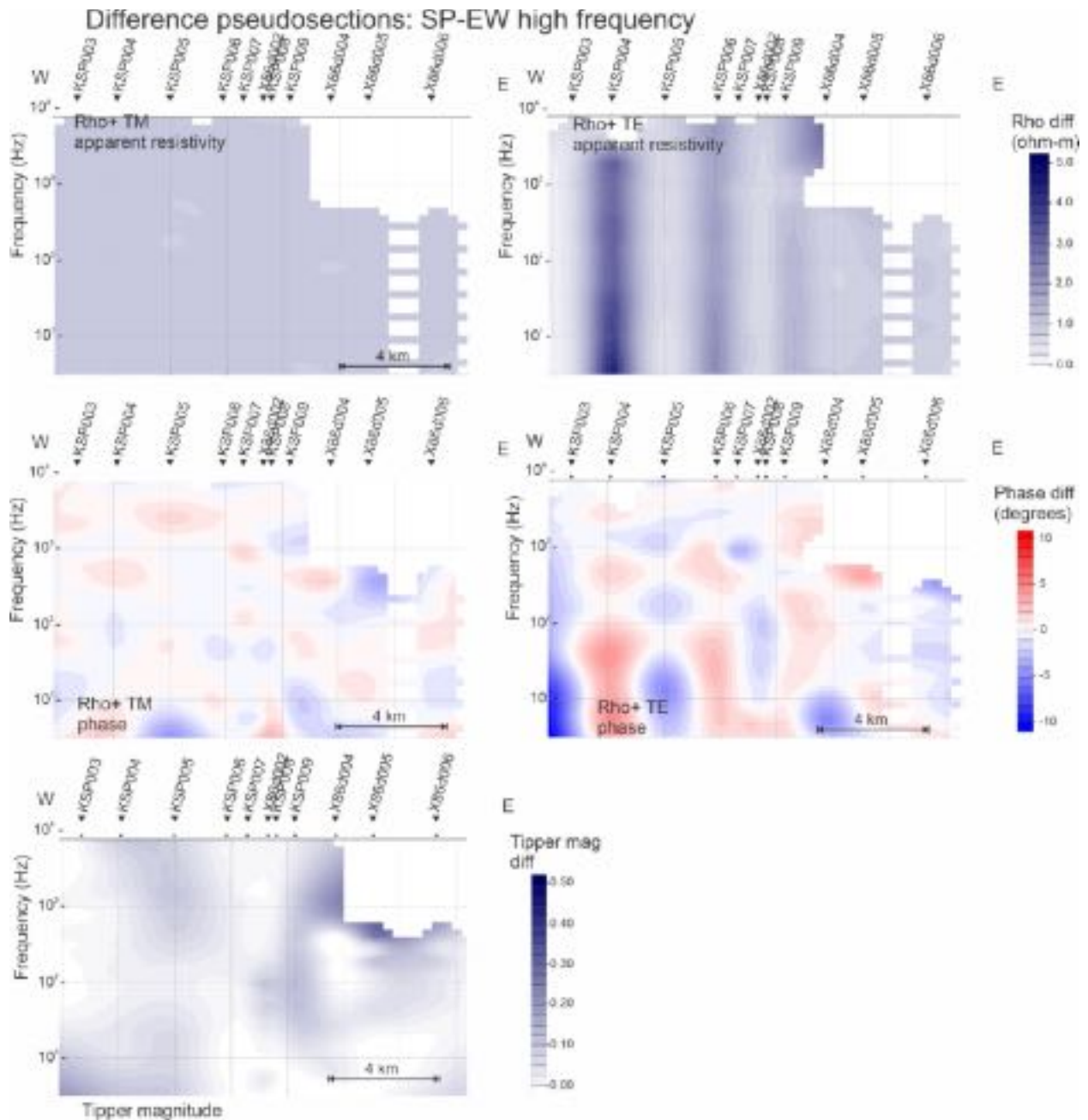


Figure 56: Difference pseudosections for the high frequency model along profile SP-EW.

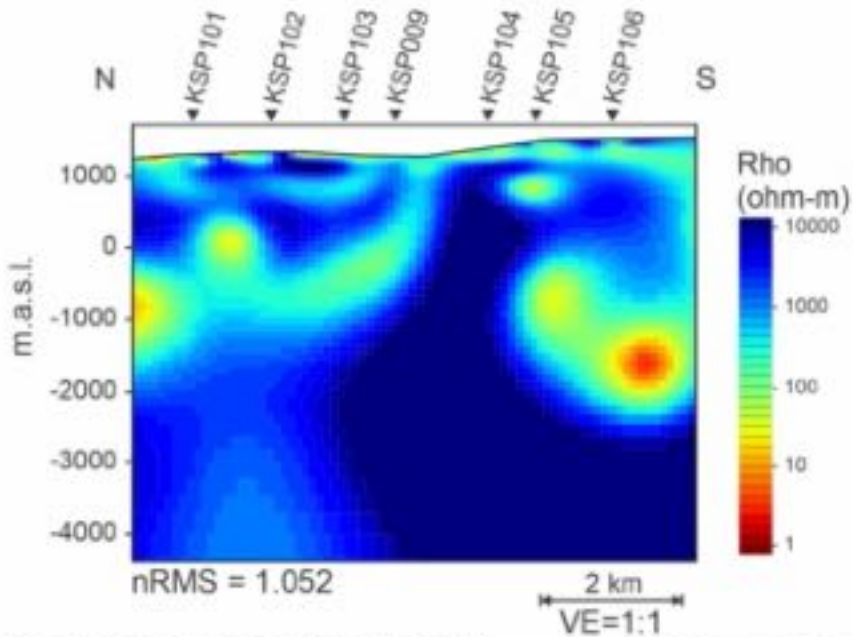
5.4. Profile SP-NS

The high frequency model was generated with the data at a strike angle of N50W from a layered starting model and an overall nRMS value of 1.052 was obtained (Figure 57). Error floors of 7% on TM-mode apparent resistivity, 20% on TE-mode apparent resistivity, 3.5% for both TM- and TE-mode phase, and an absolute value of 0.025 on the vertical field data were applied. The low frequency model was generated with the data at a strike angle of N39W from

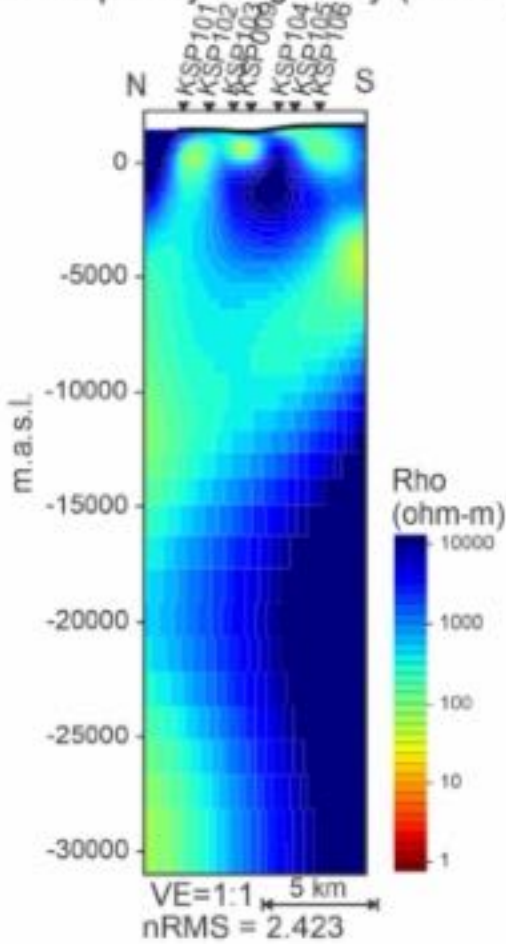
a starting model of 5000 Ωm . Error floors of 7% TM apparent resistivity, 20% TE apparent resistivity, 3.5 % phase, and an absolute value of 0.025 on the vertical field data were applied.

Difference pseudosections of the high frequency model show an excellent fit to all components of the data over the entire frequency range (Figure 58).

Preferred Models: Profiles SP-NS High frequency range only (N50W)



Low frequency range only (N39W)



All frequency range (N45W)

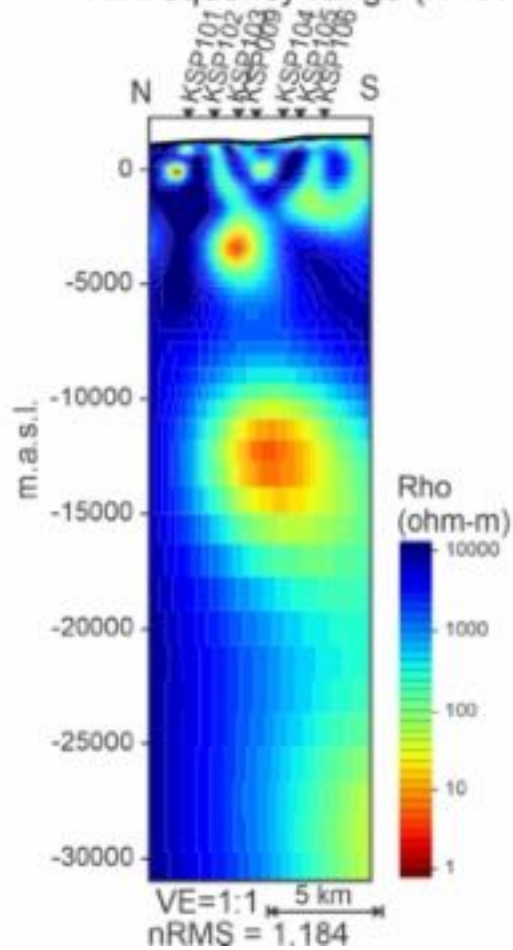


Figure 57: Preferred 2D models along Profile SP-NS.

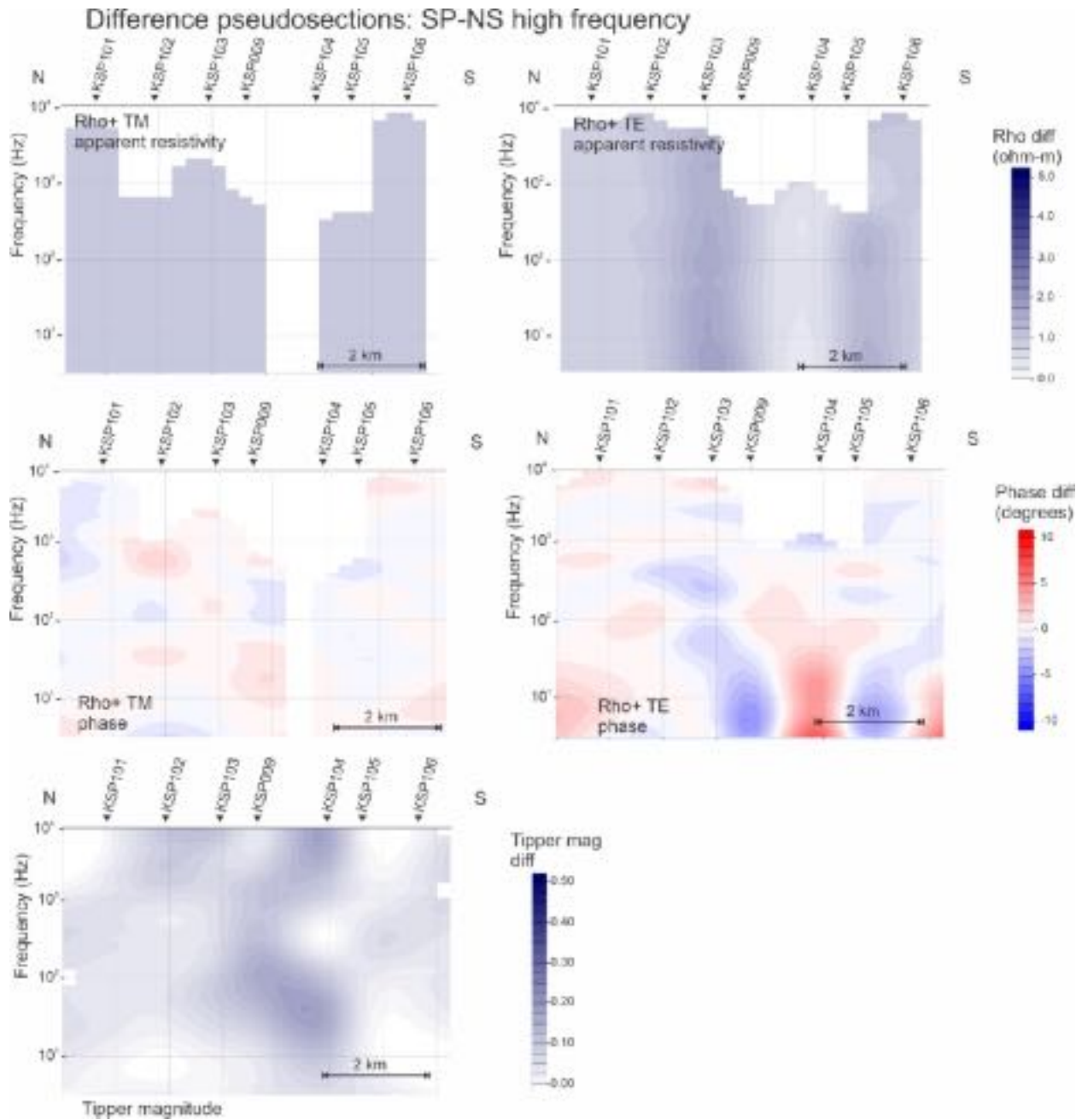


Figure 58: Difference pseudosections for the high frequency model along profile SP-NS.

5.5. Profile MO

For the MO area, analysis showed that one strike angle of N39W was appropriate for the entire frequency range of 10 kHz – 0.001 Hz. The model along the East-West profile was generated from a layered starting model and yielded an overall nRMS value of 2.116 (Figure 59). Error floors of 11% on TM-mode apparent resistivity, 20% on TE-mode apparent resistivity, 6% for both TM- and TE-mode phase, and an absolute value of 0.025 on the vertical field data were

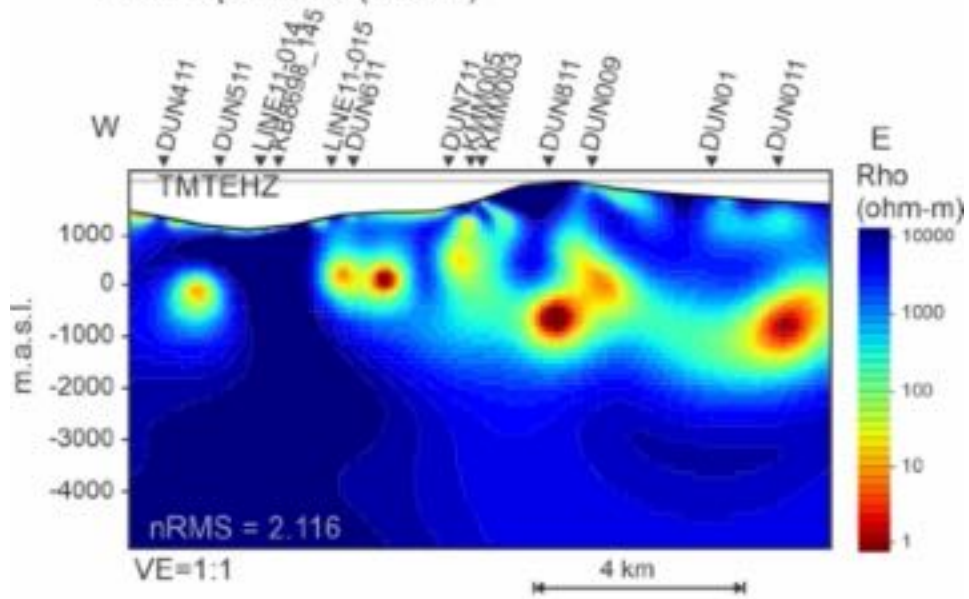
applied. The North-South model comprised of newly acquired data used error floors of 3.5% TM apparent resistivity, 20% TE apparent resistivity, 1.75 % phase, and an absolute value of 0.025 on the vertical field data were applied and has an nRMS value of 1.919.

Difference pseudosections for the East-West profile show a reasonable fit to the data, with the exception of the TE-mode phases (Figure 60). The poor fit may be a result of the higher error floors that were imposed on the data due to the lower quality of the older DUN data.

Difference pseudosections for the North-South MO profile show an excellent fit to all components of the data over the entire frequency range (Figure 61).

Preferred Models: Profiles MO

All frequencies (N39W)



All frequencies (N39W)

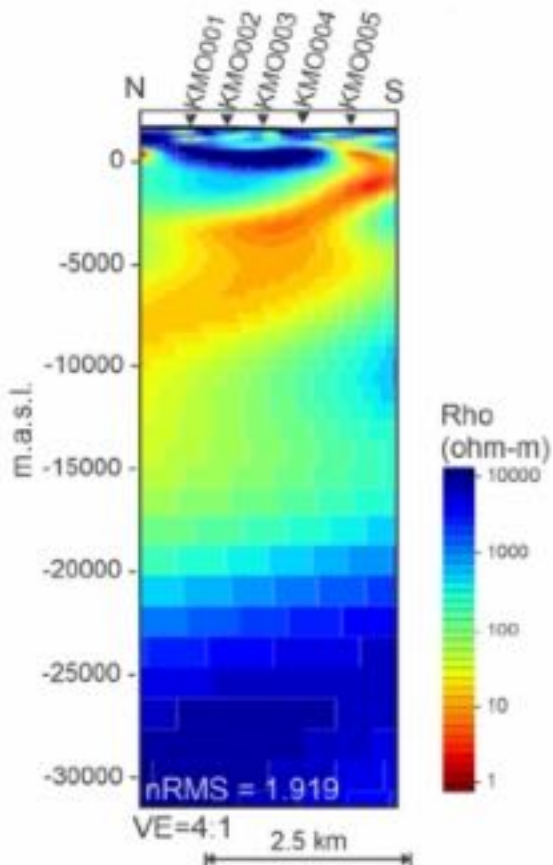


Figure 59: Preferred 2D models along Profiles MO-EW and MO-NS.

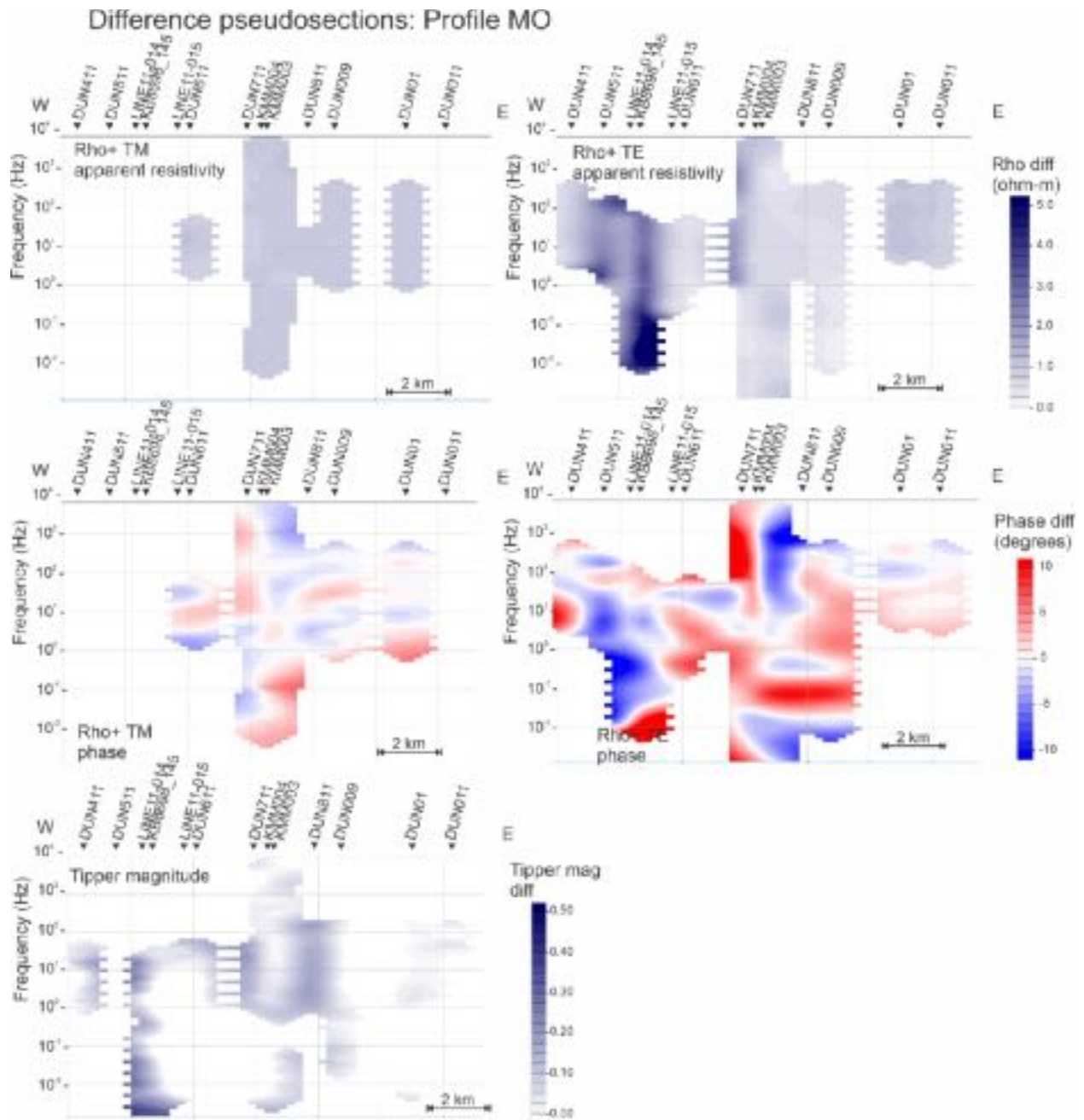


Figure 60: Difference pseudosections for Profile MO-EW.

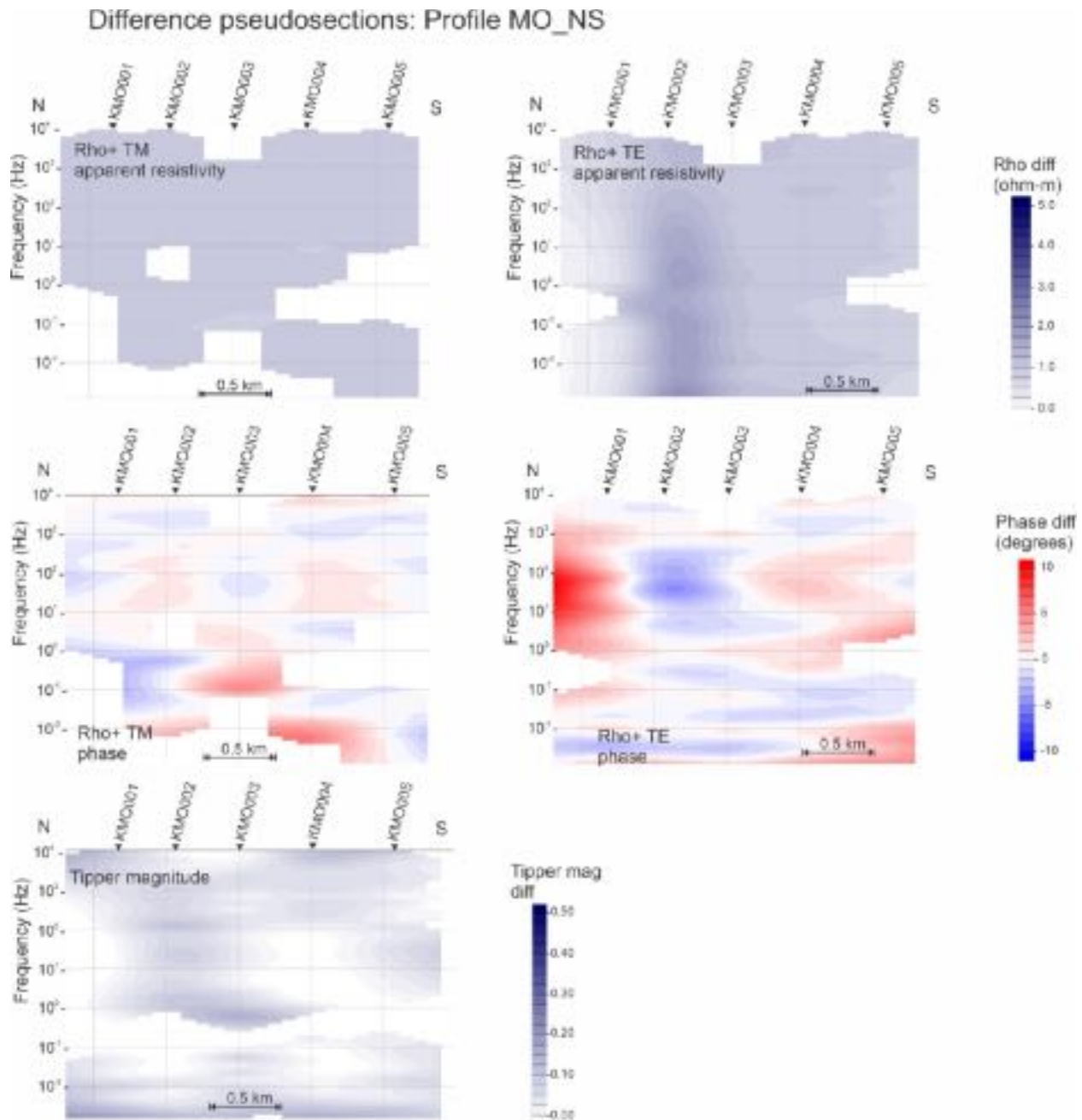


Figure 61: Difference pseudosections for Profile MO-NS.

5.6. Profile MM0

The high frequency model was generated with the data at a strike angle of N12E from a layered starting model and an overall nRMS value of 1.600 was obtained (Figure 62). Error floors of 5.25% on TM-mode apparent resistivity, 10% on TE-mode apparent resistivity, 5.25% for both TM- and TE-mode phase, and an absolute value of 0.025 on the vertical field data were applied. The low frequency model was generated with the data at a strike angle of N55W from a starting

model of 5000 Ωm . Error floors of 8.75% TM apparent resistivity, 20% TE apparent resistivity, 4.35 % phase, and an absolute value of 0.025 on the vertical field data were applied.

Difference pseudosections of the high frequency model show a very good fit to all components of the data over the entire frequency range (Figure 63).

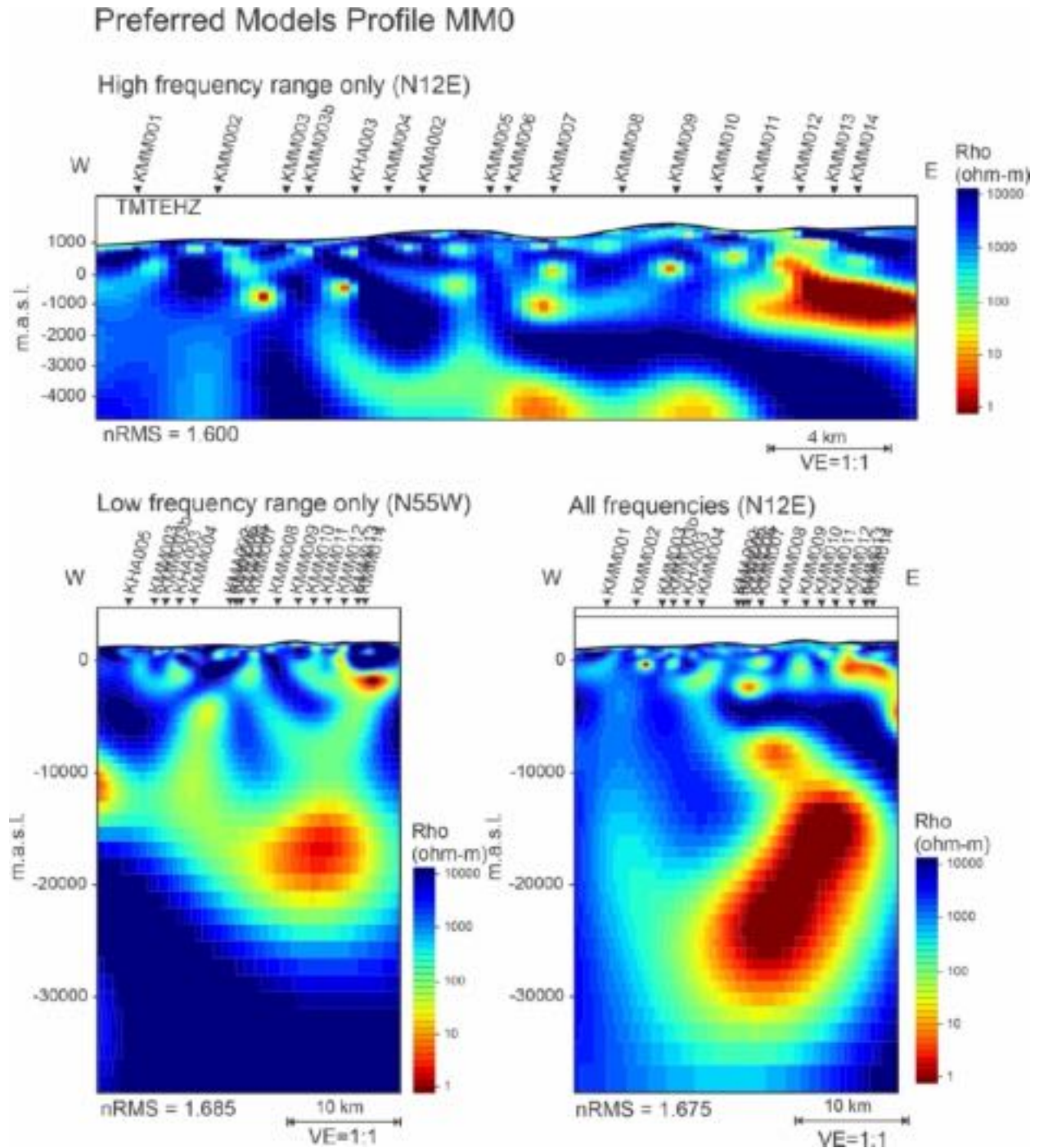


Figure 62: Preferred 2D models along Profile MM0.

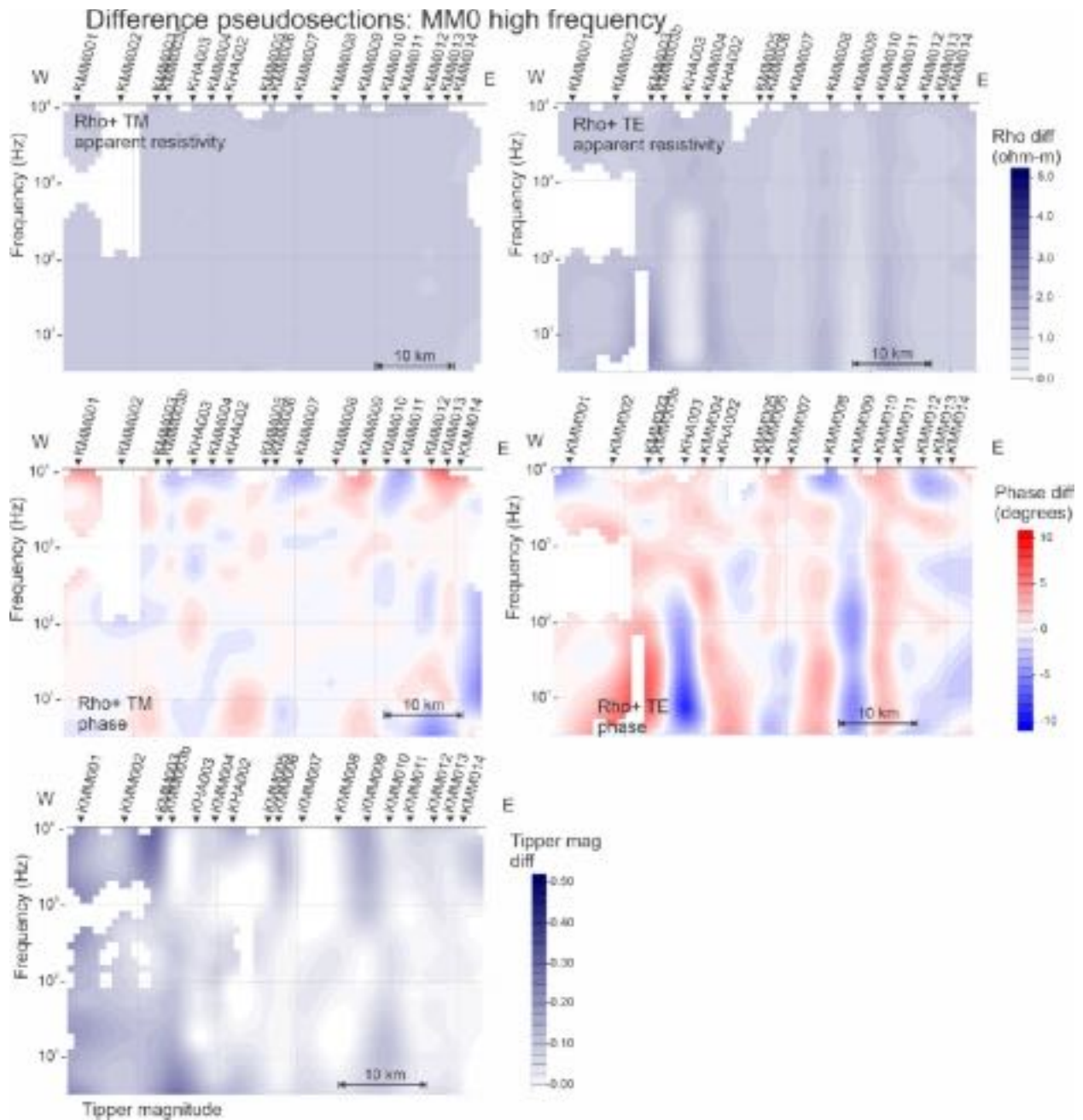


Figure 63: Difference pseudosections for high frequency model along Profile MM0.

5.7. Profile MM2

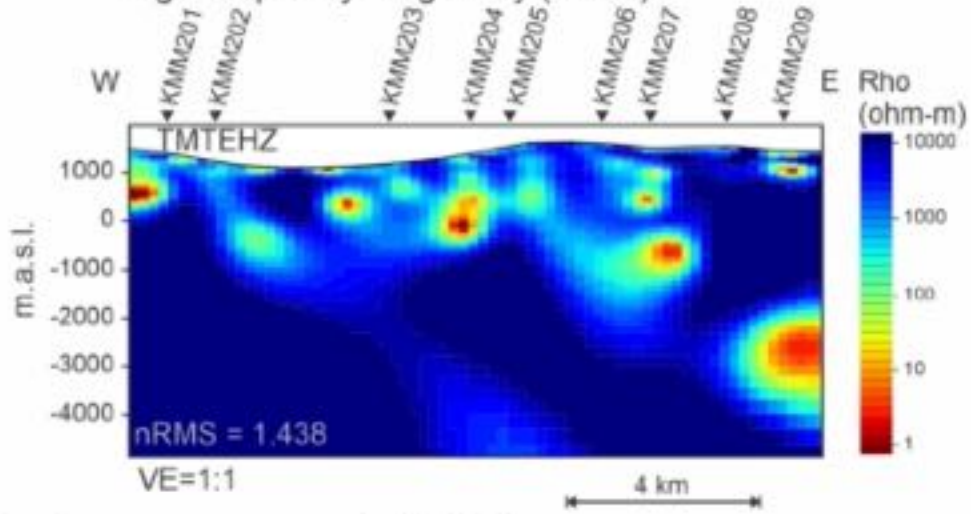
The high frequency model was generated with the data at a strike angle of N12E from a layered starting model and an overall nRMS value of 1.438 was obtained (Figure 64). Error floors of 5.25% on TM-mode apparent resistivity, 10% on TE-mode apparent resistivity, 5.25% for both TM- and TE-mode phase, and an absolute value of 0.025 on the vertical field data were applied. The low frequency model was generated with the data at a strike angle of N55W from a starting

model of 5000 Ωm . Error floors of 8.75% TM apparent resistivity, 20% TE apparent resistivity, 4.35 % phase, and an absolute value of 0.025 on the vertical field data were applied.

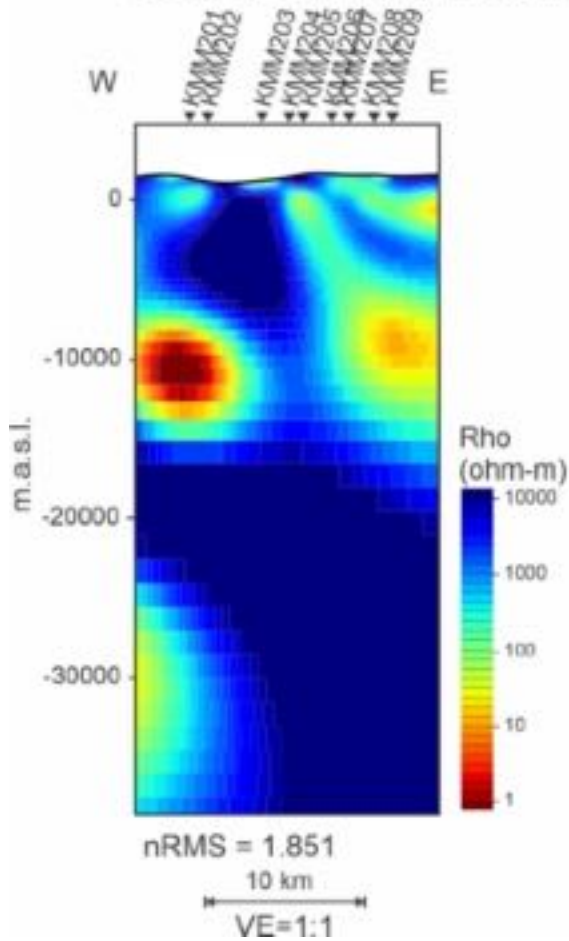
Difference pseudosections of the high frequency model show a very good fit to all components of the data over the entire frequency range (Figure 65). One area of exception is the eastern extend of the profile, the TE-phase beneath site KMM209. This may be an indication that this site is sensitive to structure to the east of the profile.

Preferred Models: Profile MM2

High frequency range only (N12E)



Low frequency range only (N55W)



All frequencies (N12E)

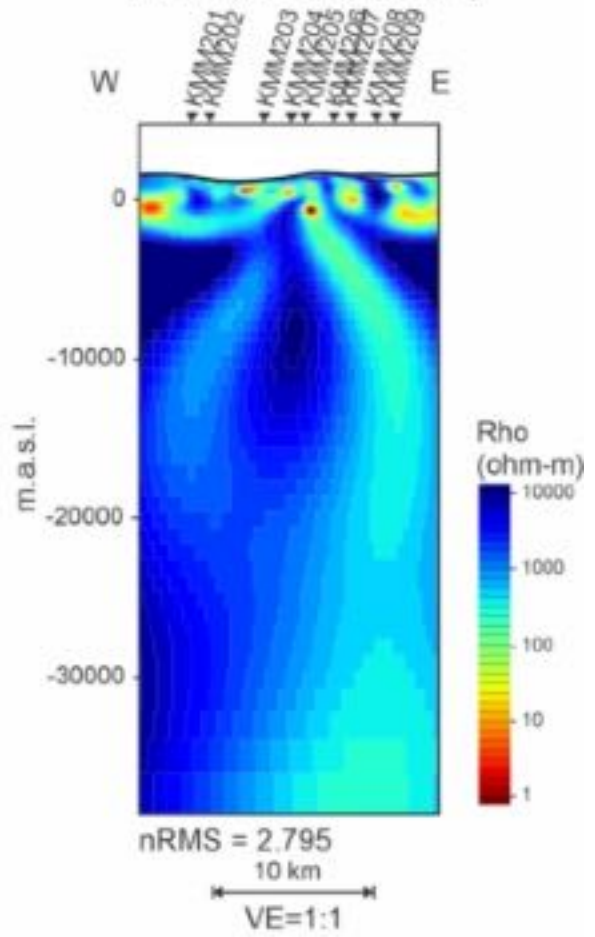


Figure 64: Preferred 2D models along Profile MM2.

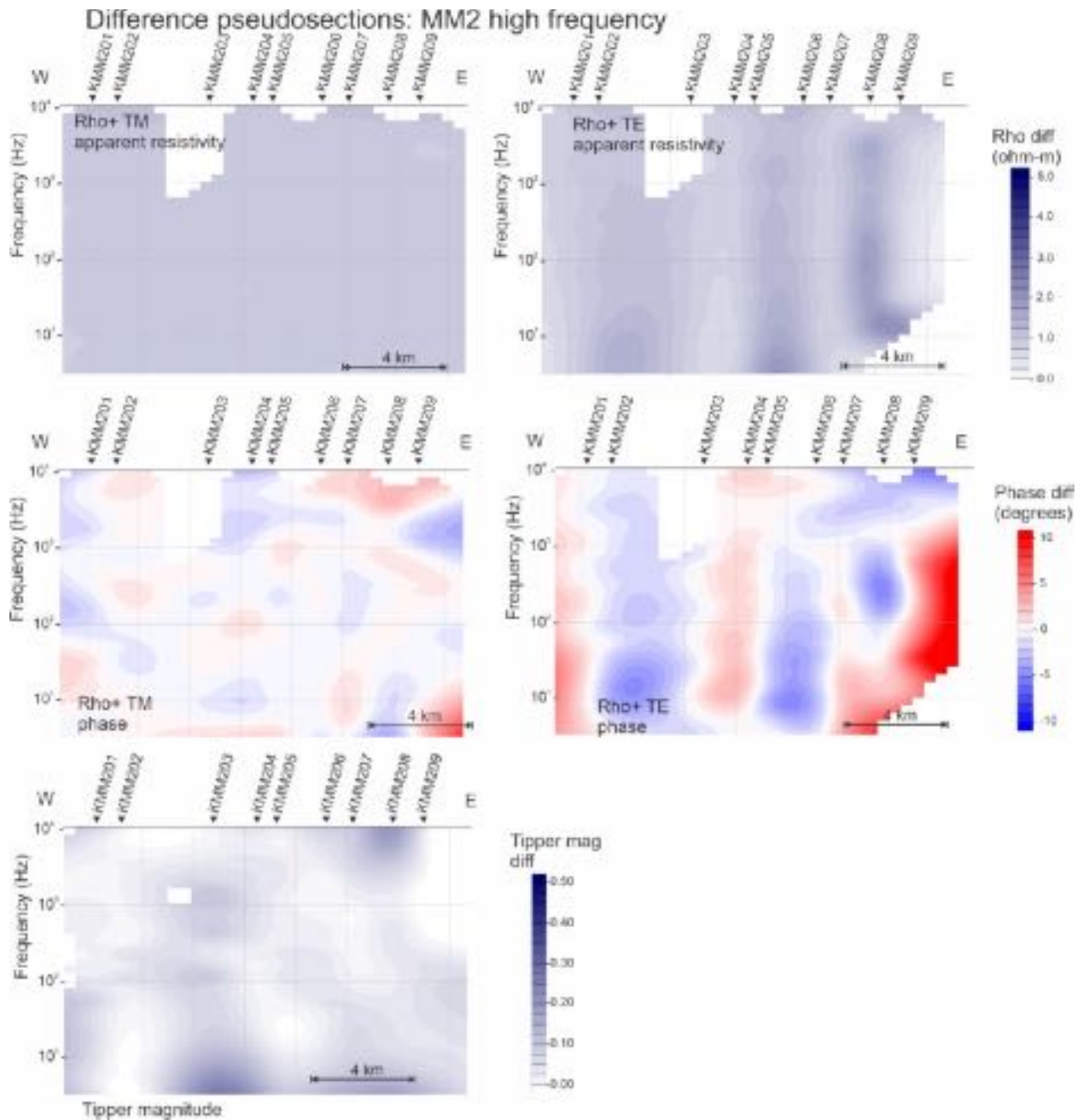


Figure 65: Difference pseudosections for high frequency model along Profile MM2.

6. Conclusions

Two-dimensional models have been generated along 6 east-west and 2 north-south profiles in the Southern Kootenay area imaging the conductivity structure of the subsurface. Models generated include the shallow structure to depths of ~ 4 km as well as the deeper crustal structure of the region. Results are consistent between the different profiles and identify a

strong conductor at the eastern margin of the survey area. Results are also consistent with previous models of previously existing data for the area.

7. Declarations and Signature

I, Jessica Spratt, do hereby certify that:

- I am a Senior Geophysicist with residence in Wakefield, Quebec and I am presently working in this capacity as Director of Interpretation of Compete MT Solutions Ltd. of Ottawa Ontario; responsible for 2D inversions.
- I obtained a B.Sc. (Hons, Geology, Carleton University, Ottawa Canada) in 1998, an M.Sc. (Applied Geophysics, Syracuse University, New York) in 2004
- I have derived the results presented in this report without consultation with any other person or persons, except for Alan Jones of CMTS.
- I have no interest, nor do I expect to receive any interest in the properties or securities of Kootenay Resources Ltd., its subsidiaries or its joint-venture partners.

Signed:

A handwritten signature in black ink, appearing to read 'J. Spratt', written in a cursive style.

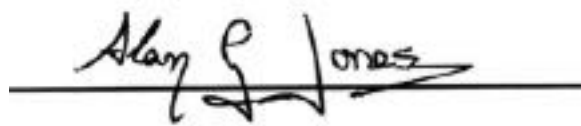
Jessica Spratt
Complete MT Solutions Inc.

I, Alan G. Jones, do hereby certify that:

- I am a Senior Geophysicist with residence in Ottawa, Ontario and I am presently working in this capacity as President and Managing Director of Compete MT Solutions Ltd. of Ottawa, Ontario and President and Managing Director of ManoTick GeoSolutions Ltd. of Ottawa, Ontario and Vice-President of Moombarriga Canada Ltd. of Ottawa, Ontario;
- I obtained a B.Sc. in Hons. Physics at the Univ. Nottingham, England in 1972, an M.Sc. in Applied Geophysics at the Univ. Birmingham, England in 1973, and a Ph.D. in Geophysics at the Univ. Edinburgh, Scotland in 1977;

- I undertook PostDoctoral Fellowships in Germany at the Univ. Munster from 1977 to mid-1981, in Sweden at the Swedish Geological Survey in 1981, and in Canada at the Univ. Toronto in 1982-1983;
- I subsequently joined the Geological Survey of Canada (Ottawa) in 1984 to 2003, rising from Research Scientist RES-2 level to Senior Research Scientist RES-5 level (the top level in the Canadian Government).
- I then became the Senior Professor and Head of Geophysics at the Dublin Institute for Advanced Sciences from 2004 to January, 2015.
- I am a registered geophysicist and a member in good standing with a license to practice in the Province of Ontario (PGO member #2790);
- I have been awarded academic distinction in Canada (J. Tuzo Wilson medal, Canadian Geophysical Union, 2006), in the USA (Fellow, American Geophysical Union, 2019), in Ireland (Member, Royal Irish Academy, 2010), in Europe (Member, Academia Europaea, 2010), in China (International Member, Geo-Electromagnetism Committee, Chinese Geophysical Society, 2009), and in South Africa (Life Affiliate member, Geological Society of South Africa, 2016).
- I am also a member of the Society of Exploration Geophysicists (SEG) and the Canadian Exploration Geophysical Society (KEGS);
- I have reviewed and approve the results presented in this report, and have done so without consultation with any other person or persons, except for Jessica Spratt;
- I have no interest, nor do I expect to receive any interest in the properties or securities of Kootenay Resources Ltd., its subsidiaries or its joint-venture partners.

Signed:



Alan G. Jones, Ph.D., P.Geo. (PGO #2790)
President, Complete MT Solutions Inc.

References

- Hansen, P. C. (1992), Analysis of discrete ill-posed problems by means of the L-curve, *Siam Review*, 34(4), 561-580, doi:10.1137/1034115.
- Rodi, W., and R. L. Mackie (2001), Nonlinear conjugate gradients algorithm for 2-D magnetotelluric inversion, *Geophysics*, 66(1), 174-187.

Appendix 3: Analysis Report - CMTS



**COMPLETE MT
SOLUTIONS**

CMTS Contract CMTS-2021-KootenayResources

Report CMTS-2021-KootenayResources-R2

Analyses of MT data acquired in the southern
Kootenays

for

Kootenay Resources Inc.

Dr. Alan G. Jones, P.Geol.

10th January, 2021

Table of Contents

EXECUTIVE SUMMARY	5
1. INTRODUCTION	5
1.1. PRIMARY AND SECONDARY TARGET DEPTHS	6
1.2. EXISTING DATA	6
1.3. COMPARISONS OF NEW AND OLD DATA	7
1.3.1. KSP104 AND 86D003	7
1.3.2. KSP105 AND 86D003	11
1.3.3. KMO004 AND DUN711	13
1.3.4. KSS106 AND SS_14	16
1.3.5. KSS108 AND SS_32	18
1.4. PROFILES	20
1.5. EXISTING MODELS	22
2. NEW ACQUISITION	23
2.1. CONTACT RESISTANCES	23
2.2. DC VALUES	27
2.3. AC VALUES	28
3. MT QUALITY FACTORS	28
3.1. QF PLOTS	29
3.1.1. CHANGE OF QF WITH SURVEY TIME	38
3.2. EXAMPLE SITES	40
3.2.1. EXAMPLE OF EXCELLENT QUALITY SITES, QF = 1.00 – 1.25	40
3.2.2. EXAMPLE OF VERY HIGH-QUALITY SITES, QF = 1.25 – 1.50	41
3.2.3. EXAMPLE OF HIGH QUALITY SITES, QF = 1.5 – 2.0	41
3.2.4. EXAMPLE OF GOOD TO MEDIUM QUALITY SITES, QF = 2.0 – 3.0	42
3.2.5. EXAMPLE OF MEDIOCRE QUALITY SITES, QF = 3.0 – 4.25	43
3.3. QF CF. ELECTRODE ARRAY PARAMETERS	45
3.4. QF CONCLUSIONS	47
4. TIPPER QUALITY FACTORS	48
5. AVERAGE RHOA/PHA CURVES	50

6.	QUALITATIVE IMAGES	53
6.1.	FREQUENCIES FOR PRIMARY DEPTHS OF INVESTIGATION	53
6.2.	DEPTHS OF PENETRATION FOR VARIOUS FREQUENCIES	55
6.3.	APPROXIMATE RESISTIVITY IMAGES FOR VARIOUS DEPTHS	57
6.4.	QUALITATIVE DIMENSIONALITY PLOTS	61
7.	GEOELECTRICAL STRIKE – PHASE TENSORS	63
7.1.	PHASE TENSOR DIMENSIONALITY	64
7.2.	PHASE TENSOR DIRECTIONALITY	65
8.	VERTICAL FIELD TRANSFER FUNCTIONS	66
8.1.	INDUCTION VECTORS	66
8.2.	TIPPER MAGNITUDE	67
8.3.	INDUCTION VECTOR AND TIPPER PLOTS	67
9.	STRIKE DECOMPOSITION	71
9.1.	SINGLE SITE ANALYSES	73
9.1.1.	SINGLE-SITE, DECADE-WIDE BANDS	73
9.1.2.	SINGLE-SITE, SINGLE FREQUENCY BANDS	76
9.1.2.1.	10 kHz – 3 Hz	77
9.1.2.2.	800 Hz – 8 Hz	79
9.1.3.	SINGLE-SITE: MISFIT SENSITIVITY WITH STRIKE DIRECTION	80
9.1.4.	SINGLE-SITE: CONCLUSIONS	83
9.2.	MULTI-SITE BY PROFILE	83
9.2.1.	PROFILE MM1	83
9.2.1.1.	Whole profile analysis	84
9.2.1.2.	Lateral variation along profile	85
9.2.1.3.	Imposed strike directions – N10E and N35W	86
9.2.1.4.	Conclusions	87
9.2.2.	PROFILE MO	88
9.2.3.	PROFILE SS	92
9.2.4.	PROFILE MM0	93
9.2.5.	PROFILE MM2	94
9.2.6.	PROFILE SP-EW	95
9.2.7.	PROFILE SP-NS	97
9.2.8.	AREA SP: PROFILES SP-NS & SP-EW TAKEN TOGETHER	97
9.2.8.1.	High frequencies: 10 kHz – 3 Hz	98

9.2.8.2.	Low frequencies: 3 Hz – 0.01 Hz	98
9.2.8.3.	All frequencies: 10 kHz – 0.01 Hz	98
9.2.9.	AREA SOUTH	99
9.2.9.1.	High frequency robust fitting	102
9.2.9.2.	Low frequency robust fitting	102
9.2.10.	PROFILE AND AREA STRIKE DIRECTIONS: CONCLUSIONS	103
9.3.	STRIKE: CONCLUSIONS	104
9.4.	CORRECTION FOR LOCAL SITE ANISOTROPY	104
10.	<u>RHO⁺ CONSISTENCY CHECK</u>	105
11.	<u>CONCLUSIONS</u>	107
12.	<u>RECOMMENDATIONS</u>	108
13.	<u>DELIVERABLES</u>	108
14.	<u>DECLARATION AND SIGNATURE</u>	108
15.	<u>REFERENCES</u>	110
16.	<u>APPENDIX A: MT ACQUISITION EQUIPMENT</u>	113
16.1.	RECORDERS	113
16.2.	MAGNETIC SENSORS	113
16.3.	ELECTRODES	114
16.3.1.	GENERAL	114
16.3.2.	ELECTRODES AND ELECTRODE ARRAY	115
16.3.3.	ELECTRIC ARRAY MEASUREMENTS	115
17.	<u>APPENDIX B: AMT DEADBAND</u>	117
18.	<u>APPENDIX C: QUALITY FACTORS DETERMINATION</u>	118
18.1.	MT QUALITY FACTORS	118
18.2.	TIPPER QUALITY FACTORS	120

Executive Summary

Newly-acquired data in the Kootenays were analysed together with older (1980s vintage) existing data from Duncan Oil. Quantec data along the southernmost profile give responses that are not consistent with the newly-acquired ones, especially for the diagonal terms (XX and YY), so are not used.

Generally the response estimates of the newly-acquired are of high quality, except for estimates in the AMT deadband (4 kHz – 900 Hz) and the MT deadband (10 Hz – 0.1 Hz) during times of low signal. Appropriate error floors are 3.5% in RhoA and 1° in Pha.

Consideration of depth penetration shows that the estimates from 10 kHz – 3 Hz optimally sense the depths of primary interest (to 4 km), and lower frequencies (3 Hz – 0.001 Hz) sense down to the base of the crust.

Some areas of interest are inferred from the qualitative maps of phases, resistivities and induction vectors.

The data can be inverted in 2-D but with varying strike direction for the high and low frequencies, and with larger error floors.

3-D inversion is recommended for the southern sites.

1. Introduction

Complete MT Solutions Inc. (“CMTS”) was contracted by Kootenay Resources Inc. (“Kootenay” or “client”) to acquire and process new data, and to analyse and model the new data together with existing data at locations shown in Figure 1.

The new data were acquired for the client under sub-contract by Moombarriga Canada Ltd. of Ottawa, a subsidiary of Moombarriga Geoscience Pty. Ltd. of Perth, Australia. Data were acquired at eighty-six (86) locations, (red circles in Figure 1). as described in report CMTS-2021-KootenayResources-R1. Direction during fieldwork was through daily contact with the client’s representative, Professor Fred Cook (“Cook” or “client’s representative”).

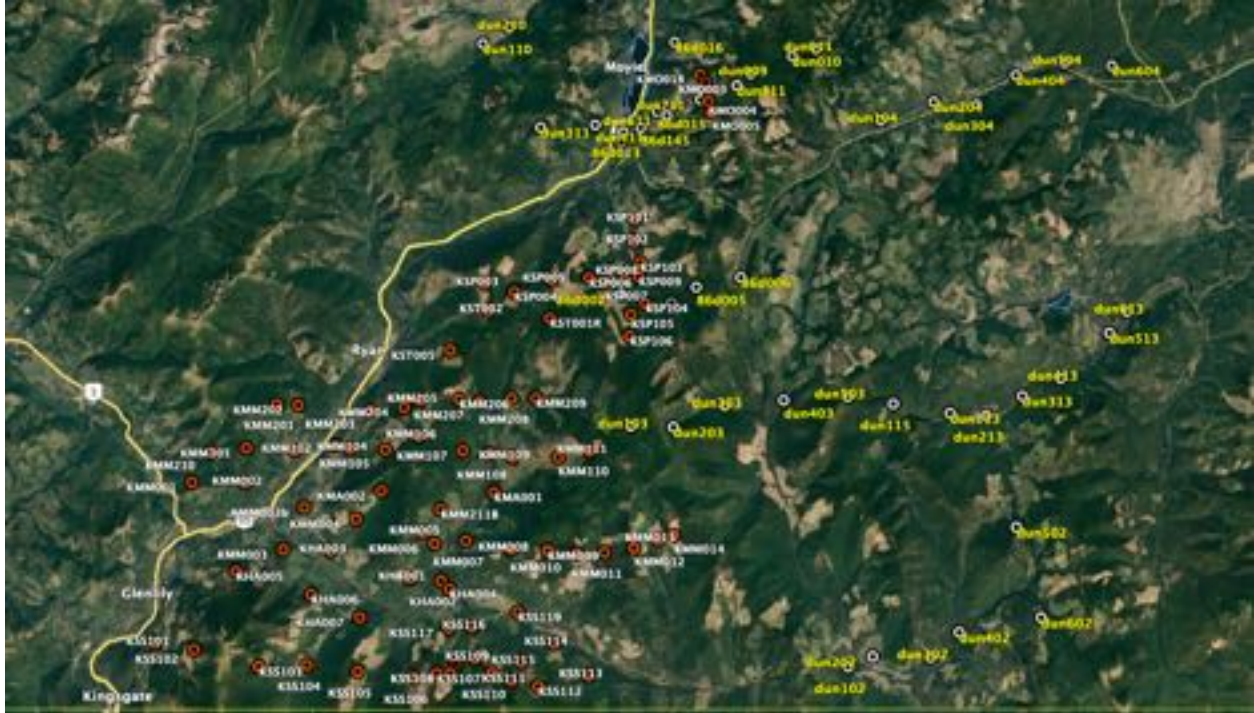


Figure 1: New MT data acquired for the client (red circles, white names). Also shown are the locations of existing data (white circles, yellow names).

1.1. Primary and Secondary target depths

As per the email from Fred Cook on 7th Nov, 2021:

“The primary target depth has to be the upper 2-4 km as that represents drilling depths.

We are also trying to image conduits in order to link them to conductors/showings near the surface. So, deeper information (middle to lower crust) will also be valuable.”

1.2. Existing data

In addition, existing data were included for consideration. These comprised two separate sets of data.

First, high-quality MT data in southeastern British Columbia were collected in 1985 (sites named “dunxxx”) and 1986 (sites named “86dxxx”) by Phoenix Geophysics Ltd. for Duncan Exploration Co. (Denver, Colo.). The locations are denoted by white circles in Figure 1. These data were donated to the Lithoprobe project by Duncan Exploration, and are now in the public domain. These data, and data over the Purcell Anticlinorium in the adjacent U.S.A., were analysed and modelled previously by Gupta and Jones (1995).

Second, a 5 km dense, high-resolution profile of 46 stations was acquired by Quantec Geoscience Ltd. (“Quantec”) for Teck Resources just north of the Canada/US border. These are named “SS_xx”, and were made available to Kootenay Resources.



1.3. Comparisons of new and old data

1.3.1. *KSP104 and 86d003*

The centres of new site KSP104 and Duncan site 86d003 are 240 m apart (Figure 2). Side-by-side comparisons of the two are shown in the upper row of Figure 3, and an overlap of them on top of each other in the lower row of Figure 3, with “1” being KSP104 and “2” being 86d003.

Both sets of estimates were derived using Phoenix equipment and Phoenix processing, but the equipment used in 2021 was very different from the MT-16 system used in 1986. Also, the new hybrid coils were used in 2021 whereas the older broadband MTC50 coils were used in 1986. The processing was essentially the same though. Note that site 86d003 only has estimates to 384 Hz as Phoenix did not have AMT acquisition until the very late-1980s.

There is visually significant differences between the two sets of estimates. But clearly there are significant galvanic distortions on both sets of data. The KSP104 PhaYX goes out of quadrant at frequencies <1 Hz.

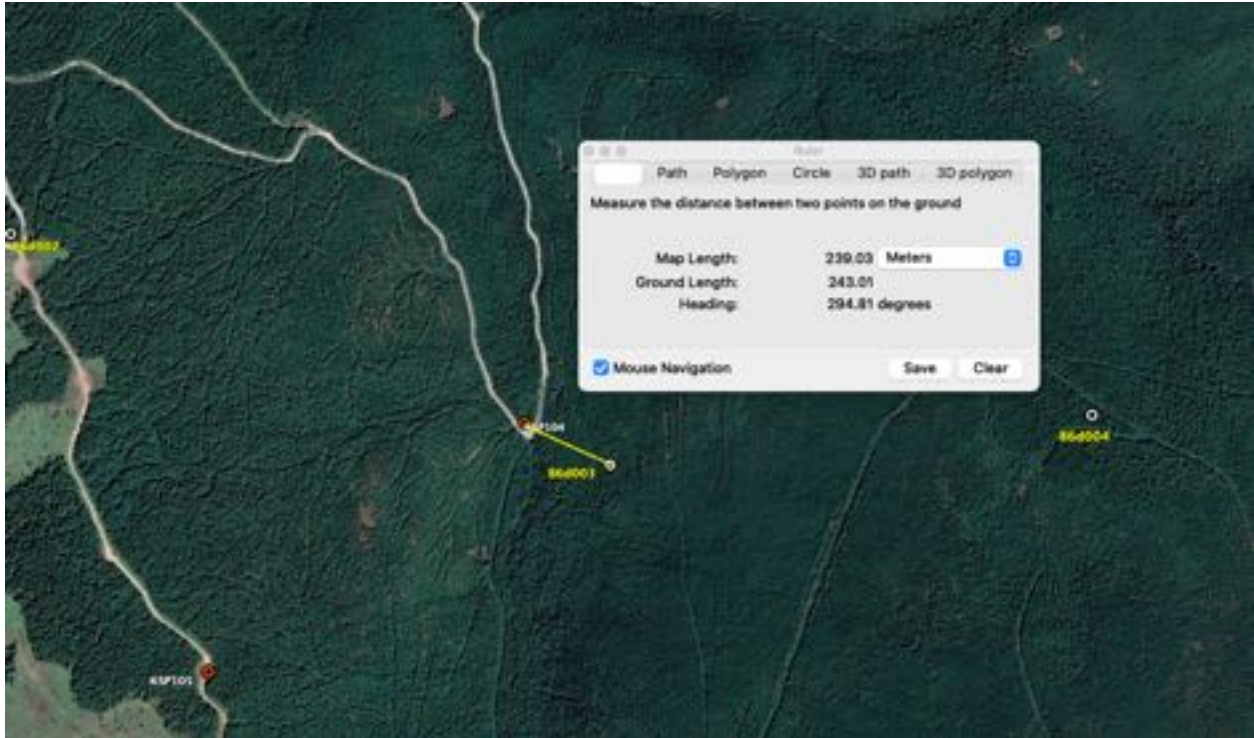
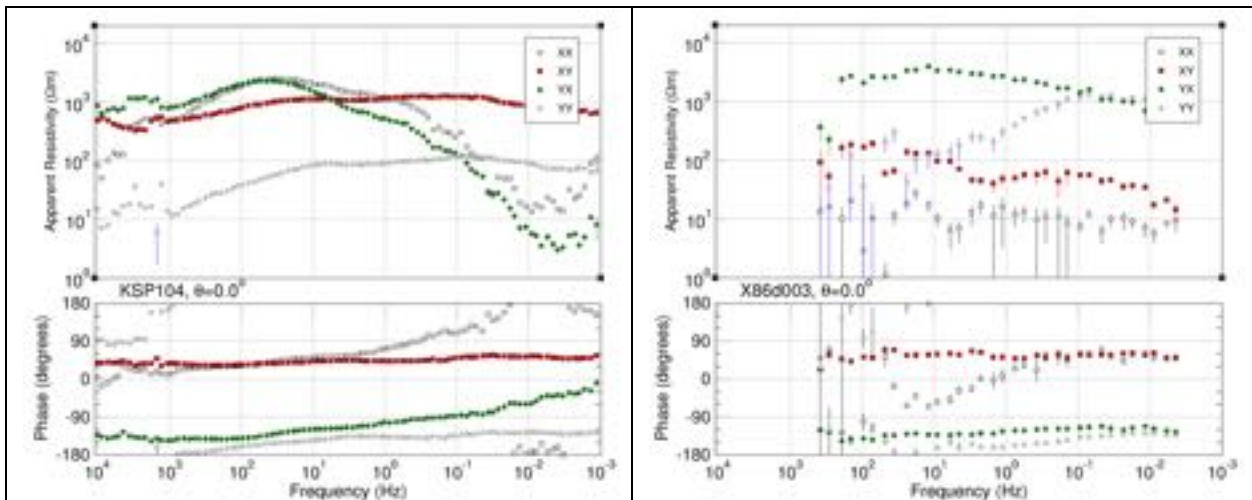


Figure 2: Locations of new site KSP104 and existing Duncan site 86d003.



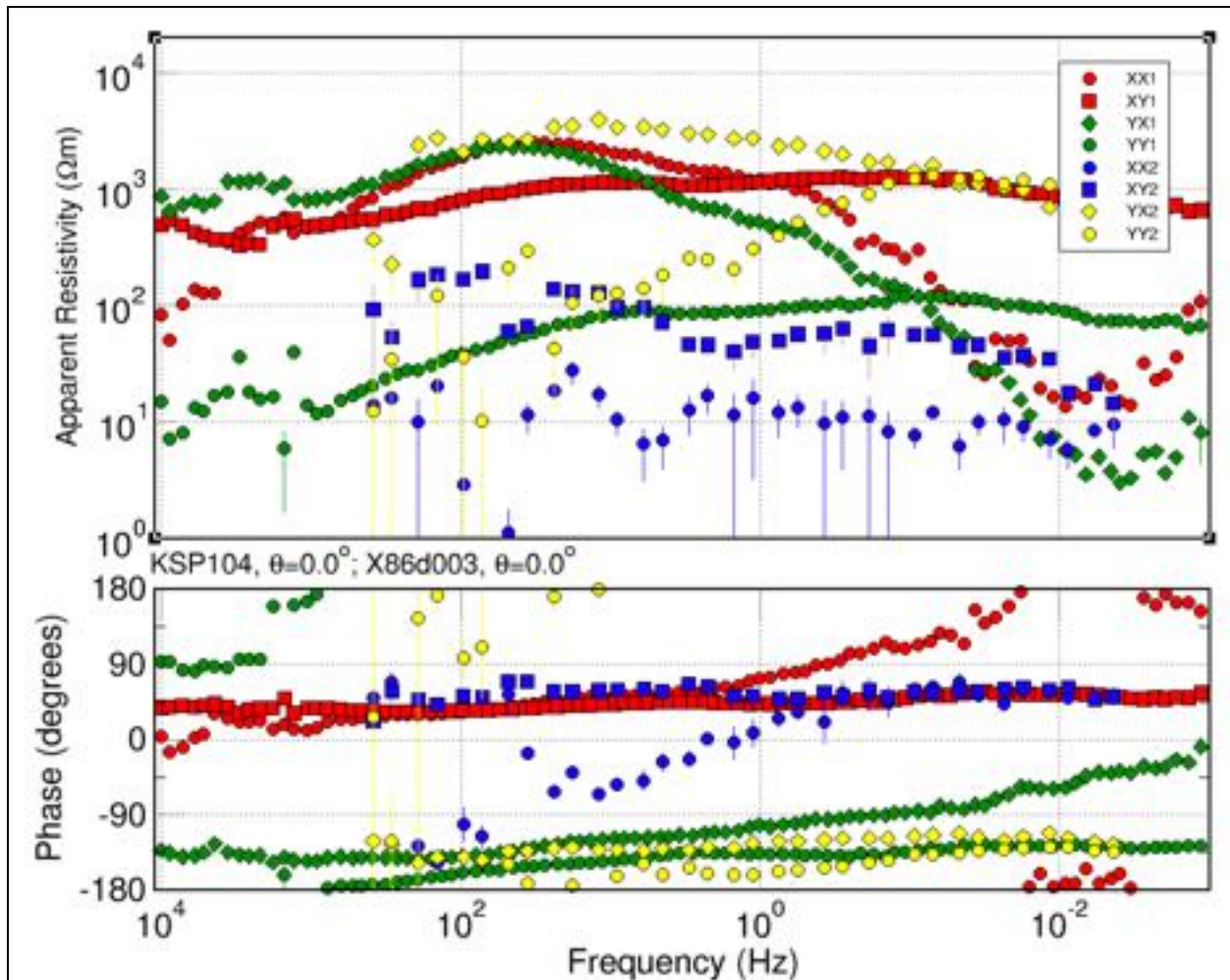


Figure 3: Comparison of new site KSP104 with Duncan site 86d003. Top row: Plots of separate sites. Bottom row: Overlay of the two sets of data - "1" is KSP104 and "2" is 86d003.

We can see if galvanic distortion decomposition removal will bring these two into better agreement – see description of the McNeice and Jones (2001) approach in the section below on *Strike decomposition*.

Performing single-site, multi-frequency decompositions for the frequency band 400 – 1 Hz yields the 2-D regional responses in Figure 4. There is some scatter in the Duncan data, but the phases are now in substantial agreement, and the RhoA curves have the same shapes but are displaced by residual static shift effects.

The only problem is that the geoelectricstrike direction determined from the new data, KSP104, is N24W, whereas the strike direction from the older data, 86d003, is N29E!

This may infer that one or both of the phases of the diagonal terms, XX and YY, in the original data are in opposite quadrants from each other. A comparison of the two (Figure 5) shows that indeed the PhaXX data (black and blue squares) are 90° apart.

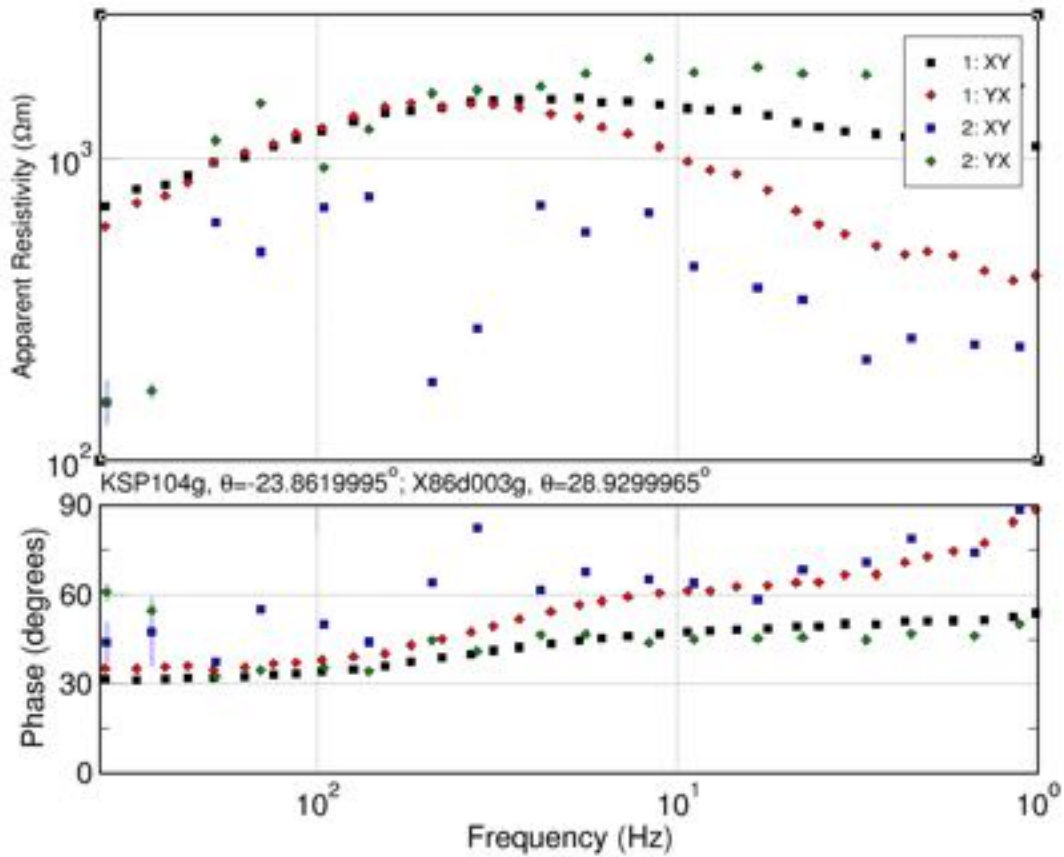


Figure 4: Comparison of KSP104 ("1") and 86d003 ("2") after distortion decomposition.

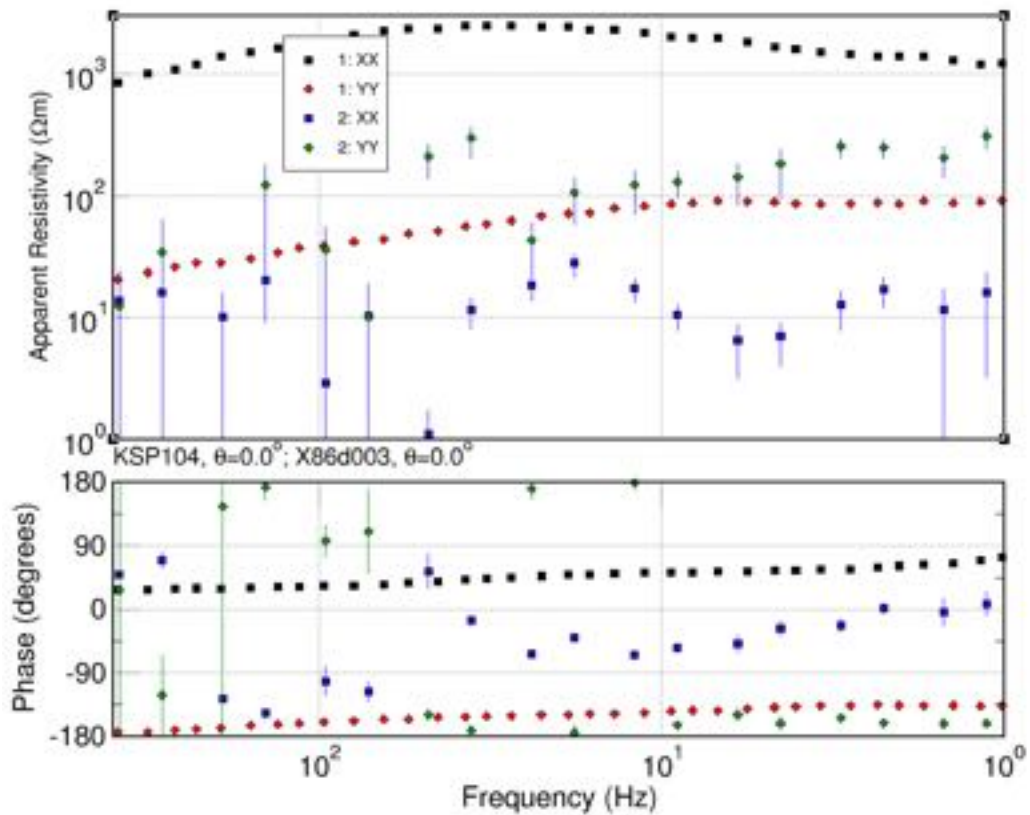


Figure 5: Comparison of the XX and YY estimates for new site KSP104 and Duncan site 86d003.

1.3.2. *KSP105 and 86d003*

The centres of new site KSP105 and Duncan site 86d002 are just over 1 km apart (Figure 6), so their high-frequency estimates may differ to about 100 Hz, but their lower frequency responses should be comparable.

Side-by-side comparisons of the two are shown in the upper row of Figure 7, and an overlap of them on top of each other in the lower row of Figure 7, with “1” being KSP105 and “2” being 86d002.

Again, both sets of estimates were derived using Phoenix equipment and Phoenix processing, site 86d003 used older BBMT coils (MTC-50s) and receiver (MT-16), whereas KSP105 used very modern coils (MTC-150s) and receiver (MTU-5C v2)

There is very good agreement of the off-diagonal (XY and YX, squares and diamonds) estimates – the phases overlap and the RhoA curves have the same shape but are slightly shifted from each other. The diagonal estimates are though not in agreement.

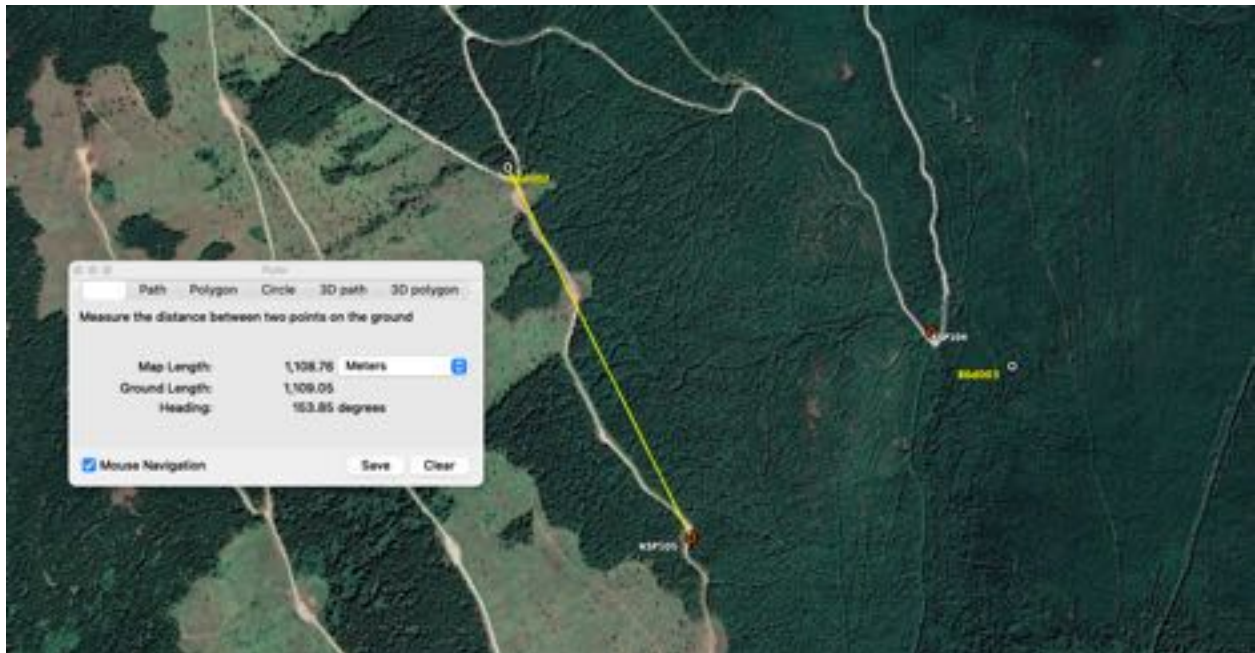


Figure 6: Locations of new site KSP105 and existing Duncan site 86d002.

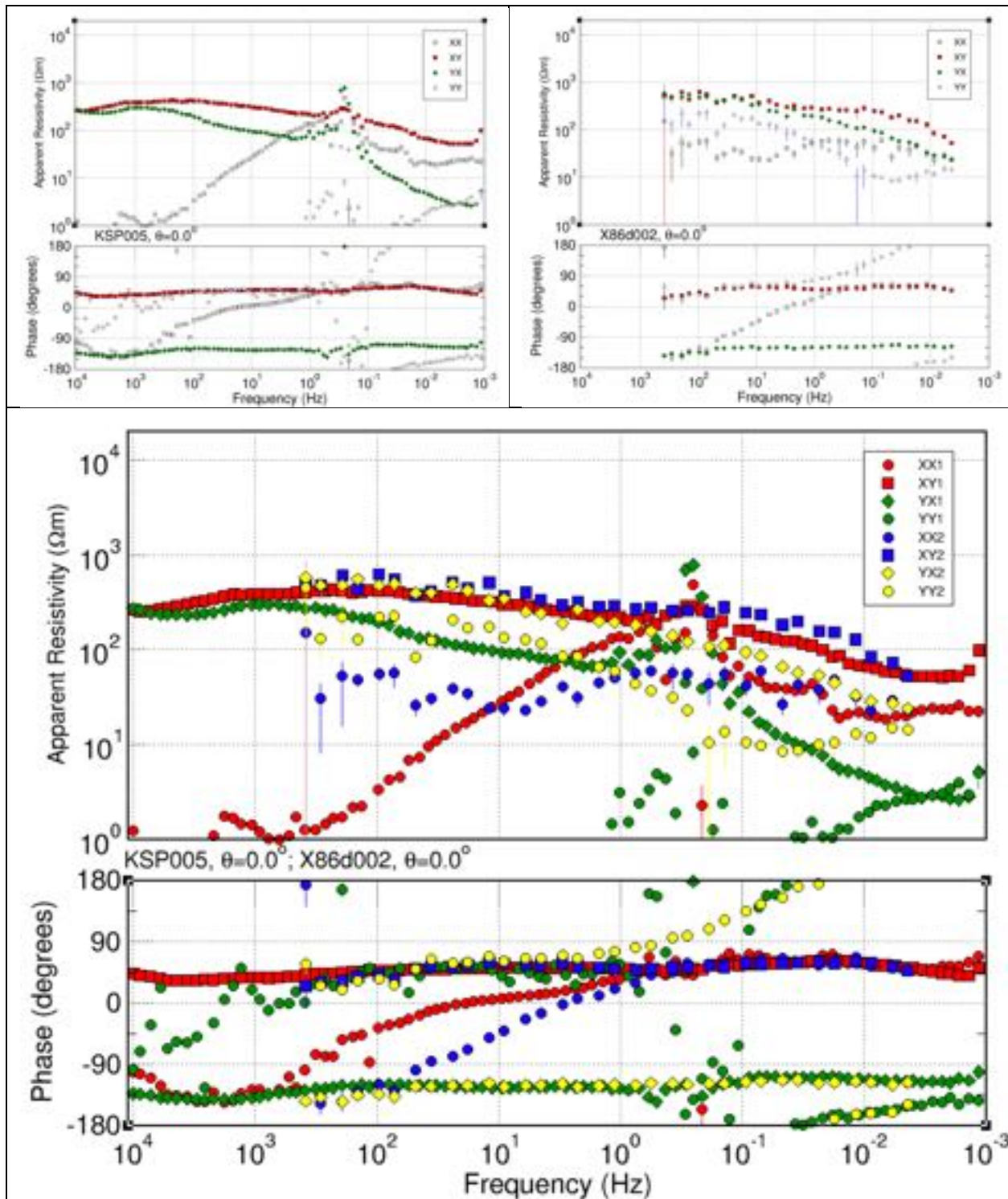


Figure 7: Comparison of new site KSP105 with Duncan site 86d002. Top row: Plots of separate sites. Bottom row: Overlay of the two sets of data - "1" is KSP105 and "2" is 86d002.

Again, we can see if galvanic distortion decomposition removal will bring these two into better agreement. Undertaking independent model fits we find geoelectric strikes of N43W and N45W (or N47E and N45E) for KSP005 and 86d002 respectively in the frequency band of 400 – 0.05 Hz.

A multi-station, multi-site decomposition of the two simultaneously yields a geoelectrical strike of N44E (or N46W), and the data are in excellent agreement (Figure 8). The phases are the same to 1 Hz, and the RhoA curves have the same shape but are displaced from each other by static shift effects.

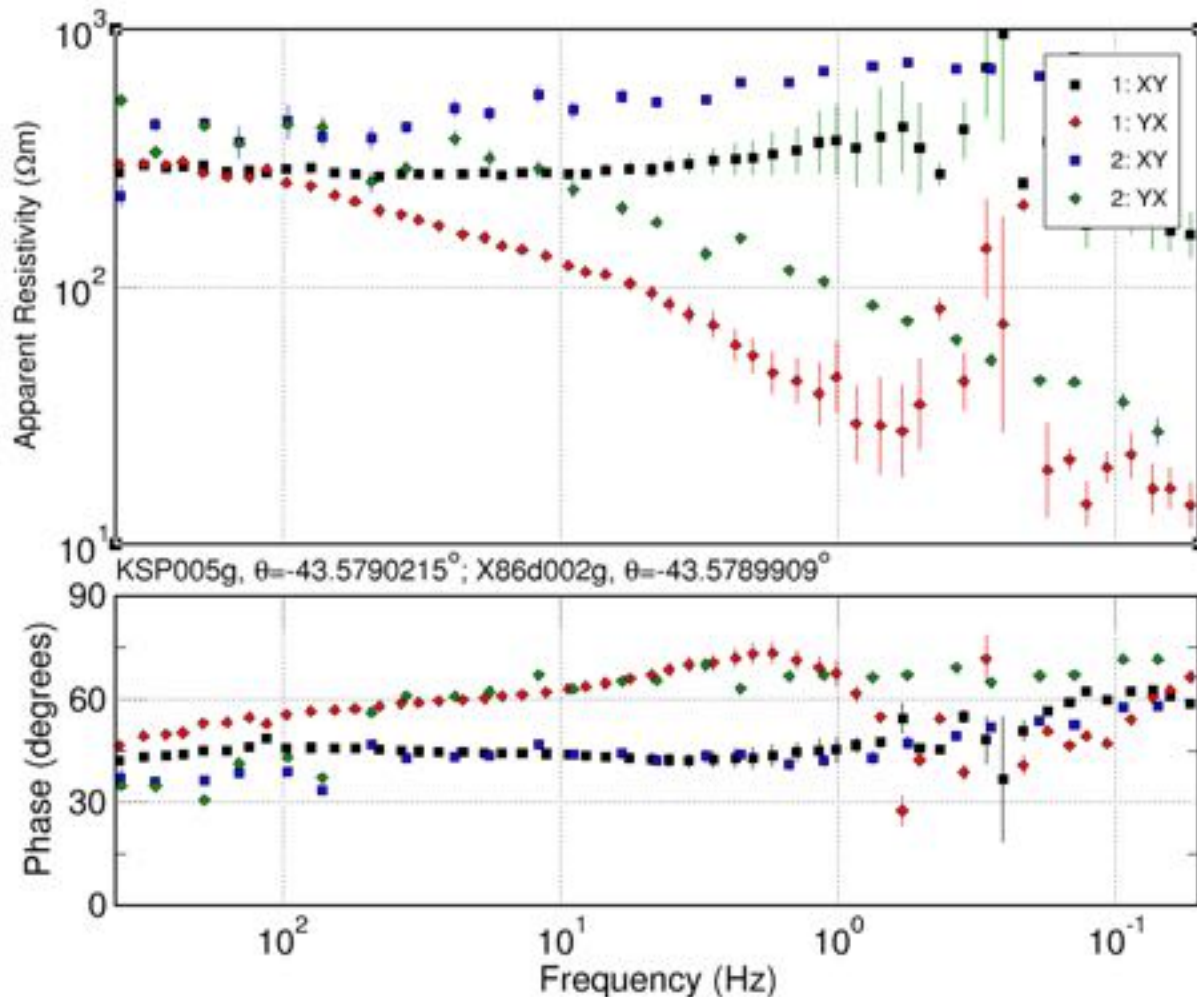


Figure 8: Comparison of KSP105 ("1") and 86d002 ("2") after distortion decomposition.

1.3.3. KMO004 and dun711

The centres of sites KMO004 and dun711 are 430 m from each other (Figure 9). Unfortunately, the dun711 data are very poor and are only over a very restricted frequency range of 384 – 1 Hz.

Nevertheless, the overlap comparison plot (Figure 10, bottom row) shows excellent agreement in the off-diagonals, XY (red and blue squares) and YX (green and tallow diamonds), even the RhoA levels are the same. There is though no agreement in the diagonal estimates, XX (red and blue circles) and YY (blue and yellow circles).

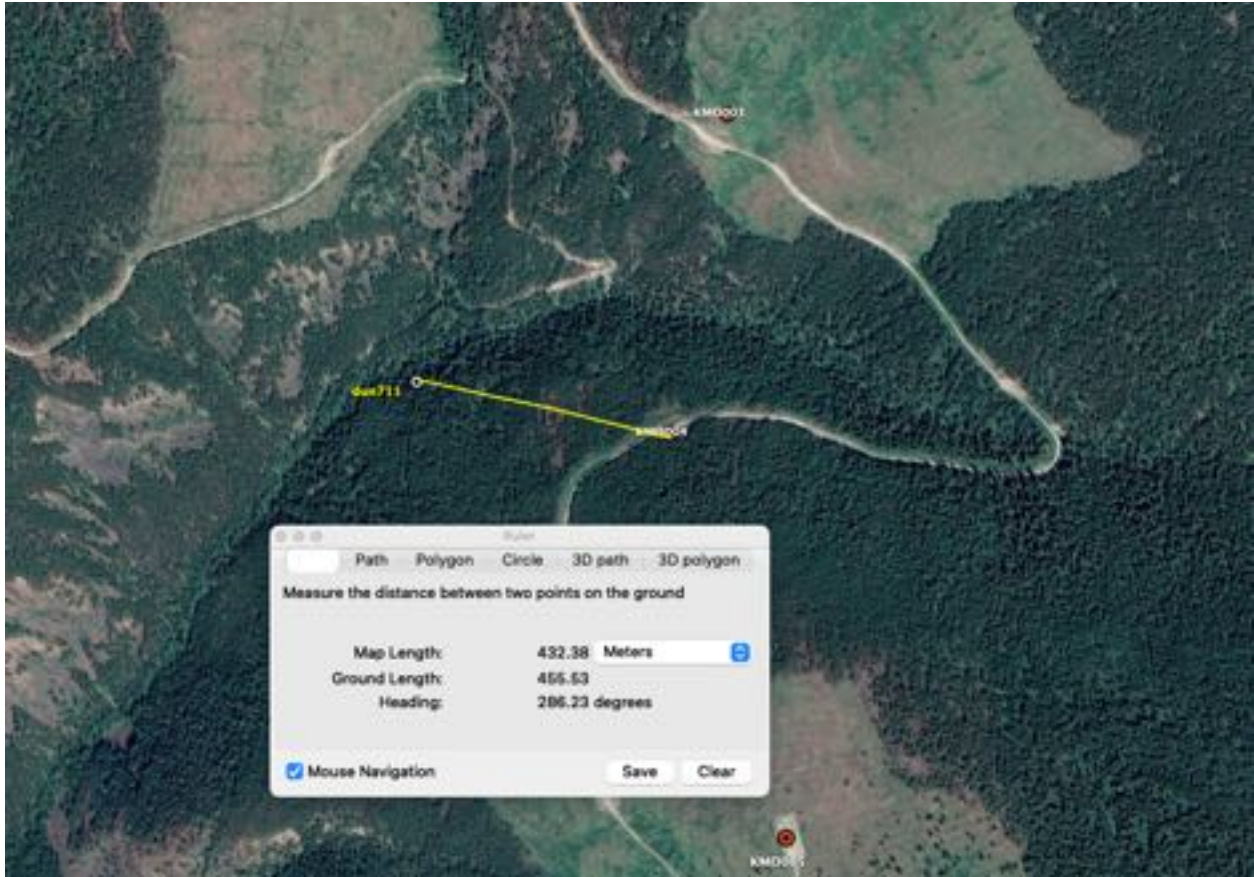
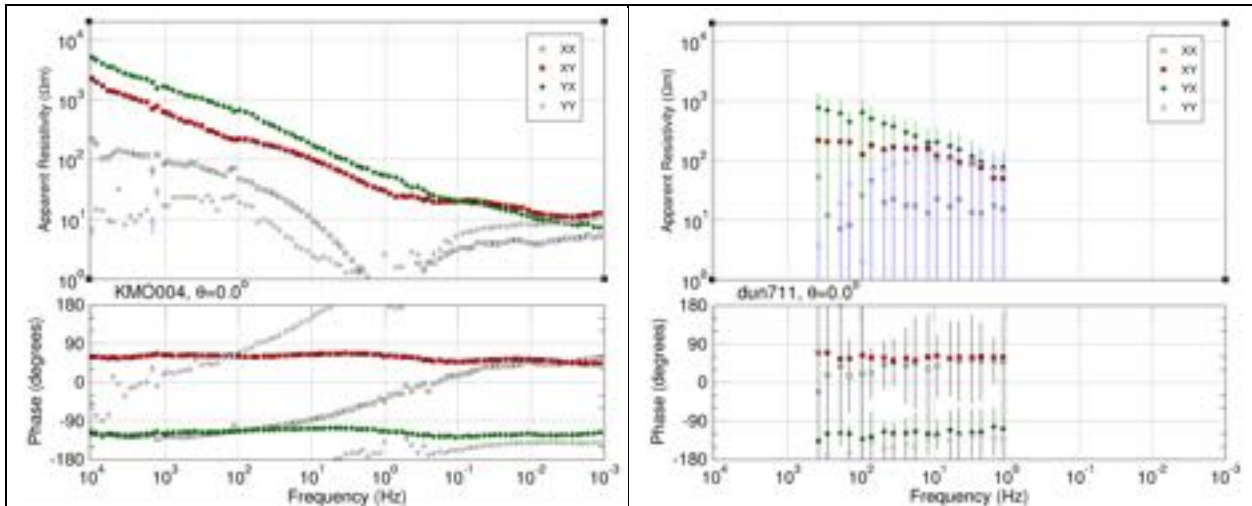


Figure 9: Locations of new site KMO004 and existing Duncan site dun711.



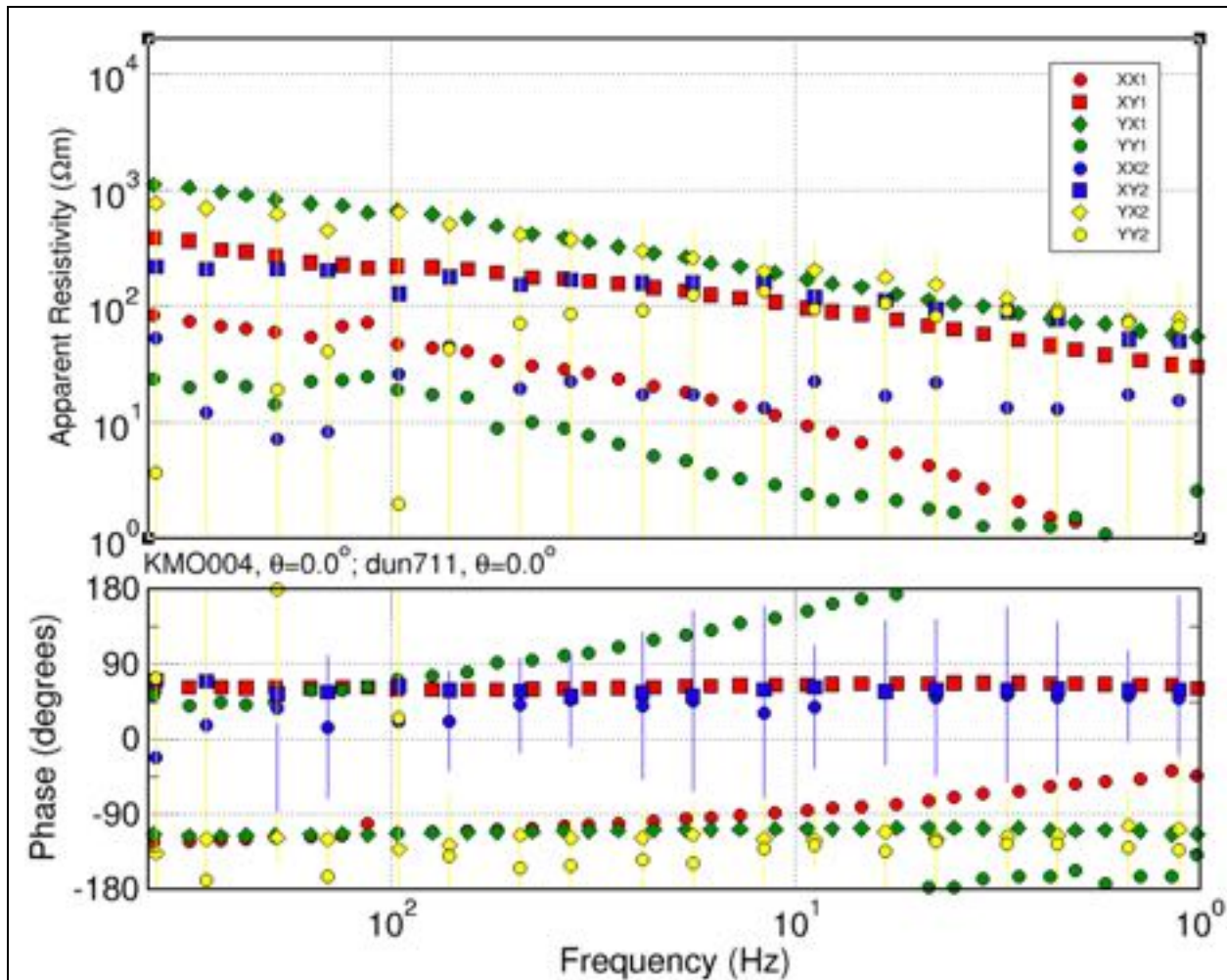


Figure 10: Comparison of new site KMO004 with Duncan site dun711. Top row: Plots of separate sites. Bottom row: Overlay of the two sets of data - "1" is KMO004 and "2" is dun711.

In contrast though to the first pair of sites, KSP104 and 86d003, separate distortion decompositions yield approximately the same strike directions, N29W for KMO004 and N33W for 86d003. Fitting the two together simultaneously in multi-site, multi-frequency mode yields 2-D response estimates with a common geoelectrical strike of N29W shown in Figure 11, and given the 35 years between the two, there is very good agreement (the shifts in the ρ_a curves are static shifts that are easily corrected for).

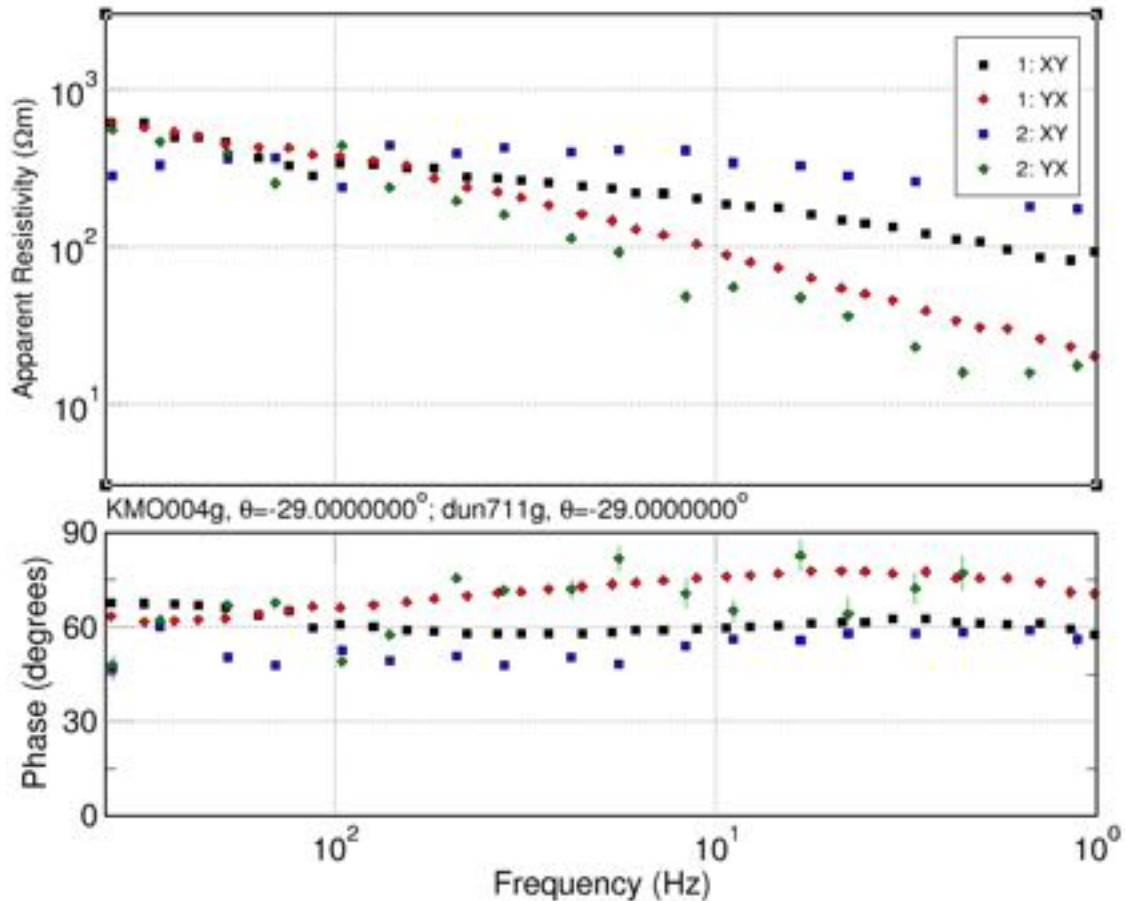


Figure 11: Comparison of distortion decomposed new site KMO004 and Duncan site dun711.

➔ We can conclude that the Duncan data is usable at most sites.

1.3.4. KSS106 and SS_14

New site KSS106 lies 400 m directly north of Quantec station SS_14 (Figure 12).

A comparison of the two sets of data is shown in Figure 13. The upper row plots the two sites separately, and the lower row overlays the two – “1” is KSS106 and “2” is SS_14.

Note that there is reasonable agreement between the off-diagonal estimates, XY and YX. There is some static shift effects evident in the Quantec data, but the ρ_{XY} and ρ_{YX} curves have mostly the same shape at frequencies >0.1 Hz. Below 0.1 Hz the Quantec Pha_{XY} estimates are very different from the new ones, with Quantec Pha_{XY} estimates leaving the 1st quadrant.

Of serious concern is the differences observable in the diagonal estimates, XX and YY. There is clearly a “tear” in the Quantec ρ_{YY} estimates at 10 Hz – such problems have been observed before in Quantec data provided by other clients and it appears to be at the overlap between the high frequency (HF) coil and the low frequency (LF) coil.

→ If the data are truly 2-D with a strike of N-S, then the diagonal terms are not used and this issue is unimportant. However, if the subsurface is 3-D, OR the strike is not exactly N-S, then all four elements of the impedance tensor are needed, and problems with the diagonal terms will influence the model of the subsurface.

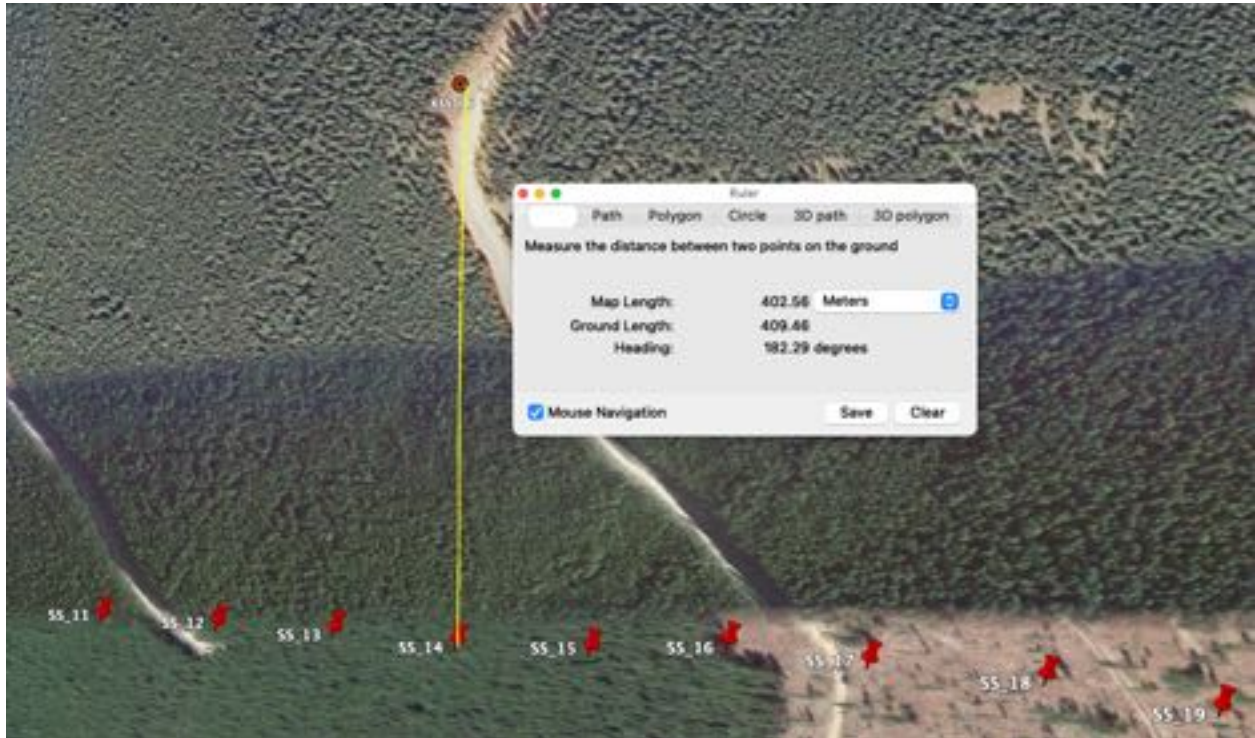
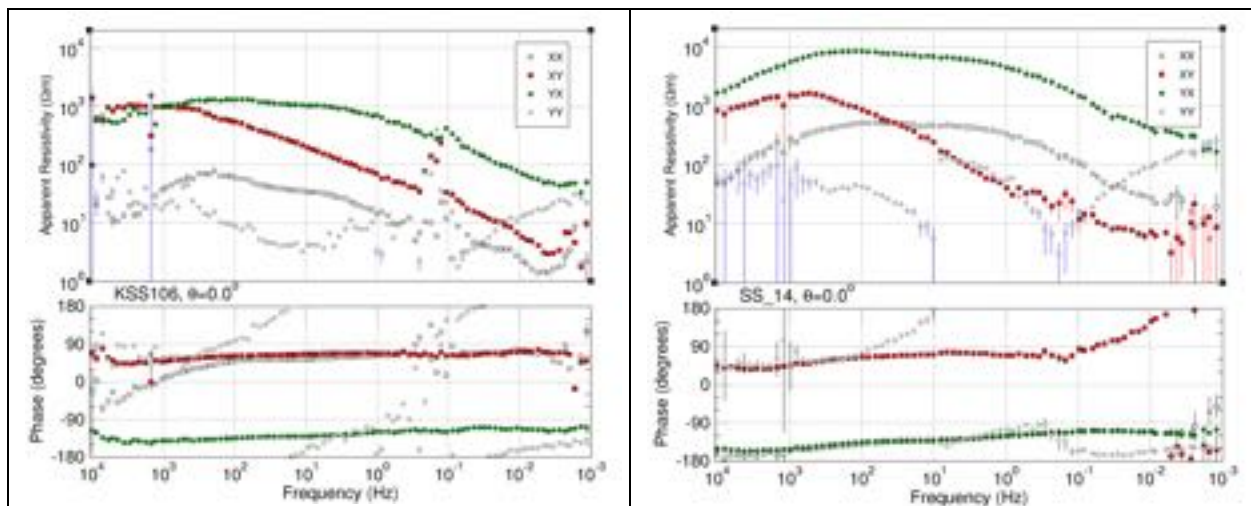


Figure 12: Locations of new site KSS106 and existing Quantec site SS_14.



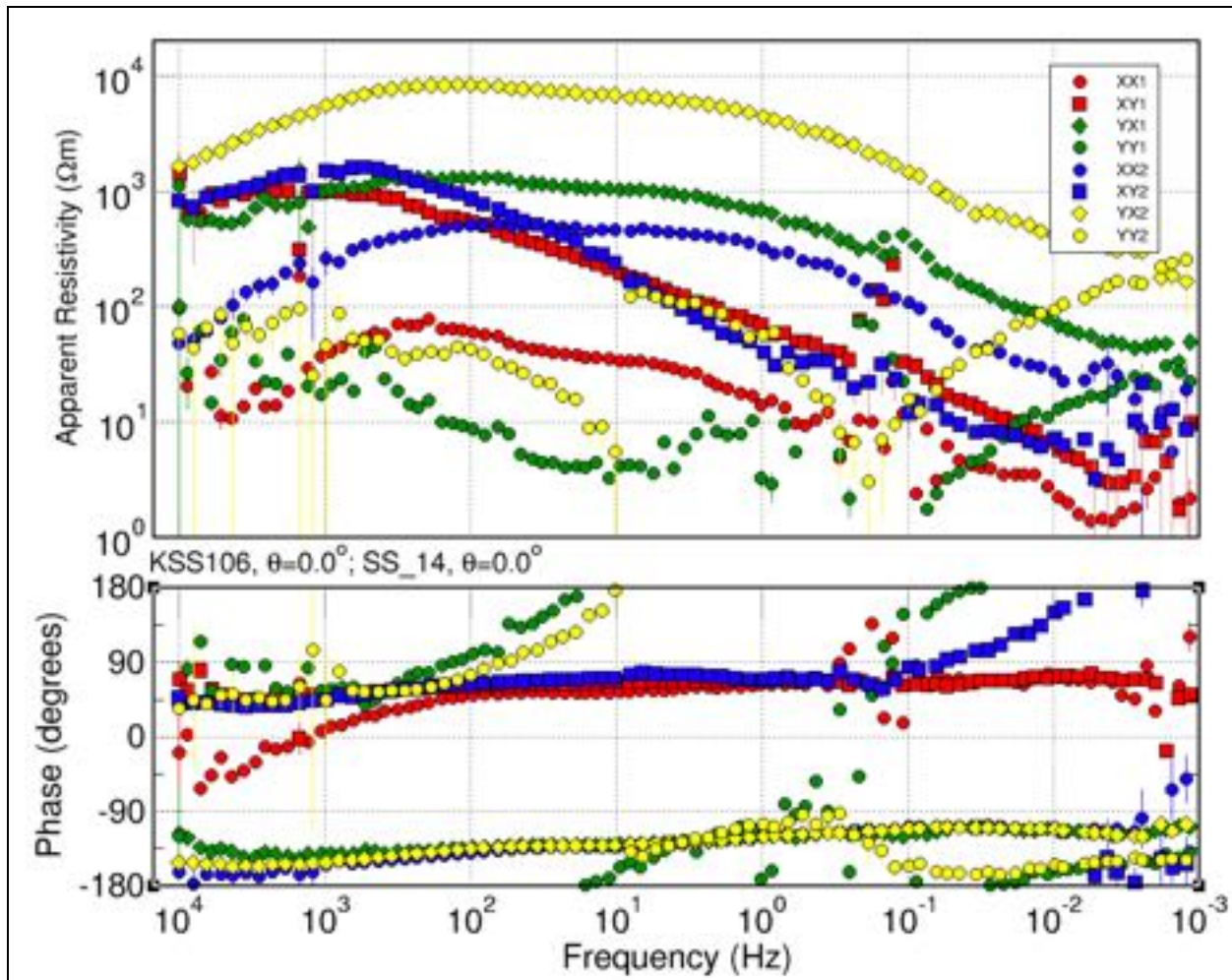


Figure 13: Comparison of new site KSS106 with Quantec site SS_14. Top row: Plots of separate sites. Bottom row: Overlay of the two sets of data - "1" is KSS106 and "2" is SS_14.

1.3.5. KSS108 and SS_32

Sites KSS108 and Quantec site SS_32 are 640 m from each other (Figure 14). Their comparison (Figure 15) is again somewhat reasonable for the off-diagonal components, XY and YX, but the diagonal terms are in very poor agreement.

In particular the PhaYY estimates (green and yellow circles) are 180° different from each other at high frequencies, but come into agreement at very low frequencies (<0.001 Hz). This problem has also been observed on data from other clients.

➔ **The Quantec diagonal elements are not in good agreement with the new Phoenix estimates, and should be used with caution.**

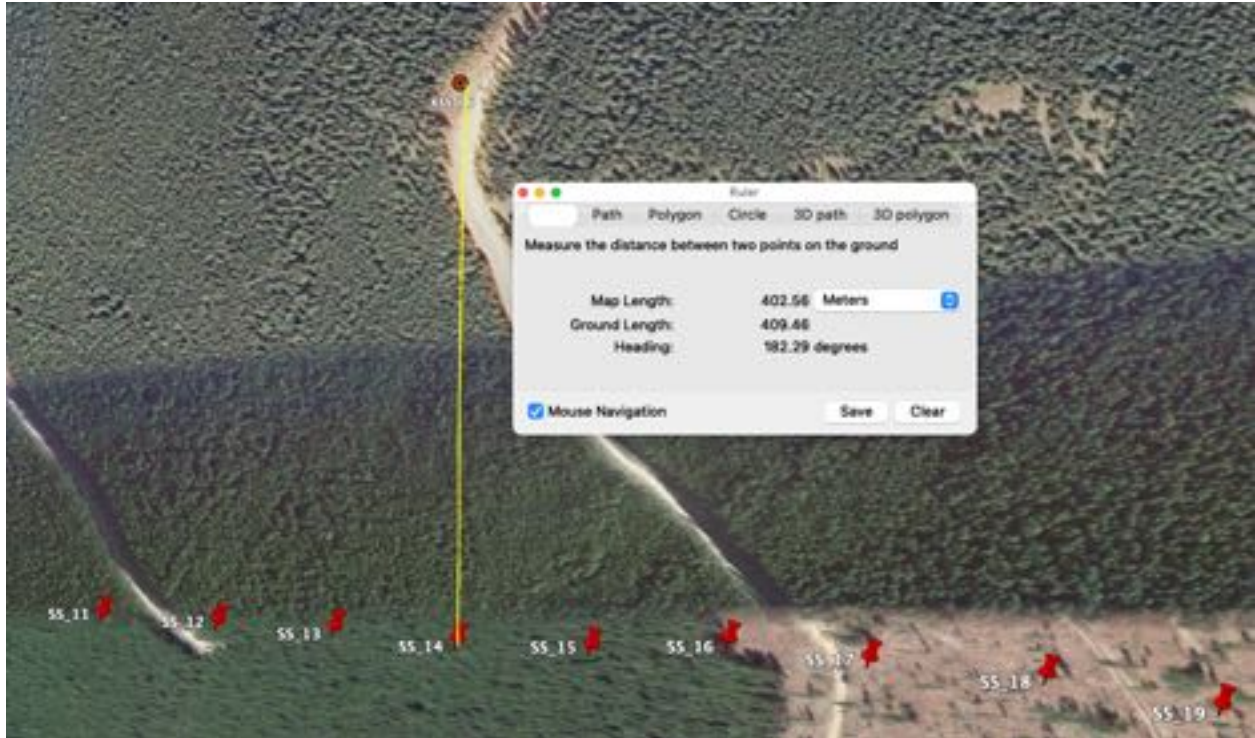
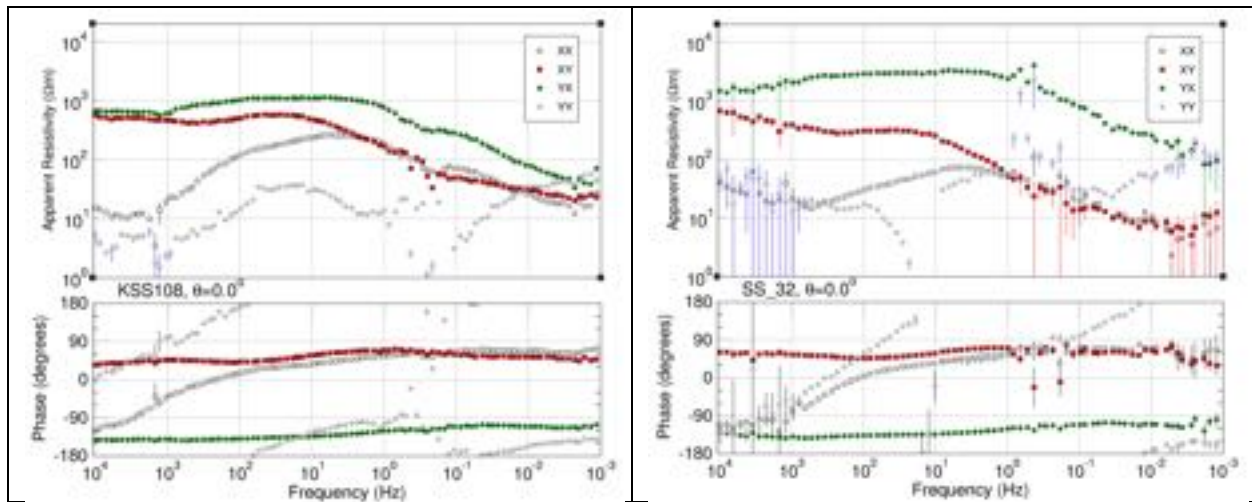


Figure 14: Locations of new site KSS108 and existing Quantec site SS_32.



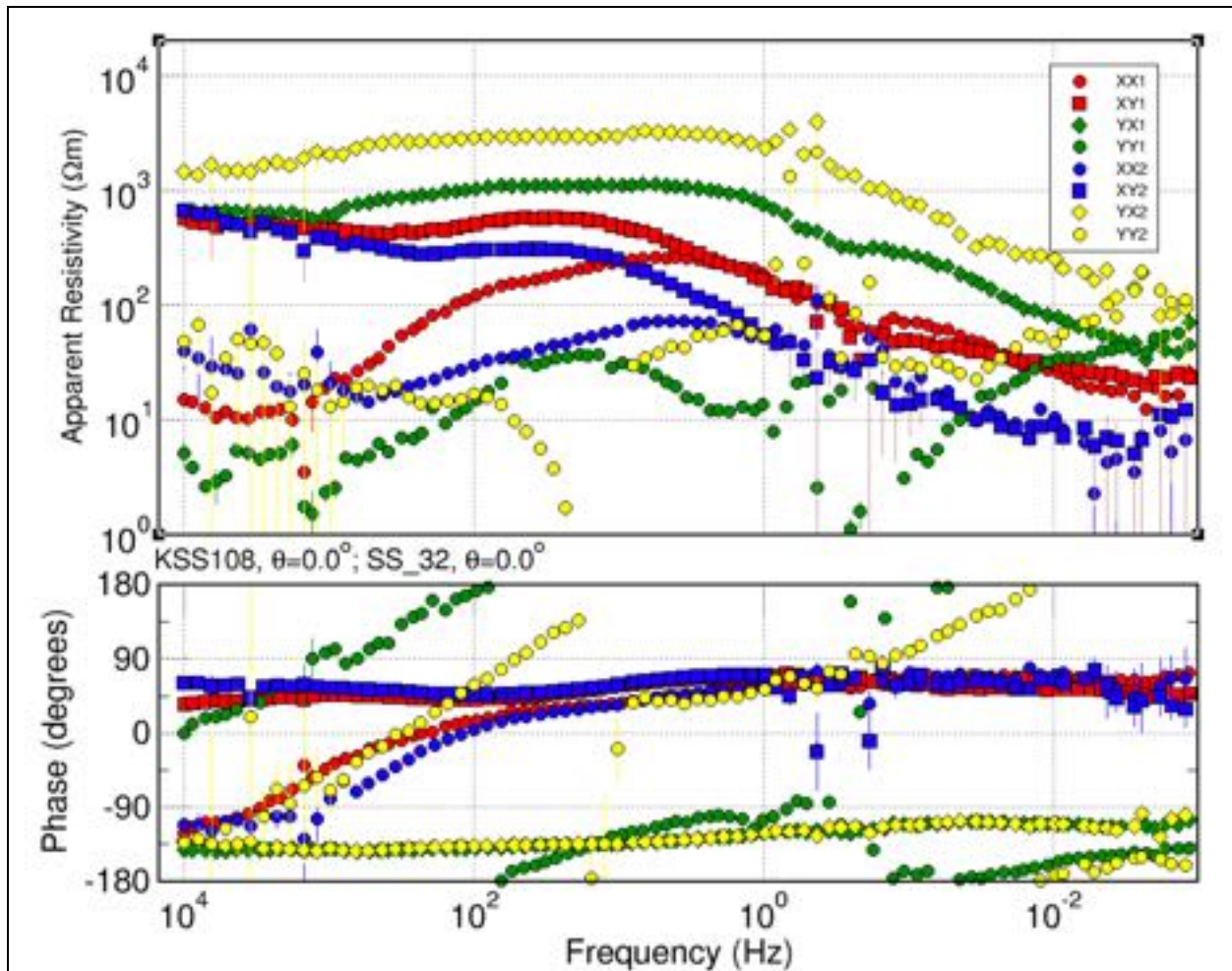


Figure 15: Comparison of new site KSS108 with Quantec site SS_32. Top row: Plots of separate sites. Bottom row: Overlay of the two sets of data - "1" is KSS108 and "2" is SS_32.

1.4. Profiles

The client's representative, Fred Cook, defined seven profiles of interest (Figure 16), with the cross-lines SP defined as two profiles, SP-EW and SP-NS. Profile MM1 uses both new data and Duncan data, and profile MO is only Duncan data for which a model already exists (see below).

Sites were assigned to the profiles as follows, from west to east.

Table 1: Site assignment to profiles.

Profile	Nsites	Sites
SS	15	KSS101, KSS102, KSS103, KSS104, KSS105, KSS106, KSS107, KSS108, KSS118, KSS109, KSS110, KSS111, KSS115, KSS112, KSS113
MM0	17	KMM001, KMM002, KMM003, KMM003b, KMM004, KMA002, KMM005, KMM006, KMM007, KMA001, KMM008, KMM009, KMM010, KMM011, KMM012, KMM013, KMM014
MM1	24	KMM210, KMM101, KMM102, KMM103, KMM104, KMM105, KMM106, KMM107, KMM108, KMM109, KMM110, KMM111, dun103, dun203,

		dun303, dun403, dun503, dun115, dun113, dun213, dun313, dun413, dun513, dun613
MM2	9	KMM201, KMM202, KMM203, KMM204, KMM205, KMM206, KMM207, KMM208, KMM209
SP-EW	12	KSP003, KSP004, KSP005, KSP006, KSP007, 86d002, KSP008, KSP009, KSP104, 86d004, 86d005, 86d006
SP-NS	9	KSP106, KSP105, KSP104, 86d002, KSP009, KSP008, KSP103, KSP102, KSP101
MO	14	dun311, dun411, dun511, 86d014, 86d145, 86d015, dun611, dun711, KMO004, KMO003, dun811, dun009, dun010, dun011

Note that the Quantec data are not assigned to profile SS.

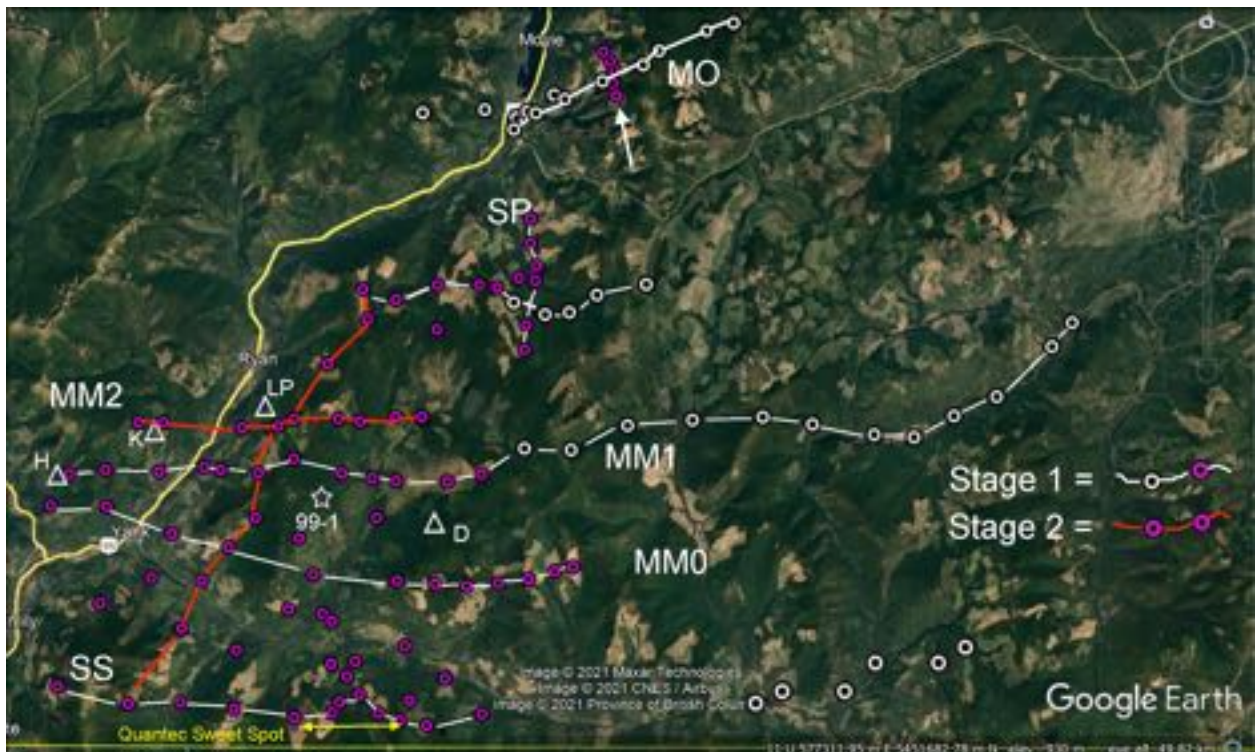


Figure 16: 2-D profiles defined by the client's representative. Purple sites are new sites and white ones are existing Duncan data.

Some of these existing data, namely stations along Duncan profile 3 (dunxx3) are used to extend profile “MM1”, others to extend profile SP-EW to the east (86d0xx), and others are used to define profile MO along Duncan profile 11.

Note that these existing data are broadband MT (BBMT) only, and the highest frequency of them is 384 Hz. Also note that they are on a different frequency set than the new data, so interpolation has to occur to get all 190 sites on the same set for inversion.

1.5. Existing models

Also note that profile MO, for Moyie, was modelled by Gupta and Jones (1995) where it is named the “Longfarrell” profile, as it combines sites along Farrell Creek and those along Teepee Creek. It is labelled profile B in Gupta and Jones (1995). These data were also modelled by Cook and Jones (1995).

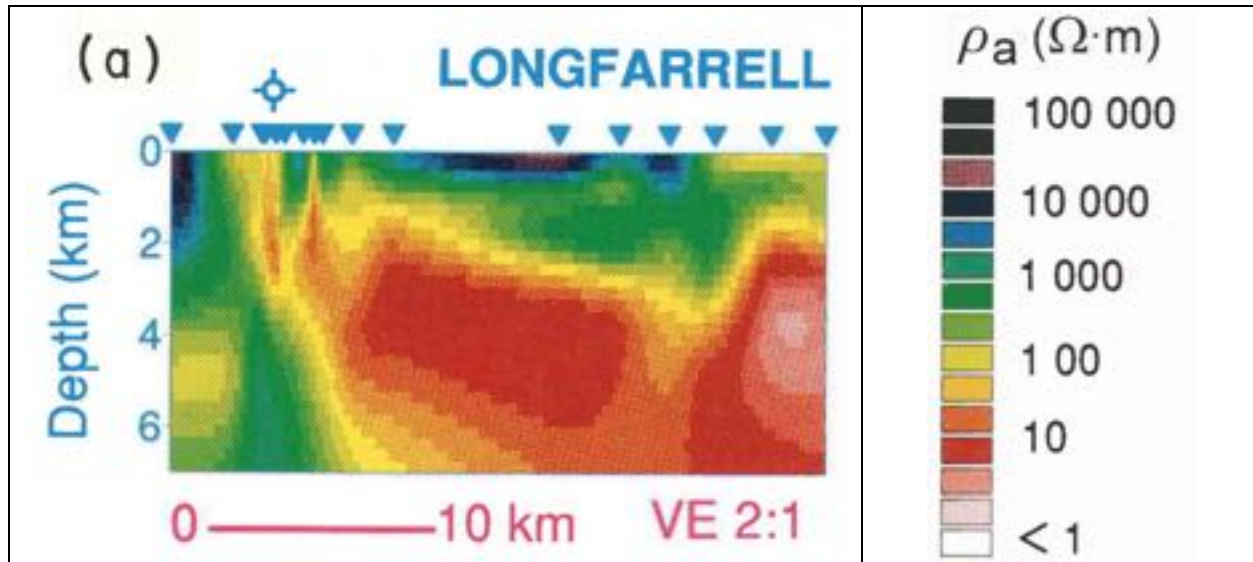


Figure 17: 2-D model derived by Gupta and Jones (1995) for the MO (Longfarrell) profile data.

The 2-D model derived for those data by Gupta and Jones (1995) is shown in Figure 17. This model was derived using the Rapid Relaxation Inversion (RRI) 2-D code that was current for the day, but modern codes are far superior. It will be interesting to see the model that we derive from these data.

Cook and Jones (1995) focus on only those sites in the close proximity to the drillhole at Moyie, and their model is shown in Figure 18.

Note that these two models had different adopted geoelectrical strike directions. The more regional Gupta and Jones (1995) model assumed a strike of N30W, whereas the more focussed Cook and Jones (1995) model had a strike of N50W.

The adopted strike angle is absolutely critical for correct modelling of the subsurface. If the wrong strike direction is chosen, then there is “mode switching”, i.e., the TE-mode data are modelled as TM-mode data, and vice-versa.

As we will discuss below, it is possible that both Gupta and Jones (1995) and Cook and Jones (1995) made errors in their assumed strike directions, and the correct strike directions were orthogonal to those assumed, i.e., N60E and N40E.

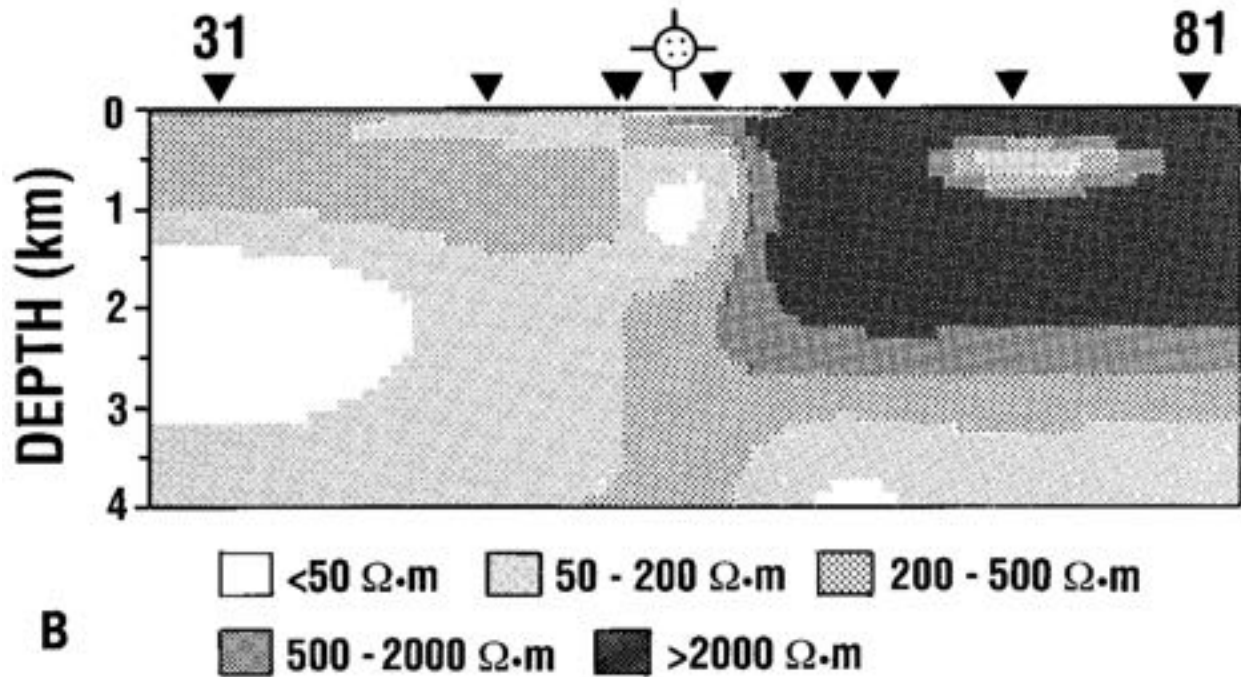


Figure 18: 2-D model derived by Cook and Jones (1995) for the sites around the Moyie drillhole.

2. New Acquisition

As described in the Logistics report, CMTS-2021-KootenayResources-R1, data were acquired at the 86 sites, and prior to each run measurements were made of the electric field parameters; contact resistances, AC and DC levels. For a discussion of these, see Appendix A.

The electrode array parameters measured at the commencement of acquisition are plotted in Figure 24.

2.1. Contact resistances

The contact resistances are, for the most part, reasonably low. The median values for E_x and E_y are $3.4 \Omega\mu$ and $3.6 \Omega m$, with the third quartiles of $5.9 \Omega m$ and $6.5 \Omega m$. The five sites in the NE corner, sites KMOxxx, all have high contact resistances, likely due to the surface conditions.

Ex Contact Resistance	Ey Contact Resistance
-----------------------	-----------------------

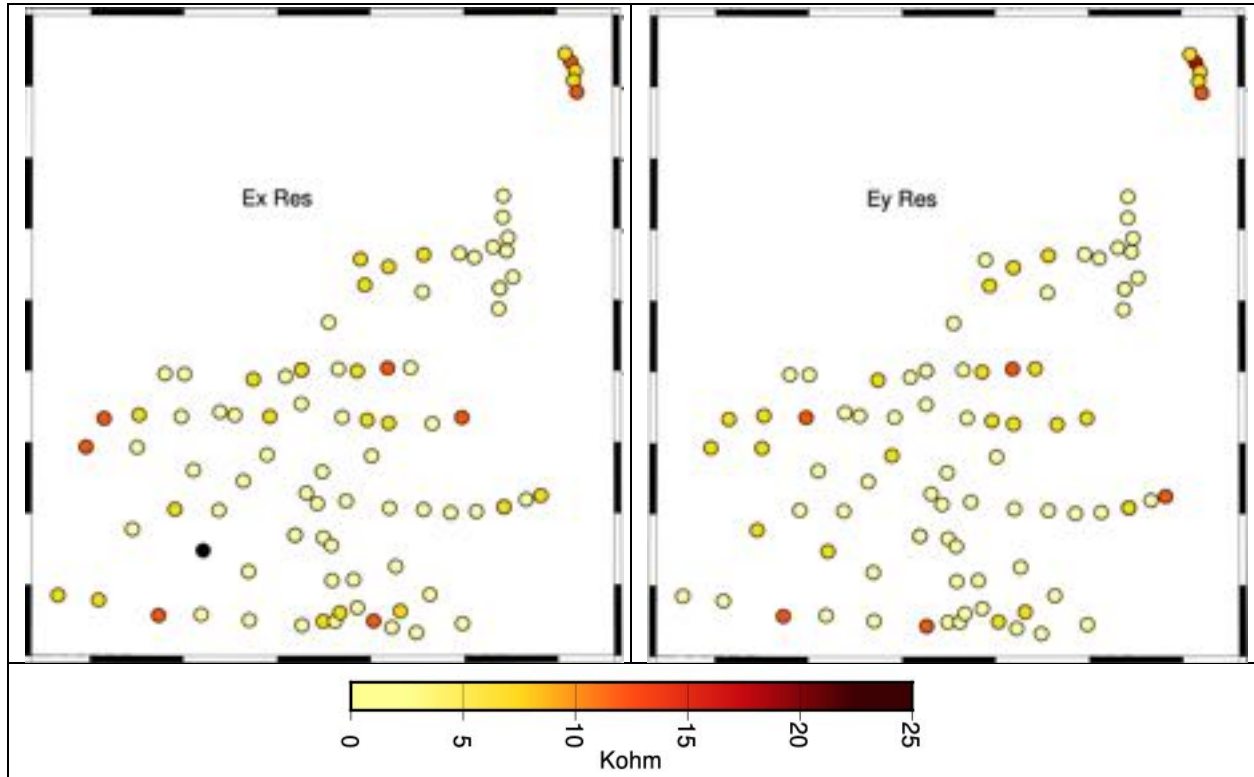


Figure 19: Electrode contact resistance measurements.

The most extreme value of 29.1 Ωm was recorded for the Ex line at site KHA006. The corresponding Ey line recorded a far lower value of 8.4 Ωm . The MT off-diagonal (XY & YX) estimates for this site exhibit high-frequency “pull-ups” in RhoXY and PhaXY (black squares, Figure 20) which may be a consequence of the high Ex contact resistance.

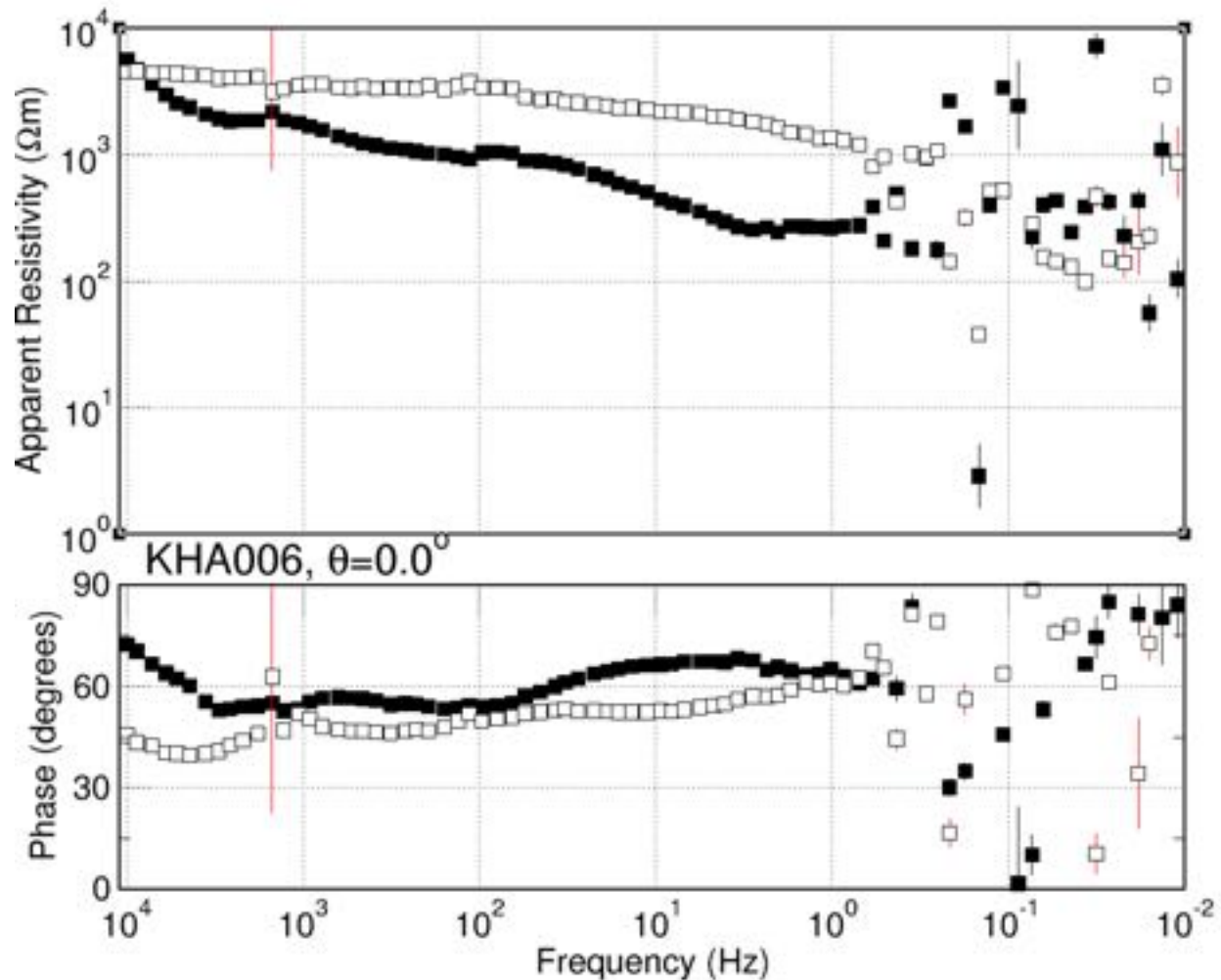


Figure 20: MT off-diagonal estimates for site KHA006.

We can check this by plotting the E_x contact resistance against the high frequency Pha_{XY} , and E_y against Pha_{YX} , for all sites. The cross-plot (Figure 21) shows that apart from this one outlier, there is the statistically weak suggestion of an increasing high frequency phase with increasing contact resistance. The best-fit linear regression through the data, excluding the anomalous KHA006 Pha_{XY} value, is

$$\text{Pha} = 31.1 (33.8 - 40.5) + 1.25 (0.67 - 1.84) R$$

(red line, Figure 21) where R = contact resistance and the ranges are the 95% confidence intervals of the intercept and the gradient. However, the R-squared goodness-of-fit statistic is only 0.097, which indicates very low confidence in the relationship.

Taking the logarithm of the contact resistances, the R-squared goodness-of-fit statistic is even lower at 0.081 with the linear regression model

$$\text{Pha} = 35.1 (30.5 - 39.6) + 13.60 (6.61 - 20.60) \log_{10}(R)$$

(blue line, Figure 21).

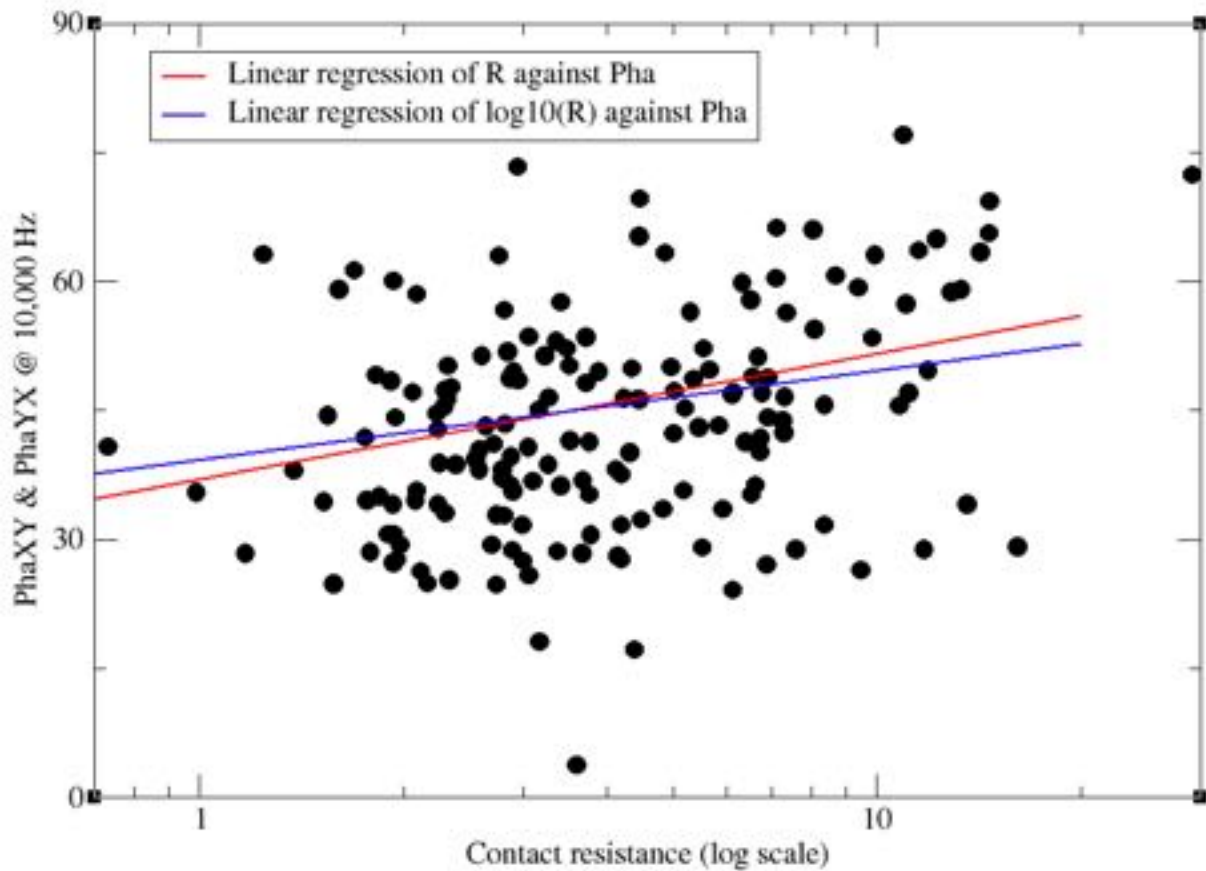


Figure 21: High frequency (10 kHz) PhaXY and PhaYX phase compared to contact resistance measured. Linear regression lines of R against Pha and $\log_{10}(R)$ against Pha shown.

One could conclude that there is a weak correlation of contract resistance with high frequency phase, but one must beware that correlation does not mean causation.

Plotted in Figure 22 are maps of the high frequency phases, plus smoothed median versions. The sites exhibiting anomalous phases compared to their neighbours can be compared with the sites showing high contact resistances in Figure 19.

There are some correlations, but others not.

→ Care should be taken when modelling sites with high contact resistances as the very high frequency phases may have been affects.

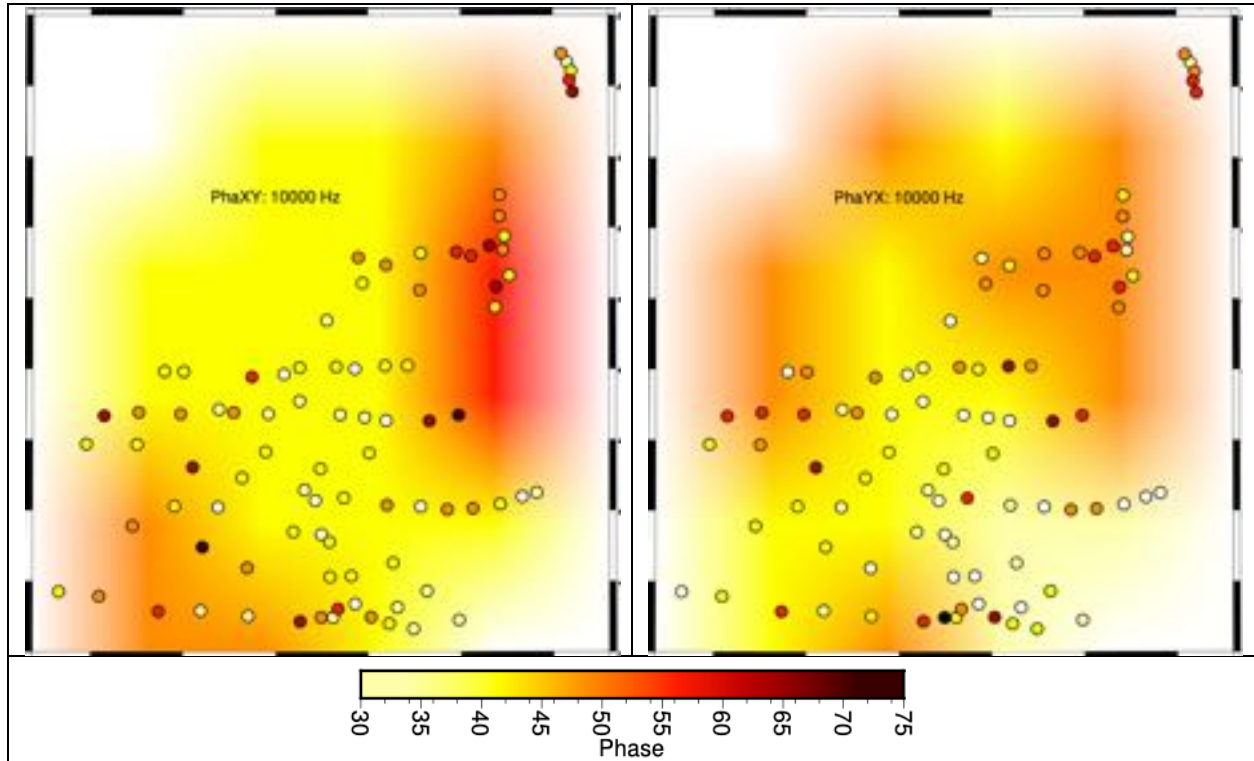
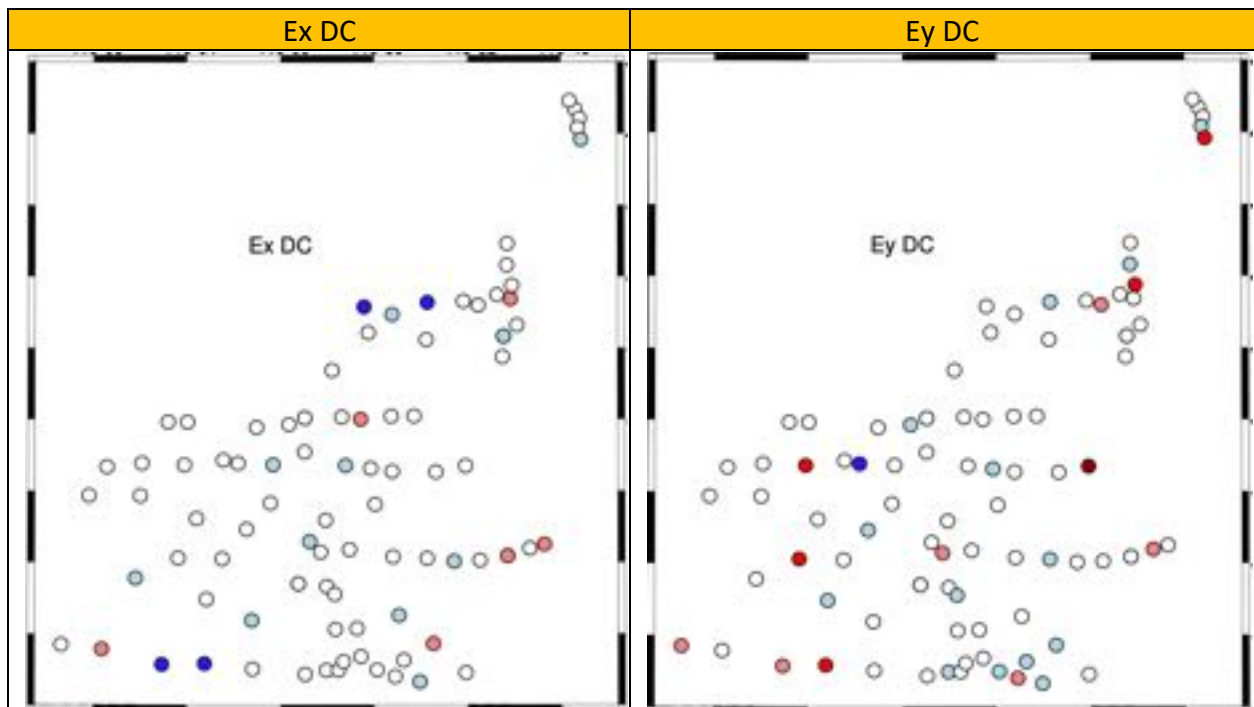


Figure 22: 10 kHz PhaXY (left) and PhaYX (right). Values at each site are shown by the coloured circles, and the contours are smoothed median maps of the values..

2.2. DC values

The DC values show that the electrodes were in good to very good condition



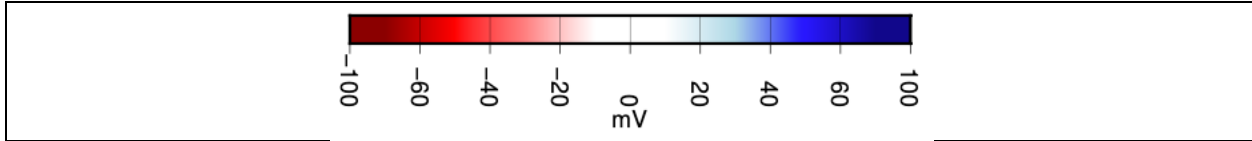


Figure 23: Electrode DC measurements.

2.3. AC values

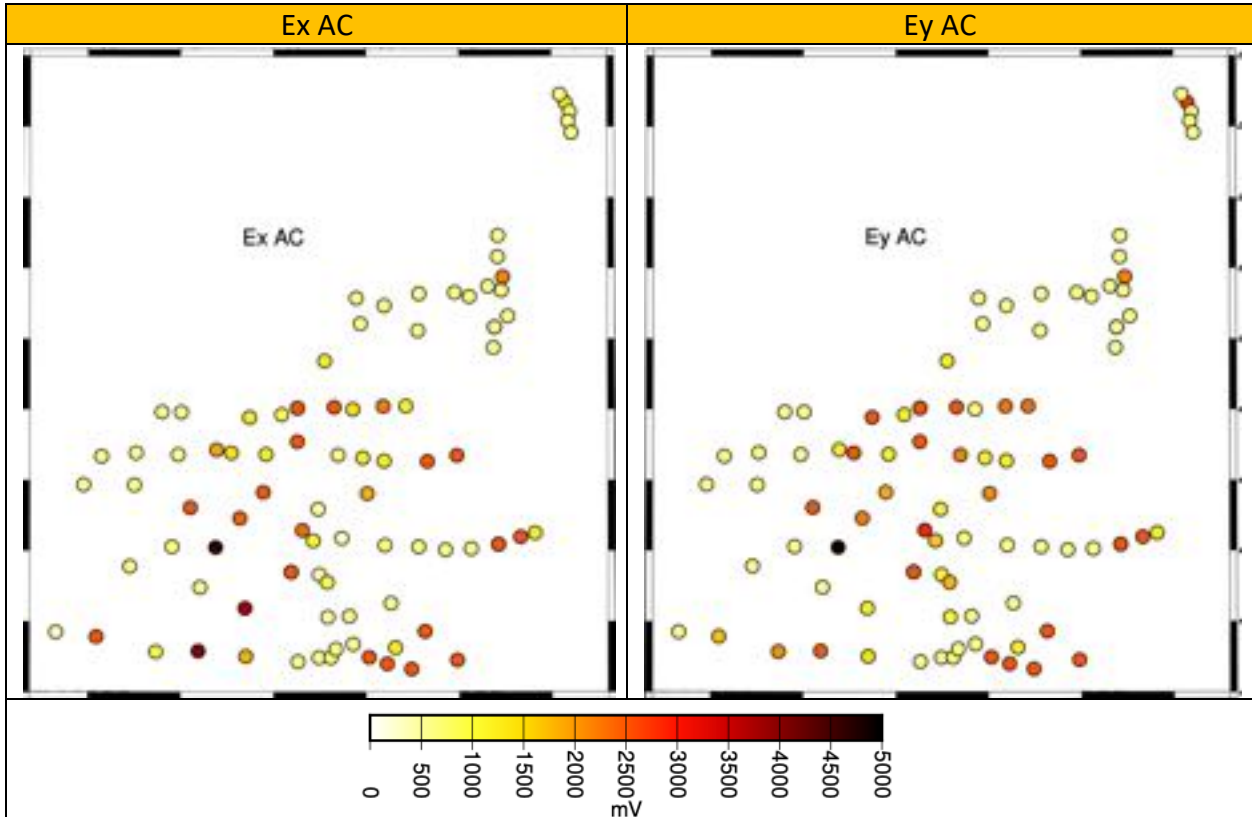


Figure 24: Electrode AC measurements.

3. MT Quality Factors

The derivation of the Smoothness Factor (SF), Error Factor (EF) and Quality Factor (QF) is described in Appendix C.

3.1. QF Plots

I plot sets of SF, EF and QF maps for each of five frequency/period bands for the MT data (Figure 25), assuming an error floor of 1° in phase/3.5% in apparent resistivity (which are levels for high quality data in the MT community).

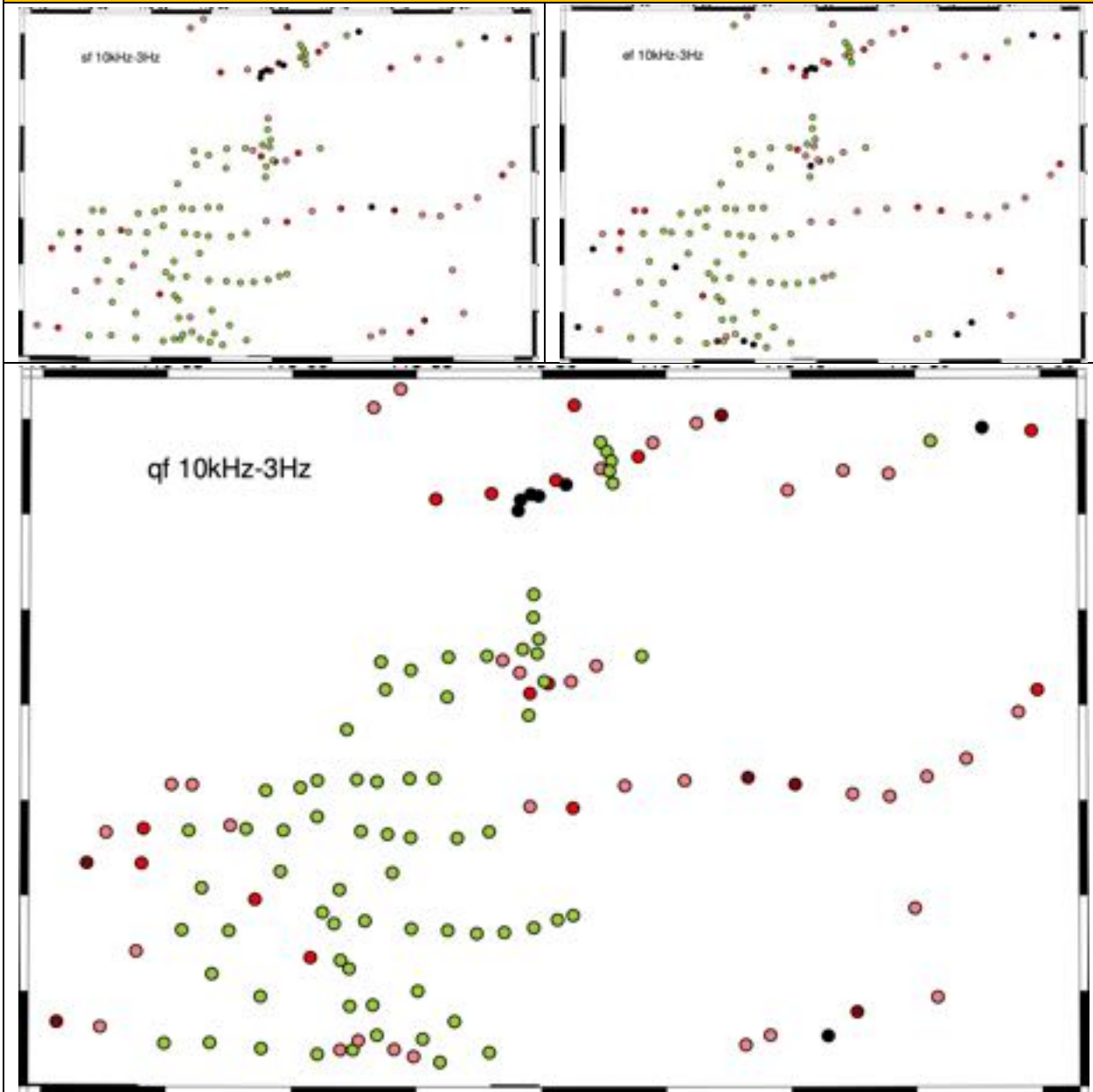
The frequency/period bands are:

- 1) 10 kHz – 3 Hz: These three-and-a-half decades cover all of the data that may be of interest, penetrating down to on average 4-5 km at the lowest frequency.
- 2) 3 Hz – 0.001 Hz: These three-and-a-half decades cover all of the data that may be of interest for crustal imaging, penetrating down to below the Moho at the lowest frequency.
- 3) 4 kHz – 800 Hz: This half decade covers the AMT dead-band, and has a depth penetration on average of 150 – 400 m.
- 4) 8 Hz – 0.1 Hz: This decade-and-a-half covers the MT deadband.
- 5) 800 Hz – 8 Hz: These two decades are where the best signals are that are sensing from 400 m to 3-4 km.
- 6) 0.1 Hz – 0.002 Hz (10 s – 500 s): This decade-and-a-half are where the best signals are sensing from 8 km to 25 km.

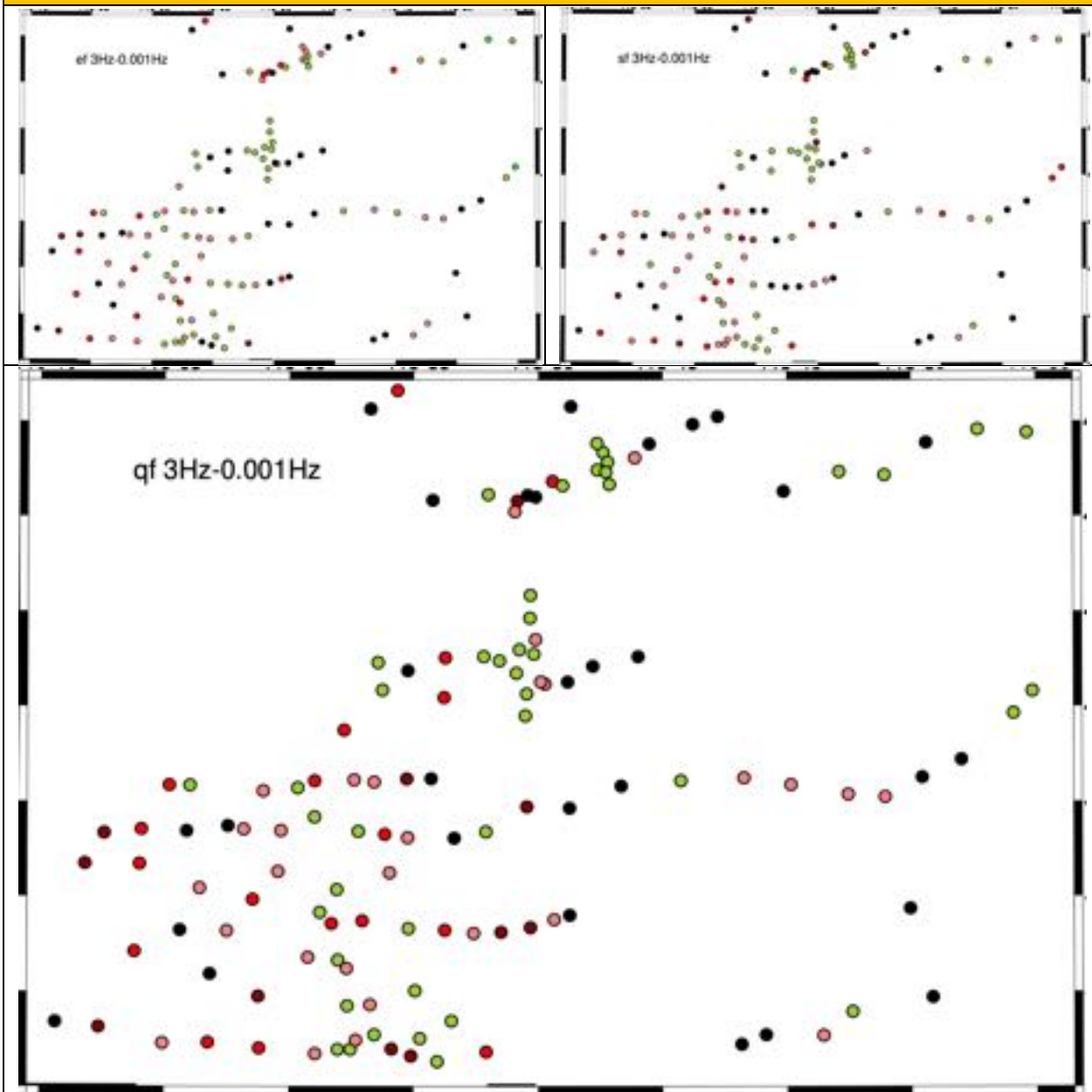
The median PHA errors for the frequency band 800 Hz – 8 Hz (avoiding the scatter in the AMT deadband) are $\text{PhaXY} = 0.025^\circ$ and $\text{PhaYX} = 0.0046^\circ$, which are ridiculously low. Even the diagonal phases are very low, $\text{PhaXX} = 0.17^\circ$ and $\text{PhaYX} = 0.11^\circ$. There is no way that errors can be that low. The problem is the Stodt parametric error estimator used by Phoenix to calculate the errors.

A brute force way of dealing with them is to assume an error floor, i.e., error estimates LESS than the floor are raised to the floor, and estimates greater than the floor are unchanged. An error floor of 1° in phase/3.5% in apparent resistivity was assumed – such an error floor is appropriate for high quality MT response estimates. Viewing the plots this is appropriate at some sites for some frequencies, but certainly not appropriate at all sites for all frequencies.

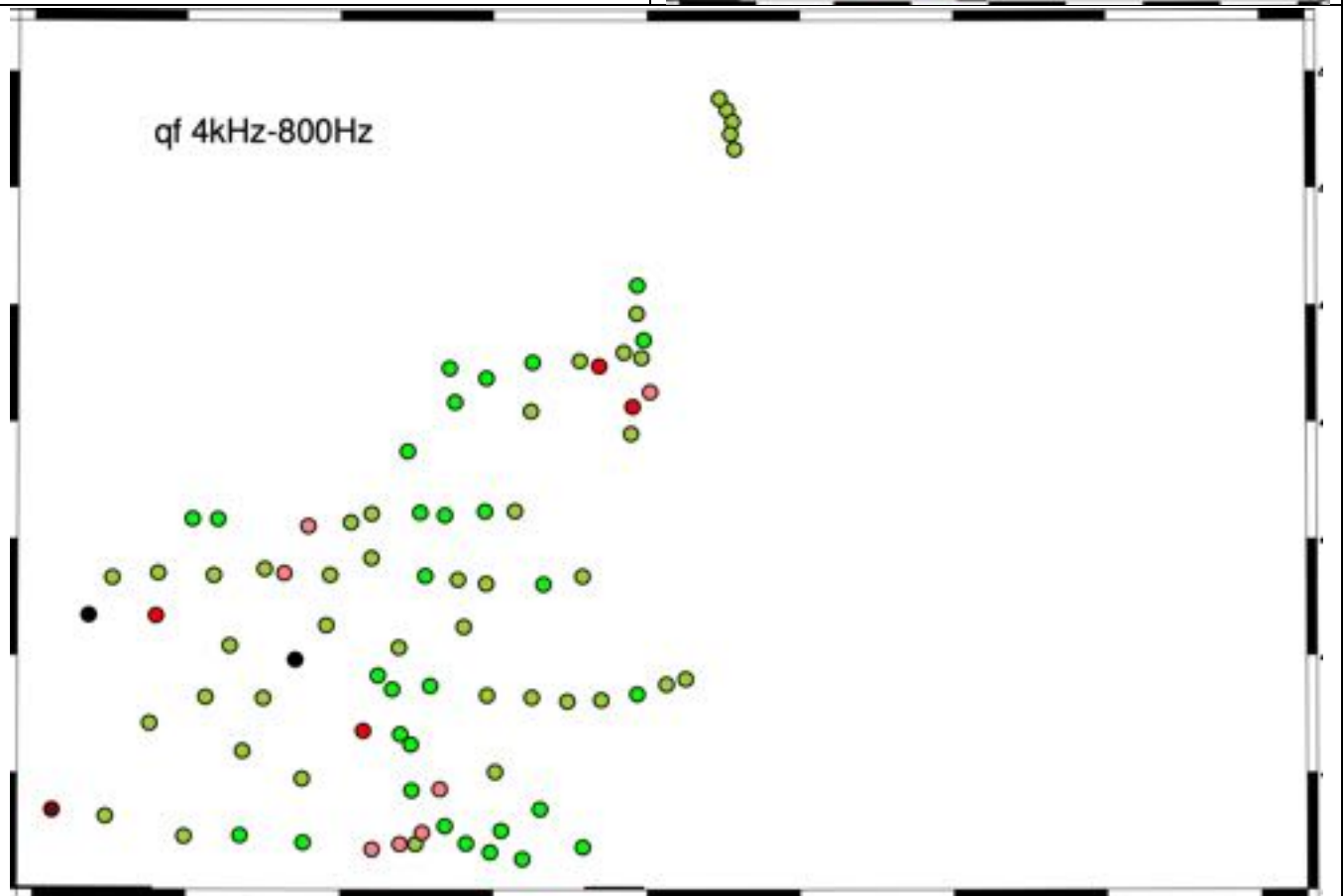
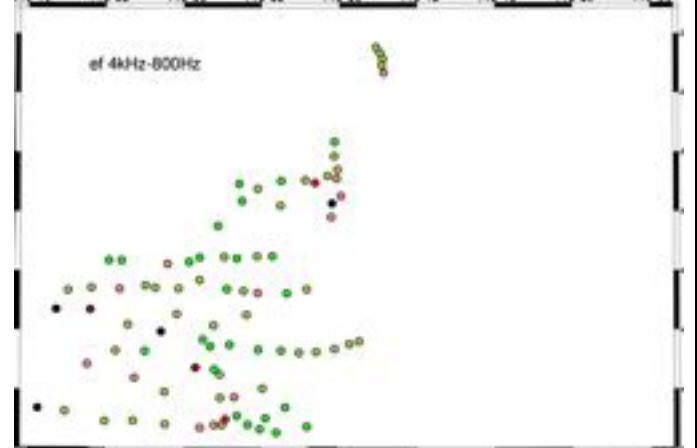
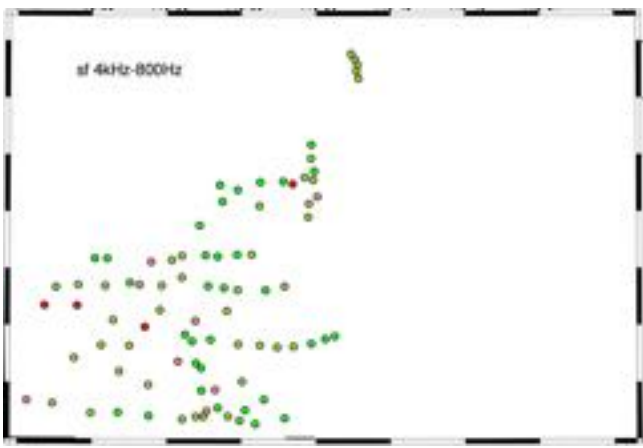
10 kHz – 3 Hz: Surface to 4-5 km



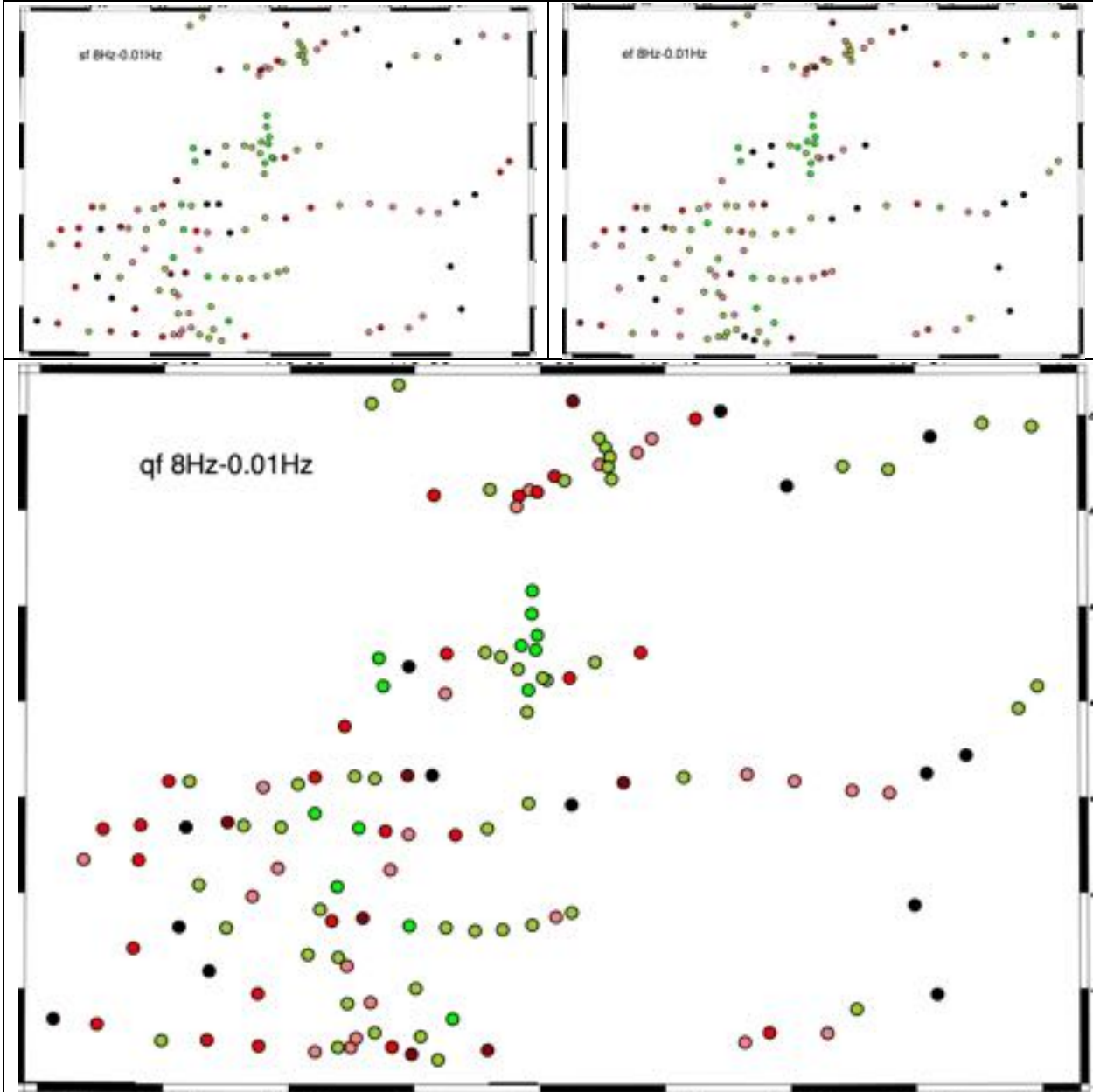
3 Hz – 0.001 Hz: 4-5 km to Moho



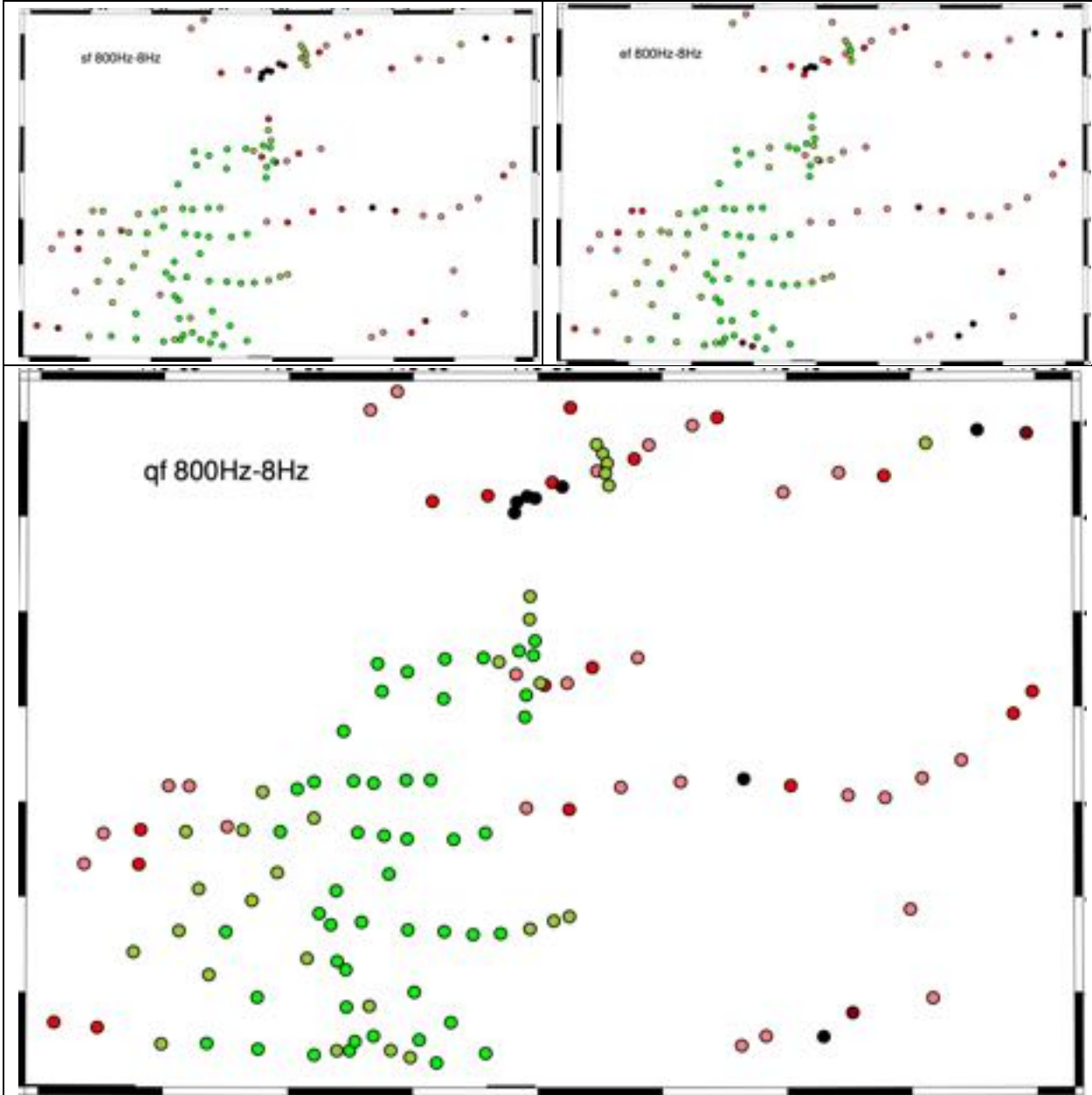
4 kHz – 800 Hz: AMT deadband



8 Hz – 0.1 Hz: MT deadband



800 Hz – 8 Hz: Optimum frequency band for shallow imaging



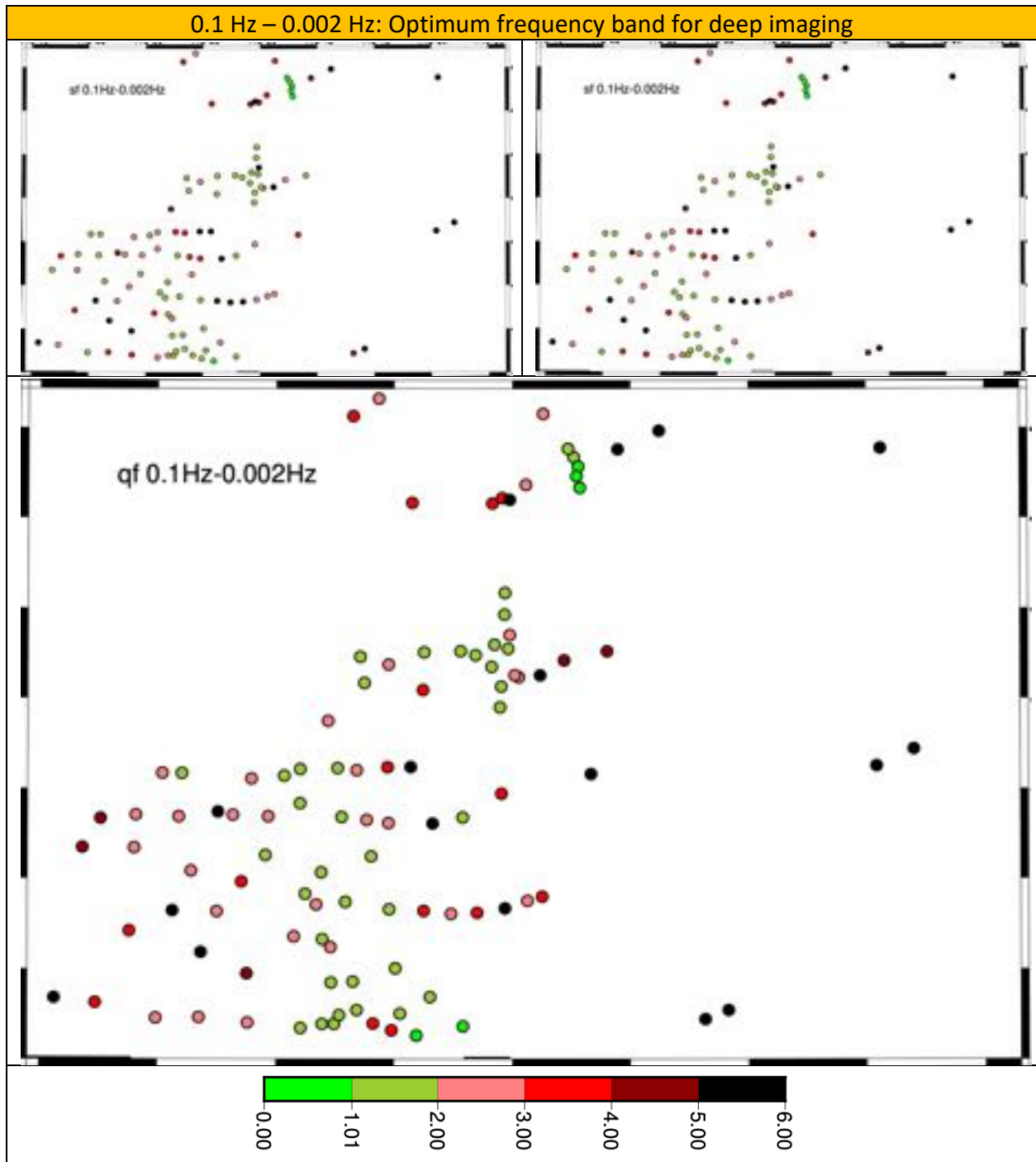
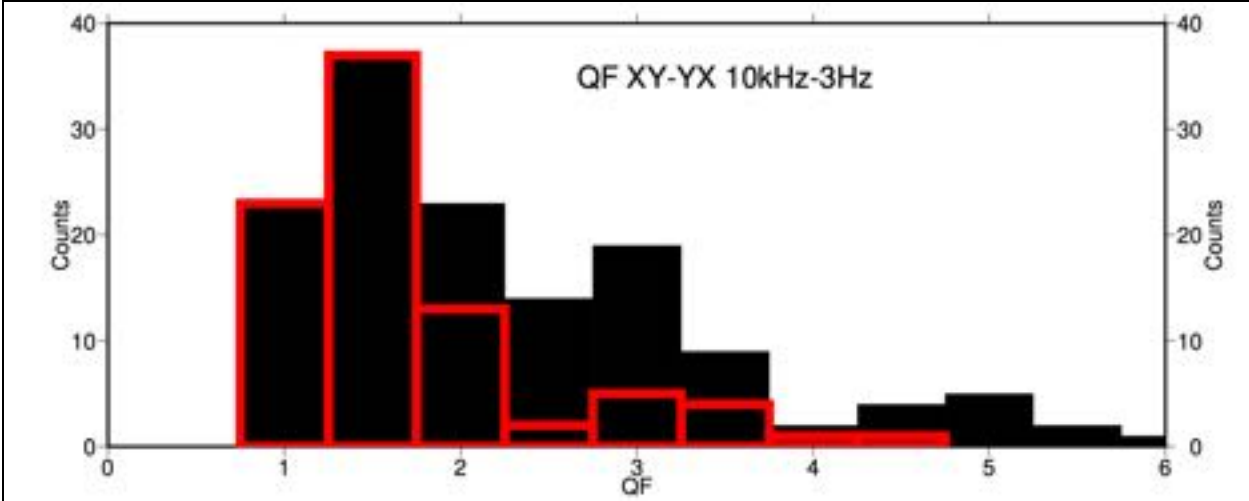


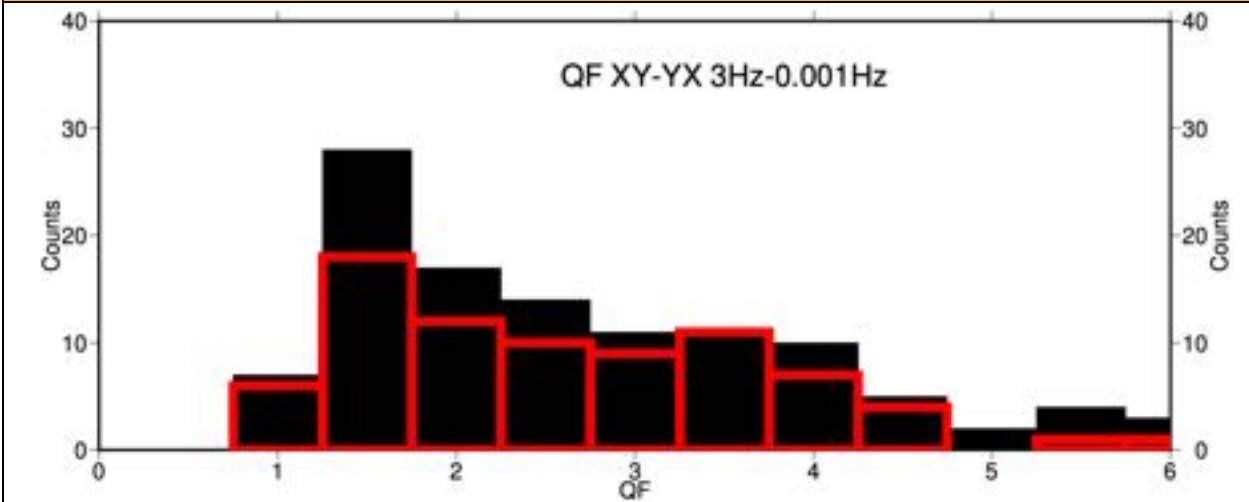
Figure 25: Maps of the Smoothness Factor (SF, left column), Error Factor (EF, right column) and Quality Factor (QF, bottom row), for an adopted error floor of 1° in Pha and 3.5% in RhoA..

The histograms of the QFs are shown in Figure 26. Histograms for all data are plotted in black, and those for the new Kootenay data only are with thick red lines.

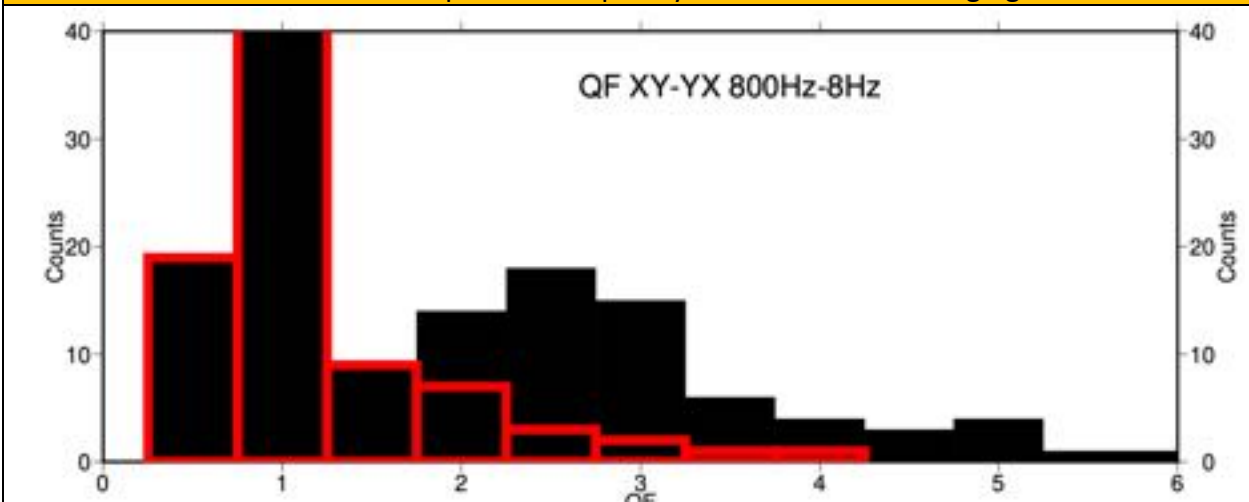
10 kHz – 3 Hz: Surface to 4-5 km



3 Hz – 0.001 Hz: 4-5 km to Moho



800 Hz – 8 Hz: Optimum frequency band for shallow imaging



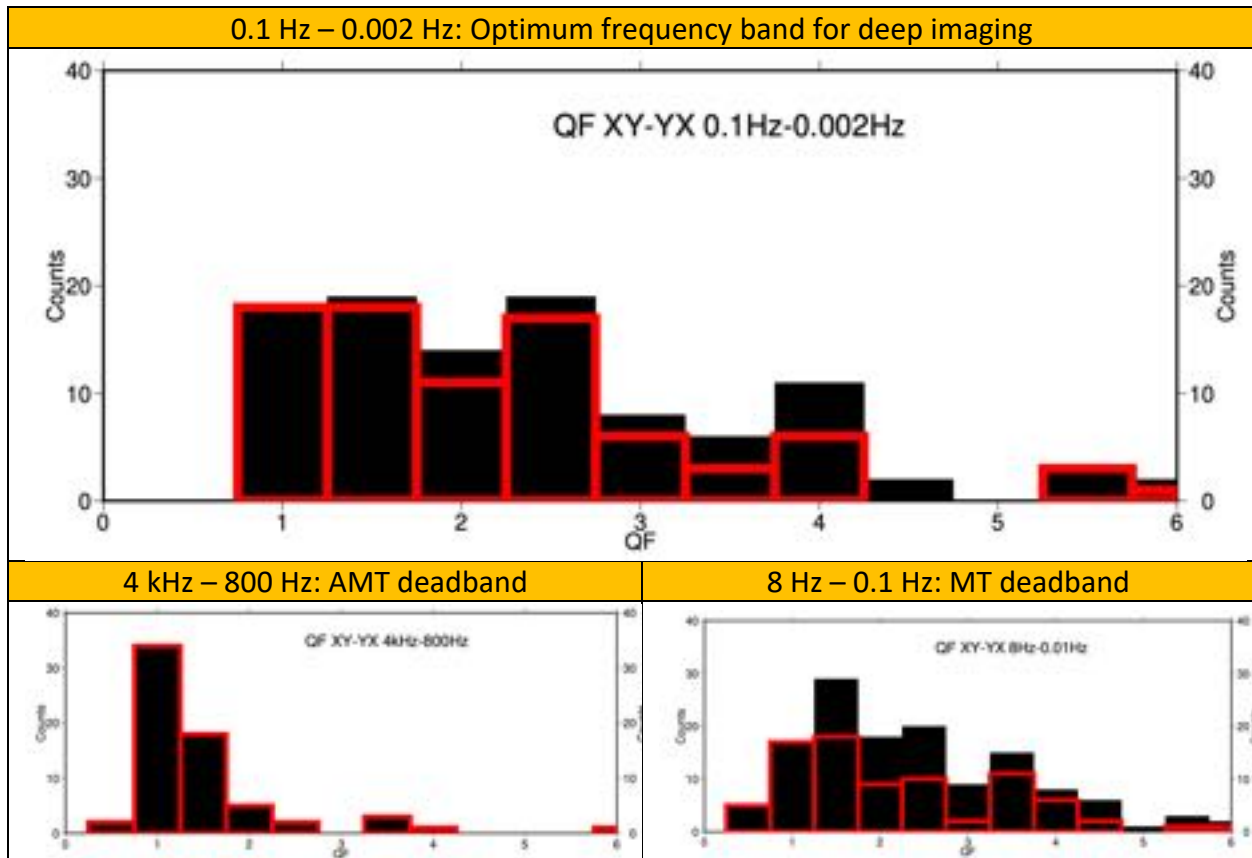


Figure 26: Histograms of the Quality Factors for various frequency bands for an adopted error floor of 1° in Pha and 3.5% in RhoA. Note: Only QFs to 6 are plotted, larger values are omitted from these plots. The black histograms are for all data, and the red lines indicate the new Kootenay data only

Overall, in the 10 kHz – 3 Hz band the QFs are well peaked at QF=1.25-1.75, with the Kootenay data having far lower QFs (= better quality) than the older Duncan data. The overall mean and median are 2.49 and 2.09, with first and third quartiles of 1.34 and 2.89. For the Kootenay data only, the mean and median are 1.71 and 1.44, with first and third quartiles of 1.23 and 1.82, statistical testament to the far higher quality of the new Kootenay data compared to the older Duncan data in this frequency band. Recall also that the older data only goes to a maximum frequency of 384 Hz.

At the lower frequency band however of 3 Hz – 0.001 Hz, the QF histogram is flatter, but nevertheless exhibits a peak at 1.25-1.75, albeit not as strong a peak. Also the distribution is very long tailed, with almost 25% of the QFs being >6 so not plotted. The overall mean and median are 4.32 and 2.89, with first and third quartiles of 1.75 and 5.73. For the Kootenay data only, the mean and median are 2.69 and 2.44, with first and third quartiles of 1.62 and 3.41, meaning there are fewer sites with very high QF so generally the Kootenay data are superior.

In the optimum frequency band of 800 Hz – 8 Hz, the Kootenay data are clearly far superior to the older data. The overall mean and median are 2.23 and 1.58, with first and third quartiles of 0.89 and 2.92. For the Kootenay data only, the mean and median are 1.18 and 0.94, with first

and third quartiles of 0.76 and 1.27. For the Duncan data, these values are 3.80, 3.04, 3.42 and 3.86. This again provides statistical evidence of the far higher quality of the new Kootenay data compared to the older Duncan data at frequencies probing down to 4-5 km.

→ We can conclude that the appropriate error floors for the new Kootenay data is 3.56%/1° for RhoA and Pha respectively for frequencies probing down to 4-5 km, whereas for the Duncan data higher error floors of 10.86%/3° are appropriate.

→ At the deeper-probing frequencies down to the Moho, then overall error floors of 9.61%/2.7° are appropriate for the Kootenay data

3.1.1. Change of QF with survey time

The QFs over the length of the survey for the new Kootenay data are shown in Figure 27 for the shallow-probing (red) and deep-probing (black) frequency bands.

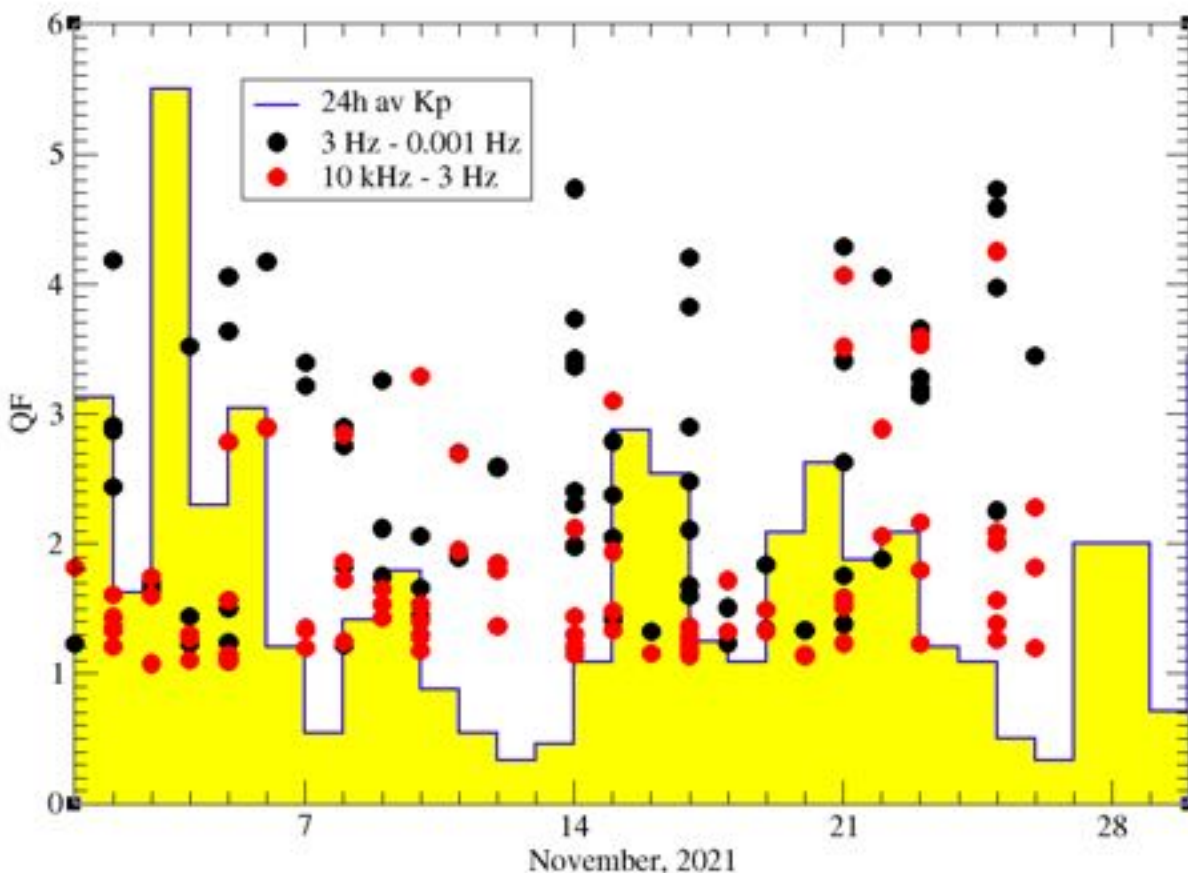


Figure 27: QFs in the frequency ranges 10 kHz - 3 Hz (black) and 10 kHz - 3Hz (red), with acquisition start day since 1st November, 2021. The yellow histogram gives the daily averaged Kp values.

There is clearly variation with time of the quality of the data in both bands. These are both signal related. The 3 hour Kp indices ⁽¹⁾ for November have been averaged from midday to midday on the day. There was significant low frequency (<8 Hz) magnetic activity at the beginning of November, and again from 15th onwards, but there was a deep lull in magnetic activity from 7th to 14th.

A plot of the Kp indices against derived QFs for the impedance estimates in the 3 Hz – 0.001 Hz band (Figure 28) shows a strong visual relationship; high Kp correlates with low QF (= high quality data), and vice-versa. Omitting the three anomalous points with very high Kp of 5.5, the others are fit to a linear regression (red line) with a correlation coefficient of -0.42.

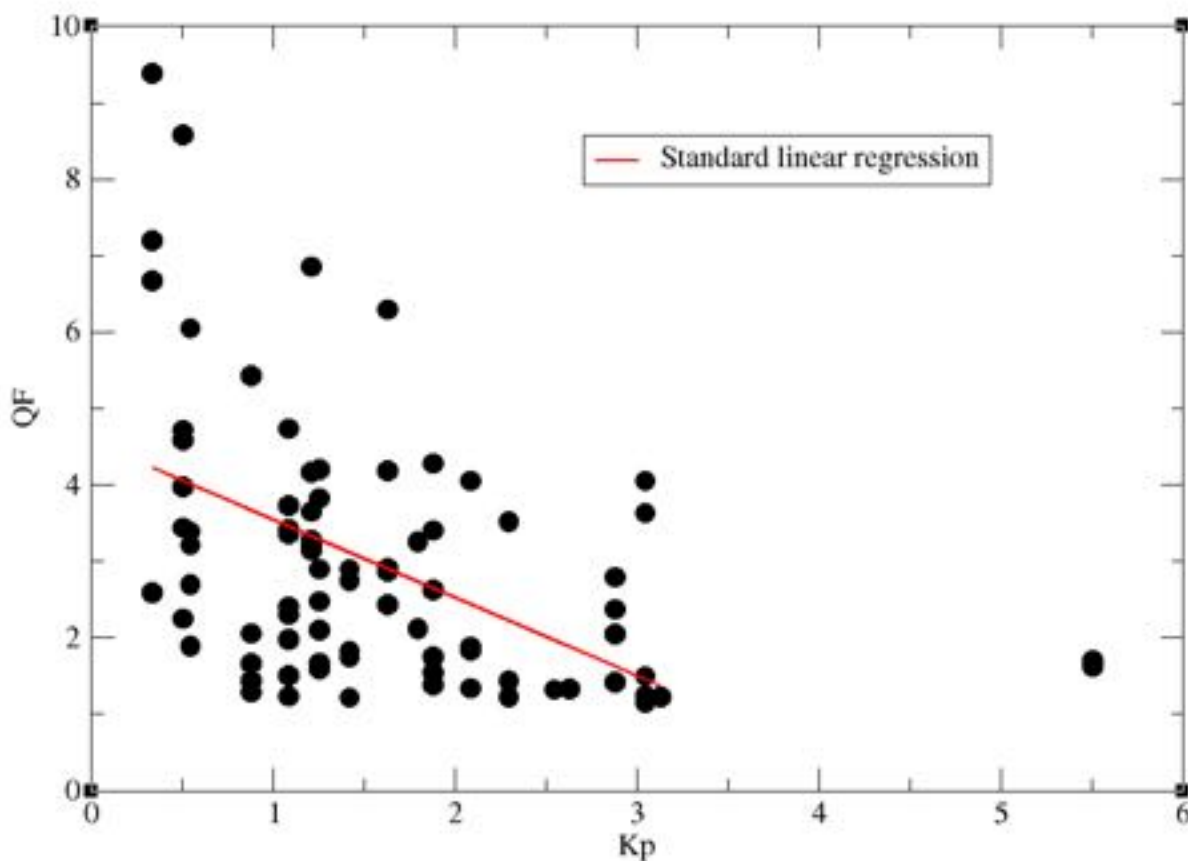


Figure 28: Kp indices against QFs for 3 Hz - 0.001 Hz band

¹ The Kp-index is the global geomagnetic activity index that is based on 3-hour measurements from ground-based magnetometers around the world. The Kp-index is a three hour long quasi-logarithmic index of the geomagnetic activity. The Kp-index ranges from 0 to 9 where a value of 0 means that there is very little geomagnetic activity and a value of 9 means extreme geomagnetic storming.

→ The quality of the low frequency responses (<8 Hz) is directly correlated with signal activity.

3.2. Example sites

Below I show examples of data for varying quality sites for the band 10 kHz to 3 Hz, which is the band of primary interest to the client.

3.2.1. Example of excellent quality sites, $QF = 1.00 - 1.25$

Of the 86 sites, over one quarter (23) have a $QF < 1.25$. The lowest of all is site KSS114 with a QF of 1.077 (Figure 29). These are really beautiful data – both the main off-diagonals (XY & YX) are smooth, and the diagonal elements (XX & YY) are well-determined.

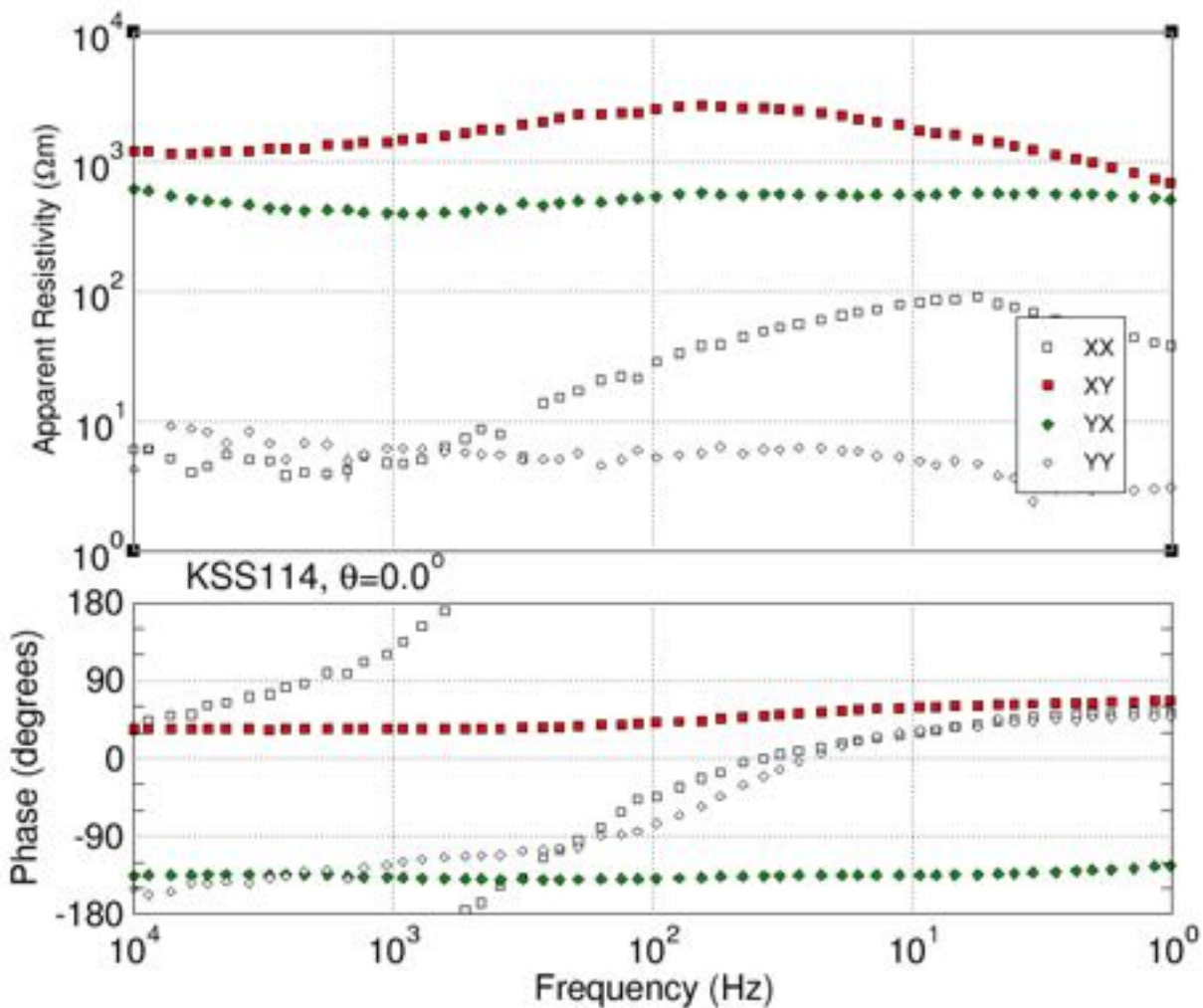


Figure 29: Example of excellent quality sites with lowest QF in the range 1.00 – 1.25.

One point to note is that at frequencies <300 Hz the Pha_{XX} and Pha_{YY} curves are on top of each other. This is a sign that the data can be validly fit with an anisotropic 1-D model.

3.2.2. Example of very high-quality sites, $QF = 1.25 - 1.50$

The next one quarter (23 sites) have a QF in the range 1.25 – 1.50. The example chosen is in the middle of this range, and is site KMM209 with $QF = 1.367$

There is now some visible scatter, particularly at a couple of frequencies in the AMT deadband and into the MT deadband, which is why the QFs are not 1. Note also the more poorly determined diagonal elements at low frequency, particularly XX.

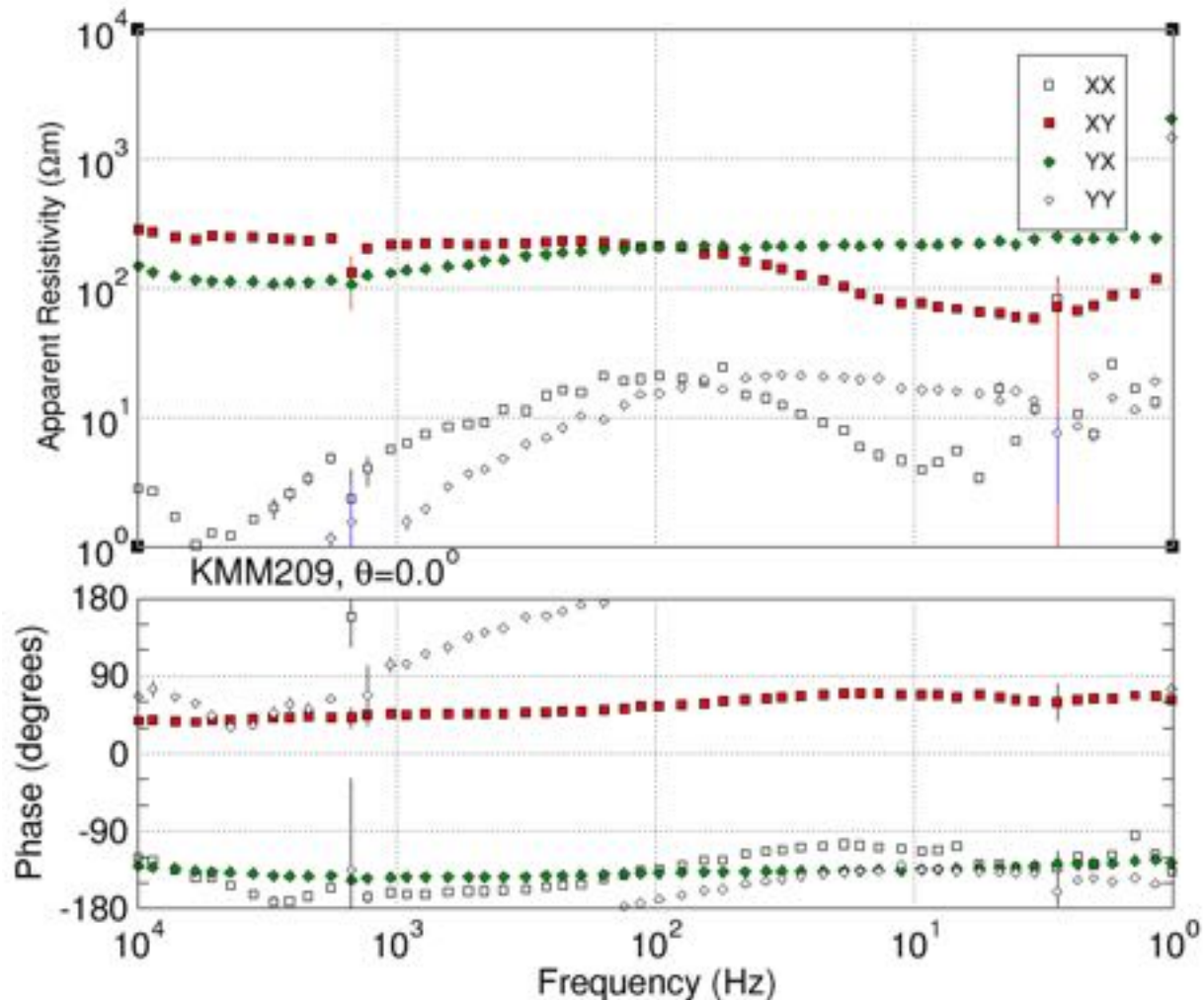


Figure 30: Example of very high quality site with QF in the range 1.25 – 1.50

3.2.3. Example of high quality sites, $QF = 1.5 - 2.0$

The next quarter (22) of sites have QF in the range 1.5 – 2.0. The site with the QF closest to the middle of this range is KSP009 with a $QF = 1.743$ (Figure 31).

Most of the XY and YX estimates are visibly very good, but with a small amount of scatter visible at the AMT deadband frequencies and up to 10 kHz, especially in YX (green diamonds). The diagonal elements XX and YY are more scattered above 1 kHz, especially YY (open diamonds).

These two shared the same electric field, E_y , so the high frequency noise was predominantly on that channel.

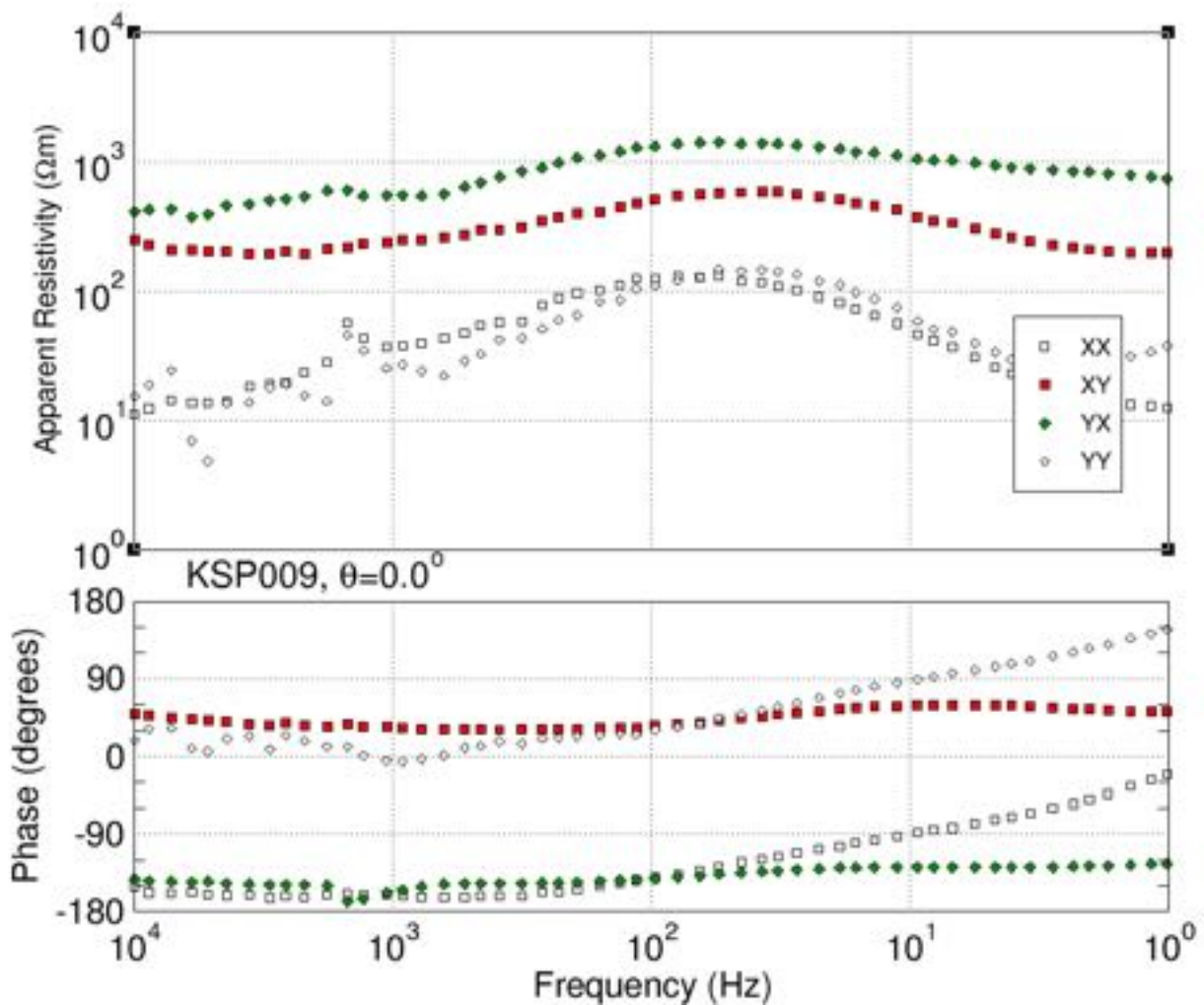


Figure 31: Example of high quality site with the QF in the range 1.5 – 2.0

3.2.4. Example of good to medium quality sites, QF = 2.0 – 3.0

There are eleven (11) sites with QF between 2.0 to 3.0. (Figure 32). The example is site KSS107 with QF = 2.688.

There is now far more visible scatter at high frequencies above 900 Hz, but the lower frequencies are still beautiful.

The diagonal elements, especially YY, are poorly estimated with a lot of scatter at high frequencies, and also below 10 Hz.

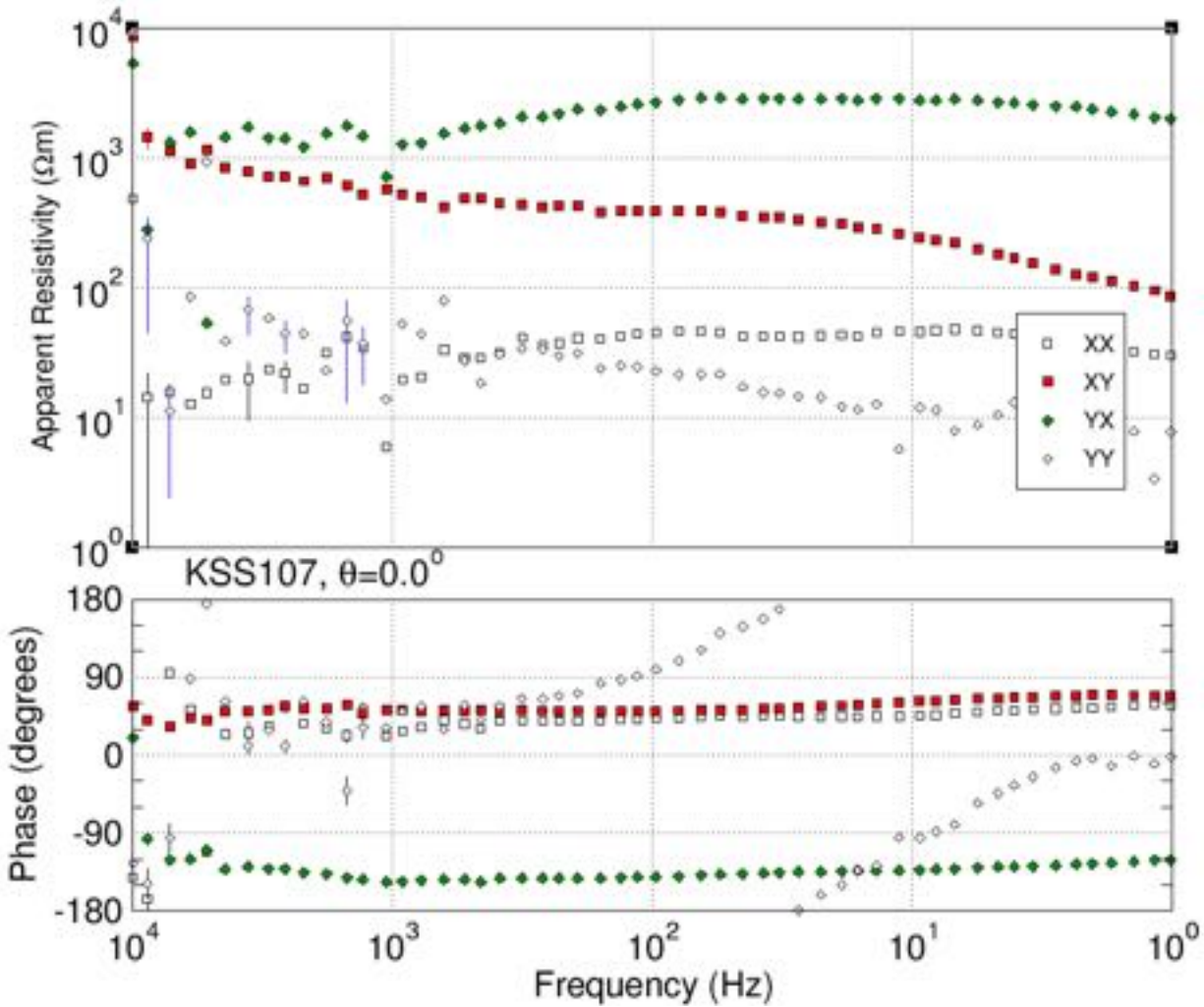


Figure 32: Example of good quality site with QF in the range 2.0 - 3.0.

3.2.5. Example of mediocre quality sites, QF = 3.0 – 4.25

Finally, there are eight (8) sites with QF in the range 3.0 – 4.25. The worst quality is KSS101 with QF = 4.251 (Figure 33).

For this site the scatter is primarily between 300 – 100 Hz, not in the AMT or MT deadbands.

Site KSS101 was located up the Emer Creek Forest Service Road some 1 km off Highway 95, and is some 3 km from the border areas of Kingsgate (CA) and Eastport (USA), with significant industrial structures and railways. I suspect that the scatter is caused by electrical interference from harmonics of 60 Hz (120 Hz, 180 Hz, 240 Hz, 300 Hz) that is not being adequately rejected by the processing software.

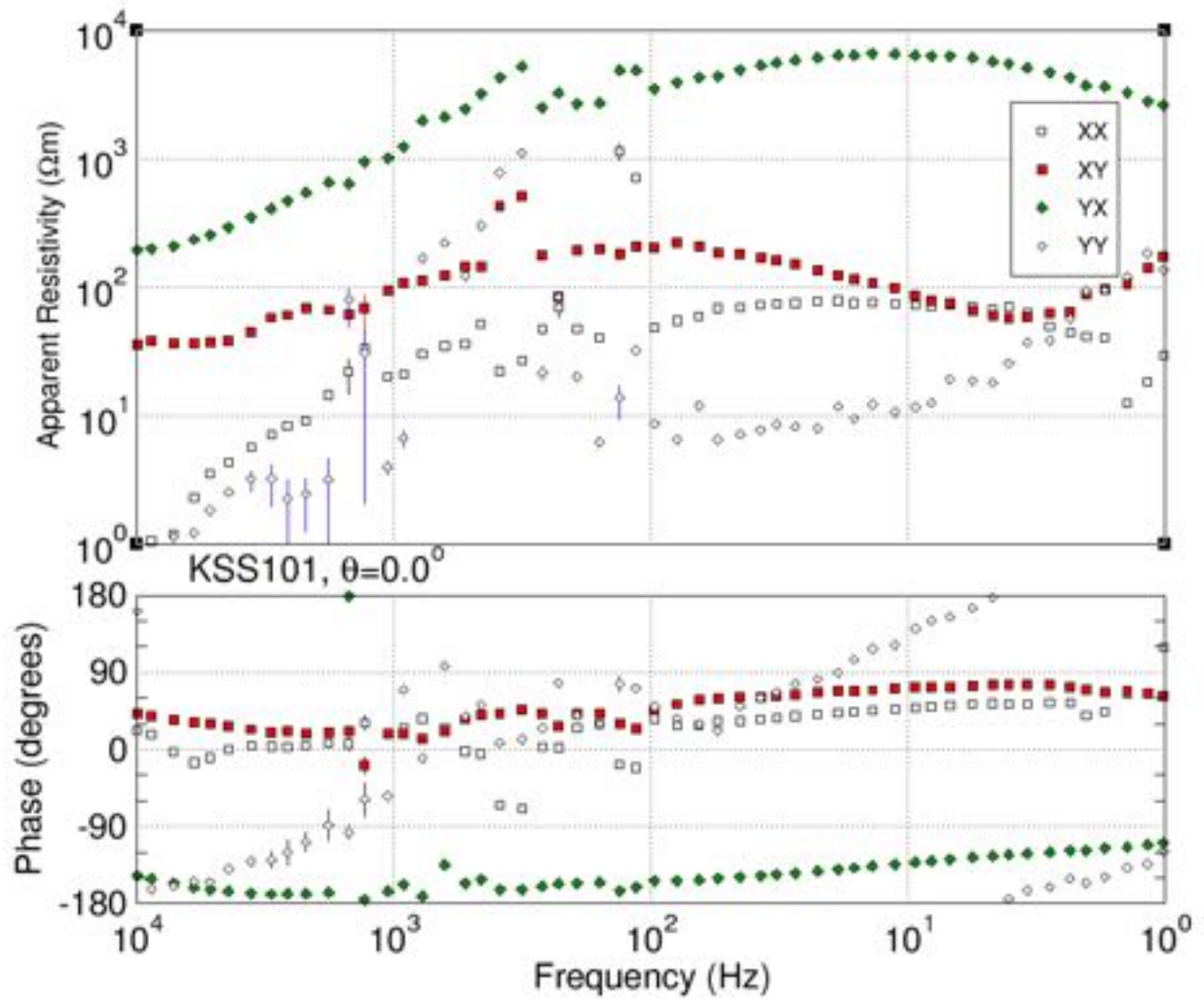


Figure 33: Example of mediocre quality sites with QF in the range 3.0 – 4.25.

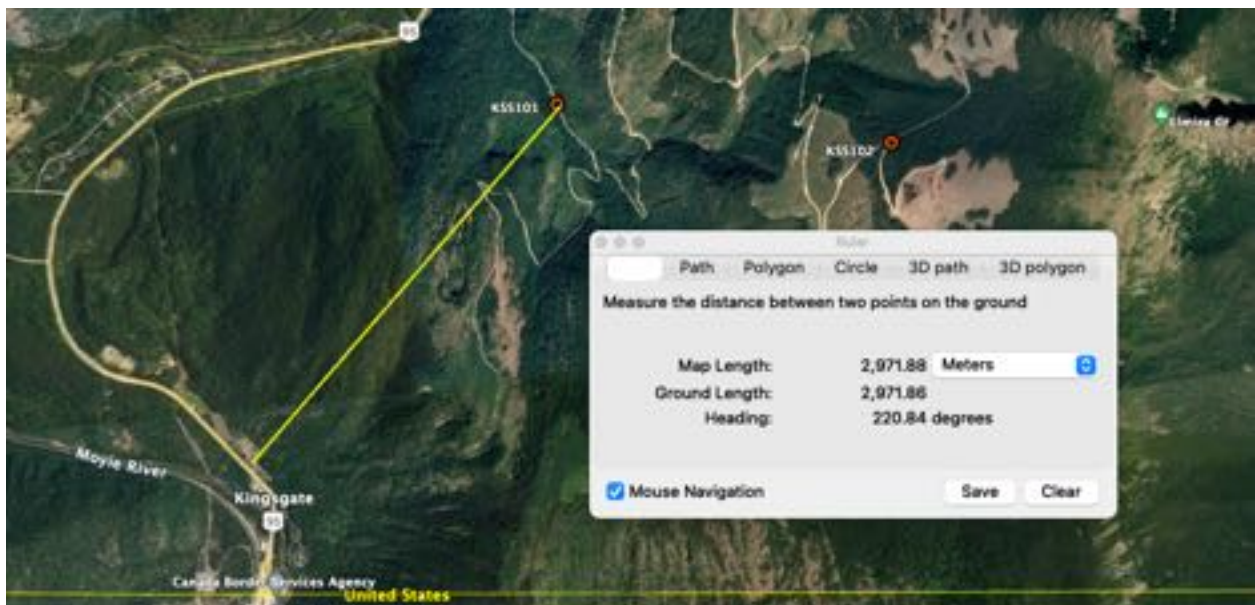


Figure 34: Location of site KSS101.

3.3. QF cf. electrode array parameters

Finally, we cross-plot the QF values derived in the frequency band 10 kHz – 3 Hz against the electrode array parameters, contact resistance, AC and DC values, to see if electrode array installation affected the quality of the data.

The plot of QFs against contact resistances (Figure 35) do not show any correlation between contact resistance and the QF values.

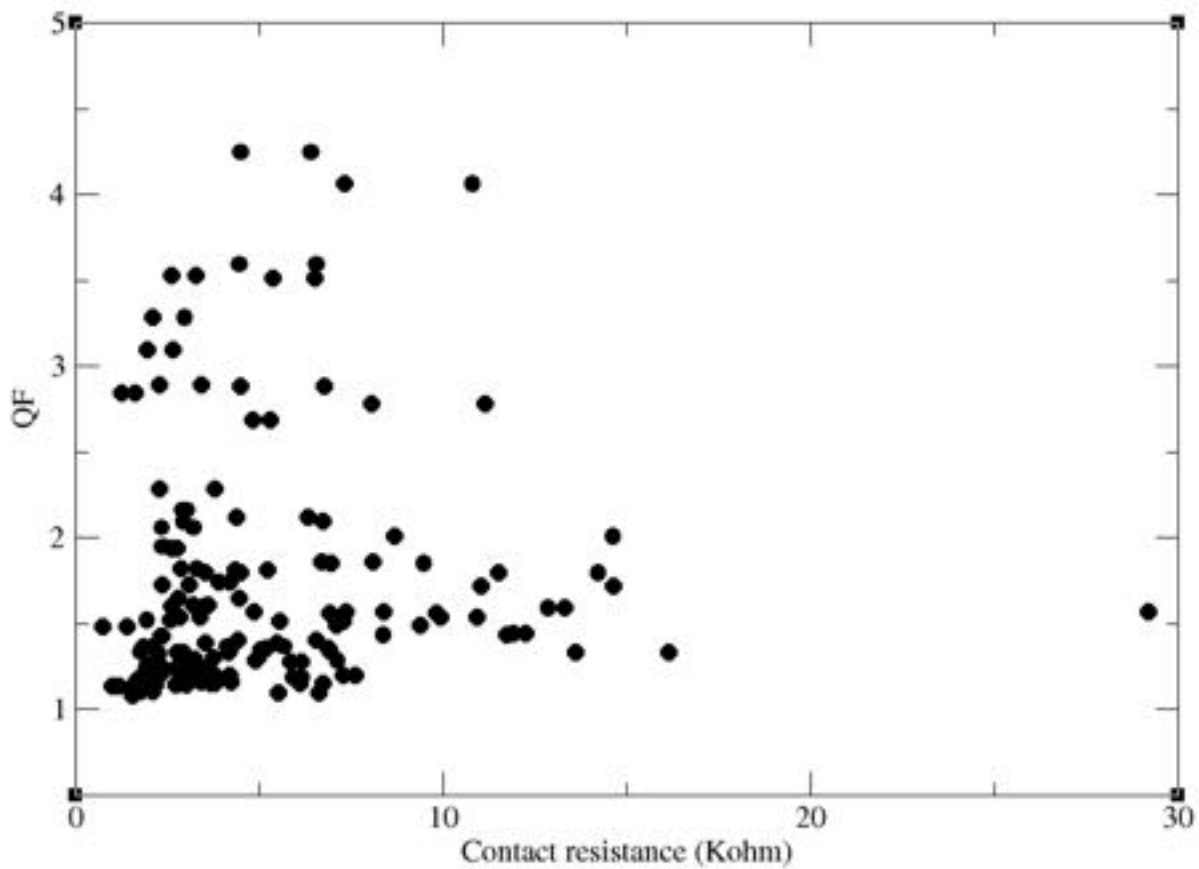


Figure 35: Cross-plot of QFs against contact resistances.

The cross-plot of measured AC against QFs is plotted in Figure 36. Again, no visible correlation of the two is evident.

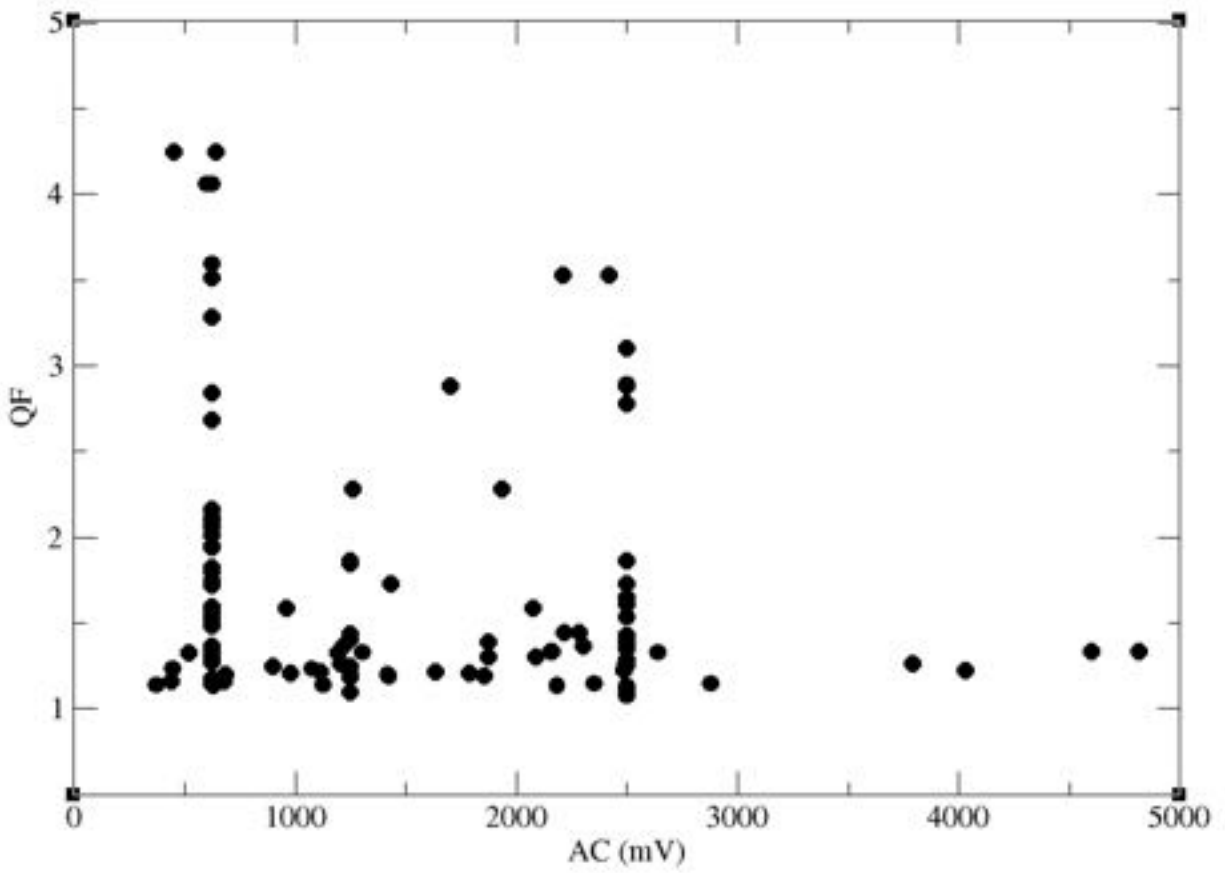


Figure 36: Cross-plot of AC against QFs

The cross-plot of the absolute values of the measured DC against QFs is plotted in Figure 37. Again, no discernible correlation is evident.

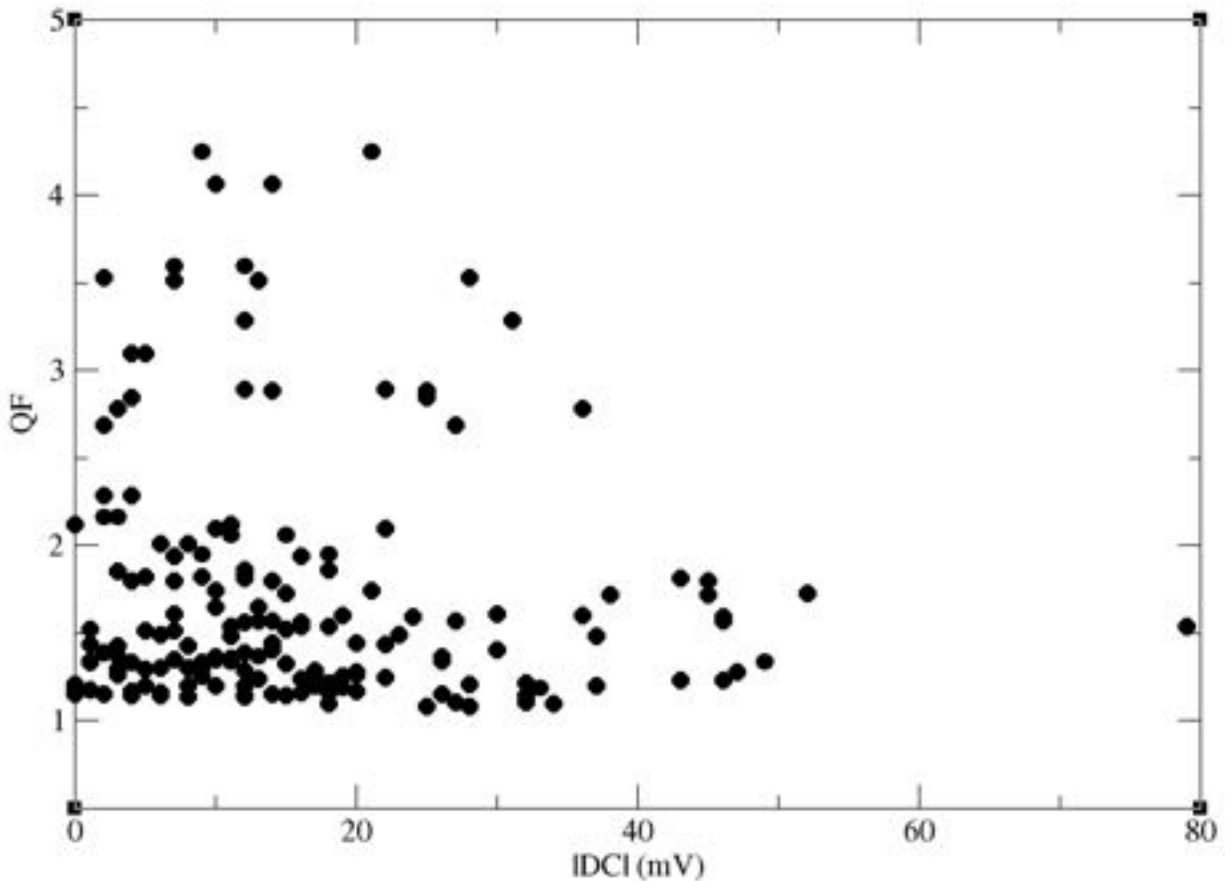


Figure 37: Cross-plot of DC against QFs

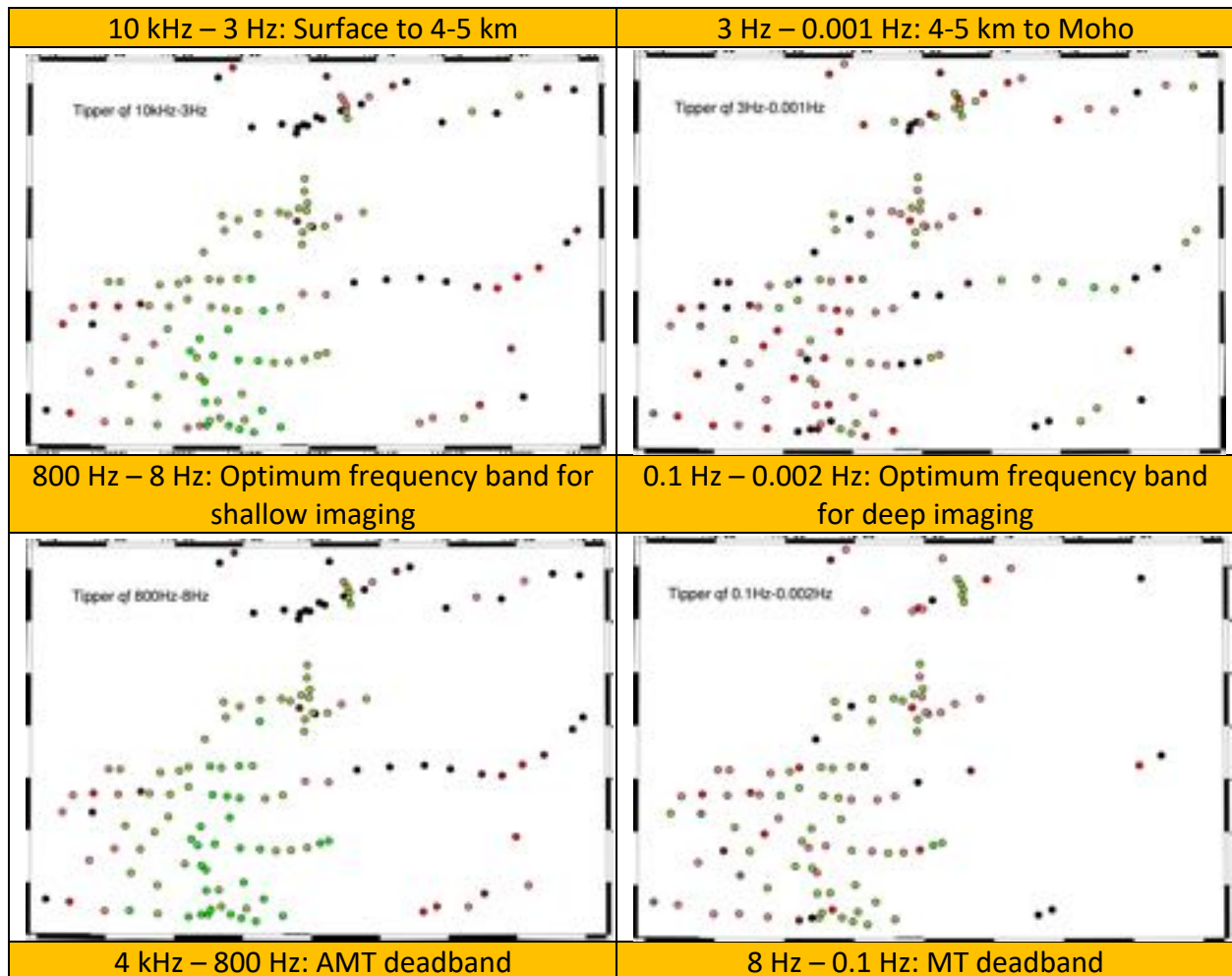
3.4. QF Conclusions

1. At the high frequencies probing down to 4-5 km, Quality Factor analyses of the data have shown that for most sites the newly-acquired data are very good to excellent, especially in the frequency range of most importance from 800 Hz – 8 Hz. For those with somewhat higher QFs, most of the noisy data are in the AMT or MT deadbands. The appropriate error floors to use are 3.56% in RhoA and 1.0° in Pha for all newly-acquired data. The existing Duncan data are poorer in quality, and the appropriate error floors to use are of order three times higher, i.e., 10.68% in RhoA and 3.0° in Pha.
2. At the lower frequencies, both the newly-acquired data and the Duncan data have appropriate error floors of order 8.90% in RhoA and 2.5° in Pha.
3. There is a strong correlation of data quality (measured by QF) with signal strength (measured by Kp). When Kp was high, QF was low.
4. There are no discernible correlations of QFs with any of the electrode array parameters.

4. Tipper Quality Factors

The vertical magnetic fields (Hz) were acquired for the newly-acquired data, so we can perform a Quality Factor analysis of the Tipper estimates, as described in Appendix C. I adopt an error floor of 0.02 for these data, which is the error level one would expect for high quality data.

The QF maps for the same frequency bands as the MT data are shown in Figure 38. Clearly the newly-acquired data are superior than the existing Duncan data.



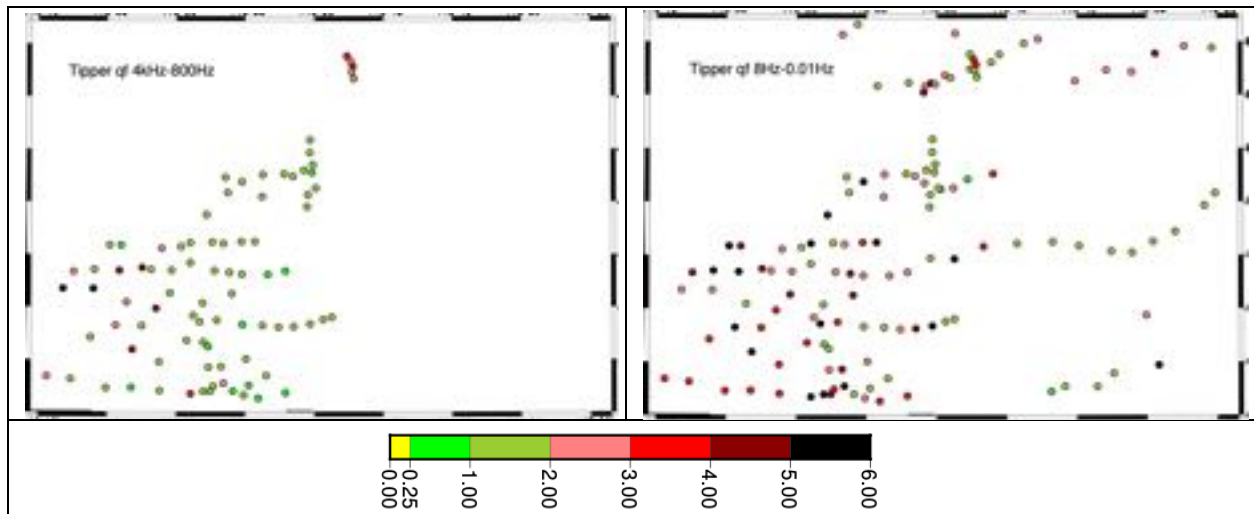


Figure 38: Tipper QFs in various frequency bands.

Histograms of the Tipper QFs are shown in Figure 39, and the 1st, median and 3rd quartiles of them are listed in Table 2. The superior quality of the newly-acquired data is proven statistically.

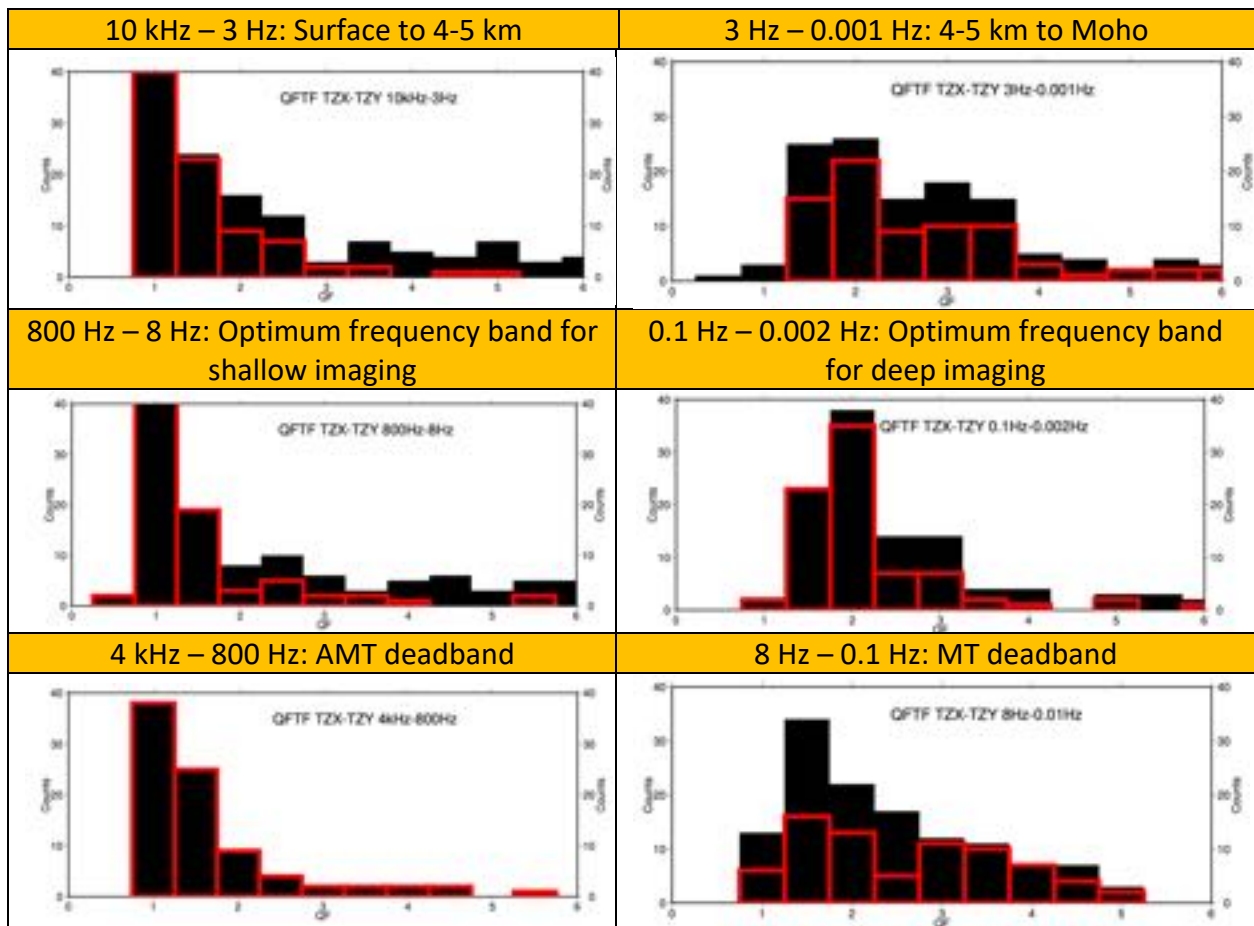


Figure 39: Histograms of Tipper QFs in various frequency bands.

Table 2: First quartile, median, and third quartile for all data and for the new Kootenay data only in the frequency bands indicated.

Frequency band	All data			New data			Duncan data		
	Q1	Median	Q3	Q1	Median	Q3	Q1	Median	Q3
10 kHz – 3 Hz	1.22	1.93	4.22	1.04	1.28	1.80	3.04	4.92	6.60
3 Hz – 0.001 Hz	1.90	2.76	3.86	1.90	2.63	3.58	1.72	3.03	5.31
800 Hz – 8 Hz	1.06	1.78	4.53	0.92	1.11	1.39	3.07	5.36	7.82
0.1 Hz – 0.002	1.77	2.12	2.96	1.69	1.91	2.26	1.28	3.09	5.07
4 kHz – 800 Hz*	1.10	1.28	1.76	1.10	1.28	1.76	-	-	-
8 Hz – 0.1 Hz	1.51	2.30	3.61	1.72	2.83	4.02	1.34	1.90	2.60

*: No Duncan data above 384 Hz

- ➔ At high frequencies, 10 kHz – 3 Hz, the error floor of 0.025 is appropriate for the newly-acquired Kootenay data, but for the existing Duncan data the appropriate error floor is higher at 0.1, which is 5 times the assumed floor of 0.02.
- ➔ At low frequencies, 3 Hz – 0.001 Hz, both the newly-acquired data and the existing Duncan data can take as their error floor a value of 0.05.

5. Average RhoA/Pha curves

To get a sense of the average resistivity structure, I average the RhoA and Pha curves from all of the sites to give the averaged XY and YX curves. This is done in a logarithmic manner for the RhoA curves and in an arithmetic manner for the Pha curves.

These averaged curves are plotted in Figure 40, where XY data are plotted as full squares, and YX data as open squares. Both curves start at some 800-1,000 Ωm . The RhoYX curve stays at 1,000 Ωm to 3 Hz, then starts to descend. The RhoXY curve starts to descend already from 30 Hz, and always lies below the RhoYX curve, indicating less penetration at the same frequency.

The Niblett-Bostick penetration depth for 1,000 Ωm at 10 kHz is 100 m. At the low frequency of 0.001 Hz (1,000 s period) the RhoA values are 10 Ωm and 30 Ωm for RhoXY and RhoYX respectively. These imply penetration to 36 km and 60 km respectively.

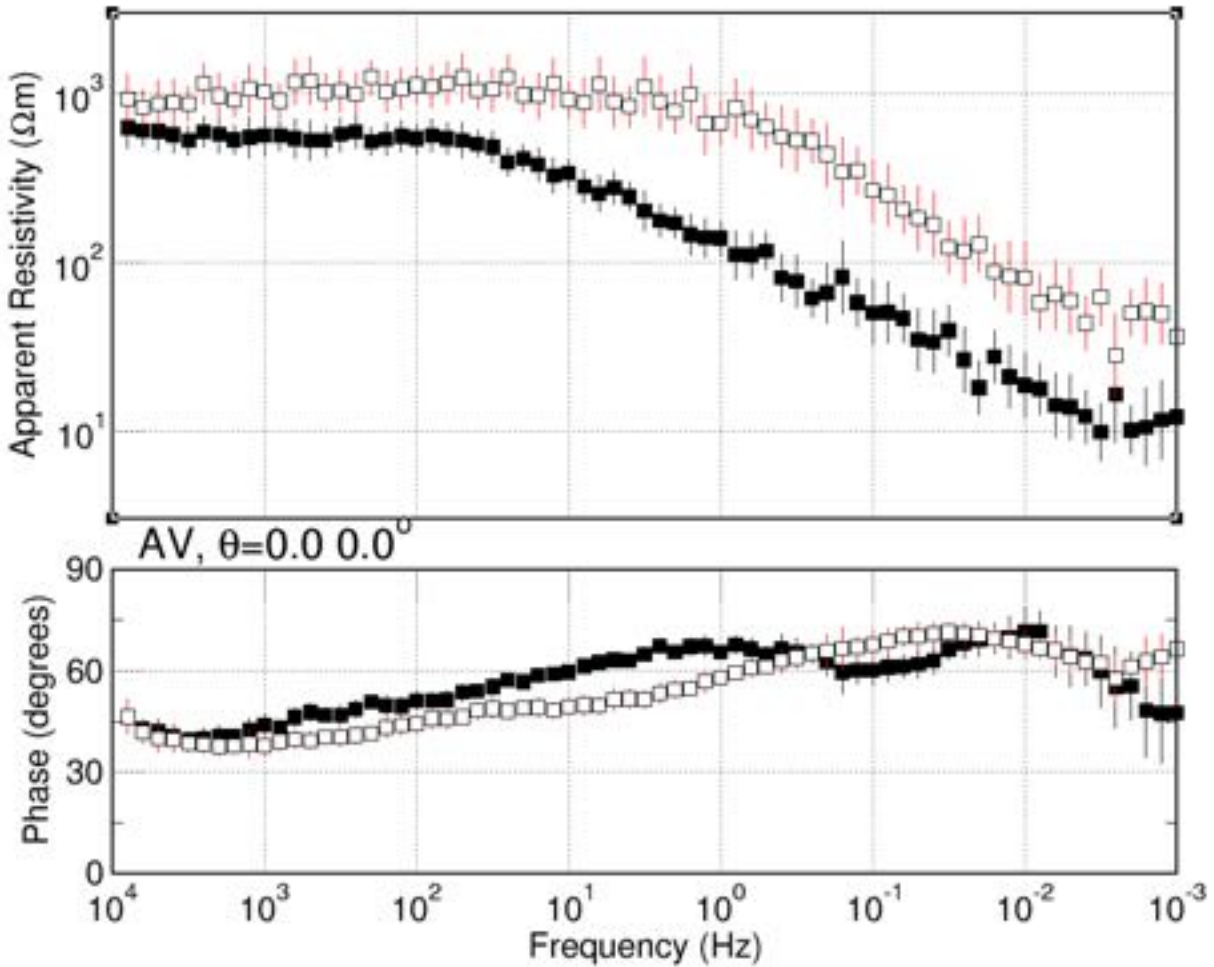


Figure 40: Averaged curves for all sites.

These estimates are transformed from period into the approx. depth, using the Niblett-Bostick transformation (Jones, 1983), in Figure 41 (top: depths to 3,000 m; bottom: depths to 30 km). The data are colour coded in with:

black: 10 kHz – 1 kHz red: 1 kHz – 100 Hz blue: 100 Hz – 10 Hz
 green: 10 Hz – 1 Hz orange: 1 Hz – 0.1 Hz magenta: 0.1 Hz – 0.01 Hz
 violet: 0.01 Hz – 0.001 Hz

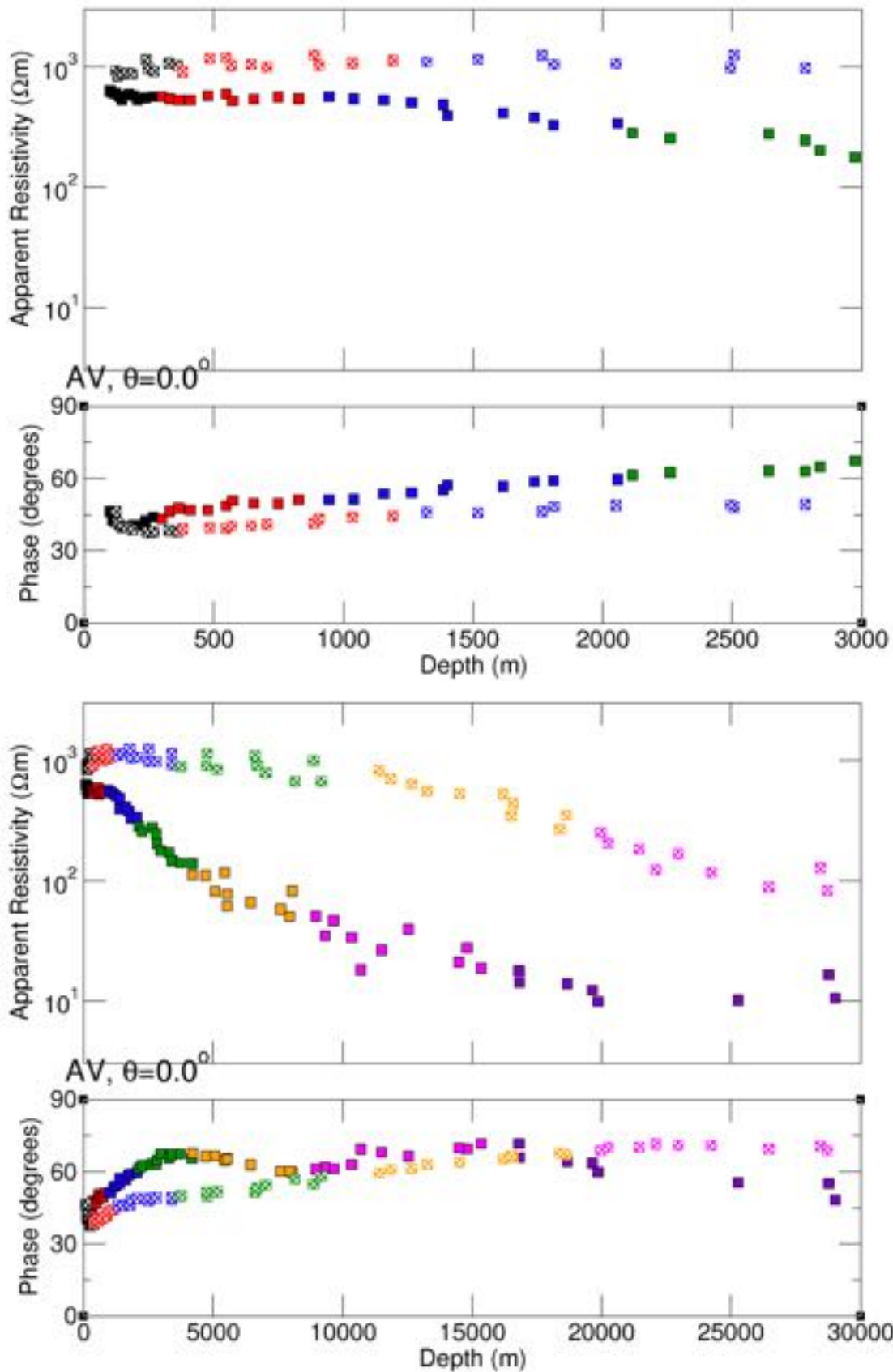


Figure 41: Averaged estimates plotted against approximate depth. Top: to 3000 m. Bottom: to 30 km

The Niblett-Bostick approximate average depths for the frequency/period bands are listed in Table 3. Taking data at frequencies much lower than 30 Hz serves no purpose for detecting the presence and imaging the top of structures at depths to 2,500 m. However, for delineation and full resolution, given the strong attenuation within any conductor present, data to 30 Hz are required.

Table 3: Niblett-Bostick penetration depths (below surface) for the XY and YX data averages.

Frequency band	XY (m)	YX (m)
10 kHz – 1 kHz	100 – 250	120 – 350
1 kHz – 100 Hz	250 – 825	350 – 1,200
100 Hz – 10 Hz	825 – 2,000	1,200 – 3,500
10 Hz – 1 Hz	2,000 – 4,000	3,500 – 9,000
1 Hz – 0.1 Hz	4,000 – 8,000	9,000 – 18,000
0.1 Hz – 0.01 Hz	8,000 – 15,000	18,000 – 32,000
0.01 Hz – 0.001 Hz	15,000 – 40,000	32,000 – 68,000

➔ This defines for us the data of primary interest for imaging depths of 2-4 km, which lies in the four decades 10 kHz – 1 Hz.

➔ The secondary depth of interest to the base of the crust comes from data down to 0.001 Hz.

6. Qualitative images

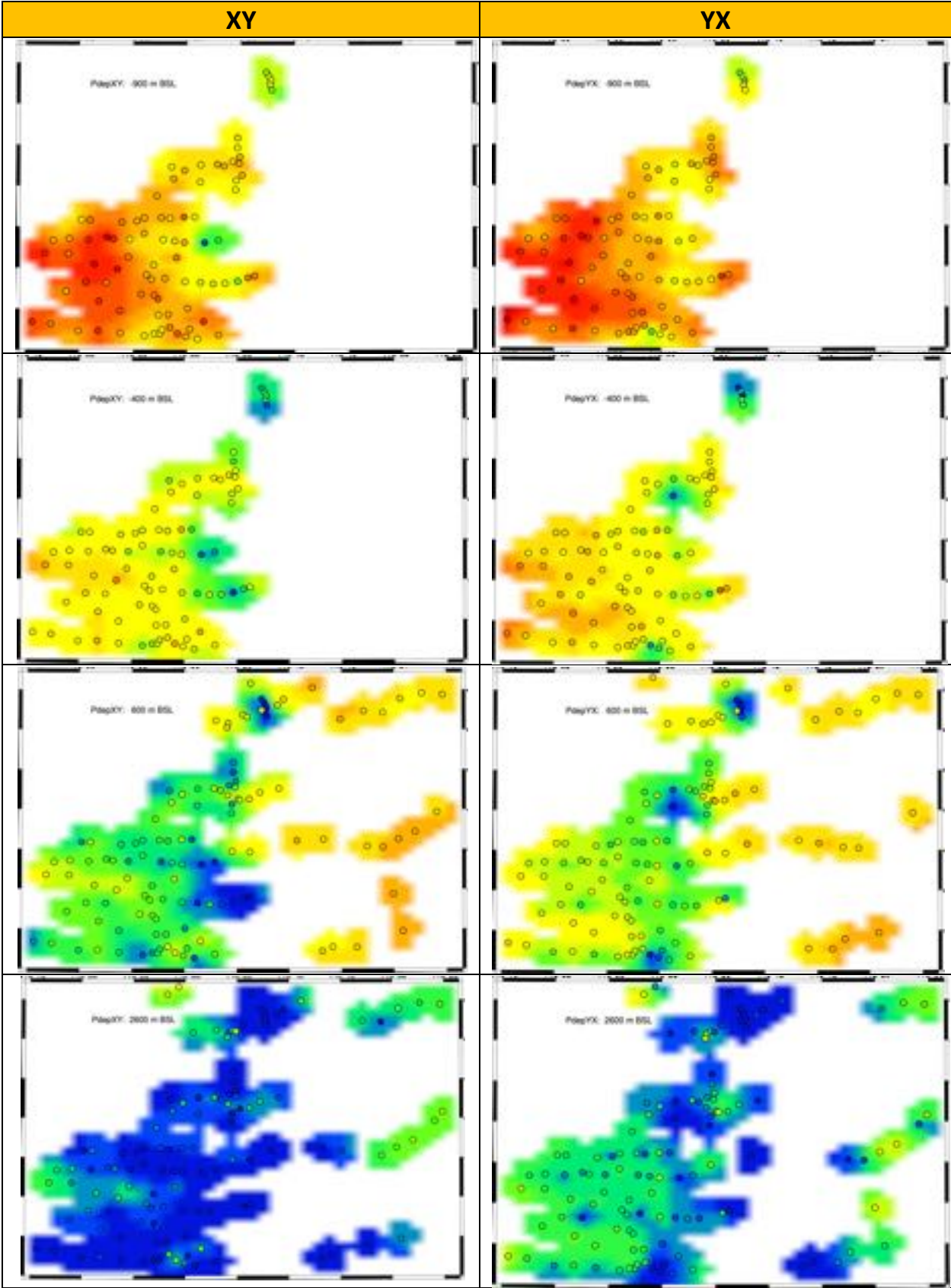
I obtain qualitative information from these data to guide analyses and subsequent inversions.

6.1. Frequencies for primary Depths of Investigation

The frequency at each site for a given Depth of Investigation is useful for identifying those frequencies most sensitive to the target depths. Below are plotted the frequencies sensing depths, defined as the Niblett-Bostick depths (Jones, 1983) rather than skin depths, for approximate depths of 500 m, 1000 m, 2000 m, and 4000 m bs (below surface) (Figure 42) for the XY and YX data at each site. The actual depths are -900 m, -400 m, 600 m and 1600 m below sea level at each site, and the approximate depths below surface are derived using the average elevation of 1400 m.

Both the XY and YX plots are visually very similar, attesting to rotational invariance at the large scale.

Note that the penetration depth of the highest frequency of the Duncan data is greater than 1000 m, hence those data do not plot on the first two rows.



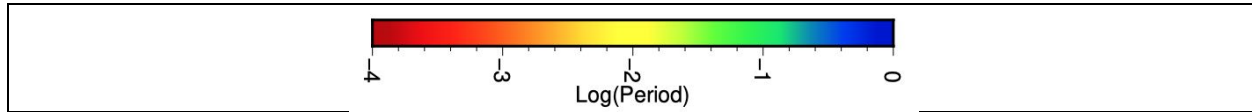


Figure 42: Frequency for Niblett-Bostick penetration to approximate depths of 500 m (top row, -900 m below sea level), 1000 m (2nd row, -400 m bsl), 2000 m (3rd row, 600 m bsl), and 4000 m (bottom row, 2600 m bsl). Left: XY; Right: YX.

From the data plotted in Figure 42 we can derive the frequencies most sensitive to the four depths are given by Table 4, which lists the median frequency plus the first and third quartiles to penetrate to each depth. Thus, the frequency range of 5 kHz to 100 Hz will cover depths of 500 m to 2,500 m on average. Where there are conductors present however, then we will need to use data to lower frequency. This is true of some parts of the grid, where frequencies down to 10 Hz appear to be needed to penetrate to 2,500 m at some sites.

Table 4: Median and 1st and 3rd quartiles for frequency to penetrate to the given depths.

Depth	XY			YX		
	Q1 (Hz)	Median (Hz)	Q3 (Hz)	Q1 (Hz)	Median (Hz)	Q3 (Hz)
500 m	800	400	160	920	460	260
1000 m	160	80	30	260	120	65
2000 m	100	25	7	145	45	25
4000 m	6	2	0.8	15	7	2

Note that this is an important point – there is no point modelling/inverting data at frequencies that penetrate too deeply to be of interest. The fit to those inconsequential data contaminates the overall fit and biases the search for the minimum to the inversion objective function. The problems associated with overfitting data of little consequence are discussed and demonstrated in Jones (1993).

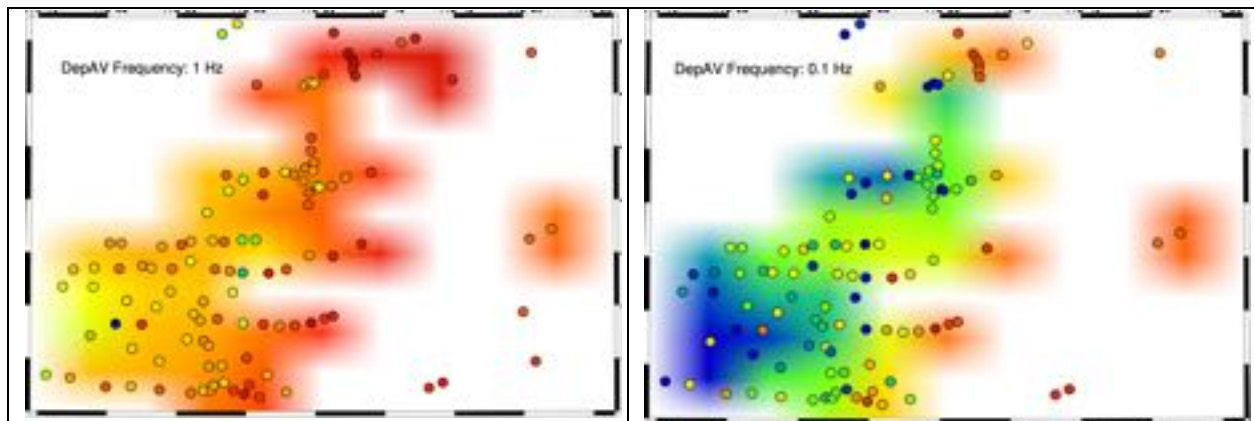
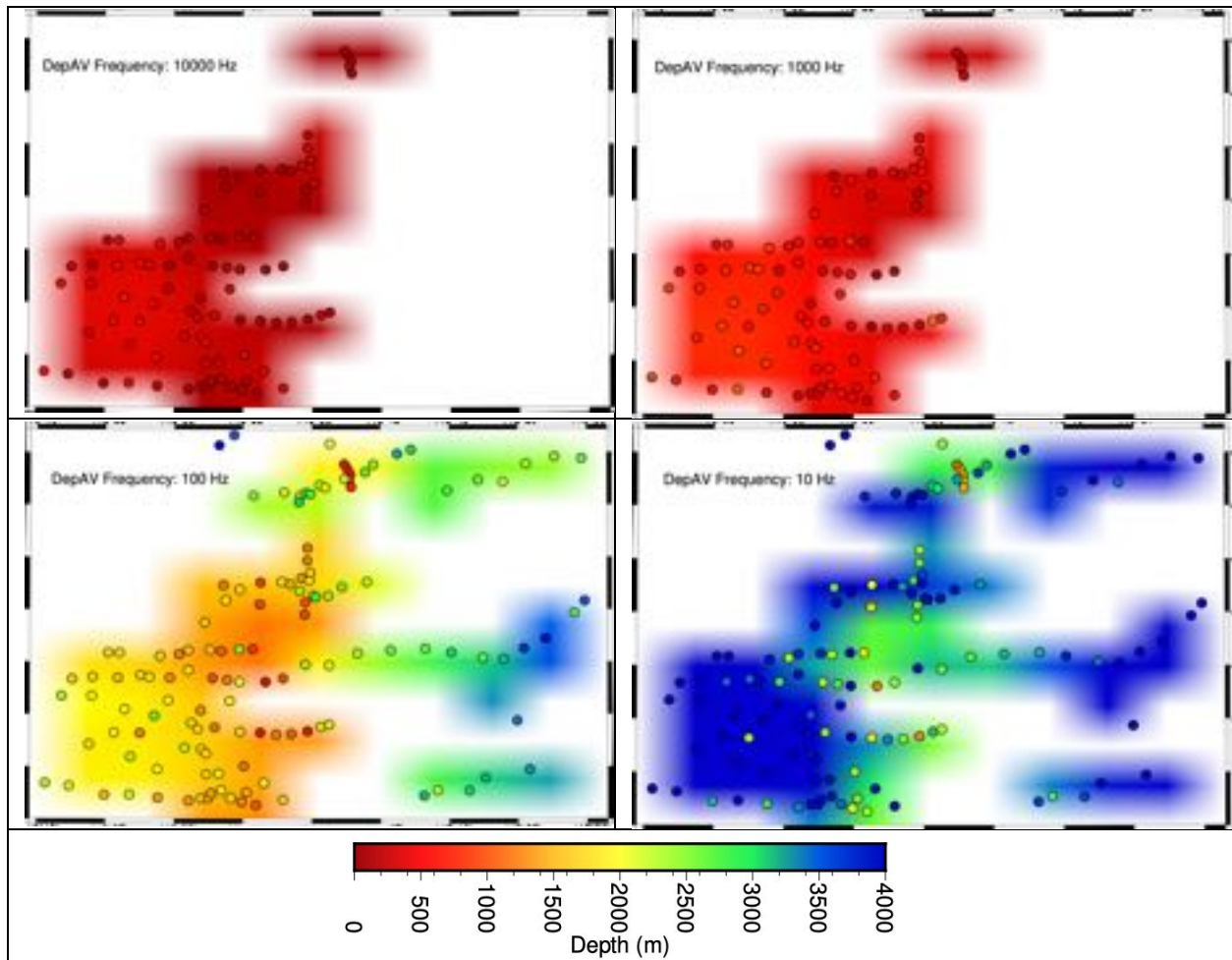
Of course, the frequencies required for optimum resolution of the subsurface are not generally known beforehand, as the conductivity structure is unknown – which is the whole point of the survey – so it always makes sense to analyse data half a decade on either side of those inferred from penetration depth arguments.

➔ **Modelling of the data needs to use frequencies from 10.5 kHz to 3 Hz for the primary target depths**

6.2. Depths of penetration for various frequencies

Another way to view the penetration information is to consider the depths for given frequencies. Below in Figure 43 are the plots of the Niblett-Bostick penetration depths (below surface) for frequencies of 10 kHz (top left row), 1 kHz (top right), 100 Hz (2nd row left), 10 Hz (2nd row right), 1 Hz (3rd row left), 0.1 Hz (3rd row right), 0.01 Hz (bottom left), and 0.001 Hz (bottom right), for the averaged impedances. Depths here are depths below surface, for an assumed average elevation of 1,400 m.

Note that the maps for frequencies above 1 Hz are on a different depth scale from those 1 Hz and below.



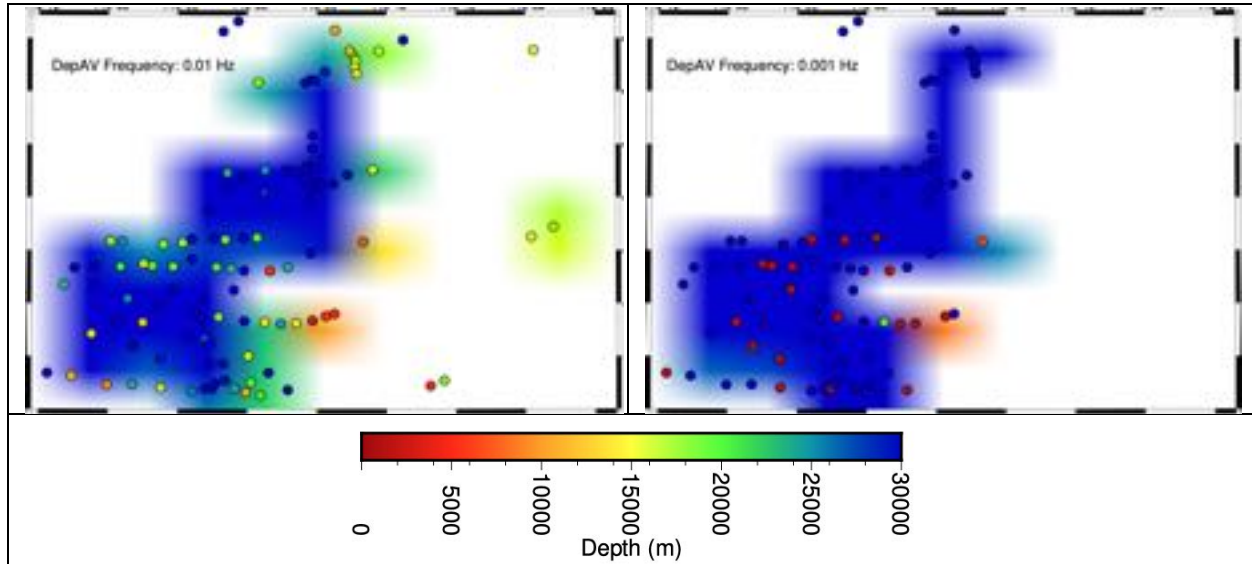


Figure 43: Depth of penetration (based on Niblett-Bostick) below surface for averaged impedances at frequencies of 10 kHz (top left), 1 kHz (top right), 100 Hz (2nd row left), 10 Hz (2nd row right), 1 Hz (3rd row left), 0.1 Hz (3rd row right), 0.01 Hz (bottom left) and 0.001 Hz (bottom right). Note the change of colour scale for frequencies above and below 1 Hz.

The statistics of the penetration depths are given in Table 5.

Table 5: Median and 1st and 3rd quartiles for depth of penetration at each frequency.

Frequency	Q1 (m)	Median (m)	Q3 (m)
10,000 Hz	8	120	260
1,000 Hz	260	440	590
100 Hz	1,225	1,800	2,500
10 Hz	2,800	3,900	4,800
1 Hz	5,650	8,675	11,700
0.1 Hz	10,700	17,700	24,150
0.01 Hz	17,750	28,600	38,700
0.001 Hz	36,500	63,500	92,500

This confirms that the frequencies of primary interest for imaging the top 4 km are from 10 kHz to around 3 Hz, and that the lower frequencies down to 0.001 Hz are essential to reach the base of the crust.

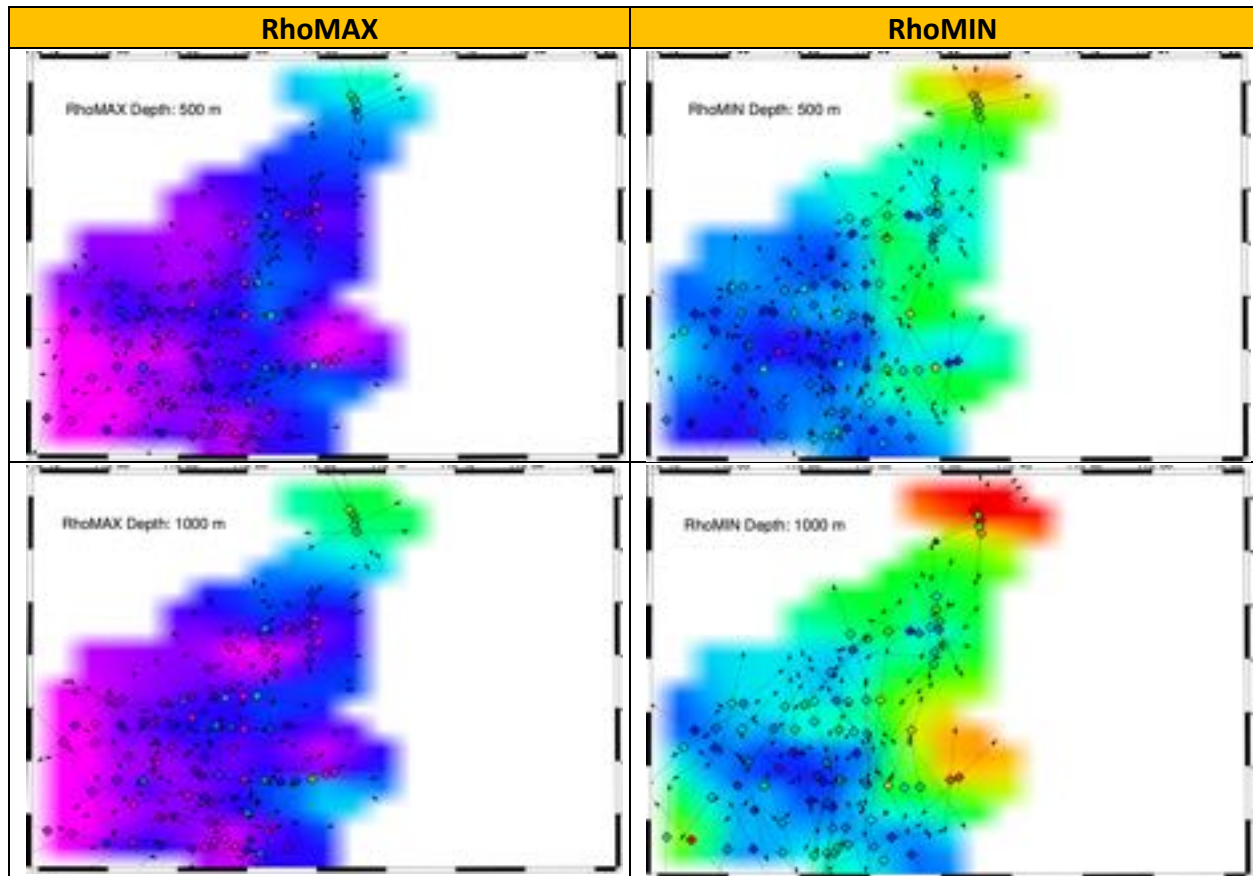
6.3. Approximate resistivity images for various depths

A quickview way of imaging the data is to obtain an approximate resistivity at a given depth using the Niblett-Bostick transform (Jones, 1983). This is done for depths of -900 m, -400 m, 600

m and 1600 m below sea level at each site for RhoMAX and RhoMIN ⁽²⁾. These depths are approx. 500 m, 1000 m, 2000 m and 4000 m below surface given the average elevation of 1400 m.

The maps for RhoMAX (left) and RhoMIN (right) are shown in Figure 44. Sites are plotted only when both orthogonal directions (XY and YX) reach to the desired depth.

The arrows indicate the direction of RhoMAX for the RhoMAX maps, and RhoMIN for the RhoMIN plots.



² RhoMAX is the maximum resistivity at that depth, and RhoMIN is the minimum resistivity. These RhoMAX and RhoMIN values are determined by rotating the data through 90° at each frequency for each site and recording the maximum and minimum resistivities and their directions. Note that these two directions are not necessarily at right angles to one another.

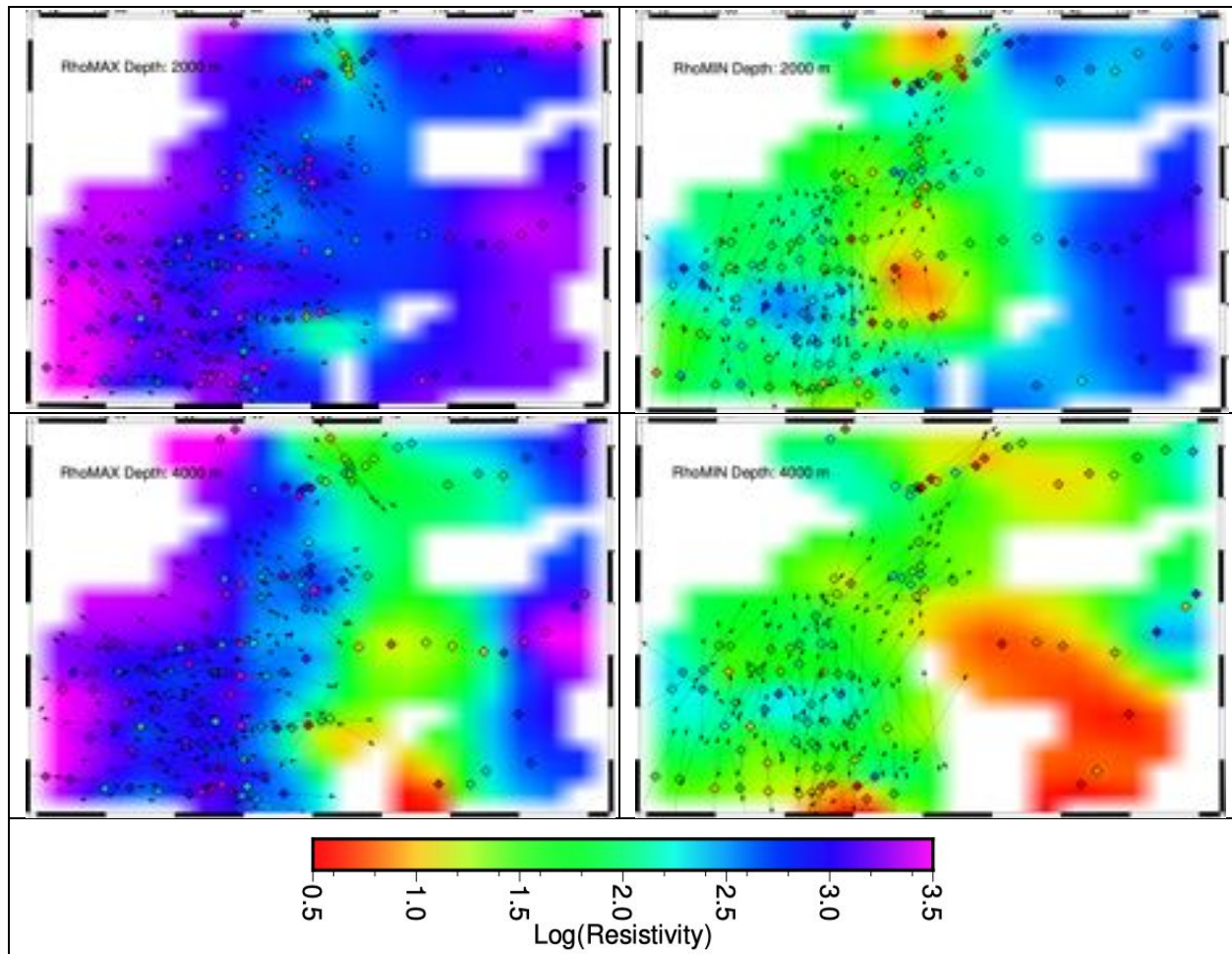


Figure 44: RhoMAX (left) and RhoMIN (right) approx. resistivity maps at depths (below sea level) of -900 m (top row, 500 m below surface), -400 m (2nd row, 1000 m bs), 600 m (3rd row, 2000 m bs), and 2600 m (4th row, 4000 m bs). Note: sites are plotted only when both orthogonal directions (XY and YX) reach to the desired depth.

There are some regions of interest in these maps. Three prominent ones are indicated in the RhoMIN plot at 4 km Figure 45, and are:

Anomaly A: A low conductivity anomaly associated with the eastern sites along the southern profile KSS.

Anomaly B: A low conductivity anomaly associated with the Purcell sulphides and mapped by Gupta and Jones (1995).

Anomaly C: A low conductivity anomaly also associated with the Purcell sulphides and mapped and modelled by Gupta and Jones (1995) – see Figure 17 above.

➔ **There are a number of regions of interest identified in the RhoMIN plots. The main new one, labelled Anomaly A, is in the eastern part of line KSS (see RhoMIN @ 4000 m depth).**

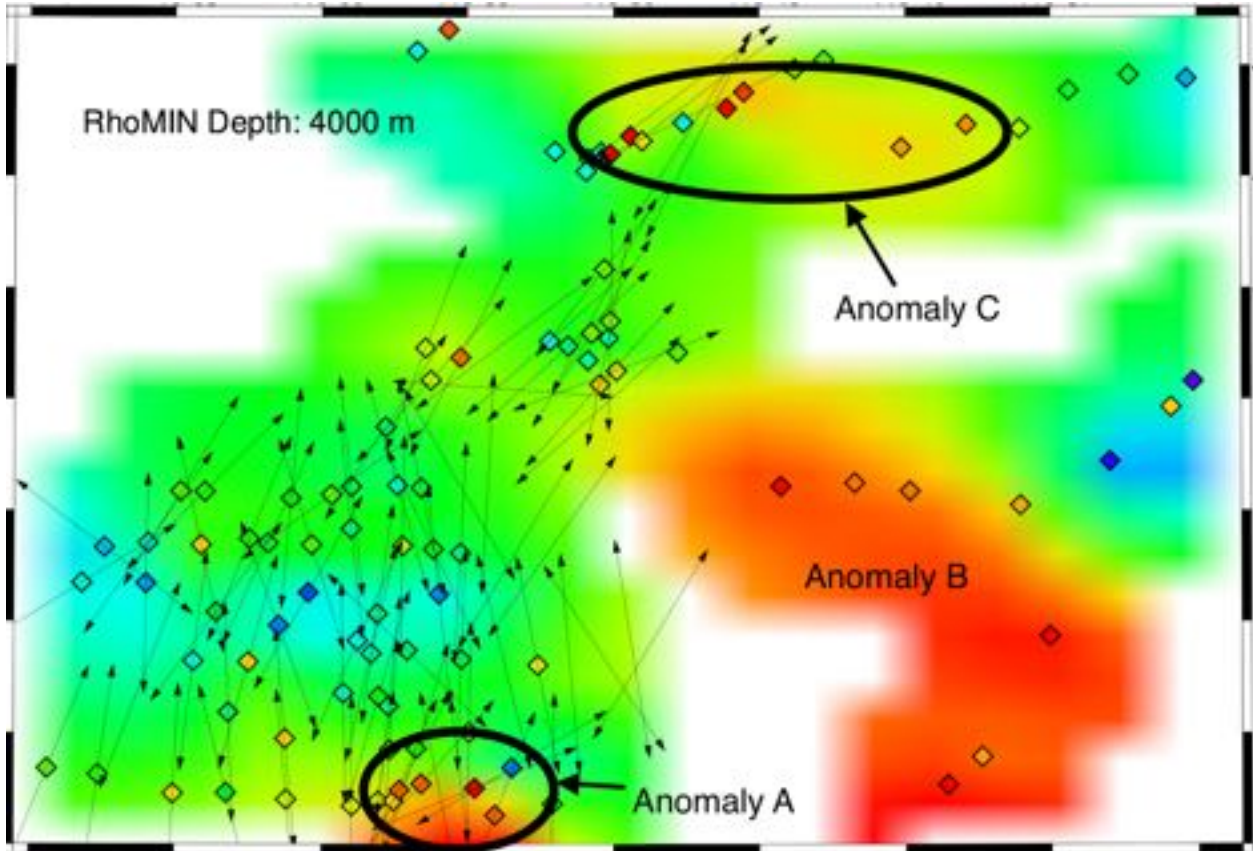


Figure 45: RhoMIN plot at approximate depth of 4 km.

The directions of the arrows are plotted as histograms on Figure 46.

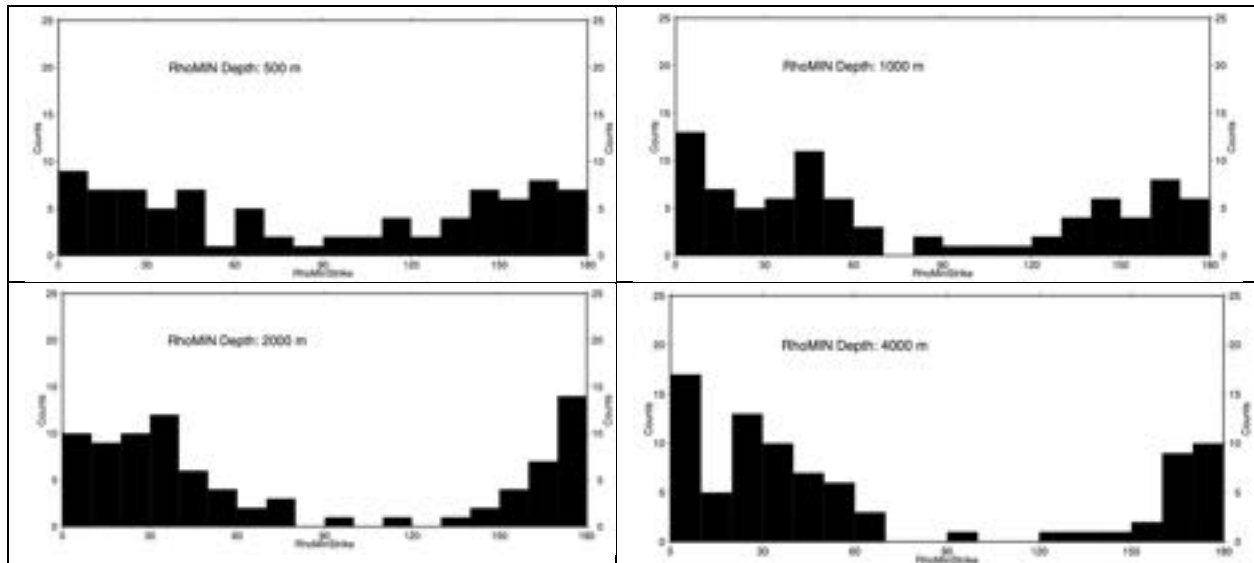


Figure 46: Histograms of RhoMIN strike directions for depths (below sea level) of -900 m (top left, 500 m below surface), -400 m (top right, 1000 m bs), 600 m (bottom left, 2000 m bs), and 2600 m (bottom right, 4000 m bs).

Using circular statistics with a pi repetition (Mardia, 1972), the means of these histograms are N11E, N14E, N15E and N2E for depths of 500 m, 1000 m, 2000 m and 4000 m respectively.

There is though clearly S-N variation, with the southern sites striking more N-S and the northernmost sites striking NNE-SSW.

6.4. Qualitative Dimensionality plots

Given the observed differences in the RhoXY and RhoYX plots at different depths shown in Figure 44, we can obtain qualitative information about the strength of dimensionality by considering the maximum differences in phase in orthogonal directions when the data are rotated through 360°.

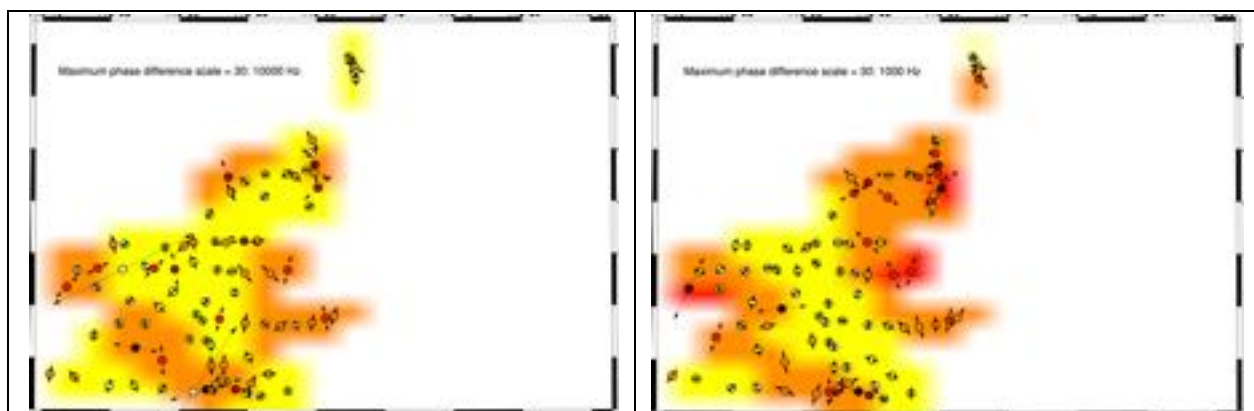
For a 1-D Earth, the phase is the same regardless of strike direction, so the phase difference is zero.

For a 2-D Earth phase difference maximises when the data are in the strike and orthogonal-to-strike directions, so the direction of maximum phase difference is indicative of geoelectrical strike.

For a 3-D Earth the extent of “3-Dness” affects whether the phase maximises at the quasi-2-D direction or not.

Below are plotted the phase difference maps at four frequencies, 10 kHz, 1 kHz, 100 Hz and 10 Hz (Figure 47), which are approximately penetrating to maximum depths of 120 m, 440 m, 1,800 m and 4,000 m respectively (Table 5).

Yellow means very little phase difference with rotation (<10 degrees), which means 1-D or subtle 2-D/3-D. Red and dark red indicate areas with strong sensitivity of phase to strike direction, so are areas that are 2-D or 3-D.



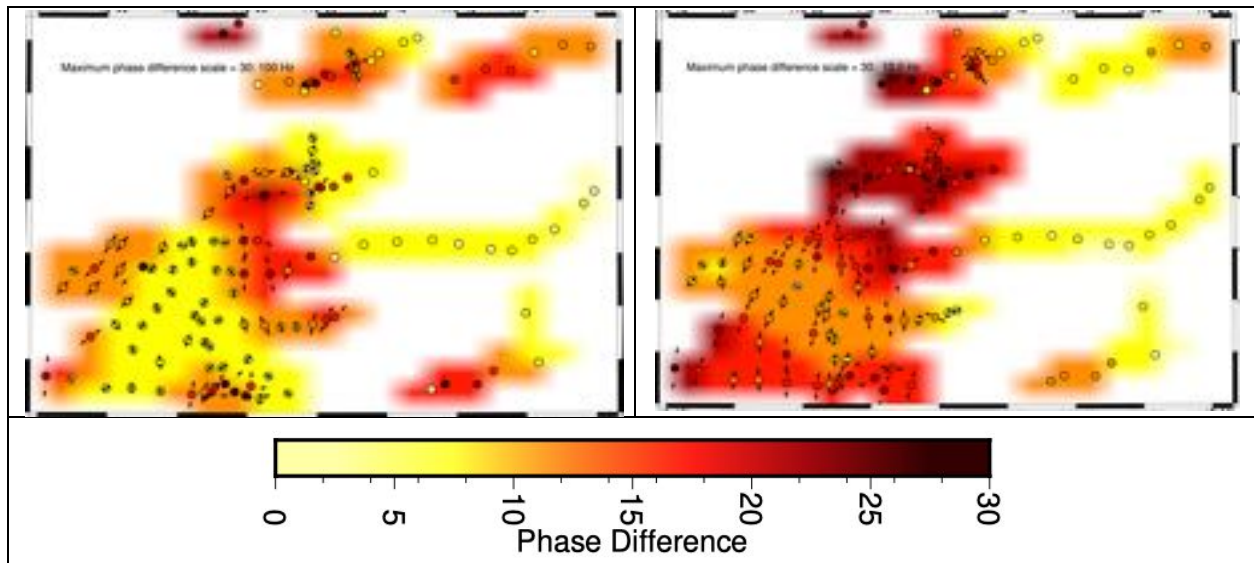


Figure 47: Phase differences at 10 kHz (top left), 1 kHz (top right), 100 Hz (bottom left) and 10 Hz (bottom right).

For much of the grid there are no strong phase differences in orthogonal directions at high frequencies. Strong phase sensitivity comes in below 100 Hz, i.e., below 2 km depth.

The directions of maximum phase difference are plotted as histograms in Figure 48. Note that these are the directions of the higher phase, and the strike direction changes by 90 degrees on either side of a boundary in conductivity (see the footnote about Phase Tensor direction – the same applies to anisotropy direction).

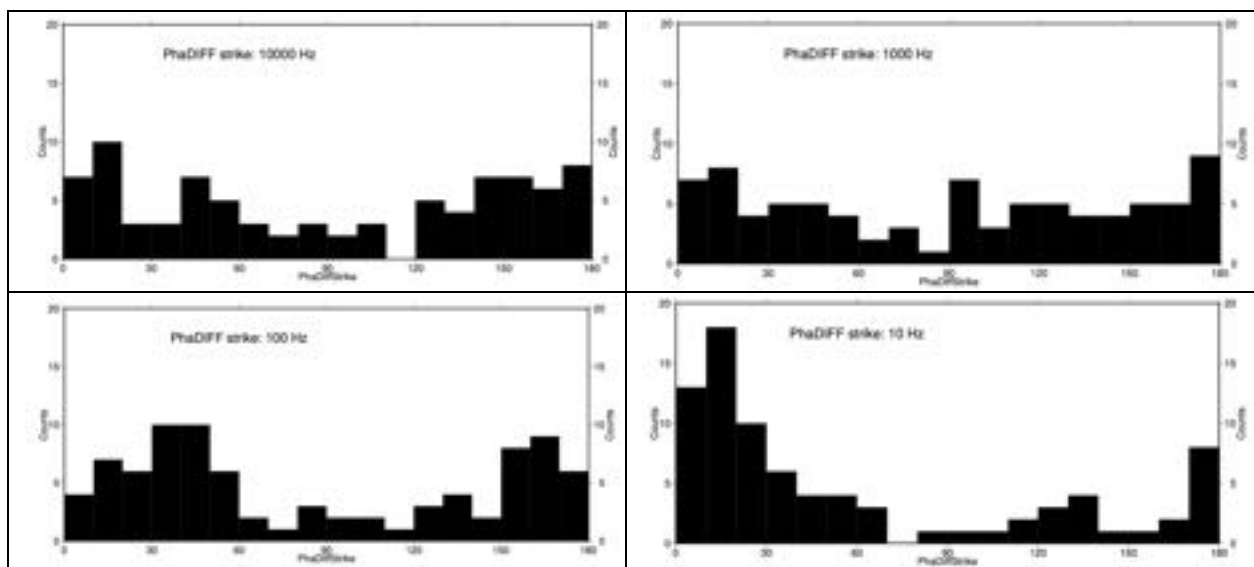


Figure 48: Histograms of maximum phase differences at frequencies of 10 kHz (top left), 1 kHz (top right), 100 Hz (bottom left) and 10 Hz (bottom right).

At high frequencies the strike is poorly defined, as we would expect from a quasi-1-D- subsurface down to 500 m. A predominant strike direction is formed by 100 Hz, with a peak at NE-SW and another at the almost conjugate direction. By 10 Hz there is one single dominant

peak at N15E. Circular statistical analyses of these histograms, assuming a repetition of π , yields means of N10E, N11E, N12E and N14E for 10 kHz, 1 kHz, 100 Hz and 10 Hz respectively, with the standard deviation reducing with decreasing frequency.

7. Geoelectrical strike – Phase Tensors

For two-dimensional (2-D) structures, in conventional MT the along-strike e-field (E_x , where “x” is defined as being along strike) divided by the across-strike h-field (H_y , “y” is across strike) is defined as the transverse-electric (TE) mode ⁽³⁾ of induction in MT. In contrast, the across-strike e-field (E_y) divided by the along strike h-field (H_x) is defined as the transverse magnetic I mode.

It is vitally important that the correct geoelectrical strike be defined for 2-D data – an incorrect strike direction will lead to erroneous models, and thereby erroneous interpretations and conclusions.

A rapid visual way for assessing dimensionality and directionality is to plot the MT Phase Tensors (Caldwell et al., 2004). The great attraction of Phase Tensors (PT) is that local galvanic distortion caused by near-surface inhomogeneities of no interest is removed, and only directionality and dimensionality of the Earth structure are indicated in the PT parameters. However, as discussed by Jones (2012), Phase Tensors should only be used in a qualitative manner as their determination is unstable in the presence of high noise and/or high distortion. For quantitative assessment then more sophisticated approaches must be adopted.

The Phase Tensors at frequencies of 3 kHz, 300 Hz, 30 Hz, 3 Hz, 0.3 Hz and 0.03 Hz, which are on average approximately penetrating to maximum depths of approx. 200 m, 650 m, 2,000 m, 6,500 m, 15 km, 22 km and 50 km respectively (Table 5), are plotted in Figure 49.

Note that there are no PTs at 3,000 Hz for the existing data as the highest frequency for those data is 384 Hz.

³ In 2-D, Maxwell’s Equations separate into two independent sets. One set describes electric currents travelling along the structures, and is called the TE mode. The other set describes electric currents travelling perpendicular to structures, and is called the TM mode. Essentially, the TE mode is responsive to current flow, whereas the TM mode is responsive to charge distribution. Hence, the two sense the subsurface resistivity distribution differently, and a joint inversion of both TE and TM mode data together is a true Joint Inversion in an inversion manner as the two trade-off against each other.

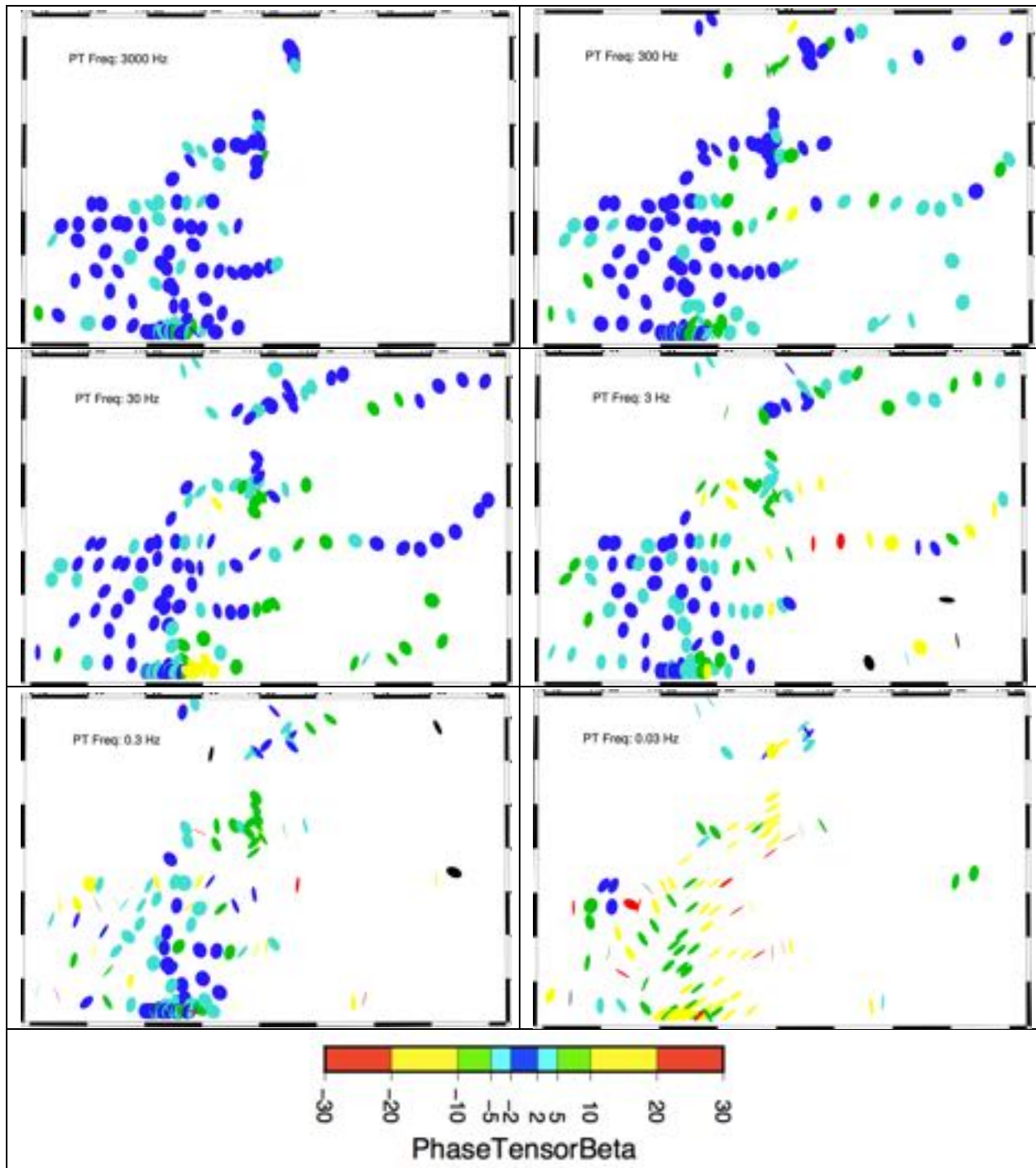


Figure 49 : Phase Tensors at frequencies of 3 kHz (top left), 300 Hz (top right), 30 Hz (middle left), 3 Hz (middle right), 0.3 Hz (bottom left), and 0.03 Hz (bottom right). The colours of the ellipses are the phase tensor beta values.

7.1. Phase Tensor Dimensionality

The colours of the ellipses indicate the PT absolute beta angle ($|β|$) values, which is a measure of 3-dimensionality, and the axes indicate the geoelectric co-ordinate system at that depth for that site. Low beta values (dark or light blue, $<5^\circ$) means that the data conform to either a 1-D

or 2-D representation of the structure below. High beta values (yellows and reds) indicate that the data are either representative of 3-D structures, OR that the data are scattered and noisy. (Note that the estimation of PT values is from algebraic manipulation of the MT impedance tensors, and so is totally non-robust.)

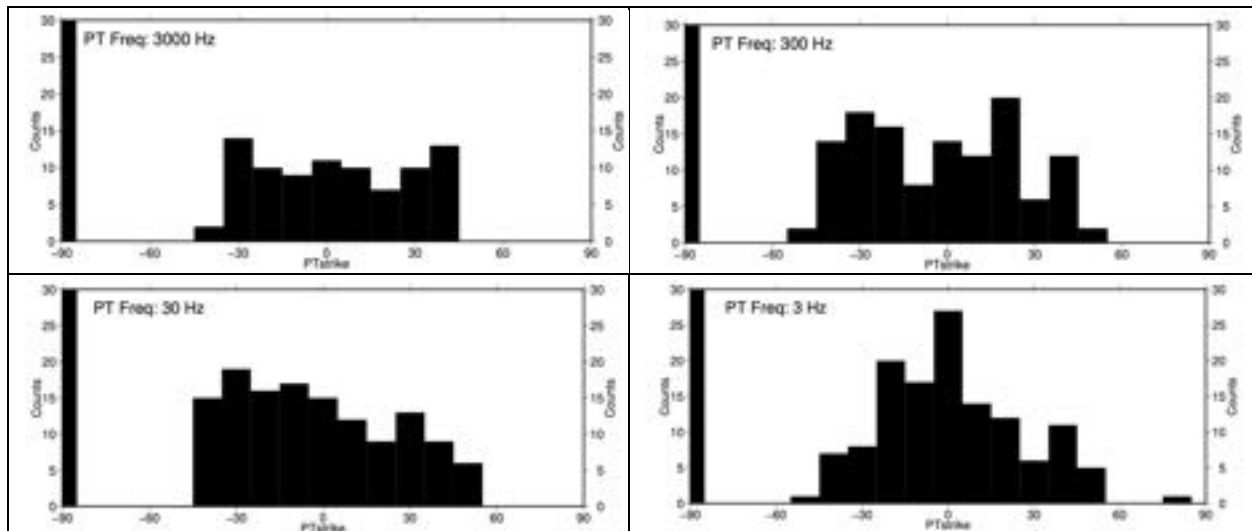
Disregarding a few obviously noisy sites (very high betas and/or very strongly distorted ellipses), at the high frequencies >3 Hz of primary interest to the client, most of the ellipses are dark to light blue, which indicates very low to low PT absolute skew ($|\beta|$) below 5° . For those sites an assumption of 1-D or 2-D interpretation is valid. Some of the dark blue ellipses are almost circular, which is evidence of a 1-D subsurface, and 1-D tools can be used for the data from those sites for imaging the top 4-5 km.

As frequency decreases below 0.3 Hz, then the data become more 3-D, and/or become very noisy.

7.2. Phase Tensor Directionality

The shape of the ellipses indicates whether the data are 1-D, which is true if the ellipse is near circular, or 2-D for low beta. If 2-D then the geoelectric strike direction is represented by the major or minor axis, depending on whether the site is on or off a conductor.

Histograms of the PT strike directions for the six frequencies are shown in Figure 50. PT-defined strike directions are scattered at high frequencies, indicative of no strong strike direction across the area, but show peaks at lower frequencies of 3 Hz and below, with directions consistent with prior observations.



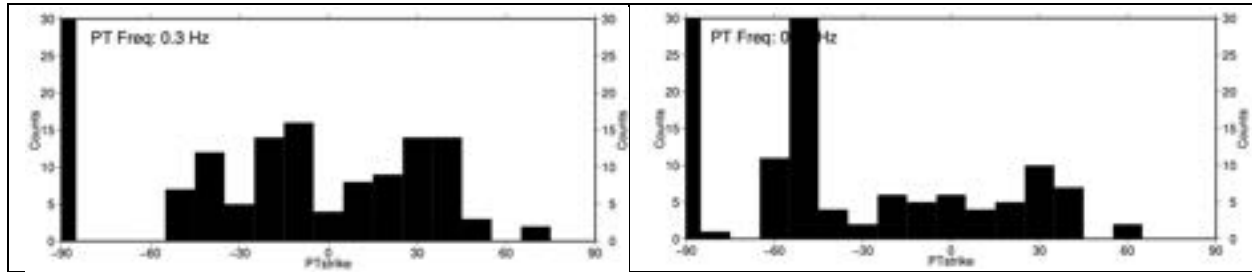


Figure 50: Histograms of the Phase Tensor strike direction for frequencies of 3 kHz (top left), 300 Hz (top right), 30 Hz (middle left), 3 Hz (middle right), 0.3 Hz (bottom left), and 0.03 Hz (bottom right).

There is in MT a 90° ambiguity in the determination of geoelectrical strike from MT data alone – there is no intrinsic way to know which is the TE mode and which is the TM mode; mode assignment must be done through considering other factors, such as the tipper induction arrow vectors (but these were not acquired), or local geology.

8. Vertical field transfer functions

There is a linear transfer functions between the observed vertical magnetic field and the two components of the horizontal magnetic field, viz.

$$H_z = T_{zx} H_x + T_{zy} H_y$$

(dependence on frequency assumed). The two transfer functions T_{zx} and T_{zy} are commonly referred to as “tippers”, taken from AFMAG, and are a measure of how much horizontal field is “tipped” into the vertical field. For a uniform source field there are no tippers over an isotropic 1-D Earth, so the presence of tippers is indicative of either a non-uniform source field (Jones & Spratt, 2002) or of non-isotropic 1-D subsurface, i.e. anisotropic 1-D, or isotropic or anisotropic 2-D or 3-D.

Tippers have not been much used in the mineral exploration industry, as often the vertical magnetic field, H_z , is not recorded in an attempt to reduce costs. This is a mistake in my view, as the tippers contain complementary information to the MT responses.

8.1. Induction vectors

The two transfer functions T_{zx} and T_{zy} are usually represented graphically as real and imaginary “induction vectors”, where the real induction vector is given by the amplitude and direction of the real parts of T_{zx} and T_{zy} , and the imaginary induction vector given by the same for the imaginary parts of T_{zx} and T_{zy} . The real part is usually reversed in the so-called Parkinson convention to point towards current concentration in conductors (Parkinson, 1959, 1962), except at high frequencies above the skin depth to the conductor (Jones, 1986). When not reversed the real vector is in the so-called Wiese convention, and the arrows point away from

structures of interest. The visually-confusing Wiese convention is generally used by central Europeans, and the far more sensible Parkinson convention by everyone else. The imaginary arrow is not reversed, as it undergoes a direction change at the frequency where the real arrow maximises – this is because the two induction arrows form a Hilbert transform pair.

Besides being used as part of inversion for structure, one common use of induction vectors is to define strike direction for 2-D modelling, given by the direction perpendicular to the real vector.

8.2. Tipper magnitude

Another informative plot is that of the tipper magnitude, given by

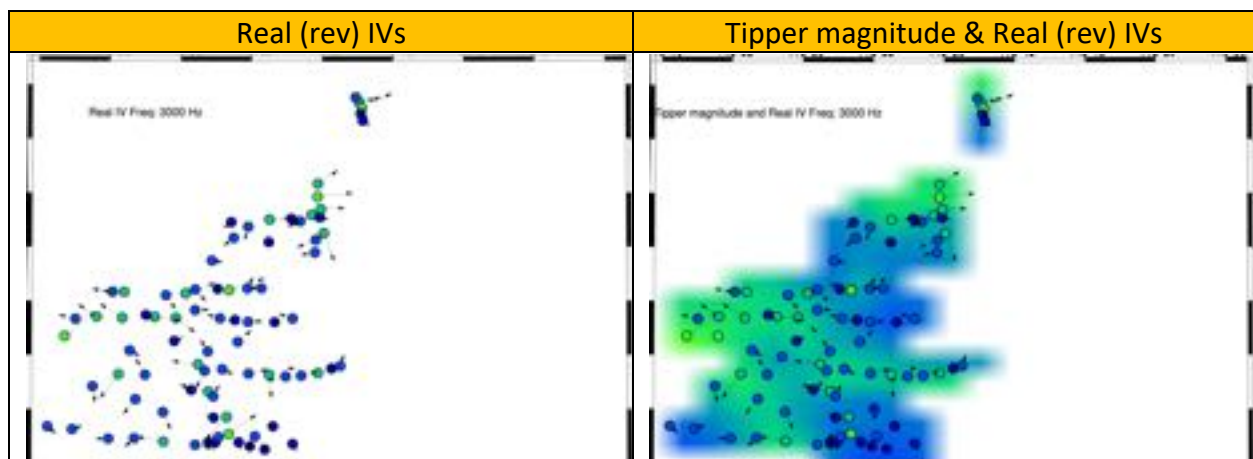
$$T = \text{SQRT} (T_{zx}^2 + T_{zy}^2).$$

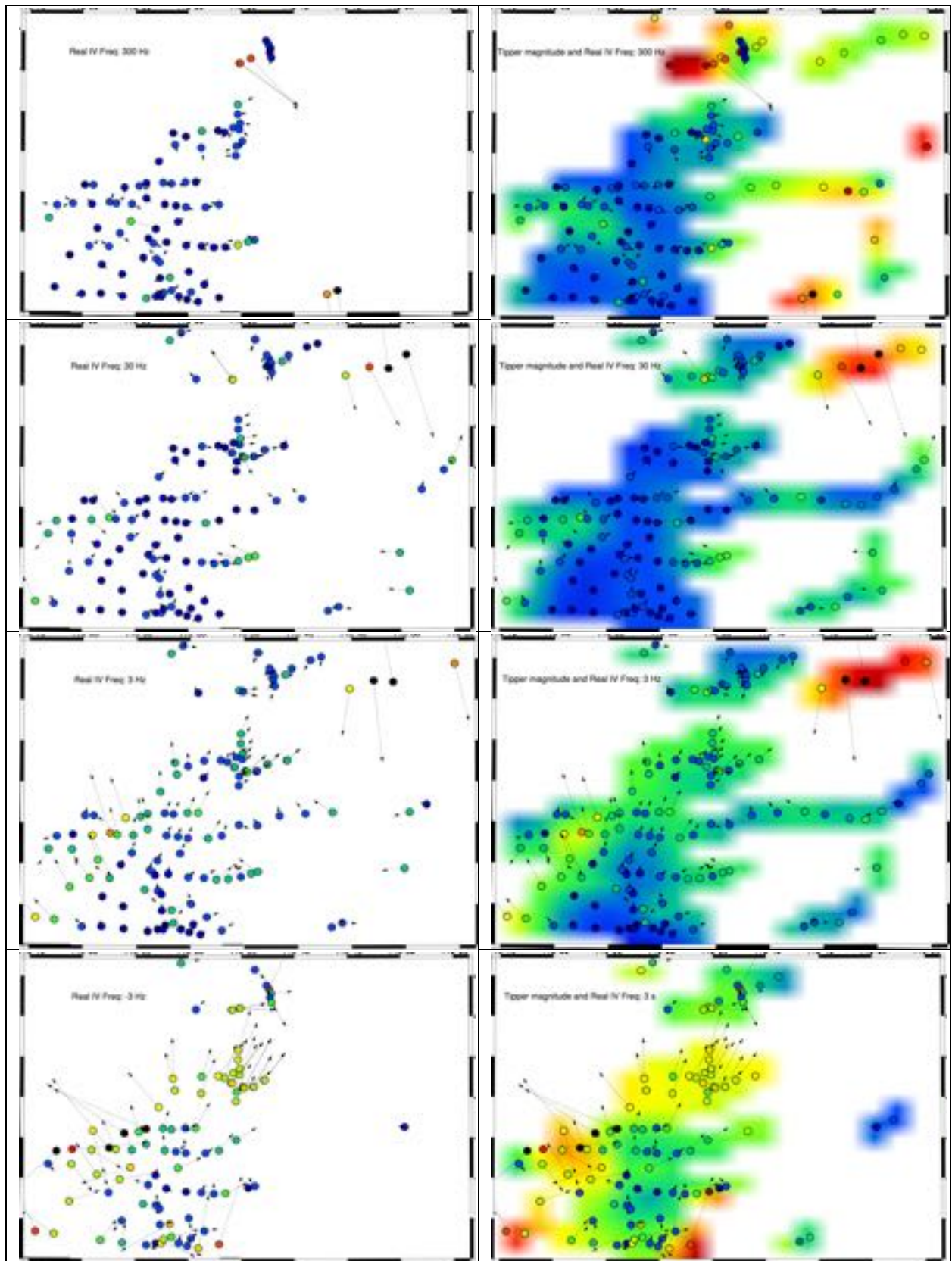
A recent paper discussing the advantages of considering Tipper Magnitude is that of Shalivahan et al. (2017)

8.3. Induction Vector and Tipper plots

Below are plots of the real (reversed) induction arrows at frequencies of 3 kHz, 300 Hz, 30 Hz, 3 Hz, 0.3 Hz and 0.03 Hz. For comparison to approximate depth, refer to Table 3, but recall that vertical magnetic field (Hz) penetration is less than electric field penetration (E_x or E_y), so tipper penetration (which is the ratio $\text{Hz}/(H_x, H_y)$) is less than MT penetration (which is the ratio $(E_x, E_y)/(H_x, H_y)$).

Real (reversed) induction vectors point towards current concentration, and in a 2-D case this means they are orthogonal to the strike of the 2-D anomaly. Note that on either side of a 2-D conductor, the vectors will have opposite directions, i.e., for a N-S striking 2-D conductor, on the east side the vectors will point west, and on the west side the vectors will point east. Thus there will be two peaks in a histogram plot of directions.





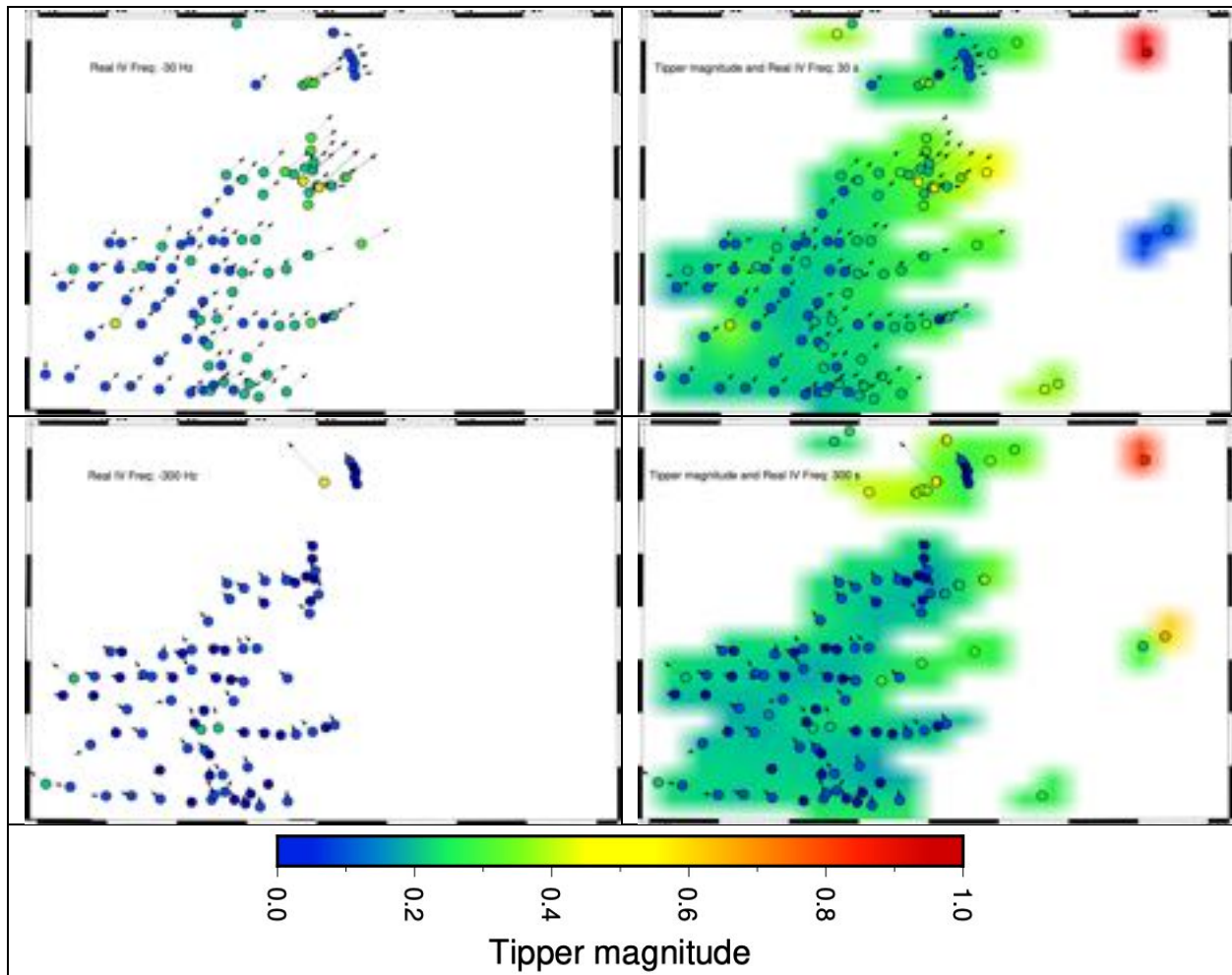


Figure 51: Plots of the real (reversed) induction arrows (left) and of the arrows and tipper magnitude (right) at frequencies of 3000 Hz (top row), 300 Hz (2nd row), 30 Hz (3rd row), 3 Hz (4th row), 0.3 Hz (3 s, 5th row), 0.03 Hz (30 s, 6th row), and 0.003 Hz (300 s, bottom row). The colour of the symbol is the magnitude of the real arrow, and the colour contour is that of the smoothed tipper magnitude.

Histograms of the induction arrow directions at the frequencies above plus the intermediate frequencies are shown in Figure 52.

The Duncan data are clearly noisy, with induction arrows that are far too large in places. There are no high frequency (>384 Hz) estimates at any Duncan sites, and also no low frequency estimates at most Duncan sites (acquisition time too short for determining estimates at low frequencies).

At high frequencies >100 Hz, generally, the tipper is relatively small, below 0.4, and is scattered without any strong dominant direction. This is indicative of small scale structures without a dominant trend.

The only immediately strongly anomalous region is in the NE at 3 Hz, but those sites are from Duncan data, and are not reliable – especially when two stations right next to each other point in opposite directions (could imply that one of the mag coils was laid in the wrong way).

At 0.3 Hz (3 s), there is some lateral variation, indicative of lateral variation in electrical conductivity. There is a strong peak at N30E – N60E that is maintained down to 0.01 Hz (100 s).

It is interesting to note the arrows and Tipper Magnitude in the location identified as Anomaly A at the eastern end of profile KSS.

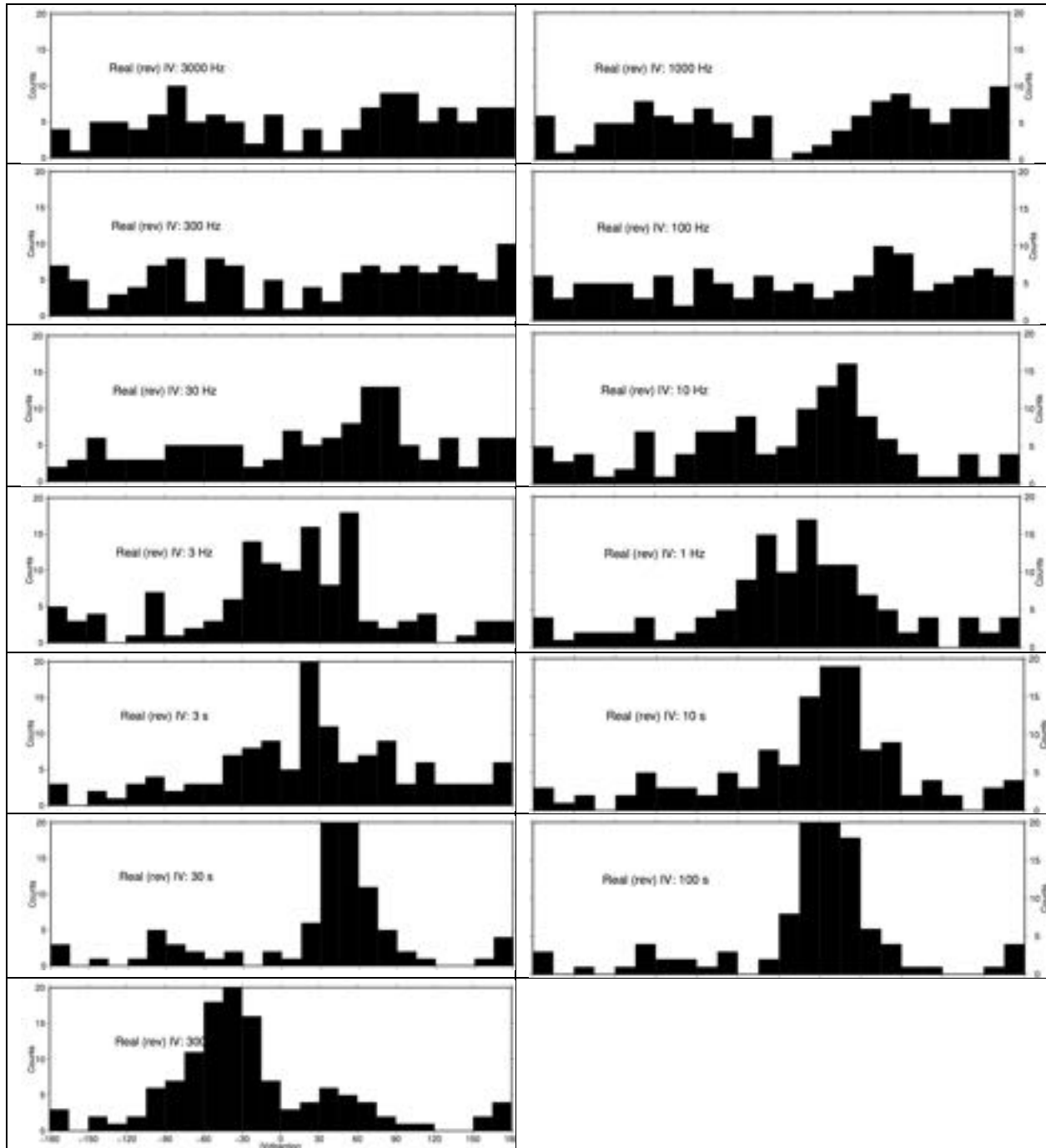


Figure 52: Histograms of Real (rev) IVs at various frequencies/periods.

- At high frequencies >100 Hz, there is no dominant strike direction apparent for the whole region.
- The induction arrows below 100 Hz are predominantly pointing NE – this means that the dominant geoelectric strike of the major structures is NW.

This justifies the choices made by Gupta and Jones (1995) and Cook and Jones (1995) of N50W and N30W respectively, rather than the orthogonal direction of N20E for the regional strike chosen by Marquis et al. (1995).

9. Strike decomposition

The purpose of geoelectrical strike determination is two-fold; first it is to ascertain **IF** a 2-D model of the data is valid, and second, if a 2-D model is valid then to derive the best strike angle to adopt for 2-D inversion and to derive the regional responses in that strike angle ⁽⁴⁾. This has to be performed in a statistical manner to derive the angle that fits the data at most sites and most frequencies.

The most-consistent geoelectrical strike over a series of sites and frequencies is best determined using the multi-site, multi-frequency distortion decomposition code of McNeice and Jones (2001), based on the approach of *Groom and Bailey* (1989, 1991). The primary objective when using any strike approach is to determine the most consistent strike direction acceptable to the majority of sites for the majority of frequencies. The optimum manner to determine that direction is in a stepwise mode, going from single-station to multi-station and from a few frequencies to broad frequency bands, to locate significant departures from uniformity, rather than utilizing all data immediately.

Strike decompositions were previously performed for this region by Gupta and Jones (1995) over decade-wide frequency bandwidths (Figure 53).

- One important point is that Gupta and Jones (1995) assumed that strike was dominantly WEST of North.

From MT data alone, there is a 90° ambiguity in the direction of strike.

⁴ Note: The data are NOT rotated into the strike direction, but a distortion model fit with that direction and estimates made of the regional responses. Jones and Groom (1993) and McNeice and Jones (2001) show the superiority of distortion model fitting over rotation.

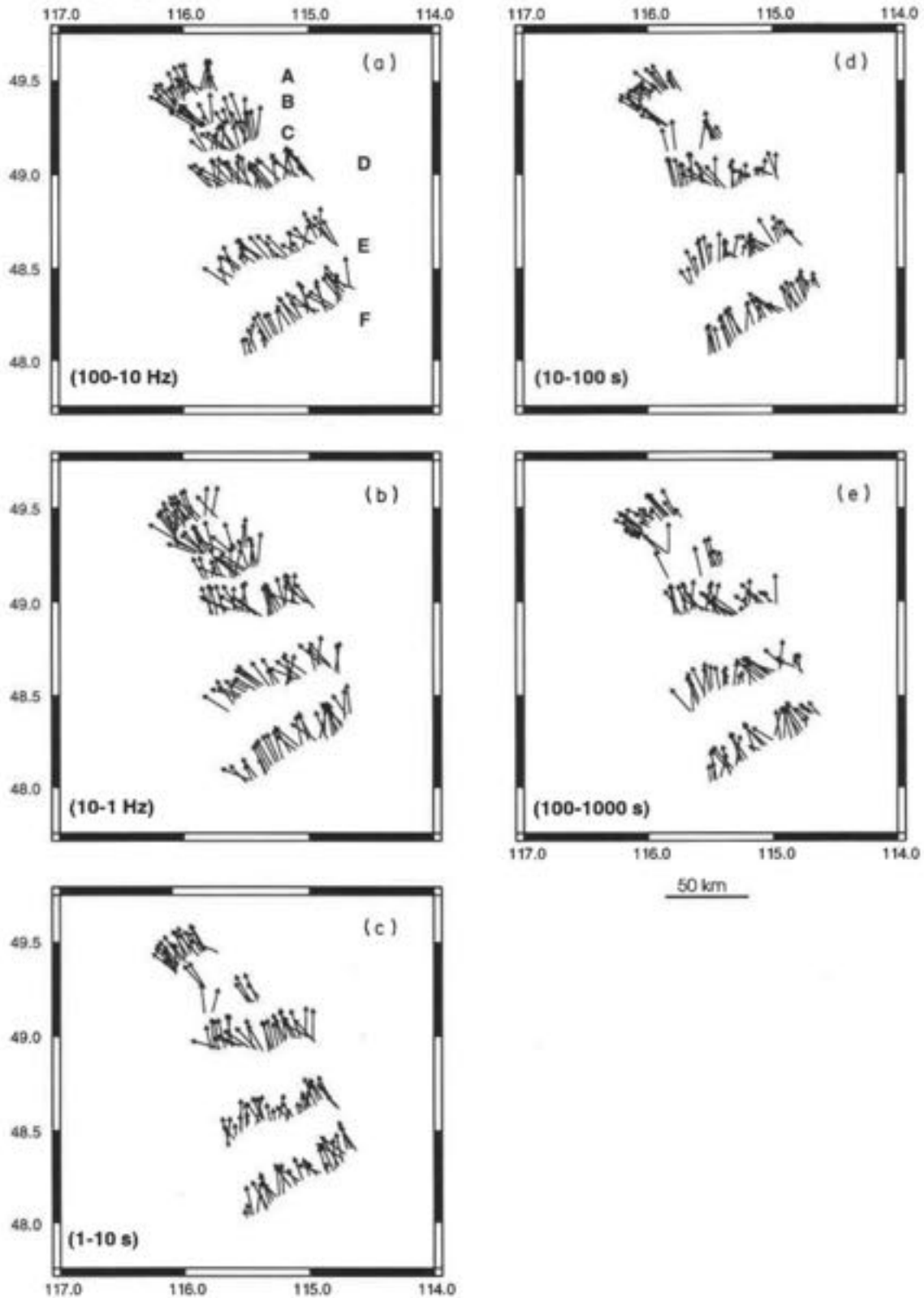


Figure 53: Strike directions calculated for five period bands: (a) 100-10 Hz; (b) 10-1 Hz; (c) 1-10 s; (d) 10-100 s; and (e) 100- 1000 s. The length of an arrow is a measure of the fit of the data to a Groom-Bailey distortion model calculated for the ID or 2D Earth under the influence of a 3D body that distorts the electric field only: long arrows indicate a good fit between the data and the model and the short arrows imply a poor fit between the two. Copied from Figure 4 in Gupta and Jones (1995).

9.1. Single site analyses

First, we run the code in single-site, multi-frequency mode, averaging data in various frequency or depth bands. We assume an error floor ⁽⁵⁾ of 1.75% in impedance throughout; this is equivalent to 3.56% in apparent resistivity and 1° in phase.

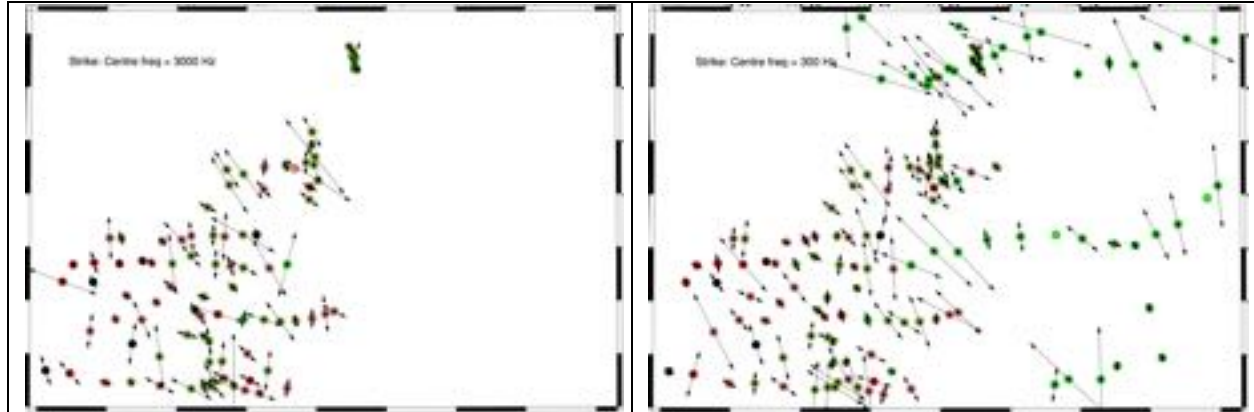
9.1.1. *Single-site, decade-wide bands*

We start by analysing data in seven decade-wide bands, from 10 kHz to 0.001 Hz.

The geoelectric strike directions for the seven are shown in Figure 54.

The lengths of the arrows indicate the phase difference between modes at the middle of each range, i.e., the phase in the strike direction minus the phase in the perpendicular-to-strike direction, which is a measure of the strength of the dimensionality. This phase difference is zero for 1-D structures, and is large for strong 2-D or 3-D structures.

The colours at each site indicate how well the model of distortion fits the data. Light green (RMS<1) and dark green (1<RMS<2) are both acceptable, pink (2<RMS<3) is moderately acceptable, and >4 (red, brown black) is not acceptable and is indicative of either 3-D structures or errors that are too low. Single site outliers are expressions of noisy scattered data.



⁵ An error floor is the minimum value of the error. Errors that are less than the error floor are increased to the error floor value, whereas errors that are greater than the error floor are unchanged. We routinely adopt an error floor when undertaking data fitting as most error estimates are derived from parametric error estimators, and are known to be far too small (see, e.g. (Chave & Jones, 1997)).

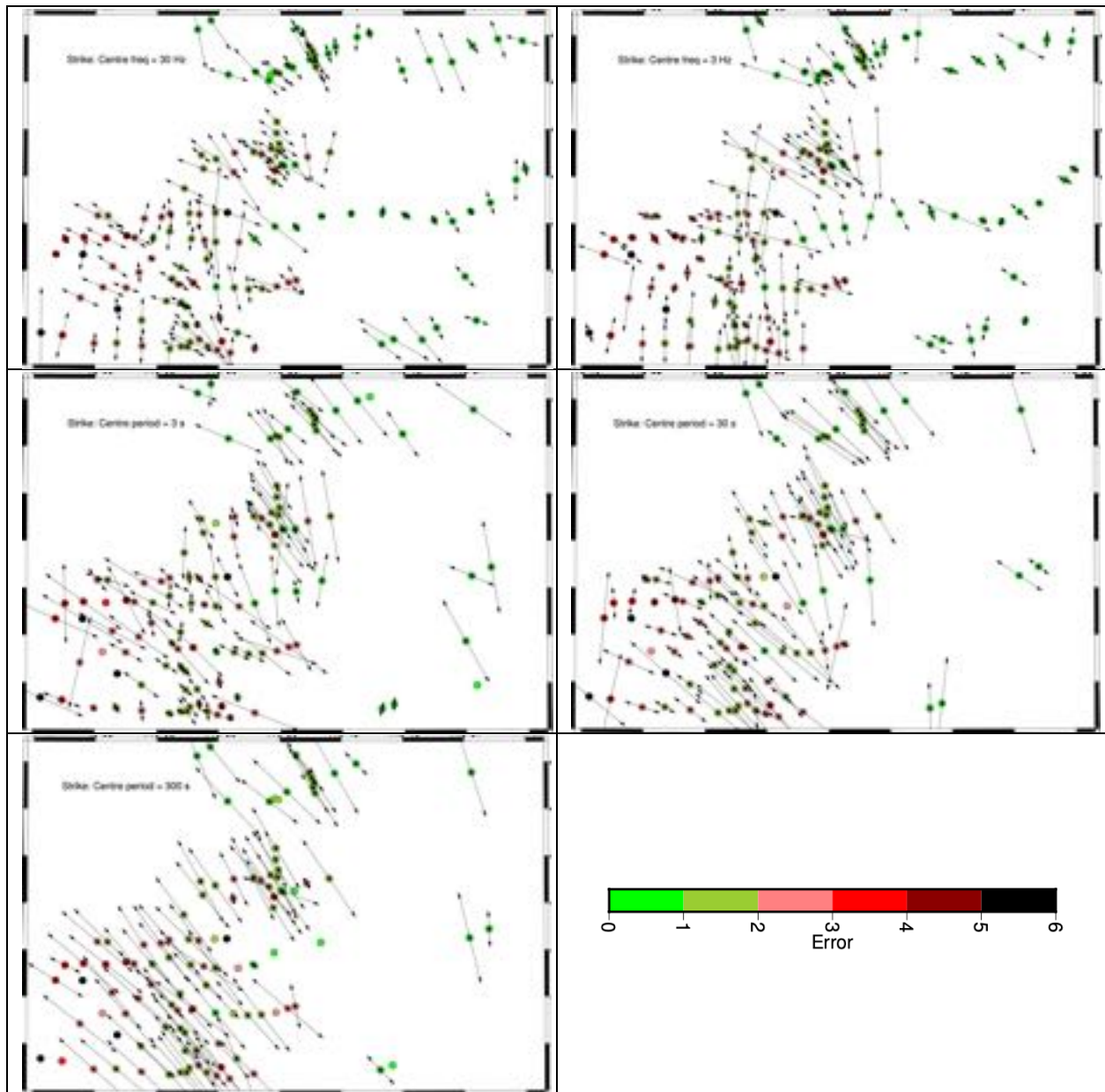
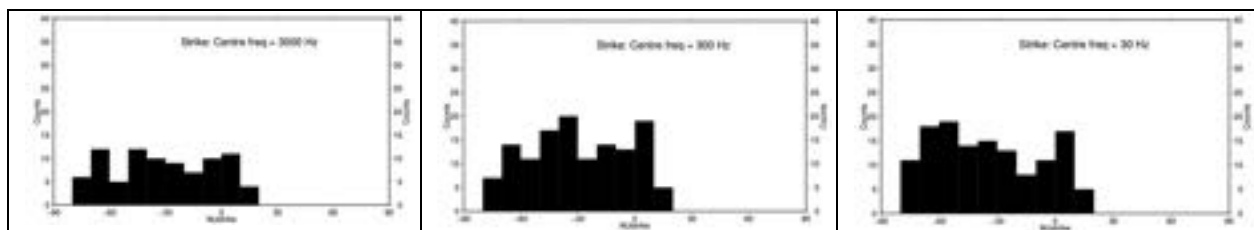


Figure 54: Single-site, multi-frequency strike directions for decade-wide bands from 10 kHz to 0.001 Hz. The length of the arrows indicates the phase difference, which is a measure of the strength of dimensionality, and the colour indicates the nRMS, with green inferring an acceptable fit and red and black unacceptable.



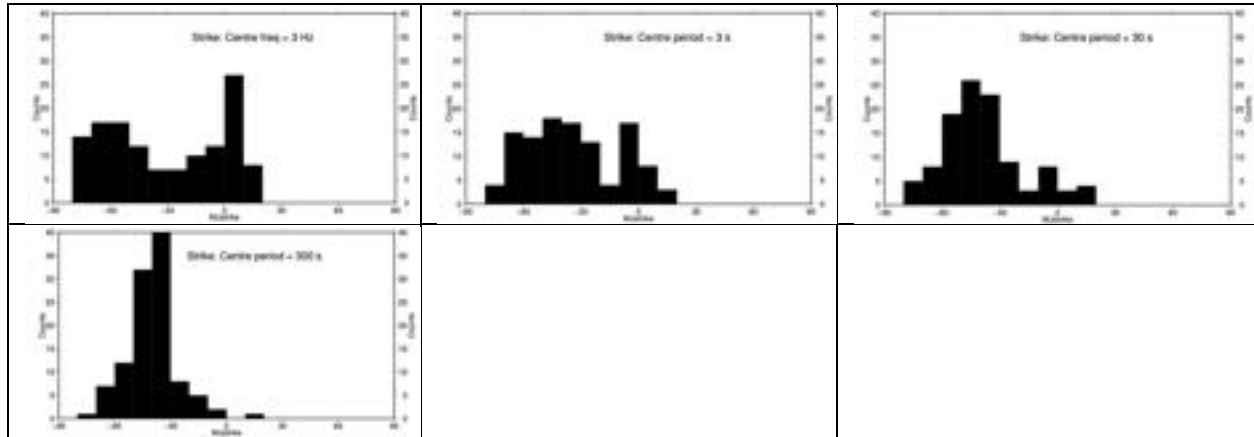


Figure 55: Histograms of the strike directions in decade-wide frequency bands from 10 kHz – 0.001 Hz.

Both visibly in the strike maps (Figure 54) and in the histograms (Figure 55) there is certainly an increasing concentration on a strike direction of initially N-S then NW-SE with decreasing frequency then finally rotating around to N30W at almost all sites at the lowest frequencies.

This rotation with decreasing frequency (=increasing period) is consistent with the directions observed by Marquis et al. (1995) to the west at the Intermontane/Omineca boundary (Figure 55).

→ However, Marquis et al. (1995) decided that the low frequencies were directed N30E, whereas here we prefer N60W, consistent with the strike directions of Gupta and Jones (1995).

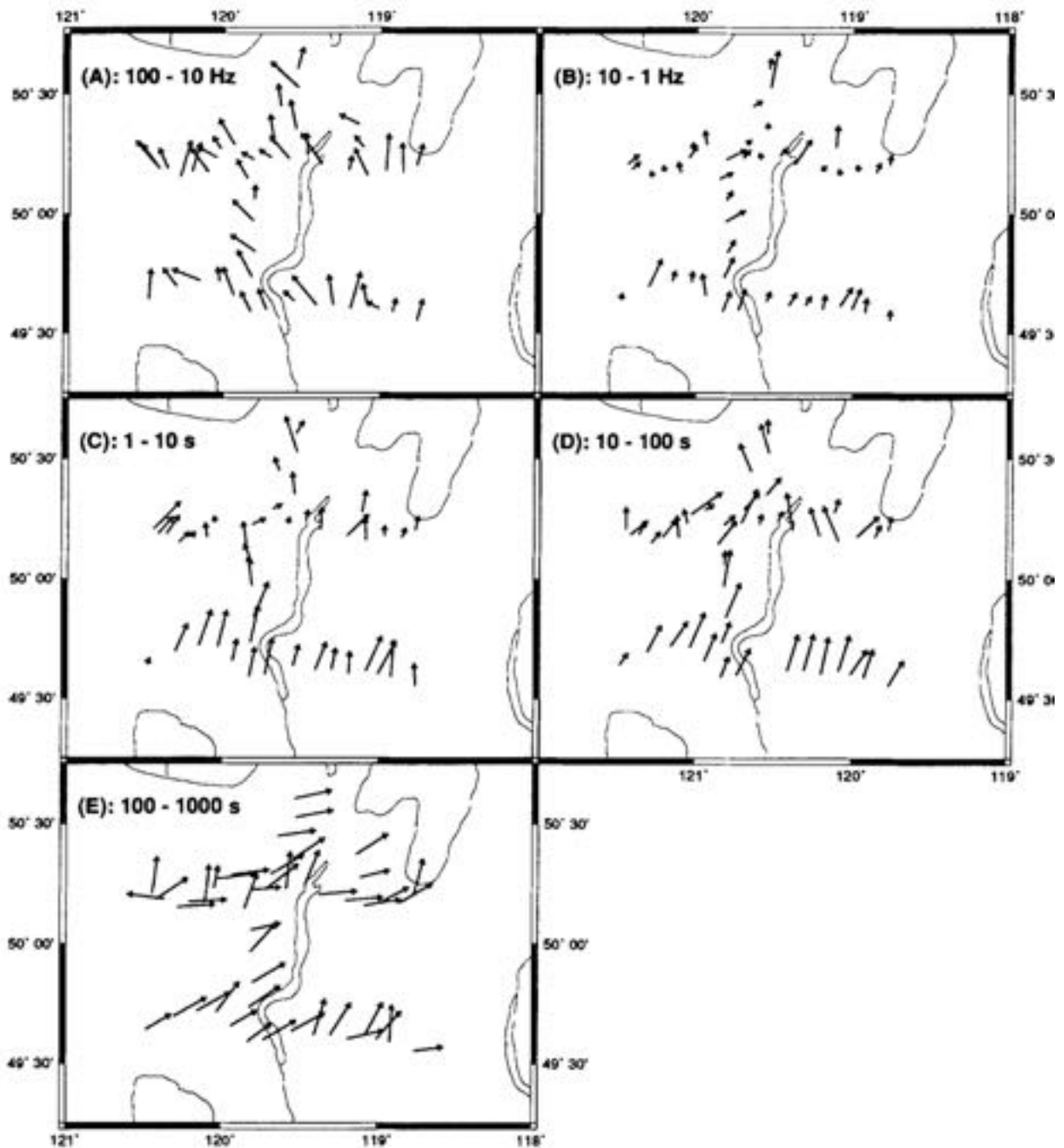


Figure 56: Strike directions for sites at the boundary of the Omineca and Intermontane Belts. Taken from Marquis et al. (1995).

9.1.2. Single-site, single frequency bands

Next we examine the strike directions determined when we seek the strike that is acceptable at each site for all frequencies in single bands.

9.1.2.1. 10 kHz – 3 Hz

The first set is the almost four-decade band of 10 kHz – 3 Hz, which is sampling from 100 m down to 4-5 km. The strike directions and error of distortion model fits at each site are shown in Figure 57, a histogram of the errors in Figure 58, and a histogram of the strike directions in Figure 59.

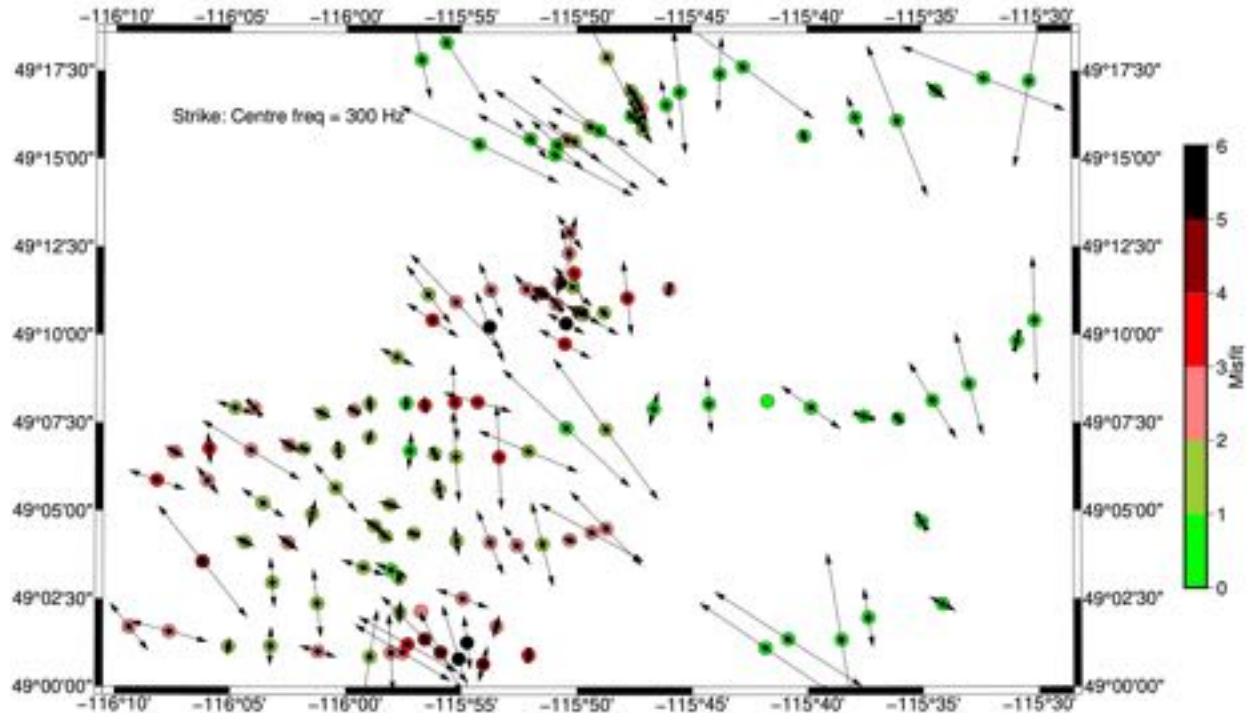


Figure 57: Strike direction for each site in the frequency band 10 kHz – 3 Hz. The scale is the average error of misfit of the distortion model to the data. Green = acceptable; Red = unacceptable.

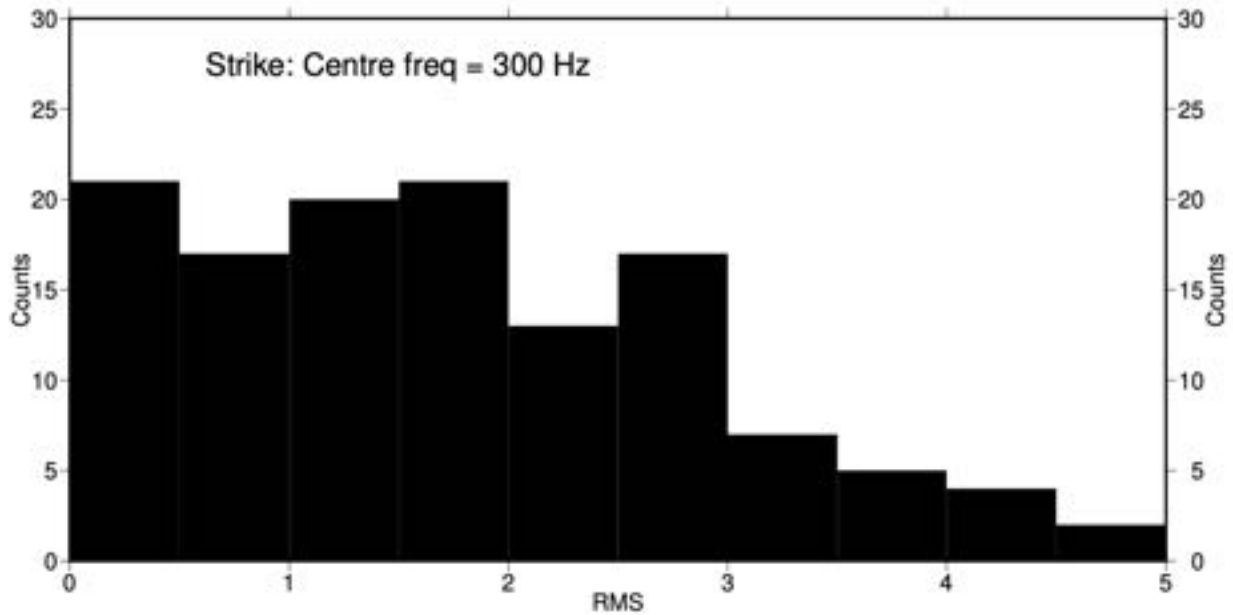


Figure 58: Histogram of nRMS misfits to the distortion model at each site as shown in Figure 57.

Of the 112 sites analysed, over half of them (759, have an nRMS < 2, so the 2-D distortion model with a single strike direction over the whole band of 10 kHz – 3 Hz is acceptable to them. A further 30 are marginally acceptable (2 < nRMS < 3), which means if the error floor is increased x1.5 from 3.75%/1° for RhoA/Pha to 5.625%/1.5°, those 30 would be acceptable also.

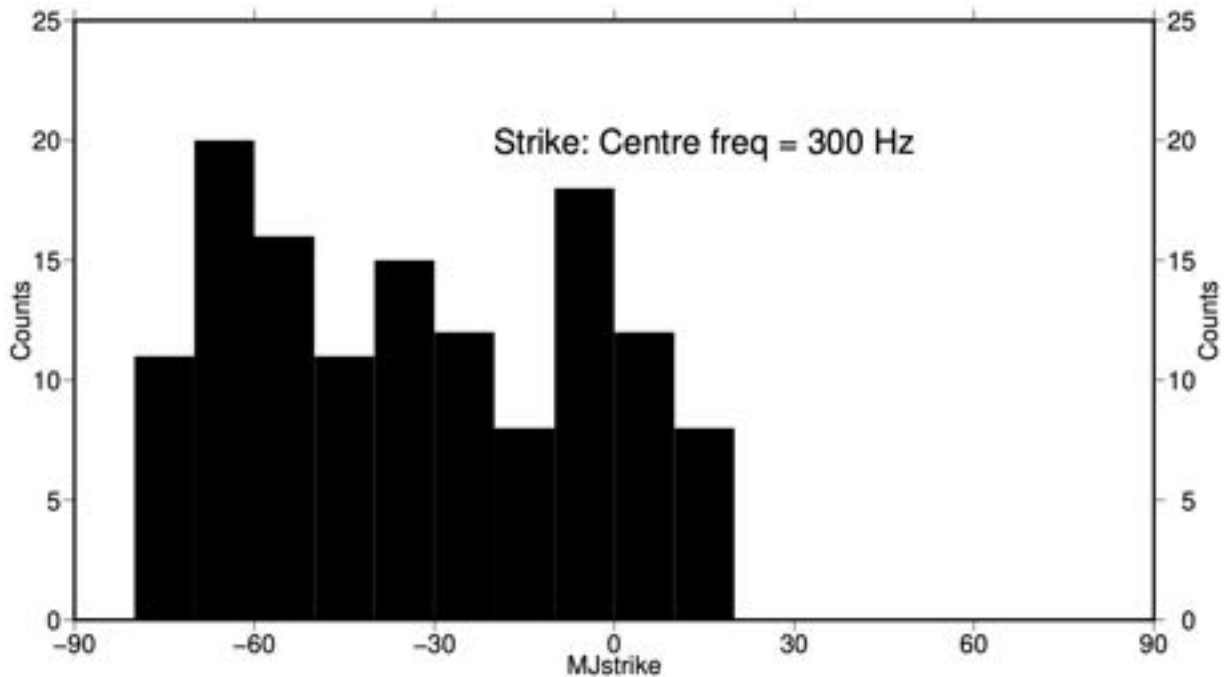


Figure 59: Histogram of strike directions in the three-decade band 10 kHz - 3 Hz.

The histogram of the strike directions is shown in Figure 59, and there are three visible peaks, at -70° - -60°, at -40° - -30° and at -10°- 0° (or their orthogonal directions).

9.1.2.2. 800 Hz – 8 Hz

The next band to analyse is the two decades of highest quality data from 800 Hz – 8 Hz. This band is primarily sensing depths from 500 m to 3-4 km. Here we see decent fits to most of the sites, with nRMS < 2.00 for about 2/3 of them.

Strike directions show the same three peaks as for the broader frequency range (Figure 61) at -70°- -60°, at -30° - -20° and at -10° - 00°, but with the peak at -70°- -60° far more pronounced.

The distortion models fits the sites excellently well (Figure 62), with over one third half (51 of 144) having an nRMS misfit <1, and two-thirds (92 of 144) having a misfit <2. There are 27 marginally-fit sites with misfit between 2 – 3, so those would be acceptable with a 50% increase in the adopted error floor. Only four sites poorly fit the distortion model with misfit >3.

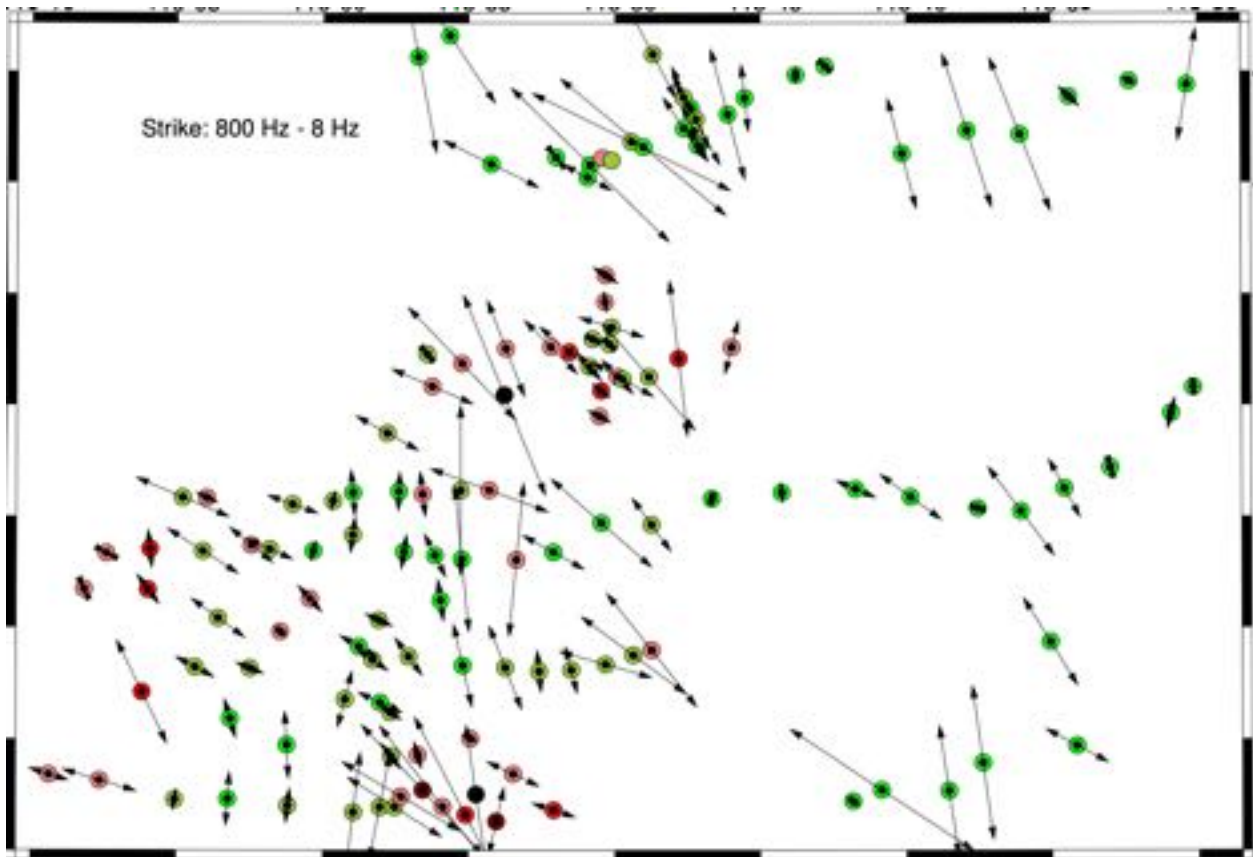


Figure 60: Strike direction for each site in the frequency band 800 Hz – 8 Hz. The scale is the average error of misfit of the distortion model to the data. Green = acceptable; Red = unacceptable.

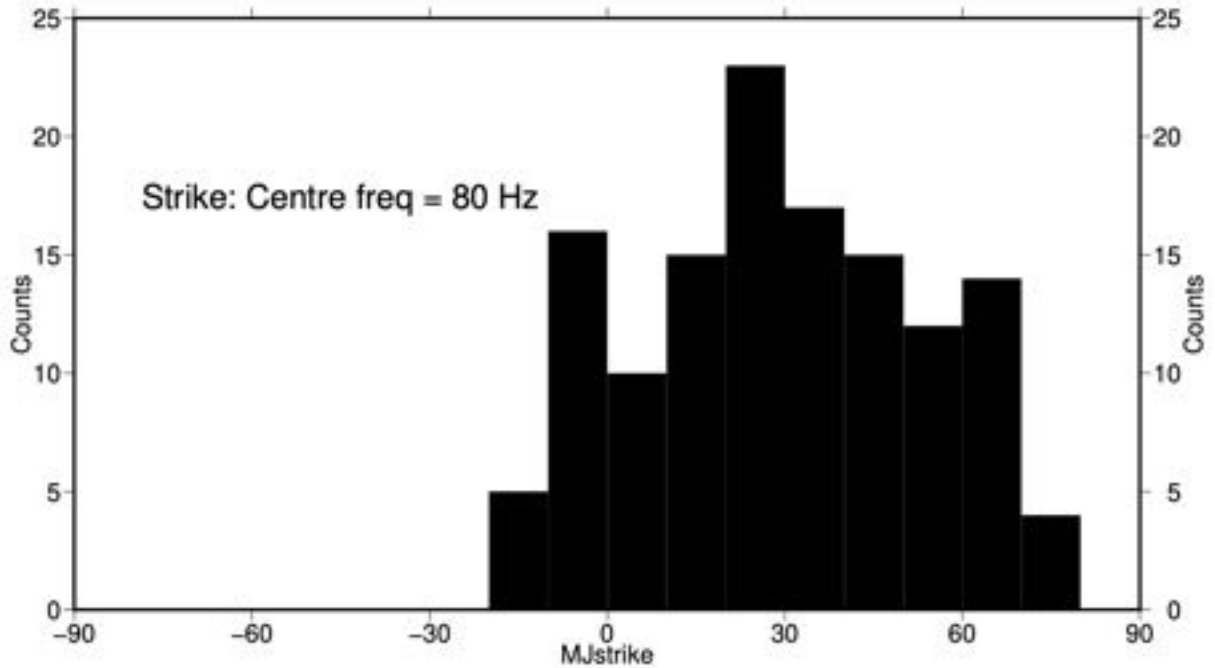


Figure 61: Histogram of strike directions in the two decade band 800 Hz - 8 Hz.

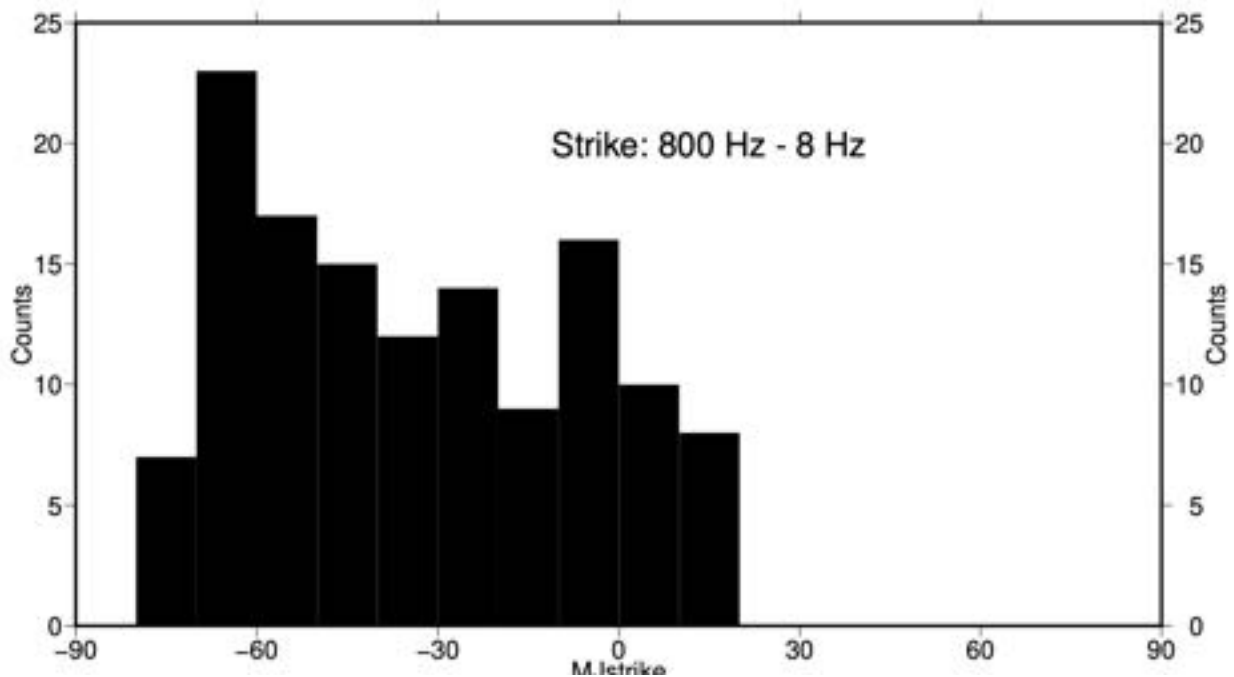


Figure 62: Histogram of strike directions in the two-decade band 800 Hz - 8 Hz.

9.1.3. Single-site: Misfit sensitivity with strike direction

One way of determining sensitivity to strike direction, i.e., intrinsic dimensionality, is to rotate the data at each site through 90° by 1° increments, and determine the minimum and maximum misfits found, then derive the ratio of the maximum RMS/minimum RMS. This ratio is plotted in

Figure 63 for the whole band 10 kHz – 3 Hz, and the sites with greatest sensitivity to strike are shown in dark red and black squares.

The histogram of the ratios (Figure 64).

The sites with little sensitivity to strike can be modelled in 1-D or anisotropic 1-D, and that is over one third (56 of 144) of them (ratio <1.5, white circles). The next 51 sites are mildly dimensional, with a ratio in the range 1.5 – 2.0 (yellow circles). Only 16 sites exhibit sensitivity to strike direction, with a ratio >2.5. These are mostly rather scattered, and most likely the sensitivity is more a function of the noise in the data than the dimensionality of the subsurface.

There is though a cluster of sites in the middle of the long central E-W profile, labelled MM1 by the client's representative. These sites do show sensitivity to strike direction.

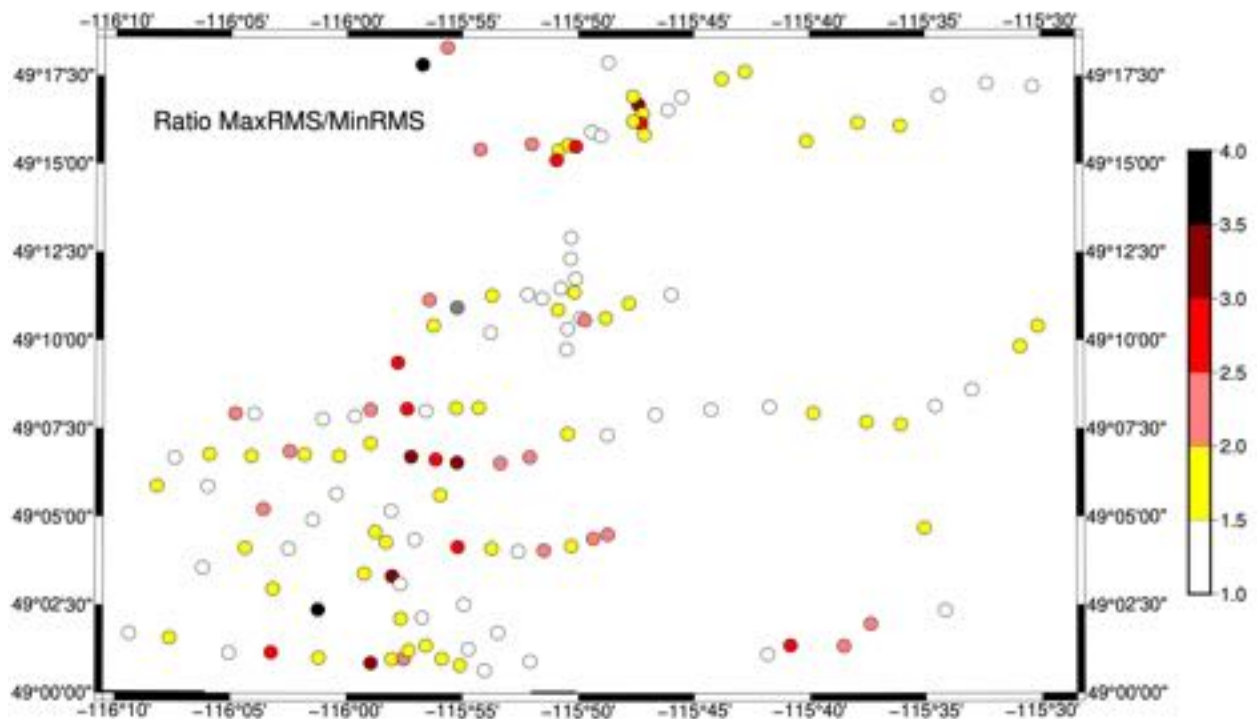


Figure 63: Ratio of the maximum RMS/minimum RMS for each site for the frequency band 10 kHz – 3 Hz.

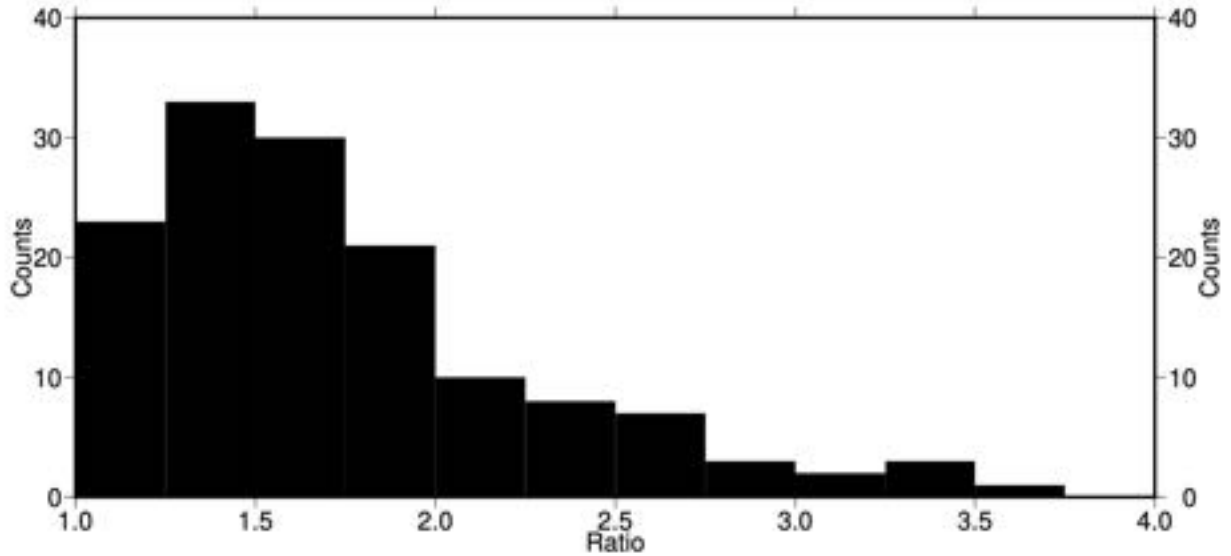


Figure 64: Histogram of the ratios of MaxRMS/MinRMS for single-site strike directions in the frequency band 10 kHz – 3 Hz.

The same plots but for the two decades 800 Hz – 8 Hz are shown in Figure 65 and Figure 66, and essentially the same information is portrayed. 51 sites have a ratio <1.5, and a total of 89 have a ratio <2.0. Only 25 sites have a ratio > 2.5.

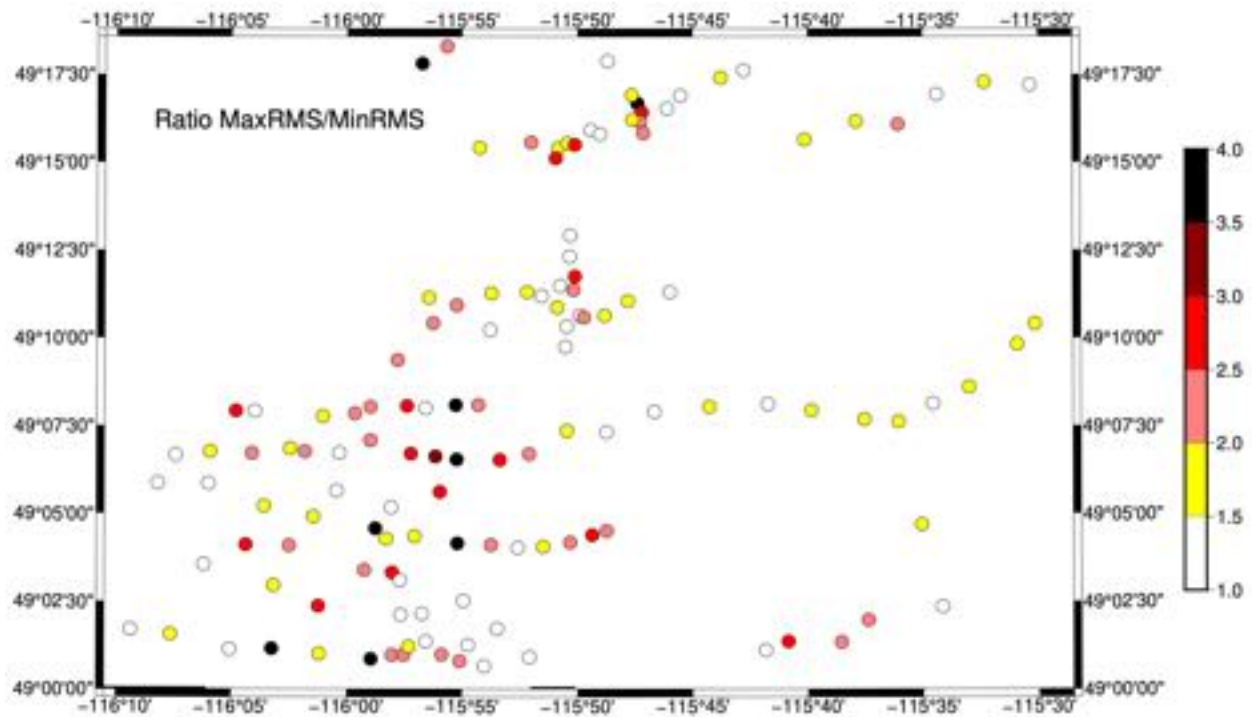


Figure 65: Ratio of the maximum RMS/minimum RMS for each site for the frequency band 800 Hz – 8 Hz.

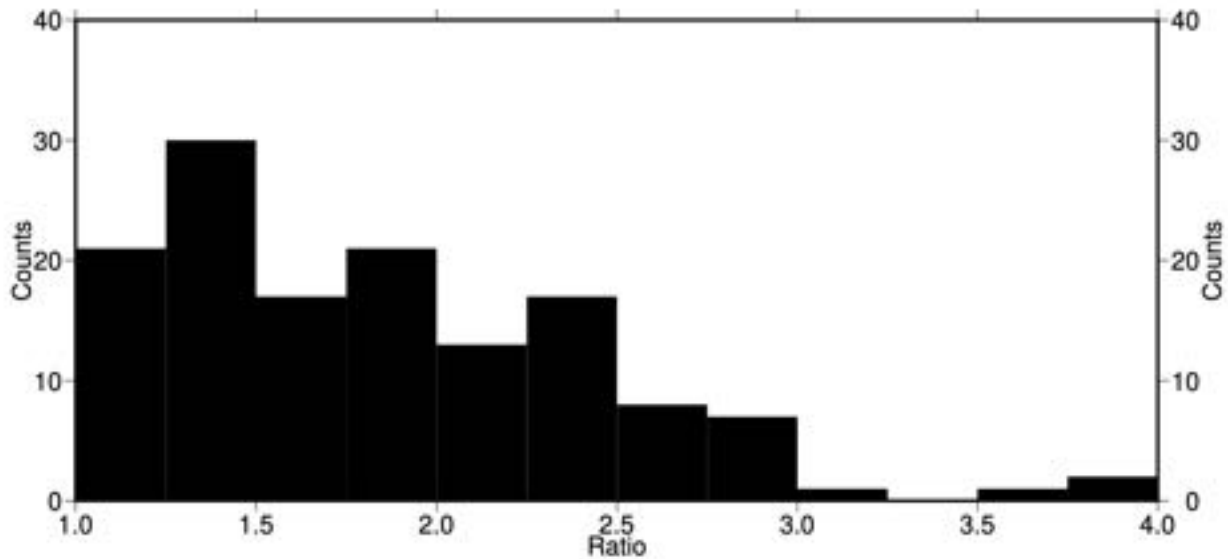


Figure 66: Histogram of the ratios of MaxRMS/MinRMS for single-site strike directions in the frequency band 800 Hz – 8 Hz.

9.1.4. *Single-site: Conclusions*

Single site analysis shows that the area is varying somewhat laterally and but very strongly vertically in the direction of strike of electrical conductivity. Some sites may be amenable to anisotropic 1-D inversion, and some small groups of sites to 2-D inversion.

Generally, the high frequencies strike N-S, the mid-frequencies NW-SE, and the lowest frequencies N60W. Hence the three peaks observed in the strike direction histograms.

9.2. Multi-site by profile

Multi-site, multi-frequency analyses were performed along each profile. The stations on each profile are listed in Table 1. Given the priority of analyses to provide Spratt with regional responses for 2-D parameter testing, the profiles were analysed starting with MM1 and MO.

Extra effort was expended on profile MM1 given its length and its importance for defining the parameters for 2-D inversion.

9.2.1. *Profile MM1*

Profile MM1 comprises 24 sites, 12 newly-acquired sites and 12 from the 1985 Duncan survey line 3 (Figure 67). The Duncan sites only have data up to 384 Hz, and are of poorer quality.

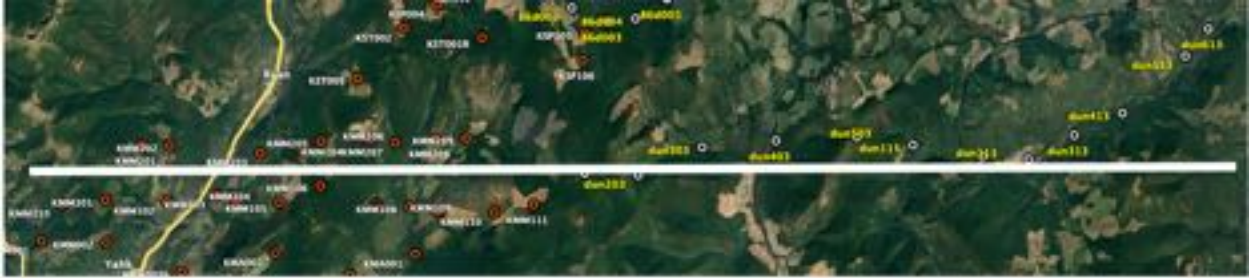


Figure 67: Profile MM1

9.2.1.1. Whole profile analysis

Performing single frequency, multi-site analyses of all the sites simultaneously along the profile (black points in Figure 68), there is significant scatter, but nonetheless a transition is visible from around N-S at the highest frequencies rotating clockwise to N45E at the lowest frequencies. This is consistent with what is being observed regionally.

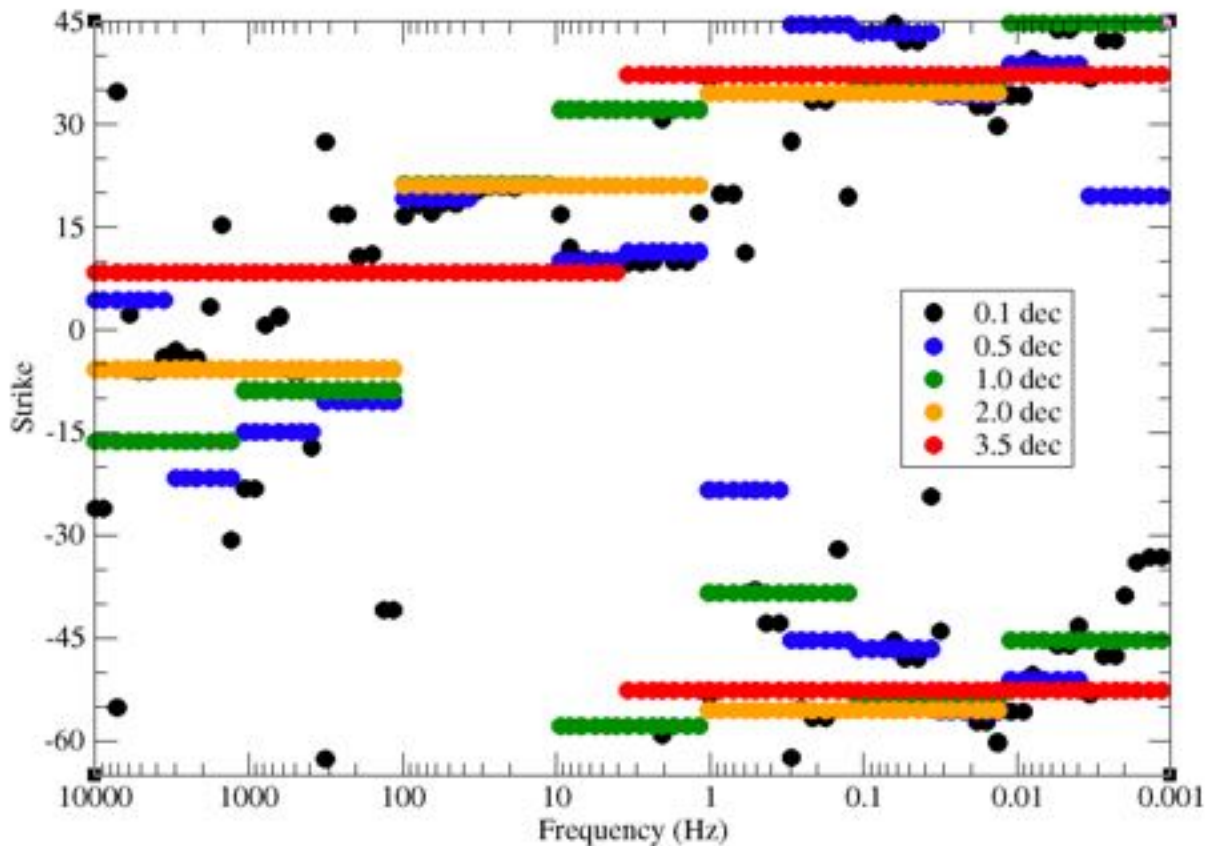


Figure 68: Strike directions for multi-site analyses with different bandwidths for sites on profile MM1.

Multi-site, multi-frequency analysis, with increasing widths of the frequency band from 0.5 decades to 3.5 decades, confirms this trend.

The 3.5 decade directions, from 10 kHz – 3 Hz and from 3 Hz – 0.001 Hz (red points) are essentially a N08E geoelectric strike direction to around 4 km and a N55W or (N35E) strike direction for the rest of the crust.

Such a layered situation was observed by Marquis et al. (1995) for sites at the boundary of the Omineca and Intermontane Belts (Figure 56). Marquis et al. (1995) found that the strike directions above 10 Hz were on average N25W, which is very different from those below 10 Hz, N20E, and at the lowest frequency of N60E.

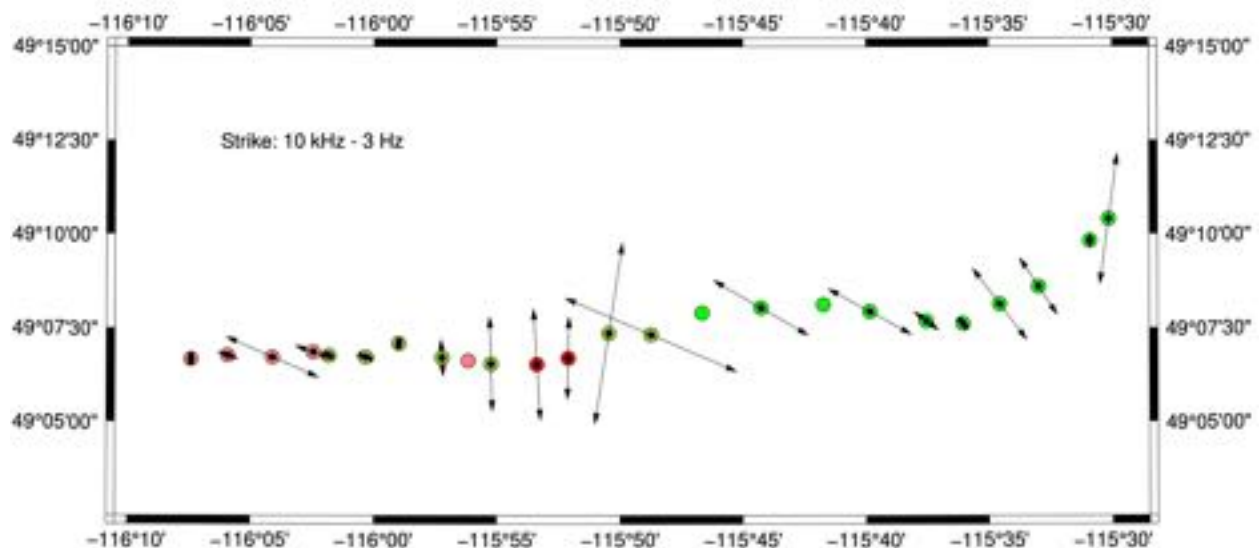
The interpretation of Marquis et al. (1995) was that the high frequency strike represents the geoelectrical strike of the allochthonous terranes, whereas the lower frequency strike is the strike of autochthonous basement. And the lowest frequency strike is that of the lowermost crust/upper mantle.

However, based on the Induction Vector directions, we assume that crustal strike is WEST of north.

9.2.1.2. *Lateral variation along profile*

To test variation of preferred strike direction along the profile, groups of sites were taken. Each group was of 5 sites, the centre one and its two neighbours on either side. The end sites were modified to include only one or two neighbours.

The analyses were performed for the two frequency bands of interest, namely 10 kHz – 3 Hz for the upper 4-5 km or so, and 3 Hz – 0.001 Hz for the middle and lower crust to the Moho. Analysis was also performed of the two-decade band from 800 Hz – 8 Hz, as these represent the best quality data. (Remember though that the Duncan data only goes to 384 Hz.)



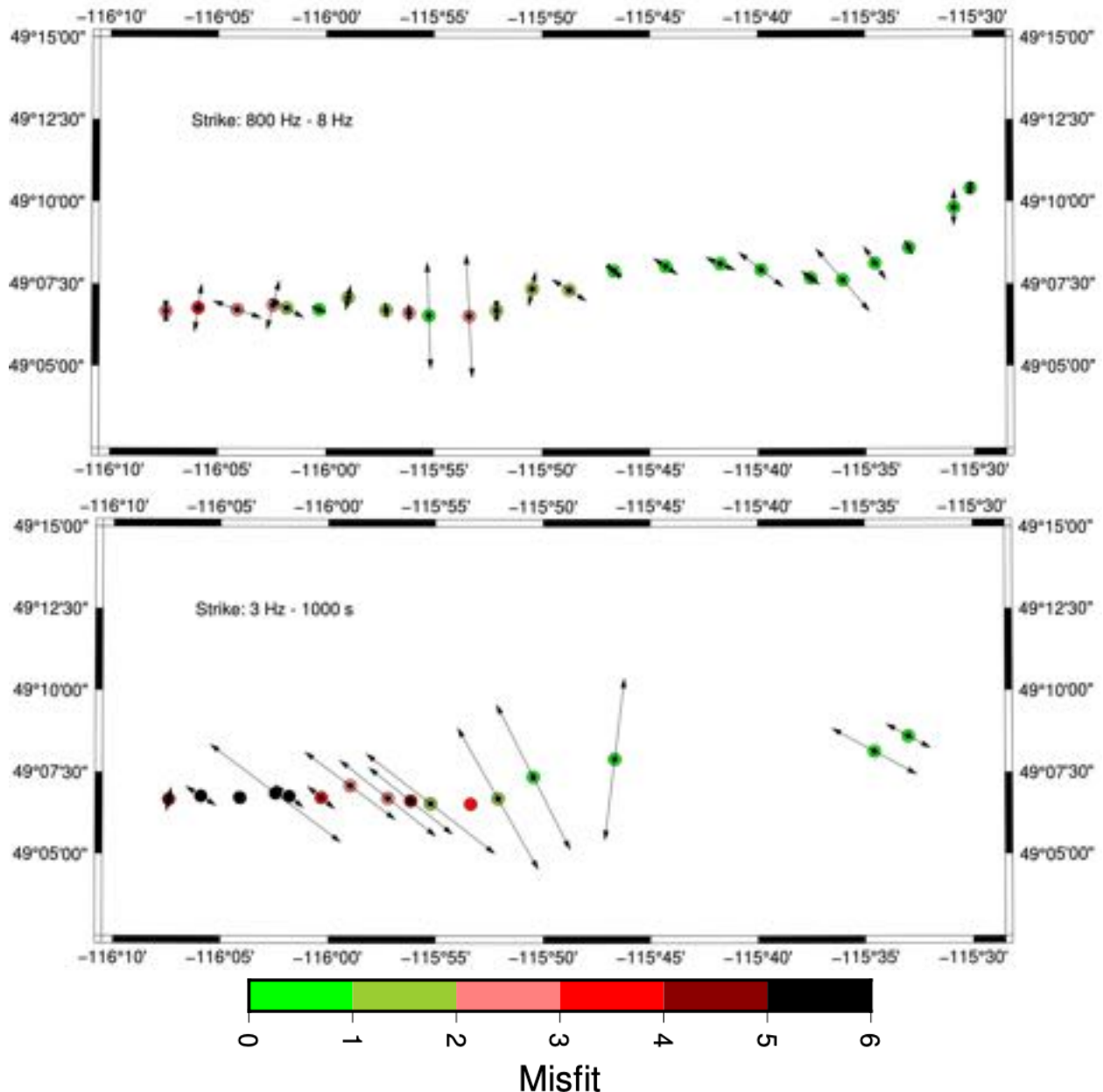


Figure 69: Strike directions for groups of five sites in the three frequency bands.

We still see a strong preference for approx. N-S at high frequencies and approx. NW-SE at the low frequencies.

9.2.1.3. Imposed strike directions – N10E and N35W

Finally, we can impose a single strike direction on all of the data, and see how well the distortion model fits.

We impose two directions, the uppermost crust direction of N10E (Figure 70, top) and the rest-of-the-crust direction of N35W (Figure 70, bottom) for all frequencies from 10 kHz – 0.001 Hz.

What we find is that the Duncan sites to the east are really not that sensitive to strike direction, and accept both directions over all frequencies. However the newly-acquired sites to the west are far more sensitive, and they poorly accept one direction over all frequencies.

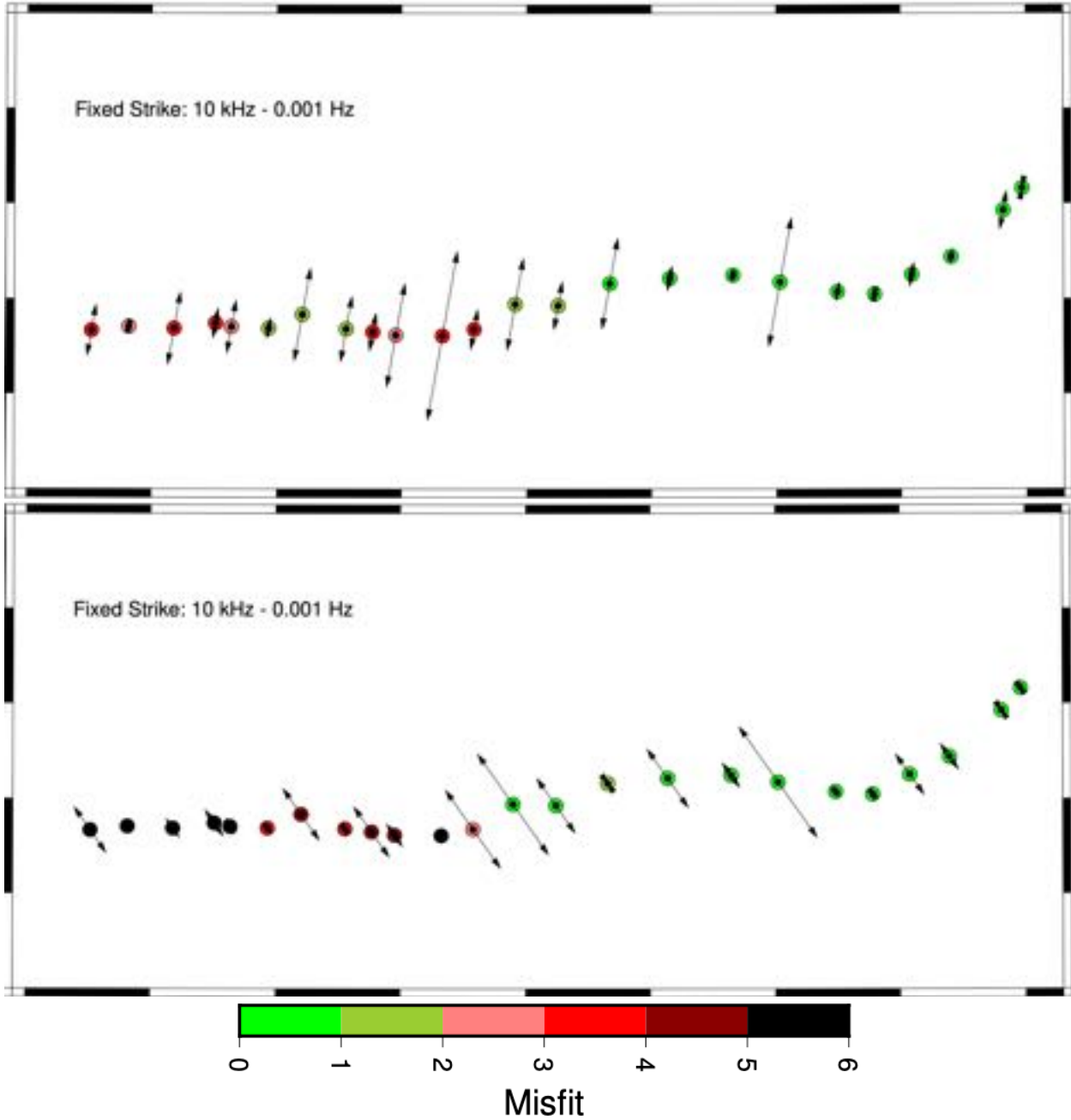


Figure 70: Imposed strike directions of N10E (top) and N35W (bottom) for all sites and all frequencies from 10 kHz – 0.001 Hz.

9.2.1.4. Conclusions

1. Profile MM1 exhibits both lateral and vertical variation in geoelectrical strike direction.
2. Sites to the east – the existing Duncan data – allow a broad range of strike directions, whereas those to the west – the newly-acquired Kootenay data – are more selective.

3. Generally, the data require a direction on N10E for frequencies sampling the top 4-5 km and N35W for the rest of the crust.
4. For optimal imaging, two models need to be generated, one for the upper 4 km with an assumed strike of N10E and using frequencies from 10 kHz – 3 Hz, and the other for the whole of the crust with an assumed strike of N35E and using frequencies from say 30 Hz – 0.001 Hz.
5. A single crustal model with a strike of N10E would be reasonable for the upper crust, but would not optimally image structures in the middle and lower crust.
6. Similarly, a single crustal model with a strike of N34E would be reasonable for the middle and lower crust, but would not optimally image structures in the upper crust.

→ **Two sets of final estimates were prepared, one set at N10E and the other set at N35E.**

9.2.2. Profile MO

Profile MO (Moyie) is the most northern sites and is an ENE-SWS one comprising primarily existing Duncan data (Figure 71). In addition, a short N-S profile of five sites labelled KMOxxx was newly-acquired, and all of those data are included in the analysis to define the appropriate strike direction(s).



Figure 71: Profile MMO. Existing Duncan data shown in yellow, and newly-acquired KMOxxx sites in white. The location of the Moyie drillhole is indicated by the blue triangle.

Thus, the 17 sites assigned to this profile are:

dun311, dun411, dun511, 86d014, 86d145, 86d015, dun611, dun711, KMO01R, KMO002, KMO003, KMO004, KMO005, dun811, dun009, dun010, dun011.

The Duncan data were previously modelled by Gupta and Jones (1995), with an assumed strike of N50W, and their model is shown in Figure 17. A subset of the data around the Moyie drillhole was previously modelled by Cook and Jones (1995), with an assumed strike of N30W, and their model is shown in Figure 18.

The multi-site analyses for different frequency bandwidths is shown in Figure 72, and there is certainly stability with frequencies lower than 10 Hz.

Note that the high frequency strike of N32W and a lower frequency strike of N43W is fully consistent with the prior analyses of Cook and Jones (1995), for the high frequency data, and Gupta and Jones (1995) for the regional scale data.

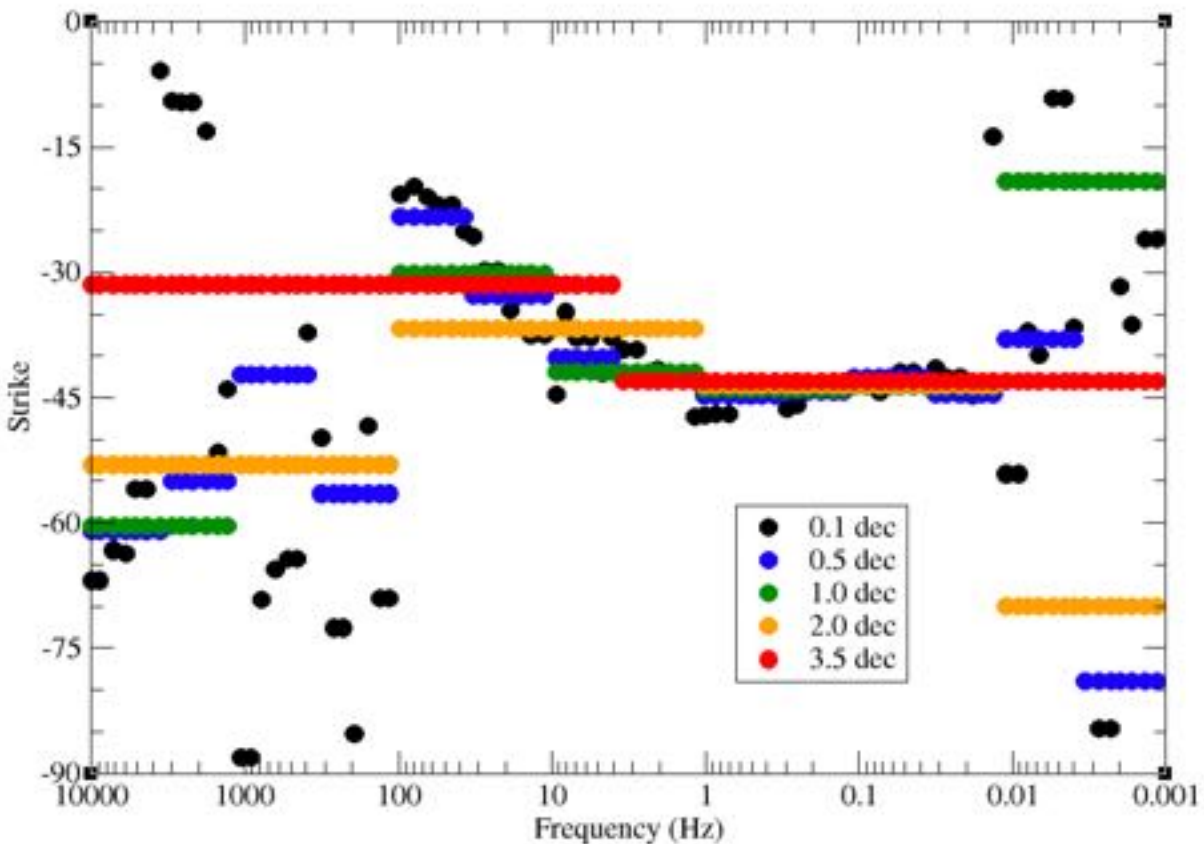


Figure 72: Strike directions for multi-site analyses with different bandwidths for sites on profile MO

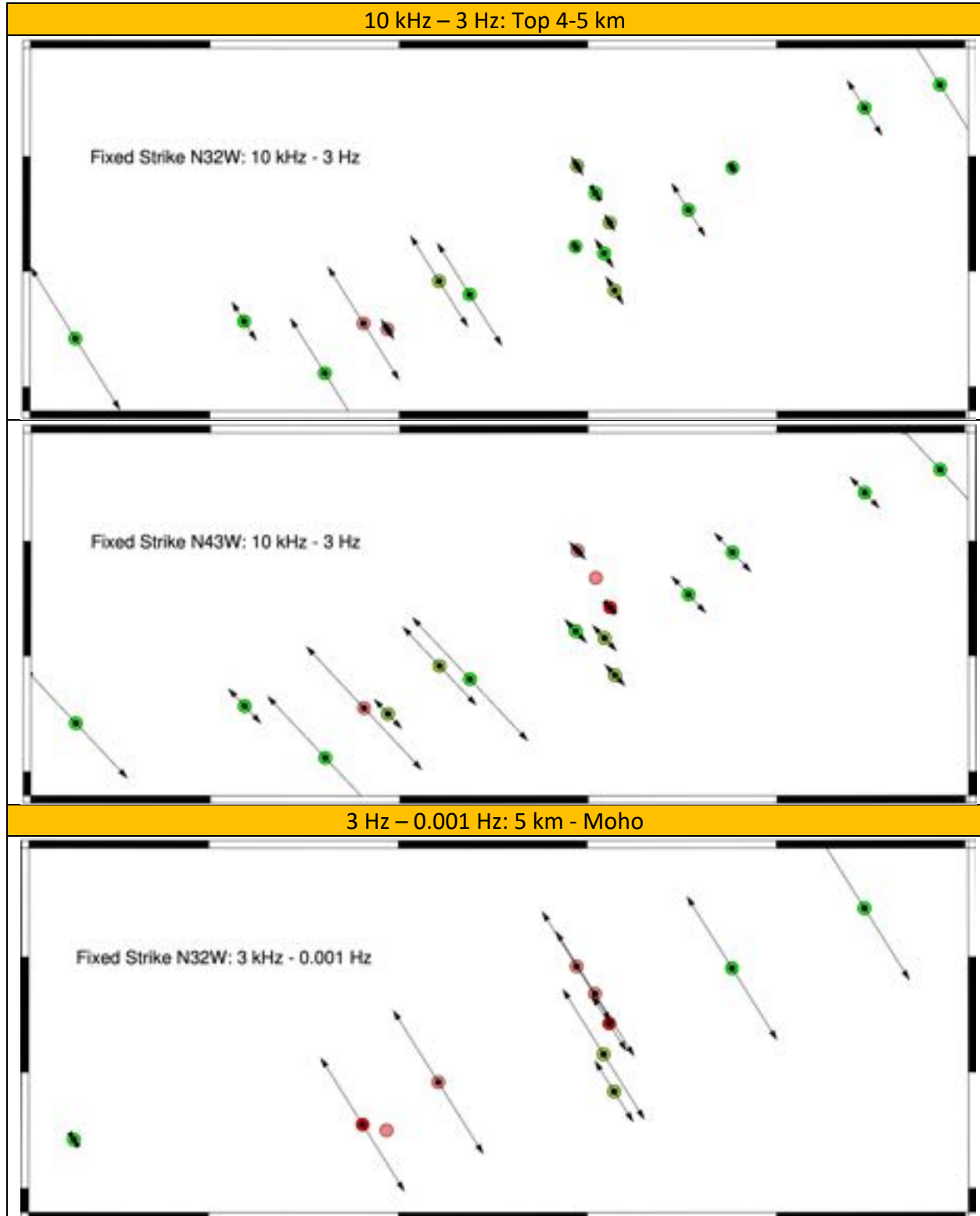
Taking all six decades from 10 kHz to 0.01 Hz together, the most consistent strike direction found is N39W, and the misfit is acceptable for most sites with an average RMS = 1.06 and first and third quartiles of 0.30 and 1.60, which is acceptable.

Fixing the strike to either N32W or N43W for the frequency band 10 kHz – 3 Hz (appropriate for N32W), 3 Hz to 0.001 Hz (appropriate for N43W), and for the whole bandwidth of 10 kHz – 0.001 Hz, we can judge how well a single strike direction fits the data.

As we can see in the error plots (Figure 73) that one strike direction is poorly appropriate for the whole frequency band of 10 kHz – 0.001 Hz (depths from the surface to the Moho). The top 4-5 km require a strike of N32W, especially the newly-acquired data. The 5 km to Moho best accepts a direction of N43W.

→ Optimally, the data from this profile should also be modelled in two bands with two different strikes, for the upper 5 km and for 5 km to the Moho.

→ However, a good first-order model for the whole crust can be obtained at N39W.



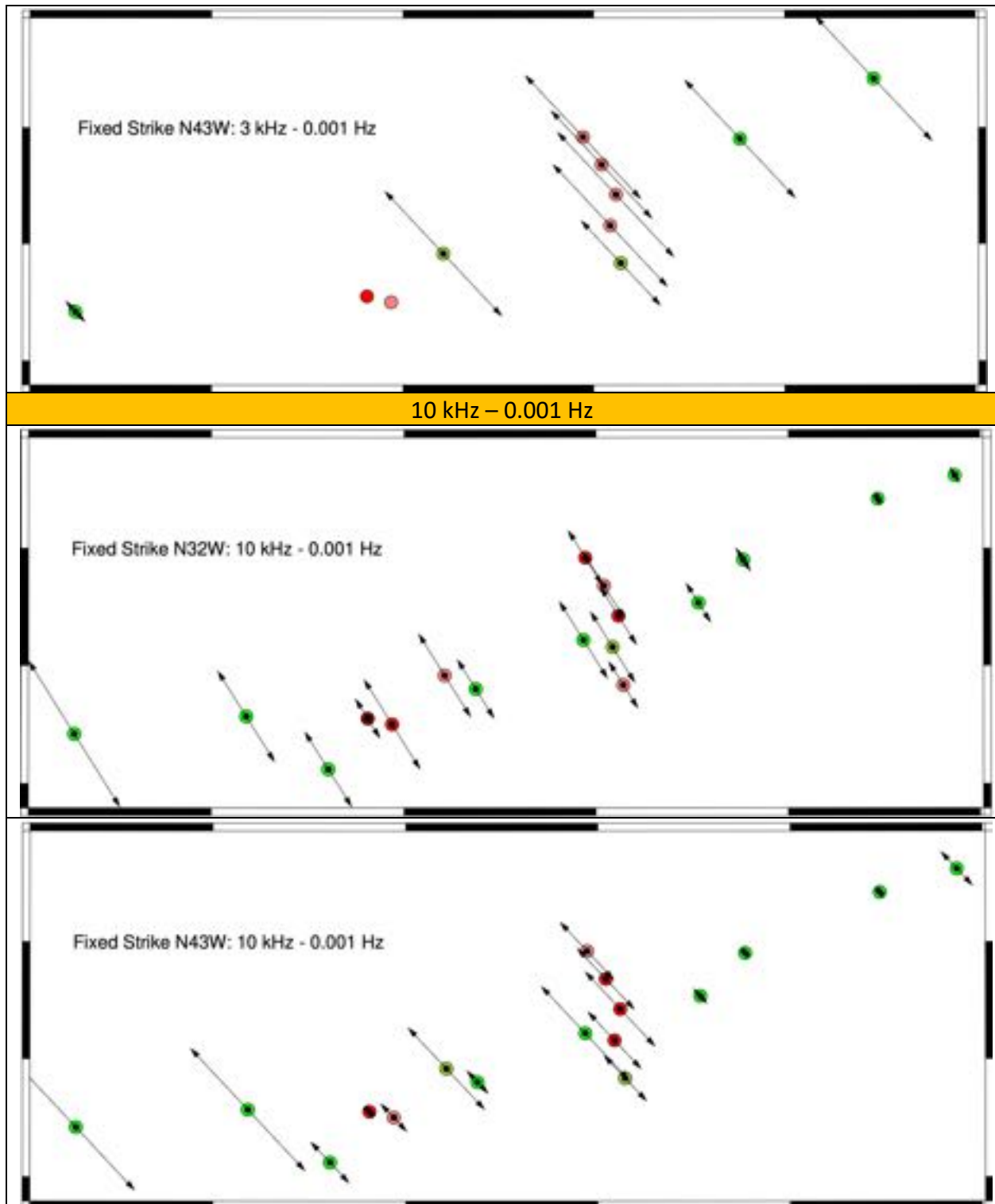


Figure 73: Errors for fixed strike directions. Top panels: Upper 5 km strike of N32W (top is correct, bottom is incorrect). Middle panels: 5 km to Moho strike of N43W (top is incorrect, bottom is correct). Bottom panels: Fixed strikes over the whole frequency band.

9.2.3. Profile SS

Profile SS comprises 14 sites KSSxxx:

KSS101, KSS102, KSS103, KSS104, KSS105, KSS106, KSS107, KSS108, KSS118, KSS109, KSS110, KSS111, KSS115, KSS112, KSS113

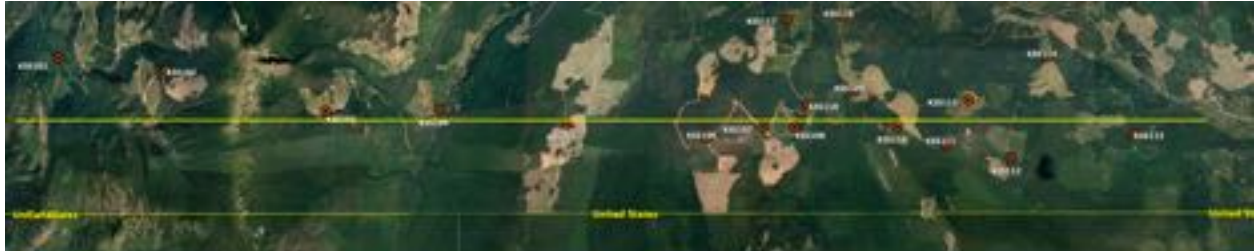


Figure 74: Sites along profile SS.

Four other KSS sites, namely KSS114, KSS116, KSS117, and KSS119, were deemed to be too far off the profile.

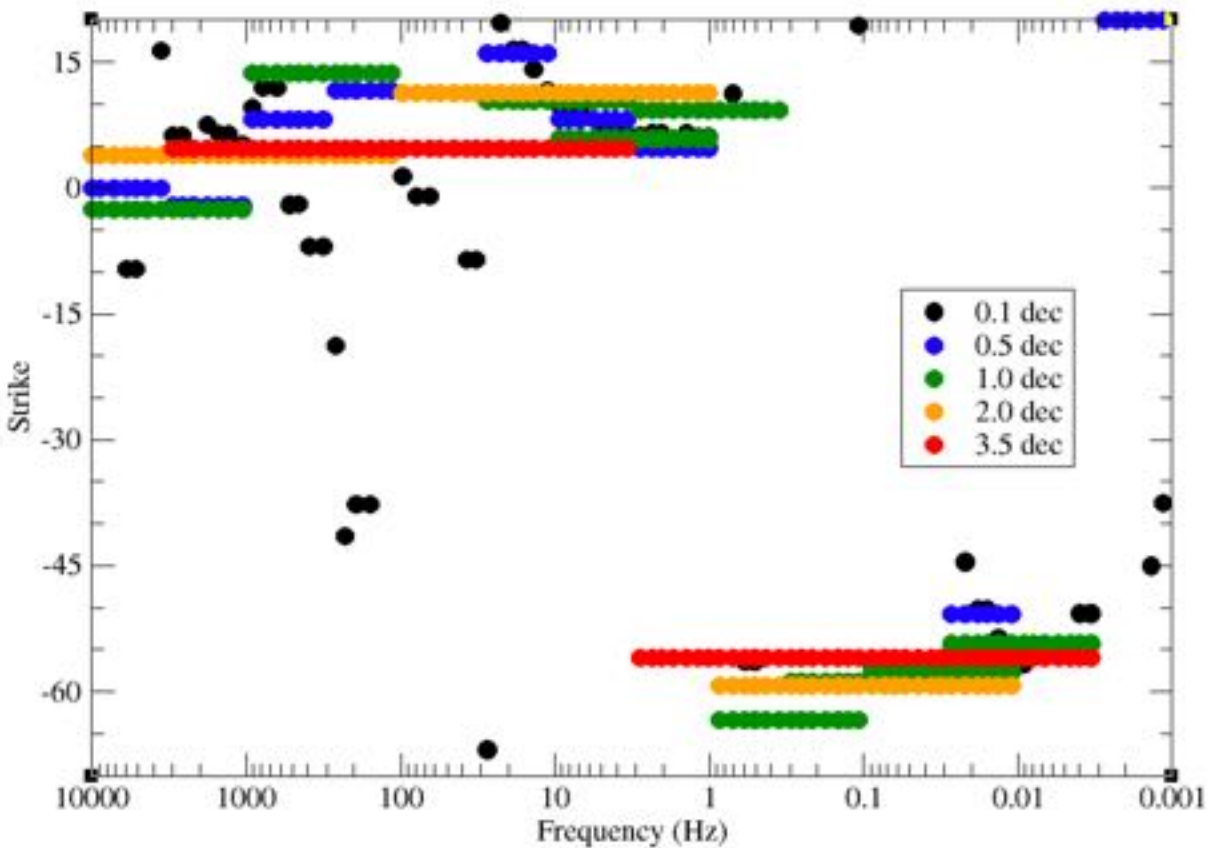


Figure 75: Strike directions for multi-site analyses with different bandwidths for sites on profile SS.

Multi-site, multi-frequency analyses with different frequency bandwidths are shown in Figure 75. As with the prior profiles, we see a systematic change in strike direction from approx. N-S (N05E) at high frequencies to N55W at low frequencies, with a cross-over at around 3 Hz.

9.2.4. Profile MM0

Profile MM0 comprises 17 sites, 15 KMM0xx and 2 KMA00x (Figure 76).

KMM001, KMM002, KMM003, KMM003b, KMM004, KMA002, KMM005, KMM006, KMM007, KMA001, KMM008, KMM009, KMM010, KMM011, KMM012, KMM013, KMM014



Figure 76: Sites along profile MM0.

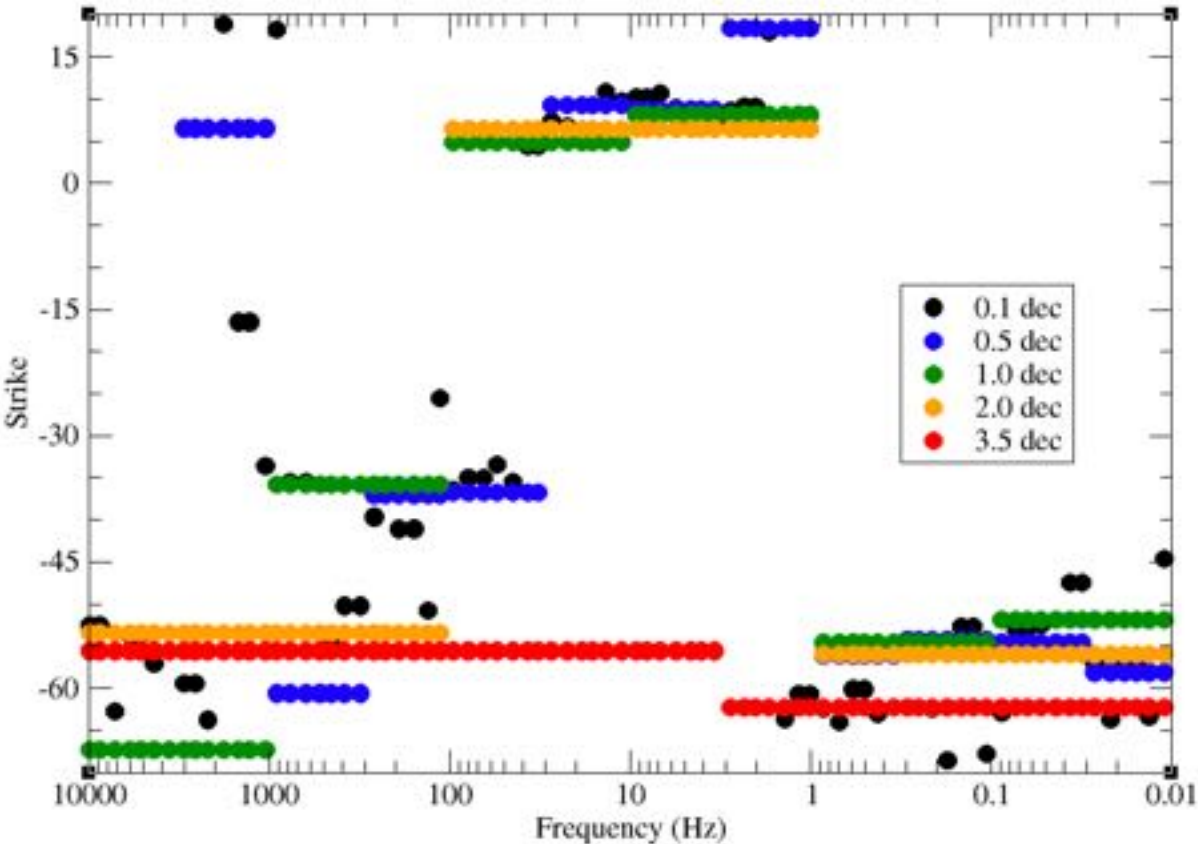


Figure 77: Strike directions for multi-site analyses with different bandwidths for sites on profile MM0.

Multi-site, multi-frequency analyses with different frequency bandwidths are shown in Figure 77. We see now a difference compared to the profile to the South (profile SS), in that the top layer to around 200 Hz has a strike direction of N55W, whereas the layer from 200 Hz to around 30 Hz has a strike of N35W, and from 30 Hz to 0.1 Hz a strike of N05E, as we saw for profile SS. Beneath that is a layer with a strike of N60W, again as we saw for profile SS.

At 200 Hz the maximum depth of penetration is of order 800 m. So we have a 4-layered strike, with N55E from the surface to 800 m (200 Hz), N35E from 800 m to 2,000 m, N05E from 2,000 m to 10,000 m, and N60W below that for the rest of the crust.

The best-fit average strike from 10 kHz – 3 Hz is N56W, and from 3 Hz – 0.01 Hz is N62W, and for the whole 6-decade frequency band of 10 kHz – 0.01 Hz is N66W.

9.2.5. Profile MM2

Profile MM2 comprises 9 sites KMM20x (Figure 78):

KMM201, KMM202, KMM203, KMM204, KMM205, KMM206, KMM207, KMM208, KMM209



Figure 78: Sites along profile MM2.

Multi-site, multi-frequency analyses with different frequency bandwidths are shown in Figure 79. The highest frequencies >1 kHz, i.e. to a depth of order 300 m, show significant change, but from 1 kHz down to 3 Hz there is strike stability in the direction N10E. As with the other profiles, at low frequencies <3 Hz the strike rotates around clockwise to N65W.

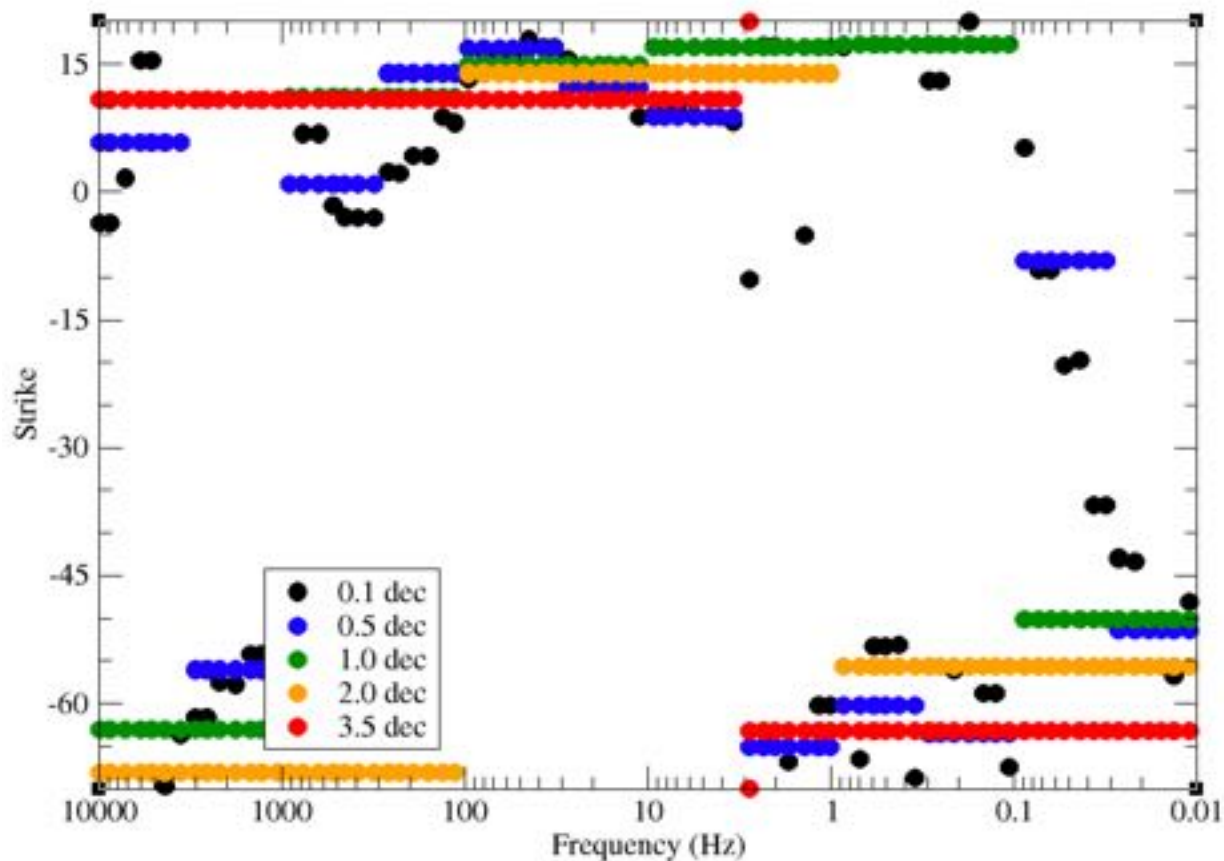


Figure 79: Strike directions for multi-site analyses with different bandwidths for sites on profile MM2.

9.2.6. Profile SP-EW

Profile SP-EW comprises 12 sites, 8 newly-acquired ones (KSPxxx) and 4 Duncan ones (86d00x) (Figure 80):

KSP003, KSP004, KSP005, KSP006, KSP007, 86d002, KSP008, KSP009, KSP104, 86d004, 86d005, 86d006

Recall that the Duncan sites only go to 384 Hz as their highest frequency.

Multi-site, multi-frequency analyses with different frequency bandwidths are shown in Figure 81. There is clearly for this profile greater agreement in strike direction between the uppermost parts of the crust and the bulk of the crust, with a direction of N45W for the upper 4 km and N35W for the rest of the crust.

Analysing all 6 decades of frequency from 10 kHz to 0.01 Hz together, the common strike direction is N44W (NW-SE).



Figure 80: Sites along profiles SP-EW (red) and SP-NS (blue).

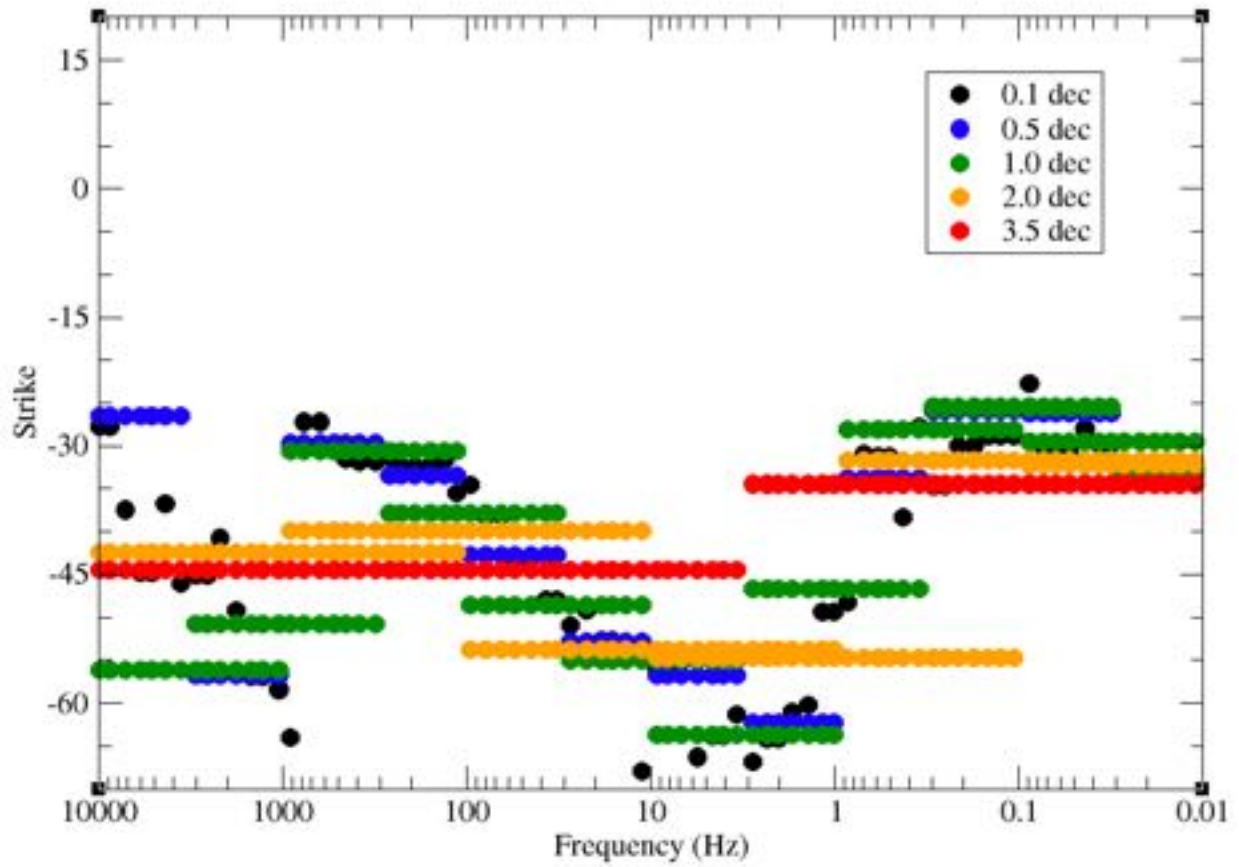


Figure 81: Strike directions for multi-site analyses with different bandwidths for sites on profile SP-EW.

9.2.7. Profile SP-NS

Profile SP-NS comprises 9 sites, 8 newly-acquired ones (KSPxxx), and one Duncan one (Figure 80):

KSP106, KSP105, KSP104, 86d002, KSP009, KSP008, KSP103, KSP102, KSP101

Multi-site, multi-frequency analyses with different frequency bandwidths are shown in Figure 82. High frequencies show a strike around N62W, whereas low frequencies show a strike of N36W.

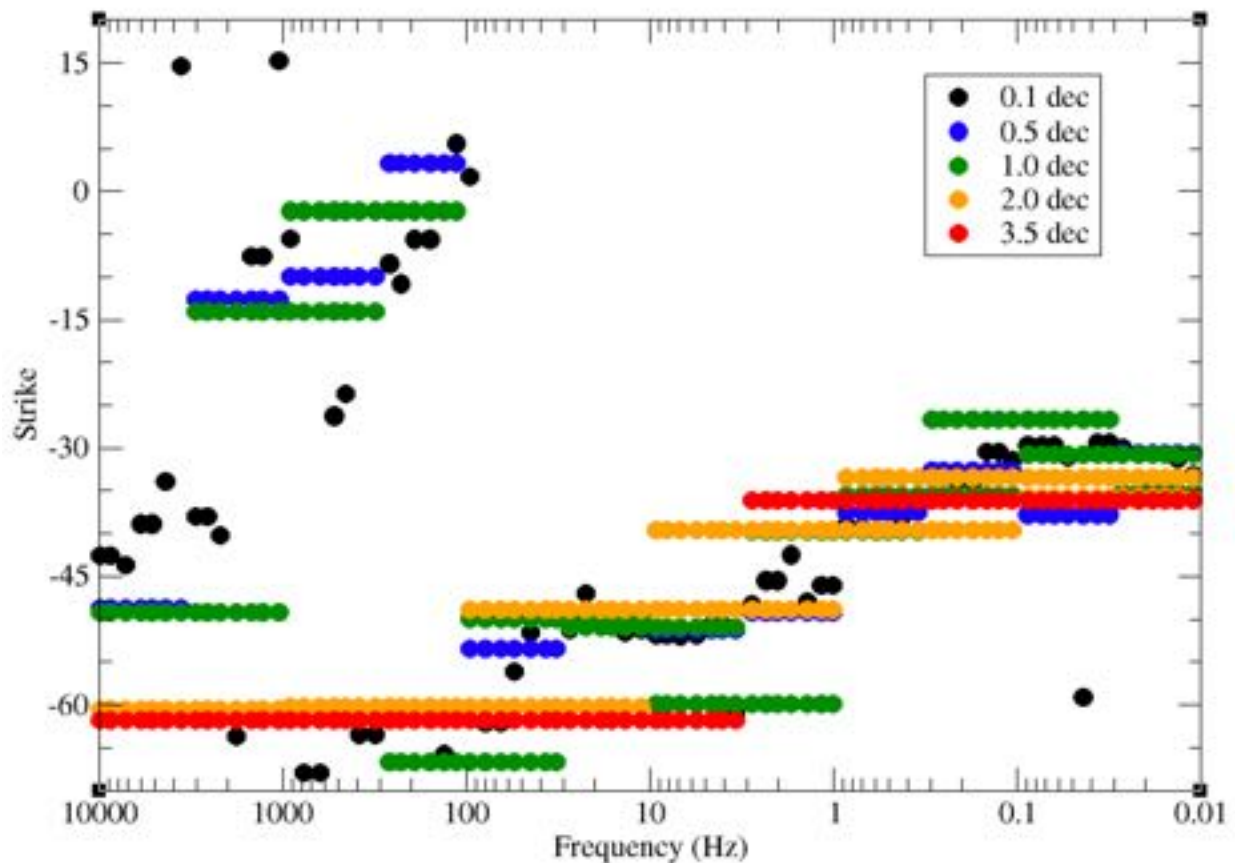


Figure 82: Strike directions for multi-site analyses with different bandwidths for sites on profile SP-NS.

9.2.8. Area SP: Profiles SP-NS & SP-EW taken together

Given that the two profiles SP-NW and SP-NS give very close strike directions at angles to them both, we can analyse all 17 sites simultaneously.

Multi-site, multi-frequency analyses with different frequency bandwidths are shown in Figure 83. High frequencies show a strike around N50W, whereas low frequencies show a strike of N39W.

9.2.8.1. *High frequencies: 10 kHz – 3 Hz*

The average misfit at high frequencies (10 kHz – 3 Hz) for a strike of N50W is 3.02, with first and third quartiles of 2.31 and 3.36. This means that the 2-D model of the subsurface is not statistically acceptable to most sites when error floors are set to 3.5% in RhoA and 1° in Pha. Again, to be statistically acceptable, 95% of the sites have to have an RMS < 2.00 (95% confidence limit). We can achieve this by doubling the error floor to 7% in RhoA and 2° in Pha.

9.2.8.2. *Low frequencies: 3 Hz – 0.01 Hz*

The average misfit at low frequencies (3 Hz – 0.01 Hz) for a strike of N39W is 1.62, with first and third quartiles of 2.44 and 3.83. This means that the 2-D model of the subsurface is not statistically acceptable to most sites when error floors are set to 3.5% in RhoA and 1° in Pha. To be statistically acceptable, 95% of the sites have to have an RMS < 2.00 (95% confidence limit). We can achieve this by doubling the error floor to 7% in RhoA and 2° in Pha

9.2.8.3. *All frequencies: 10 kHz – 0.01 Hz*

Taking all 6 decades of frequency from 10 kHz to 0.01 Hz, the best-fitting strike direction is N44E for all sites simultaneously. But this strike has a high average RMS misfit = 4.5, with three four sites disagreeing vehemently with RMS >7.0 (86d006 RMS = 8.13; 86d005 = 7.96, KSP104 = 8.30). Those three sites could potentially distort the strike direction acceptable to the rest of the sites because of their “leverage” effect on the least-squares model fitting.

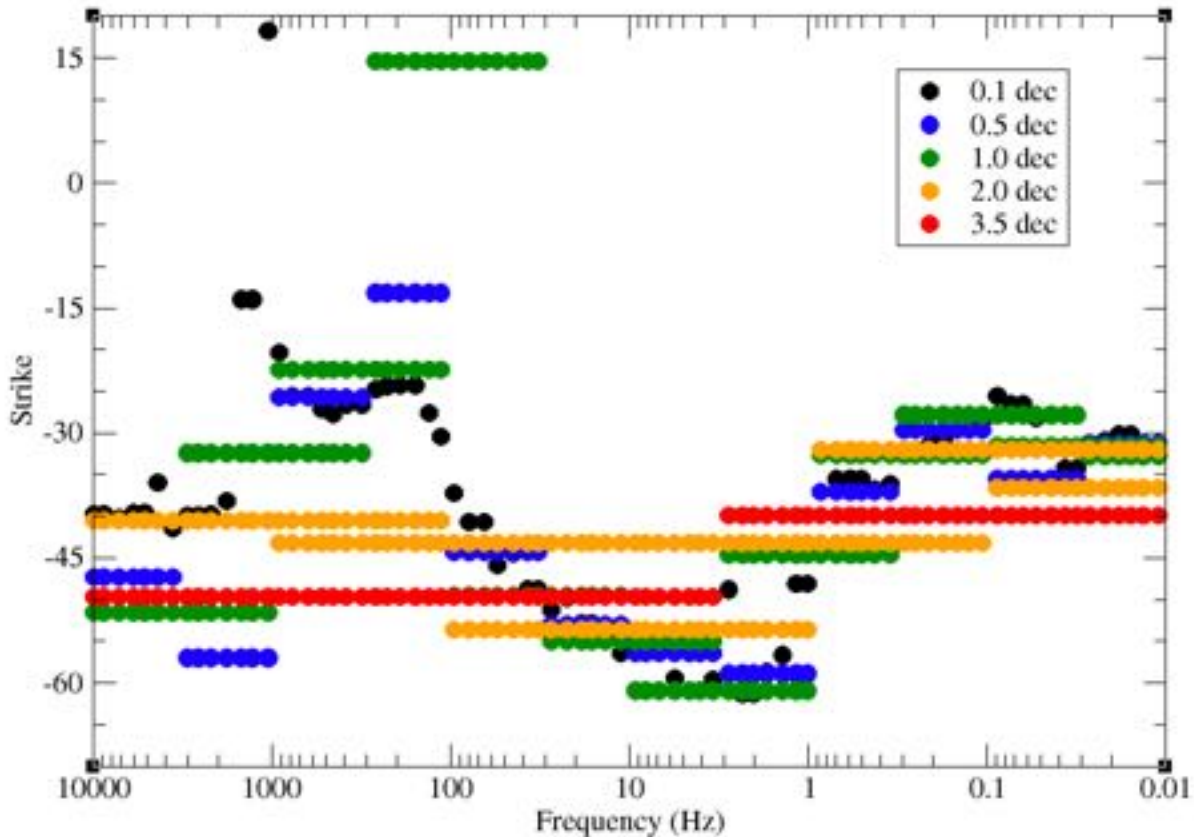


Figure 83: Strike directions for multi-site analyses with different bandwidths for sites in area SP.

Taking the reduced set of 14 sites, the best-fitting strikes is N45E with average RMS misfit = 3.73 with first and third quartiles of 2.50 and 4.31.

To make these data acceptable for 2-D inversion, 95% of them (12) should have an RMS <2.00 (95% confidence interval). If we increase the error floor from 3.5% in RhoA and 1° in Pha to 4x those values, i.e., 14% in RhoA and 4° in Pha, then the strike is N44W and the average misfit is RMS = 1.00, which is too good a fit as all sites have an RMS <1.5. Reducing the error floor to 3x original values, i.e., 10.5% in RhoA and 3° in Pha, results in a strike of N45W and an average RMS = 1.32, which is acceptable.

9.2.9. Area South

In a similar manner, we can take all 65 sites in the south, KSSxxx, KHAxxx and KMMxxx, and analyse them together for unified strike directions. (Given the high number of sites, it is not possible to conduct multi-frequency analysis with more than 28 frequencies (due to memory limitations), so the 3.5 decade wide bands are not computed.)

Multi-site, multi-frequency analyses with different frequency bandwidths are shown in Figure 85. High frequencies show a strike around N10E, whereas low frequencies show a strike of N54W, with the change in strike occurring at around 1 Hz (approx. 5 km).



Figure 84: Locations of sites in area "South".

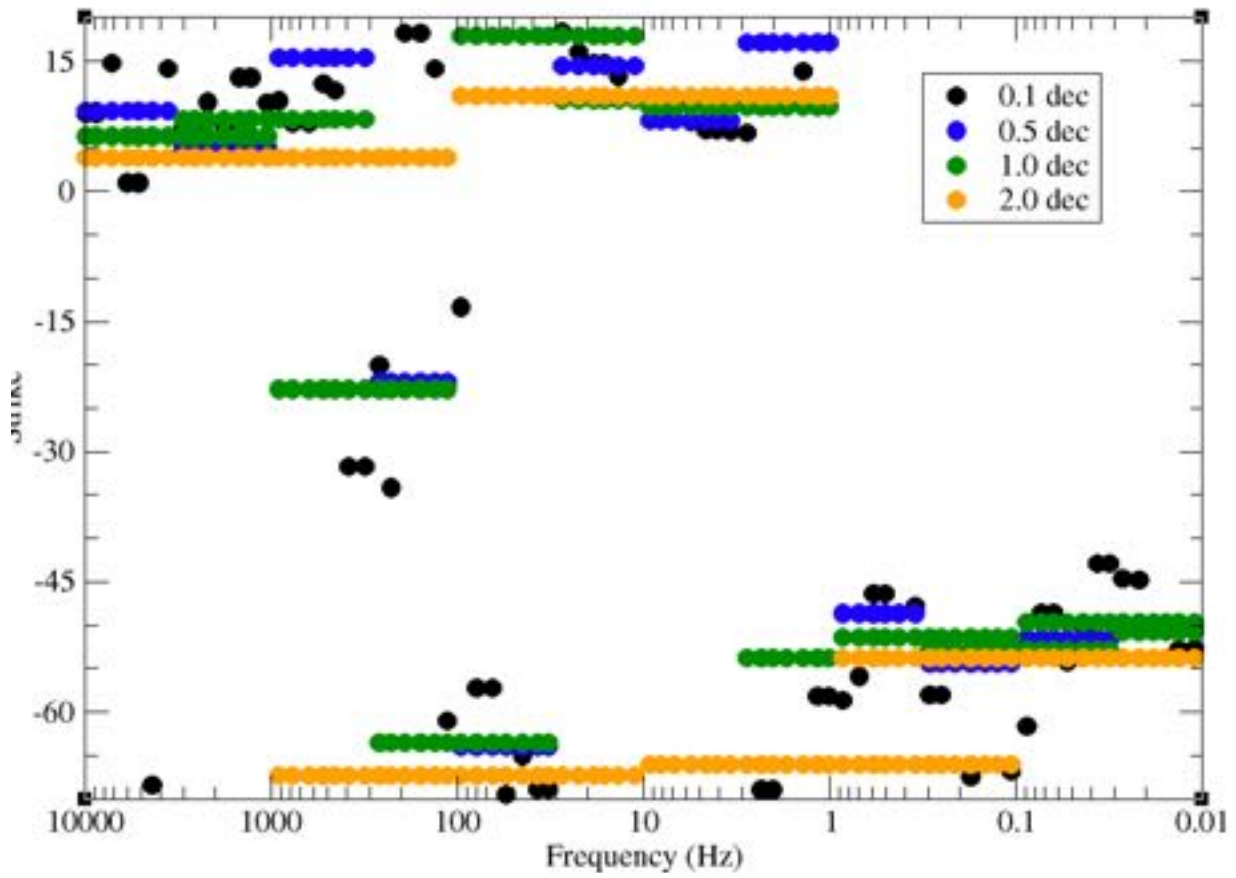


Figure 85: Strike directions for multi-site analyses with different bandwidths for sites in area "South".

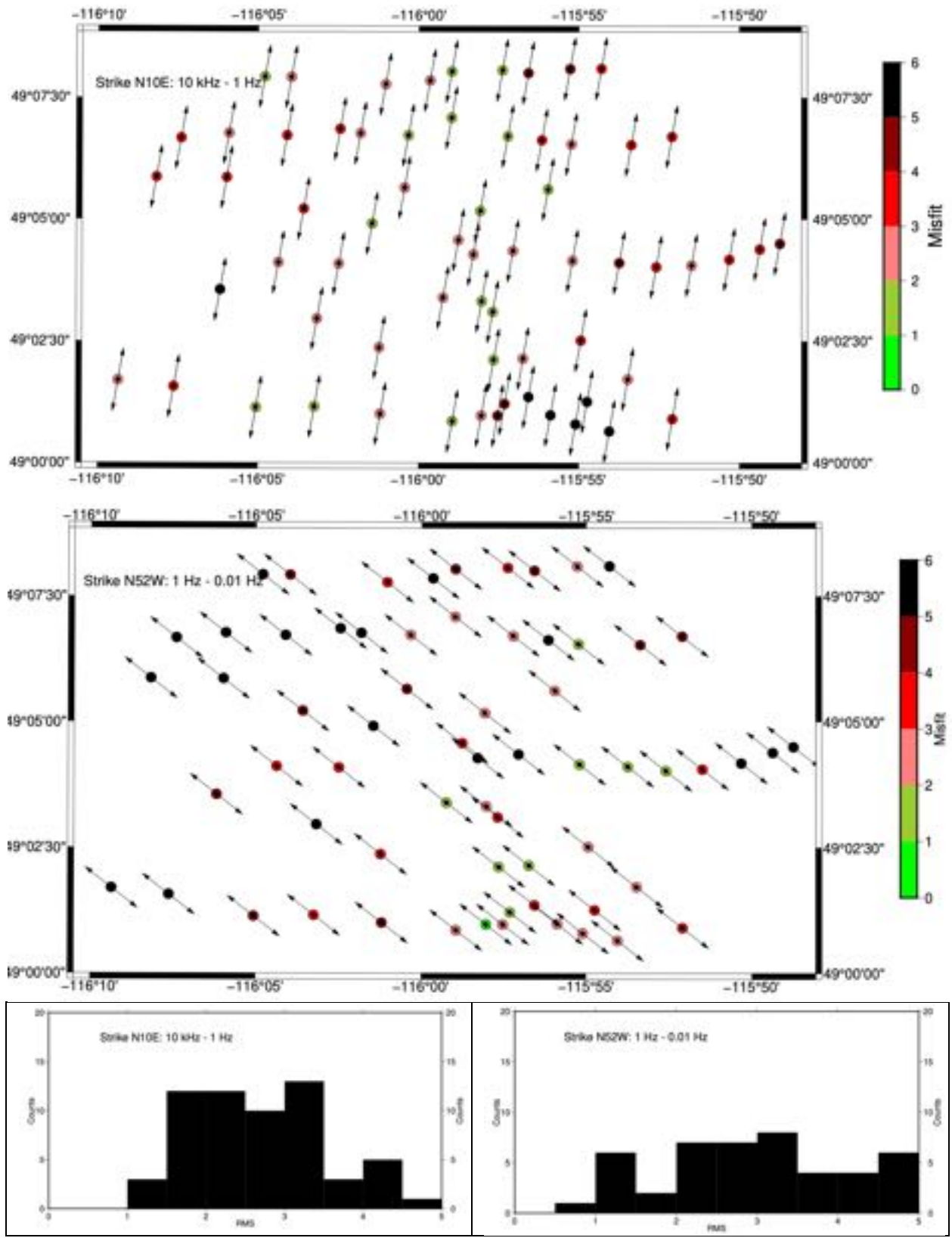


Figure 86: Fixed strike direction of N10E at high frequencies (top row) and N52W at low frequencies (middle row), and the misfit histograms (bottom row).

Note that the RMS misfits (Figure 86) show that most sites are >2.0 , which means that the distortion model does not fit the data within the errors of the data – an error floor of 1.75% in $|Z|$ was assumed, which is 3.5% in RhoA and 1° in Pha . These were judged to be the error floors for the newly-acquired data in the Quality Factor analysis. Below we adjust those floors to accommodate the data.

9.2.9.1. High frequency robust fitting

The misfits of the distortion model to the high frequency data (10 kHz – 1 Hz, Figure 86, bottom left) have a median of 2.6 with first and third quartiles of 2.03 and 3.37. The “problem” with high misfits is that with a least-squares approach those with high misfits are outliers than can distort the model, the so-called “leverage effect”.

To address this and to fit the data robustly, if we increase the error floor to 1.5 times the prior values, then approx. 3/4 of the misfits will be acceptable (<2.0) and the effect of high misfits will be less severe. Also, to guard against outlier leverage effects, we remove the four sites that fit most poorly (RMS >6.0), namely KSS115 (RMS=11.19), KSS111 (9.83), KSS109 (7.08) and KSS110 (6.01).

When we do this, we find a consistent angle for high frequencies >1 Hz of N12E (Figure 87). The RMS errors are now statistically acceptable, with 58 (=93%) falling within the 95% confidence limit (RMS < 2.00).

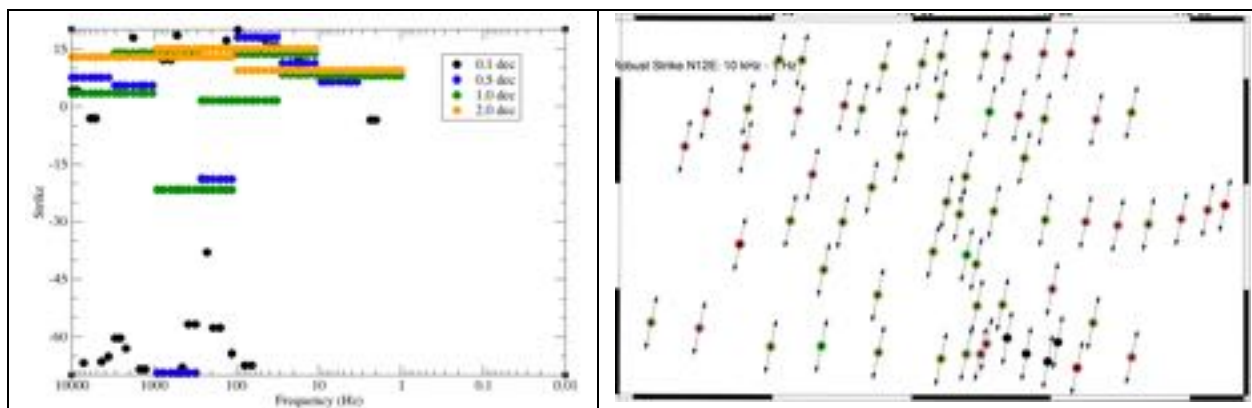


Figure 87: High frequency strike directions for multi-site analyses with different bandwidths for the reduced set of sites in area “South” with error floors set to 5.25% for RhoA and 1.5° for Pha .

9.2.9.2. Low frequency robust fitting

At low frequencies (1 Hz – 0.01 Hz, Figure 86, bottom right), misfits are higher, with a mode of 3.76 and first and third quartiles of 2.45 and 5.32. We need to increase the error floor by 2.5x to get most sites fitting acceptably, and to guard against outlier leverage, we remove seven sites with high misfit above 7.0, namely KMM102 (RMS=9.42), KHA006 (8.59), KMM103 (8.19), KSS101 (7.46), KSS102 (7.34), KMM007 (7.28), and KMM002 (7.03).

When we do this, we find a consistent angle for low frequencies <1 Hz of N55W (Figure 88). The RMS errors are now statistically acceptable, with 45 (=89%) falling within the 95% confidence limit (RMS < 2.00).

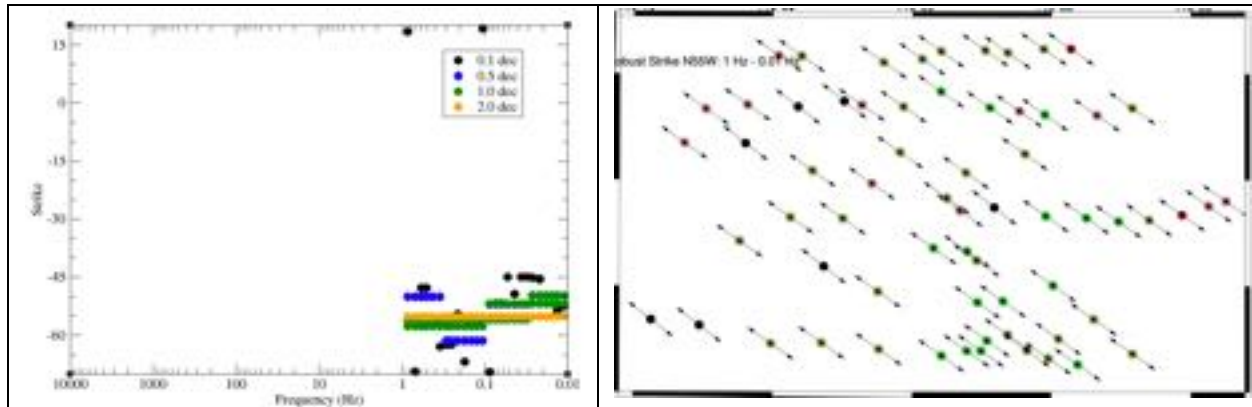


Figure 88: Low frequency strike directions for multi-site analyses with different bandwidths for the reduced set of sites in area “South” with error floors set to 8.75 % for RhoA and 2.5° for Pha.

9.2.10. Profile and Area Strike directions: Conclusions

A summary of the strike directions found for each profile and for the two areas is given in Table 6.

Table 6: Summary of strike directions along profiles and for areas.

Profile	High frequency 10 kHz – 3 Hz	Low frequency 3 Hz – 0.01 Hz	Comments
SS	N05E	N55W	
MM0	N56W	N62W	High frequency strike not consistent with neighbouring profiles SS, MM1 and MM2 nor with Area “South”.
MM1	N10E	N35W	Low frequency strike not consistent with neighbouring profiles SS, MM0 and MM2, nor with Area “South”.
MM2	N10E	N65W	
Area South	N12E	N55W	Combines all 65 newly-acquired sites KSSxxx, KHAXxx and KMMxxx. Cross-over at 1 Hz. Strikes are from reduced sets with larger error floors. Error floors for the newly-acquired data should be set to 5.25% for RhoA and 1.5° for Pha for the high frequency data (10 kHz – 3 Hz), and to 8.75 % for RhoA and 2.5° for Pha for the low frequency data (3 Hz – 0.001 Hz) for 2-D inversion
SP-EW	N45W	N35W	
SP-NS	N62W	N36W	
Area SP	N50W	N39W	Combines sites on SP-EW and SP-NS. Error floors of 7% in RhoA and 2° in Pha required at both HF and LF.
	N45E		Can use N45E for all freqs. Need to set error floors to 10.5% in RhoA and 3° in Pha.

MO	N32W	N43W	Can use N39W for all freqs. Error floors set to 3.5% in RhoA and 1° in Pha.
	N39W		

9.3. Strike: Conclusions

1. Southern profiles – SS, MM0, MM1 & MM2:

- 1.1. The southern profiles are all consistent with a two-layered crust, with a top layer striking N12E down to of order 5 km, and the rest of the crust striking N55W.
- 1.2. Error floors for the newly-acquired data should be set to 5.25% for RhoA and 1.5° for Pha for the high frequency data (10 kHz – 3 Hz), and to 8.75 % for RhoA and 2.5° for Pha for the low frequency data (3 Hz – 0.001 Hz) for 2-D inversion.

2. Central profiles – SP-EW & SP-NS:

- 2.1. For the central SP cross, the strike is consistent for both SP-EW and SP-NS, with again a two-layer crust with the uppermost crust striking N50W and the rest of the crust striking N39W. Error floors need to be set to 7% in RhoA and 2° in Pha
- 2.2. A single strike of N45E is acceptable when the error floors are increased to 10.5% in RhoA and 3° in Pha.

3. Northern profile – MO:

- 3.1. Again a two-layered Earth is found in strike, but with directions very close to each other, N32W for the upper 4 km and N43W for the rest of the crust.
- 3.2. A single strike direction of N39W is acceptable for all data, with error floors set to 3.5% in RhoA and 1° in Pha.

9.4. Correction for local site anisotropy

The final distortion correction that can be applied is for local site anisotropy, “*a*” in Groom-Bailey parlance, whereby the high frequency asymptotes of the two apparent resistivity curves are moved to their geometric mean values at each site. This is performed on the “*dcmp*” files output by the proprietary *strike* code using another proprietary code *dcmp2j*.

An example is for a site named P3-24 from another client’s survey. The original data (left, Figure 89) show RhoXY and RhoYX curves that are parallel but separated at high frequencies.

Application of the site anisotropy correction brings them together (right, Figure 89).

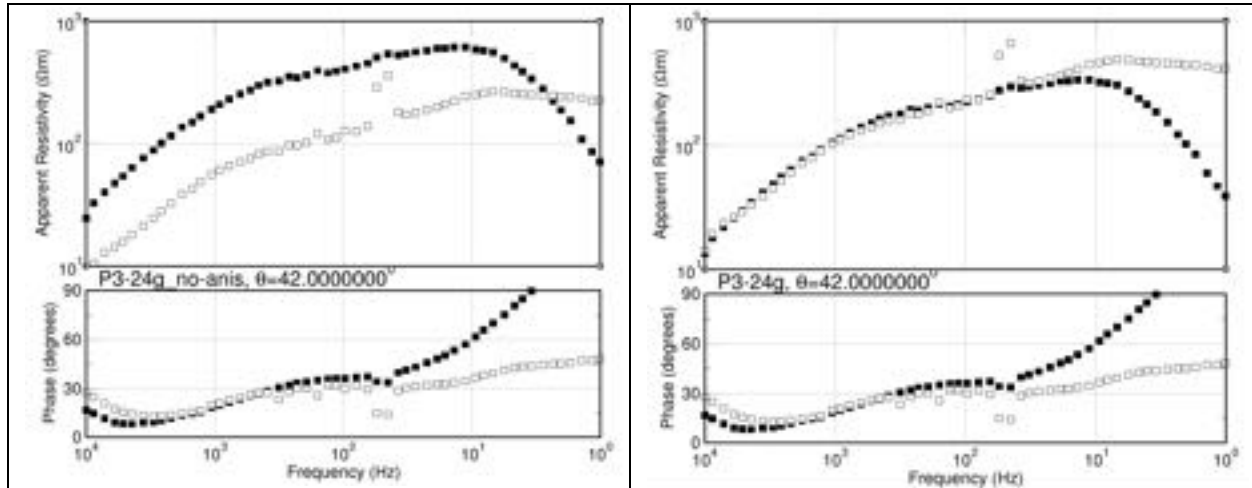


Figure 89: Example of application of anisotropy correction for site P3-24. The decomposed data (left) show Rho_{XY} and Rho_{YX} curves that are parallel but separated at high frequencies. Application of the site anisotropy correction brings them together (right).

10. Rho^+ consistency check

Formally in 1-D (Weidelt, 1972) and for the TM mode in 2-D (Weidelt & Kaikkonen, 1994) the MT responses at a site must be internally consistent such that the apparent resistivity Rho_A curve and the phase Pha curve are the Hilbert Transform of each other. There are also a number of other constraints on the nature of the impedances when expressed as impulse response functions in the time domain, but these are rarely exploited (Jones, 1980).

For extreme numerical models this is not upheld in the TE mode in 2D (Parker, 2010), but experience shows that there are few 2-D TE data for which this Hilbert Transformation relationship is not valid. It also has some merit in 3-D for testing internal compatibility the off-diagonal terms (Z_{xy} and Z_{yx}), but the diagonal terms (Z_{xx} and Z_{yy}) cannot be tested in the same manner as they are routinely “out-of-quadrant”.

Parker and Booker (1996) present an algorithm, called Rho^+ , which tests this compatibility between the Rho_A and Pha curves. This is an extension of a previous algorithm, called D^+ , of Parker (1980) that yields the best-fitting model possible to a 1-D MT response but operated on the real and imaginary parts of the impedances ⁽⁶⁾.

⁶ Note: All physically realizable systems do not respond before input is received. This means that the impulse response function describing the system must be zero for lags less than zero. This leads to a Hilbert Transformation relationship between the real and imaginary parts of the frequency domain response function. This was used by Jones [1980]. For some special systems, called “minimum phase” systems, then the amplitude and phase also form a Hilbert Transform pair.

I have adapted the Rho^+ algorithm and made it robust to outliers, that would otherwise perturb the results, using a Least Trimmed Squares approach (Rousseeuw & Leroy, 1987). This iterative procedure identifies those points that are inconsistent, to within statistical error, of the Hilbert Transform relationship between the RhoA and Pha curves. The outliers are replaced by their predictions, and errors are assigned to signify the magnitude of the shift involved.

For the example of site P3-24, the data after distortion decomposition and anisotropy correction are shown in Figure 90 (left plot), and clearly even after distortion decomposition there are problems with scatter in the especially the YX component. The Robust Rho^+ algorithm smoothed through the obvious scatter in the data, as shown in the right plot.

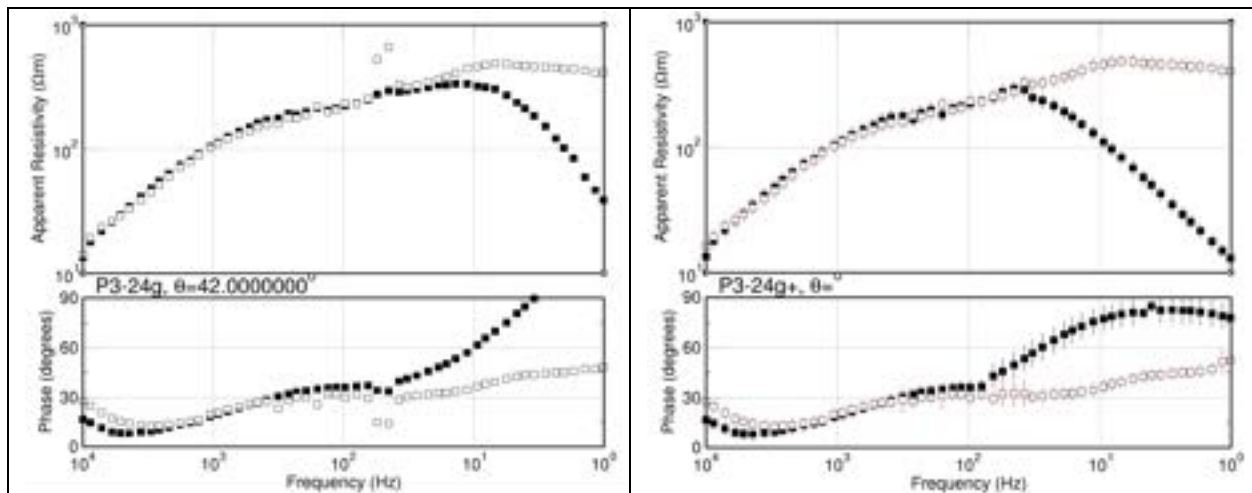


Figure 90: Site P3-24: Left plot is the distortion decomposed and anisotropy-corrected data. Right plot: Robust Rho^+ corrected data. Filled circles are XY (=TE) data, open circles are YX (=TM) data.

Some of the sites in this survey exhibit the same behaviour of Phase Roll Out of Quadrant (PROQ).

This is an important pre-processing step prior to inversion, as otherwise all least-squares based inversion codes will try to reduce the misfit to the largest outliers, if they are not culled before initiation of inversion. It is important to ensure that RhoA and Pha are consistent, and that outliers are dealt with prior to inversion, or a lot of human and computer time will be wasted.

Note: It should be noted that no-one else, neither in academia nor industry, offers such a robust Rho^+ algorithm to apply to the data. In Geotools there is the standard Rho^+ algorithm, but I have developed this robust variant that is proprietary to ManoTick GeoSolutions (MTGS).

Decomposition and Rho^+ does not necessarily result in 2-D responses that should be inverted for structure. In some cases, one of the phases rolls out-of-quadrant (PROQ – phase roll out of quadrant) and the apparent resistivity curves rise or drop at >45 degrees. Such behaviour is impossible in the TM mode in 2-D, and is only seen in the TE mode for extremely paranoid and

sharp structures, such as the corner of an ocean basin (Ichihara & Mogi, 2009), and even then the departure from the correct phase quadrant for the TE phase is less than 10 degrees.

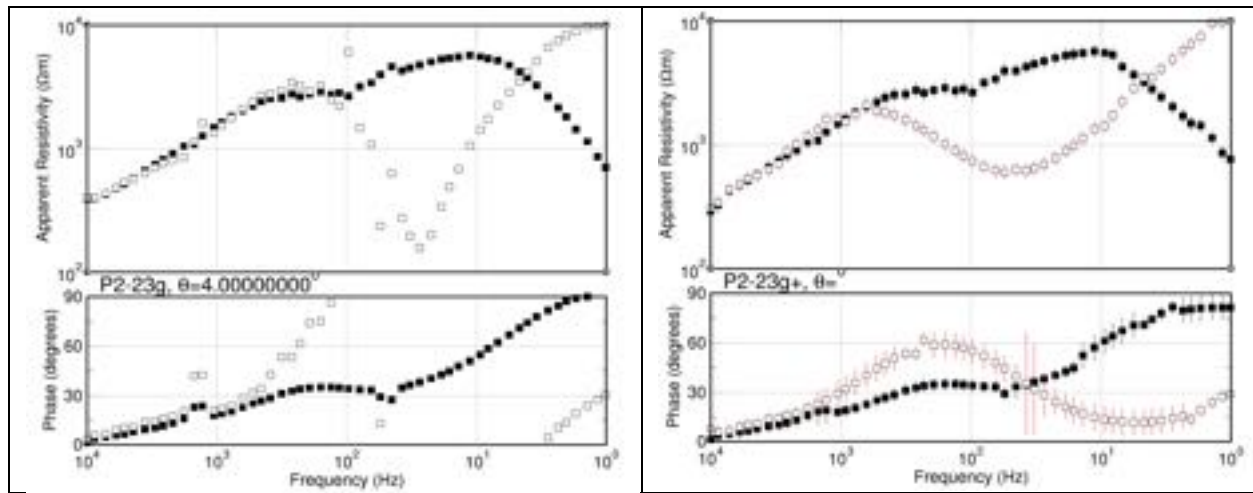


Figure 91: Site P2-23: Left plot is the distortion decomposed and anisotropy-corrected data. Right plot: Robust Rho+ corrected data. Filled circles are XY (=TE) data, open circles are YX (=TM) data.

An example is shown for site P2-23 of another client, where the original data and the decomposed data both exhibit phases rolling out-of-quadrant at frequencies <100 Hz (Figure 91, left). Applying robust Rho⁺ forces the PhaXY to stay within quadrant (Figure 91, right), but one cannot have any confidence in the XY responses below 300 Hz as the shapes of the curves have been dramatically modified. In this case the suspect data are culled prior to inversion.

To guard against this issue, visual inspection of the comparisons of before-and-after application of robust Rho⁺ must be performed for all sites prior to inversion, and suspect/inconsistent data must be culled.

11. Conclusions

Deep analyses of the data show that they are of generally high quality, except for some bands (especially the AMT and MT deadbands) due to low signal during those times of acquisition.

Quantec data along the southernmost profile give responses that are not consistent with the newly-acquired ones, especially for the diagonal terms (XX and YY), so are not used.

For the depths of interest to the client, the high frequencies from 10 kHz – 3 Hz probe down to 4 km. For crustal probing, frequencies from 3 Hz down to 0.01 Hz or even 0.001 Hz need to be taken.

Qualitative mapping of the responses does show some areas of potential interest.

Careful and exhaustive geoelectrical strike analyses shows that the southern area sites are all consistent expressing a two-layer situation, with a top layer striking approx. N-S, and the lower

layer striking approx. NW-SE. This lower strike is consistent with prior work (Gupta & Jones, 1995).

Strikes directions and appropriate error floors to use for 2-D inversion are summarized in Table 6.

Subsequently, the 2-D regional response estimates were checked for internal consistency.

12. Recommendations

- 1) Perform 2-D inversions along the profiles using the distortion-corrected data.
- 2) Perform 3-D inversion of the southern sites.

13. Deliverables

The deliverables for this part of the contract comprise:

1. Deliverables/Report: This report.
2. Deliverables/*profile*/Appendix A: Plots of all four MT components and both Tipper components for all sites.
3. Deliverables/*profile*/Appendices B: Plots of all distortion decomposed and Rho+ distortion decomposed MT components and for all sites along each of the profiles
4. Deliverables/*profile*/Appendices C: Plots of all Rho+ distortion decomposed MT components compared with the original data and for all sites along each of the profiles
5. Deliverables/*profile*/Appendices D: Plots of all Rho+ distortion decomposed MT components compared with the distortion decomposed data and for all sites along each of the profiles
6. Deliverables/*profile*/Appendices E: Plots of all distortion decomposed MT components compared with the original data and for all sites along each of the profiles
7. Deliverables/*profile*/Appendices F: Distortion-corrected (“g.edi”) and Rho+ distortion-corrected (“g+.edi”) estimates in EDI format.

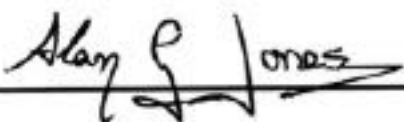
14. Declaration and Signature

I, Alan G. Jones, do hereby certify that:

- I am a Senior Geophysicist with residence in Ottawa, Ontario and I am presently working in this capacity as President and Managing Director of Compete MT Solutions Ltd. of Ottawa (Ontario), President and Managing Director of ManoTick GeoSolutions Ltd. of Ottawa (Ontario), and Vice-President of Moombarriga Canada Ltd. of Ottawa (Ontario);

- I obtained a B.Sc. in Hons. Physics at the Univ. Nottingham (England) in 1972, an M.Sc. in Applied Geophysics at the Univ. Birmingham (England) in 1973, and a Ph.D. in Geophysics at the Univ. Edinburgh (Scotland) in 1977;
- I undertook PostDoctoral Fellowships in Germany at the Univ. Munster from 1977 to mid-1981, in Sweden at the Swedish Geological Survey in 1981, and in Canada at the Univ. Toronto in 1982-1983;
- I subsequently joined the Geological Survey of Canada (Ottawa) in 1984 to 2003, rising from Research Scientist RES-2 level to Senior Research Scientist RES-5 level (the top scientist level in the Canadian Government).
- I then became the Senior Professor and Head of Geophysics at the Dublin Institute for Advanced Sciences (Ireland) from 2004 to January, 2015.
- I am a registered geophysicist and a member in good standing with a license to practice in the Province of Ontario (PGO member #2790);
- I have been awarded academic distinction in Canada (J. Tuzo Wilson medal, Canadian Geophysical Union, 2006), in the USA (Fellow, American Geophysical Union, 2019), in Ireland (Member, Royal Irish Academy, 2010), in Europe (Member, Academia Europaea, 2010), in China (International Member, Geo-Electromagnetism Committee, Chinese Geophysical Society, 2009), and in South Africa (Life Affiliate member, Geological Society of South Africa, 2016).
- I am also a member of the Society of Exploration Geophysicists (SEG), the Canadian Exploration Geophysical Society (KEGS), and the South African Geophysical Association (SAGA);
- I have derived the results presented in this report without consultation with any other person or persons;
- I have no interest, nor do I expect to receive any interest in the properties or securities of Kootenay Resources Inc., any of its subsidiaries or controlling interests, or any of its joint-venture partners.

Signed:



Alan G. Jones, Ph.D., P.Geo.
President, Complete MT Solutions Inc.

15. References

- Caldwell, T. G., Bibby, H. M., & Brown, C. (2004). The magnetotelluric phase tensor. *Geophysical Journal International*, 158(2), 457-469. Article.
- Chave, A. D., & Jones, A. G. (1997). Electric and magnetic field galvanic distortion decomposition of BC87 data. *Journal of Geomagnetism and Geoelectricity*, 49(6), 767-789.
- Chave, A. D., & Jones, A. G. (Eds.). (2012). *The Magnetotelluric Method - Theory and Practice*: Cambridge University Press.
- Cook, F. A., & Jones, A. G. (1995). Seismic reflections and electrical conductivity: A case of Holmes' curious dog? *Geology*, 23(2), 141-144. Article.
<http://homepages.dias.ie/~ajones/papers/58.pdf>
- Evans, S., Jones, A. G., Spratt, J., & Katsube, J. (2005). Central Baffin electromagnetic experiment (CBEX): Mapping the North American Central Plains (NACP) conductivity anomaly in the Canadian arctic. *Physics of the Earth and Planetary Interiors*, 150(1-3), 107-122.
- Ferguson, I. J. (2012). Instrumentation and field procedures. In A. D. Chave & A. G. Jones (Eds.), *The Magnetotelluric Method: Theory and Practice* (pp. 421-479). Cambridge, UK: Cambridge University Press.
- Garcia, X., & Jones, A. G. (2002). Atmospheric sources for audio-magnetotelluric (AMT) sounding. *Geophysics*, 67(2), 448-458.
- Groom, R. W., & Bailey, R. C. (1989). Decomposition of magnetotelluric impedance tensors in the presence of local three dimensional galvanic distortion. *Journal of Geophysical Research*, 94, 1913-1925.
- Groom, R. W., & Bailey, R. C. (1991). Analytical investigations of the effects of near surface three dimensional galvanic scatterers on MT tensor decomposition. *Geophysics*, 56(4), 496-518. Article.
- Gupta, J. C., & Jones, A. G. (1995). Electrical conductivity structure of the Purcell Anticlinorium in southeast British Columbia and northwest Montana. *Canadian Journal of Earth Sciences*, 32, 1564-1583.
- Haines, G. V., & Jones, A. G. (1988). Logarithmic Fourier Transformation. *Geophysical Journal*, 92, 171-178. <http://homepages.dias.ie/~ajones/papers/28.pdf>
- Hutton, V. R. S., & Jones, A. G. (1980). Magnetovariational and magnetotelluric investigations in S. Scotland. In U. Schmucker (Ed.), *Electromagnetic Induction in the Earth and Moon* (pp. 141-150): Centr. Acad. Publ. Japan, Tokio and D. Reidel Publ. Co., Dordrecht.
- Ichihara, H., & Mogi, T. (2009). A realistic 3-D resistivity model explaining anomalous large magnetotelluric phases: the L-shaped conductor model. *Geophysical Journal International*, 179(1), 14-17.
- Jones, A. G. (1980). Geomagnetic induction studies in Scandinavia - I. Determination of the inductive response function from the magnetometer data. *Journal of Geophysics (Zeitschrift fuer Geophysik)*, 48, 181-194.
- Jones, A. G. (1983). On the equivalence of the Niblett and Bostick transformations in the magnetotelluric method. *Journal of Geophysics-Zeitschrift Fur Geophysik*, 53(1), 72-73. Letter.

- Jones, A. G. (1986). Parkinson's pointers' potential perfidy! *Geophysical Journal of the Royal Astronomical Society*, 87, 1215-1224. <http://homepages.dias.ie/~ajones/papers/25.pdf>
- Jones, A. G. (1993). The COPROD2 dataset - tectonic setting, recorded MT data, and comparison of models. *Journal of Geomagnetism and Geoelectricity*, 45(9), 933-955.
- Jones, A. G. (2012). Distortion of magnetotelluric data: its identification and removal. In A. D. Chave & A. G. Jones (Eds.), *The Magnetotelluric Method: Theory and Practice*. Cambridge (UK): Cambridge University Press.
- Jones, A. G., & Groom, R. W. (1993). Strike angle determination from the magnetotelluric impedance tensor in the presence of noise and local distortion - rotate at your peril. *Geophysical Journal International*, 113(2), 524-534. Note.
- Jones, A. G., & Spratt, J. (2002). A simple method for deriving the uniform field MT responses in auroral zones. *Earth Planets and Space*, 54(5), 443-450.
- Mardia, K. V. (1972). *Statistics of Directional Data*: Academic Press, New York.
- Marquis, G., Jones, A. G., & Hyndman, R. D. (1995). Coincident conductive and reflective middle and lower crust in Southern British Columbia. *Geophysical Journal International*, 120(1), 111-131. Article.
- McNeice, G. W., & Jones, A. G. (2001). Multisite, multifrequency tensor decomposition of magnetotelluric data. *Geophysics*, 66(1), 158-173.
- Parker, R. L. (1980). The inverse problem of electromagnetic induction: Existence and construction of solutions based on incomplete data. *Journal of Geophysics*, 85(B8), 4421-4428.
- Parker, R. L. (2010). Can a 2-D MT frequency response always be interpreted as a 1-D response? *Geophysical Journal International*, 181(1), 269-274. <Go to ISI>://WOS:000275884300015
- Parker, R. L., & Booker, J. R. (1996). Optimal one-dimensional inversion and bounding of magnetotelluric apparent resistivity and phase measurements. *Physics of the Earth and Planetary Interiors*, 98(3-4), 269-282. <Go to ISI>://WOS:A1996WB25300010
- Parkinson, W. D. (1959). Directions of rapid geomagnetic fluctuations. *Geophysical Journal of the Royal Astronomical Society*, 2(1), 1-14. <Go to ISI>://WOS:A1959WW35400001
- Parkinson, W. D. (1962). The influence of continents and oceans on geomagnetic variations. *Geophysical Journal of the Royal Astronomical Society*, 6(4), 441-449. <Go to ISI>://WOS:A1962WU73100003
- Petiau, G., & Dupis, A. (1980). Noise, temperature-coefficient, and long-time stability of electrodes for telluric observations. *Geophysical Prospecting*, 28(5), 792-804. <Go to ISI>://WOS:A1980KM25200009
- Rousseeuw, P. J., & Leroy, A. M. (1987). *Robust Regression and Outlier Detection*: Wiley.
- Shalivahan, Maurya, V. P., Bhattacharya, B. B., & Singh, R. K. (2017). Tipper Magnitude Revisited. In *15th International Congress of the Brazilian Geophysical Society & EXPOGEEF, Rio de Janeiro, Brazil, 31 July-3 August 2017* (pp. 189-193).
- Weidelt, P. (1972). The inverse problem of geomagnetic induction. *Geophysical Journal of the Royal Astronomical Society*, 35(1-3), 379-379. Abstract of Published Item.
- Weidelt, P., & Kaikkonen, P. (1994). Local 1-D interpretation of magnetotelluric B-polarization impedances. *Geophysical Journal International*, 117(3), 733-748. Article.

16. Appendix A: MT acquisition equipment

16.1. Recorders

MT recorders are often specially designed for MT, such as those used by Phoenix, Metronix, and Lviv. Some contractors use generic recorders, such as RefTeks (Quantec) or gDAS (Southernrock Geophysics).

What is important in a recorder is a high dynamic range, true 24-bit A/D at a minimum, and a high input impedance.

16.2. Magnetic sensors

In induction coil design there is a trade-off to be made between having greater sensitivity, which comes from having more windings around the core (i.e., a longer, heavier sensor) and minimising eddy current noise, which comes from having fewer windings and a smaller core. Induction coil design is discussed in detail in Ferguson's Chapter 9 (Ferguson, 2012) in Chave and Jones (2012).

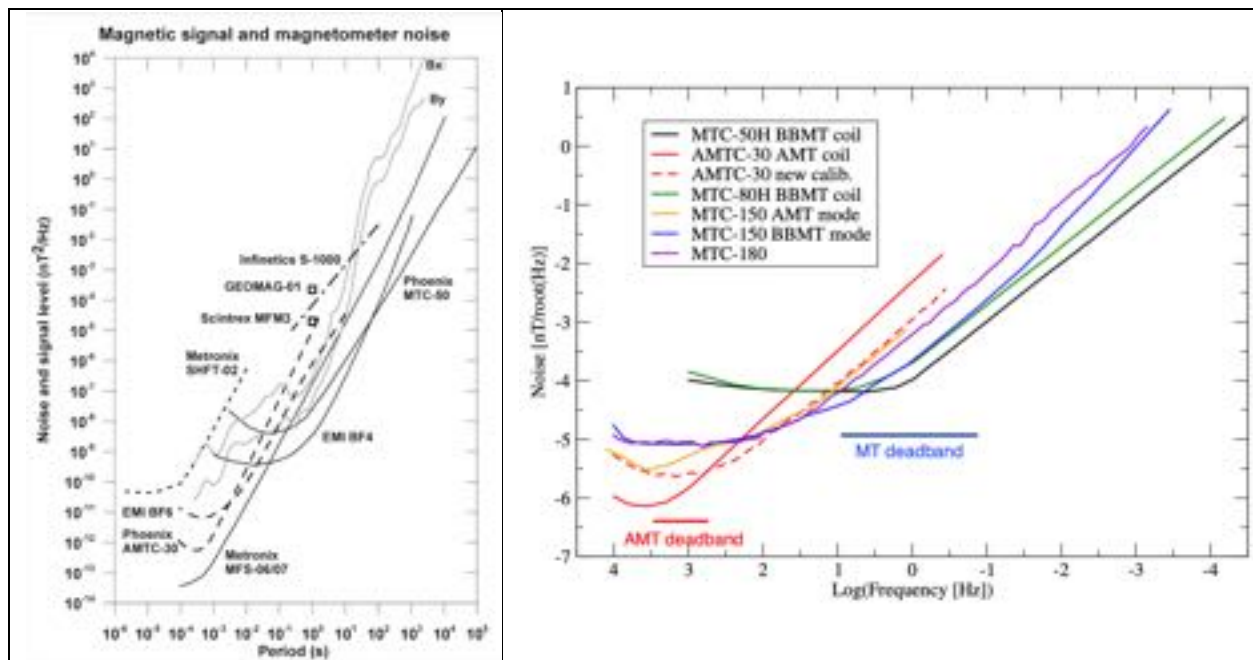


Figure 92: Left: Noise levels of common MT coils, from Ferguson (2012). Right: Noise levels of Phoenix's family of coils.

A comparison of common MT coils is shown in Figure 92. Left shows a number of manufacturers and was compiled by Ferguson (2012), and right compares the Phoenix family of coils and was compiled by me.

16.3. Electrodes

16.3.1. General

Electric field sensors, called “electrodes”, in the early days of MT were initially solid metal, such as steel, Pb or Cu in rods, tubes or plates. However, it was realized in the late-1970s that polarization charges on metal surfaces caused significant noise on the electric fields, particularly in the MT deadband of 8 Hz to 0.1 Hz where signal is very low and noise is high (due primarily to microseismic activity caused by e.g. wind coupling to the ground through tree roots). Hence non-polarizing electrodes came into common use for MT from the late-1970s onwards.

Non-polarizing electrodes comprise a metal and its salt, and for land acquisition are usually Pb-PbCl₂ or Cu-CuSO₄. Pb-PbCl₂ are intrinsically lower noise, given the lower potential between Pb and its salt. For marine use, the more expensive Ag-AgCl electrodes are used as Ag-AgCl has the lowest potential between a metal and its salt of all three, so give the lowest noise specs.

Parallel comparison tests by Petiau and Dupis (1980) showed the superiority of non-polarizing electrodes, particularly at lower frequencies Figure 93.

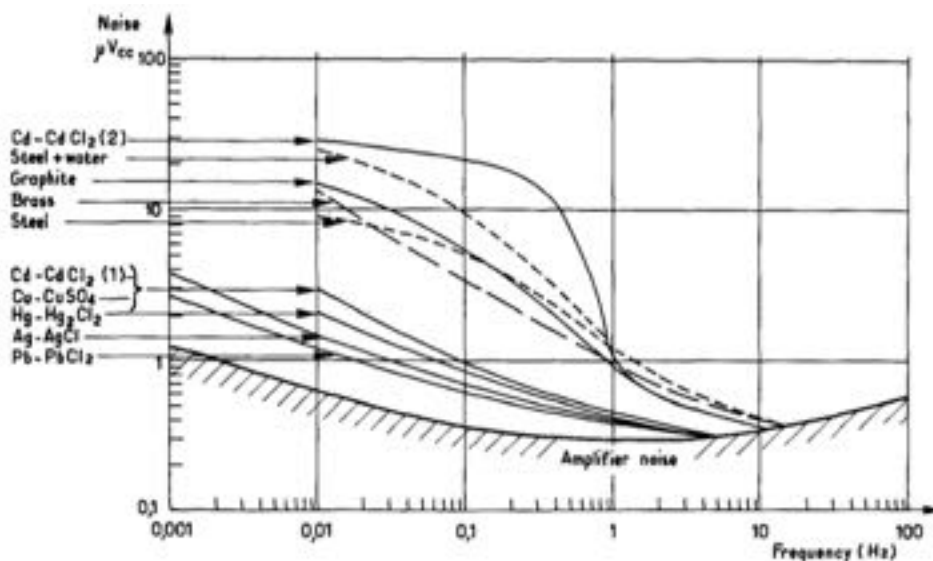


Figure 93: Noise of different electrodes 30 min – 1 hour after setting up. Taken from Petiau and Dupis (1980).

For the late-1970s recording system used by Petiau and Dupis (1980), all electrodes performed as well as each other at frequencies above 10 Hz. Modern systems are far more sensitive, so the difference between polarizing and non-polarizing electrodes persists to higher frequencies, to at least 100 Hz.

Care has to be taken of electrodes, however they are constructed. Metal ones need to be cleaned daily to ensure there are no oxidation effects on them, and non-polarizing ones have to

be checked for DC levels to ensure that there is no precipitation of the salt on the metal surface causing internal resistances. Any of these effects cause noise on the electric field.

16.3.2. *Electrodes and electrode array*

Acquisition was performed using stainless steel rods. As shown above, these are noisier than non-polarizing electrodes, by more than half an order of magnitude, even to high frequencies.

Solid metal electrodes have a high contact resistance. For a rod of length L , diameter a , in a half-space of resistivity ρ , the Faradaic contact resistance R is given by

$$R = \frac{\rho}{2\pi L} \left[\ln\left(\frac{2L}{a}\right) - 1 \right]$$

(Ferguson, 2012). Assume a 1 cm diameter rod pushed 50 cm into the ground with an intrinsic resistance of 2,000 Ωm , this yields a Faradaic resistance of 2.3 k Ω . That is assuming 100% contact along the whole surface of the rod and that there is no rusting or other effects that will cause resistance to be increased.

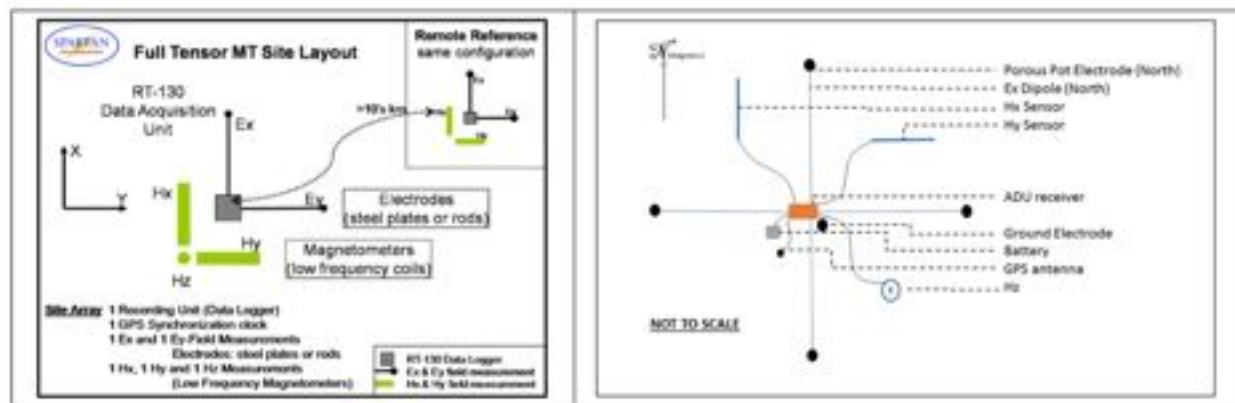


Figure 94: L-shaped (left, typically used by Quantec) and X-shaped (right, used by CMTS) electrode arrays.

Two electrode arrays are shown in Figure 94.

16.3.3. *Electric array measurements*

It is necessary when performing MT acquisition to make three measurements at the beginning and the end of acquisition of the electrode array. These are:

1) **DC voltages between various pairs of electrodes.**

- The point of measuring the DC voltages between various pairs of electrodes, N-S, N-G, S-G, etc., is to determine whether an electrode is holding charge. Charges on electrodes introduce noise into the electric channels.

- Solid metal electrodes intrinsically have this problem, as discussed above.
- Excellent, newly-made, non-polarizing electrodes should have very low DC, of order 5 mV. Over time, and especially if the electrodes are not properly cared-for, the salt paste begins to dry, and this causes precipitation of the salt onto the metal. This introduces noise in the electrode, and its effect is to make the electrode hold charge, ie it turns the electrode into a weak battery. The DC level will rise to large values above say 25 mV. Any electrode that shows high DC levels should be immediately taken out of service and reconditioned or discarded.

2) AC voltages between N-S and E-W electrodes.

The AC voltage is measured for the two pair of electric field channels in order to ensure that ambient AC noise, from nearby powerlines, will not swamp the input and cause clipping. This was more of a problem when recorders were only 16 bit in the 1980s. The 24 bit recorders used by both Quantec and Moombarriga will have had sufficient dynamic range for this not to be an issue. Also, as noted in Moobarriga's report, there is no cultural noise in the vicinity of the project area.

3) Contact resistance between N-S and E-W electrodes.

The issue with contact impedance is the circuit between the electrodes, the ground, and the receiver, such that if the contact impedance approaches the input impedance of the receiver, then there are *RL* inductive effects on the data due to attenuation (and phase advances) of the electric field amplitudes at high frequencies. The most egregious example in the literature is that from a recently-deglaciated site on Baffin Island acquired by Evans et al. (2005) with a measured contact resistance of 2 M Ω . No data at high frequencies >5 Hz (periods <0.2 s) are usable (Figure 95).

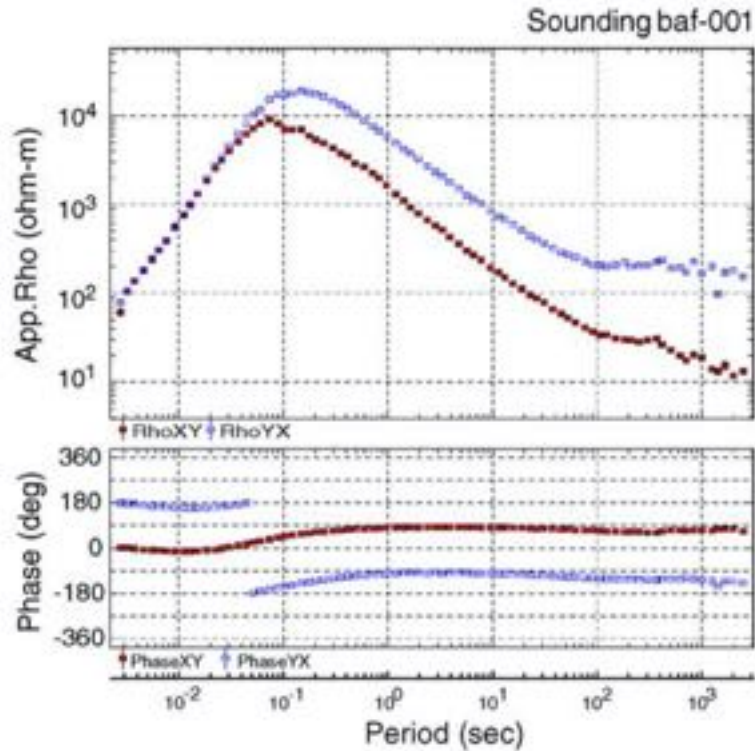


Figure 95: Site baf001 of Evans et al. (2005) .

The information on these values should be read from the EDI files. Note that many contractors do not provide this information, or if they do it is not within the EDI file.

17. Appendix B: AMT deadband

The sensitivity of the available coils is important for assessing the likely quality of the time series, especially in the AMT deadband ⁽⁷⁾. Tests by Garcia and Jones (2002) analysing data acquired with the Phoenix AMTC-30 sensors showed that typically signal was estimated to be one to two orders of magnitude less than sensor noise, at about 5×10^{-8} nT/sqrt(Hz) at 1 kHz (based on the electric field amplitudes), during the daytime. As soon as the Sun rises atmospheric electrical conductivity goes up by two to three orders of magnitude due to solar ionization of the atmosphere. Thus, energy from distant lightning storms travelling along sunlit paths are attenuated by 100 to 1,000 times more than nighttime paths. This phenomenon is shown in the Hx and Hy spectral amplitudes at 1 kHz over 24 hours of Figure 96. There is decent signal from sunset at 21:00 to sunrise at 06:30, but as soon as the Sun rises the signal level

⁷ The AMT deadband is the band of frequencies from around 5 kHz to around 800 Hz, and is caused by a natural low in the signal spectrum from the two different sources of lightning energy. High frequency cloud-to-ground energy is at frequencies from 5 kHz and above, and low frequency cloud-to-ionsphere energy is from around 800 Hz to the Schumann resonance (7.8 Hz).

drops instantly and decreases to below sensor noise levels, and the spectral amplitude hovers at the sensor noise level.

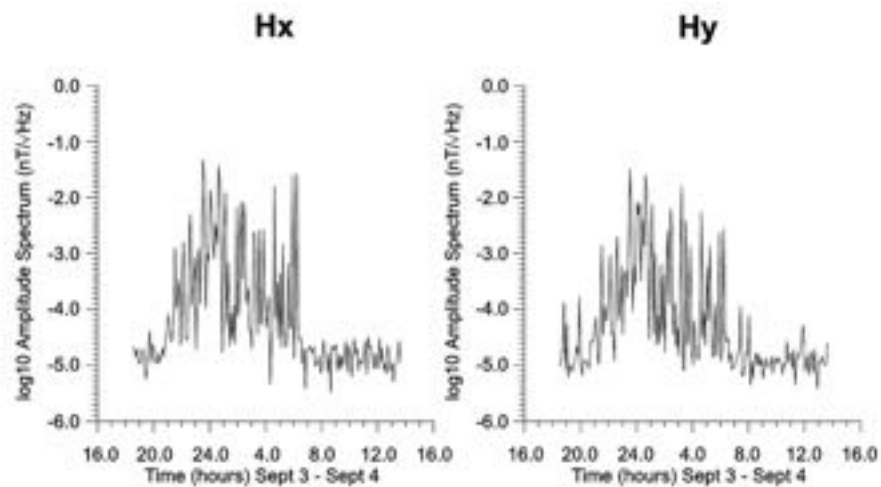


Figure 96: Power spectra amplitude calculated for a frequency of 1000 Hz for the two magnetic channels recorded between the afternoon of September 3 and the morning of September 4. (Reproduced from Fig. 6 of Garcia and Jones (2002).)

The important point here is that it is virtually impossible to obtain high quality data in the AMT deadband during sunlit acquisition with any sensors, even with the currently very best AMT coils available (Metronix MFS-06/07 coils, Figure 92), if one uses normal processing methods that derives estimates the continuum.

18. Appendix C: Quality Factors determination

18.1. MT Quality Factors

Currently, there is no accepted way in the MT community of quantitatively assessing the quality of MT response curves. Generally, curves can be rated on a 5-point qualitative scale from excellent (1) to good (2) to average (3) to poor (4) to unusable (5), based on visual inspection. However, the response estimates usually vary in their quality with period – data in the AMT deadband (5 kHz – 800 Hz) and the MT deadband (10 Hz – 0.1 Hz) are often far poorer than neighbouring data, especially if acquisition was in the daytime only. The lowest frequency/longest period data can also be poor due to insufficient recording times, non-uniform source fields, lack of source field energy (=low sunspot number), etc.

The quality of the RhoA and Pha curves is basically a function of the smoothness of the curves, i.e., point to point consistency, and the errors associated with the estimates. Smooth XX, XY, YX and YY curves that have consistent errors such that small scale scatter of the estimates lies within small errors are desirable. To undertake quantitative assessment of quality, and to

automate the process of poor data identification, I devised a “Quality Factor” of the XY and YX curves that is a combination of a measure of smoothness and a measure of error.

Smoothness Factor (SF): For this I use the Rho+ algorithm of Parker and Booker (1996). This algorithm tests the compatibility of the off-diagonal RhoA and Pha curves to each other. High quality response curves should have a chi-squared misfit of the best-fitting possible model (which is of conductance spikes) equivalent to a normalised RMS (nRMS) of one. Formally, this Rho+ test only applies for 1-D data (Weidelt, 1972) and the TM mode in 2-D data (Weidelt & Kaikkonen, 1994), and in practice to almost all TE mode data. Some extreme and pathological theoretical models in the TE-mode in 2-D fail this test as their phases go slightly outside the 0-90 degree phase bounds (Ichihara & Mogi, 2009; Parker, 2010), but only by a few degrees. In 3-D there is no general statement, but it often is applicable. There are two SFs, one for the XY component (SF_{xy}) and one for YX (SF_{yx}).

Error Factor (EF): The error factor is the average error divided by the assumed error floor. Typically, we assume a minimum error floor of order 1° in phase/3.5% in apparent resistivity for high quality data. When an error floor is set, the EF has a minimum value of 1.

Alternatively, if no error floor is set, then the EF is the average error without normalization. There are four EFs, for each off-diagonal element there is one for RhoA and one for Pha, and for each component these are arithmetically averaged, i.e., EF_{xy} = (EFRhoXY + EFPhaXY)/2, and similarly for EF_{yx}.

For each component, XY and YX, the Quality Factor is given by the geometric mean of the SF and EF, i.e., QF_{xy} = SQRT(SF_{xy} * EF_{xy}), and similarly for QF_{yx}.

The **Average Quality Factor** is given by **QF_{av} = SQRT(QF_{xy} * QF_{yx})**

Quality Factors will be of order 1 for high quality data, and QF increases with decreasing quality of data.

→ Note: The QFs are only for the XY and YX off-diagonal elements of the MT impedance tensor. I do not test the XX and YY diagonal elements, but they are just as important when one wants to undertake anything that involves the complete tensor (e.g., dimensionality analyses, anisotropic 1-D inversion, 2-D inversion with strike not perpendicular to the profile direction, 3-D inversion).

18.2. Tipper Quality Factors

Given the potential importance of tippers in MT, Quality Factor determinations for tippers would be highly useful to identify those sites with problems and those with good quality data without laboriously viewing all of the tipper plots.

As with MT responses, there is no accepted automated way of assessing the quality of the tipper responses, and so I have developed one. I have used the fact that the Real and Imaginary parts of the tipper responses, T_{zx} and T_{zy} , given by

$$H_z = T_{zx} H_x + T_{zy} H_y$$

(dependence on frequency assumed), must form a Hilbert Transform pair relationship as the tipper equation describes a realizable, linear system. By “realizable” that means that there is no output to the system before there is any input, i.e., the impulse response functions in the lag domain are zero for lags less than zero. That translates into the Hilbert Transform relationship in the frequency domain. This relationship was discovered independently in a number of fields, and is called the Kramers-Kronig relationship in atomic scattering theory, Bode’s relations in servo-mechanics, and the Kertz operator in Geomagnetic Depth Sounding studies.

This relationship is the basis of the D^+ and Rho^+ algorithms of Parker (1980) and Parker and Booker (1996), but otherwise is little exploited in MT. Jones (1980) used Hilbert Transformation to show that the real part of his Scandinavian C-response function was consistent with the imaginary part through Hilbert transformation.

The Hilbert transformation integral is

$$H_R(\omega) = \mathcal{H}\{H_I(\omega)\} = \frac{1}{\pi} P \int_{-\infty}^{\infty} \frac{H_I(w)}{\omega - w} dw$$
$$H_I(\omega) = -\mathcal{H}\{H_R(\omega)\} = -\frac{1}{\pi} P \int_{-\infty}^{\infty} \frac{H_R(w)}{\omega - w} dw$$

where $H_R(\omega)$ and $H_I(\omega)$ are the real and imaginary parts of the transfer function $H(\omega)$, and P denotes the Cauchy principal value of the integral. The integral is defined over all frequencies in a linear manner, so is difficult to implement. It is usually determined using Fourier Transformation, but as our data are in a log domain, we would have to interpolate significantly at 10 kHz sampling to cover the whole range to 1,000 s (=time series of 10^7 points). This could be performed more efficiently using the Logarithmic Fourier Transform of Haines and Jones (1988), but still the computational effort is large.

Instead, I adopted an approximate method using a 5-point numerical differentiation to determine the predicted Imaginary part from the Real part.

An example is shown for the tippers from a site named L50N_2750W. The Real parts are shown as filled circles, and the imaginary parts as unfilled circles in Figure 97. Also shown for the imaginary data are the +/- 0.02 ranges (dashed lines), which represents a realistic error floor for tipper estimates. The 5-point numerical differentiation of the real part (after 5-point smoothing to reduce scatter effects) as an estimate of the predicted imaginary part is shown as the blue line (Tz-i pred).

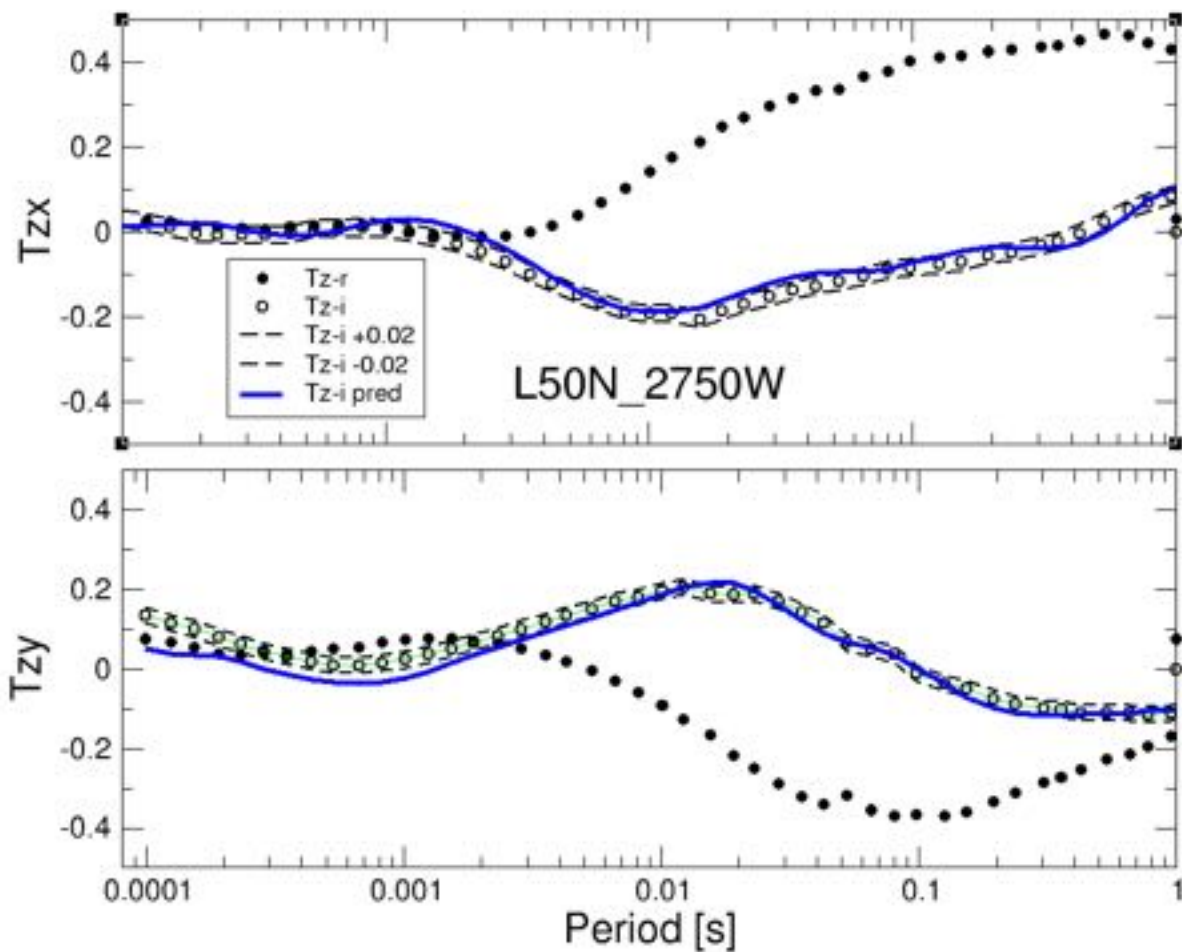


Figure 97: Tippers for site L50N_2750W shown as filled (Real, $Tz-r$) and unfilled (Imaginary, $Tz-i$) points. An error floor of 0.02 is shown as the black dashed lines on the imaginary parts. The 5-point numerical differentiation prediction of $Tz-i$ from $Tz-r$ is shown as the blue lines ($Tz-i$ pred).

The averaged absolute difference between the $\text{Im}(Tz_x)$ and $\text{Im}(Tz_y)$ and their predictions for the 46 data points between 10 kHz and 1 Hz is 0.017 and 0.026 respectively, which is consistent with an assumed error floor of 0.02. The higher Tz_y prediction difference is due to the rising $\text{Im}(Tz_y)$ at high frequencies, which may not be real. So these data would have Smoothness Factors of 0.85 and 1.30 for Tz_x and Tz_y respectively for an adopted error floor of 0.02.

This approach can be used as a tool to determine the Smoothness Factors in exactly the same way as for MT data. The Error Factors can be derived in the same manner also, as the average

error over an interval scaled by the error floor. And the Quality Factors are the average of these two.